

**Synthese und Eigenschaften poröser
metall-organischer
Gerüstverbindungen basierend auf
dreiwertigen Kationen**

**Kumulative Dissertation
zur Erlangung des Doktorgrades
der Mathematisch-Naturwissenschaftlichen Fakultät
der Christian-Albrechts-Universität zu Kiel**

vorgelegt von
Helge Reinsch

**Institut für Anorganische Chemie
der Christian-Albrechts-Universität zu Kiel**

Oktober 2012

1. Gutachter/in: Prof. Dr. Norbert Stock

2. Gutachter/in: Prof. Dr. Wolfgang Bensch

Tag der mündlichen Prüfung: 7.12.2012

Zum Druck genehmigt, Kiel, 7.12.2012, Prof. Dr. Wolfgang J. Duschl

Der Dekan

Meiner Familie

Synthese und Eigenschaften poröser metall-organischer Gerüstverbindungen basierend auf dreiwertigen Kationen

In der vorliegenden Arbeit wurden die Synthese und die Eigenschaften neuer poröser Gerüstverbindungen basierend auf Al^{3+} - und Mn^{3+} -Ionen und aromatischen Polycarboxylaten (Linkermolekülen) verschiedener Geometrie und Größe untersucht. Zur Entdeckung und zur Syntheseoptimierung der neuen Verbindungen wurden dabei in fast allen Fällen Hochdurchsatzmethoden genutzt. Ausgehend von Linkermolekülen linearer Geometrie konnten zwei neue Netzwerkstrukturen entdeckt werden. In Methanol konnten unter solvothermalen Bedingungen drei zueinander isoretikuläre Verbindungen hergestellt werden. Alle drei Verbindungen basieren auf $[\text{Al}_{12}(\text{OCH}_3)_{24}]^{12+}$ -Clustern, die durch lineare Dicarboxylate dreidimensional verknüpft werden. Durch die Wahl des Linkermoleküls konnten die Porengrößen und damit die Sorptionseigenschaften moduliert werden. In Isopropanol konnte des Weiteren eine Verbindung erhalten werden, die auf 2-Aminoterephthalat und säulenförmigen Aluminium-Sauerstoff-Baueinheiten basiert. Die Ladung des kationischen Gerüsts wird durch eingelagerte Chlorid-Ionen ausgeglichen, deren polare Natur in Kombination mit protischen funktionellen Gruppen zu einer stark hydrophilen Oberfläche des Gerüsts führt. Zwei weitere Verbindungen konnten durch den Einsatz tritopischer Linkermoleküle erhalten werden. Im System Al^{3+} / 1,3,5-Benzotrisbenzoesäure (H_3BTB) / DMF wurde die Verbindung $[\text{Al}(\text{BTB})]$ hergestellt. Die Struktur weist hexagonale Kanäle mit einem Durchmesser von etwa 1 nm auf. Die Verbindung $[\text{Mn}_3\text{O}(\text{H}_2\text{O})_3(\text{BTC})_2]$ wurde ausgehend von $\text{Mn}(\text{NO}_3)_2 \cdot 4\text{H}_2\text{O}$ und Trimesinsäure (H_3BTC) erhalten. Mn^{2+} -Ionen werden unter solvothermalen Bedingungen zu Mn^{3+} -Ionen oxidiert, welche dann das Gerüst ausbilden. Ausgehend von Al^{3+} -Ionen und gewinkelten Dicarbonsäuren konnten elf weitere poröse Verbindungen hergestellt werden. Basierend auf Isophthalsäure (1,3- H_2BDC) oder in 5-Position funktionalisierten Derivaten der Isophthalsäure konnten sieben verschiedene Verbindungen mit der allgemeinen Summenformel $[\text{Al}(\text{OH})(1,3\text{-BDC-X})]$ hergestellt werden. Durch den Einsatz von verschiedenen funktionalisierten Isophthalsäuren konnten drei Verbindungen erhalten werden welche dieselbe Gerüststruktur aufweisen und verschiedene Linkermoleküle enthalten. Durch die funktionellen Gruppen werden kleine Unterschiede in der Kristallstruktur induziert, die zu massiven Veränderungen des Sorptionsverhaltens führen.

Ausgehend von Benzophenondicarbonsäure (H_2BPDC) konnte außerdem die Verbindung $[\text{Al}(\text{OH})(\text{BPDC})]$ erhalten werden. Diese weist eindimensionale Kanäle auf, die mit funktionellen Ketogruppen ausgekleidet sind.

Synthesis and properties of porous metal-organic frameworks based on trivalent cations

This thesis deals with the synthesis and properties of new porous metal-organic frameworks (MOFs) based on Al^{3+} - and Mn^{3+} -ions and polytopic aromatic carboxylates of varying size and shape. For the discovery and synthesis optimisation, in most cases high-throughput methods were applied. Two new framework structures were discovered starting from linear linker molecules. Three isorecticular compounds incorporating different linker molecules were synthesised in methanol under solvothermal reaction conditions. They are all based on the same unprecedented $[\text{Al}_{12}(\text{OCH}_3)_{24}]^{12+}$ -cluster, which is connected to adjacent inorganic building units via the organic moieties. The choice of the linker molecule determines the size of the pores and thus the sorption properties of the respective compound. Another new compound based on 2-aminoterephthalic acid and infinite column-shaped aluminium-oxygen-building units was obtained in 2-propanol. The framework charge of this compound is compensated by embedded chloride ions, which results in a highly polar, hydrophilic surface. Employing tritopic linker molecules, two new MOFs were synthesized. Using 1,3,5-benzenetrisbenzoic acid (H_3BTB), the compound $[\text{Al}(\text{BTB})]$ was discovered in DMF as the solvent. Its framework exhibits large hexagonal channels with a diameter of ~ 1 nm. Starting from $\text{Mn}(\text{NO}_3)_2 \cdot 4\text{H}_2\text{O}$ and trimesic acid (H_3BTC), the compound $[\text{Mn}_3\text{O}(\text{H}_2\text{O})_3(\text{BTC})_2]$ was obtained. This MOF is based on Mn^{3+} -ions which are generated in-situ under solvothermal reaction conditions. Employing V-shaped dicarboxylates and Al^{3+} -salts, eleven new compounds were obtained. Using isophthalic acid (1,3- H_2BDC) or one of its functionalised derivatives, seven differently functionalised MOFs with isorecticular structures and the general formula $[\text{Al}(\text{OH})(1,3\text{-BDC-X})]$ could be synthesised. The use of mixtures of isophthalic acids led to the synthesis of three additional compounds incorporating at least two different linker molecules. The functional groups induce subtle structural differences which result in a massively modulated sorption behaviour. The use of benzophenonedicarboxylic acid (H_2BPDC) resulted in the formation of the new compound $[\text{Al}(\text{OH})(\text{BPDC})]$. Its framework structure exhibits onedimensional channels which are lined with keto-groups.

Danksagung

Der erste Dank an dieser Stelle geht natürlich an Professor Stock für die Betreuung dieser Arbeit und dabei insbesondere für die gewährten Freiheiten und die gebotenen Möglichkeiten, die (hoffentlich) in einer guten Arbeit resultierten.

Ein weiterer Dank geht natürlich auch an die spektroskopische Abteilung für ungezählte Messungen und an die Werkstatt. Außerdem sei auch den vielen Helfern im Institut gedankt, zum einen für zahlreiche Messungen und zum anderen für die Instandhaltung der Geräte.

Ein besonderer Dank geht natürlich auch an den AK Stock, in dem ich während der gesamten Promotion mit Freude gearbeitet habe. Dabei sollten auch die Bachelor-Studenten und Praktikanten nicht vergessen werden, die hoffentlich etwas bei mir gelernt haben. Und ein spezieller Dank geht dafür an Britta, dass sie mir so weit wie möglich die Bürokratie abgenommen hat. Einen weiteren Dank an Lici und Mark für die sehr angenehme und freundschaftliche Arbeitsatmosphäre bei uns im Labor. Und einen Dank an Nele für die netten Urlaube.

Weiterhin soll den Kooperationspartnern in München, Bayreuth, Leuven, Krakau und Versailles dafür gedankt sein, dass sie zum Gelingen dieser Arbeit beigetragen haben, ebenso wie den Mitarbeitern am DESY, die Vieles erleichtert haben. Auch die Gastfreundschaft während der Aufenthalte in Versailles und Edinburgh soll hier nicht unerwähnt bleiben.

Der wichtigste Dank geht an meine Familie, die mich fortwährend unterstützt hat und die immer für mich da war. Ohne sie wäre diese Arbeit mit Sicherheit nicht möglich gewesen.

1. Einleitung	- 2 -
2. Charakterisierungsmethoden	- 6 -
2.1 Prinzip der Röntgenbeugung	- 8 -
2.2 Indizierung und Zellverfeinerung	- 10 -
2.3 Strukturlösung und Strukturverfeinerung	- 12 -
2.4 Raumgruppen, Unter- und Obergruppen	- 15 -
2.5 Verwendete Programme	- 17 -
3. Präparative Methoden	- 18 -
3.1 Solvothermalsynthese	- 18 -
3.2 Hochdurchsatzmethoden	- 20 -
4. Kumulativer Hauptteil	- 23 -
4.1 Poröse Aluminium-basierte MOFs	- 23 -
4.2 High-Throughput Studies of Highly Porous Al-based MOFs	- 32 -
4.3 Synthese neuer poröser Aluminium-MOFs basierend auf linearen aromatischen Dicarboxylat-Ionen	- 41 -
4.3.1 CAU-3: A new family of porous MOFs with a novel Al-based brick: [Al ₂ (OCH ₃) ₄ (O ₂ C-X-CO ₂)] (X=aryl)	- 41 -
4.3.2 A new Al-MOF based on a unique column-shaped inorganic building unit exhibiting strongly hydrophilic sorption behaviour	- 51 -
4.4 Synthese neuer poröser MOFs basierend auf 1,3,5-funktionalisierten aromatischen Tricarboxylat-Ionen	- 55 -
4.4.1 A new aluminum-based microporous metal-organic framework: Al(BTB) (BTB = 1,3,5-benzenetrisbenzoate)	- 55 -
4.4.2 Formation and Characterisation of Mn-MIL-100	- 62 -
4.5 Synthese neuer poröser Aluminium-MOFs basierend auf gewinkelten aromatischen Dicarboxylat-Ionen	- 69 -
4.5.1 Structures, sorption characteristics and nonlinear optical properties of a new series of highly stable aluminium MOFs	- 69 -
4.5.2 Mixed-linker MOFs with CAU-10-structure: synthesis and gas sorption characteristics	- 87 -
4.5.3 The first keto-functionalized microporous Al-based metal-organic framework: [Al(OH)(O ₂ C-C ₆ H ₄ -CO-C ₆ H ₄ -CO ₂)]	- 97 -
5. Zusammenfassung	- 118 -
6. Ausblick	- 128 -
7. Anhänge	- 131 -
8. Literatur	- 244 -
9. Liste der Publikationen und Beiträge	- 248 -

1. Einleitung

Die Chemie der metallorganischen Gerüstverbindungen (metal-organic frameworks oder MOFs) hat innerhalb der letzten 15 Jahre beachtliches Interesse hervorgerufen, sowohl innerhalb der industriellen^{1,2} wie auch der akademischen Forschung.^{3,4,5} Dabei steht eine endgültige Definition für den Terminus MOF immer noch aus, obwohl Bestrebungen existieren, die eine eindeutige Klassifizierung ermöglichen sollen.⁶ Am häufigsten werden Verbindungen als MOFs klassifiziert, die kristallin sind und aus anorganischen und organischen Baueinheiten aufgebaut werden. Die Wechselwirkungen, die diese definierten Baueinheiten zusammen halten, sollen dabei energetisch in der Größenordnung von kovalenten Bindungen liegen.⁷ Die anorganischen Baueinheiten werden fast immer während der Synthese der Verbindungen gebildet, allerdings konnten in wenigen Fällen auch definierte Vorläuferverbindungen eingesetzt werden, deren prinzipieller Aufbau während der Synthese des MOFs erhalten bleibt.^{8,9,10} Es werden hauptsächlich nulldimensionale Kationen oder Metall-Oxo-Cluster beobachtet,¹¹ allerdings existieren auch eine Reihe von Verbindungen, die auf eindimensionalen Metall-Sauerstoff-Ketten basieren.^{12,13} Seltener sind zweidimensionale Schichten¹⁴ oder dreidimensionale anorganische Gerüste¹⁵ beobachtet worden. Als organische Baueinheiten (Linker) werden am häufigsten aromatische Polycarbonsäuren eingesetzt, welche in ihrer deprotonierten Form die anorganischen Baueinheiten dreidimensional verknüpfen. Des Weiteren werden auch Phosphon-¹⁶ oder Sulfonsäuren¹⁷ verwendet, sowie leicht deprotonierbare heterocyclische Aromaten wie Imidazole,¹⁸ Triazole¹⁹ und Tetrazole.²⁰

Durch diese Art der Verknüpfung werden häufig poröse Verbindungen erhalten, die gegenüber konventionellen porösen Verbindungen wie Zeolithen oder Aktivkohle diverse Vorteile besitzen. Die kristalline Natur der MOFs resultiert in klar definierten Porengrößen und -eigenschaften, im Gegensatz zu den breiten Porengrößenverteilungen amorpher Adsorbentien wie Aktivkohlen oder Silica-Materialien. Die Vielfalt der Baueinheiten stellt den größten Vorteil gegenüber den Zeolithen dar, deren Struktur durch die tetraedrische Geometrie der TO_4 -Baueinheiten limitiert wird. Des Weiteren können zur Synthese der erwähnten Verbindungsklassen nur wenige Elemente verwendet werden, während für die Synthese von MOFs im Prinzip fast jedes Element eingesetzt werden kann. Im

Hinblick auf die Eigenschaften der porösen Verbindungen besteht der größte Nachteil der MOFs in der limitierten Stabilität. Während Zeolithe in industriellen Prozessen bei Temperaturen über 500 °C eingesetzt werden, werden die stabilsten MOFs unter diesen Bedingungen bereits zerstört.^{21,22} Für potentielle Anwendungen ist der größte Nachteil hingegen der Preis für die Ausgangsstoffe und die teilweise drastischen Synthesebedingungen.²

Neben der strukturellen Vielfalt liegt ein Hauptaugenmerk bei der Synthese von MOFs auf ihrem modularen Aufbau. Während die Vielfalt der potentiellen Baueinheiten zu einer theoretisch unendlichen Anzahl von Verbindungen mit verschiedenen Strukturen und somit auch Eigenschaften führt, lassen sich durch das modulare Bauprinzip die separaten Baueinheiten theoretisch durch andere Bausteine gleicher Geometrie ersetzen, während die Topologie des Gerüsts erhalten bleibt. Diese Herangehensweise an die Synthese neuer Verbindungen wird als isoretikuläre Synthese bezeichnet.²³ So lassen sich beispielsweise die magnetischen Eigenschaften durch den Austausch von Ni^{2+} durch Co^{2+} verändern.^{24,25} Ebenso kann das Sorptionsverhalten gegenüber Gasen durch die Verwendung von Al^{3+} , Fe^{3+} , Cr^{3+} oder V^{3+} variiert werden.²⁶ Die Größe der Poren im Netzwerk kann durch den Einsatz von kleineren oder größeren organischen Baueinheiten verändert werden.^{21,27,28} Durch die Verwendung von chemisch funktionalisierten Linkermolekülen lässt sich zudem Einfluss auf die Eigenschaften der Porenoberfläche nehmen, wodurch insbesondere die Affinität gegenüber Adsorbaten verändert wird.²⁹ Weitere Möglichkeiten zur Manipulation der Eigenschaften sind die Verwendung von verschiedenen Metallionen bei der Synthese³⁰ oder von Gemischen von geometrisch äquivalenten Linkermolekülen.³¹ Allerdings sind diesem einfachen Prinzip durch die Realität Grenzen gesetzt, denn die theoretische Möglichkeit der Synthese garantiert nicht die präparative Zugänglichkeit einer Verbindung.

Diese Vielfalt an Möglichkeiten zur Einflussnahme auf die Eigenschaften von Verbindungen mit gleicher Netzwerkstruktur sind einzigartig innerhalb der Festkörperchemie und wahrscheinlich der Hauptgrund für das konstant starke Interesse an MOFs. Auf Grund der Modulierbarkeit der Eigenschaften und der teilweise unübertroffenen Porosität³² werden MOFs auch als potentiell interessante Materialien für diverse Anwendungen wie Gasspeicherung³³ und -trennung³⁴, als Katalysatoren³⁵ oder Sensoren³⁶ oder in medizinischen Anwendungen³⁷ diskutiert.

MOFs die auf Al^{3+} -Ionen und aromatischen Polycarboxylaten basieren haben in der Vergangenheit bereits gezeigt, dass sie einige wünschenswerte Eigenschaften vereinen. So zeigen sie eine hohe thermische und chemische Stabilität.³⁸ Des Weiteren sind die Ausgangsstoffe meist kostengünstig und nicht toxisch, was für potentielle Anwendungen von Interesse ist.² Die Komplexität der wässrigen Chemie von Al^{3+} -Ionen verheißt außerdem eine große Strukturvielfalt. Dies wurde in einigen Fällen bereits gezeigt, indem ausgehend von identischen Ausgangsstoffen verschiedene Verbindungen hergestellt werden konnten.^{14,39,40} Basierend auf der sehr häufig beobachteten MIL-53-Topologie (MIL steht für *Materiaux de l'Institute Lavoisier*) konnte bereits gezeigt werden, dass das modulare Syntheseprinzip für Al-MIL-53 in vollem Umfang angewendet werden kann. Linkermoleküle verschiedener Größe^{2,41,42} und mit verschiedenen funktionellen Gruppen^{43,44} konnten für die Synthese von MOFs mit MIL-53-Struktur verwendet werden. Die größte Herausforderung und auch das größte Problem bei der Synthese neuer Al-MOFs liegt dabei in der Tatsache begründet, dass in fast allen Fällen mikrokristalline Produkte erhalten werden. Die Strukturbestimmung erfolgt daher nur in den wenigsten Fällen mittels konventioneller Einkristall-Röntgenbeugung,¹⁴ sondern in vielen Fällen mittels Einkristall-Mikrodiffraction mit Synchrotronstrahlung^{39,40,45} oder aus Röntgenpulverbeugungsdaten.^{46,47,48} Die variable Strukturchemie der Al^{3+} -Ionen führt dabei oft zu Synthesebedingungen, die sehr empfindlich auf geringe Änderungen der Syntheseparameter reagieren. Deshalb haben sich Hochdurchsatzmethoden als wertvolles Werkzeug zur Synthese von Al-MOFs erwiesen.^{47,49} Durch die Miniaturisierung der Reaktoren, die parallelisierte Syntheseführung und die automatisierte Charakterisierung lassen sich schnell und kostengünstig große Parameterräume untersuchen, was sowohl die Entdeckung neuer Verbindungen als auch die Optimierung von Synthesebedingungen erleichtert.

Diese Arbeit beschäftigt sich mit der Synthese neuer, poröser Al^{3+} - und Mn^{3+} -basierter MOFs mittels Hochdurchsatzmethoden. Dabei wurden im ersten Teil der Arbeit Linkermoleküle linearer Geometrie eingesetzt, wobei insbesondere der Einfluss des Lösungsmittels auf die Struktur des MOFs von Interesse war. Zum einen wurde dabei mittels Hochdurchsatzmethoden das komplexe quaternäre System Al^{3+} / Linker / Base / Methanol untersucht. Außerdem wurde erstmalig Isopropanol als Lösungsmittel zur Synthese von Al-MOFs verwendet. Im zweiten Teil wurden dreizählige Linkermoleküle verwendet. Dabei wurden die Systeme Al^{3+} / Linker /

Additiv / DMF und Mn^{2+} / Linker / Lösungsmittel untersucht. In letzterem stand insbesondere die in-situ Oxidation von Mn^{2+} - zu Mn^{3+} -Ionen im Fokus. Im dritten Teil der Arbeit wurden erstmalig V-förmige Linkermoleküle zur Synthese von Al-MOFs eingesetzt. Insbesondere die Verwendung von verschiedenen funktionalisierten Isophthalsäuren und deren Einfluss auf die Struktur und die Sorptionseigenschaften waren dabei von Interesse.

2. Charakterisierungsmethoden

Zur Charakterisierung der in dieser Arbeit vorgestellten Verbindungen wurden hauptsächlich die folgenden Methoden eingesetzt:

- Röntgenpulverdiffraktometrie
- Einkristalldiffraktometrie
- Thermogravimetrische Analyse und differentielle Thermoanalyse
- CHNS-Elementaranalyse
- IR- und Raman-Spektroskopie
- UV/Vis-Spektroskopie
- NMR-Spektroskopie in Lösung und an Festkörpern
- Rasterelektronenmikroskopie
- Volumetrische Gassorption

Die für die jeweiligen Messungen verwendeten Geräte sind in Tabelle 2.1 aufgelistet. Weitere Röntgenbeugungsexperimente wurden am Deutschen Elektronen Synchrotron (DESY) in Hamburg durchgeführt. Diese Messungen fanden an der Beamline G3 am DORIS Beschleuniger-Ring und an Beamline P8 am PETRA Beschleuniger-Ring statt. Des Weiteren wurden während der Synthese *in-situ* Röntgenbeugungsexperimente an der Beamline F3 am DORIS Beschleuniger-Ring durchgeführt, die zur Untersuchung der Kinetik des Kristallisationsprozesses dienen. Als eine weitere Methode wurde innerhalb einer Kooperation mit der KU Leuven (Belgien) die SHG-Mikroskopie eingesetzt. Dabei wird die Frequenzverdopplung von monochromatischem Licht an nicht-zentrosymmetrischen Strukturen gemessen. Die mit Abstand wichtigste Methode für diese Arbeit ist die Röntgenpulverdiffraktometrie und die Ermittlung der Kristallstruktur aus Pulverbeugungsdaten. Das Grundprinzip der Röntgenbeugung an Pulvern und die darauffolgenden Schritte zur Bestimmung einer Kristallstruktur sind deshalb in den weiteren Abschnitten näher erläutert.

Tabelle 2.1: Die hauptsächlich in dieser Arbeit verwendeten Methoden und die jeweiligen Geräte und Besonderheiten.

Methode	Geräteart	Anmerkung
Röntgenpulverdiffraktometrie	STOE Stadi P Combi	Transmissionsgeometrie, $\text{CuK}_{\alpha 1}$ -Strahlung, Image Plate Detektor, Hochdurchsatzdiffraktometer
	STOE Stadi P	Transmissionsgeometrie, $\text{CuK}_{\alpha 1}$ -Strahlung, Position Sensitive Detektor
	Panalytical Xpert	Reflektionsgeometrie, CuK_{α} -Strahlung, Halbleiterdetektor
	Panalytical Empyrean	Transmissionsgeometrie, CuK_{α} -Strahlung, Halbleiterdetektor
Einkristalldiffraktometrie	Bruker X8-APEX2	$\text{MoK}_{\alpha 1}$ -Radiation, CCD-Detektor
Thermogravimetrische Analyse / Differentielle Thermoanalyse	NETSCH STA 409 CD	Messungen in Al_2O_3 -Tiegeln in Luft, Heizrate von 4 K/min
CHNS-Analyse	Eurovektor EuroEA	
IR-Spektroskopie	ALPHA-FT-IR A220/D-01	ATR-Einheit
	ATI Matheson Genesis	Messungen als KBr-Tablette
	Bruker Tensor 27	Temperaturabhängige Messungen
Raman-Spektroskopie	Bruker IFS 66 FRA 106	Nd/YAG-Laser als Lichtquelle
UV/Vis-Spektroskopie	Varian Cary 5000	Messung der reinen Verbindungen
NMR-Spektroskopie	Bruker DRX 500	Spektroskopie in Lösung (^1H)
	Bruker DSX Avance 400 FT	Festkörperspektren (^{13}C , ^{15}N)
	Bruker Avance II 300	Festkörperspektren (^{27}Al)
Rasterelektronenmikroskopie	Philips ESEM-XL 30	EDX-Detektor
	Zeiss Gemini Ultra Plus	
Volumetrische Gassorption	BEL JAPAN INC. Belsorp _{max}	Messungen von N_2 , H_2 , CO_2 und H_2O bis 1 bar

2.1 Prinzip der Röntgenbeugung

Kristalle sind dreidimensional periodische, homogene Festkörper mit anisotropen Eigenschaften. Der Beugung von Röntgenstrahlen an kristallinen Verbindungen liegt die Bragg'sche Gleichung (Glg. 2.1) zu Grunde:

$$n \cdot \lambda = 2d \sin \Theta \quad (2.1)$$

In dieser Gleichung bezeichnet n die Beugungsordnung, λ gibt die Wellenlänge der gebeugten Strahlung an, d entspricht dem Abstand zwischen zwei Netzebenen und Θ ist der Beugungswinkel. Für die Beugung wird die Tatsache genutzt, dass die interatomaren Abstände in Kristallen in derselben Größenordnung liegen wie die Wellenlänge der Röntgenstrahlung. Durch den periodischen Aufbau entstehen sogenannte Netzebenen, welche immer im Abstand d parallel zueinander angeordnet sind. Da diese d -Werte und λ in derselben Größenordnung liegen, wirkt die Anordnung der Scharen von Netzebenen wie ein Beugungsgitter, das heißt Strahlung die unter einem bestimmten Winkel Θ relativ zu einer Netzebenenschar auftrifft wird gebeugt und tritt unter diesem Winkel Θ relativ zu den Netzebenen wieder aus. Dabei tragen alle Atome der Kristallstruktur zur Beugung bei. Das Beugungsphänomen beruht auf der Interferenz der an den Atomen des Kristalls gestreuten Strahlung. Während dabei die Streuung an den Atomen auf den Netzebenen nur zur konstruktiven Interferenz führt, tragen die exakt zwischen den Netzebenen liegenden Atome nur zur destruktiven Interferenz bei. Die Streuung an allen weiteren Atomen liefert einen Beitrag zu beiden Phänomenen.

Für die analytische Anwendung wird monochromatische Strahlung verwendet und die Detektion der gebeugten Strahlung erfolgt in Abhängigkeit von 2Θ . Die so erhaltenen Beugungsmaxima werden Reflexe genannt, in Anlehnung an das von Bragg entwickelte geometrische Modell.⁵⁰ Wird an einem einzelnen Kristall gebeugt, so sorgt der dreidimensional periodische Aufbau von Kristallen dafür, dass der Kristall um alle drei Raumachsen rotiert werden muss, damit jede Ebenenschar in Beugungsbedingung liegen kann. Dadurch wird eine dreidimensionale Anordnung der Reflexe erhalten. Wird an einem (idealen) mikrokristallinen Pulver gebeugt, so ist die Lage der Kristallite statistisch und jede Ebenenschar liegt mit gleicher Wahrscheinlichkeit in Beugungsbedingung, so dass die Probe nicht rotiert werden muss. Stattdessen kann zeitgleich die Beugung von allen Ebenenscharen winkelabhängig detektiert werden. Allerdings geht hierbei die Orientierung der

Netzebenen und damit auch die Orientierung der Reflexe im Raum verloren. Mit Hilfe der Gleichung 2.1 lassen sich so die d-Werte einer kristallinen Substanz bestimmen. Die zweite elementare Gleichung der Röntgenbeugung ist die Strukturfaktorgleichung (Gleichung 2.2, vereinfacht für zentrosymmetrische Kristallstrukturen), über die die Intensität der gemessenen Reflexe mit der Anordnung der Atome im Kristall verknüpft werden kann:

$$F_c = \sum f_n \{ \cos 2\pi(hx_n + ky_n + lz_n) + i \sin 2\pi(hx_n + ky_n + lz_n) \} \quad (2.2)$$

Die Intensität eines gemessenen Reflexes ist proportional zum Quadrat des Strukturfaktors F_c . Der Parameter f_n ist der Atomformfaktor, der den Streubeitrag eines Atoms angibt und von der Elektronendichte um das Atom herum und dem Beugungswinkel abhängig ist. Die Werte h , k und l werden Miller'sche Indizes genannt und bezeichnen eindeutig die jeweilige Netzebenenchar, während x_n , y_n und z_n die relative Lage der Atome in der Elementarzelle angeben.⁵¹ Der dreidimensional periodische Aufbau eines Kristalls führt dazu, dass sich der gesamte Kristall durch eine Elementarzelle beschreiben lässt. Diese Elementarzelle wird durch ihre Abmessungen a , b und c beschrieben, die auch als Vektoren betrachtet werden. Zwischen diesen Vektoren definierter Länge spannen sich die Winkel α , β und γ auf, so dass jede Elementarzelle ein Parallelepiped darstellt. Die Anordnung der Atome in der Elementarzelle wird dann in fraktionellen Koordinaten relativ zu den Vektoren angegeben. Durch Aneinanderreihung von beliebig vielen Elementarzellen in allen drei Raumrichtungen kann so der Aufbau des Kristalls beschrieben werden. Die Miller'schen Indizes identifizieren die jeweiligen Netzebenen indem sie den Schnittpunkt der Ebene mit den Achsen der Zelle angeben. Dabei wird a bei $1/h$, b bei $1/k$, und c bei $1/l$ geschnitten, wobei alle Indizes immer ganze Zahlen sind. Die Vektoren a , b und c entspringen in einem Punkt mit den fraktionellen Koordinaten $(0,0,0)$, der als Bezugspunkt für die Koordinaten x_n , y_n und z_n für die jeweiligen weiteren Atome dient.

Ist der Inhalt der Elementarzelle einer kristallinen Verbindung bekannt, so lässt sich mit Hilfe der beiden Gleichungen in sehr kurzer Zeit das Beugungsbild für einen Kristall ebenso wie für ein mikrokristallines Pulver berechnen, wodurch eine Verbindung schnell durch den direkten Vergleich der experimentellen mit den berechneten Daten identifiziert werden kann. Dies ist das Hauptanwendungsgebiet der Röntgenpulverdiffraktometrie, da auch komplexe Phasengemische identifiziert werden können. Der umgekehrte Gang der Strukturbestimmung aus Beugungsdaten

ist häufig auf Einkristalle beschränkt, da für diese ein dreidimensionales Beugungsbild gemessen werden kann. Dies ist daher heutzutage eine Routinemethode. Dagegen ist die Bestimmung von Kristallstrukturen aus Pulverbeugungsdaten häufig sehr mühsam, da das dreidimensionale Beugungsbild auf eine Dimension projiziert wird. Seit der Entwicklung von kostengünstigen, leistungsstarken Computern ist allerdings auch diese Methode zu einem leichter gangbaren Weg geworden. Für diese Arbeit war es sogar die hauptsächlich angewandte Methode, weshalb einige elementare Schritte für die Strukturlösung aus Pulverbeugungsdaten beziehungsweise das Aufstellen eines Strukturmodells und dessen Verfeinerung in den Folgenden Abschnitten beschrieben werden.

2.2 Indizierung und Zellverfeinerung

Der erste Schritt zur Strukturbestimmung einer unbekanntes Substanz ist die Indizierung der gemessenen Reflexe, das heißt die Zuordnung der ermittelten d -Werte zu den jeweiligen Miller'schen Indizes. Der Aufwand hängt dabei von den Zellparametern und der Komplexität der Elementarzelle ab. Je mehr unabhängige Zellparameter existieren, desto komplexer ist auch das Beugungsbild. Je nach Zugehörigkeit zu einem bestimmten Kristallsystem sind dabei nur bestimmte Reflexe zu beobachten. Beispielsweise ist im kubischen Kristallsystem nur der Zellparameter $a = b = c$ zu bestimmen, die Winkel betragen alle 90° . Daher ist die Lage der (100)-, (010)- und (001)-Reflexe und der zu bestimmende d -Wert identisch. Die hohe Symmetrie innerhalb der Zelle führt dazu, dass nur d -Werte beobachtet werden können, die der Gleichung 2.3 (der sogenannten quadratischen Bragg'schen Gleichung) genügen:

$$1/d^2 = (h^2 + k^2 + l^2) \cdot 1/a^2 \quad (2.3)$$

Werden also nur Reflexe beobachtet für die Gleichung 2.3 für einen bestimmten Zellparameter a erfüllt ist, so kann das Diffraktogramm kubisch indiziert werden. Ähnlich Gleichungen gelten auch für alle anderen Kristallsysteme.⁵² Mit abnehmender Symmetrie werden diese Gleichungen komplexer, weshalb verschiedene Algorithmen entwickelt wurden, die die Indizierung ausführen. Die TREOR-⁵³ und DICVOL-Algorithmen⁵⁴ starten dabei mit Indizierungsversuchen im kubischen Kristallsystem, und erhöhen dann schrittweise die Komplexität der Gleichungen und damit die Anzahl der möglichen Zellparameter, die auch

Freiheitsgrade genannt werden. Den umgekehrten Weg geht der von Visser⁵⁵ programmierte Algorithmus, der eine triklinische Zelle annimmt und eine höhere Symmetrie nur bei Übereinstimmungen mit den Beugungsbedingungen für höhersymmetrische Systeme annimmt, beispielsweise wenn zwei oder mehr Winkel laut Indizierung 90° aufweisen. So lassen sich über die Indizierung die Metrik der Elementarzelle und das Kristallsystem einer Verbindung bestimmen.

Des Weiteren können Zentrierungen und translatorische Symmetrieelemente beobachtet werden. Beide Eigenschaften führen zu systematischen Auslöschungen, was bedeutet, dass bestimmte Reflexe nicht beobachtet werden können, obwohl das Kristallsystem dies erlauben würde. Während im kubisch primitiven Gitter der (100)-Reflex beobachtet wird, ist dieser im kubisch flächenzentrierten Gitter systematisch ausgelöscht. Diese Auslöschung resultiert daraus, dass die Beugung am Gitter auf der konstruktiven und destruktiven Interferenz der gebeugten Strahlung beruht. Interferieren Wellen mit passendem Gangunterschied destruktiv, so wie im kubisch flächenzentrierten Gitter, so führt dies zur systematischen Auslöschung von Reflexen. Ganz allgemein sind bei solch einer Flächenzentrierung nur Reflexe erlaubt, bei denen alle Miller'schen Indizes gerade oder alle ungerade sind ($h+k$, $k+l$ und $h+l$ müssen gerade Zahlen ergeben).⁵² Allerdings müssen auch andere Ursachen für die Abwesenheit der Reflexe in Betracht gezogen werden. Beispielsweise kann dies auch auf die Kristallstruktur selbst zurückzuführen sein, auf Grund derer manche Reflexe eine sehr geringe Intensität aufweisen. Ebenso kann eine gestörte Fernordnung der Atome innerhalb der Kristallstruktur oder experimentelle Fehler bei der Probenpräparation und der Messung zur scheinbaren Auslöschung von Reflexen führen, die allerdings eigentlich nur sehr geringe Intensität besitzen. Deshalb sollte die Bestimmung von Zentrierungen und translatorischen Symmetrieelementen aus Pulverbeugungsdaten kritisch behandelt werden. Basierend auf den indizierten Zellparametern und dem Kristallsystem sowie den systematischen Auslöschungen lassen sich so eine oder mehrere Raumgruppen ermitteln, die dem Beugungsbild genügen. Sind mehrere Raumgruppen möglich, lassen sich diese in einer Auslöschungsgruppe zusammenfassen. Eine endgültige Bestätigung einer bestimmten Raumgruppe lässt sich allerdings nur durch eine erfolgreiche Strukturverfeinerung erreichen. Um die erhaltenen Zellparameter zu präzisieren kann eine Verfeinerung der Zellparameter durchgeführt werden. Dabei werden die Zellparameter iterativ geändert, bis die Abweichung der beobachteten

Werte von den theoretischen Idealwerten für die zu optimierende Zelle möglichst klein wird. Für diese Verfeinerung wird die Summe der Fehlerquadrate (Gleichung 2.4) minimiert:

$$\sum_j (d_{obs} - d_{calc})^2 = Minimal \quad (2.4)$$

Diese Verfeinerung der Zellparameter lässt sich basierend auf den beobachteten Reflexlagen durchführen. Es kann allerdings auch eine Profilanpassung eines theoretischen Diffraktogramms an das experimentell gemessene vorgenommen werden, bei der weitere Faktoren verfeinert werden, wie zum Beispiel eine lineare Verschiebung oder stark anisotrope Reflexformen. Eine solche Methode wurde von Pawley,⁵⁶ eine weitere von Le Bail⁵⁷ entwickelt. Bei diesem Verfahren können dann zeitgleich auch die Intensitäten der Reflexe extrahiert und verfeinert werden, was für die Strukturbestimmung ein entscheidender nächster Schritt ist.

Die Güte einer Indizierung oder einer Zellverfeinerung nach Pawley oder Le Bail lässt sich zum einen optisch durch einen Vergleich von theoretischen und experimentellen Werten ermitteln. Zum anderen existieren verschiedene Gütefaktoren, die die Qualität mathematisch beschreiben. Einer dieser Faktoren ist der für die Profilanpassung gebräuchliche R_{WP} -Wert (Gleichung 2.5):

$$R_{WP} = \{\sum[w_i \cdot (I_{iobs} - I_{icalc})^2] / \sum[w_i \cdot (I_{iobs} + I_{icalc})^2]\} \quad (2.5)$$

Dabei stellt w_i einen Gewichtungsfaktor dar, der von der Messgenauigkeit der Intensität abhängt ($w_i = \text{Zählrate} \cdot \text{Messzeit}$).⁵² I_{iobs} und I_{icalc} geben die gemessenen und berechneten Intensitäten am Punkt i wieder. Der so ermittelte Gütefaktor für die gewichtete Profilanpassung sollte gegen Null gehen. Ein weiterer Faktor ist der GoF („Goodness of Fit“), der möglichst nahe bei 1 liegen sollte. Dieser Wert wird über Gleichung 2.6 ermittelt:

$$GoF = \{\sum[w_i \cdot (I_{iobs} - I_{icalc})^2] / n \cdot p\}^{0.5} \quad (2.6)$$

Dabei gibt n die Anzahl der verwendeten Messpunkte an und p ist die Anzahl der verfeinerten Parameter.

2.3 Strukturlösung und Strukturverfeinerung

Die Strukturlösung aus Röntgenpulverbeugungsdaten verläuft oft analog zur Methode ausgehend von Einkristallbeugungsdaten. Allerdings sind statt tausender Reflexe, wie im Falle von Einkristallbeugungsdaten, meist nur wenige hundert oder noch weniger Reflexe eindeutig zuzuordnen. Daher ist die Menge an Informationen

eher limitiert, was die Strukturlösung praktisch immer zu einem trial-and-error Prozess macht, der oft erst nach vielen Versuchen ein sinnvolles Ergebnis liefert.

Das Beugungsbild kann als Fouriertransformierte der Elektronendichte im Kristall verstanden werden. Diese Elektronendichte steht mit den Strukturformfaktoren nach Gleichung 2.7 im direkten Zusammenhang⁵¹:

$$\rho_{xyz} = \frac{1}{V} \sum_{hkl} F_{hkl} \cdot e^{-i2\pi(hx+ky+lz)} \quad (2.7)$$

Die Elektronendichte lässt sich also bestimmen, wenn die Strukturformfaktoren F_{hkl} bekannt sind. Allerdings lassen sich nur die Intensitäten von Reflexen bestimmen. Diese sind zwar quadratisch proportional zu $|F_{hkl}|^2$, aber die Phase der Reflexe kann nicht direkt bestimmt werden.

Bei der Strukturlösung aus Pulverdaten werden meist direkte Methoden⁵⁸ angewandt, um dieses Problem zu umgehen. Die direkten Methoden nutzen hauptsächlich die Tatsache aus, dass die Phasen von bestimmten Reflexgruppen, sogenannten Reflextripletts, mit einer bestimmten Wahrscheinlichkeit voneinander ableitbar sind. Dadurch kann bei einigen besonders starken Reflexen die Phase angenommen werden, woraus die Phase weiterer Reflexe ermittelt werden kann. Allerdings basiert diese Phasenbestimmung auf Wahrscheinlichkeiten und ist somit nicht zwingend eindeutig. Im Falle der Strukturlösung aus Pulverbeugungsdaten bleibt dann noch das Problem der Reflexüberlappung. Da das Beugungsbild nicht dreidimensional sondern eindimensional ist, können Reflexe mit ähnlichen d -Werten leicht überlappen, wodurch die eindeutige Zuordnung zu einer Netzebene erschwert werden kann. Sind allerdings die Strukturformfaktoren einer genügend hohen Anzahl an Reflexen ermittelt, lässt sich daraus die Anordnung der Atome innerhalb der Elementarzelle bestimmen. Der rechnerische Aufwand steigt dabei mit der Anzahl der zu bestimmenden Parameter. Allerdings kann ein hohes Maß an Symmetrie ebenfalls zu Problemen führen, da nur wenige Reflexe erlaubt sind, was die Menge ermittelter Information limitiert. Daher wurden verschiedene weitere Methoden entwickelt, um Kristallstrukturen aus Röntgenbeugungsdaten zu bestimmen.

Ein solcher Ansatz zur Strukturlösung sind die Realraum-Methoden⁵⁹, die einen hohen Rechenaufwand erfordern. Dabei wird, basierend auf der ermittelten Summenformel und den bestimmten kristallographischen Parametern, eine zufällige Kristallstruktur erzeugt. Diese Kristallstruktur wird dann schrittweise geändert, bis das theoretische Diffraktogramm möglichst gut mit dem experimentellen Diffraktogramm

übereinstimmt. Damit gehört der Realraum-Ansatz zu den Monte-Carlo-Methoden. Dieser Prozess zur Strukturlösung kann sich allerdings beliebig lange hinziehen und eignet sich besonders gut, wenn strukturelle Fragmente bereits bekannt sind. Diese Fragmente lassen sich dann als definierte Baueinheiten nutzen, so dass die Komplexität der Struktur herabgesetzt wird. Insbesondere werden Koordinationspolyeder oder - bei molekularen Verbindungen - die Molekülstruktur vorgegeben. Dennoch ist die Bestimmung der Struktur in diesem Fall stark vom Zufall abhängig.

Ein Ansatz zur Aufstellung eines Strukturmodells, der sich besonders bei den modular aufgebauten MOFs als vielversprechend erwiesen hat, ist die Verwendung von Kraftfeldmethoden. Dabei wird von einer bekannten Kristallstruktur ausgegangen und einzelne Baueinheiten der Verbindung werden durch strukturell ähnliche Baueinheiten ersetzt, beispielsweise ein Linkermolekül durch ein größeres, topologisch gleichwertiges Linkermolekül. Die so erhaltene hypothetische Kristallstruktur wird im Anschluss energetisch optimiert. Das heißt, dass für jede definierte Bindung eine bestimmte Kraftkonstante und ein optimaler Abstand angenommen werden. Durch schrittweise Änderungen an der Struktur werden nun die energetischen Eigenschaften dieser Bindungen optimiert und eine neue, optimierte Struktur minimaler Energie erhalten. Diese Methoden sind insbesondere durch die Kraftfeld-Parameter limitiert, da für die anorganischen Baueinheiten nur wenige Kraftfeldparameter literaturbekannt sind. Außerdem werden schwache Wechselwirkungen meistens nicht berücksichtigt. Die Methode eignet sich besonders gut, wenn basierend auf den Eigenschaften einer unbekanntes Verbindung und den ermittelten kristallographischen Parametern eine strukturelle Verwandtschaft zu einer bekannten Verbindung plausibel ist.

Alle beschriebenen Methoden dienen zur Aufstellung eines Strukturmodells. Bei ausreichender Qualität der Pulverbeugungsdaten und einem sinnvollen und ausreichend guten Strukturmodell kann dieses dann mittels Rietveld-Methoden verfeinert werden um die exakte Struktur zu ermitteln.⁶⁰ Dabei wird das Strukturmodell solange an die experimentellen Messdaten angepasst, bis eine ausreichende Übereinstimmung erreicht ist. Sowohl die Zellparameter als auch die Position der Atome, sowie deren thermische Auslenkungsparameter können dabei verfeinert werden. Neben den bereits beschriebenen Gütefaktoren R_{WP} und GoF

existiert noch der R_{Bragg} -Wert, der die Übereinstimmung der theoretischen Reflexintensitäten mit den experimentell ermittelten beschreibt (Gleichung 2.8):

$$R_{\text{Bragg}} = \frac{\sum_k (I_{\text{kobs}} - I_{\text{kcalc}})}{\sum_k I_{\text{kobs}}} \quad (2.8)$$

Mittels dieser Methoden lässt sich so die Kristallstruktur von Verbindungen aus Pulverbeugungsdaten bestimmen. Die Qualität der so ermittelten Struktur hängt dabei von einer Vielzahl von experimentellen Parametern ab, kann aber im Optimalfall als gleichwertig zu einer aus Einkristallbeugungsdaten bestimmten Kristallstruktur angesehen werden. Der Vorteil der Methode für die Strukturbestimmung liegt darin, dass die Struktur einer Vielzahl von Kristalliten simultan bestimmt wird, so dass eine gemittelte Struktur erhalten und bestätigt wird. Im Gegensatz dazu lässt sich aus Einkristallbeugungsdaten zwar meist schneller und detaillierter die Struktur bestimmen, allerdings ist diese Methode im Prinzip auf einen individuellen Kristall begrenzt.

2.4 Raumgruppen, Unter- und Obergruppen

Das Konzept der Elementarzelle beinhaltet, dass alle im Kristall vorhandenen Symmetrieelemente auf die Symmetrie einer Elementarzelle reduziert werden können. Fasst man die möglichen Symmetrieelemente einer Elementarzelle zusammen, so lassen sich insgesamt 32 verschiedene Kristallklassen im dreidimensionalen Raum erzeugen. Die Kristallklasse entspricht dabei der Punktgruppe der Elementarzelle.⁶¹ Erweitert man die Symmetrieelemente um die translatorischen Symmetriebeziehungen zwischen den Elementarzellen so ergeben sich 230 mögliche Raumgruppen. In manchen Fällen erlaubt die Symmetrie verschiedene Elementarzellen. Die Wahl der richtigen Elementarzelle anhand der beobachteten Symmetrieelemente geschieht dann nach bestimmten festgelegten Konventionen.⁶¹ So sollte die Elementarzelle beispielsweise möglichst klein aber auch möglichst hochsymmetrisch sein.

Die Raumgruppen weisen untereinander verschieden starke Verwandtschaft auf. Ein Spezialfall ist dabei die Gruppe-Untergruppe Beziehung. Werden formal aus einer Raumgruppe X einzelne oder kombinierte Symmetrieelemente entfernt, so ergibt sich eine neue Raumgruppe Z . Diese Raumgruppe Z ist eine maximale Untergruppe von X , wenn sich keine Raumgruppe Y erzeugen lässt, die durch Entfernung von weniger Symmetrieelementen erzeugt werden kann. In diesem Fall wäre Z dann eine

maximale Untergruppe von Y . Ist Z eine maximale Untergruppe von X , so lässt sich X auch als minimale Obergruppe bezeichnen. Abgesehen von den Symmetrieelementen kann sich dabei auch das Translationsgitter verändern.

Man unterscheidet drei Gruppe-Untergruppe Beziehungen.⁵¹ Die translationsgleichen Untergruppen (Übergang t) enthalten weniger Symmetrieelemente als die jeweilige Raumgruppe während das Translationsgitter erhalten bleibt. Je nach Grad der Ausdünnung an Symmetrie lassen sich Indices festlegen, die Beschreiben wie viel Symmetrie verschwindet (Index 2 \rightarrow Halbierung der Symmetrieelemente). Dabei ändert sich die Kristallklasse der Raumgruppe.

Als klassengleiche Untergruppen (Übergang k) werden die Raumgruppen bezeichnet, die unter Erhalt der Kristallklasse erzeugt werden können. Dabei fällt beispielsweise eine Zentrierung weg oder die Gitterparameter von einer oder mehreren Achsen verdoppeln oder verdreifachen sich. Isomorphe Untergruppen (Übergang l) entsprechen einem Spezialfall der klassengleichen Untergruppen. Dabei ändern sich nur die Gitterparameter, während der Raumgruppentyp komplett unverändert bleibt.

Von Bedeutung sind diese Beziehungen in der Strukturchemie der MOFs, weil Verbindungen mit ähnlichen oder fast identischen Strukturen ihre Verwandtschaft oftmals auch in den Raumgruppen wiedergeben. So können die verschiedenen Pseudopolymorphe der Struktur von Cr-MIL-53⁶² (Raumgruppen $Imcm$, $Pnam$ und $C2/c$) auch erzeugt werden, indem von $Imcm$ ein klassengleicher Übergang zu $Pnam$ stattfindet. Der Übergang von $Imcm$ zu $C2/c$ ist dagegen ein translationsgleicher Übergang. Da die Gruppe-Untergruppe Beziehungen bekannt sind, lassen sich mit speziellen Programmen aus bekannten Kristallstrukturen hypothetische Kristallstrukturen in den jeweiligen Ober- und Untergruppen erzeugen. Dies stellt dann einen Spezialfall für die Erstellung eines Strukturmodells dar, das zur Strukturverfeinerung dienen kann. Details und Beispiele zu Gruppe-Untergruppe Beziehungen finden sich in den Kapiteln 4.4.1 und 4.5.1 in dieser Arbeit.

2.5 Verwendete Programme

Die verwendete Software für die verschiedenen Techniken, die im vorherigen Teil beschrieben wurden, ist in Tabelle 2.2 zusammengefasst.

Tabelle 2.2: In dieser Arbeit verwendete Software.

Methode	Geräteart	Anmerkung
Strukturlösung	Expo 2009 ⁶³	Direkte Methoden
Strukturverfeinerung	TOPAS ⁶⁴	Rietveld-Methode
Pulverdiffraktometrie	STOE WINXPOW ⁶⁵	Messung und Auswertung
Visualisierung von Strukturen	Diamond 3.1	
Indizierung	STOE WINXPOW ⁶⁵	ITO/TREOR/DICVOL-Algorithmus
	TOPAS ⁶⁴	modifizierter DICVOL-Algorithmus
	Expo 2009	
Raugruppen-Konvertierung	Powdercell ⁶⁶	Transformation in Ober- und Untergruppen
Kraftfeldrechnungen	Materials Studio 5.0 ⁶⁷	

3. Präparative Methoden

Die Synthesebedingungen, unter denen MOFs hergestellt werden können, umfassen einen sehr weiten Bereich. Obwohl in einigen wenigen Beispielen lösungsmittelfrei⁶⁸ oder annähernd lösungsmittelfrei⁶⁹ MOFs hergestellt werden konnten, wird in fast allen Fällen die Kristallisation aus Lösung zur Synthese genutzt. In vielen Fällen wird bei Raumtemperatur oder unter moderat erhöhten Temperaturen aber ohne autogenen Druck im Reaktor gearbeitet.⁷⁰ In dieser Arbeit wurde allerdings ausschließlich unter solvothermalen Bedingungen gearbeitet. Obwohl der Begriff solvothermal manchmal verwendet wird, um die Synthese in einem geschlossenen Reaktor zu beschreiben, wird sie hier benutzt, um das Erhitzen eines Reaktionsgemisches in einem geschlossenen Reaktor über den Siedepunkt mindestens eines verwendeten Lösungsmittels zu beschreiben. Die Methoden um dem Reaktionsgemisch für die Synthese eines MOFs Energie zuzuführen sind vielfältig und umfassen die Verwendung von Mikrowellenöfen,⁷¹ die mechanochemische Synthese,⁶⁸ die elektrochemische Synthese⁷² und die sonochemische Synthese.⁷³ In dieser Arbeit wurde allerdings fast ausschließlich die konventionelle dielektrische Heizmethode im Ofen genutzt, da hierfür die im Arbeitskreis entwickelte Hochdurchsatz-Ausrüstung für das Arbeiten unter solvothermalen Bedingungen vorhanden war.

3.1 Solvothermalsynthese

Die Solvothermalsynthese umfasst Reaktionsbedingungen, die erzeugt werden, wenn ein Lösungsmittel im geschlossenen Reaktor über seinen Siedepunkt erhitzt wird, so dass innerhalb des Reaktors ein autogener Druck aufgebaut wird. Aufgrund dieses Drucks wird meistens in dickwandigen Glasreaktoren oder Stahlautoklaven mit innerten Tefloneinsätzen gearbeitet. Die Eigenschaften des Lösungsmittels verändern sich unter diesen Bedingungen drastisch, sind allerdings bisher, außer für Wasser als Lösungsmittel, kaum untersucht. Die auftretenden Effekte werden daher hauptsächlich für diesen Spezialfall erklärt.⁷⁴ In diesem Fall wird die Methode auch Hydrothermalsynthese genannt.

Unter hydrothermalen Bedingungen nimmt das Ionenprodukt des Wassers zu, während die Viskosität und die Dielektrizitätskonstante abnehmen. Insgesamt führt

dies dazu, dass gelöste Spezies unter hydrothermalen Bedingungen assoziieren können. Die niedrigere Viskosität führt außerdem zu einer hohen Mobilität der gelösten Ionen und Moleküle und damit zu einer guten Durchmischung. Die Löslichkeit der Ausgangsstoffe kann dabei durch den Zusatz von sogenannten Mineralisatoren erhöht werden, zum Beispiel durch den Einsatz von Basen oder Fluoriden. Im Vergleich zu klassischen, lösungsmittelfreien Festkörperreaktionen erfordern Hydrothermalsynthesen relativ geringe Temperaturen zwischen 100 °C und 300 °C. Daher bilden sich häufig nicht die thermodynamisch stabilen Produkte, sondern kinetisch stabile Verbindungen (Hochporöse MOFs werden häufig als kinetisch stabil betrachtet, so dass die Solvothermalsynthese oft die einzige Möglichkeit zur Synthese darstellt). Des Weiteren kann durch die gute Durchmischung meist ein homogenes Produkt erhalten werden. So lassen sich beispielsweise Quarzkristalle oder Perowskite mit definierter, gleichmäßiger Kristallitgröße herstellen.^{74,75} Auch Chalkogenide oder anderweitig nicht zugängliches eisensubstituiertes Ceroxid können solvothermal synthetisiert werden.⁷⁶ Eine weitere wichtige Verbindungsklasse die unter solvothermalen Bedingungen hergestellt wird sind die mikroporösen Zeolithe,⁷⁷ die als metastabile Zwischenprodukte betrachtet werden. Die thermodynamisch stabile Modifikation dieser porösen Alumosilicate stellen die dichten Oxide dar.

Für die Synthese von MOFs ist insbesondere von Bedeutung, dass sich die organischen Ausgangsstoffe unter keramischen Reaktionsbedingungen zersetzen würden. Daher bietet die Kristallisation aus Lösung einen vielversprechenden Ansatz zur Synthese. Unter solvothermalen Bedingungen wird häufig dann gearbeitet, wenn die organische Komponente unter milderer Bedingungen nicht ausreichend löslich ist, beispielsweise für die Synthese von MOFs basierend auf Terephthalsäure in Wasser.^{78,79} Dabei bilden sich in manchen Fällen anorganische Spezies, die durch die Kristallisation als MOF stabilisiert werden und ansonsten präparativ nicht zugänglich wären. Häufig werden MOFs auch in anderen Lösungsmitteln als Wasser unter solvothermalen Bedingungen hergestellt, zum Beispiel in Methanol⁸⁰ oder N,N-Dimethylformamid.⁸¹ Hierbei ist allerdings zu beachten, dass in Analogie zu Wassermolekülen und Hydroxidionen, die in die Struktur des Produkts eingebaut werden können, die Lösungsmittelmoleküle ebenfalls als Reaktanden fungieren können. Außerdem zersetzen sich organische Lösungsmittel häufig unter solvothermalen Reaktionsbedingungen. So wurde bereits beobachtet, dass Methanol

als methylierendes Reagens wirken kann.⁸² Dimethylformamid hydrolysiert in Gegenwart von Spuren von Wasser zu Ameisensäure und Dimethylamin. Dieser Effekt muss bei der Synthese in Betracht gezogen werden, ebenso wie die Reaktivität der Edukte. Metallnitrate und -perchlorate wirken beispielsweise als Oxidationsmittel und Metallionen können während der Synthese ihre Wertigkeit ändern.

3.2 Hochdurchsatzmethoden

Die Komplexität der chemischen Systeme und die nicht exakt bekannten Reaktionsbedingungen führen dazu, dass das Produkt einer Synthese unter solvothermalen Bedingungen praktisch nicht vorhergesagt werden kann. Deshalb sind Aussagen über solch ein System nur auf empirischer Basis möglich. Als ein wertvolles Werkzeug für die Synthese von MOFs haben sich daher Hochdurchsatz-(HD-)Methoden bewährt. Nimmt man in einem hypothetischen Reaktionssystem mit vier unterschiedlichen Ausgangsstoffen an, dass deren Menge in jeweils vier Schritten variiert werden soll, so ergeben sich bei ansonsten konstanten Reaktionsbedingungen bereits $4^4 = 256$ mögliche Zusammensetzungen der Ausgangsmischung. Um eine begründete Aussage über dieses hypothetische System machen zu können, müssten diese 256 Reaktionen durchgeführt und die Produkte charakterisiert werden. Gerade bei komplexen Reaktionssystemen mit mehr als zwei Ausgangsstoffen und bei der Verwendung von kommerziell nicht erhältlichen Chemikalien können Hochdurchsatzmethoden deshalb hervorragende Dienste leisten. Diese Methoden basieren darauf, dass einzelne präparative und analytische Schritte parallelisiert, miniaturisiert und automatisiert ausgeführt werden. Abgesehen von der Synthese von MOFs⁸³ hat sich dieser Ansatz auch in vielen anderen Bereichen bewährt, zum Beispiel in der Präparation von Proteinkristallen,⁸⁴ der Synthese und Charakterisierung von Katalysatoren⁸⁵ oder der Entwicklung von Sensoren.⁸⁶

Die in dieser Arbeit verwendeten Gerätschaften und Vorrichtungen wurden speziell für das Arbeiten unter solvothermalen Bedingungen konstruiert. Am Anfang der Untersuchung eines solvothermalen Systems steht dabei immer die sorgfältige Planung des HD-Experiments. Dabei sollten Parameter wie die Löslichkeit der Edukte im verwendeten Lösungsmittel, die Reaktivität und Stabilität der Reaktanden

(beispielsweise die oxidierende Wirkung von Nitraten) und nicht zuletzt auch die Verfügbarkeit der Ausgangsstoffe in Betracht gezogen werden. Auch die Prozessparameter wie Synthesetemperatur und –dauer sollten vernünftig begründet sein.

Die Dosierung der Ausgangsstoffe kann dann manuell oder automatisiert erfolgen, beispielsweise mittels eines Pipettierroboters (Abb. 3.1, links). Dabei werden die Reaktanden direkt in die Teflonreaktoren (Maximalvolumen von 2000 oder 300 μL) eindosiert. Diese Reaktoren werden dann in spezielle Multiklaven eingesetzt, die 48 Reaktoren mit 300 μL oder 24 Reaktoren mit 2000 μL Volumen fassen (Abb. 3.1, rechts).

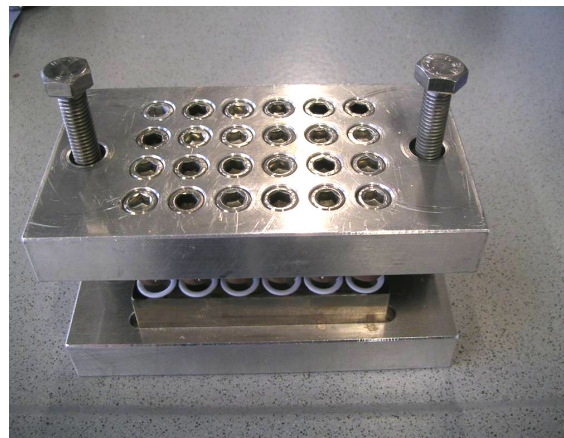


Abbildung 3.1: Links der im AK Stock verwendete Pipettierroboter, rechts ein 24er-Multiklav mit eingesetzten Teflonreaktoren.

Diese Multiklaven werden dann mittels einer Presse unter Druck verschlossen und einem definierten Temperaturprogramm unterworfen. Dabei dienen Teflonfolien auf den Reaktoren als Dichtung, um diese druckdicht zu verschließen. Nach dem Abkühlen werden die festen Produkte mit einem HD-Filterblock abgetrennt und auf einen Probenträger mit 48 Positionen transferiert. Dieser Probenträger ist kompatibel mit dem HD-Pulverdiffraktometer STOE Stadi P Combi (Abb. 3.2). Nach der Charakterisierung können die Proben in well-plates gelagert werden. Die durch die Charakterisierung mittels Röntgenpulverdiffraktometrie gewonnenen Informationen dienen dann als Grundlage zur Planung des nächsten HD-Experiments. Mit diesem Arbeitsablauf lassen sich schnell chemische Trends im Reaktionssystem erkennen. Dies erleichtert zum einen die Entdeckung neuer Verbindungen und beschleunigt zum anderen die Optimierung der Synthesebedingungen.

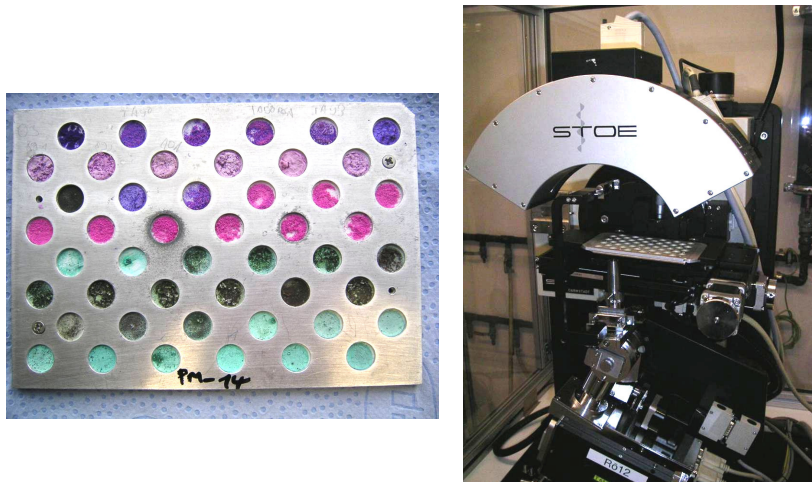


Abbildung 3.2: Links ein HD-Probenträger mit 48 Proben, rechts der eingelegte Probenträger im HD-Pulverdiffraktometer.

Die Automatisierung umfasst in diesem Fall die Dosierung und die Charakterisierung. Die Reaktionsansätze werden miniaturisiert und die Synthese und Produktisolierung werden parallelisiert durchgeführt. Der Vorteil des geringen Chemikalienverbrauchs ist gleichzeitig der größte Nachteil der HD-Methoden, denn die Menge an Produkt ist somit eher gering. Sollen größere Mengen zur ausführlichen Charakterisierung hergestellt werden, müssen die Syntheseparameter in manchen Fällen neu eingestellt werden, da diese empfindlich von der Reaktorgröße abhängen können. Im schlechtesten Fall kann die Synthese sogar so empfindlich sein, dass eine Aufskalierung auf größere Reaktoren nicht möglich ist.

Zusätzlich zu dieser Ausrüstung stehen im Arbeitskreis weitere HD-Geräte bereit. So kann eine HD-Mikrowelle verwendet werden, die für Teflon- und Glasreaktoren geeignet ist. Die Nutzung von Mikrowellen zum Erhitzen verkürzt dabei in drastischem Maß die Aufheizzeiten. Auch ein Temperaturgradienten-Reaktor kann verwendet werden.⁸⁷ In diesem lässt sich nicht nur die Zusammensetzung der Ausgangsstoffe variieren, sondern zusätzlich ein Temperaturgradient zwischen den Reaktoren anlegen, um den Einfluss der Temperatur auf die Produktbildung zu untersuchen. Allerdings ist dieser Reaktor nicht für hydrothermale Bedingungen geeignet. Der HD-Mikrowellenofen wurde im Verlauf dieser Arbeit zwar genutzt, allerdings konnte kein starker Einfluss auf die Produktbildung beobachtet werden.

4. Kumulativer Hauptteil

4.1 Poröse Aluminium-basierte MOFs

Trotz der Herausforderungen, die sich daraus ergeben, dass Aluminium-MOFs nur selten makroskopische Einkristalle ausbilden, sind bereits mehrere Verbindungen bekannt und ausführlich charakterisiert worden. Einige von diesen Verbindungen sollen hier kurz beschrieben werden, um einen Überblick über die auftretenden anorganischen Baueinheiten und die strukturellen Tendenzen sowie die potentiellen Anwendungsmöglichkeiten zu geben.

Der als erstes synthetisierte Aluminium-MOF [Al(OH)BDC] wurde durch die Reaktion von Terephthalsäure (H_2BDC) und $Al(NO_3)_3 \cdot 9H_2O$ in Wasser erhalten. Dieser basiert auf Ketten eckenverknüpfter AlO_6 -Polyeder die über Terephthalationen miteinander verknüpft werden. Dieser MOF ist unter dem Trivialnamen Al-MIL-53 (MIL steht für *Materiaux de l'Institut Lavoisier*) bekannt.⁸⁸ Durch die Verknüpfung der Ketten untereinander entsteht ein dreidimensionales Netzwerk mit rautenförmigen Kanälen (Abb. 4.1). In Abhängigkeit von eingelagerten Gastmolekülen adaptiert das Gerüst verschiedene Formen und weist damit den sogenannten „breathing“-Effekt auf.

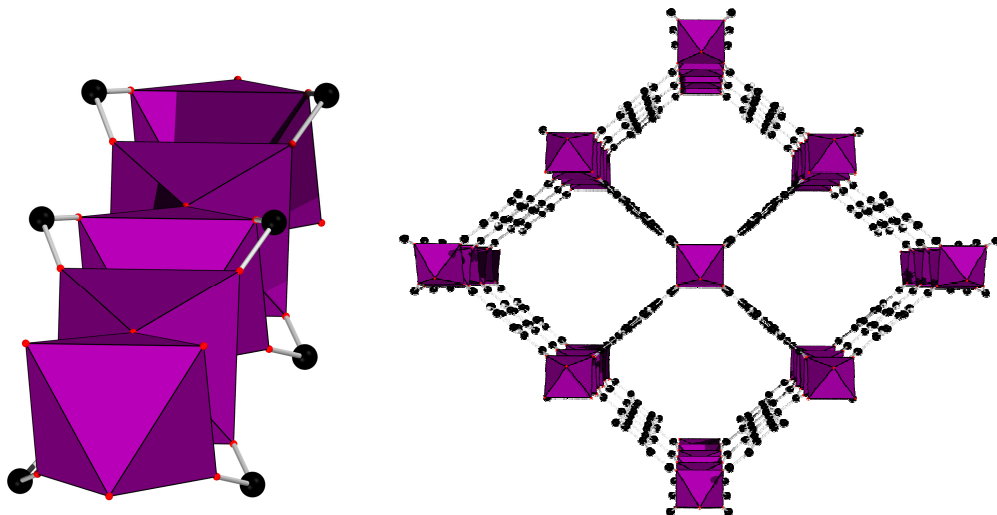


Abbildung 4.1: Links die Kette von AlO_6 -Polyedern gezeigt mit Carboxylat-Gruppen, rechts die Netzwerk-Struktur von Al-MIL-53 in der offenen Form betrachtet entlang der c -Achse. AlO_6 -Polyeder sind in violett dargestellt, Sauerstoffatome sind in rot, Kohlenstoffatome in schwarz gezeichnet.

Der Durchmesser der Kanäle hängt dabei von den eingelagerten Gastmolekülen ab. Die Flexibilität des Netzwerks in Abhängigkeit von den eingelagerten Gastmolekülen führt dazu, dass eine hohe Selektivität für Al-MIL-53 bei der Trennung von Xylenisomeren beobachtet werden kann.⁸⁹ Sowohl die Sorptionseigenschaften als auch die strukturelle Variation des Netzwerks lassen sich durch die Verwendung von funktionalisierten Linkermolekülen beeinflussen.^{90,91} Werden größere Linkermoleküle verwendet, wie zum Beispiel 4,4'-Biphenyldicarbonsäure oder 2,6-Naphtalendicarbonsäure, lässt sich die Atmung sogar komplett unterdrücken.^{92,93} Dabei bestimmen die Synthesebedingungen darüber, ob eine komplett geöffnete oder eine vollständig geschlossene Konformation der Kanäle beobachtet wird.

Die Verwendung von 2-Aminoterephthalsäure ($\text{H}_2\text{BDC-NH}_2$) zur Synthese von $[\text{Al}(\text{OH})\text{BDC-NH}_2]$ oder Al-MIL-53-NH₂ ruft besonders vielversprechende Eigenschaften hervor, weshalb dieser MOF bereits sehr detailliert untersucht wurde. So konnten die NH₂-Gruppen bereits post-synthetisch durch Umsetzung mit Ameisensäure modifiziert werden.⁹⁴ Des Weiteren zeigte Al-MIL-53-NH₂ hervorragende Selektivitäten bei der Trennung von Gemischen von CO₂ und CH₄.⁹⁵ Auch die Verwendung als NLO-Material (NLO = Nicht-Lineare Optik) wurde bereits diskutiert, da durch die atmende Struktur zwischen SHG-aktiver und -inaktiver Form mit herausragend hohen Kontrastwerten gewechselt werden kann.⁹⁶

Die Vielzahl an Verbindungen mit MIL-53-Topologie kann dadurch erklärt werden, dass diese Netzwerkstruktur scheinbar thermodynamisch am stabilsten ist. In-situ-Experimente zur Untersuchung der Kristallisation von Al-MIL-53-NH₂ konnten zeigen, dass Al-MIL-53-NH₂ das Endprodukt einer Synthese ist, bei der als Zwischenstufe unter anderem $[\text{Al}_3\text{O}(\text{OH})(\text{H}_2\text{O})_2(\text{BDC-NH}_2)_3]$ oder Al-MIL-101-NH₂ erhalten wird.⁹⁷ Im Gegensatz zur MIL-53-Topologie weist letztere Verbindung trimere Baueinheiten μ_3 -O-eckenverknüpfter AlO₆-Polyeder auf. Diese sind mittels Aminoterephthalatanionen zu sogenannten Supertetraedern verknüpft (Abb. 4.2). Diese Supertetraeder sind analog zu den tetraedrischen Knotenpunkten im zeotypen MTN-Netzwerk angeordnet. Die Linkermoleküle bilden dabei die Kanten des Supertetraeders.

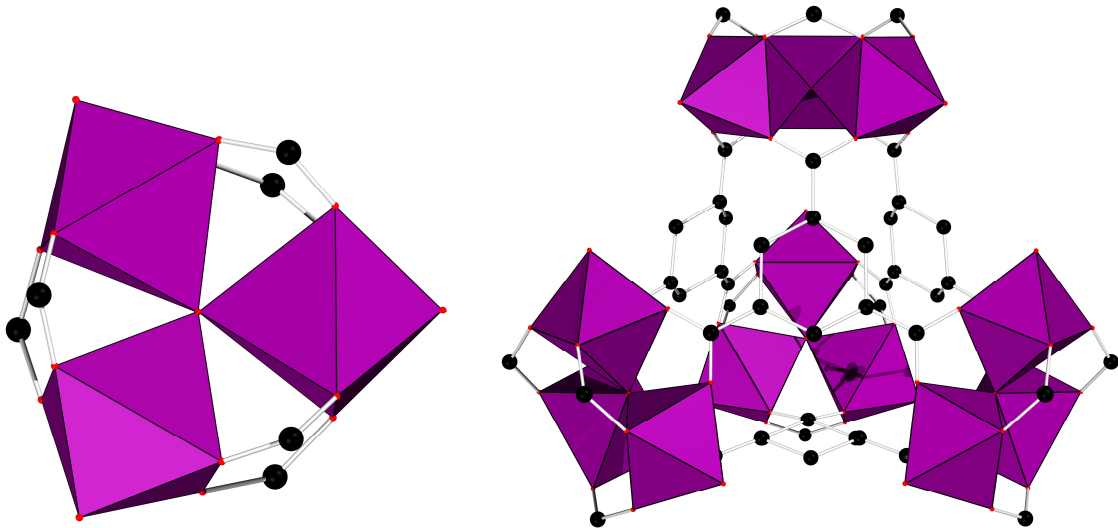


Abbildung 4.2: Links die trimere Baueinheit aus AlO₆-Polyedern, rechts die Struktur eines Supertetraeders in MIL-101 dargestellt ohne Aminogruppen. AlO₆-Polyeder sind in violett dargestellt, Sauerstoffatome sind in rot, Kohlenstoffatome in schwarz gezeigt.

Im Gegensatz zu Al-MIL-53-NH₂ weist Al-MIL-101-NH₂ damit ein starres, mesoporöses Netzwerk mit drastisch erhöhter Sorptionskapazität auf. Al-MIL-101-NH₂ konnte zum einen bereits selbst als basischer Katalysator eingesetzt werden,⁹⁸ zum anderen stellt es aufgrund der Porengröße ein passendes Trägermaterial für molekulare Katalysatoren dar.⁹⁹

Eine Serie von drei unfunktionalisierten Aluminium-MOFs konnte basierend auf 1,3,5-Benzentricarbonsäure (Trimesinsäure oder H₃BTC) hergestellt werden. Die Struktur von [Al₃O(OH)(H₂O)₂(BTC)₂] (Al-MIL-100) weist dabei starke Ähnlichkeit zur Struktur von MIL-101 auf.¹⁰⁰ Allerdings sind die trimeren anorganischen Baueinheiten über Trimesatanionen verknüpft, die nicht die Kanten, sondern die Flächen des Supertetraeders bilden. Diese verkleinerten Supertetraeder sind ebenfalls analog zum zeotypen MTN-Netzwerk angeordnet, so dass ein mesoporöser MOF entsteht. Während im Fall von Al-MIL-101-NH₂ bisher noch keine Daten zur lokalen Koordinationsumgebung von Al³⁺ publiziert wurden, konnte für Al-MIL-100 bereits gezeigt werden, dass die Spitzen der AlO₆-Polyeder, die für gewöhnlich von zwei Wassermolekülen und einem Hydroxidion gebildet werden, teilweise entfernt werden können.¹⁰¹ So lässt sich die oktaedrische Koordination des Al³⁺-Ions durch Entfernung der koordinierten Wassermoleküle partiell in eine quadratisch pyramidale Umgebung umwandeln, so dass Al³⁺ als Lewissäure wirkt.¹⁰²

Ein weiteres Aluminiumtrimesat, mit verringerter Sorptionskapazität im Vergleich zu Al-MIL-100, stellt $[\text{Al}_8(\text{OH})_{12}(\text{H}_2\text{O})_3(\text{OH})_3(\text{BTC})_3]$ (Al-MIL-110) dar. In diesem MOF sind achtkernige Aluminium-Oxo-Cluster über Trimesatanionen so verknüpft, dass hexagonale Kanäle mit einem Durchmesser von 1.6 nm entstehen (Abbildung 4.3).¹⁰³

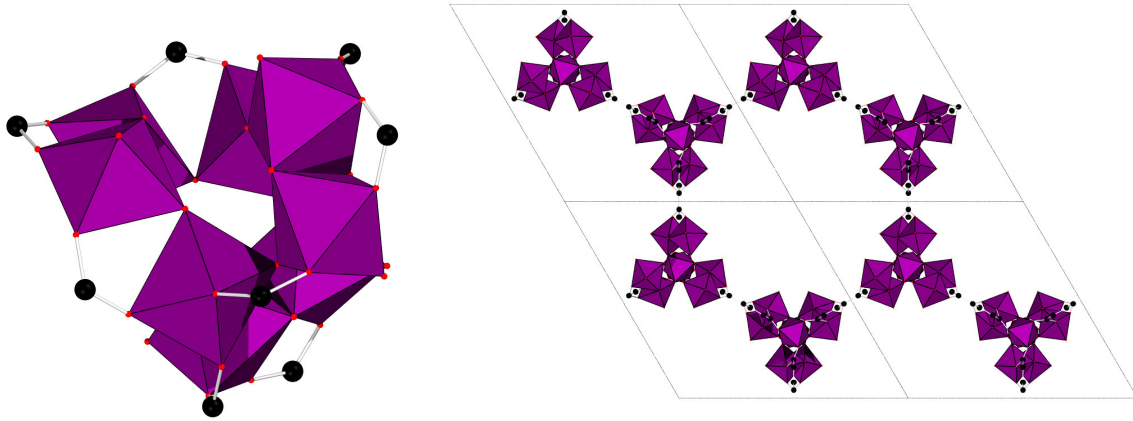


Abbildung 4.3: Links der achtkernige Aluminium-Oxo-Cluster aus MIL-110 inklusive der Carboxylatgruppen, rechts eine 2x2x2-Superzelle mit der Netzwerk-Struktur von Al-MIL-110 betrachtet entlang der *c*-Achse. AlO_6 -Polyeder sind in violett dargestellt, Sauerstoffatome sind in rot, Kohlenstoffatome in schwarz gezeigt.

Zur Strukturbestimmung für Al-MIL-110 wurde ein spezieller Aufbau zur Einkristallröntgenbeugung entwickelt, da die maximale Kristallgröße nur $3 \times 3 \times 10 \mu\text{m}$ betrug. Dieses Mikrodiffraktion-Setup konnte soweit perfektioniert werden, dass sogar die Strukturbestimmung von Al-MIL-100 möglich war, dessen Kristallgröße nur $8 \mu\text{m}^3$ betrug. Beide Verbindungen entstehen im selben hydrothermalen System Al^{3+} / Trimesinsäuretrimethylester / Wasser / Salpetersäure. Während Al-MIL-110 nach mehreren Tagen bei pH-Werten nahe 0 entsteht, kann reines Al-MIL-100 nur bei einem pH-Wert nahe 1 nach wenigen Stunden Reaktionszeit erhalten werden. Die dritte Verbindung in der Reihe der Aluminiumtrimesate ist $[\text{Al}_{12}\text{O}(\text{OH})_{18}(\text{H}_2\text{O})_3(\text{Al}_2(\text{OH})_4)(\text{BTC})_6]$ oder Al-MIL-96,¹⁰⁴ das bei höherem pH-Wert bereits nach einem Tag isoliert werden kann. Die Ähnlichkeit der Synthesebedingungen zeigt zum einen eine Empfindlichkeit der Synthese, die für Al-MOFs häufig beobachtet wird. Zum anderen demonstriert sie aber auch die Vielfalt an möglichen Strukturen, die beim Einsatz von Al^{3+} -Salzen erwartet werden kann. Diese Vielfalt ist wahrscheinlich durch die komplexe wässrige Chemie von Al^{3+} -Ionen begründet.¹⁰⁵ Die Struktur von Al-MIL-96 enthält ebenfalls die trimeren Baueinheiten, die in MIL-100 und MIL-101 beobachtet werden, basiert aber hauptsächlich auf zweidimensionalen, gewellten Schichten von kondensierten AlO_6 -Polyedern. Die

Trimesatanionen dienen dann der Verknüpfung zu einem dreidimensionalen Netzwerk. Im Vergleich mit Al-MIL-100 und Al-MIL-110 weist Al-MIL-96 die kleinsten Poren und die geringste Kapazität auf. Durch die starke Wechselwirkung mit Adsorbaten ist allerdings eine vielversprechende Selektivität bei der Trennung von fünfgliedrigen Kohlenwasserstoffen zu beobachten.¹⁰⁶

Tetracarbonsäuren wurden ebenfalls erfolgreich zur Synthese poröser Aluminium-MOFs eingesetzt. Ausgehend von 1,2,4,5-Benzentetracarbonsäure (H_4BTeC) konnte zum einen die zu Al-MIL-53 analoge Verbindung $[Al(OH)(H_2BTeC)]$ oder MIL-121 beobachtet werden.¹⁰⁷ Allerdings besitzt dieser MOF nur eine sehr limitierte Porosität, da zwei nichtkoordinierende Carbonsäuregruppen pro Linkermolekül in die Kanäle ragen. Eine weitere Verbindung die auf diesem Linkermolekül basiert ist $[Al_4(OH)_8(BTeC)]$ oder Al-MIL-120.¹⁰⁸ In diesem MOF basiert die anorganische Baueinheit auf Ketten von kantenverknüpften AlO_6 -Polyedern, die über die komplett deprotonierten Tetracarboxylat-Ionen verknüpft werden (Abb. 4.4). So bilden sich schmale hexagonale Kanäle, die in einer permanenten Porosität resultieren.

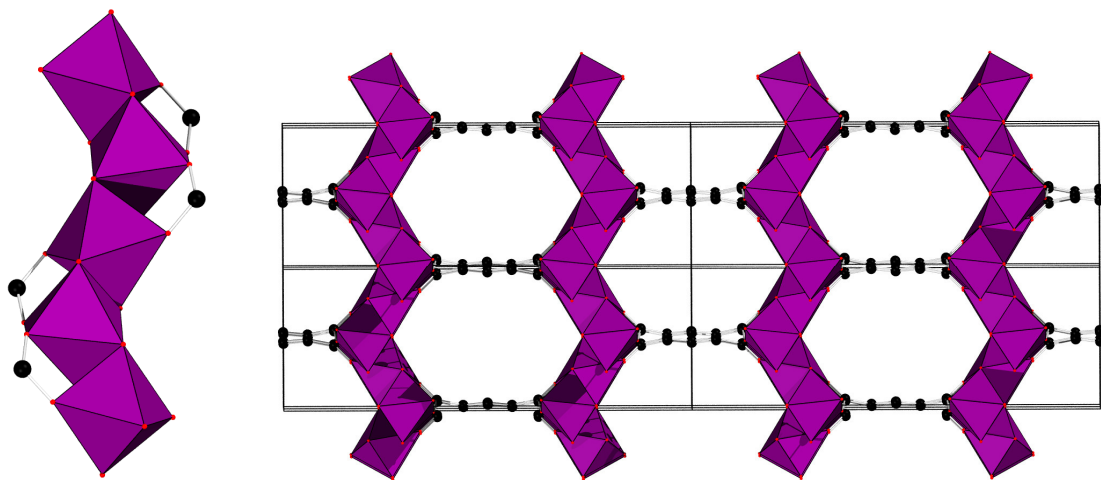


Abbildung 4.4: Links ein Ausschnitt aus der Kette von kantenverknüpften AlO_6 -Polyedern inklusive der Carboxylatgruppen, rechts eine $2 \times 2 \times 2$ -Superzelle mit der Netzwerk-Struktur von Al-MIL-120 betrachtet entlang der c -Achse. AlO_6 -Polyeder sind in violett dargestellt, Sauerstoffatome sind in rot, Kohlenstoffatome in schwarz gezeigt.

Eine weitere Kristallstruktur basierend auf H_4BTeC wurde bei niedrigerem pH-Wert beobachtet. In diesem Fall bildet sich $[Al_2(OH)_2(H_2O)_2(BTeC)]$ oder MIL-118.¹⁰⁹ Die anorganische Baueinheit ähnelt derjenigen in Al-MIL-53 und MIL-121, allerdings koordinieren die Carboxylatgruppen teilweise nicht direkt an die Al^{3+} -Ionen. Stattdessen sind Wassermoleküle an die Kationen koordiniert. Diese Wassermoleküle sind wiederum über Wasserstoffbrückenbindungen an die

Carboxylatgruppen gebunden (Abb. 4.5 links). Wird der MOF kalziniert so werden die Wassermoleküle entfernt und die Carboxylatgruppen koordinieren direkt an die Al^{3+} -Ionen (Abb. 4.5 rechts).

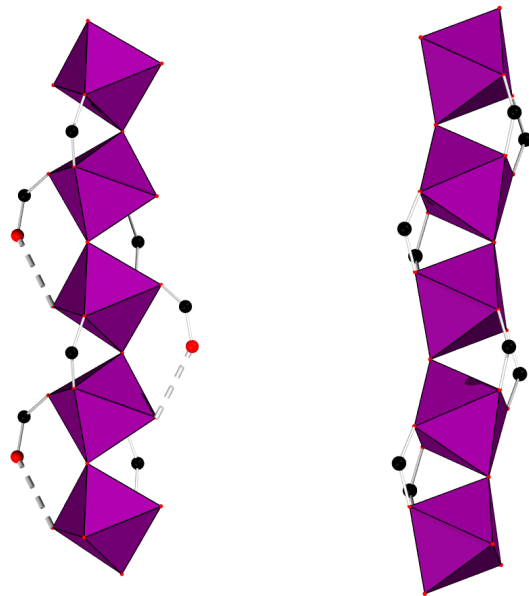


Abbildung 4.5: Links ist ein Ausschnitt aus der anorganischen Baueinheit in MIL-118 gezeigt. Wasserstoffbrückenbindungen sind gestrichelt dargestellt. Rechts ein Ausschnitt aus der anorganischen Baueinheit in kalziniertem MIL-118. AlO_6 -Polyeder sind in violett dargestellt, Sauerstoffatome sind in rot, Kohlenstoffatome in schwarz gezeigt.

Diese Koordination bleibt auch erhalten, wenn Wasser readsorbiert. Die Wassermoleküle werden dann in die Kanäle der Verbindungen eingelagert. Die drei verschiedenen Kristallstrukturen, die für MIL-118 beobachtet werden, sind in Abbildung 4.6 dargestellt.

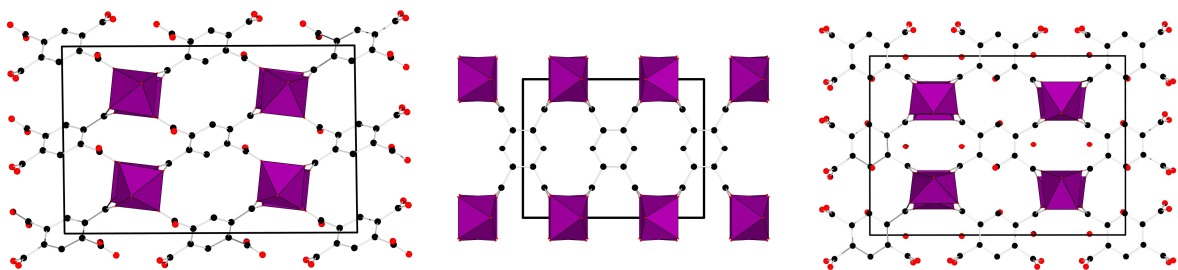


Abbildung 4.6: Elementarzellen der verschiedenen Kristallstrukturen für MIL-118 betrachtet entlang der b -Achse. Links: MIL-118; Mitte: Kalziniertes MIL-118; Rechts: Kalziniertes MIL-118 nach Readsorption von Wasser. AlO_6 -Polyeder sind in violett dargestellt, Sauerstoffatome sind in rot, Kohlenstoffatome in schwarz gezeigt.

Die Porosität von MIL-118 ist allerdings auf die Adsorption von Wasser beschränkt. Ein weiterer Aluminium-MOF, der für photokatalytische Experimente eingesetzt wurde ist $[\text{Al}_2(\text{OH})_2(\text{PTB})]$ oder Al-PMOF.¹¹⁰ Die anorganische Komponente ist die

Gleiche wie in Al-MIL-53, allerdings sind die Ketten über Porphyrintetrabenzoat-Ionen (PTB, Abb. 4.7 links) verknüpft, wodurch ein Netzwerk mit permanenter Porosität entsteht (Abb. 4.7 rechts).

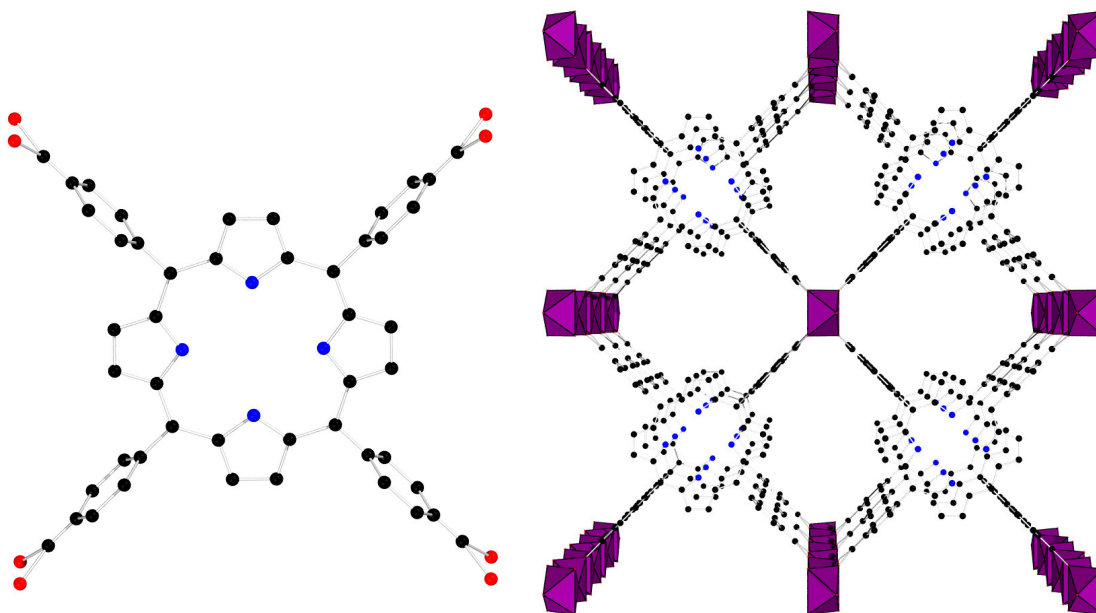


Abbildung 4.7: Links der Porphyrintetrabenzoat-Linker, rechts die Netzwerk-Struktur des Al-PMOF betrachtet entlang der *b*-Achse. AlO₆-Polyeder sind in violett dargestellt, Sauerstoffatome sind in rot, Kohlenstoffatome in schwarz und Stickstoffatome in blau gezeigt.

Die photokatalytischen Eigenschaften dieses MOFs werden durch das Linkermolekül bestimmt. Dabei können die Protonen innerhalb des Porphyrinkerns auch durch Zn²⁺-Ionen ausgetauscht werden. Beide MOFs zeigten eine katalytische Aktivität bei der photochemischen Wasserspaltung in O₂ und H₂.¹¹⁰

Alle bisher beschriebenen Verbindungen haben gemein, dass entweder Wasser oder DMF als Lösungsmittel eingesetzt wurde. Eine Ausnahme stellt die Verbindung [Al₄(OH)₂(OCH₃)₄(BDC-NH₂)₃] oder CAU-1 dar.¹¹¹ Diese wird in Methanol ausgehend von 2-Aminoterephthalsäure hergestellt. Die anorganische Baueinheit ist ein achtkerniger, zyklischer Cluster der aus mittels Hydroxidionen ecken- und mittels Methanolationen kantenverknüpften Al³⁺-Ionen aufgebaut ist (Abb. 4.8 links). Die Cluster sind zwölfmal zu benachbarten Baueinheiten verknüpft, so dass ein Netzwerk entsteht, das analog zur kubisch innenzentrierten Kugelpackung aufgebaut ist (Abb. 4.8 rechts). So entstehen in Analogie zur Kugelpackung tetraedrische und oktaedrische Kavitäten, die über trigonale Fenster miteinander verbunden werden.

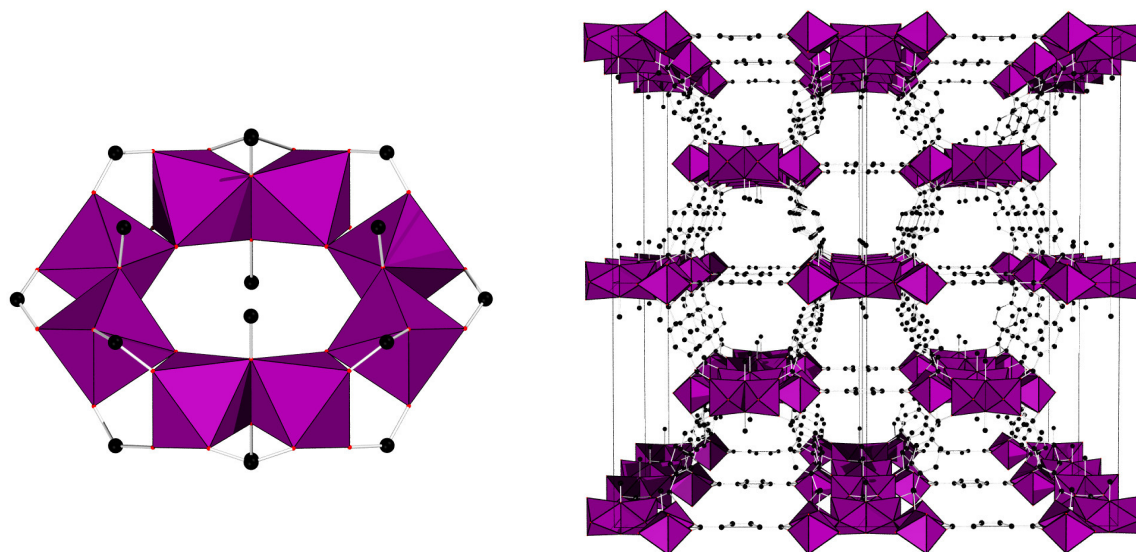


Abbildung 4.8: Links die oktamere Baueinheit aus AlO_6 -Polyedern gezeigt mit Carboxylatgruppen, rechts eine $2 \times 2 \times 2$ -Superzelle mit der Struktur des CAU-1 Netzwerks dargestellt ohne Aminogruppen und betrachtet entlang der b -Achse. AlO_6 -Polyeder sind in violett dargestellt, Sauerstoffatome sind in rot, Kohlenstoffatome in schwarz gezeigt.

CAU-1 konnte unter Einsatz von 2-Aminoterephthalsäure und 2,5-Dihydroxyterephthalsäure hergestellt werden.¹¹² Es wurde auch gezeigt, dass das Lösungsmittel Methanol während der Synthese als methylierendes Reagens auf die Aminogruppen wirken kann.¹¹³ Außerdem können die in die anorganische Baueinheit eingebauten Methanolationen nach der Synthese durch thermische Behandlung gegen Hydroxidionen ausgetauscht werden.

Das dominierende Strukturmotiv für Aluminium-MOFs ist also die Verknüpfung von AlO_6 -Polyedern zu Ketten, die sowohl über Ecken als auch über Kanten vollzogen werden kann. Dieses Motiv findet sich auch in weiteren, nicht-porösen Aluminium-MOFs wie in $[\text{Al}_2(\text{OH})_2(\text{NTeC})]$ oder Al-MIL-122 (basierend auf 1,4,5,8-Naphthalentetracarboxylationen = NTeC)¹¹⁴ und $[\text{Al}(\text{OH})(\text{ABDC})]$ oder Al-MIL-129 (basierend auf 4,4'-Azobenzendicarboxylationen = ABDC).¹¹⁵ Die Baueinheit wird auch bei anderen Verbindungen basierend auf dreiwertigen Ionen gefunden, so zum Beispiel für Ga^{3+} ,^{116,117} oder In^{3+} ,^{118,119} aber auch für Übergangsmetalle wie Fe^{3+} ,¹²⁰ Cr^{3+} ¹²¹ oder V^{3+} .¹²² Aber auch die trimeren Baueinheiten sind in der Chemie der Übergangsmetall-MOFs häufig zu beobachten, zum Beispiel für Sc^{3+} ,¹²³ V^{3+} ,¹²⁴ Cr^{3+} ¹²⁵ oder Fe^{3+} .¹²⁰ Auch für die oktamere Baueinheit in CAU-1 existiert ein Analogon, welches allerdings ungewöhnlicherweise durch den Ti^{4+} -basierten MOF MIL-125 dargestellt wird.¹²⁶

Die Zusammensetzungen und das jeweilige verwendete Lösungsmittel, sowie die thermischen Stabilitäten und spezifischen Oberflächen der hier beschriebenen porösen Al-basierten Verbindungen sind in Tabelle 4.1 zusammengefasst.

Tabelle 4.1: Eigenschaften der beschriebenen porösen Aluminium-MOFs soweit in der Literatur berichtet.

Trivialname	ideale Summenformel	Lösungsmittel	Zersetzung bei	S _{BET} [m ² /g]
Al-MIL-53	[Al(OH)(BDC)]	H ₂ O	500 °C	1590 (S _{Langmuir})
Al-MIL-53-NH ₂	[Al(OH)(BDC-NH ₂)]	H ₂ O	350 °C	-
DUT-4	[Al(OH)(NDC)]	DMF	430 °C	1308
DUT-5	[Al(OH)(BPDC)]	DMF	430 °C	1613
Al-MIL-101-NH ₂	[Al ₃ (O)OH(H ₂ O) ₂ (BDC-NH ₂) ₃]	DMF	380 °C	2100
Al-MIL-100	[Al ₃ (O)OH(H ₂ O) ₂ (BTC) ₂]	H ₂ O	370 °C	2152
Al-ML-110	[Al ₈ (OH) ₁₂ (OH) ₃ (H ₂ O) ₃ (BTC)]	H ₂ O	-	1408
Al-MIL-118	[Al ₂ (OH) ₂ (H ₂ O) ₂ (BTeC)]	H ₂ O	480 °C	-
MIL-120	[Al ₄ (OH) ₈ (BtetC)]	H ₂ O	340 °C	308
MIL-121	[Al(OH)(BDC(-CO ₂ H) ₂)]	H ₂ O	380 °C	162
Al-PMOF	[Al ₂ (OH) ₂ (PTB)]	DMF	370 °C	1400
CAU-1-NH ₂	[Al ₄ (OH) ₂ (OCH ₃) ₄ (BDC-NH ₂) ₃]	Methanol	310 °C	1500
CAU-1-(OH) ₂	[Al ₄ (OH) ₂ (OCH ₃) ₄ (BDC(-OH) ₂) ₃]	Methanol	300 °C	1370

4.2 High-Throughput Studies of Highly Porous Al-based MOFs

Dieses Manuskript wurde in der vorliegenden Fassung im Dezember 2011 im Journal „Microporous and Mesoporous Materials“ eingereicht.

Die in der Literatur beschriebenen Ergebnisse zur Verwendung von Hochdurchsatzmethoden für die Synthese von Aluminium-MOFs wurde detailliert zusammengefasst. Im Laufe dieser Arbeit wurde außerdem das System Wasser / DMF / Al^{3+} / Linker als äußerst vielversprechend für die Synthese von Aluminium-MOFs identifiziert. Unter anderem konnten die Verbindungen Al-MIL-53-COOH, Al-MIL-96 und Al-MIL-120 ausgehend von 1,2,4-Benzentricarbonsäure, 1,3,5-Benzentricarbonsäure und 1,2,4,5-Benzentetracarbonsäure hergestellt werden. Für alle Synthesen wurde ein archetypisches Hochdurchsatz-Schema verwendet, in dem die Verhältnisse Al^{3+} : Linkermolekül und H_2O : DMF variiert wurden. Dieses Hochdurchsatzexperiment wurde ausgehend von den drei verschiedenen Linkermolekülen durchgeführt, wobei die beschriebenen Verbindungen erhalten wurden. Dies demonstriert klar die Vielseitigkeit des solvothermalen Systems für die Synthese von Al-MOFs. Die schnelle und effiziente Identifizierung von optimalen Synthesebedingungen mittels Hochdurchsatzmethoden sowie die Aufskalierung der Synthese im Mikrowellen-Ofen beweisen die Effizienz der diskutierten Methoden. Im Vergleich zu den Originalsynthesen konnten die Verbindungen unter sehr viel mildereren Synthesebedingungen erhalten werden. Die Reaktionsprodukte wurden mittels Röntgenpulverbeugung, IR-Spektroskopie, CHNS-Analyse und Stickstoff-Sorption charakterisiert. Dabei zeigte sich, dass die unterschiedlichen Synthesebedingungen zu teilweise drastisch veränderten Eigenschaften führen können. Die Einlagerung von Linkermolekülen in die Poren von MIL-53-COOH führte zu einer offenen Gerüstkonformation und damit zu einer permanenten Porosität für die in dieser Arbeit hergestellte Verbindung, während die literaturbekannte Verbindung $[\text{Al}(\text{OH})(\text{O}_2\text{C}-\text{C}_6\text{H}_3-\text{COOH}-\text{CO}_2)]$ keine Porosität gegenüber Stickstoff aufweist. Und während für Al-MIL-120 $[\text{Al}_4(\text{OH})_8(\text{C}_{10}\text{O}_8\text{H}_2)]$ permanente Porosität beobachtet wurde, zeigte die in dieser Arbeit hergestellte Verbindung keine Adsorption von Stickstoff und eine verringerte Stabilität. Im Gegensatz dazu wurde für Al-MIL-96 $[\text{Al}_{12}\text{O}(\text{OH})_{18}(\text{H}_2\text{O})_3(\text{Al}_2(\text{OH})_4)(\text{btc})_6]$ keine Stickstoffadsorption beobachtet, während das in dieser Arbeit hergestellte Produkt geringe Verunreinigungen aber auch eine permanente Porosität aufwies.

High-Throughput Studies of Highly Porous Al-based MOFs

Helge Reinsch, Norbert Stock

Abstract:

The use of high-throughput (HT) methods for the discovery of compounds as well as for the synthesis optimization in the field of porous aluminium MOFs is summarized. Taking the requirements of an industrial process into account, new synthesis procedures have been developed that demonstrate the versatility of the HT method. This is exemplified by the results that were obtained for the solvothermal system $\text{Al}_2(\text{SO}_4)_3 \cdot 18\text{H}_2\text{O}$ / polycarboxylic acid / H_2O / DMF. Under rather mild reaction conditions, compared to the previously reported procedures, the Al-MOFs MIL-53-COOH, MIL-96, and MIL-120 were obtained employing 1,2,4-benzenetricarboxylic acid, 1,3,5-benzenetricarboxylic acid, and 1,2,4,5-benzenetetracarboxylic acid, respectively. Applying the HT methodology combined with microwave(MW)-assisted heating, the synthesis procedure were rapidly established, optimized and scaled up. The obtained solids were characterized by X-ray powder diffraction (XRPD), elemental analysis, vibrational spectroscopy and nitrogen sorption measurements. The properties of these MOFs are discussed in comparison with literature values.

1. Introduction

Among the still increasing number of porous metal-organic frameworks (MOFs), the materials based on aluminium and aromatic carboxylates take an exceptional position. Aluminium is an attractive inorganic component for the construction of MOFs since its salts are non-toxic readily commercially available at low-cost. The low toxicity plays an important role in the handling of the materials as well as for the use in medical applications. The low molar mass of aluminium is especially of interest for the gravimetric capacity for gas storage applications. Furthermore, most of the reported Al-based MOF materials exhibit remarkable thermal and chemical stabilities, which are only excelled by chromium- or zirconium-based MOFs.^[1,2] Thus, Al-based MOFs are already commercially available and are used for tests in large-scale applications.^[3] Despite these promising developments, the research in the field of Al-MOFs remains challenging and rather scarce, due to several reasons. For example the mostly polycrystalline nature of the reaction products impedes structure determination especially since the structural diversity of polynuclear Al-clusters leads to the formation of unique framework structures.^[4] Therefore, the known materials are very limited in number. Their structures were determined from single crystal microdiffraction data,^[5,6] XRPD measurements^[7,8] or deduced from related framework structures.^[9,10] These methods necessitate a synthesis procedure that is optimized towards a maximum crystal size or the highest possible crystallinity to give reliable results. In this context, the use of high-throughput-methods has shown to be perfectly suitable.^[11,12] The three main principles for this methodology are miniaturization, parallelization and automation of process steps.^[13] In our case, the reactor size is miniaturized which results in a lower consumption of chemicals, while the parallelized synthesis in multiclaves assures the identity of reaction conditions. The automated dosing of chemicals and the characterization by means of HT-XRPD help to save time and assist in working economically more efficient. Therefore, the HT-methods are an ideal tool for the discovery of new materials as well as for the optimization of the reaction conditions towards a certain property of the product.^[14]

Herein, we briefly summarize in section 2 the use of HT methods for the synthesis of new Al-MOFs and describe in section 3 an easy synthesis protocol for the HT-assisted discovery of Al-MOFs under mild reaction conditions, the synthesis optimizations by automated MW synthesis and the scale up of the syntheses up to the 500 mg scale.

2. High-throughput methods for the synthesis of aluminium MOFs

The HT-methods that are applied in our group were developed over years towards a multifunctional tool for the synthesis of inorganic-organic hybrid compounds. Besides the conventional dielectric heating method, we also implemented MW-assisted heating^[15] and a reactor with a programmable temperature gradient^[16] into our high-throughput workflow. One focus of our work lies on the synthesis of inorganic-organic hybrid compounds based on phosphonates^[17] or functionalized phosphonates^[18] which display a broad variety of interesting structures and properties.^[19] The HT-methods are also an ideal tool for the synthesis of porous MOFs.^[20,21,22] These methods provide an excellent performance in the systematic investigation of even complex solvothermal systems as shown in our recent work, especially in the challenging field of Al-MOFs.^[23,24,25,26]

The multiclaves for conventional heating that are employed in our group contain small Teflon vessels and can be heated up to a maximum temperature of 200°C. The smaller vessels with a volume of 300 μL are used for the 48-multiclave, while the reactors in the 24-multiclave contain up to 2 mL. The latter are preferentially used when solid reactants are employed, due to the easier dosage. For MW-assisted heating, we also use 24-multiclaves, but the Teflon reactors ($V = 2$ mL) are embedded in siliconcarbide blocks.^[15] The temperature-gradient oven (TGradient, Biometra, $T_{\text{max}} = 99.9$ °C) is equipped with small plastic vials ($V = 200$ μL). The maximum gradient that can be accomplished in one reaction is 40 °C.^[16]

For the automated characterization by XRPD a diffractometer with an x,y-stage is used that allows the measurement of up to 96 samples. The characterization is

further accelerated due to the use of an image-plate detector, which enables us to measure the powder patterns for all products of a 48-multiclave within 3 hours. For the experiments that are discussed in this article, the 24-multiclaves for conventional heating were employed.

Parameters that are of great importance in the solvothermal synthesis of MOFs can be generally categorized as process and chemical parameters. Process parameters comprise reactor material, heating method, heating/cooling rate, reaction temperature and time, while chemical parameters cover the chemical composition of the starting mixture, e.g. molar ratio of the starting materials, pH, solvents/solvent mixtures, overall concentration, cation source and the use of templates or precursors. Studies on aluminium MOFs looking at the different aspects are summarized in the following sections.

2.1 Influence of cation source

The system $\text{Al}^{3+}/\text{H}_3\text{BTB}/\text{DMF}$ (H_3BTB = 1,3,5-benzene-tribenzoic acid) was investigated at 180 °C using the 24 multiclave.^[23] Two metal sources, $\text{AlCl}_3 \cdot 6\text{H}_2\text{O}$ and $\text{Al}(\text{NO}_3)_3 \cdot 9\text{H}_2\text{O}$, were employed in four molar ratios $\text{Al}^{3+} : \text{H}_3\text{BTB}$ for three overall concentration ($2 \times 4 \times 3 = 24$ reactions). The setup as well as the results obtained from the HT-XRPD measurements is presented in Figure 1. The use of aluminium chloride leads exclusively to X-ray amorphous products, while the use of aluminium nitrate results in the formation of $[\text{Al}(\text{BTB})]$, denoted CAU-4. Excess of Al^{3+} leads to the formation of X-ray amorphous or crystalline by-products. The overall concentration hardly affects the purity of the compounds, but the most crystalline products were obtained at high concentrations.

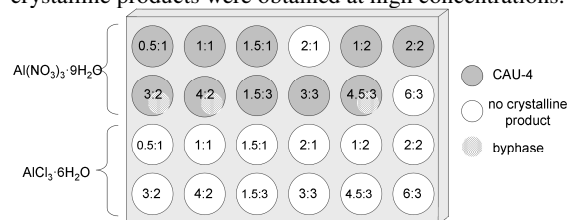


Figure 1: Experiments and results obtained in the system $\text{Al}^{3+}/\text{H}_3\text{BTB}/\text{DMF}$ (H_3BTB = 1,3,5-benzene-tribenzoic acid) varying the aluminium source, the overall concentration and the molar ratios. The numbers correspond to the amount of Al^{3+} relative to the amount of H_3BTB (1 = 0.09 mmol).

Further optimization of the process parameters and the use of benzoic acid as an additive led to the formation of the highly porous and stable MOF. CAU-4 exhibits a honeycomb network with one-dimensional pores with diameter of 9.6 Å, is thermally stable up to 400 °C in air and has a BET-surface area of 1520 m²/g and a micropore volume of 0.61 cm³/g.^[23]

2.2 Solvent Screening

Considering a given system consisting of a metal ion and a linker molecule, the solvent has the most profound influence on the product formation.^[21,27] Therefore, the system $\text{Al}^{3+}/\text{H}_2\text{BDC-NH}_2/\text{solvent}$ ($\text{H}_2\text{BDC-NH}_2$ = aminoterephthalic acid) was investigated at 125 °C.^[24] The two metal sources, $\text{AlCl}_3 \cdot 6\text{H}_2\text{O}$ and $\text{Al}(\text{NO}_3)_3 \cdot 9\text{H}_2\text{O}$, were used in three molar ratios $\text{Al}^{3+} : \text{H}_2\text{BDC-NH}_2$ and in addition to DMF the solvents CH_3OH , $\text{C}_2\text{H}_5\text{OH}$ and CH_3CN were employed, i.e. $2 \times 3 \times 4 = 24$ reactions (Figure 2). Acetonitrile as the solvent only yields recrystallized $\text{H}_2\text{BDC-NH}_2$ as the crystalline product. The

use of $\text{Al}(\text{NO}_3)_3 \cdot 9\text{H}_2\text{O}$ results exclusively in the formation of Al-MIL-53-NH_2 , which is known to form under a wide variety of reaction conditions.^[28,29] The system is especially interesting when DMF and methanol is employed in combination with $\text{AlCl}_3 \cdot 6\text{H}_2\text{O}$. Thus Al-MIL-101-NH_2 was observed for the first time using DMF as the solvent. The synthesis optimization led to a highly crystalline product whose formation was recently studied by in situ X-ray diffraction.^[29] In methanol the thitherto unprecedented MOF CAU-1 [$[\text{Al}_4(\text{OH})_2(\text{OCH}_3)_4(\text{BDC-NH}_2)_3]$] was obtained.

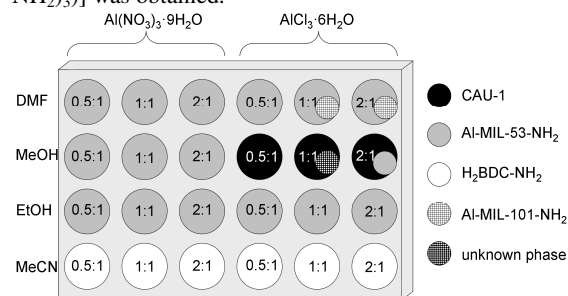


Figure 2: Experiments and results obtained in the system $\text{Al}^{3+}/\text{H}_2\text{BDC-NH}_2/\text{solvent}$ ($\text{H}_2\text{BDC-NH}_2$ = aminoterephthalic acid) varying the aluminium source, the overall concentration, the molar ratios and the solvent. The numbers in the circles represent the molar ratio of $\text{Al}^{3+} : \text{H}_2\text{BDC-NH}_2$.

Further optimization of the reaction conditions resulted in a highly crystalline, phase pure product. Under microwave irradiation this compound is even formed within a few minutes.^[30,31] The reliable synthesis procedure resulted in the thorough characterization and application of CAU-1. Thus, the separation of gases^[32] and liquids^[33] as well as the post-synthetic modification has been described.^[34] The precise control of the synthesis and activation conditions allowed the modification of the inorganic and organic brick in an Al-based MOF by direct and post-synthetic synthesis routes.^[35]

2.3 Ternary Systems

The pH of a reaction mixture is another commonly discussed parameter that determines the product formation. The addition of an acid or a base increases the complexity of a reaction system and therefore the number of reactions that need to be carried out for a systematic investigation. Based on the results of CAU-1, the influence of the addition of a base to the system $\text{Al}^{3+}/\text{H}_2\text{BDC}/\text{methanol}$ (H_2BDC = terephthalic acid) was studied (Figure 3). Thus at a constant molar ratio of $\text{Al} : \text{H}_2\text{BDC} = 4:1$ the investigation of the influence of the overall concentration and the amount of NaOH led to the discovery of the archetype of a new family of MOFs, denoted CAU-3.^[25] At a high pH and low overall concentration of the reactants [$\text{Al}_2(\text{OCH}_3)_4(\text{BDC})$], denoted CAU-3-BDC, is formed as a pure phase material. Higher concentrations and more acidic conditions resulted in formation of the well known compounds MIL-53 and CAU-1-BDC.

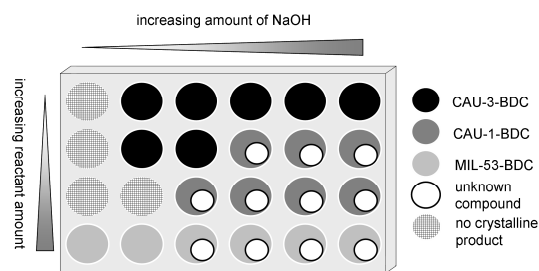


Figure 3: Results obtained in the system $\text{Al}^{3+}/\text{H}_2\text{BDC}/\text{CH}_3\text{OH}/\text{NaOH}$ (H_2BDC = terephthalic acid) varying the overall concentration and the amount of NaOH.

Based on these results the reaction conditions for the isoreticular compounds containing aminoterephthalate (CAU-3-BDC- NH_2) or 2,6-naphthalenedicarboxylate ions (CAU-3-NDC) could be established in an elaborate process. All three compounds were shown to be highly porous and to the best of our knowledge CAU-3-NDC exhibits the highest porosity reported for an Al-based MOF hitherto.

3. Experimental Section

3.1. General

All chemicals used for the synthesis are commercially available and were used without further purification. For the HT-assisted synthesis we used our 24-high-throughput reactor system based on multiclaves with Teflon inserts with a volume of 2 mL. For the upscaled reactions, we employed a Biotage initiator microwave synthesizer. The high-throughput XRPD studies were carried out on a STOE HT diffractometer equipped with a xy-stage and an IPDS system ($\text{Cu-K}_{\alpha 1}$ radiation) in transmission geometry. High-precision powder diffraction data for MIL-96 and MIL-120 was measured on a STOE Stadi-P powder diffractometer equipped with a linear position sensitive detector system ($\text{Cu-K}_{\alpha 1}$ radiation). The data for the Al-MIL-53-COOH was measured on a Panalytical X-pert Highscore in reflection geometry ($\text{Cu-K}_{\alpha 1}$ radiation). MIR spectra were recorded on an ATI Matheson Genesis spectrometer in the spectral range of 400-4000 cm^{-1} equipped with an ATR unit. The CHNS-analyses were measured with an Eurovektor EuroEA elemental analyzer. Sorption experiments were performed using a Belsorp-max instrument (BEL JAPAN INC.). Before the sorption experiments, the samples were activated at 200 °C under vacuum (0.1 mbar) over night. The software package used for the indexing and lattice parameter refinement was TOPAS Academics.^[36]

3.2 Synthesis Principle

For the synthesis of porous aluminium based MOFs, it is often necessary to apply rather high temperatures (> 200°C), which leads to a high autogenous pressure in the reactor (> 20 bar). These drastic conditions, the utilization of precursors or the price of the organic solvent are important drawbacks for the direct transfer of the synthesis protocol from lab-scale to the industrial scale.^[3] Another complication in industrial scale up synthesis is the source of the metal ions. Metal chlorides are highly corrosive and metal nitrates and perchlorates are undesirable due to their oxidizing properties.^[3] During our ongoing research in the field of porous Al-MOFs, we observed that in the solvothermal system $\text{Al}_2(\text{SO}_4)_3 \cdot 18\text{H}_2\text{O}$ / polycarboxylic acid / H_2O / DMF with H_2O as the major solvent, several Al-based MOFs

can be readily obtained under mild reaction conditions. The use of $\text{Al}_2(\text{SO}_4)_3 \cdot 18\text{H}_2\text{O}$ avoids the afore mentioned problems and although the organic solvents is not excluded from the synthesis, its amount is only in the range of 10 – 40 %. Due to the low reaction temperatures (125 – 145 °C) the autogenous pressure inside the reactor does not exceed 5 bar. To demonstrate the versatility of our approach, we created an “archetype” working scheme which was used for the screening of three different systems. Here, we present the results using 1,2,4-benzenetricarboxylic acid, 1,3,5- benzenetricarboxylic acid and 1,2,4,5-benzenetetracarboxylic acid. These were chosen on the basis of their commercial availability and price.

In the first step of our synthesis approach, we screened the solvothermal systems for the optimal reaction conditions. The setup was for all investigated linker molecules as follows: in one 24-HT reactor we carried out the reactions for four different solvent ratios H_2O : DMF, using two different ratios of Al^{3+} : linker at three different concentrations (Fig. 4).

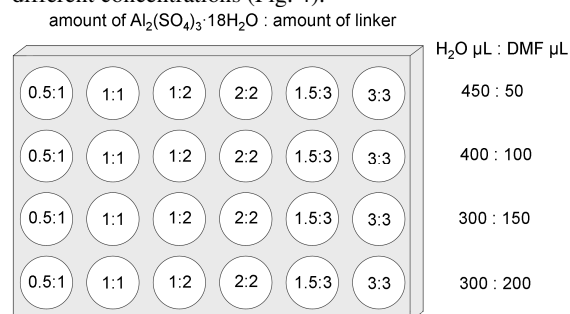


Figure 4: The archetype scheme for the high-throughput reactions carried out in the first step of our synthesis approach. A value of 1 corresponds to 0.05 mmol of reactant.

The filling degree was kept at 500 μL and the reactors were in all cases heated at 135 °C for 5 hours. To identify the reaction products, they were characterized by HT-XRPD measurements. The data also allowed judging the quality of the products regarding their purity and crystallinity. The optimal conditions were used in step 2 of our approach to scale up the synthesis in glass reactors using MW assisted heating ($V_{\text{max}} = 5 \text{ mL}$).

In the second step, four MW reactions per linker were carried out: in the first three the temperature was varied (125 °C, 135 °C and 145 °C) and in the fourth reactor, the influence of stirring on the product formation at 135 °C was identified. Thus, the sensitivity of the solvothermal system towards up-scaling is also tested. Since solvothermal reactions can be quite sensitive to the heating method (dielectric / microwave) and the reactor material used (glass / Teflon), the robustness of the synthesis procedure is checked. Due to the faster heating in a microwave oven,^[31] the reaction times were decreased to 4 hours. In the third step, the optimized conditions were further applied to larger MW-reactors ($V_{\text{max}} = 20 \text{ mL}$) and the resulting products were finally characterized in detail.

3.3 HT-Study using 1,2,4-Benzenetricarboxylic acid, Al-MIL-53-COOH

In the solvothermal system Al^{3+} / 1,2,4-Benzenetricarboxylic acid / H_2O / DMF, we exclusively observed the formation of the COOH-functionalized analogue of large-pore form of Al-MIL-53 (figure not shown). The product with the highest crystallinity was

obtained from a mixture with the composition of 0.15 mmol 1,2,4-benzenetricarboxylic acid (trimellitic acid), 0.15 mmol $\text{Al}_2(\text{SO}_4)_3 \cdot 18\text{H}_2\text{O}$, 400 μL H_2O and 100 μL DMF. Other fractions of DMF led to a decrease in crystallinity. At the lowest overall concentrations of the reactants, the obtained solids were only weakly crystalline showing very few and broad Bragg-peaks (Fig. S1). The reactions in the MW oven showed, that an increase in temperature had a negative influence on the formation of Al-MIL-53-COOH, while a temperature of 125 °C or stirring at 135 °C resulted in almost no differences in the powder pattern.

3.4 HT-Study using 1,3,5-Benzenetricarboxylic acid – Al-MIL-96

Employing 1,3,5-benzenetricarboxylic acid (trimesic acid) as the linker molecule, the formation of two different crystalline MOFs could be observed in the system Al^{3+} / trimesic acid / H_2O / DMF (Fig. 5). Other researchers have shown that the well-known trimesate-based Al-MOFs Al-MIL-100,^[37] Al-MIL-110,^[5] and Al-MIL-96^[38] can be obtained under the same reaction conditions at high reaction temperatures in water just by varying the reaction time.^[39] Corresponding to their density as well as their thermodynamic stability, Al-MIL-100 is observed first, Al-MIL-110 at an intermediate stage and the most stable compound obtained in the end is Al-MIL-96. These findings are in good agreement with our results. Although we applied rather mild reaction conditions, the formation of MIL-96 is observed in all vessels and thus it is the dominant phase (Fig. 5).

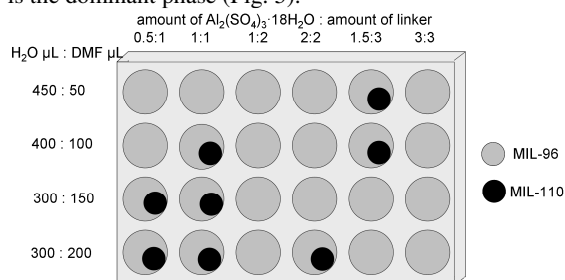


Figure 5: The results of the high-throughput reactions carried out with trimesic acid applying the archetype scheme. A value of 1 corresponds to 0.05 mmol of reactant.

Based on the composition 0.1 mmol carboxylic acid, 0.1 mmol $\text{Al}_2(\text{SO}_4)_3 \cdot 18\text{H}_2\text{O}$, 450 μL H_2O and 50 μL DMF, the pure compound with highest crystallinity was observed. The increase of the fraction of DMF results in the formation of MIL-110 as a minor product, especially at lower overall concentrations (Fig. S2). Thus the composition of the solvent mixture is crucial for the synthesis of the pure MIL-96. At higher overall concentrations and increased fractions of DMF, broad Bragg-peaks are observed; the formation of Al-MIL-100 was not detected under these reaction conditions. The MW reactions demonstrate the sensitivity of the systems towards the changed reaction conditions employing the MW-assisted heating. At 125 °C and 135 °C, the formation of MIL-110 as an impurity is observed, but at 135 °C under stirring or at the elevated temperature of 145 °C, the pure product was obtained.

3.5 HT-Study using 1,2,4,5-Benzenetetracarboxylic acid – Al-MIL-120

The use of benzenetetracarboxylic acid (pyromellitic acid) results in the formation of two different crystalline

products in well-defined fields of formation (Fig. 6). Al-MIL-121^[26], which is a doubly COOH-functionalized analogue of Al-MIL-53, is observed at low fractions of DMF, especially for higher overall concentrations of Al^{3+} and linker (Fig. S3). It is exclusively observed for the ratios $\text{Al}_2(\text{SO}_4)_3 \cdot 18\text{H}_2\text{O}$: linker = 1:2 and 1.5:3, i.e. equimolar amounts of Al^{3+} and linker = 2:2 and 3:3 (Fig. 6).

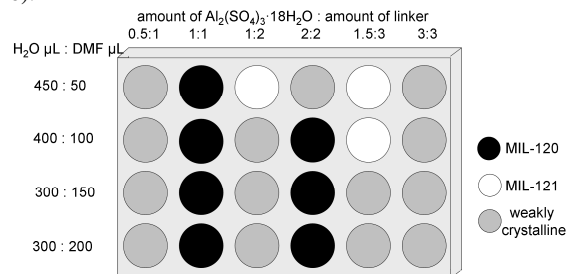


Figure 6: The results of the high-throughput reactions carried out with pyromellitic acid applying the archetype scheme. A value of 1 corresponds to 0.05 mmol of reactant.

The second MOF observed is MIL-120,^[6] which is mainly formed at low and intermediate overall concentrations and an excess of Al^{3+} . Thus, the molar ratios Al^{3+} : linker in the starting mixture correspond to the ones in the products, which is 1:1 for MIL-121 and 1:2 for MIL-120. The MIL-120 product of highest crystallinity is obtained from mixtures with a high DMF fraction. Due to its reported microporous nature, further steps for the synthesis optimization were applied starting with the composition 0.05 mmol pyromellitic acid, 0.05 mmol $\text{Al}_2(\text{SO}_4)_3 \cdot 18\text{H}_2\text{O}$, 300 μL H_2O and 200 μL DMF. The increase of the reaction temperature is beneficial but not essential for the crystallinity of the product, while stirring clearly decreases the quality of the product (Fig. S4).

3.6 Scale-up syntheses

In the third step of our approach, the optimized conditions of step 2 were scaled up further and applied to larger MW-reactors ($V_{\text{max}} = 20$ mL). Thus, Al-MIL-53-COOH was obtained from a mixture of 1,2,4-benzenetricarboxylic acid (945 mg, 4.5 mmol), 9 mL of a 0.5 M aqueous solution of $\text{Al}_2(\text{SO}_4)_3 \cdot 18\text{H}_2\text{O}$ (4.5 mmol) and 3.0 mL N,N-dimethylformamide with 3.0 mL H_2O in a 30 mL vial. The reactor was heated in the MW oven without stirring at 135 °C for 4 h. The product was washed with water and dried under ambient conditions. To remove most of the adsorbed solvent molecules (see IR-section), the MOF was activated at 200 °C in vacuum (0.1 mbar) for 12 h. Elemental analysis after activation: found (%): C: 41.5, H 2.5, N 0.5. The high amount of carbon indicates, that linker molecules are embedded inside the channels, which is a common phenomenon for MIL-53-compounds.^[7,20] The sum formula was calculated from the elemental analysis to be $[\text{Al}(\text{OH})(\text{O}_2\text{C}-\text{C}_6\text{H}_3(\text{CO}_2\text{H})-\text{CO}_2)] \cdot (\text{C}_6\text{H}_3(\text{CO}_2\text{H})_{3,0,27}(\text{H}_2\text{O})_{1,08}(\text{DMF})_{0,13}$. For the optimized, upscaled synthesis procedure for MIL-96, a mixture of 1,3,5-benzenetricarboxylic acid (630 mg, 3 mmol), 6 mL of a 0.5 M aqueous solution of $\text{Al}_2(\text{SO}_4)_3 \cdot 18\text{H}_2\text{O}$ (3 mmol) and 1.5 mL N,N-dimethylformamide with 7.5 mL H_2O was heated in a 30 mL vial under stirring up to 135 °C for 4 h. The product was washed with water and dried under ambient conditions. Elemental analysis for MIL-96 $[\text{Al}_{12}\text{O}(\text{OH})_{18}(\text{H}_2\text{O})_3(\text{Al}_2(\text{OH})_4(\text{btc})_6)] \cdot 24\text{H}_2\text{O}$: expected values: C 26.0, H 3.7, found (%): C 31.7, H 3.0, N 1.7, S

2.2. The differing values for carbon and hydrogen and the detection of nitrogen and sulfur indicate, that due to the different synthesis procedure sulfate ions and residual DMF molecules or a decomposition product of the latter are embedded inside the cavities of the framework. Further washing and activation in vacuum did not result in a removal of the nitrogen and sulphur containing species.

For the optimized synthesis procedure for MIL-120, a mixture of 1,2,4,5-benzenetetracarboxylic acid (305 mg, 1.2 mmol), 2.4 mL of a 0.5 M aqueous solution of $\text{Al}_2(\text{SO}_4)_3 \cdot 18\text{H}_2\text{O}$ (1.2 mmol) and 4.8 mL N,N-dimethylformamide together with 4.8 mL H_2O in a 30 mL vial was heated without stirring up to 145 °C for 4 h. The product was washed with water and dried under ambient conditions. Elemental analysis: found (%): C 26.8 H 3.3, N 2.4. Expected values (%) for MIL-120 $[\text{Al}_4(\text{OH})_8(\text{C}_{10}\text{O}_8\text{H}_2)] \cdot 3.5\text{H}_2\text{O}$: C 20.5 H 3.4. We attribute the deviation to the inclusion of DMF molecules or dimethylamine ions, formed during the reaction by hydrolysis of DMF. Washing and thermal activation in vacuum did not lead to a complete removal of these nitrogen species.

4 Results and Discussion

4.1 XRPD measurements

MIL-53-COOH exhibits a rather poor degree of crystallinity, but according to the position of the reflections, the framework is present in the large-pore form. Due to the low number of resolved reflections, the pattern was not indexed. The comparison with the simulated pattern of the large-pore form of Al-MIL-53 shows a reasonable agreement with a small shift towards lower angles (Fig. 7).

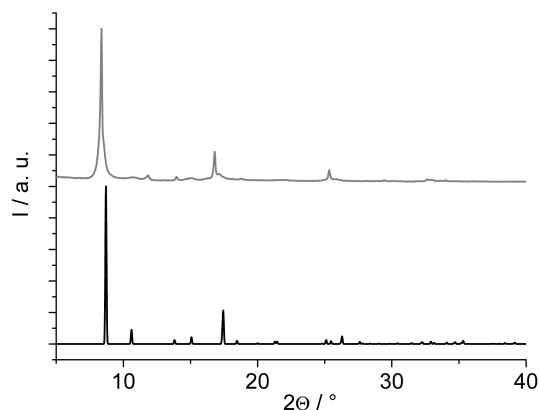


Figure 7: Comparison of the calculated pattern of Al-MIL-53-ht in black and the measured pattern for Al-MIL-53-COOH in grey.

The high degree of crystallinity of MIL-96 allowed the refinement of the cell parameters. The powder pattern was successfully indexed with a hexagonal cell ($a = 14.2942 \text{ \AA}$, $b = 31.2217 \text{ \AA}$, $\text{GoF} = 68$). Due to the extinction conditions, the correct space group $P6_3/mmc$ was suggested by the program. The cell refinement by Pawley methods in this space group led to the refined cell parameters $a = 14.2917(3) \text{ \AA}$ and $b = 31.210(1) \text{ \AA}$ (Fig. 8).

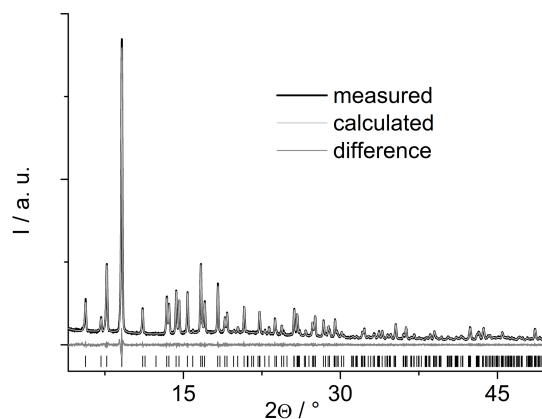


Figure 8: Pawley-Fit for the obtained MIL-96. The measured values are in black, the calculated intensity is in light grey and the difference plot in dark grey. The vertical bars mark the allowed reflections.

The quality of the fit is underlined by the low R_{WP} -value of 5.1%. The refined cell parameters are in excellent agreement with the cell parameters reported in the literature ($a = 14.2074(2) \text{ \AA}$ and $b = 31.2302(9) \text{ \AA}$, space group $P6_3/mmc$).^[38]

The indexing of the powder pattern of MIL-120 led to a monoclinic cell with the parameters $a = 9.8161 \text{ \AA}$, $b = 19.8599 \text{ \AA}$, $c = 7.5324 \text{ \AA}$ and $\beta = 134.72^\circ$. The extinction conditions led to the space group $C2/m$. The cell refinement by Pawley methods (Fig. 9) resulted in the cell parameters $a = 9.8211(2) \text{ \AA}$, $b = 19.8791(5) \text{ \AA}$, $c = 7.5365(2) \text{ \AA}$ and $\beta = 134.73(1)^\circ$.

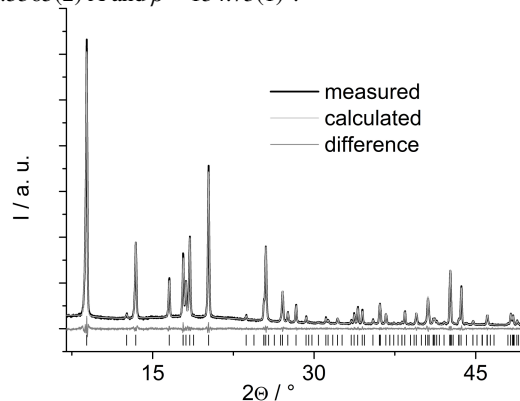


Figure 9: Pawley-Fit for the obtained MIL-120. The measured values are in black, the calculated pattern is in light grey and the difference plot in dark grey. The vertical bars mark the allowed reflections.

These values are in quite good agreement with the ones reported in the literature (space group $C2/m$, $a = 9.748(1) \text{ \AA}$, $b = 20.048(1) \text{ \AA}$, $c = 7.489(1) \text{ \AA}$ and $\beta = 134.42(1)^\circ$).^[6] The R_{WP} -value amounts to 5.0 %

4.2 Nitrogen Sorption

The sorption measurements were carried out on the activated samples that were heated overnight at 200 °C in vacuum (0.1 mbar) to remove solvent from the pores. The isotherm for MIL-120 shows almost no uptake of N_2 before the condensation at $p/p_0 = 1$. Thus, the pores are not accessible for nitrogen molecules. The isotherms of Al-MIL-96 and the Al-MIL-53-COOH exhibit type-I isotherms which indicate the existence of micropores (Fig. 10).

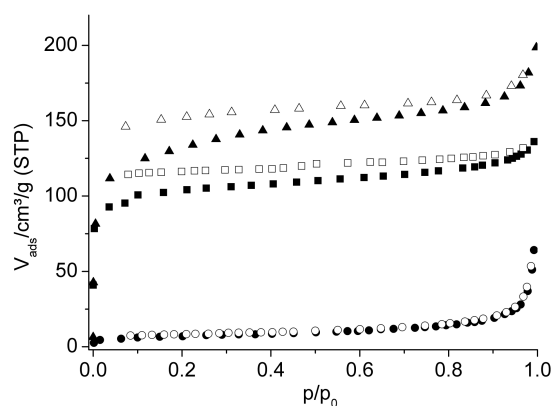


Figure 10: Nitrogen sorption isotherms for the described compounds. Triangles represent the data for MIL-96, squares for MIL-53-COOH and circles for MIL-120. Filled symbols represent the adsorption-, empty symbols represent the desorption branch.

The apparent specific BET surface areas are $A_{\text{BET}} = 393 \text{ m}^2/\text{g}$ for Al-MIL-53-COOH and $A_{\text{BET}} = 483 \text{ m}^2/\text{g}$ for Al-MIL-96. The micropore volumes, determined from the amount adsorbed at $p/p_0 = 0.5$ are $V_{\text{MIC}} = 0.23 \text{ cm}^3/\text{g}$ for MIL-96 and $V_{\text{MIC}} = 0.17 \text{ cm}^3/\text{g}$ for MIL-53-COOH, respectively. The desorption branches for the two porous compounds exhibit an atypical hysteresis. This could be attributed to the presence of molecules that were not fully removed from the cavities and to the small pores of the frameworks that slow down the desorption kinetics.

4.3 Vibrational Spectroscopy

All IR-spectra were measured before and after thermal activation under vacuum. For Al-MIL-53-COOH significant changes in the spectra are observed (Fig.11).

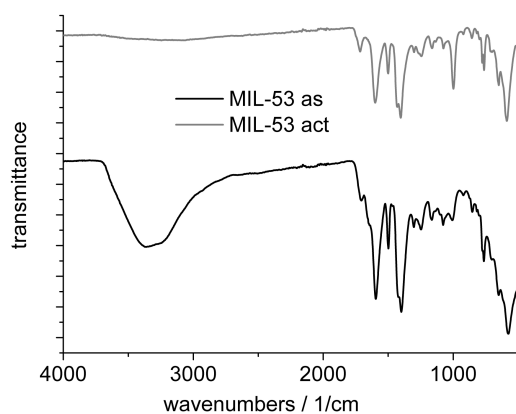


Figure 11: IR-spectra for the as synthesized Al-MIL-53-COOH and for the same compound activated in vacuum.

The almost complete disappearance of the broad absorption band around 3400 cm^{-1} is correlated to the removal of adsorbed water during the activation. The same observation is made for the band at 1680 cm^{-1} , which is attributed to the C=O-vibration of adsorbed DMF molecules.

In both spectra the band at 1715 cm^{-1} corresponds to the C=O-vibration of free carboxylic acid groups. At 1595 cm^{-1} and 1498 cm^{-1} , the absorption of C=O-vibrations of carboxylate groups and the C=C-vibrations of the aromatic ring respectively is observed. The two overlapping bands around 1400 cm^{-1} can be attributed to both of the two aforementioned groups. At 762 cm^{-1} and

852 cm^{-1} , the characteristic C-H deformation vibrations of the 1,2,4-substituted aromatic ring is observed.^[40] In contrast to the spectrum of as synthesized Al-MIL-53-COOH only minor amounts of water are observed for as synthesized MIL-96 (Fig. 12).

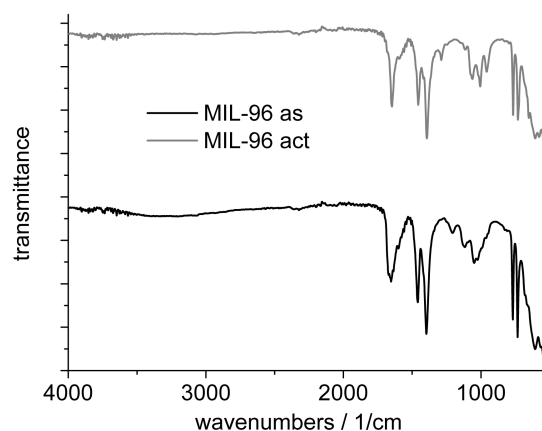


Figure 12: IR-spectra for the as synthesized MIL-96 and for the same MOF activated at 200°C in vacuum.

While the C=O-vibration of the carboxylate groups is observed at 1650 cm^{-1} in the spectrum of the activated MOF, the additional band for the C=O-vibration of DMF included inside the pores leads to a rather broad absorption in the spectrum of the as synthesized compound in the range of 1600 cm^{-1} to 1700 cm^{-1} . The absorption bands at 1460 cm^{-1} and 1398 cm^{-1} can be attributed to the C=C-vibrations of the aromatic ring and the symmetric C=O stretching vibration of the carboxylate groups. The two bands at 770 cm^{-1} and 735 cm^{-1} corresponds to the 1,3,5-substitution of the benzene core.

In the spectra of MIL-120, only the absorption bands of the as synthesized compound are well defined. This spectrum exhibits two well defined absorptions of an O-H-vibration at 3650 cm^{-1} and 3530 cm^{-1} , which are removed upon activation (Fig. 13).

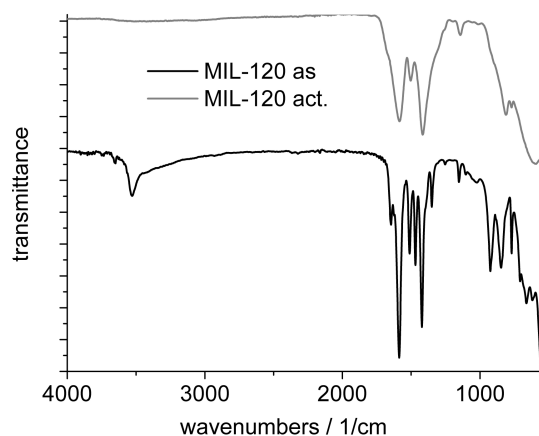


Figure 13: IR-spectra of the as synthesized and the activated MIL-120.

At 1640 cm^{-1} and 1583 cm^{-1} the bands for the C=O-vibrations of the carboxylate groups are observed and below this peak the band of the C=C-bonds of the aromatic ring at 1510 cm^{-1} . However, the drastic changes in the spectrum upon activation clearly indicate a structural change upon activation. The bands in the

spectrum of the activated MOF are generally broadened due to the thermal treatment. The decomposition of the product is also supported by the broadening of the Bragg-reflections upon activation (Fig. S5).

5 Structural Descriptions and Discussion

The structure of the hybrid compound formed with trimellitic acid is a functionalized analogue of Al-MIL-53. This MOF's framework is based on the connection of chains of *trans*-connected AlO_6 -octahedra via the aromatic dicarboxylates. Thus rhombic channels are formed, which are usually accessible after the removal of the embedded solvent molecules (Fig. 14).

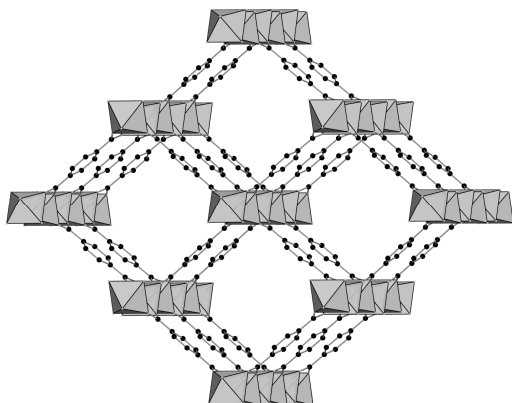


Figure 14: Framework structure of the open conformation of unfunctionalized Al-MIL-53. Hydrogen atoms are omitted for clarity. The figure was drawn using crystallographic data from reference [7].

Upon exchange or removal of these guest molecules, the MIL-53 materials exhibit remarkable changes in their structure due to host-guest interactions. These changes depend further on the constituents of the MIL-53 network, i.e. the trivalent metal ion and the dicarboxylate ion.^[41] Using exclusively H_2O as the solvent for the synthesis of Al-MIL-53-COOH the reversible structure transition between the narrow pore and the large pore form is also observed.^[42] By the use of $\text{H}_2\text{O}/\text{DMF}$ solvent mixture, the framework exclusively adapts a structure similar to the large pore form of unfunctionalized Al-MIL-53. This is due to the bulky functional group and the embedded linker molecules. Even after thermal activation we could not observe any structural change according to the XRPD data or the IR spectra. Thus as a consequence of the synthesis procedure described herein, the MOF does not exhibit the breathing effect. This structural behavior can be advantageous, since the shrinking of the framework can inhibit the adsorption of molecules.

The framework of MIL-96 is based on wave-shaped inorganic layers which contain 18-membered rings of AlO_6 -octahedra. The layers are connected via the trimellitate ions to the trimeric $\{\text{Al}_3(\mu_3\text{-O})(\text{OH}(\text{H}_2\text{O})_2)\}$ building units along [001]. Thus the continuous 2D-layers and the trimeric units alternate in the hexagonal framework (Fig. 15).

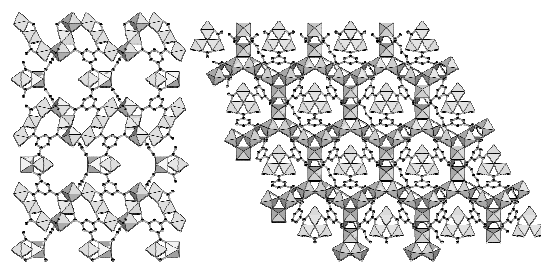


Figure 15: Left: Structure of MIL-96 as seen along the *b*-axis showing the layered arrangement. Right: Structure seen along the *c*-axis showing the hexagonal framework. Hydrogen atoms are omitted for clarity. The figure was drawn using crystallographic data from reference [38].

In contrast to the MIL-96 reported earlier, the material synthesized by the described method contains residual sulfate ions and DMF molecules or a decomposition product of the latter. Due to the narrow pores, these impurities could not be removed from the cavities by washing with water or thermal activation. Nevertheless the material is highly porous towards nitrogen, although MIL-96 originally wasn't reported to be porous towards N_2 .^[38] The apparent specific BET-surface ($A_{\text{BET}} = 483 \text{ m}^2/\text{g}$) and the micropore volume ($V_{\text{MIC}} = 0.23 \text{ cm}^3/\text{g}$) are comparable to the values found in another study^[43] ($A_{\text{BET}} = 532 \text{ m}^2/\text{g}$), taking the small impurities into account. While the original synthesis conditions are quite harsh ($210 \text{ }^\circ\text{C}$ for 24 hours in water) and $\text{Al}(\text{NO}_3)_3 \cdot 9\text{H}_2\text{O}$ as metal source as well as trimesic acid trimethylester as a precursor must be employed, the synthesis procedure described herein eliminates all three of these disadvantages and greatly accelerates the synthesis. Thus, it should allow the transfer to industrial scale.

The third compound obtained by our three-step approach is MIL-120. Its structure is built up from chains of edge-sharing AlO_6 -octahedra. These are interconnected via pyromellitate linker molecules. The resulting channels are running perpendicular to these chains and exhibit a diameter of $5.4 \times 4.7 \text{ \AA}$ (Fig. 16).

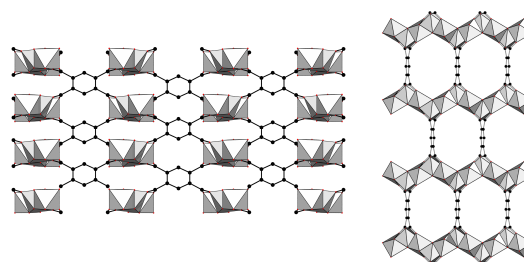


Figure 16: Left: Structure of MIL-120 as seen along [102], showing the arrangement of the edge-sharing chains. Right: Structure seen along the *c*-axis showing the hexagonal channels inside the framework. Hydrogen atoms are omitted for clarity. The figure was drawn using crystallographic data from reference [6].

Although a highly crystalline product could be obtained, it does not show any measurable porosity. The change of the activation temperature did also not result in an uptake of nitrogen. This could be due to the inclusion of molecules inside the cavities. Another possible reason is a change of the structure of the framework upon thermal activation, as indicated by the IR-spectra. This latter is supported by the XRPD measurements (Fig. S5).

6 Conclusions

Applying our three-step approach, we have successfully synthesized three Al-MOFs applying HT-methods in combination with MW-assisted heating and characterized them regarding their structure and porosity. The advantage of the described approach lies in the chemical composition of the reaction mixtures (reactants and solvents) and the mild conditions, which are both suitable for the application in industrial processes. The combination of HT-methods and microwave heating can obviously accelerate the discovery of compounds in solvothermal systems and speed up the optimization of synthesis procedures. Although the MOFs that were obtained apparently exhibit the same structure as literature-known compounds, they exhibit different compositions and therefore different sorption properties. Thus, under mild reaction conditions a new microporous, carboxylic acid functionalized Al-MIL-53 was obtained that does not exhibit the usually observed breathing behavior. For MIL-96 and MIL-120 the reaction temperature could be decreased from 210°C by 75°C and 65 °C respectively. While the reaction conditions have only a minor impact on the sorption properties of MIL-96 these changes lead to non-porous MIL-120. Thus we have presented evidence that the properties of the obtained compounds are strongly dependent on the synthesis method.

References

- 1 I. J. Kang, N. A. Khan, E. Haque, S. Hwa Jung, *Chem. Eur. J.* 17 (2011) 6437.
- 2 M. Kandiah, M. H. Nilsen, S. Usseglio, S. Jakobsen, U. Olsbye, M. Tilset, C. Larabi, E. A. Quadrelli, F. Bonino, K. P. Lillerud, *Chem. Mater.* 22 (2010) 6632.
- 3 M. Gaab, N. Trukhan, S. Maurer, R. Gummaraju, U. Müller, *Micropor. Mesopor. Mater.* (2011), doi:10.1016/j.micromeso.2011.08.016
- 4 W. H. Casey, *Chem. Rev.* 106 (2006) 1.
- 5 C. Volkringer, D. Popov, T. Loiseau, N. Guillou, G. Férey, M. Haouas, F. Taulelle, C. Mellot-Draznieks, M. Burghammer, C. Riekel, *Nature Materials* 6 (2007) 760.
- 6 C. Volkringer, D. Popov, T. Loiseau, G. Férey, M. Burghammer, C. Riekel, M. Haouas, F. Taulelle, *Chem. Mater.* 21 (2009) 5695.
- 7 T. Loiseau, C. Serre, C. Huguenard, G. Fink, F. Taulelle, M. Henry, T. Bataille, G. Férey, *Chem. Eur. J.* 10 (2004) 1373
- 8 T. Loiseau, C. Mellot-Draznieks, H. Muguerra, G. Férey, M. Haouas, F. Taulelle, C. R. *Chimie* 8 (2005) 765.
- 9 I. Senkovska, F. Hoffmann, M. Fröba, J. Getzschmann, W. Böhlmann, S. Kaskel, *Micropor. Mesopor. Mater.* 122 (2009) 93.
- 10 S. Biswas, T. Ahnfeldt, N. Stock, *Inorg. Chem.* 50 (2011) 9518.
- 11 C. Volkringer, T. Loiseau, N. Guillou, G. Férey, M. Haouas, F. Taulelle, E. Elkaim, N. Stock, *Inorg. Chem.* 49 (2010) 9852.
- 12 A. Sonnauer, F. Hoffmann, M. Fröba, L. Kienle, V. Duppel, M. Thommes, C. Serre, G. Férey, N. Stock, *Angew. Chem. Int. Ed.* 48 (2009) 3791.
- 13 N. Stock, *Micropor. Mesopor. Mater.* 129 (2010) 287.
- 14 E. Biemmi, S. Christian, N. Stock, T. Bein, *Micropor. Mesopor. Mater.* 117 (2009) 111.
- 15 P. Maniam, N. Stock, *Inorg. Chem.* 50 (2011) 5085.
- 16 S. Bauer, N. Stock, *Angew. Chem. Int. Ed.* 46 (2007) 6857.
- 17 S. Bauer, N. Stock, *J. Solid State Chem.* 180 (2007) 3111.
- 18 A. Sonnauer, N. Stock, *Eur. J. Inorg. Chem.* 32 (2008) 5038.
- 19 K. J. Gagnon, H. P. Perry, A. Clearfield, *Chem. Rev.* (2011), doi: 10.1021/cr2002257.
- 20 T. Ahnfeldt, D. Gunzelmann, T. Loiseau, D. Hirsemann, G. Férey, J. Senker, N. Stock, *Inorg. Chem.* 48 (2009) 3057.
- 21 S. Bauer, C. Serre, T. Devic, P. Horcajada, J. Marrot, G. Férey, N. Stock, *Inorg. Chem.* 47 (2008) 7568.
- 22 S. Bernt, M. Feyand, A. Modrow, J. Wack, J. Senker, N. Stock, *Eur. J. Inorg. Chem.* 35 (2011) 5378.
- 23 H. Reinsch, M. Krüger, J. Wack, J. Senker, F. Salles, G. Maurin, N. Stock, *Micropor. Mesopor. Mater.* (2011), doi:10.1016/j.micromeso.2011.05.029
- 24 T. Ahnfeldt, N. Guillou, D. Gunzelmann, I. Margiolaki, T. Loiseau, G. Férey, J. Senker, N. Stock, *Angew. Chem. Int. Ed.* 21 (2009) 5265.
- 25 H. Reinsch, M. Feyand, T. Ahnfeldt, N. Stock, *Dalton Trans.* (2012), doi:10.1039/C2DT12005D.
- 26 C. Volkringer, T. Loiseau, N. Guillou, G. Férey, M. Haouas, F. Taulelle, E. Elkaim, N. Stock, *Inorg. Chem.* 49 (2010) 9852.
- 27 S. Chen, Z. Zhang, K. Huang, Q. Chen, M. He, A. Cui, C. Li, Q. Liu, M. Du, *Cryst. Growth Des.* 8 (2008) 3437.
- 28 S. Couck, J. F. M. Denayer, G. V. Baron, T. Remy, J. Gascon, F. Kapteijn, *J. Am. Chem. Soc.* 132 (2009) 6326.
- 29 E. Stavitski, M. Goesten, J. Juan-Alcañiz, A. Martinez-Joaristi, P. Serra-Crespo, A. V. Petukhov, J. Gascon, F. Kapteijn, *Angew. Chem. Int. Ed.* 41 (2011) 9624.
- 30 T. Ahnfeldt, N. Stock, *CrystEngComm* (2011), doi: 10.1039/c1ce05956d.
- 31 T. Ahnfeldt, J. Moellmer, V. Guillerme, R. Staudt, C. Serre, N. Stock, *Chem. Eur. J.* 2011, 17, 6462-6468.
- 32 X. Si, C. Jiao, F. Li, J. Zhang, S. Wang, S. Liu, Z. Li, L. Sun, F. Xu, Z. Gabelica, C. Schick, *Energy Environ. Sci.* 4 (2011) 4522.
- 33 F. Vermoortele, M. Maes, P. Modhadam, M. Lennox, F. Ragon, M. Brouhaout, S. Biswas, K. Laurier, I. Beurroies, R. Denoyel, M. Roeffaers, N. Stock, T. Dören, C. Serre, D. De Vos, *J. Am. Chem. Soc.* 133 (2011) 18529.
- 34 M. Savonnet, E. Kockrick, A. Camarata, D. Bazer-Bachi, N. Bats, V. Lecocq, C. Pinel, D. Farrusseng, *New J. Chem.* 35 (2011) 1892.
- 35 T. Ahnfeldt, D. Gunzelmann, J. Wack, J. Senker, N. Stock, *CrystEngComm* submitted.
- 36 Topas V4.1: General Profile and Structure Analysis Software for Powder Diffraction Data Bruker AXS Ltd, 2004.
- 37 C. Volkringer, D. Popov, T. Loiseau, G. Férey, M. Burghammer, C. Riekel, M. Haouas, F. Taulelle, *Chem. Mater.* 21 (2009) 5695.
- 38 T. Loiseau, L. Lecroq, C. Volkringer, J. Marrot, G. Férey, M. Haouas, F. Taulelle, S. Bourrelly, P. L. Llewellyn, M. Latroche, *J. Am. Chem. Soc.* 128 (2006) 10223.
- 39 N.A. Khan, J.S. Lee, C-H. Jun, S.H. Jung, *Micropor. Mesopor. Mater.* (2011), doi: 10.1016/j.micromeso.2011.11.025
- 40 G. Sokrates, *Infrared and Raman characteristic group frequencies: tables and charts*, third Ed., John Wiley & Sons Ltd., Chichester, 2001.
- 41 G. Férey, C. Serre, *Chem. Soc. Rev.* 38 (2009) 1380.
- 42 N. Reimer, N. Stock, submitted.
- 43 Ji Sun Lee a, Sung Hwa Jung, *Micropor. Mesopor. Mater.* 129 (2010) 274.

4.3 Synthese neuer poröser Aluminium-MOFs basierend auf linearen aromatischen Dicarboxylat-Ionen

4.3.1 CAU-3: A new family of porous MOFs with a novel Al-based brick: $[Al_2(OCH_3)_4(O_2C-X-CO_2)]$ (X=aryl)

Dieser Artikel wurde in „Dalton Transactions“ veröffentlicht (reproduced with permission from RSC, *Dalton Trans.*, **2012**, *41*, 4164-4171).

Anknüpfend an vormalige Forschungsergebnisse aus der Arbeitsgruppe wurde die Verwendung von Methanol als Lösungsmittel untersucht. Basierend auf 2-Aminoterephthalsäure konnte bereits die Verbindung CAU-1 hergestellt und charakterisiert werden. Die Erhöhung der Komplexität des solvothermalen Systems durch Zusatz einer Base führte zur Entdeckung neuer Verbindungen. Mittels Hochdurchsatzmethoden wurde eine neue Familie poröser, Aluminium-basierter MOFs in dem solvothermalen System Al^{3+} / Linker / Methanol / NaOH synthetisiert. Alle Verbindungen dieser Familie basieren auf demselben neuartigen anorganischen Baustein, einem $[Al_{12}(OCH_3)_{24}]^{12+}$ -Cluster. Dieser Baustein besitzt eine zyklische Form und ähnelt den bekannten molekularen Verbindungen der „ferric wheels“. Zusammen mit dem oktameren $[Al_8(OH)_4(OCH_3)_8]^{12+}$ -Cluster der in CAU-1 beobachtet wurde stellen diese Verbindungen bisher die einzigen Beispiele für zyklische Aluminium-Oxo-Cluster. Die anorganischen Baueinheiten in CAU-3 sind zwölfmal zu benachbarten Clustern verknüpft, wodurch ein Netzwerk mit verzerrter kubisch flächenzentrierter Topologie aufgebaut wird. Die Poren entsprechen den Tetraeder- beziehungsweise den Oktaederlücken in der kubisch flächenzentrierten Kugelpackung. Es konnten mittels Hochdurchsatzmethoden optimierte Synthesebedingungen gefunden werden, die zur Synthese von MOFs basierend auf Terephthalat-Ionen (CAU-3-BDC oder $[Al_2(OCH_3)_4(O_2C-C_6H_4-CO_2)]$), 2-Aminoterephthalat-Ionen (CAU-3-BDC-NH₂ oder $[Al_2(OCH_3)_4(O_2C-C_6H_3NH_2-CO_2)]$) und 2,6-Naphthalendicarboxylat-Ionen (CAU-3-NDC oder $[Al_2(OCH_3)_4(O_2C-C_{10}H_6-CO_2)]$) führten. Der Porendurchmesser der tetraedrischen und oktaedrischen Poren variiert zwischen 1 nm und 1.1 nm in CAU-3-BDC-NH₂ und 1.4 nm und 1.5 nm in CAU-3-NDC. Durch die anisotrope Form der Kavitäten beträgt die größte Abmessung der Poren in CAU-3-NDC allerdings 3.8 nm.

Alle Verbindungen wurden mittels IR- und Raman-Spektroskopie, Elementaranalyse, Thermogravimetrie, Röntgenpulverdiffraktometrie und Gassorption charakterisiert. Die Struktur von CAU-3-BDC konnte aus Pulverbeugungsdaten gelöst werden, während ein Strukturmodell von CAU-3-NDC mittels Kraftfeldrechnungen erhalten wurde. Zur Erstellung eines Modells von CAU-3-BDC-NH₂ wurde die Kristallstruktur von CAU-3-BDC mittels Fouriersynthese ergänzt. Alle Kristallstrukturen konnten mittels Rietveldmethoden verfeinert werden. Durch den Einsatz der verschiedenen Linkermoleküle konnte das Sorptionsverhalten gegenüber Stickstoff und Wasserdampf moduliert werden.

Cite this: *Dalton Trans.*, 2012, **41**, 4164

www.rsc.org/dalton

PAPER

CAU-3: A new family of porous MOFs with a novel Al-based brick: $[\text{Al}_2(\text{OCH}_3)_4(\text{O}_2\text{C-X-CO}_2)]$ (X = aryl)†

Helge Reinsch, Mark Feyand, Tim Ahnfeldt and Norbert Stock*

Received 21st October 2011, Accepted 7th December 2011

DOI: 10.1039/c2dt12005d

A new family of Al-based MOFs denoted as CAU-3 (CAU = Christian-Albrechts-Universität) was discovered in the solvothermal system Al^{3+} /aryldicarboxylic acid/NaOH/methanol by applying high-throughput-methods. The three compounds reported in this article $[\text{Al}_2(\text{OCH}_3)_4\text{BDC}]$, $[\text{Al}_2(\text{OCH}_3)_4\text{BDC-NH}_2]$ and $[\text{Al}_2(\text{OCH}_3)_4\text{NDC}]$ (BDC = 1,4-benzenedicarboxylate; NDC = 2,6-naphthalenedicarboxylate) are all based on the same unprecedented inorganic building unit $[\text{Al}_{12}(\text{OCH}_3)_{24}]^{12+}$, which is a dodecameric cyclic aluminium-methanolate-cluster. The material CAU-3-NDC was found to exhibit the highest surface area as well as the highest micropore volume of all Al-based MOFs reported until now.

Introduction

During the past few years, the research on highly porous MOFs with tailored properties has become a main objective for scientists in the field of porous materials.^{1–5} This relatively new class of materials is built up from inorganic vertices, most often metal ions or cationic metal-oxo-clusters, which are connected to each other using polytopic organic linker-molecules. These organic parts of the network usually consist of organic anions often bearing carboxylate- or phosphonate-groups. To create pores by separating the inorganic vertices from each another, the linker molecule is often based on a rigid aromatic unit like benzene or naphthalene. Once the reaction conditions for the formation of such a hybrid compound are known, similar reaction parameters should in principle allow the incorporation of further functionalized and also larger organic molecules into the structure, while keeping the inorganic brick unchanged. This approach towards the synthesis of new compounds is commonly referred to as isoreticular synthesis.⁶ There are only few examples for the synthesis of isoreticular families of MOFs, consisting of more than two materials based on the same inorganic building unit.^{7–12} An example is the MIL-88-series, which is based on dicarboxylate ions but contains trimeric $\text{M}(\text{III})_3\text{-}\mu_3\text{O}^{7+}$ -clusters, where M(III) stands for a Cr^{3+} or Fe^{3+} . These compounds exhibit enormous changes in their lattice parameters, depending not only upon the metal ion (Fe^{3+} , Cr^{3+}) and the dicarboxylate-molecule, but also

on the presence and the nature of guest molecules inside the pores.⁹ Another example was reported for the Zr^{4+} -based MOFs called UiO-66, -67, and 68.^{10,11} In this case, $\text{Zr}_6\text{O}_4(\text{OH})_4^{12+}$ -clusters are twelvefold connected by linear dicarboxylate ions to form a **fcu**-net, which corresponds to a fcc-packing of inorganic building blocks. Due to their outstanding chemical stability, the functionalized analogues of the UiO-66 (based on 1,4-benzenedicarboxylate) have shown to be ideal candidates for further post-synthetic modification reactions.¹²

One reason for this limited number of examples is due to the complexity of solvothermal reactions. Small changes of the organic linker molecule have often a strong influence on the solubility as well as the acid–base and the coordination properties. Thus, the reaction conditions have to be established and optimized for each organic linker molecule separately. In this context, high-throughput-methods have proven to be a highly valuable tool for the intentional synthesis of MOFs.^{13,14} Applying this methodology, we were recently able to synthesize the amino-functionalized Al-MIL-53,¹⁵ a MOF with lozenge-shaped channels bearing NH_2 -groups which can be further chemically modified, and Cr-MIL-101-NDC,¹⁶ which exhibits giant pores with a diameter of 4.6 nm. The miniaturization of the reaction vessels, the parallelization of the synthesis and the automated characterization open the opportunity to screen even complex reaction systems with large parameter-spaces. Therefore, chemical trends can be easily identified, and synthesis parameters can be rapidly optimized with a rather low consumption of starting materials.

Recently we have started a systematic high-throughput investigation on the role of the solvent in the synthesis of Al-based MOFs. In contrast to MOFs based on divalent cations, only few Al-based MOFs have been reported in the literature since mostly very small μm -sized crystals have been obtained, which complicates the structure determination. The frameworks of these known porous Al-MOF structures contain only six different

Christian-Albrechts-Universität zu Kiel, Institut für Anorganische Chemie, Max-Eyth-Str. 2, 24118 Kiel, Germany. E-mail: stock@ac.uni-kiel.de; Fax: +49 431 8801775; Tel: +49 431 8801675

† Electronic supplementary information (ESI) available: Crystallographic data, details of the Rietveld refinements and further XRPD data, selected bond lengths, TG curves. CCDC reference numbers 799242–799244 for CAU-3-NDC, CAU-3-BDC, and CAU-3-BDC-NH₂, respectively. For ESI and crystallographic data in CIF or other electronic format see DOI: 10.1039/c2dt12005d

Al–O bricks.^{17–23} This rather limited number of structures is in sharp contrast to the diversity of polynuclear species that are known from the solvolysis reactions of aluminium salts.^{24,25} For this reason, the field of Al³⁺-based MOFs still is a promising chemical system for the discovery of new materials. Due to the high thermal and chemical stability of the known Al-based MOFs, as well as to the cost-effective availability of the usually nontoxic starting materials, these yet unknown compounds could be of high interest for commercial applications.

Especially linear dicarboxylic acids have shown to be useful for the synthesis of isorecticular compounds, not only but also due to the commercial availability of a variety of dicarboxylic acids with different size and functionalization. In combination with one-dimensional chains of corner-sharing AlO₆-octahedra, several porous compounds based on the MIL-53 structure are known, showing interesting sorption behaviour as well as high thermal stabilities.^{26–30} Another example for a dicarboxylate-based Al-MOF is CAU-1, which contains twelvefold connected octanuclear Al-oxo-clusters.^{23,31} Herein we report the synthesis and characterization of a new family of porous MOFs based on linear aryldicarboxylate ions, which contain the novel dodecameric Al-based brick [Al₁₂(OCH₃)₂₄]¹²⁺.

Experimental

Materials and methods

Chemicals. AlCl₃·6H₂O (Riedel-de Haen, ≥99%), Al(NO₃)₃·9H₂O (Merck, ≥99%), H₂BDC (Aldrich, ≥98%), H₂BDC-NH₂ (Fluka, ≥98%), NaOH (Baker, ≥97%), methanol (BASF, purum), and *N,N*-dimethyl-formamide (BASF, tech.) were used as purchased. 2,6-Naphthalenedicarboxylic acid was synthesized by hydrolysis of dimethyl 2,6-naphthalenedicarboxylate (Aldrich, 98%).

Methods. Most reactions were carried out using our 24-high-throughput reactor system.³² The upscaled synthesis was performed in custom made Teflon inserts in steel autoclaves with a volume of 30 mL. The high-throughput X-ray analyses were performed in transmission geometry using a STOE HT powder diffractometer equipped with a xy-stage and an image plate detector (IPDS) system (Cu-Kα1 radiation). Temperature dependent X-ray powder diffraction (XRPD) data was measured on a STOE Stadi-P diffractometer in transmission geometry equipped with an image plate detector (IPDS) using Cu-Kα1 radiation. High-precision X-ray powder diffraction data for the structure solution was collected on a STOE Stadi-P powder diffractometer equipped with a linear position sensitive detector (PSD) system (monochromated Cu-Kα1 radiation) in transmission geometry. XRPD data for the structure refinement was recorded on a Panalytical X-pert Highscore diffractometer in reflection-geometry. MIR spectra were recorded on an ATI Matheson Genesis spectrometer in the spectral range of 4000–400 cm⁻¹ using the KBr disk method. FT-Raman spectra were recorded on a Bruker IFS 66 FRA 106 in the range of 0–3300 cm⁻¹ using a Nd/YAG-Laser (1064 nm). The thermogravimetric analyses were recorded using a NETZSCH STA 409 CD analyzer. The samples were heated in Al₂O₃ crucibles at a rate of 4 K min⁻¹ under a flow of air (25 ml min⁻¹). The TG data were corrected for buoyancy and

current effects. The molecular modelling software used was Materials Studio 5.0.³³ Sorption experiments were performed using a BEL JAPAN INC. Belsorp_{max}.

Synthesis and high-throughput-investigations

Discovery and synthesis optimisation of CAU-3-BDC, [Al₂(OCH₃)₄BDC]. The compound CAU-3-BDC (**1**) was discovered in a high throughput-experiment using AlCl₃·6H₂O, terephthalic acid (H₂BDC), methanol and 2 M methanolic NaOH as starting materials. After the reaction at 125 °C for 5 h, the tendencies in the product formation shown in Fig. 1 could be observed. Exact amounts of starting materials can be found in Table S5.† The molar ratio Al³⁺:H₂BDC was kept constant at 4, the absolute amount of starting material was increased from row to row and from column to column, the amount of base was raised.

The compound was obtained from a highly diluted basic solution. Under more acidic and more concentrated conditions the well known compounds CAU-1 and MIL-53 are formed. Furthermore an unknown product of very low crystallinity was observed. Although the material obtained under these conditions already exhibited a remarkable porosity (apparent specific surface area of A_{BET} ~1200 m² g⁻¹), the crystallinity of the sample was rather low. A detailed high-throughput-investigation (~200 reactions) led to an improved synthesis procedure for CAU-3-BDC and the crystallinity was improved substantially. Therefore, the Al³⁺-source was varied (nitrate, chloride and perchlorate), as well as the molar ratios and the absolute amounts of starting materials. We also investigated the influence of H₂O on the product formation. While the use of Al(ClO₄)₃·9H₂O or the addition of small amounts of water led to the formation of X-ray amorphous products or Al₂O₃, we observed highest crystallinity only for very small concentrations of H₂BDC and large excess of Al(NO₃)₃·9H₂O and NaOH. To achieve an optimum of crystallinity we also varied the heating program. The progress during this synthesis optimization is visualized in Fig. 2.

The optimized synthesis procedure of **1** in the 24 reactor system is as follows: a mixture of Al(NO₃)₃·9H₂O (45.2 mg, 0.120 mmol), terephthalic acid (H₂BDC; 2.5 mg, 0.015 mmol) and a solution of NaOH in methanol (2 M, 60 μL, 0.120 mmol) was suspended in methanol (1.340 mL). The reactor was heated up to 125 °C in 12 h. The temperature was held for 5 h and the reactor was allowed to cool down to room temperature in 4 h.

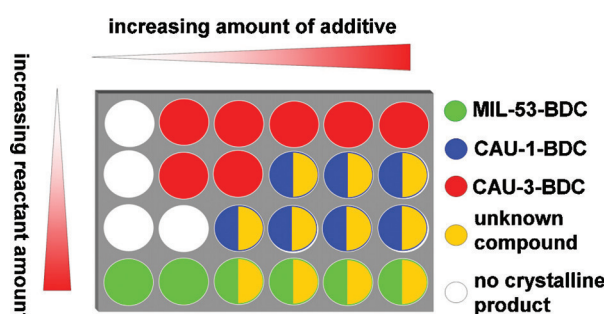


Fig. 1 Results of the high-throughput investigation for the discovery of CAU-3-BDC.

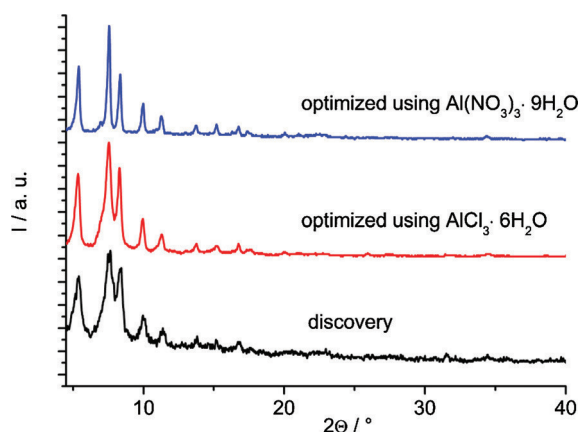


Fig. 2 Improvement of the crystallinity of the products during the HT-assisted synthesis optimization.

Scale-up of the reaction was performed in a 30 mL custom-made autoclave with Teflon insert. For this synthesis, the reaction parameters were stepwise adjusted to the larger reactor.

$\text{Al}(\text{NO}_3)_3 \cdot 9\text{H}_2\text{O}$ (540 mg, 1.44 mmol), H_2BDC (40 mg, 0.240 mmol) and a solution of NaOH in methanol (2 M, 720 μL , 1.44 mmol) were suspended in methanol (16.0 mL). The reactor was heated up to 125 °C in 12 h. The temperature was held for 3 h and the reactor was allowed to cool down to room temperature in 1 h.

After the filtration, a white microcrystalline powder was obtained. Thermogravimetric analysis and TEM-images revealed, that a large amount of an X-ray amorphous byproduct was formed. To remove this byproduct, 100 mg of the reaction product were treated with 10 mL of DMF in a microwave oven (Biotage Initiator) at 150 °C for 1 h under stirring. To remove the DMF, the filtrated solid was treated with 10 mL methanol and heated up in the microwave oven to 100 °C for 1 h. The product was dried at room temperature in air, and further activated under vacuum for the sorption experiments (160 °C/12 h/0.1 mbar). Since the crystallinity slightly decreases during this process (Fig. S1), the structure solution and refinement were performed using the XRPD measurements of the “as synthesized” compound. All other analytical data was measured for the activated product stored under ambient conditions prior to the measurements.

Elemental analysis on an activated sample: found: C: 35.43%, H: 4.07%. Calculated values, based on the deduced formula $[\text{Al}_2(\text{OCH}_3)_4(\text{O}_2\text{CC}_6\text{H}_4\text{CO}_2)] \cdot 3.6\text{H}_2\text{O}$: C: 35.4%, H: 5.7%.

Discovery and synthesis optimisation of CAU-3-BDC-NH₂, $[\text{Al}_2(\text{OCH}_3)_4\text{BDC-NH}_2]$. Starting from the optimized reaction conditions for **1**, the synthesis of the amino-functionalized analogue CAU-3-BDC-NH₂ (**2**) was attempted. Surprisingly, the reaction conditions are very similar. For the optimized synthesis of **2** in the multiclave, a mixture of $\text{Al}(\text{NO}_3)_3 \cdot 9\text{H}_2\text{O}$ (52 mg, 0.139 mmol), 2-aminoterephthalic acid ($\text{H}_2\text{BDC-NH}_2$, 2.5 mg, 0.014 mmol) and a 2 M solution of NaOH in methanol (69 μL , 0.138 mmol) were suspended in methanol (1.330 mL). The reactor was heated up to 125 °C in 8 h. The temperature was held for 6 h and the reactor was allowed to cool down to room temperature in 1 h.

For the up-scaling of the reaction we used again our 30 mL custom-made autoclave with a Teflon insert. For this synthesis, $\text{Al}(\text{NO}_3)_3 \cdot 9\text{H}_2\text{O}$ (540 mg, 1.44 mmol), $\text{H}_2\text{BDC-NH}_2$ (40 mg, 0.220 mmol) and a solution of NaOH in methanol (2 M, 720 μL , 1.44 mmol) were suspended in methanol (16.0 mL). The reactor was heated up to 125 °C in 12 h. The temperature was held for 3 h and the reactor was allowed to cool down to room temperature in 1 h.

After the filtration, a yellow microcrystalline product was obtained. Thermogravimetric measurements revealed the presence of an X-ray amorphous byproduct, which was removed by applying the same procedure as for CAU-3-BDC. The crystallinity of CAU-3-BDC-NH₂ decreased slightly during this treatment (Fig. S2†). Therefore, XRPD data of the as-synthesized product was used for the structure refinement while all other analytical data was measured for the activated material. Elemental analysis on an activated sample (160 °C/12 h/0.1 mbar) stored under ambient conditions: found: C: 31.02%, H: 3.81%, N: 1.96%; These values differ from the assumed formula $[\text{Al}_2(\text{OCH}_3)_4(\text{O}_2\text{C-C}_6\text{H}_3\text{NH}_2\text{-CO}_2)] \cdot 3.6\text{H}_2\text{O}$ which are calculated to be: C: 34.1%, H: 5.7%, N: 3.3%. After dissolution in $\text{D}_2\text{O}/\text{NaOD}$ we observed in the NMR-spectrum, that CAU-3-NH₂ not only contains aminoterephthalate ions, but also terephthalate anions and N-methylated aminoterephthalate ions. We attribute the discrepancy between the experimental values and the ideal formula to this *in situ* conversion of the linker and to small amounts of X-ray amorphous Al-species (see also TG-measurement). Further investigations of this phenomenon are in progress.

Discovery and synthesis optimisation of CAU-3-NDC, $[\text{Al}_2(\text{OCH}_3)_4\text{NDC}]$. The synthesis of CAU-3-NDC (**3**) needed much more effort, since it is highly sensitive to every single parameter during the synthesis, and every small change leads to the formation of crystalline byproducts, whose structures and compositions are a subject of current research. Without the use of high-throughput-methods, optimization of the synthesis conditions (~800 reactions) would have been hardly possible. Due to the large number of reactions that were performed, a detailed description of the HT-investigations is not given. The varied parameters comprise the Al^{3+} -source (nitrate, chloride and perchlorate) and the molar ratios and absolute amounts of starting materials. Due to the sensitivity of the reaction towards the thermal process, the chemical composition of the starting mixture had to be screened using different heating programs. This finally led to the optimized synthesis of **3** in the 24 reactor system, which is as follows: a mixture of $\text{AlCl}_3 \cdot 6\text{H}_2\text{O}$ (29.3 mg, 0.12 mmol), 2,6-naphthalenedicarboxylic acid (H_2NDC ; 7.5 mg, 0.03 mmol) and a 2 M solution of NaOH (52 μL , 0.1 mmol) in methanol was suspended in methanol (448 μL) and heated to 130 °C in 1 h. The temperature was kept for 4 h and the reactor was allowed to cool down in 1 h. The white, as-synthesized product contains traces of sodium chloride (see also structure refinement) and X-ray amorphous byproducts like residual linker molecules in the pores. EDX measurements showed molar ratios of Al: Cl ranging from 2.5 to 3. IR-spectroscopy proved the presence of residual naphthalene dicarboxylic acid. Elemental analysis on a thermally activated sample (160 °C/12 h/0.1 mbar) stored under ambient conditions prior to the measurement:

found: C: 47.97%, H: 3.81%. Calculated values, based on the ideal formula $[\text{Al}_2(\text{OCH}_3)_4(\text{O}_2\text{CC}_{10}\text{H}_6\text{CO}_2)]$: C: 48.9%, H: 4.6%. Although these values are in quite good agreement, the described material still contains the mentioned byproducts.

All measurements were performed with the as-synthesized microcrystalline product. The only activation step for the sorption measurements was heating under vacuum, which hardly influences the crystallinity (Fig. S3†). Several attempts were made, to perform a scale-up of the synthesis and to further activate the as-synthesized compound. The products of the synthesis in larger reactors exhibit a much lower specific surface area, although, based on the XRPD measurements, no differences were observed. Further activation steps were attempted in several solvents, but the raw material decomposes in water, DMF and even ethanol. The solvent treatment in methanol led only to a reduction of the amount of chloride ions.

The absolute amounts synthesized are in all three cases quite low. In the case of CAU-3-BDC and CAU-3-BDC-NH₂, we usually obtain ~25 mg of fully activated sample from one up-scaled reaction. One reason is the low overall concentration of the linker molecule that is necessary to obtain the title compounds. The other reason is the elaborate activation procedure to remove the X-ray amorphous byproducts. In the case of CAU-3-NDC, around 8 mg are obtained from one HT-reaction.

Structure determination and refinement

The experimental XRPD pattern of CAU-3-BDC was successfully indexed with Topas Academics³⁴ as a hexagonal crystal system with the lattice parameters $a = 21.0480(4)$ Å and $c = 34.8305(7)$ Å with a goodness of fit of 23. Based on the extinction conditions, the rhombohedral space group $R\bar{3}m$ was suggested by the program. The structure solution was carried out successfully with the Expo2004³⁵ software package using Direct Methods. Starting from the space group $R\bar{3}m$, the positions of the aluminum based brick were determined. By recycling these fragments in a new intensity extraction, in addition parts of the BDC²⁻ ion were localized. This starting model was completed by force field calculations with the software package Forcite implemented in Materials Studio 5.0.³³ For the calculations, the universal force field was used without an optimization of the cell parameters. The completed model was refined with Rietveld techniques using Topas Academics.³⁴ The final Rietveld refinement involved 15 background parameters, 15 atomic parameters, 4 temperature factors, 1 scale factor and 2 cell parameters. The peak shape was modeled using a pearson VII function and anisotropic peak broadening effects were taken into account using a spherical harmonics series. The C–C distances and the C–O distances of the methoxy groups were restrained. The final Rietveld plot shown in Fig. 3 led to satisfying structural model indicators ($R_{\text{Bragg}} = 0.4\%$, $R_{\text{wp}} = 4.76\%$ and $\text{GoF} = 1.64$). Selected bond lengths and the asymmetric unit can be found in the supporting informations in Fig. S4 and Table S1,† respectively.

The structural model of CAU-3-BDC was used for the Rietveld refinement of CAU-3-BDC-NH₂. The difference Fourier calculations showed electron densities at a distance of 1.5 Å from the lateral carbon atoms of the phenyl ring. Assigning these electron densities to a nitrogen atom with a site occupation of 0.25 led to a significant lowering of the R -values R_{bragg} and R_{wp}

by 1 and 0.5%. The results of the final Rietveld refinement are shown in Fig. S5.† The C–C distances, C–O distances of the methoxy groups as well as the C–N distances were restrained and an overall temperature factor was used. The refinement led to good structure indicators of $R_{\text{Bragg}} = 0.59\%$, $R_{\text{wp}} = 4.17\%$ and $\text{GoF} = 1.71$. Selected bond lengths are given in Table S2.†

The indexing and lattice parameter refinement of the experimental powder pattern of **3** was carried out with the Stoe WinXpow software package.³⁶ The hexagonal cell parameters $a = 23.1533(5)$ Å and $c = 40.4120(9)$ Å were obtained. For the construction of a model of CAU-3-NDC, we started from the structure of CAU-3-BDC. The space group was converted to $P1$ and the terephthalate ions were replaced by naphthalene dicarboxylate ions after adjusting the cell parameters to the ones obtained from the indexing process, using Materials Studio 5.0. The model was submitted to a full energy minimization without an optimization of the unit cell constants with the universal force field (UFF) implemented in the software. For this simulation, the aluminum atoms were replaced by iron due to their very similar ionic radii (0.67 vs. 0.69) and the missing parameters for octahedrally coordinated aluminum in the parameter set. Van der Waals interactions were represented by a classical 12-6 Lennard Jones potential. The convergence criteria were set to 1.0×10^{-4} kcal mol⁻¹ and 0.005 kcal mol⁻¹ Å⁻¹ and 5.0×10^{-5} Å (displacement) respectively. The obtained structural model possesses lower symmetry than the parent-structure CAU-3-BDC and exhibits the space group $R\bar{3}$, due to the break of the symmetry caused by the naphthalene dicarboxylate ions (atomic coordinates and a simulated powder pattern of this model can be found in Table S3 and Fig. S6†). This structural model was used to carry out the Rietveld refinement. Due to the lower crystallinity and the two-fold number of atomic parameters caused by the lower symmetry, the atomic positions of the NDC²⁻ ions were restrained and an overall temperature factor was used. The final refinement leads to satisfying structure indicators ($R_{\text{Bragg}} = 4.47\%$, $R_{\text{wp}} = 9.41\%$ and $\text{GoF} = 4.80$). The final Rietveld plot is shown in Figure S7† and selected bond lengths are given in Table S4.† Two reflections at 32.62° and 45.42° are observed which are due to NaCl as an impurity. The final parameters of all three refinements are summarized in Table 1.

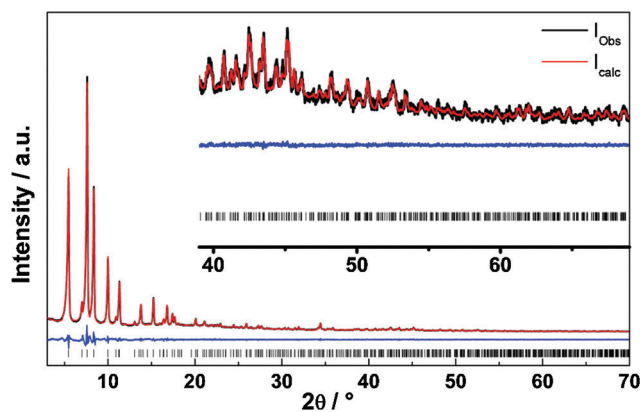
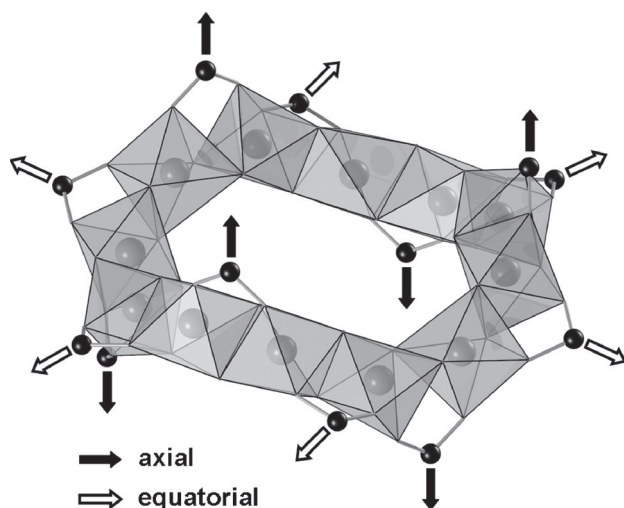


Fig. 3 Final Rietveld-plot for **1**. Measured intensities are in black, calculated intensities are in red, the difference plot is blue. The vertical bars mark the Bragg-positions.

Table 1 Final parameters obtained from the Rietveld-refinements

	CAU-3-BDC	CAU-3-BDC-NH ₂	CAU-3-NDC
Empirical formula	Al ₂ O ₈ C ₁₂ H ₁₆	Al ₂ O ₈ C ₁₂ N ₁ H ₁₇	Al ₂ O ₈ C ₁₆ H ₁₈
M g mol ⁻¹	342.21	357.23	368.25
Crystal system	Rhombohedral	Rhombohedral	Rhombohedral
Space group	<i>R</i> $\bar{3}m$	<i>R</i> $\bar{3}m$	<i>R</i> $\bar{3}$
<i>a</i> /pm	2110.51(5)	2093.5(1)	2320.56(2)
<i>c</i> /pm	3488.8(1)	3481.3(2)	4063.51(4)
<i>V</i> /10 ⁶ pm ³	13458.1(8)	13214(1)	18950.(3)
<i>Z</i>	18	18	18
<i>R</i> _{wp} /%	4.76	4.17	9.41
<i>R</i> _{Bragg} /%	0.4	0.59	4.47
GoF	1.64	1.71	4.8
weighted Durbin-Watson statistic	0.594	0.312	0.120

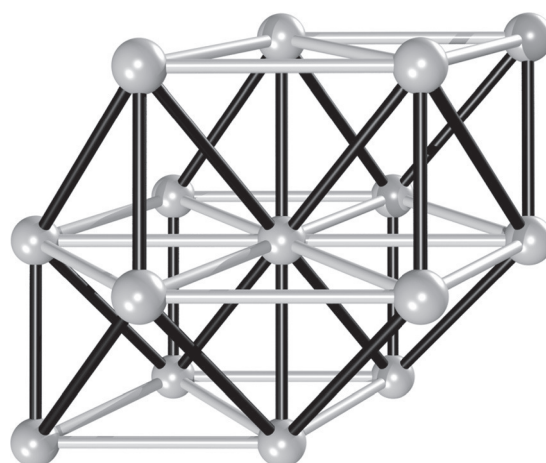
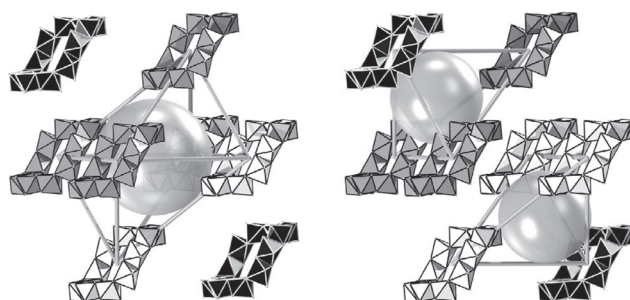
**Fig. 4** Dodecameric building unit and its connectivity mode in the framework of CAU-3-BDC. Methyl-groups are omitted for clarity.

Results and discussion

Structural description

The structure of CAU-3-BDC is based on dodecameric [Al₁₂(OCH₃)₂₄]¹²⁺ cations, to which twelve carboxylate moieties are coordinated, each one bridging two Al-ions (Fig. 4).

Thus, the inorganic units are composed of twelve edge-sharing AlO₆-polyhedra. The edge-sharing oxygen atoms are part of methanolate ions, while the other oxygen-atoms result from the coordination of the bridging carboxylate-groups. Similar dodecameric clusters have been only observed twice in molecular complexes containing the transition metals Fe³⁺ and Mn³⁺/Cr³⁺ ions.^{37,38} To the best of our knowledge this is the first time, that this cluster has been observed in Al chemistry as well as in the chemistry of MOFs. Recently, the Mn³⁺/Cr³⁺ building block was proposed as a possible brick for the formation of new metal-organic frameworks.³⁹ Besides the octanuclear cyclic cluster incorporated in the framework of CAU-1,²³ this building unit is the second example of an wheel-shaped aluminium carboxylate, whose occurrence is again strictly limited to the incorporation into a metal-organic framework.

**Fig. 5** Schematic representation of a part of the distorted fcu-net. The white bonds represent the connectivity in the *xy*-plane of the inorganic brick, the black ones the connectivity along the *z*-axis.**Fig. 6** The two different types of cavities in the fcu-framework. Different colours emphasize the ABC stacking of the of the Al-based bricks [Al₁₂(OCH₃)₂₄]¹²⁺.

The twelvefold connectivity by dicarboxylate units leads to the formation of a fcu-net (Fig. 5).

This high connectivity is remarkable, since only few examples of such MOFs have been reported. Besides the well known UiO-66,¹⁰ for example the frameworks of CAU-1²³ and its Ti-analogue MIL-125⁴⁰ exhibit this connectivity mode. While the latter two MOFs show a distorted pseudo-bcc packing of clusters, the assembly in CAU-3 leads to a fcc-packing like in UiO-66. Due to the anisotropic shape of the cluster a strongly distorted packing is observed (Fig. S7†).

Accordingly, the [Al₁₂(OCH₃)₂₄]¹²⁺ clusters are connected sixfold in their *xy*-plane and sixfold alternating in both directions along the *z*-axis of the cyclic cluster. The resulting network contains tetrahedral and octahedral cavities which are strongly distorted due to the anisotropic shape of the Al-containing brick (Fig. 6).

Assuming a spherical shape, the diameters of the tetrahedral and octahedral cavities are approximately 10 and 11 Å (calculated based on van-der-Waals radii), respectively. In reality larger molecules could be accommodated and based on the estimated available free space, the incorporation of rod-shaped guests with maximum length of 27 Å should be possible. The triangular apertures of these cavities differ only slightly in size and should be accessible for molecules up to a diameter of 7 Å.

The dimensionality and shape of the pores differ only slightly for compound **2**, since the amino-group is statistically distributed over the four possible positions of the aromatic ring. The larger linker molecule in **3** leads to an extended, non-interpenetrating framework containing distorted tetrahedral and octahedral cavities of ~ 14 Å and ~ 15 Å in diameter, assuming a spherical guest. Based on the structure, rod-shaped guests with maximum length of 38 Å should fit into the octahedral cavities.

Spectroscopic and thermal properties

The vibrational spectra (Fig. 7) of the three title compounds are very similar. The characteristic bands for the carboxylate vibrations around 1580 cm^{-1} and 1420 cm^{-1} clearly show the presence of the dicarboxylate ions coordinating to the Al^{3+} -ions. The aliphatic C–H vibrations at 2950 cm^{-1} and 2840 cm^{-1} are due to the bridging methanolate ions in the Al-based brick. In the case of as synthesized CAU-3-NDC, the absorption band around 1700 cm^{-1} is attributed to residual naphthalene dicarboxylic acid molecules occluded in the pores.

The band at 1250 cm^{-1} (C–N-vibration) in the spectrum of CAU-3-BDC-NH₂ proves the incorporation of aminoterephthalic acid, although the characteristic NH₂-bands around 3450 cm^{-1} are not observed, probably due to the presence of hydrogen-bonded water inside the pores. In the Raman-spectra, especially the aromatic C–C-vibrations between 1640 cm^{-1} and 1380 cm^{-1} are well resolved.

The thermal stability of all three MOFs was investigated in air atmosphere up to at least $800\text{ }^\circ\text{C}$ with a heating rate of 4 K

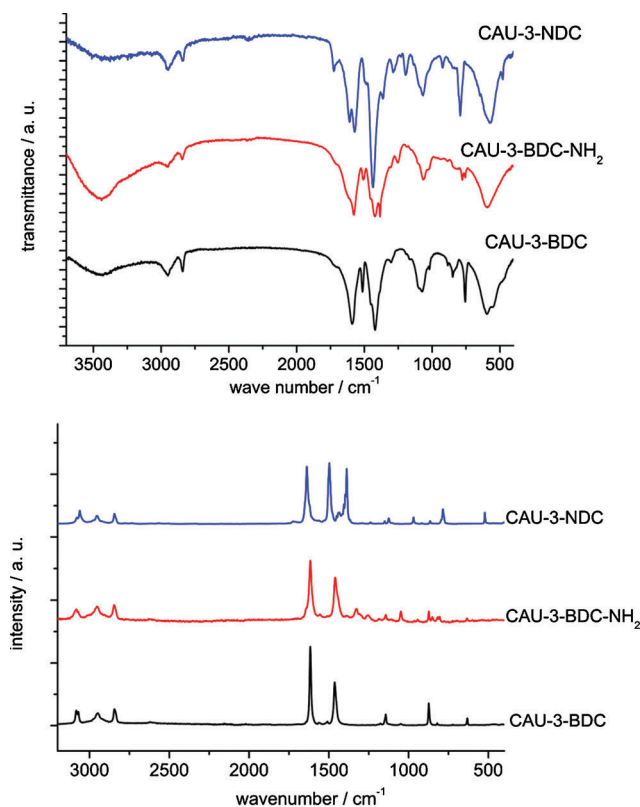


Fig. 7 IR- (top) and Raman-spectra (bottom) of the different CAU-3 MOFs.

min^{-1} (Fig. S9, S10 and S11†). For **1**, the first weight loss of -16.5% corresponds to the removal of incorporated solvent molecules. At higher temperatures ($\sim 200\text{ }^\circ\text{C}$), the decomposition of the frameworks and thus the structural collapse proceeds in two steps (calc.: 58.7% , obs.: 60.9%). The product formed in the end is weakly crystalline Al_2O_3 . In the case of CAU-3-BDC, we were also able to prove the structural rigidity of the framework during the activation process. Temperature-dependent XRPD data (Fig. 8) demonstrates, that no uncommon cell parameter shifts can be observed.

While the chemical decomposition of **1** shows a stepwise mechanism in the TG curve, the structure of the framework collapses directly during the second weight loss. The increased stability during the TDXRPD experiment compared to the TG-data is attributed to the different experimental set ups.

The decomposition of CAU-3-BDC-NH₂ (**2**) is similar to that of **1**. Like for CAU-3-BDC, the decomposition starts after the removal of adsorbed solvent (10.3%) at a temperature of $\sim 180\text{ }^\circ\text{C}$. The two last weight losses correspond quite well to the decomposition of **2** (calc.: 66.4% , obs.: 62.4%), although the difference could be attributed to a small amount of X-ray-amorphous Al-oxo-species.

The decomposition of **3** during the TG-experiment shows a similar stability ($\sim 180\text{ }^\circ\text{C}$), but due to the observed byproducts, we did not attribute the weight losses to defined steps of decomposition.

Sorption properties

For the sorption measurements, the samples were activated in vacuum (10^{-2} mbar) at $160\text{ }^\circ\text{C}$ for 12 h. The XRPD patterns of the samples after the sorption experiments can be found in the supporting information (Fig. S1–S3). The nitrogen isotherms (Fig. 9) were measured at 77 K . The BET-method was applied to calculate the apparent surface area and the micropore volumes were calculated from the amount adsorbed at $p/p_0 = 0.5$.

The sorption experiments confirm the tendencies that we expected. The incorporation of the amino-group leads to a decrease of micropore volume as well as apparent surface area,

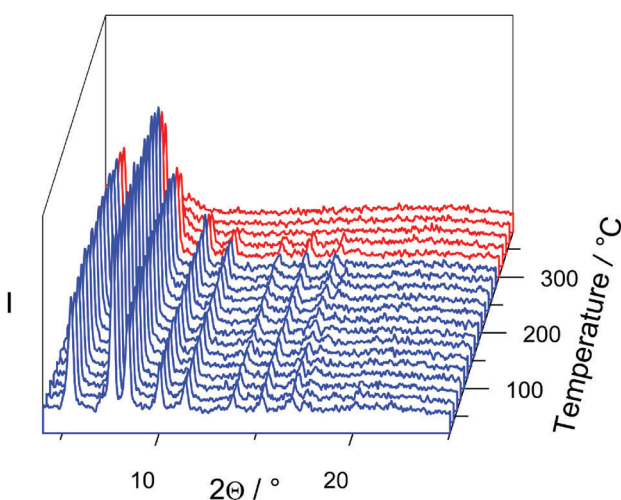


Fig. 8 Temperature-dependent XRPD patterns of CAU-3-BDC (**1**), measured under air.

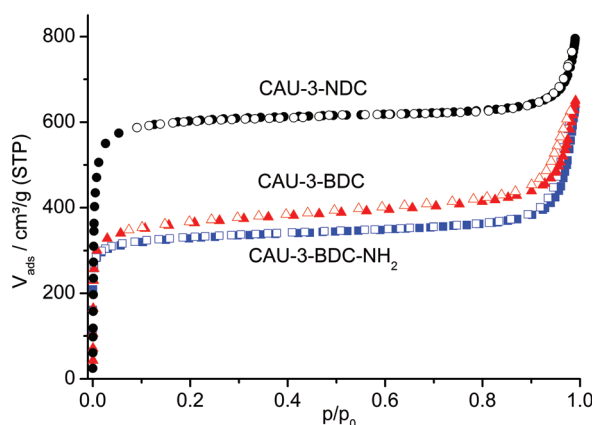


Fig. 9 N₂-Sorption isotherms for **1**, **2** and **3** measured at 77 K.

Table 2 Apparent specific surface areas and V_{mic} values of the CAU-3-MOFs

Compound	$A_{\text{BET}} \text{ m}^2 \text{ g}^{-1}$	$A_{\text{Langmuir}} \text{ m}^2 \text{ g}^{-1}$	$V_{\text{mic}} \text{ cm}^3 \text{ g}^{-1}$
CAU-3-BDC	1550	1920	0.64
CAU-3-BDC-NH ₂	1250	1520	0.53
CAU-3-NDC	2320	2750	0.95

while the enlargement of the linker molecule results in a drastically increased uptake. The BET-surfaces as well as the micropore volumes are summarized in Table 2.

The apparent specific surface areas and the micropore volume measured for CAU-3-NDC **3** are to the best of our knowledge the highest reported so far for any literature known Al-MOF. Changing the adsorbate from N₂ to H₂O, the influence of the functional group is clearly visible (Fig. 10). The use of H₂O vapour leads to strong hysteresis. The absolute amount of adsorbed water is similar for both CAU-3-BDC and CAU-3-BDC-NH₂, but due to the presence of the polar amino group, the adsorbed amount of water vapour at lower partial pressures is higher in CAU-3-NH₂.

Although this is a purely qualitative sorption study, the influence of the amino group with its ability for hydrogen bonding is obvious.

Conclusion

Summarizing our results, we have synthesized three new Al-containing MOFs by applying our high-throughput-methods and characterized them in detail. This new family of MOFs contains an unprecedented brick, [Al₁₂(OCH₃)₂₄]¹²⁺, which is twelvefold connected by dicarboxylate molecules to form a **fcu**-net. This inorganic unit is the second example for the occurrence of a wheel-shaped aluminium cluster in a metal-organic framework. All three compounds of the CAU-3-family are highly porous and exhibit BET-surface areas larger than 1200 m² g⁻¹ and micropore volumes higher than 0.5 cm³ g⁻¹. They are thermally stable up to at least 180 °C in air. The sorption properties are altered upon incorporation of a functional group or a larger linker molecule, respectively.

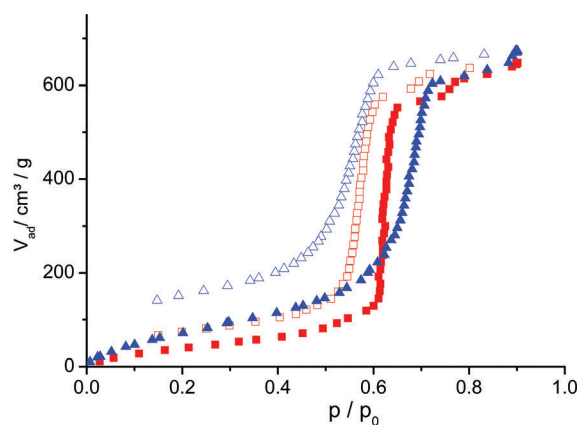


Fig. 10 Water vapour isotherms for **1** and **2** measured at 25 °C. Blue triangles for the NH₂-functionalized compound **2**, red squares for **1**. Empty symbols represent the desorption-, filled symbols represent the adsorption-branch.

Acknowledgements

This work has been financially supported by the DFG (SPP 1362). The research leading to these results has received funding from the European Community's Seventh Framework Programme (FP7/2007–20013) under grant agreement n° 228862'.

Notes and references

- G. Férey, *Chem. Soc. Rev.*, 2008, **37**, 191.
- Z. Wang and S. M. Cohen, *Chem. Soc. Rev.*, 2009, **38**, 1315.
- S. Kitagawa, R. Kitaura and S. Noro, *Angew. Chem., Int. Ed.*, 2004, **43**, 2334.
- C. Janiak, *Dalton Trans.*, 2003, 2781.
- R. Long and O. M. Yaghi, *Chem. Soc. Rev.*, 2009, **38**, 1213.
- O. M. Yaghi, M. O'Keeffe, N. W. Ockwig, H. K. Chae, M. Eddaoudi and J. Kim, *Nature*, 2003, **423**, 705.
- T. Devic, P. Horcajada, C. Serre, F. Salles, G. Maurin, B. Moulin, D. Heurtaux, G. Clet, A. Vimont, J.-M. Greneche, B. Le Ouay, F. Moreau, E. Magnier, Y. Filinchuk, J. Marrot, J.-C. Lavalley, M. Daturi and G. Férey, *J. Am. Chem. Soc.*, 2010, **132**, 1127.
- M. Eddaoudi, J. Kim, N. Rosi, D. Vodak, J. Wachter, M. O'Keeffe and O. M. Yaghi, *Science*, 2002, **295**, 469.
- C. Serre, C. Mellot-Draznieks, S. Surblé, N. Audebrand, Y. Filinchuk and G. Férey, *Science*, 2007, **315**, 1828.
- J. H. Cavka, S. Jakobsen, U. Olsbye, N. Guillou, C. Lamberti, S. Bordiga and K. P. Lillerud, *J. Am. Chem. Soc.*, 2008, **130**, 13850.
- A. Schaate, P. Roy, A. Godt, J. Lippke, F. Waltz, M. Wiebcke and P. Behrens, *Chem.-Eur. J.*, 2011, **17**, 6643.
- M. Kandiah, S. Usseglio, S. Svelle, U. Olsbye, K. P. Lillerud and M. Tilset, *J. Mater. Chem.*, 2010, **20**, 9848.
- S. Bauer, C. Serre, T. Devic, P. Horcajada, J. Marrot, G. Férey and N. Stock, *Inorg. Chem.*, 2008, **47**, 7568.
- P. Maniam and N. Stock, *Inorg. Chem.*, 2011, **50**, 5085.
- T. Ahnfeldt, D. Gunzelmann, T. Loiseau, D. Hirsemann, G. Férey, J. Senker and N. Stock, *Inorg. Chem.*, 2009, **48**, 3057.
- A. Sonnauer, F. Hoffmann, M. Fröba, L. Kienle, V. Duppel, M. Thommes, C. Serre, G. Férey and N. Stock, *Angew. Chem., Int. Ed.*, 2009, **48**, 3791.
- C. Volkringer, D. Popov, T. Loiseau, G. Férey, M. Burghammer, C. Riekel, M. Haouas and F. Taulelle, *Chem. Mater.*, 2009, **21**, 5695.
- C. Volkringer, D. Popov, T. Loiseau, N. Guillou, G. Férey, M. Haouas, F. Taulelle, C. Mellot-Draznieks, M. Burghammer and C. Riekel, *Nat. Mater.*, 2007, **6**, 760.
- C. Volkringer, T. Loiseau, N. Guillou, G. Férey, M. Haouas, F. Taulelle, N. Audebrand, I. Margiolaki, D. Popov, M. Burghammer and C. Riekel, *Cryst. Growth Des.*, 2009, **9**, 2927.
- C. Volkringer, T. Loiseau, M. Haouas, F. Taulelle, D. Popov, M. Burghammer, C. Riekel, C. Zlotea, F. Cuevas, M. Latroche,

- D. Phanon, C. Knöfelv, P. L. Llewellyn and G. Férey, *Chem. Mater.*, 2009, **21**, 5783.
- 21 C. Volkringer, T. Loiseau, N. Guillou, G. Férey, M. Haouas, F. Taulelle, E. Elkaim and N. Stock, *Inorg. Chem.*, 2010, **49**, 9852.
- 22 C. Volkringer, T. Loiseau, N. Guillou, G. Férey and E. Elkaim, *Solid State Sci.*, 2009, **11**, 1507.
- 23 T. Ahnfeldt, N. Guillou, D. Gunzelmann, I. Margiolaki, T. Loiseau, G. Férey, J. Senker and N. Stock, *Angew. Chem., Int. Ed.*, 2009, **48**, 5163.
- 24 W. Schmitt, E. Baissa, A. Mandel, C. E. Anson and A. K. Powell, *Angew. Chem., Int. Ed.*, 2001, **40**, 3577.
- 25 E. A. Mainicheva, O. A. Gerasko, L. A. Sheludyakova, D. Y. Naumov, M. I. Naumova and V. P. Fedin, *Russ. Chem. Bull.*, 2006, **55**, 267.
- 26 T. Loiseau, C. Serre, C. Huguenard, G. Fink, F. Taulelle, M. Henry, T. Bataille and G. Férey, *Chem.–Eur. J.*, 2004, **10**, 1373.
- 27 I. Senkovska, F. Hoffmann, M. Fröba, J. Getzschmann, W. Böhlmann and S. Kaskel, *Microporous Mesoporous Mater.*, 2009, **122**, 93.
- 28 A. Comotti, S. Bracco, P. Sozzani, S. Horike, R. Matsuda, J. Chen, M. Takata, Y. Kubota and S. Kitagawa, *J. Am. Chem. Soc.*, 2008, **130**, 13664.
- 29 J. Gascon, U. Aktay, M. D. Hernandez-Alonso, G. P. M. Van Klink and F. Kapteijn, *J. Catal.*, 2009, **261**, 75.
- 30 S. Couck, J. F. Denayer, G. V. Baron, T. Remy, J. Gascon and F. Kapteijn, *J. Am. Chem. Soc.*, 2009, **131**, 6326.
- 31 T. Ahnfeldt, J. Moellmer, V. Guillermin, R. Staudt, C. Serre and N. Stock, *Chem.–Eur. J.*, 2011, **17**, 6462.
- 32 E. Biemmi, S. Christian, N. Stock and T. Bein, *Microporous Mesoporous Mater.*, 2009, **117**, 111.
- 33 Materials Studio Version 5.0, Accelrys Inc., San Diego, CA, 2009.
- 34 Topas Academics 4.2, Coelho Software, 2007.
- 35 A. Altomare, M. Cavalli, R. Calandro, C. Cuocci, C. Giacovazzo, A. Gagliardi, A. G. G. Moliterni and R. Rizzi, EXPO2004. Program for Solving Crystal Structures from Powder Data by direct Methods, 2004.
- 36 STOE WinXPOW version 2.11, Stoe & Cie GmbH, 2005, Darmstadt, Germany.
- 37 T. C. Stamatatos, A. G. Christou, C. M. Jones, B. J. O'Callaghan, K. A. Abboud, T. A. O'Brien and G. Christou, *J. Am. Chem. Soc.*, 2007, **129**, 9840.
- 38 M. Helliwell, A. A. Smith, S. J. Teat and R. E. P. Winpenny, *Inorg. Chim. Acta*, 2003, **354**, 49.
- 39 D. J. Tranchemontagne, J. L. Mendoza-Cortes, M. O'Keeffe and O. M. Yaghi, *Chem. Soc. Rev.*, 2009, **38**, 1257.
- 40 M. Dan-Hardi, C. Serre, T. Frot, L. Rozes, G. Maurin, C. Sanchez and G. Férey, *J. Am. Chem. Soc.*, 2009, **131**, 10857.

4.3.2 A new Al-MOF based on a unique column-shaped inorganic building unit exhibiting strongly hydrophilic sorption behaviour

Der vorliegende Artikel wurde in „Chemical Communications“ veröffentlicht (reproduced with permission from RSC, *Chem. Commun.*, **2012**, *48*, 9486-9488).

Die Synthese der Verbindungen CAU-1 und CAU-3 in Methanol gab den Anlass zur Untersuchung weiterer solvothermalen Systeme mit Alkoholen als Lösungsmittel. Während in Ethanol ausschließlich literaturbekannte Phasen erhalten wurden konnten in 2-Propanol die Verbindungen Al-MIL-68 und CAU-6 hergestellt werden. Während Al-MIL-68 das Aluminium-basierte Analogon eines Vanadium-MOFs darstellt, handelt es sich bei CAU-6 um eine neue Verbindung. Die Summenformel $[Al_{13}Cl_6(H_2O)_6(OH)_{27}(O_2C-C_6H_3NH_2-CO_2)_3(C_3H_7OH)_6]$ konnte durch Kombination von Elementaranalyse, Thermogravimetrie, IR-Spektroskopie, energiedispersiver Röntgenfluoreszenz und Festkörper-NMR-Spektroskopie bestimmt werden. Basierend auf dieser Summenformel und Synchrotron-Pulverbeugungsdaten wurde ein Strukturmodell erstellt, das mittels Kraftfeldrechnungen optimiert wurde.

Die Struktur von CAU-6 basiert auf anorganischen Baueinheiten, die eine säulenförmige Architektur aufweisen. Heptamere von kantenverknüpften AlO_6 -Polyedern sind über Dimere eckenverknüpfter AlO_6 -Polyeder zu formal unendlich langen Säulen verknüpft. Diese Säulen können gedanklich auch erstellt werden, wenn die literaturbekannten dreizehnkernigen Al-Oxo-Cluster $[Al_{13}(OH)_{24}(H_2O)_{24}]Cl_{15} \cdot 13H_2O$ zu Säulen kondensiert würden. Die Anorganischen Baueinheiten in CAU-6 sind über 2-Aminoterephthalationen verknüpft, so dass trigonale Kanäle entstehen. Diese Kanäle sind mit Chlorid-Ionen und 2-Propanol Molekülen gefüllt, die nur teilweise entfernt werden können. Da diese nicht kristallographisch geordnet sind, konnte die Struktur nicht mittels Rietveldverfeinerung bestätigt werden. Allerdings stimmen alle weiteren Analyseergebnisse gut mit dem Strukturmodell überein. Die durch die eingelagerten Anionen stark polarisierte Oberfläche der Kanäle in Verbindung mit den protischen funktionellen OH- und NH_2 -Gruppen führt zu einem stark hydrophilen Sorptionsverhalten. Daher wird eine untypische Typ-I-Isotherme für die Wasserdampf-Sorption an CAU-6 beobachtet.

Cite this: *Chem. Commun.*, 2012, **48**, 9486–9488

www.rsc.org/chemcomm

A new Al-MOF based on a unique column-shaped inorganic building unit exhibiting strongly hydrophilic sorption behaviour†‡

Helge Reinsch,^a Bartosz Marszałek,^b Julia Wack,^c Jürgen Senker,^c Barbara Gil^b and Norbert Stock^{*a}

Received 9th July 2012, Accepted 7th August 2012

DOI: 10.1039/c2cc34909d

The new Al-based metal–organic framework $[Al_{13}(OH)_{27}(H_2O)_6(BDC-NH_2)_3Cl_6(C_3H_7OH)_6]$ denoted CAU-6 (CAU = Christian-Albrechts-Universität) was solvothermally synthesized in 2-propanol and was thoroughly characterized. The framework structure exhibits a unique column-shaped inorganic building unit, which is based on stacked, corner-sharing Al_{13} -clusters. The compound exhibits unprecedented hydrophilicity for metal–organic frameworks.

Metal–organic frameworks or MOFs are often the subject of research directed towards possible applications in separation processes¹ as well as in gas storage² and catalysis.³ Besides their often unparalleled performances in such areas, they are also investigated regarding their architectural beauty and sometimes unique inorganic building units. Al^{3+} ions exhibit a rich structural variability in aqueous solutions and many Al-oxo clusters have been reported.⁴ In contrast only a few Al^{3+} containing building units have been reported for Al-based MOFs synthesized under hydrothermal reaction conditions compared to *e.g.* In^{3+} -based MOFs.⁵ Besides trimeric and octameric clusters,^{6,7} one-dimensional infinite chains of corner- or edge-sharing AlO_6 -octahedra^{8,9} as well as continuous two-dimensional layers were observed.¹⁰ The change of the solvent to methanol induces the stabilization of other structural motifs (Fig. 1). Cyclic cationic clusters based on eight or twelve aluminium ions, *i.e.* $[Al_8(OH)_4(OCH_3)_8]^{12+}$ and $[Al_{12}(OCH_3)_{24}]^{12+}$, were shown to be stabilized by the incorporation into a MOF, while they were never observed elsewhere.^{11,12} In principle, these inorganic building units should also be accessible as discrete clusters and *vice versa* known molecular Al-oxo species could act as inorganic units in MOFs.

Our long-standing interest in the chemistry of Al-based MOFs has been assisted by the use of high-throughput (HT) methods.¹³ Since the structural diversity of this class of compounds is often

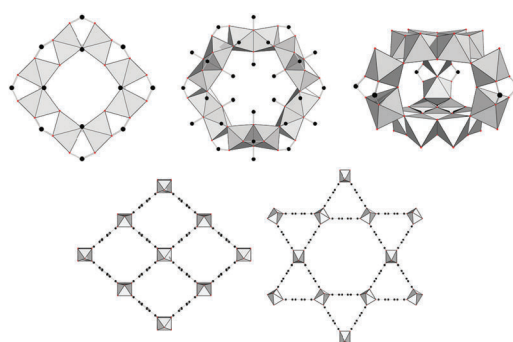


Fig. 1 Structural motifs and framework topologies that are observed in Al-MOFs synthesized from alcohols. Top: inorganic building units in CAU-1 (left), CAU-3 (middle) and CAU-6 (right). Bottom: topologies of MIL-53 (left) and MIL-68 (right).

accompanied by a high sensitivity towards synthesis parameters, these methods have been proven to be very useful for the discovery as well as the synthesis optimization.^{14,15} The new structural motifs observed for the synthesis in methanol inspired us to further employ alcohols as solvents in the system Al^{3+} - H_2BDC -X-solvent (H_2BDC -X stands for benzene-1,4-dicarboxylic acid with X = H, $-NH_2$). The use of ethanol yielded the corresponding well known compounds of the MIL-53-family Al-MIL-53 and Al-MIL-53- NH_2 (MIL = Matériaux d'Institut Lavoisier), independently of the aluminium source. Using the more hydrophobic solvent 2-propanol, the use of $AlCl_3 \cdot 6H_2O$ yielded different framework structures. Employing terephthalic acid, the formation of Al-MIL-68¹⁶ could be observed (Fig. S2, ESI†), while the use of 2-aminoterephthalic acid resulted in the formation of the new compound CAU-6 (Fig. 1). A list of HT reactions carried out and the obtained reaction products are given in the ESI† (Table S1 and Fig. S1, ESI†).

After establishing and optimising the synthetic route by using HT-methods, the reaction was scaled up. In a Teflon-lined autoclave ($V_{Max} = 37$ mL), 150 mg (0.83 mmol) of 2-aminoterephthalic acid ($H_2BDC-NH_2$), 800 mg (3.32 mmol) of $AlCl_3 \cdot 6H_2O$ and 5 mL of 2-propanol were heated for twelve hours to 120 °C, held at this temperature for twelve hours and cooled to room temperature over twelve hours. The precipitate was filtered and redispersed in 300 mL of water by stirring for several hours. After filtration and drying under ambient conditions, this washing procedure was repeated four more times.

^a Institute of Inorganic Chemistry, Christian-Albrechts-Universität Kiel, Max-Eyth-Straße 2, 24118 Kiel, Germany.
E-mail: stock@ac.uni-kiel.de

^b Faculty of Chemistry, Jagiellonian University, ul. Ingardena 3, 30-060 Kraków, Poland

^c Inorganic Chemistry I, Universität Bayreuth, Universitätsstraße 30, 95447 Bayreuth, Germany

† This article is part of the ChemComm metal–organic frameworks web themed issue.

‡ Electronic supplementary information (ESI) available: Materials and methods, details about synthesis and characterisation, analytical data for Al-MIL-68. See DOI: 10.1039/c2cc34909d

Upon this treatment, the cell parameters shift slightly (Fig. S3 and S4, ESI†).

By a combination of elemental analysis, EDX-spectroscopy, thermogravimetry, IR-spectroscopy and solid-state NMR-spectroscopy, the empirical formula of CAU-6 was established to be $[\text{Al}_{13}(\text{OH})_{27}(\text{H}_2\text{O})_6(\text{BDC-NH}_2)_3\text{Cl}_6(\text{C}_3\text{H}_7\text{OH})_6]$. For the structure determination, due to the absence of suitable single crystals, high-resolution XRPD data were recorded at the beamline G3 at the DESY-synchrotron source in Hamburg. Indexing of the pattern gave a hexagonal cell, which was confirmed and refined by the Le Bail method, resulting in the cell parameters $a = b = 19.2275(3)$ Å and $c = 14.0741(3)$ Å. The extinction conditions are in agreement with the space groups $P\bar{3}1c$, $P\bar{6}2c$ and $P6_3/mmc$ (Fig. S10, ESI†). The inorganic building unit could be unambiguously identified using direct methods for the structure determination in the space groups $P\bar{3}1c$ and $P\bar{6}2c$.¹⁷ Both structural models exhibited the higher symmetry of the space group $P6_3/mmc$. The complete model of the framework was therefore constructed in the space group $P6_3/mmc$ by insertion of the linker molecules and subsequently optimised using force field calculations.¹⁸ The framework of CAU-6 is based on the well known Al_{13} -cluster as found in the basic aluminium chloride $[\text{Al}_{13}(\text{OH})_{24}(\text{H}_2\text{O})_{24}]\text{Cl}_{15} \cdot 13\text{H}_2\text{O}$ (Fig. 2).¹⁹ In CAU-6 these clusters are stacked along the c -axis and the corner-sharing connectivity leads to the formation of infinite columns (Fig. S13 and S14, ESI†). Alternatively, the structure can be described as composed of heptanuclear cores of edge-sharing

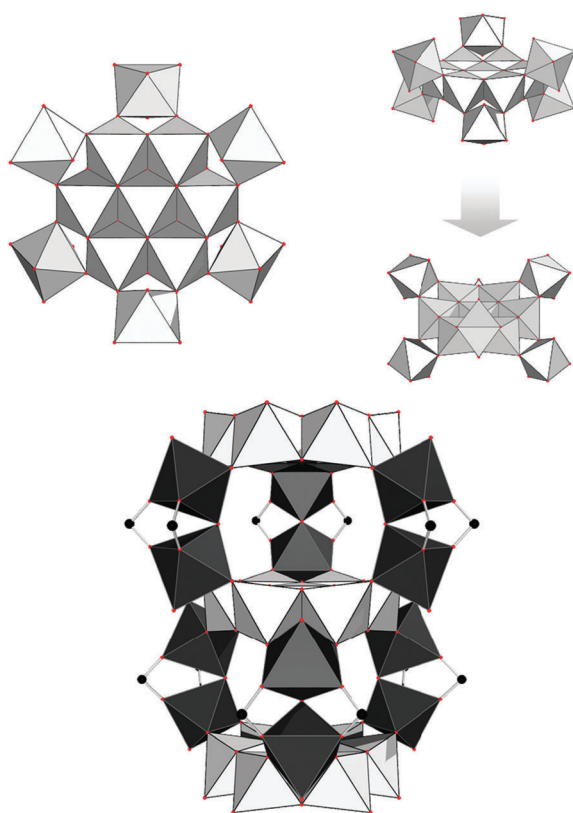


Fig. 2 The Al_{13} -subunit, its mode of condensation and a section of the condensed infinite column as found in the framework of CAU-6. In the latter, heptameric subunits are drawn in light gray, while the bridging dimers are emphasized in black. Bridging carboxylate groups are shown.

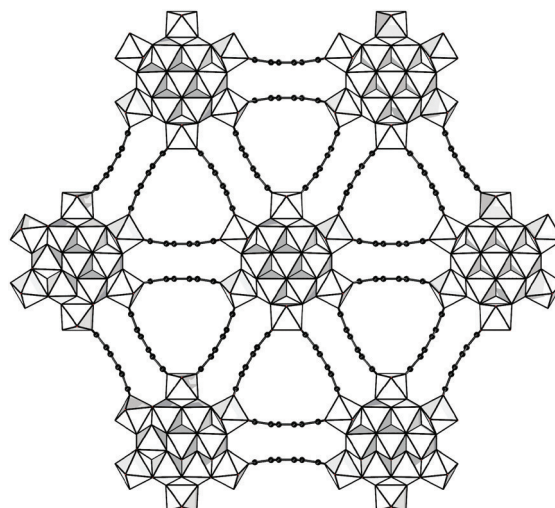


Fig. 3 Framework structure of CAU-6 as seen along the c -axis.

AlO_6 -polyhedra, which are interconnected by dimers of corner-sharing AlO_6 -polyhedra (Fig. 2).

The interconnection of these infinite columns is achieved by aminoterephthalate ions. Two carboxylate groups coordinate to each dimer. Thus, each column is connected to six of their neighbouring columns (Fig. 3). By this connection, sinusoidal trigonal channels with a diameter between 5 and 10 Å are formed. In addition, small cavities with a diameter of ~ 2.4 Å are found between the heptanuclear cores inside the columns.

These pores are partially occupied by chloride ions, 2-propanol and water molecules in a non-ordered fashion. Therefore, the structural model could not be refined by Rietveld methods, although the simulated pattern is in good agreement with the measured one (Fig. S11, ESI†).

The solid-state 1D-NMR-experiments confirm the incorporation of the linker molecules and 2-propanol into the MOF, and prove that the Al^{3+} ion is exclusively octahedrally coordinated to six oxygen atoms (Fig. S15 and S16, ESI†). 2-Propanol molecules could not be removed even by extensive treatment with water and thermal activation at 130 °C. The 2D-NMR-spectrum for ^{27}Al proves that the inorganic unit is built up by Al^{3+} ions in two different chemical environments in the approximate ratio 7 : 6 (Fig. 4).

This is in good agreement with the structural model. The connection of Al^{3+} ions within a column must be accomplished by hydroxide ions or solvent molecules. The chloride ions act as counterions. Although some chloride is washed out during the extensive aqueous work-up, residual ions remain inside the channels, as measured by EDX. The occluded water molecules can be only partially removed by thermal activation without damaging the framework structure, as proven by thermogravimetry and *in situ* IR-spectroscopy (Fig. S6 and S18, ESI†). Thermal treatment in vacuum up to 100 °C reduces the intensity of the ν_{OH} -bands of hydrogen bonded water and propanol molecules around 3400 cm^{-1} . The complete removal of water and propanol molecules at temperatures > 150 °C leads to the decomposition of the framework. This is clearly observed by broadening and flattening of the ν_{CO} -bands between 1400 and 1700 cm^{-1} . Thus, it is not possible by thermal activation to obtain the solvent-free framework structure without structural

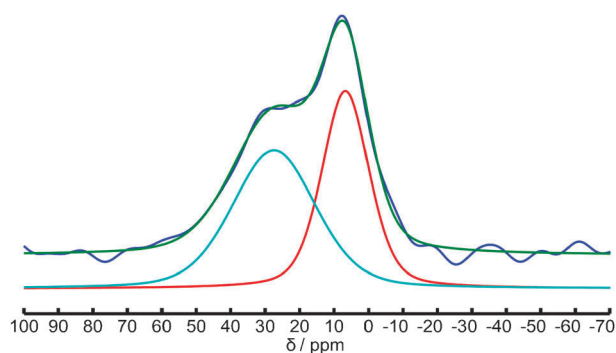


Fig. 4 Deconvoluted F1 projection of the ^{27}Al MQMAS-spectrum. Measured signal (blue) fit (green), simulated signals in red, turquoise.

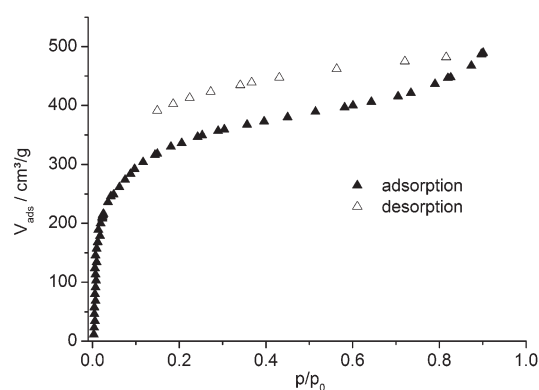


Fig. 5 Water vapour sorption isotherm for CAU-6, measured at 298 K.

collapse. Therefore the residual solvent and water molecules and the counterions must be considered as part of the MOF.

The thermally activated (130 °C, 12 h, 0.1 mbar), *i.e.* partially dehydrated MOF still exhibits remarkable porosity towards nitrogen (Fig. S8, ESI†). The apparent specific BET-surface area is $A_{\text{BET}} = 620 \text{ m}^2 \text{ g}^{-1}$ and the micropore volume is $V_{\text{Mic}} = 0.25 \text{ cm}^3 \text{ g}^{-1}$, as calculated from the amount adsorbed at $p/p_0 = 0.5$. More interestingly, the highly polar surface built up by the protic OH- and NH_2 -groups, chloride ions and solvent molecules induces a strong affinity towards polar adsorbents like CO_2 (Fig. S9, ESI†) and especially towards H_2O (Fig. 5). The amount of CO_2 adsorbed at 1 bar at 298 K is $V_{\text{ads}} = 84 \text{ mg g}^{-1}$.

The type-I-isotherm for the H_2O -vapour adsorption is exceptional for MOFs, and to the best of our knowledge, such hydrophilicity has not been reported for MOFs yet. Most often, MOFs are hydrophobic or require a certain partial pressure, before H_2O is adsorbed.^{20–22} For CAU-6, the combination of the protic OH- and NH_2 -groups, guest molecules and counterions results in hydrophilic properties. Substantial amounts of H_2O -vapour are already adsorbed at low p/p_0 and the gravimetric capacity at $p/p_0 = 0.9$ is $\sim 37\%$.

Summarizing the results, we were able to synthesize a new MOF based on unique column-shaped inorganic building units based on Al_{13} -clusters. Although the crystal structure could not be refined by conventional methods, the combination of various analytical techniques allowed us to establish a coherent structural model. The combination of micropores,

surface decorating protic groups, solvent molecules and counterions leads to exceptionally hydrophilic properties.

The research leading to these results has received funding from the European Community's Seventh Framework Programme (FP7/2007-2013) under grant agreement no. 228862. The work has been supported by the DFG (SPP 1362) and the European Regional Development Fund in the framework of the Polish Innovation Economy Operational Program (contract no. POIG.02.01.00-12-023/08). The help of Andre Rothkirch (DESY, Hamburg) during the collection of XRPD-data is gratefully acknowledged, as well as the recording of the SEM-micrographs by Markus Döblinger (LMU Munich).

Notes and references

- 1 F. Vermoortele, M. Maes, P. Modhadam, M. Lennox, F. Ragon, M. Boulhout, S. Biswas, K. Laurier, I. Beurroies, R. Denoyel, M. Roeffaers, N. Stock, T. Dürren, C. Serre and D. De Vos, *J. Am. Chem. Soc.*, 2011, **133**, 18529.
- 2 M. P. Suh, H. J. Park, T. K. Prasad and D. Lim, *Chem. Rev.*, 2012, **112**, 782.
- 3 A. Corma, H. García and F. X. Llabrés i Xamena, *Chem. Rev.*, 2010, **110**, 4606.
- 4 E. A. Mainicheva, O. A. Gerasko, L. A. Sheludyakova, D. Y. Naumov, M. I. Naumova and V. P. Fedin, *Russ. Chem. Bull.*, 2006, **55**, 267.
- 5 S. Zheng, J. J. Bu, T. Wu, C. Chou, P. Feng and X. Bu, *Angew. Chem., Int. Ed.*, 2011, **50**, 8858; S. Zheng, C. Mao, T. Wu, S. Lee, P. Feng and X. Bu, *J. Am. Chem. Soc.*, 2012, **134**, 11936.
- 6 C. Volkringer, D. Popov, T. Loiseau, G. Férey, M. Burghammer, C. Riekkel, M. Haouas and F. Taulelle, *Chem. Mater.*, 2009, **21**, 5695.
- 7 C. Volkringer, D. Popov, T. Loiseau, N. Guillou, G. Férey, M. Haouas, F. Taulelle, C. Mellot-Draznieks, M. Burghammer and C. Riekkel, *Nat. Mater.*, 2007, **6**, 760.
- 8 T. Loiseau, C. Serre, C. Huguenard, G. Fink, F. Taulelle, M. Henry, T. Bataille and G. Férey, *Chem.–Eur. J.*, 2004, **10**, 1373.
- 9 C. Volkringer, T. Loiseau, M. Haouas, F. Taulelle, D. Popov, M. Burghammer, C. Riekkel, C. Zlotea, F. Cuevas, M. Latroche, D. Phanon, C. Knöfel, P. L. Llewellyn and G. Férey, *Chem. Mater.*, 2009, **21**, 5783.
- 10 T. Loiseau, L. Lecroq, C. Volkringer, J. Marrot, G. Férey, M. Haouas, F. Taulelle, S. Bourrelly, P. L. Llewellyn and M. Latroche, *J. Am. Chem. Soc.*, 2006, **128**, 10223.
- 11 T. Ahnfeldt, N. Guillou, D. Gunzelmann, I. Margiolaki, T. Loiseau, G. Férey, J. Senker and N. Stock, *Angew. Chem., Int. Ed.*, 2009, **48**, 5163.
- 12 H. Reinsch, M. Feyand, T. Ahnfeldt and N. Stock, *Dalton Trans.*, 2012, **41**, 4164.
- 13 N. Stock, *Microporous. Mesoporous. Mater.*, 2010, **129**, 287.
- 14 H. Reinsch, M. Krüger, J. Wack, J. Senker, F. Salles, G. Maurin and N. Stock, *Microporous. Mesoporous. Mater.*, 2012, **157**, 50.
- 15 A. Sonnauer, F. Hoffmann, M. Fröba, L. Kienle, V. Duppel, M. Thommes, C. Serre, G. Férey and N. Stock, *Angew. Chem., Int. Ed.*, 2009, **48**, 3791.
- 16 M. Schubert, U. Mueller and S. Marx, *Patent US*, 2010/0076220 A1, 2010.
- 17 A. Altomare, M. Cavalli, R. Calandro, C. Cuocci, C. Giacobozzo, A. Gagliardi, A. G. G. Moliterni, R. Rizzi, *EXPO2004. Program for Solving Crystal Structures from Powder Data by direct Methods*, 2004.
- 18 *Materials Studio Version 5.0*, Accelrys Inc., San Diego, CA, 2009.
- 19 W. Seichter, H. Mögel, P. Brand and D. Salah, *Eur. J. Inorg. Chem.*, 1998, 795.
- 20 P. Küsgens, M. Rose, I. Senkovska, H. Fröde, A. Henschel, S. Siegle and S. Kaskel, *Microporous. Mesoporous. Mater.*, 2008, **120**, 325.
- 21 S. K. Henninger, F. Jeremias, H. Kummer and C. Janiak, *Eur. J. Inorg. Chem.*, 2012, **16**, 2525.
- 22 G. Akiyama, R. Matsuda, H. Sato, A. Hori, M. Takata and S. Kitagawa, *Microporous. Mesoporous. Mater.*, 2012, **157**, 89.

4.4 Synthese neuer poröser MOFs basierend auf 1,3,5-funktionalisierten aromatischen Tricarboxylat-Ionen

4.4.1 A new aluminum-based microporous metal-organic framework: Al(BTB) (BTB = 1,3,5-benzenetrisbenzoate)

Dieses Manuskript wurde in der vorliegenden Fassung in „Microporous and Mesoporous Materials“ veröffentlicht (*Micropor. Mesopor. Mater.*, **2012**, 157, 50-55). In dem solvothermalen System Al^{3+} / 1,3,5-Benzentris-*p*-benzoesäure (H_3BTB) / DMF wurde die Bildung des mikroporösen MOFs [Al(BTB)] oder CAU-4 beobachtet. Durch Zusatz von Benzoesäure als Additiv konnte die Verbindung phasenrein isoliert werden. Ausgehend von der Kristallstruktur des Lanthanoid-basierten MOFs Tb-MIL-103 [Tb(BTB)(H_2O)] konnte mittels Kraftfeldrechnungen ein Strukturmodell der Verbindung erstellt werden, das mit allen Analyseergebnissen übereinstimmt. Aufgrund der geringen Kristallinität konnte dieses Modell allerdings nicht mittels Rietveldmethoden verfeinert werden. CAU-4 wurde mittels Elementaranalyse, IR-Spektroskopie, Thermogravimetrie, Röntgenpulverbeugung, Festkörper-NMR-Spektroskopie und Stickstoff-Sorption charakterisiert. Die anorganischen Baueinheiten sind isolierte Al^{3+} -Ionen, die über die Carboxylatgruppen des BTB-Moleküls zu einer formal unendlich langen Kette verbunden werden. Dadurch entstehen hexagonale Kanäle mit einem Porendurchmesser von ~ 1 nm.



A new aluminium-based microporous metal–organic framework: Al(BTB) (BTB = 1,3,5-benzenetrisbenzoate)

Helge Reinsch^a, Martin Krüger^a, Julia Wack^b, Jürgen Senker^b, Fabrice Salles^c, Guillaume Maurin^c, Norbert Stock^{a,*}

^a Institut für Anorganische Chemie, Christian-Albrechts-Universität, Max-Eyth Straße 2, D-24118 Kiel, Germany

^b Anorganische Chemie I, Universität Bayreuth, Universitätsstr. 30, D-95447 Bayreuth, Germany

^c Institut Charles Gerhardt – UMR CNRS 5253, UMR2, ENSCM, Université de Montpellier II, Place Eugène Bataillon CC 003, F-34095 Montpellier cedex 5, France

ARTICLE INFO

Article history:

Received 23 December 2010

Received in revised form 12 May 2011

Accepted 13 May 2011

Available online 16 June 2011

Keywords:

Metal organic framework

High-throughput methods

Solvothermal synthesis

Metal carboxylate

Aluminium

ABSTRACT

The system $\text{Al}^{3+}/\text{H}_3\text{BTB}/\text{DMF}/\text{additive}$ was systematically investigated using high-throughput methods and the new, microporous MOF [Al(BTB)] (BTB = 1,3,5-benzenetrisbenzoate), named CAU-4 (CAU = Christian-Albrechts-University), was discovered. The synthesis was optimized changing chemical and process parameters and the final synthesis procedure was scaled up to the gram scale. CAU-4 is thermally stable up to 400 °C in air and exhibits a BET-surface area of 1520 m²/g and a micropore volume of 0.61 cm³/g. A structure model was developed using a computationally assisted structure determination that was further validated by a good agreement with the experimental X-ray diffraction patterns and the geometrical features. The framework structure consists of isolated [AlO₆]-octahedra which are bridged by carboxylate groups of the BTB-linker to form chains. These chains are connected by the tritopic aromatic building blocks, to form one-dimensional hexagonal channels with a diameter of ca. 9.6 Å.

© 2011 Elsevier Inc. All rights reserved.

1. Introduction

In the last decade, the research on metal–organic frameworks (MOFs) has produced an amazing number of new porous framework materials [1]. These compounds are built up from organic linker molecules, typically containing carboxylate or phosphonate groups, and inorganic building blocks (bricks) like metal cations or metal-oxo-clusters [2]. Once the synthesis conditions of the inorganic building blocks are established, isoreticular synthesis can be employed to adjust the pore size and pore functionality [3–8]. Through post-synthetic modification the properties of the MOFs can be fine-tuned. The so-obtained compounds are investigated for their use in gas sorption or separation, in drug delivery or as catalysts [9,10].

MOFs which are based on trivalent cations have shown to be materials with highly desirable properties. Thus, many chromium- and aluminium-based MOFs show a very high thermal and chemical stability such as Al-MIL-53 [11], MIL-100 [12–14], and Cr-MIL-101 [15]. These MOFs are based on terephthalic acid (H₂BDC) or trimesic acid (H₃BTC). Extension of the organic linker has led to isoreticular compounds exhibiting larger pores and cavities. The use of the ditopic ligands naphthylidicarboxylic acid and biphenyldicarboxylic acid resulted in the formation of the

porous analogues of the Al-MIL-53 (DUT-4 and DUT-5) [16]. The tritopic ligand H₃BTC has been observed in the Al-based MOFs Al-MIL-96 [17], Al-MIL-100 [12], and MIL-110 [18] which exhibit large specific BET-surfaces and micropore volumes. The extension of H₃BTC by insertion of phenyl rings leads to 1,3,5-benzenetrisbenzoic acid (H₃BTB). Although there is a large number of MOFs containing this linker molecule that are based on beryllium [19], magnesium [20], copper [21], zinc [22–25] nickel [26], terbium [27] or iron [28], there is no example in the chemistry of aluminium.

In the course of our systematic investigation of Al-containing MOFs, we selected the tritopic linker H₃BTB for the exploration of the system $\text{Al}^{3+}/\text{H}_3\text{BTB}/\text{DMF}/\text{additive}$. Here, we present the synthesis and detailed characterization of the first Al- and BTB-containing MOF [Al(BTB)].

2. Experimental section

2.1. General

All chemicals used for the synthesis of CAU-4 are commercially available and were used without further purification. For the discovery and synthesis optimization high-throughput methods comprising our 24-high-throughput reactor system were employed [29,30]. The high-throughput XRPD measurements were performed using a STOE HT diffractometer equipped with a xy-stage and an IPDS system (Cu K_{α1} radiation) in transmission geometry.

* Corresponding author. Tel.: +49 (0) 431 880 1675; fax: +49 (0) 431 880 1775.
E-mail address: stock@ac.uni-kiel.de (N. Stock).

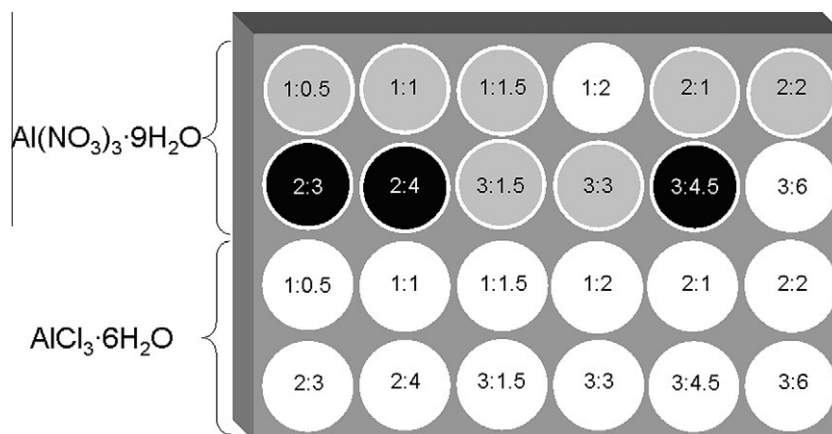


Fig. 1. Results of the high-throughput investigation of the system $\text{Al}^{3+}/\text{H}_3\text{BTB}/\text{DMF}$ at a reaction temperature of $190\text{ }^\circ\text{C}$. Grey (CAU-4), black (mixture of CAU-4 and the crystalline byproduct), white (X-ray amorphous product). The numbers represent the molar ratios $\text{H}_3\text{BTB}:\text{Al}^{3+}$.

High-precision powder diffraction data was measured on a STOE Stadi-P powder diffractometer equipped with a linear position sensitive detector system ($\text{Cu}-\text{K}\alpha_1$ radiation). MIR spectra were recorded on an ATI Matheson Genesis spectrometer in the spectral range of $400\text{--}4000\text{ cm}^{-1}$ using the KBr disk method. FT-Raman spectra were recorded on a Bruker IFS 66 FRA 106 in the range of $0\text{--}3500\text{ cm}^{-1}$ using a Nd/YAG-Laser (1064 nm). The thermogravimetric analyses were performed using a NETSCH STA 409 CD analyzer. The samples were heated in Al_2O_3 crucibles at a rate of 4 K min^{-1} under a flow of air (75 ml min^{-1}). The TG data were corrected for buoyancy and current effects. Sorption experiments were carried out using a Belsorp-max instrument (BEL JAPAN INC.) Before the sorption experiments, the samples were activated at $200\text{ }^\circ\text{C}$ under vacuum (10^{-2} kPa) over night. ^{27}Al and ^{13}C solid-state NMR studies were performed on a commercial BRUKER Avance II 300 spectrometer operating at 7.05 T . The relative reference for ^{13}C shifts was TMS and for ^{27}Al shifts a hydrochloric solution of AlCl_3 . The measurements were taken in a 4 mm triple-resonance probe from BRUKER. All experiments were measured under magic angle spinning (MAS) with spinning frequencies of 12.5 kHz for the ^{13}C - and 14430 Hz for the ^{27}Al -MQMAS spectrum. A ramped cross-polarization sequence with a contact time of 5 ms was used for the excitation of the ^{13}C nuclei, where the power of the ^1H radiation was linearly varied from 100% to 50% . During the acquisition a broadband proton decoupling with a nutation frequency of 70 kHz and SPINAL64 was applied. The ^{27}Al -MQMAS spectrum was recorded with a three-pulse sequence [31] with nutation frequencies of 108 kHz , 300 kHz and 11 kHz for the excitation, conversion and selective 90° pulses, respectively. The

coherence pathway $0 \pm 30\text{--}1$ was selected via a cog-wheel phase cycle [32] $\text{COG60}\{11,1,0;30\}$.

2.2. Preparation

The optimized synthesis of CAU-4 in the HT reactor system ($V_{\text{max}} = 2.0\text{ ml}$ per Teflon insert) is as follows: $\text{Al}(\text{NO}_3)_3 \cdot 9\text{H}_2\text{O}$ ($45.7\text{ }\mu\text{mol}$, 17.1 mg , Merck), benzoic acid ($81.9\text{ }\mu\text{mol}$, 10.0 mg , Merck) and 1,3,5-benzenetrisbenzoic acid ($91.3\text{ }\mu\text{mol}$, 40.0 mg , BASF) were dissolved in *N,N*-dimethylformamide (6.50 mmol , 0.50 mL , BASF). The reactor was heated for 24 h at $180\text{ }^\circ\text{C}$.

The reaction can be scaled up to the fourfold amount, using Pyrex glass tubes, or to the tenfold amount, using larger steel autoclaves with Teflon inserts ($V = 30\text{ mL}$). The same molar ratios $\text{Al}^{3+}:\text{H}_3\text{BTB}:\text{benzoic acid}:\text{DMF} = 7:14:10:142$ as well as the same temperature program were used. A yield of 47% (based on H_3BTB) was obtained from the reaction in the 30 ml reactor. Elemental analysis of the scaled-up synthesis product: $[\text{Al}(\text{BTB})] \cdot 1.6(\text{DMF}) \cdot 4.7(\text{H}_2\text{O})$ calc (%): C 57.5 , H 5.4 , N 3.4 , found (%): C 58.4 H 4.2 , N 3.8 . These values correspond well to the results of the TG measurements but may change upon long term exposure to air.

2.3. Molecular simulations

2.3.1. Computational assisted structure determination

The structure model for the CAU-4 was derived from an energy minimization procedure in the space group $P1$ using the classical universal force field (UFF) [33] and imposing the unit cell

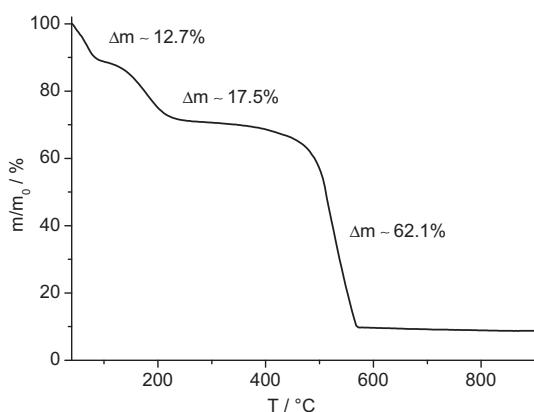


Fig. 2. TG analysis of $[\text{Al}(\text{BTB})] \cdot 1.6\text{ DMF} \cdot 4.7\text{ H}_2\text{O}$ (CAU-4-as).

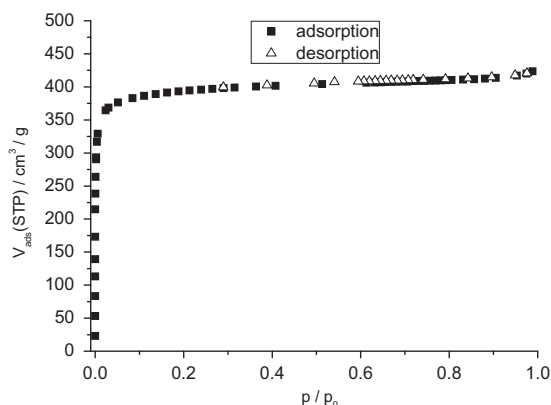


Fig. 3. Sorption isotherm of CAU-4 measured with N_2 at $-196\text{ }^\circ\text{C}$.

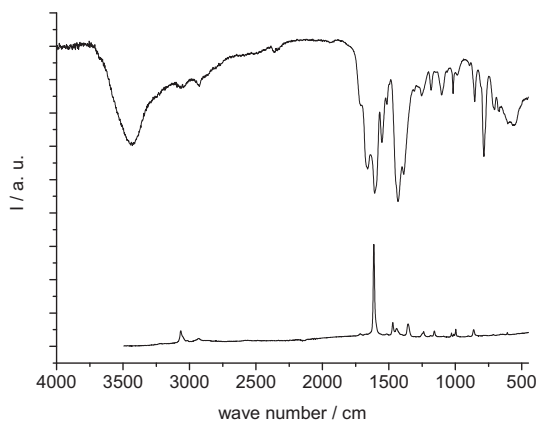


Fig. 4. IR- and Raman spectra of as synthesized CAU-4.

parameters determined experimentally. Such calculations were performed using the Forcite software implemented in Materials Studio (version 5.0) [34]. The UFF force field has been selected for its ability to reproduce successfully the structures of many metal–organic frameworks [5,35,36]. Since the UFF force field describes only aluminium with a tetrahedral coordination environment, the parameters for the octahedrally coordinated Al^{3+} present in CAU-4 were defined starting with those available for Fe^{2+} defined in an octahedral environment. This adjustment consisted of rescaling the σ -parameter taking into account the difference of ionic radii for the two elements [37]. Such a procedure was validated on the Al-MIL-53 structure with simulated Al–O distances and O–Al–O angles very similar to those experimentally determined [11]. The powder XRPD pattern for the resulting structure was further calculated using the Reflex software within Materials Studio.

2.3.2. Calculations of the geometrical features

The accessible surface area of the simulated structure model for CAU-4 was estimated using the strategy previously reported by Düren et al. [38]. The surface area was calculated from the center of a nitrogen probe molecule rolling across the surface. While the diameter of the nitrogen probe molecule was considered to be 3.681 Å, the diameters of each atom constituting the CAU-4 structure were taken from the forcefield described above. Using the same parametrization for the framework, the methodology of Gelb and Gubbins [39] was further used to calculate the pore size distribution (PSD). Finally, the solvent accessible volume was also determined from the crystal structure model using the standard setting

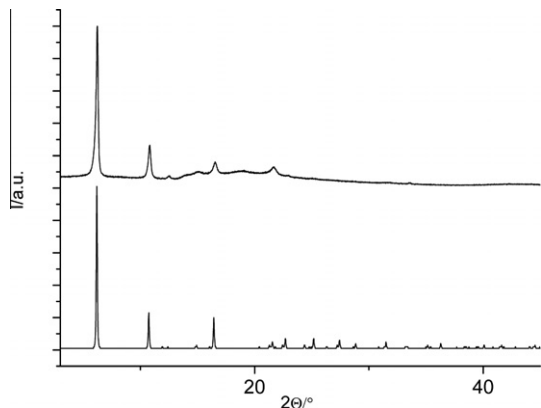


Fig. 5. Comparison of the diffractograms of MIL-103 (calculated, bottom) and CAU-4 (top).

in PLATON, which uses a random probe molecule with a diameter of 2.6 Å [40].

3. Results and discussion

3.1. Synthesis

High-throughput methods have shown to be a valuable tool for the exploration of new chemical systems. Thus, the discovery of new compounds and the optimization of synthesis procedures can be rapidly achieved while using only small amounts of starting materials [30]. Due to the large number of experiments reaction trends can be extracted and fields of formation are easily established [41–43].

CAU-4 was discovered during a high-throughput investigation of the system $\text{Al}^{3+}/\text{H}_3\text{BTB}/\text{solvent}$ using $\text{Al}(\text{NO}_3)_3 \cdot 9\text{H}_2\text{O}$ or $\text{AlCl}_3 \cdot 6\text{H}_2\text{O}$ respectively as the metal-source. Use of DMF as the solvent (190 °C/24 h) led to the formation of two new compounds depending on the molar ratios employed (Fig. 1).

Using $\text{AlCl}_3 \cdot 6\text{H}_2\text{O}$ as the aluminium source, only X-ray amorphous solids were obtained. Employing $\text{Al}(\text{NO}_3)_3 \cdot 9\text{H}_2\text{O}$, the formation of pure phase CAU-4 is observed at molar ratios $\text{H}_3\text{BTB}:\text{Al}^{3+} \geq 1$. Especially at higher concentrations (Fig. 1, 2nd row), mixtures of CAU-4 and a crystalline byproduct are formed, when $\text{Al}(\text{NO}_3)_3 \cdot 9\text{H}_2\text{O}$ is used in excess.

After the discovery of the new phase focused libraries were set up to determine the field of formation of CAU-4. First the overall concentration as well as molar ratio $\text{Al}^{3+}/\text{H}_3\text{BTB}$ were optimized. Employing the molar ratio $\text{Al}^{3+}:\text{H}_3\text{BTB}:\text{DMF} = 7:14:142$ crystalline products were obtained. To further increase the crystallinity different additives such as water, NaOH, HNO_3 , ethylenediamine or monodentate carboxylic acids were tested. Only the latter additives led to an improvement of the crystallinity. Small amounts of formic acid as well as benzoic acid had a slightly positive influence on the product formation (Fig. S1). In addition, the use of benzoic acid as the additive improves the reproducibility of synthesis procedure for CAU-4 which strongly depends on the purity of the DMF (Fig. S2). The molar ratio $\text{Al}^{3+}:\text{H}_3\text{BTB}:\text{benzoic acid}:\text{DMF} = 7:14:10:142$ was finally used for the scale-up synthesis of CAU-4.

Once the chemical parameters were established we focused on the optimization of the process parameters. The reaction temperature and the reaction time were found to be optimal at 180 °C for 24 h. Higher temperatures led to less crystalline products, while longer reaction times did not improve the product quality (Fig. S3). For the synthesis scale-up, the time-dependent formation of CAU-4 under stirring was also investigated. CAU-4 is obtained after 3 h and the crystallinity of the product improves with time (Fig. S4).

3.2. Thermal analysis and stability

The thermogravimetric experiment (Fig. 2) was performed under air with a heating rate of 4 K/min. The first weight loss between 40 and 100 °C corresponds to the removal of adsorbed water molecules (calc. 12.8%; obs. 12.7%), while the second step (120–200 °C) can be attributed to the removal of DMF molecules (calc. 17.6%; obs. 17.5%). The framework is stable up to 400 °C and decomposes under formation of X-ray amorphous Al_2O_3 (calc. 61.9%; obs. 62.1%). The observed weight losses are in very good agreement with the results of the elemental analysis. Thus the as synthesized compound has the composition $[\text{Al}(\text{BTB})] \cdot 1.6 \text{ DMF} \cdot 4.7 \text{ H}_2\text{O}$.

The XRD pattern of a sample activated at 200 °C under vacuum for 12 h shows that the framework structure is stable in air after the removal of the guest molecules (Fig. S5). Thus, CAU-4 is

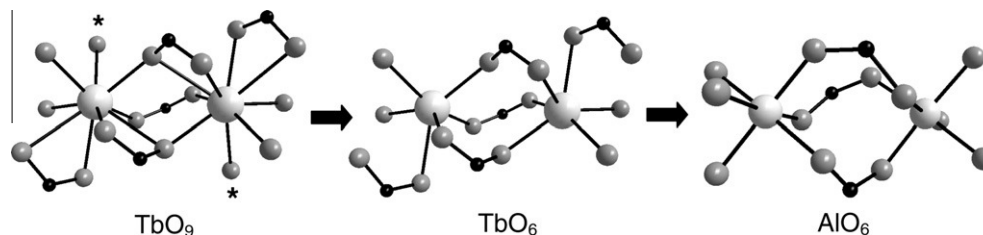


Fig. 6. Conversion of the ninefold coordination of edge-sharing $[\text{TbO}_9]$ -polyhedra observed in MIL-103 into isolated $[\text{AlO}_6]$ -octahedra connected by the carboxylate groups. The asterisk marks the water molecules coordinated to the Tb^{3+} ions. Grey: oxygen, black: carbon, white: metal.

Table 1

Cell parameters of MIL-103 (starting model), the structural model of CAU-4 (from force field calculations) and the final structural model, taking the experimental reflection positions into account.

Structure	MIL-103	CAU-4: structure of minimal energy	CAU-4: experimental lattice parameters
Space group	<i>R</i> 32	<i>P</i> 312	<i>P</i> 312
<i>a</i> = <i>b</i>	28.5344(8) Å	15.9822 Å	16.273(1) Å
<i>c</i>	12.2148(5) Å	3.7721 Å	12.956(6) Å

another example of the high stability of Al-containing MOFs. Its stability is comparable to the one observed for other Al-containing MOFs such as of DUT-4 and DUT-5 exhibiting also unfunctionalized linker molecules, similar micropore volumes and easily accessible channels [16]. A similar functionalized porous Al-MOF such as CAU-1 decomposes around 310 °C [44].

3.3. Adsorption

The structural integrity of the activated compound was also demonstrated by sorption measurements. The N_2 -isotherm was recorded at -196 °C (Fig. 3). Prior to the measurement, the sample was activated over night at 200 °C and 10^{-2} kPa. A type I isotherm is observed which is typical for microporous materials. The specific surface was calculated using the BET-equation according to the procedure proposed recently [45]. CAU-4 exhibits an apparent spe-

cific surface area of 1520 m^2/g and a micropore volume of 0.61 cm^3/g (calculated from the amount adsorbed at $p/p_0 = 0.5$). This corresponds well to the solvent accessible volume calculated from the crystal structure model using PLATON (0.67 cm^3/g) [40].

The pore size was determined from the N_2 -isotherm by means of NLDFT/GCMC-methods using the BELSORP evaluation software [46]. Assuming a cylindrical pore shape and an oxidic surface, the pore radius was determined to be 4.1 Å, which is quite close to the expected value of 4.8 Å. The PSD as well as the simulated fit can be found in the supporting information (Figs. S6 and S7).

3.4. Spectroscopy

The IR- and Raman spectra (Fig. 4) of the as synthesized CAU-4 show the presence of water (3443 cm^{-1}) and residual DMF (2926 , 1709 cm^{-1}) molecules in the pores. The presence of the coordinating carboxylate groups is demonstrated by the stretching vibrations ν_{as} and ν_{s} at 1628 cm^{-1} and 1431 cm^{-1} , respectively. The absorption at 787 cm^{-1} can be attributed to the C–H deformation vibration of the 1,3,5-substituted aromatic ring. In the Raman-spectrum, the C–H stretching vibrations of the aromatic protons are observed at 3065 cm^{-1} and the C–C ring stretching vibration at 1613 cm^{-1} .

4. Structure

Since no single crystals could be obtained, and due to the limited number of well resolved reflections in the XRPD pattern

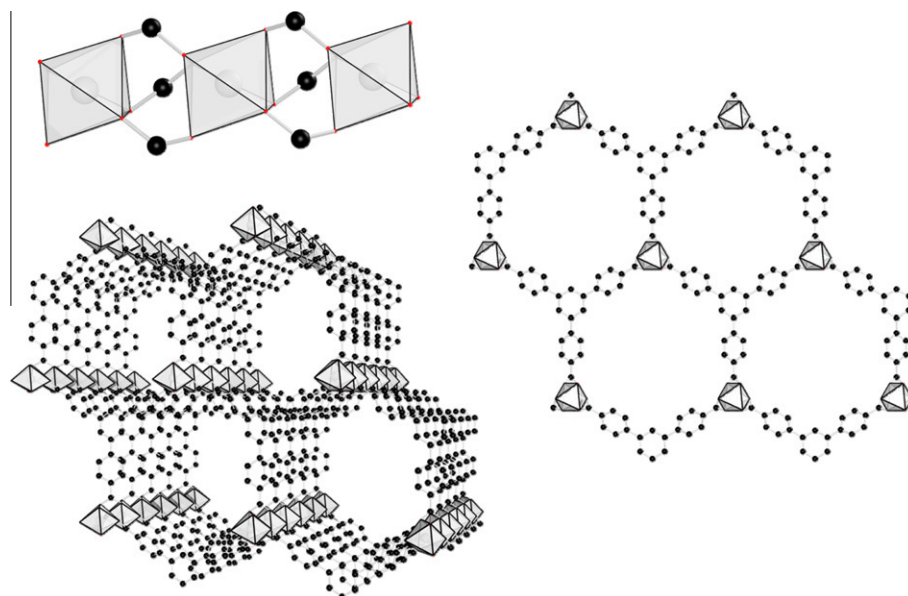


Fig. 7. Upper left: isolated $[\text{AlO}_6]$ -octahedra connected by the carboxylate groups of the BTB-linker. Right: connection of the chains by the BTB ions result in the formation of a honeycomb-like framework. Lower left: representation of the hexagonal channels.

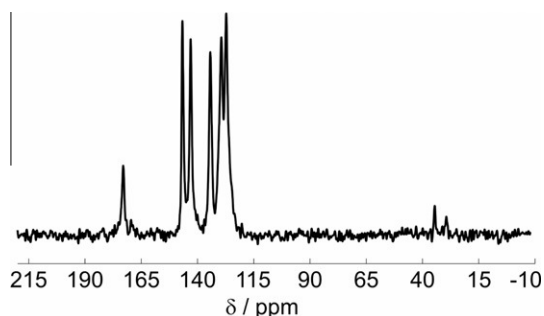


Fig. 8. ^{13}C CP-MAS spectrum of CAU-4.

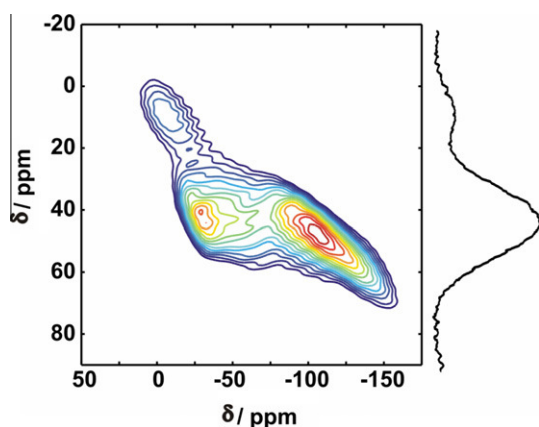


Fig. 9. ^{27}Al MQMAS Spectrum of CAU-4.

(Fig. 5), the crystal structure could not be determined using conventional methods. Comparison of the XRPD pattern of CAU-4 with calculated patterns of other BTB-containing MOFs led to the assumption that the structure of CAU-4 is related to the one of MIL-103 (Fig. 5) [27]. This MOF is built up from chains of edge-sharing $[\text{TbO}_9]$ -polyhedra, which are formed by the coordination of carboxylate moieties and water molecules. The most common coordination numbers for aluminium are CN = 4 and 6 and in carboxylate-based Al-MOFs exclusively AlO_6 polyhedra have been observed [47]. Therefore, the structure of MIL-103 was used as a starting model and the coordination was adjusted to allow a sixfold coordination of the metal center. To adjust the coordination around the metal ion in CAU-4, the water molecules were deleted from the structure and the bridging (μ_2 -) oxygen atoms of the carboxylate groups in MIL-103 were connected to only one M^{3+} ion (Fig. 6).

The computational assisted structure determination was performed in $P1$ symmetry. The so-obtained optimized structure adapts the space group $P312$ and was further transformed to the maximal isomorphous subgroup of lowest index using Powdercell [48] which results in a tripling of the c -axis parameter. This model was further adapted to the experimentally obtained cell parameters (Table 1). The final atomic positions are given in Table S1.

Employing this structure model, all reflections observed in the experimental XRPD pattern are well reproduced, leading to the Pawley-Fit shown in Fig. S8.

Further validation of the proposed structure model was also obtained by a good agreement between the simulated geometrical features and those experimentally observed. Indeed, the simulated pore diameter (9.6 Å, Fig. S9, [39]), accessible surface area (1670 m^2/g , [38]) and solvent accessible volume (0.67 cm^3/g , PLA-

TON [40]) compare well with the experimental data of 8.2 Å, 1520 m^2/g and 0.61 cm^3/g , respectively.

The resulting framework is based on single AlO_6 -octahedra, which are connected via bridging carboxylate groups in a twisted face-to-face fashion (Fig. 7). A similar bridging mode was already observed in a scandium based MOF, based on terephthalate anions [49,50]. Thus, an infinite chain of bridged octahedra is formed. Like in MIL-103, the tritopic BTB-ligands connect these units to form a honeycomb framework with one-dimensional channels. These channels exhibit a diameter of ~ 9.6 Å, taking the van-der-Waals radii of the framework atoms into account.

Solid state ^{13}C and ^{27}Al NMR spectra of the activated compound were recorded (Figs. 8 and 9). As expected the ^{13}C spectrum (Fig. 8) is mainly dominated by the signals in aromatic region (120–150 ppm). Only one signal for the carboxylate group is observed (173 ppm) confirming that all $-\text{COO}^-$ groups are connected to the Al^{3+} ions in a similar way. The small signals at 29.5 and 35 ppm are due to traces of solvent molecules in the pores. The ^{27}Al -MQMAS spectrum (Fig. 9) is typical for sixfold coordinated Al^{3+} ions in a strongly distorted octahedral environment. At least two independent Al atoms are present.

5. Conclusion

We have discovered and characterized a new Al-based MOF named CAU-4. The framework is built up from isolated AlO_6 -octahedra, which are bridged by the carboxylate groups of the incorporated BTB-anion. The synthesized sample exhibits a BET-surface area and a micropore volume of 1520 m^2/g and 0.61 cm^3/g , respectively. The low crystallinity of CAU-4 poses a challenge for the structure determination by common methods. Nevertheless a structure model could be set up that agrees well with all the analytical results.

Acknowledgements

The work has been supported by the DFG (SPP 1362). The research leading to these results has received funding from the European Community's Seventh Framework Program (FP7/2007–20013) under grant agreement n° 228862.

Appendix A. Supplementary data

Supplementary data associated with this article can be found, in the online version, at doi:10.1016/j.micromeso.2011.05.029.

References

- [1] C. Janiak, J.K. Vieth, *New J. Chem.* 34 (2010) 2366.
- [2] M. Eddaoudi, J. Kim, N. Rosi, D. Vodak, J. Wachter, M. O'Keeffe, O.M. Yaghi, *Science* 295 (2002) 469.
- [3] M. Kandiah, S. Usseglio, S. Svelle, U. Olsbye, K.P. Lillerud, M. Tilset, *J. Mater. Chem.* 20 (2010) 9848.
- [4] S. Surble, C. Serre, C. Mellot-Draznieks, F. Millange, G. Férey, *Chem. Commun.* (2006) 284.
- [5] T. Devic, P. Horcajada, C. Serre, F. Salles, G. Maurin, B. Moulin, D. Heurtaux, G. Clet, A. Vimont, J.-M. Greneche, B. Le Ouay, F. Moreau, E. Magnier, Y. Filinchuk, J. Marrot, J.-C. Lavalley, M. Daturi, G. Férey, *J. Am. Chem. Soc.* 132 (2010) 1127.
- [6] H. Chun, D.N. Dybtsev, H. Kim, K. Kim, *Chem. Eur. J.* 11 (2005) 3521.
- [7] M.T. Wharmby, J.P.S. Mowat, S.P. Thompson, P.A. Wright, *J. Am. Chem. Soc.* 133 (2011) 1266.
- [8] T. Ahnfeldt, J. Moellmer, V. Guillemin, R. Staudt, C. Serre, N. Stock, *Chem. Eur. J.* 17 (2011) 6462.
- [9] A. Czaja, N. Trukhan, U. Müller, *Chem. Soc. Rev.* 38 (2009) 1284.
- [10] P. Horcajada, T. Chalati, C. Serre, B. Gillet, C. Sebrie, T. Baati, J.F. Eubank, D. Heurtaux, P. Clayette, C. Kreuz, J.-S. Chang, Y.-K. Hwang, V. Marsaud, P.-N. Bories, L. Cynober, S. Gil, G. Férey, P. Couvreur, R. Gref, *Nature Mater* 9 (2010) 172.
- [11] T. Loiseau, C. Serre, C. Huguénard, G. Fink, F. Taulelle, M. Henry, T. Bataille, G. Férey, *Chem. Eur. J.* 10 (2004) 1373.

- [12] C. Volkringer, D. Popov, T. Loiseau, G. Férey, M. Burghammer, C. Riekel, M. Haouas, F. Taulelle, *Chem. Mater.* 21 (2009) 5695.
- [13] P. Horcajada, S. Surblé, C. Serre, D. Hong, Y. Seo, J. Chang, J.-M. Greneche, I. Margiolaki, G. Férey, *Chem. Commun.* (2007) 2820.
- [14] G. Férey, C. Serre, C. Mellot-Draznieks, F. Millange, S. Surblé, J. Dutour, I. Margiolaki, *Angew. Chem. Int. Ed.* 433 (2004) 6296.
- [15] G. Férey, C. Mellot-Draznieks, C. Serre, F. Millange, J. Dutour, S. Surblé, I. Margiolaki, *Science* 309 (2005) 2040.
- [16] I. Senkowska, F. Hoffmann, M. Fröba, J. Getzschmann, W. Böhlmann, S. Kaskel, *Micropor. Mesopor. Mater.* 122 (2009) 93.
- [17] T. Loiseau, L. Lecroq, C. Volkringer, J. Marrot, G. Férey, M. Haouas, F. Taulelle, S. Bourrelly, P.L. Llewellyn, M. Latroche, *J. Am. Chem. Soc.* 128 (2006) 10223.
- [18] C. Volkringer, D. Popov, T. Loiseau, N. Guillou, G. Férey, M. Haouas, F. Taulelle, C. Mellot-Draznieks, M. Burghammer, C. Riekel, *Nat. Mater.* 6 (2007) 760.
- [19] K. Sumida, M.R. Hill, S. Horike, A. Dailly, J.R. Long, *J. Am. Chem. Soc.* 131 (2009) 15120.
- [20] C. Volkringer, T. Loiseau, J. Marrot, G. Férey, *Cryst. Eng. Comm.* 11 (2009) 58.
- [21] B. Chen, M. Eddaoudi, S.T. Hyde, M. O’Keeffe, M. Yaghi, *Science* 291 (2001) 1021.
- [22] H.K. Chae, D.Y. Siberio-Perez, J. Kim, Y.-B. Go, M. Eddaoudi, A.J. Matzger, M. O’Keeffe, O.M. Yaghi, *Nature* 427 (2004) 523.
- [23] J. Kim, B. Chen, T.M. Reineke, H. Li, M. Eddaoudi, D.B. Moler, M. O’Keeffe, O.M. Yaghi, *J. Am. Chem. Soc.* 123 (2001) 8239.
- [24] S.R. Caskey, A.G. Wong-Foy, A.J. Matzger, *Inorg. Chem.* 47 (2008) 7751.
- [25] L. Hou, J. Zhang, X. Chen, S. Weng, *Chem. Commun.* (2008) 4019.
- [26] K. Gedrich, I. Senkowska, N. Klein, U. Stoeck, A. Henschel, M.R. Lohe, I.A. Baburin, U. Mueller, S. Kaskel, *Angew. Chem. Int. Ed.* 49 (2010) 8489.
- [27] T. Devic, C. Serre, N. Audebrand, J. Marrot, G. Férey, *J. Am. Chem. Soc.* 127 (2005) 12788.
- [28] S. Choi, M. Seo, M. Cho, Y. Kim, M. Jin, D. Jung, J. Choi, W. Ahn, J. Rowsell, J. Kim, *Cryst. Growth Des.* 7 (2007) 2290.
- [29] S. Bauer, C. Serre, T. Devic, P. Horcajada, J. Marrot, G. Férey, N. Stock, *Inorg. Chem.* 47 (2008) 7568.
- [30] N. Stock, *Micropor. Mesopor. Mater.* 129 (2010) 287.
- [31] J.P. Amoureux, C. Fernandez, S. Steuernagel, *J. Magn. Reson. A* 123 (1996) 116.
- [32] A. Jerschow, R. Kumar, *J. Magn. Reson.* 160 (2003) 59.
- [33] K. Rappé, C.J. Casewit, K.S. Colwell, W.A. Goddard III, W.M. Skiff, *J. Am. Chem. Soc.* 114 (1992) 10024.
- [34] Materials Studio Version 5.0, Accelrys Inc., San Diego, CA, 2009.
- [35] A. Sonnauer, F. Hoffmann, M. Froba, L. Kienle, V. Duppel, M. Thommes, C. Serre, G. Férey, N. Stock, *Angew. Chem. Int. Ed.* 48 (2009) 3849.
- [36] F. Salles, G. Maurin, C. Serre, P.L. Llewellyn, C. Knöfel, H.J. Choi, J.R. Long, Y. Filinchuk, G. Férey, *J. Am. Chem. Soc.* 132 (2010) 13782.
- [37] R.D. Shannon, C.T. Prewitt, *Acta Cryst. B* 25 (1969) 925.
- [38] T. Düren, F. Millange, G. Férey, K.S. Walton, R.Q. Snurr, *J. Phys. Chem. C* 111 (2007) 15350.
- [39] L.D. Gelb, K.E. Gubbins, *Langmuir* 15 (1999) 305.
- [40] A.L. Spek, PLATON, A Multipurpose Crystallographic Tool, Utrecht University, Utrecht, The Netherlands, 2010.
- [41] A. Sonnauer, N. Stock, *Eur. J. Inorg. Chem.* (2008) 5038.
- [42] N. Stock, T. Bein, *Solid State Sci.* 5 (2009) 1207.
- [43] C. Volkringer, T. Loiseau, N. Guillou, G. Férey, M. Haouas, F. Taulelle, E. Elkaim, N. Stock, *Inorg. Chem.* 49 (2010) 9852.
- [44] T. Ahnfeldt, N. Guillou, D. Gunzelmann, I. Margiolaki, T. Loiseau, G. Férey, J. Senker, N. Stock, *Angew. Chem. Int. Ed.* 21 (2009) 5265.
- [45] J. Moellmer, E.B. Celerc, R. Luebke, A.J. Cairns, R. Staudta, M. Eddaoudi, M. Thommes, *Micropor. and Mesopor. Mater.* 129 (2010) 345.
- [46] Evaluation Software BEL Japan, INC. (2008).
- [47] Cambridge Crystallographic Data Centre, CCDC Version 5.31 (2009).
- [48] W. Kraus, G. Nolze, *PowderCell* 2.4, (2000).
- [49] S.R. Miller, P.A. Wright, C. Serre, T. Loiseau, J. Marrot, G. Férey, *Chem. Commun.* (2005) 3850.
- [50] J. Perles, M. Iglesias, M. Martín-Luengo, M. Ángeles Monge, C. Ruiz-Valero, N. Snejko, *Chem. Mater.* 23 (2005) 5837.

4.4.2 Formation and Characterisation of Mn-MIL-100

Dieses Manuskript wurde in der vorliegenden Fassung im September 2012 im Journal „CrystEngComm“ eingereicht.

Das solvothermale System Mn^{2+} / Trimesinsäure (H_3BTC) / Methanol wurde untersucht. Dabei wurde bei Verwendung von $\text{Mn}(\text{NO}_3)_2 \cdot 4\text{H}_2\text{O}$ eine Oxidation von Mn^{2+} - zu Mn^{3+} -Ionen beobachtet. Nach kurzen Reaktionszeiten bildete sich Mn-MIL-100, dessen Struktur auf trimeren Baueinheiten von μ_3 -O-eckenverknüpften MnO_6 -Polyedern basiert. Diese Cluster enthalten zwei Mn^{3+} - sowie ein Mn^{2+} -Ion. Die Zusammensetzung $[\text{Mn}_3(\text{O})(\text{H}_2\text{O})_3(\text{BTC})_2] \cdot \text{Lösungsmittel}$ wurde mittels Thermogravimetrie bestätigt. Die Struktur konnte mittels Röntgenpulverbeugung eindeutig identifiziert werden. Während die koordinierten Wassermoleküle für die Al^{3+} -, Sc^{3+} -, V^{3+} -, Cr^{3+} - und Fe^{3+} -basierten Analoga von Mn-MIL-100 unter Strukturverlust entfernt werden können, führt dies in Mn-MIL-100 zur irreversiblen Amorphisierung des MOFs. Werden nur die eingelagerten, nicht koordinierenden Lösungsmittelmoleküle im Vakuum entfernt, so bleibt die Struktur allerdings erhalten. Sowohl der im Vakuum aktivierte als auch der amorphisierte MOF weisen eine hohe Porosität auf. Die kurzen Reaktionszeiten erlaubten eine in-situ Charakterisierung des Kristallisationsprozesses mittels energiedispersiver Röntgenbeugung. Die gemessenen Daten wurden mit zwei verschiedenen Modellen ausgewertet. Trotz der ungewöhnlichen in-situ Oxidation von Mn^{2+} zu Mn^{3+} sind allerdings keine ungewöhnlichen Phänomene in der Kristallisationskinetik zu beobachten.

Cite this: DOI: 10.1039/c0xx00000x

www.rsc.org/xxxxxx

ARTICLE TYPE

Formation and Characterisation of Mn-MIL-100

Helge Reinsch^a and Norbert Stock^{a,*}

Received (in XXX, XXX) Xth XXXXXXXXXX 20XX, Accepted Xth XXXXXXXXXX 20XX

DOI: 10.1039/b000000x

The synthesis and characterisation of the Mn-based analogue of the MIL-100-framework is reported. The title compound is synthesised from a methanolic solution of trimesic acid and manganese(II) nitrate in very short reaction times. During the reaction, the Mn²⁺-ions are oxidized in-situ to Mn³⁺-ions. The obtained MOF was characterised by XRPD-measurements, IR-spectroscopy, thermogravimetric measurements and sorption experiments. To have a closer look at the crystallisation occurring after the in situ metal oxidation-reaction that results in the formation of the title compound, in-situ EDXRPD-experiments under solvothermal conditions were carried out. These time-resolved measurements could be evaluated by two different kinetic models (by Avrami and Gualtieri) for crystallisation. The results indicate a two stage reaction process, which are dominated by different reaction mechanisms.

Introduction

In the field of porous materials, metal-organic frameworks (MOFs) represent a rather young but still rapidly growing class of compounds.¹ These materials are in general based on metal ions or cationic metal-oxo-clusters which are connected via anionic organic moieties, mostly carboxylate or phosphonate but also sulfonate or imidazolate ions. The metal-organic materials often exhibit highly desirable properties. Thus, large specific surface areas as well as unique sorption properties were reported.² In some cases flexible framework structures or chemically specific sorption behaviour can be observed.^{3,4}

Among the large variety of metal-organic frameworks, a remarkable number of compounds is based on the trimeric building unit $\{M(\text{III})_3\text{O}(\text{OH})(\text{O}_2\text{C-R})_6(\text{H}_2\text{O})_2\}$ shown in Fig. 1.⁵ This cluster has been known for a very long time, but the chemistry of MOFs shed a new light on its properties. Especially the compounds known as MIL-88³ (MIL stands for *Matériaux de l'Institut Lavoisier*), MIL-100⁶ and MIL-101⁷, which are all based on this building unit, must be mentioned in this context. The materials known as M(III)-MIL-100 or M(III)-MIL-101 (M(III) designates the trivalent metal ion that forms the cluster) exhibit permanent porosity with specific surface areas above $S_{\text{BET}} = 2000 \text{ m}^2/\text{g}$ and pore volumes up to $2 \text{ cm}^3/\text{g}$. Furthermore, the MOFs of the MIL-100-series $[\text{M}(\text{III})(\mu_3\text{-O})(\text{OH})(\text{H}_2\text{O})_2(\text{BTC})_2]$ (BTC = 1,3,5-benzenetricarboxylate) possess an outstanding thermal as well as chemical stability. MIL-100 could be obtained up to now with the metal ions V³⁺,⁸ Cr³⁺,⁶ Fe³⁺,⁹ Al³⁺,¹⁰ and Sc³⁺.¹¹ Besides the mentioned, desirable properties, the main interest in these materials originates from the coordination chemistry of the trimeric building unit. Since the charge of the cations is compensated by the μ_3 -oxide-ion, six carboxylate groups and one hydroxide ion, the weakly bond water molecules that complete the octahedral coordination geometry can be easily removed.¹² In this way, coordinatively unsaturated sites (*cus*) can be created

inside the framework. These are available for coordination by other ligands^{13,14,15,16} or catalytic transformations.^{9,17,18}

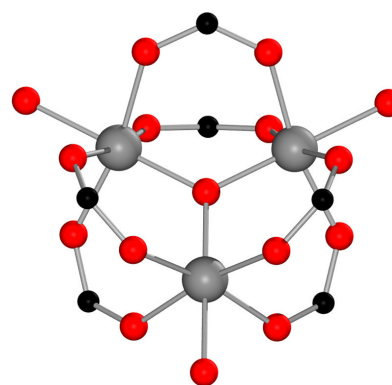


Fig. 1: The trimeric building unit observed in several MOFs based on Sc³⁺, V³⁺, Cr³⁺, Fe³⁺ or Al³⁺. M(III) atoms in grey, oxygen atoms in red, carbon atoms in black.

Fe-MIL-100 for example has been proven to be a versatile Lewis-acidic catalyst.⁹ Furthermore, the trimeric cluster based on Fe³⁺ can be partially reduced to a mixed valency, which increases the number of *cus*.¹⁹ After this post-synthetic modification, the MOF was successfully used for the separation of propane and propene. Furthermore it was successfully employed in the selective removal of N-heterocyclic aromatics from fuel feeds.²⁰ Moreover, Fe-MIL-100 can be synthesised at very large scale,²¹ which makes it also a candidate for potential applications as water adsorbent.^{22,23}

Although this trimeric unit of the MIL-100 topology is known for manganese as a mixed valent cluster of two Mn³⁺- and one Mn²⁺-ions²⁴, it has not been observed in the chemistry of MOFs yet. To the best of our knowledge, no MOF has been reported up to now based on inorganic nodes built up from Mn³⁺ and carboxylate ions, although Mn³⁺ was incorporated as part of the metal-organic linker molecule.^{25,26} Herein, we report the synthesis of the Mn-based analogue of the MIL-100 structure that could be

obtained using Mn(II)nitrate as the metal source. The divalent ions are oxidized in-situ in methanolic solution. The Mn-MIL-100 was fully characterised by TG-measurements, X-ray powder diffraction (XRPD), IR-spectroscopy and sorption experiments. To elucidate the crystallisation mechanism that comprises the oxidation step, time dependent EDXRPD-data (energy dispersive X-ray powder diffraction) under solvothermal conditions was recorded at the DESY-Synchrotron source in Hamburg. The evaluation of the data was conducted using two different kinetic models.

Experimental

Materials

Methanol and ethanol (BASF, purum), trimesic acid (H_3BTC , 1,3,5-benzenetricarboxylic acid) (Sigma) and $\text{Mn}(\text{NO}_3)_2 \cdot 4\text{H}_2\text{O}$ are commercially available and were used as obtained.

Synthesis

Mn-MIL-100 (**1**) can be synthesised from a mixture of 400 mg trimesic acid (1.9 mmol) in 18 ml methanol and 2 ml of a 1 M $\text{Mn}(\text{NO}_3)_2 \cdot 4\text{H}_2\text{O}$ solution in methanol (2 mmol). The clear reaction solution was heated for 45 min at 125 °C under stirring in a closed glass reactor ($V = 100 \text{ mL}$). After filtration, the obtained brown powder is redispersed in ethanol and filtered again. This final product is slightly sensitive to air exposure, but the crystallinity is retained for several hours and therefore it can be handled under non-inert conditions. It is noteworthy that the quality of the XRPD patterns, especially the relative intensities up to $5^\circ(2\theta)$, depends strongly on the amount of solvent molecules present in the pores.

Characterisation

The XRPD data was recorded on a Panalytical Xpert diffractometer in reflection geometry ($\text{Cu-K}\alpha_1$ -radiation). Temperature dependent XRPD data was collected on STOE Stadi P diffractometer equipped with an IPPSD detector under air in capillaries. MIR spectra were recorded on an ATI Matheson Genesis spectrometer in the spectral range of $4000\text{-}400 \text{ cm}^{-1}$ using the KBr disk method. Thermogravimetric experiments were carried out under air on a NETZSCH-STA-409 CD thermal analyzer with a heating rate of 4 K/min. The sample was heated in an Al_2O_3 crucible under a flow of air (25 ml/min) and the data was corrected for buoyancy and current effects. Sorption experiments were performed with a BELSORP Max from Bel Japan. INC.

Results and Discussion

Structure

The structure of MIL-100 is based on the connection of the trimeric building units via trimesate anions (BTC). The inorganic bricks represent the corners of a so-called supertetrahedron (ST) and are connected by the tricarboxylate ions, which represent the faces of the tetrahedron.

The resulting framework corresponds to the zeotypic MTN-

network, in which the supertetrahedra replace the tetrahedral nodes. This framework exhibits two kinds of very large pores with a diameter of 25 Å and 29 Å respectively.⁶ While the smaller cavity exhibits only pentagonal windows, the larger one also possesses hexagonal apertures.

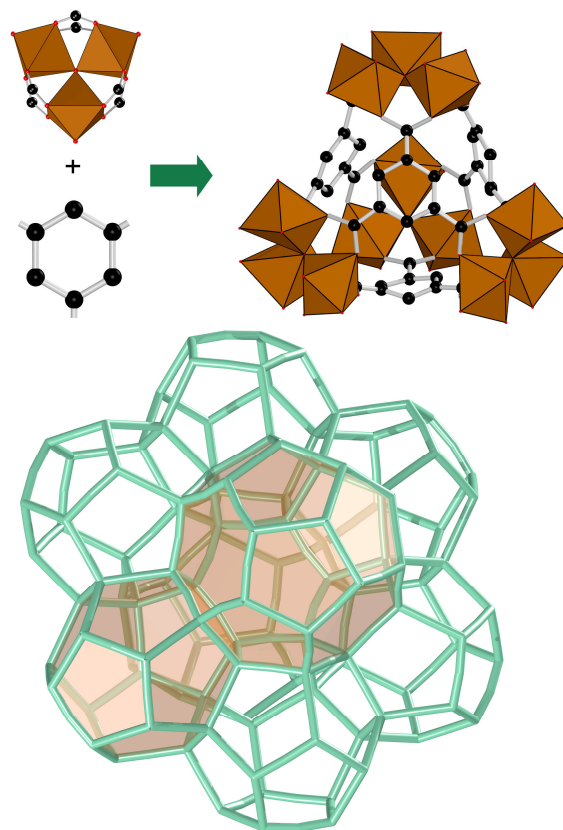


Fig. 2: Arrangement of the building units to form a supertetrahedron (top) and the MTN-framework with its two kinds of cavities emphasized in brown (bottom). Crystal data taken from reference 6.

The structure of **1** is very similar to the framework of the Cr-MIL-100, as proven by XRPD (Fig. 3).

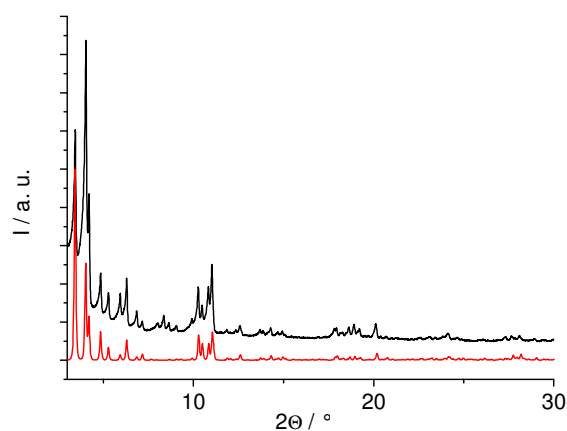


Fig. 3: Powder pattern for **1** (black) and simulated pattern for Cr-MIL-101 (red).

The lattice parameters are very similar (72.908 Å and 72.906 Å for Mn- and Cr-MIL-100 respectively) and the differences in relative intensities are mainly due to the

occluded solvent molecules. Depending on the amount and kind of solvent occluded inside the pores, the relative intensity of the reflections may strongly vary. The framework structure is stable in methanol as well as in ethanol. Upon solvent exchange with water, the crystallinity decreases substantially. The complete removal of the methanol and ethanol from the pores by heating or by heating under vacuum (0.1 mbar) results in an amorphization, while solvent removal under vacuum at room temperature retains the crystallinity (Fig. S1).

Properties

The TG-measurements in air indicate, that Mn decomposes above 400 °C in air (Fig. 4).

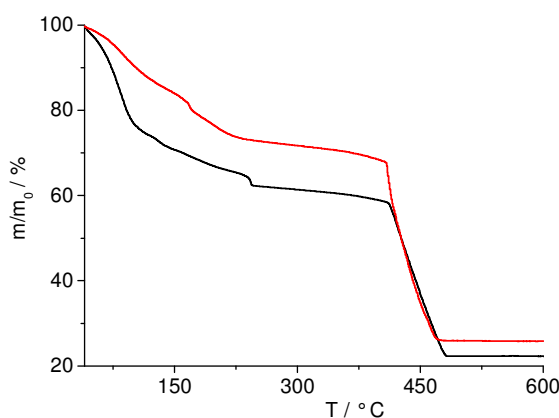


Fig. 4: TG-curves for the as synthesised material (black) and the Mn-MIL-100 washed in ethanol (red).

The as synthesised (*as*) material (Fig. 4, black curve) shows a rapid loss of solvent starting with methanol removal at 40 °C and H₂O above 75 °C. The well defined step at 240 °C, which we attribute to some residual acid (see also IR-spectrum, Fig. S3), can be easily removed by washing in ethanol. The curve for the washed material **1** in red shows a similar stepwise removal of ethanol followed by dehydration. Moreover, assuming the composition of the desolvated for Mn-MIL-100 as [Mn₃(O)(BTC)₂], the decomposition above 400 °C is in very good agreement with the theoretical value (ratio wht % residue/ wht% at 400 °C = 0.376 (observed) and 0.384 (calculated)). The residual solid after complete decomposition was identified as the crystalline mixed valence manganese oxide Mn₃O₄ by XRPD measurements. Both results indicate that the trimeric building unit in **1** exhibits most probably the mixed valency known from the corresponding trinuclear manganese carboxylate [Mn₃O(MeOH)₃(O₂C-C₁₄H₉)₆].²⁷ Temperature dependent XRPD-measurements confirm the amorphization upon solvent removal at elevated temperatures. The decrease in the crystallinity starts already at 120 °C, indicated by peak broadening and lowering of the intensities. The amorphization is completed at 200 °C. The thermally activated amorphous as well as the vacuum treated crystalline material were characterised regarding their sorption behaviour. In both cases a remarkable porosity was observed (Fig. S2 and Fig. 6, respectively). The capacity of the thermally activated materials (0.1 mbar, 4.5 h, 140 °C) strongly depends on the solvent treatment

procedure. The micropore volumina were determined from the amount adsorbed at $p/p_0 = 0.5$. Starting from the *as*-material ($S_{\text{BET}} = 1330 \text{ m}^2/\text{g}$, $V_{\text{Mic}} = 0.59 \text{ cm}^3/\text{g}$), the porosity is increased by activation in ethanol ($S_{\text{BET}} = 1410 \text{ m}^2/\text{g}$, $V_{\text{Mic}} = 0.63 \text{ cm}^3/\text{g}$). If the ethanol-washed Mn-MIL-100 is redispersed again in methanol, the exchange with the more volatile solvent further increases the porosity ($S_{\text{BET}} = 1610 \text{ m}^2/\text{g}$, $V_{\text{Mic}} = 0.73 \text{ cm}^3/\text{g}$).

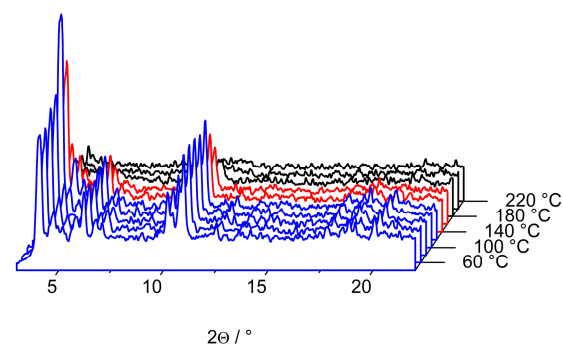


Fig. 5: Temperature dependent XRPD data for as synthesised Mn-MIL-100 measured in a capillary under air.

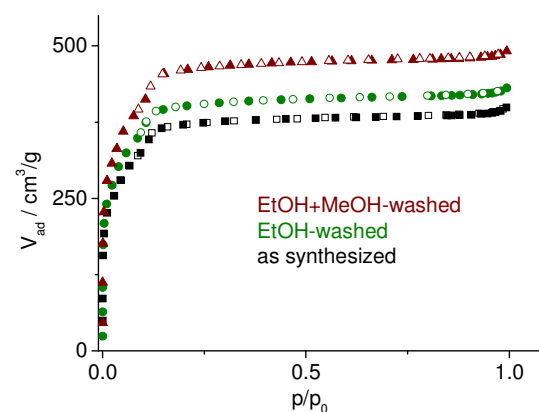


Fig. 6: N₂ isotherms of thermally activated and solvent exchanged compounds measured at 77 K. Filled symbols represent the adsorption, empty symbols represent the desorption branch.

Due to the amorphization of Mn-MIL-100 upon thermal solvent removal, the exact structure must be considered as unknown, but the steps in the sorption curves indicate, that the pore system is still topologically related to the MIL-100-framework. The slow increase in the sorption curve between $p/p_0 \sim 0.01$ and 0.2 and the inflection point at $p/p_0 \sim 0.15$ are characteristic for the filling of large pores during the adsorption, and thus can be attributed to the adsorption into the larger cages of the framework.²⁸

Interestingly, the sorption behaviour of the MOF activated only in vacuum is almost identical to the thermally activated MOF. Activation at room temperature at $p = 0.1$ mbar results in the preservation of the crystallinity (Fig. S1). This is probably due to the weakly bound solvent molecules at the trimeric unit that are not removed under vacuum at room temperature, while the thermal treatment generates reactive *cus*, which destabilise the framework. The specific surface areas of the ethanol washed, vacuum-treated MOF is 1540 m²/g and its micropore volume is 0.67 cm³/g. However, the MOF activated in vacuum at room temperature as well as the compound that was thermally

activated decompose within few hours after re-exposure to air and lose their porosity.

Reaction Mechanism

To the best of our knowledge, the in-situ formation of Mn^{3+} ions by oxidation of Mn^{2+} ions in the synthesis of MOFs has not been described previously. Therefore, the reaction conditions were investigated in detail. The crucial role can be attributed to the use of $\text{Mn}(\text{NO}_3)_2 \cdot 4\text{H}_2\text{O}$. Employing the chloride or the acetate of Mn(II) under otherwise identical reaction conditions, we were not able to observe any oxidized Mn-species. The direct use of the trivalent acetate did also not lead to the formation of **1**. Furthermore, the oxidation is independent of the atmosphere in the reactor. Purging the solution with argon followed by sealing of the reactor under inert conditions did not affect the product formation. The use of other organic acids like nitroterephthalic acid or pyridine-dicarboxylic acid also led to the oxidation of Mn(II), but no crystalline products could be obtained yet. A similar result was observed when the solvent was changed from methanol to another solvent. Above certain temperatures, the oxidation of the Mn(II) was also observed in ethanol or water employing manganese nitrate, but no Mn-MIL-100 was obtained. In contrast to this, we did not observe any oxidation in N,N-dimethylformamide as the solvent. Based on standard potentials, the oxidation of methanol by Mn^{3+} ions is expected, but the described solvothermal system seems to be unique in its ability to “capture” and stabilize the Mn(III) in its trivalent state, prior to the formation of **1**.

The rather short reaction time (45 min) that leads to the formation of Mn-MIL-100 makes it a perfectly suitable system for a kinetic evaluation of the crystallization process using synchrotron radiation.²⁹ While the synthesis of hybrid compounds often takes days, in this case the crystallisation already starts after ten minutes, as observed by clouding of the reactant solution. Thus, in-situ energy-dispersive XRPD measurements were carried out at the beamline F3 of the HASYLAB at DESY (Hamburg, Germany). The set-up that was used for the EDXRPD measurements allowed us to incorporate a microwave-oven into the beam as recently described by our group.³⁰ Polychromatic white synchrotron light is used and the energy of the diffracted X-rays is recorded under a constant detector angle by a Ge-detector. The reactions were carried out in small vials ($V_{\text{Max}} = 5$ mL, filling degree 3 mL) using a Biotage Initiator MW-oven. Time-dependent EDXRPD patterns were recorded at three different temperatures (125°C, 135°C and 145°C) with a time resolution of 30 seconds. A typical set of spectra is shown in Figure 7.

The integration of the peak area corresponds to the reaction progress α , and was used in its normalized form to study the kinetics of crystallisation. In this study the peak corresponding to the 113 reflection, which is the one with the highest intensity, was chosen. The plot of the reaction progress for the different temperatures is shown in Fig. 8.

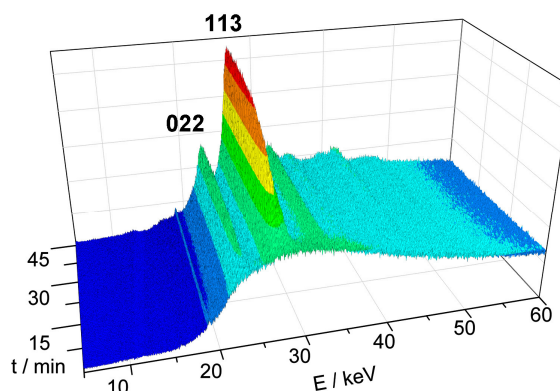


Fig. 7: EDXRPD-spectra for the reaction at 135 °C. The strongest peaks are given with their hkl-indices.

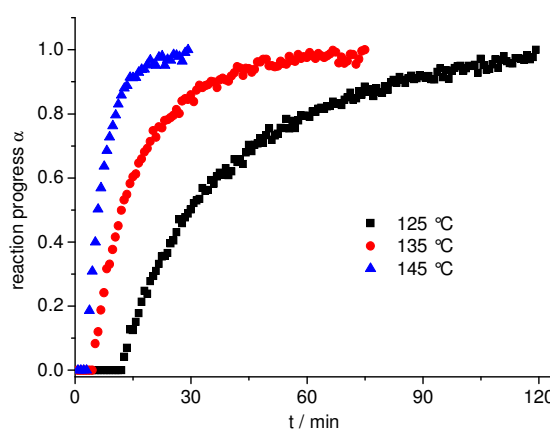


Fig. 8: Reaction progress for the synthesis of Mn-MIL-100 at the three different temperatures depending on the synthesis time.

Useful information can be directly extracted from these plots. The induction time (t_{ind}), which is the period during which no crystalline products are observed, is shortened for the synthesis at higher temperatures (at 125 °C: 12 minutes; at 135 °C: 4.5 minutes; at 145 °C: 3 minutes). Furthermore, the reaction is completed after shorter times at higher temperatures. While the crystallisation is finished after 30 minutes at 145 °C, the reaction is slowed down at 135 °C (75 minutes) and 125 °C (120 minutes).

Further information can be gained by careful evaluation of the data. Two models are commonly employed to evaluate the crystallisation. The most frequently used method is the Sharp-Hancock analysis.³¹ According to this model, the plot of $\ln[-\ln(1-\alpha)]$ over $\ln(t_{\text{Red}})$ yields a straight line with the slope m and the intercept $m \ln(k)$. Here, $t_{\text{Red}} = t - t_{\text{ind}}$ and m is the Avrami exponent, which gives information about the reaction mechanism. In the case of Mn-MIL-100, plotting $\ln[-\ln(1-\alpha)]$ vs. $\ln(t_{\text{Red}})$ leads to two linear sections with different slopes (Fig. S4-S9). Thus, two dominating mechanisms are taking place during the crystallisation of Mn-MIL-100, which was already reported in other studies.³² Therefore, the Sharp-Hancock analysis was carried out for both linear sections. The final values are summarized in Tab. 1.

Table 1 Rate constants (k_1 and k_2), Avrami exponents (m_1 and m_2) and corresponding reaction periods, evaluated according to the Sharp-Hancock model.

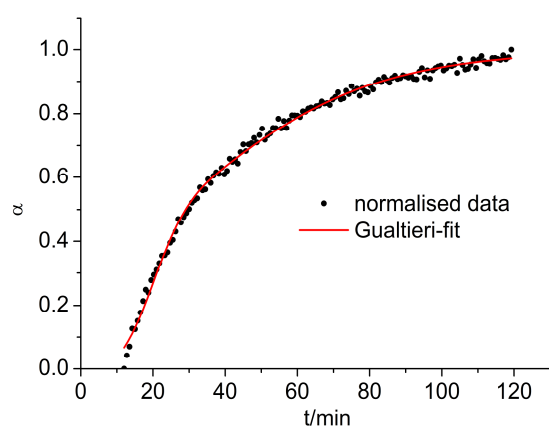
T [°C]	k_1 [min ⁻¹]	m_1	t_{Red} [min]	k_2 [min ⁻¹]	m_2	t_{Red} [min]
125	0.048(10)	1.97(17)	0-5	0.030(1)	1.009(8)	5-120
135	0.109(6)	1.77(8)	0-3	0.074(4)	0.91(2)	3-75
145	0.177(11)	1.66(8)	0-3	0.189(20)	0.90(4)	3-30

Both rate constants increase with temperature. The Avrami exponents for the first stage of the reaction indicate ($1.66(8) \leq m_1 \leq 1.97(17)$) that during the first minutes, the crystallisation mechanism is controlled by nucleation (theory, $m = 2$). During the second period of the reaction Avrami exponents are in the range of 0.90(4) to 1.009(8), which are characteristic for a first order reaction mechanism. This could be due to the in-situ generation of Mn^{3+} ions, which should then be the rate limiting step. Thus, the Sharp-Hancock model shows that the reaction can be separated in two parts that are dominated by different crystallisation mechanisms.

The second, recently more often used model to evaluate the extent of crystallisation is the Gualtieri method.³³ This model takes into account, that the nucleation and the crystal growth are two separate processes, represented in equation 1.

$$\alpha = \frac{1}{1 + \exp\left[-\left(\frac{t-a}{b}\right)^n\right]} \{1 - \exp[-(k_g t)^n]\}$$

The reaction extent or progress α is the same as in the Sharp-Hancock model, t is the time, k_g is the rate constant for the crystal growth, $a = 1/k_n$, the reciprocal rate constant of the nucleation, b is a constant also related to nucleation and n is the dimensionality of the crystal growth. Since previous measurements for isoreticular compounds have shown that the crystals of MIL-100 are mostly octahedral,¹⁰ the dimensionality of the crystal growth was set to $n = 3$. The results of the fits are shown in Fig. 9, S10, S11 and the parameters are summarized in Table 2.

**Fig. 9** Gualtieri-fit for the normalised data measured at 125 °C.**Table 2** Rate constants and nucleation parameter b as obtained by using the Gualtieri model.

T [°C]	k_n [min ⁻¹]	k_g [min ⁻¹]	b [min ⁻¹]
125	0.039(1)	0.0486(4)	26.1(4)
135	0.116(6)	0.112(1)	12.6(3)
145	0.241(25)	0.203(7)	4.7(3)

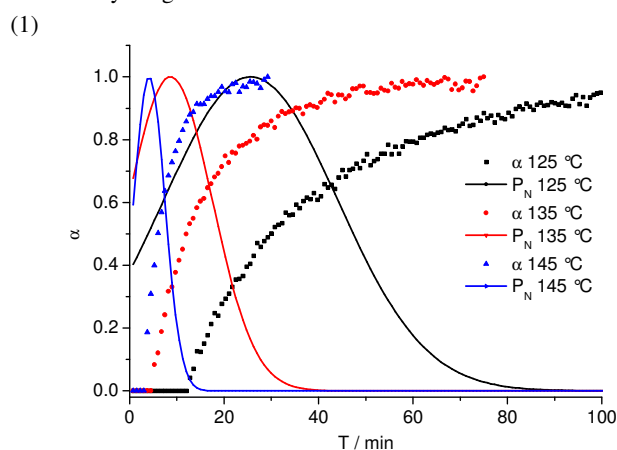
The rate constants for nucleation and growth increase with temperature. Moreover, the values are in the same order of magnitude as the ones obtained from the Sharp-Hancock model.

In comparison with the results of crystallisation studies on other hybrid compounds^{34,35,36,37} as well as inorganic materials^{38,39,40,41} the rate constants and coefficients are not drastically different. Thus the in situ oxidation of Mn^{2+} does not result in uncommon crystallisation kinetics.

The constants that are determined by the Gualtieri-method can be used to calculate the probability of nucleation P_N which is

$$P_N = e^{-\frac{(t-a)^2}{b^2}} \quad (2)$$

The plot of probability of nucleation and reaction process versus time is shown in Figure 10. Nucleation takes place after crystal growth is observed.

**Fig. 10** The reaction progress α (symbols) and the probability of nucleation P_N (solid line) as determined for the different temperatures (125 °C: black; 135 °C: red; 145 °C: blue).

The Arrhenius activation energy for the reaction can be obtained for both reaction steps by plotting $\ln(k)$ vs $1/T$ (Fig. S12-S15). These values are summarised in Tab. 3.

Table 3 Activation energies evaluated from the different reaction stages for the Sharp-Hancock and the Gualtieri model.

model rate constant E_a [kJ]	Sharp-Hancock		Gualtieri	
	k_1	k_2	k_n	k_g
	89.8±11.7	127.0±3.0	126.5±12.4	98.9±8.4

The activation energies are all in the same order of magnitude and comparable to the values reported previously for MOFs (CAU-1: 131-136 kJ,³⁵ MOF-14: 64-83 kJ,³⁴ $\text{Li}_4[\text{C}_4\text{H}_2\text{S}(\text{CO}_2)_2]_2[\text{C}_3\text{H}_7\text{NO}]_2$: 114-132 kJ,⁴²).

Conclusions

The accessibility of a Mn(III)-based MOF exhibiting permanent porosity has been demonstrated in this study. Since the structure of Mn-MIL-100 is composed of trimeric units of corner-sharing octahedra $\{Mn_3(\mu_3-O)(H_2O)_3(O_2C-R)_6\}$ the formation of other well known MOFs such as MIL-88 and MIL-101 which are also based on the same inorganic building units should be feasible. The observation of an in situ oxidation and the subsequent stabilisation of the cation in a MOF structure could be a promising approach for the discovery of new MOFs with metal ions in hard to access oxidation states.

Acknowledgements

The help of Dr. Andre Rothkirch (HASYLAB, DESY Hamburg) and Mark Feyand (CAU Kiel) during the recording and interpretation of the EDXRPD-data is gratefully acknowledged. The research leading to these results has received funding from the European Community's Seventh Framework Programme (FP7/2007-20013) under grant agreement n° 228862".

Notes and references

^a Institute of Inorganic Chemistry, Christian-Albrechts-Universität Kiel, Max-Eyth-Straße 2, 24118 Kiel, Germany; stock@ac.uni-kiel.de

† Electronic Supplementary Information (ESI) available: IR-spectrum, XRPD-data and sorption isotherm for the vacuum-treated MOF, Sharp-Hancock-plots and Fits, Gualtieri-Fits, Arrhenius-plots. See DOI: 10.1039/b000000x/

- 1 N. Stock, S. Biswas, *Chem. Rev.*, 2012, **112**, 933.
- 2 H. K. Chae, D. Y. Siberio-Perez, J. Kim, Y. Go, M. Eddaoudi, A. J. Matzger, M. O'Keeffe, O. M. Yaghi, *Science*, 2004, **427**, 523.
- 3 C. Serre, C. Mellot-Draznieks, S. Surble, N. Audebrand, Y. Filinchuk, G. Férey, *Science*, 2007, **315**, 1828.
- 4 M. I. H. Mohideen, B. Xiao, P. S. Wheatley, A. C. McKinlay, Y. Li, A. M. Z. Slawin, D. W. Aldous, N. F. Cessford, T. Düren, X. Zhao, R. Gill, K. M. Thomas, J. M. Griffin, S. E. Ashbrook, R. E. Morris, *Nature Chemistry*, 2011, **3**, 304.
- 5 C. T. Dziobkowski, T. J. Wroblewski, D. B. Brown, *Inorg. Chem.*, 1981, **20**, 671.
- 6 G. Férey, C. Serre, C. Mellot-Draznieks, F. Millange, S. Surble, J. Dutour, I. Margiolaki, *Angew. Chem. Int. Ed.* 2004, **43**, 6296.
- 7 G. Férey, C. Mellot-Draznieks, C. Serre, F. Millange, J. Dutour, S. Surblé, I. Margiolaki, *Science*, 2005, **23**, 2040.; E. Stavitski, M. Goesten, J. Juan-Alcaniz, A. Martinez-Joaristi, P. Serra-Crespo, A. V. Petukhov, J. Gascon, F. Kapteijn, *Angew. Chem. Int. Ed.*, 2011, **50**, 9624.
- 8 A. Lieb, H. Leclerc, T. Devic, C. Serre, I. Margiolaki, F. Mahjoubi, J. S. Lee, A. Vimont, M. Daturi, J.-S. Chang, *Micropor. Mesopor. Mater.*, 2012, **157**, 18.
- 9 P. Horcajada, S. Surble, C. Serre, D.-Y. Hong, Y.-K. Seo, J.-S. Chang, J.-M. Greneche, I. Margiolaki, G. Férey, *Chem. Commun.*, 2007, **27**, 2820.
- 10 C. Volkringer, D. Popov, T. Loiseau, G. Férey, M. Burghammer, C. Riekel, M. Haouas, F. Taulelle, *Chem. Mater.*, 2009, **21**, 5695.
- 11 J. P. S. Mowat, S. R. Miller, A. M. Z. Slawin, V. R. Seymour, S. E. Ashbrook, P. A. Wright, *Micropor. Mesopor. Mater.*, 2011, **142**, 322.
- 12 M. Haouas, C. Volkringer, T. Loiseau, G. Férey, F. Taulelle, *J. Phys. Chem. C*, **115**, 17934.
- 13 D.-Y. Hong, Y. K. Hwang, C. Serre, G. Férey, J.-S. Chang, *Adv. Funct. Mater.*, 2009, **19**, 1537.
- 14 H. Leclerc, A. Vimont, J.-C. Lavalley, M. Daturi, A. D. Wiersum, P. L. Llewellyn, P. Horcajada, G. Férey, C. Serre, *Phys. Chem. Chem. Phys.*, 2011, **13**, 11748.
- 15 L. Hamon, C. Serre, T. Devic, T. Loiseau, F. Millange, G. Férey, G. De Weireld, *J. Am. Chem. Soc.*, 2009, **131**, 8775.
- 16 C. Volkringer, H. Leclerc, J.-C. Lavalley, T. Loiseau, G. Férey, M. Daturi, A. Vimont, *J. Phys. Chem. C*, 2012, **116**, 5710.
- 17 L. Kurfirtova, Y.-K. Seo, Y. K. Hwang, J.-S. Chang, J. Cejka, *Catalysis Today*, 2012, **179**, 85.
- 18 F. Vermoortele, R. Ameloot, L. Alaerts, R. Matthesen, B. Carlier, E. V. Ramos Fernandez, J. Gascon, F. Kapteijn, D. E. De Vos, *J. Mater. Chem.*, 2012, **22**, 10313.
- 19 J. W. Yoon, Y.-K. Seo, Y. K. Hwang, J.-S. Chang, H. Leclerc, S. Wuttke, P. Bazin, A. Vimont, M. Daturi, E. Bloch, P. L. Llewellyn, C. Serre, P. Horcajada, J.-M. Greneche, A. E. Rodrigues, G. Férey, *Angew. Chem. Int. Ed.*, 2010, **49**, 5949.
- 20 M. Maes, M. Trekels, M. Boulhout, S. Schouteden, F. Vermoortele, L. Alaerts, D. Heurtaux, Y.-K. Seo, Y. K. Hwang, J.-S. Chang, I. Beurroies, R. Denoyel, K. Temst, A. Vantomme, P. Horcajada, C. Serre, D. E. De Vos, *Angew. Chem. Int. Ed.*, 2011, **50**, 4210.
- 21 Y.-K. Seo, J. Woong Yoon, J. Sun Lee, U.-H. Lee, Y. K. Hwang, C.-H. Jun, P. Horcajada, C. Serre, J.-S. Chang, *Micropor. Mesopor. Mater.*, 2012, **157**, 137.
- 22 Y.-K. Seo, J. W. Yoon, J. S. Lee, Y. K. Hwang, C.-H. Jun, J.-S. Chang, S. Wuttke, P. Bazin, A. Vimont, M. Daturi, S. Bourrelly, P. L. Llewellyn, P. Horcajada, C. Serre, G. Férey, *Adv. Mater.*, 2012, **24**, 806.
- 23 F. Jeremias, A. Khutia, S. K. Henninger, C. Janiak, *J. Mater. Chem.*, 2012, **22**, 10148.
- 24 T. Lis, V. Kinzhybalo, K. Zieba, *Acta Cryst.*, 2005, **E61**, 2382.
- 25 F. Song, C. Wang, J. M. Falkowski, L. Ma, W. Lin, *J. Am. Chem. Soc.*, 2010, **132**, 15390.
- 26 X.-L. Yang, M.-H. Xie, C. Zou, Y. He, B. Chen, M. O'Keeffe, C.-D. Wu, *J. Am. Chem. Soc.*, 2012, **134**, 10638.
- 27 N. Taleb, V. J. Richards, S. P. Argent, J. van Slageren, W. Lewis, A. J. Blake, N. R. Champness, *Dalton Trans.*, 2011, **40**, 5891
- 28 A. Sonnauer, F. Hoffmann, M. Fröba, L. Kienle, V. Duppel, M. Thommes, C. Serre, G. Férey, N. Stock, *Angew. Chem. Int. Ed.*, 2009, **48**, 3791.
- 29 N. Pienack, W. Bensch, *Angew. Chemie Int. Ed.*, 2011, **50**, 2014.
- 30 M. Feyand, C. Näther, A. Rothkirch, N. Stock, *Inorg. Chem.*, 2010, **49**, 11158.
- 31 J. D. Sharp, J. H. Hancock, *J. Am. Ceram. Soc.*, 1972, **55**, 74.
- 32 N. Pienack, C. Näther, W. Bensch, *Eur. J. Inorg. Chem.*, 2009, 937
- 33 A. F. Gualtieri, *Phys. Chem. Miner.*, 2001, **28**, 719.
- 34 F. Millange, R. El Osta, M. E. Medina, R.I. Walton, *CrystEngComm*. 2011, **13**, 103.
- 35 T. Ahnfeldt, J. Moellmer, V. Guillerm, R. Staudt, C. Serre, N. Stock, *Chem.-Eur. J.*, 2011, **17**, 6462.
- 36 F. Millange, M. E. Medina, N. Guillou, G. Férey, K. M. Golden, R. I. Walton, *Angew. Chem. Int. Ed.*, 2010, **49**, 763.
- 37 E. Stavitski, M. Goesten, J. Juan-Alcaniz, A. Martinez-Joaristi, P. Serra-Crespo, A. V. Petukhov, J. Gascon, F. Kapteijn, *Angew. Chem. Int. Ed.*, 2011, **50**, 9624.
- 38 R. J. Francis, S. O'Brien, A. M. Fogg, P. Shiv Halasyamani, D. O'Hare, T. Loiseau, G. Férey, *J. Am. Chem. Soc.*, 1999, **121**, 1002.
- 39 R. Kiebach, N. Pienack, M.-E. Ordolff, F. Studt, W. Bensch, *Chem. Mater.* 2006, **18**, 1196.
- 40 Y. Zhou, E. Antonova, W. Bensch, G. R. Patzke, *Nanoscale*, 2010, **2**, 2412.
- 41 Y. Zhou, E. Antonove, Y. Lin, J.-P. Grunwaldt, W. Bensch, G. R. Patzke, *Eur. J. Inorg. Chem.* 2012, 783.
- 42 R. El Osta, M. Frigoli, J. Marrot, M.E. Medina, R.I. Walton, F. Millange, *Cryst. Growth Des.*, 2012, **12**, 1531.

4.5 Synthese neuer poröser Aluminium-MOFs basierend auf gewinkelten aromatischen Dicarboxylat-Ionen

4.5.1 Structures, sorption characteristics and nonlinear optical properties of a new series of highly stable aluminium MOFs

Dieses Manuskript wurde in der vorliegenden Fassung im August 2012 im Journal „Chemistry of Materials“ eingereicht.

Mittels Hochdurchsatzmethoden konnte in dem System Al^{3+} / Isophthalsäure (H_2BDC) / H_2O / DMF unter solvothermalen Bedingungen die neue Verbindung $[\text{Al}(\text{OH})(\text{BDC})]$ oder CAU-10-H hergestellt werden. Durch Verwendung von in 5-Position funktionalisierten Isophthalsäuren konnten fünf weitere Analoga dieser Verbindung erhalten werden (CAU-10-X mit $\text{X} = \text{CH}_3, \text{OCH}_3, \text{NO}_2, \text{NH}_2$ oder OH). Alle Verbindungen wurden mittels Elementaranalyse, IR-Spektroskopie, Thermogravimetrie, Gassorption (N_2 und H_2 bei 77 K, CO_2 und H_2O bei 298 K), Rasterelektronenmikroskopie, SHG-Mikroskopie und Röntgenpulverdiffraktometrie charakterisiert. Die Kristallstrukturen der Verbindungen CAU-10-H, - CH_3 und OCH_3 konnten aus Pulverbeugungsdaten gelöst und mittels Rietveldmethoden verfeinert werden. Das Netzwerk ist aus helicalen Ketten von *cis*-eckenverknüpften AlO_6 -Polyedern aufgebaut, die über die Isophthalationen verknüpft werden, so dass Kanäle mit einem maximalen Durchmesser von ca. 7 Å entstehen.

Durch die Kombination der Ergebnisse von Röntgenpulverdiffraktometrie und SHG-Mikroskopie konnte die Raumgruppe von CAU-10- NO_2 eindeutig bestimmt werden. Im Falle von CAU-10- CH_3 konnte zusätzlich ein Phaseübergang beobachtet werden, wenn das Syntheseprodukt auf 200 °C erhitzt wird wobei die Lösungsmittelmoleküle aus den Poren entfernt werden. Auch hier konnte die Raumgruppe des Rohprodukts durch den Einsatz von SHG-Mikroskopie eindeutig bestimmt werden.

Im Falle von CAU-10- NH_2 wurde mittels NMR-Spektroskopie eine partielle Formylierung der Aminogruppen durch das Lösungsmittel nachgewiesen.

Durch den Einbau der funktionellen Gruppen verändern sich zum einen die Stabilitäten der CAU-10-Verbindungen, zum Anderen zeigen die verschiedenen Mitglieder der Serie aber auch ein stark verändertes Sorptionsverhalten. Dabei werden veränderte Kapazitäten, Affinitäten und Zugänglichkeiten beobachtet, je nachdem welche funktionelle Gruppe in das Netzwerk eingebaut ist. Außerdem

werden, obwohl die Strukturen der MOFs zueinander isoretikulär sind, sechs verschiedene Raumgruppen beobachtet, die aber alle untereinander strukturell verwandt sind. In Tabelle 4.5.1 sind die Verbindungen, die Elementarzellparameter und die Raumgruppen in denen diese kristallisieren aufgeführt.

Tabelle 4.5.1: Kristallographische Parameter der Verbindungen der CAU-10-Serie.

Verbindung	$a = b$ [Å]	c [Å]	Raumgruppe
CAU-10-H	21.55(7)	10.38(3)	$I4_1$
CAU-10-CH ₃ (as)	21.4900(6)	10.4828(4)	$P4_1$
CAU-10-CH ₃	21.4917(6)	10.1810(5)	$I4_1/amd$
CAU-10-OCH ₃	21.3609(3)	10.5699(2)	$I4_1/a$
CAU-10-NO ₂	21.4707(3)	10.3777(2)	$P4_1$
CAU-10-NH ₂	21.4567(4)	10.8452(3)	$P\bar{4}n2$
CAU-10-OH	21.3072(5)	38.6974(9)	$P4$

Die Struktur des bei 200 °C aktivierten CAU-10-CH₃ weist die höchste Symmetrie auf (Raumgruppe $I4_1/amd$, Nr.141). Durch einen translationsgleichen Übergang gelangt man zu der Raumgruppe $I4_1/a$ (Nr. 88) in der CAU-10-OCH₃ kristallisiert (Abb. 4.5.1).

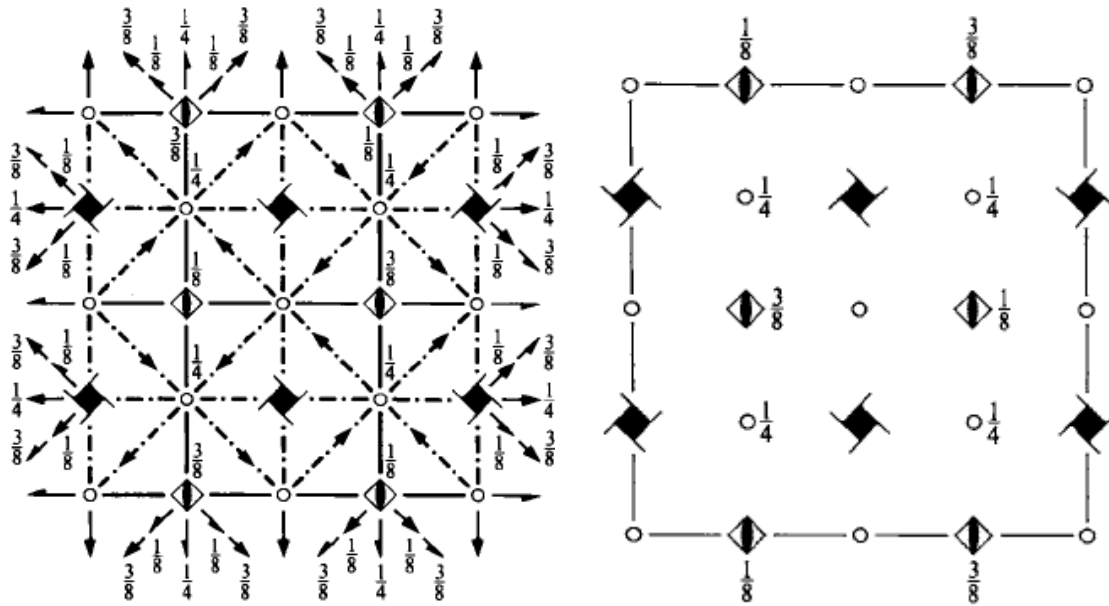


Abbildung 4.5.1: Darstellung der Symmetrieelemente der Raumgruppen $I4_1/amd$ und $I4_1/a$ entlang c aus den *International Tables for Crystallography*.¹

Bei solch einem Übergang bleibt das Translationsgitter erhalten, was sich auch in den sehr ähnlichen Zellparametern der CAU-10-Verbindungen zeigt. Die Kristallklasse ändert sich dabei von $4/mmm$ zu $4/m$. Die Spiegelebenen m (senkrecht zu a und b) und die Gleitspiegelebenen d mit den dazu orthogonal stehenden zweizähligen Drehachsen sind in $I4_1/a$ nicht mehr enthalten. Durch diesen Symmetrieverlust sinkt die Multiplizität der allgemeinen Wyckoff-Positionen von 32 auf 16, weshalb die asymmetrische Einheit von CAU-10-OCH₃ ungefähr doppelt so viele Atome enthält wie die asymmetrische Einheit von CAU-10-CH₃. Und während beispielsweise das Al³⁺-Ion in der Struktur von CAU-10-CH₃ auf einer speziellen Position liegt (Multiplizität 16), liegt das Al³⁺-Ion in der Struktur von CAU-10-OCH₃ auf einer allgemeinen Lage, deren Multiplizität allerdings ebenfalls 16 beträgt.

Durch einen weiteren translationsgleichen Übergang gelangt man von der Raumgruppe $I4_1/a$ in die Raumgruppe $I4_1$ (Nr. 80), in der CAU-10-H kristallisiert. In dieser Raumgruppe fehlt auch die Gleitspiegelebene a die parallel zur ab -Ebene liegt. Außerdem werden beim Übergang die vierzähligen Drehinversionsachsen in zweizählige Drehachsen umgewandelt. Zusätzlich verschwinden alle Inversionszentren und der Nullpunkt der Raumgruppe verschiebt sich, so das insgesamt die relative Position der Symmetrieelemente verschoben wird (Abb. 5.2).

¹ T. Hahn, *International Tables for Crystallography Vol. A, fifth Edt.*, Springer, 2005.

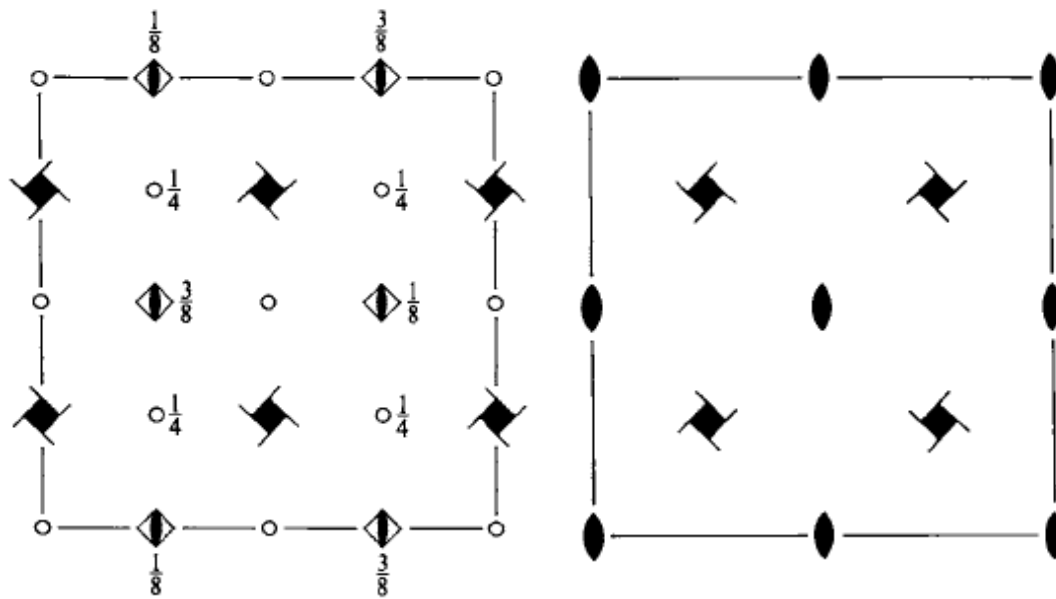


Abbildung 5.2: Darstellung der Symmetrieelemente der Raumgruppen $I4_1/a$ und $I4_1$ entlang c aus den *International Tables for Crystallography*.

Auch bei diesem Übergang halbiert sich die Symmetrie innerhalb der Zelle während die Gitterparameter annähernd unverändert bleiben. Die Multiplizität der allgemeinen Positionen liegt für $I4_1$ nur noch bei 8, weshalb die asymmetrische Einheit von CAU-10-H in etwa doppelt so viele Atome enthält wie die asymmetrische Einheit von CAU-10-OCH₃ und ungefähr viermal so viele wie CAU-10-CH₃. Die Kristallklasse ändert sich von $4/m$ zu 4 für CAU-10-H.

Von der Raumgruppe $I4_1$ gelangt man durch einen klassengleichen Übergang zur Raumgruppe $P4_1$ (Nr. 76), in der die Verbindungen CAU-10-NO₂ sowie das nicht thermisch aktivierte CAU-10-CH₃ kristallisieren. Dabei geht die Zentrierung der Elementarzelle verloren während das Translationsgitter erhalten bleibt. Die Multiplizität der allgemeinen Positionen sinkt auf 4. Die Kristallklasse 4 bleibt allerdings erhalten.

Alle Elementarzellen der CAU-10-Verbindungen sind sich untereinander sehr ähnlich (Schema 1). Sonderfälle stellen die Raumgruppen von CAU-10-NH₂ und CAU-10-OH dar. Für CAU-10-NH₂ wurde die Auslöschungsgruppe $P-4n2$ beobachtet, mit einer ähnlichen Zelle wie für die übrigen CAU-10-MOFs. Die Verbindung CAU-10-OH kristallisiert in der Auslöschungsgruppe $P4$ mit einer ungefähr vierfachen c -Achse. In beiden Fällen konnten keine 4₁-Schraubenachsen nachgewiesen werden, wodurch sie sich von den Kristallstrukturen der anderen CAU-10 Verbindungen unterscheiden.

Allerdings kann man von $P4_1$ zur klassengleichen Obergruppe $P4_2$ (Nr. 77) mit halbiertes c -Achse gelangen. Von dieser Zelle kann man mit klassengleichem Übergang in die Obergruppe $P4$ (Nr. 75) mit erneut halbiertes c -Achse gelangen. In die beobachtete Zelle gelangt man dann durch einen vierfachen isomorphen Übergang mit jeweiliger Verdoppelung der c -Achse (Schema 2).

In die Raumgruppe $P-4n2$ kann man auch ausgehend von der Raumgruppe $I4_1/amd$ durch schrittweisen Symmetrieabstieg gelangen, allerdings nicht entlang des für die anderen Verbindungen beschriebenen Zweiges. Man gelangt durch einen translationsgleichen Übergang in die Raumgruppe $I-4m2$ (Nr. 119), wobei allerdings die charakteristischen 4_1 -Schraubenachsen wegfällen. Aus dieser Raumgruppe gelangt man dann durch einen klassengleichen Übergang unter Wegfall der Zentrierung in die Raumgruppe $P-4n2$ (Nr. 118) (Schema 3).

Der Zusammenhang zwischen den Raumgruppen ist in den folgenden Schemata dargestellt:

Schema 1

Raumgruppe $I4_1/amd$, Kristallklasse $4/mmm$

↓ t_2 ↓

Raumgruppe $I4_1/a$, Kristallklasse $4/m$

↓ t_2 ↓

Raumgruppe $I4_1$, Kristallklasse 4

↓ k_2 ↓

Raumgruppe $P4_1$, Kristallklasse 4

Schema 2

Raumgruppe $P4_1$, Kristallklasse 4

↓ k_2 zur Obergruppe ↓

Raumgruppe $P4_2$, Kristallklasse 4 ($c' = 1/2 c$)

↓ k_2 zur Obergruppe ↓

Raumgruppe $P4$, Kristallklasse 4 ($c'' = 1/4 c$)

↓ 4 mal i_2 ↓

Raumgruppe $P4$, Kristallklasse $4(c''' = 8c' = 16c'' = 4c)$

Schema 3

Raumgruppe $I4_1/amd$, Kristallklasse $4/mmm$

↓ t_2 ↓

Raumgruppe $I-4m2$, Kristallklasse $-4m2$

↓ k_2 ↓

Raumgruppe $P-4n2$, Kristallklasse $-4m2$

Structures, sorption characteristics and nonlinear optical properties of a new series of highly stable aluminium MOFs

Helge Reinsch[†], Monique Van der Veen^{‡,§}, Barbara Gil[◊], Bartosz Marszalek[◊], Thierry Verbiest[§], Dirk de Vos[‡], Norbert Stock^{†*}

[†]Institut für Anorganische Chemie, Christian-Albrechts-Universität zu Kiel, Max-Eyth-Straße 2, 24118 Kiel (Germany). [‡]Centre for Surface Chemistry and Catalysis, University of Leuven, Kasteelpark Arenberg 23, 3001 Leuven (Belgium) [§]Molecular Electronics and Photonics, University of Leuven, Celestijnenlaan 200D, 3001 Leuven (Belgium). [◊] Faculty of Chemistry, Jagiellonian University, ul. Ingardena 3, 30-060 Kraków, (Poland).

KEYWORDS metal-organic frameworks; aluminium carboxylates; porous materials; nonlinear optical properties; isoreticular chemistry

ABSTRACT: Employing high-throughput methods, the synthesis conditions for a series of six new MOFs based on aluminium ions and the V-shaped linker molecule 1,3-benzene dicarboxylic acid, denoted as CAU-10-X (CAU = Christian-Albrechts-University) with the sum formula $[\text{Al}(\text{OH})(\text{C}_8\text{H}_3\text{O}_4\text{X})]$ -solvent, were established (X = functional group in 5-position of the aromatic ring; X = H (**1**), CH₃ (**2**), OCH₃ (**3**), NO₂ (**4**), NH₂ (**5**), or OH (**6**)). Due to the absence of macroscopic crystals, the obtained compounds were structurally characterized employing XRPD-methods. The crystal structures of **1**, **2** and **3** were refined using Rietveld methods. Although the described MOFs are isoreticular, they crystallize in several, sometimes chiral and polar space groups (**1**, **4**, **6**), due to slight structural changes induced by the functionalization. These space groups were confirmed with second-harmonic generation measurements. All compounds are highly stable as confirmed by temperature-dependent XRPD- and IR-experiments and decompose at temperatures above 350 °C. The stabilities of all compounds in aqueous solutions of varying pH were confirmed by XRPD-measurements and their sorption properties towards nitrogen, hydrogen, carbon dioxide and water vapor at low pressures are reported. A drastic influence of the functional group on affinity, capacity and accessibility of the pores for these gases is observed. These properties depend on the polarity and size of the functional group as well as on subtle structural differences between the CAU-10-X compounds.

Introduction

Metal-organic frameworks are often objected to as potential materials for a variety of applications like gas storage, separation processes, as sensor materials or in pharmaceutical applications.^[1,2,3,4] Their main advantage is the modular building principle rooted in the assembly of separate organic and inorganic building units. This allows in theory the facile tuning of their properties, either by the chemical functionalization of the organic building units or by replacement of the inorganic units. This approach is known as isoreticular chemistry, which is supposed to result in “tailored” properties, suitable to the application of interest.^[5] This principle has shown to be valuable for a small number of compounds, while the majority of structures remains unique. Prominent examples of the successful isoreticular synthesis are most often based on linear aromatic dicarboxylate ions, which are varied in size and by additional functional groups.^[6,7] This is most probably due to the commercial availability of a rather large number of linker molecules exhibiting this linear geometry. As an example, a large number of compounds based on the MIL-53-topology are known and well characterized (MIL stands for Matériaux d’Institut Lavoisier). The inorganic unit in this type of framework is a chain of *trans*-connected M(III)O₆-polyhedra, which are connected by linear

dicarboxylate ions.^[8] The size of these dicarboxylate ions can be varied in a wide range, thus the smallest linker incorporated until now is the fumarate ion (*trans*-1,2-ethylenedicarboxylate).^[9] The largest molecule used for the synthesis of the MIL-53-topology is the 4,4'-biphenyldicarboxylic acid.^[10] Furthermore, a manifold of compounds based on functionalized 1,4-benzenedicarboxylic acid can be synthesized.^[11,12] The diversity of this topology is increased due to the large number of cations that can act as inorganic unit, like Al³⁺^[8], Sc³⁺^[13], Fe³⁺^[14], Cr³⁺^[15], In³⁺^[16] or Ga³⁺^[17]. Among these compounds, especially the MOFs based on aluminium and chromium have shown to be chemically and thermally stable.^[18,19] Moreover, the low price and the low toxicity of aluminium salts have resulted in a profound interest of industrial research groups in these materials.^[9] These are the reasons for our interest in the synthesis of new MOFs based on aluminium. While a large number of compounds based on the MIL-53-topology can be readily synthesized, there is no example for MOFs based on aluminium and the V-shaped 1,3-benzene dicarboxylic acid (isophthalic acid or 1,3-H₂BDC). To the best of our knowledge there is no example at all for a porous compound based on this linker molecule and one of the mentioned trivalent cations, although the isophthalic acid is non-toxic and available at low cost. This is

very surprising since a variety of modified isophthalic acids are commercially available, which in principle eases the synthesis of isoreticular MOFs. Therefore, we started a systematic investigation of the solvothermal system Al^{3+} / isophthalic acid / solvent. For this investigation, we took also the requirements of industrial research into account, i.e. the preferable use of $\text{Al}_2(\text{SO}_4)_3 \cdot 18\text{H}_2\text{O}$, a low amount of organic solvents and rather mild synthesis conditions.^[9] By applying high-throughput (HT-) methods,^[20,21] we discovered a new porous aluminum isophthalate, denoted as CAU-10-H with the sum formula $[\text{Al}(\text{OH})(1,3\text{-BDC})]$. Using the reaction conditions for the synthesis of CAU-10-H as a starting point, the HT-methods were further employed to optimize the synthesis conditions for five other members of this series bearing NO_2 -, NH_2 -, CH_3 -, OCH_3 - or OH-groups. For a detailed characterization of all members of the CAU-10-series sorption experiments were carried out with N_2 and H_2 at 77 K and with CO_2 and H_2O at 298 K. In addition, thermogravimetric experiments as well as temperature dependent XRPD- and IR-measurements were performed and stability tests in a wide pH-range were carried out. To identify structural transitions and to confirm the chirality and polarity of some of these MOFs, the CAU-10-series was further characterized by means of SHG-measurements.

Experimental Section

Materials and Methods. All chemicals are commercially available and were employed without further purification. A detailed description of our HT-methods is given elsewhere.^[22] The HT-studies for the discovery and optimisation of CAU-10-H are described in the supporting information. For the upscaled reactions, custom made teflon-reactors in steel autoclaves with a volume of 37 mL or glass reactors for solvothermal conditions with a volume of 100 mL were employed. The initial characterization by means of XRPD-methods was carried out on a STOE-Stadi-P diffractometer ($\text{Cu K}\alpha_1$ -radiation) equipped with a xy-stage and an image-plate-detector. The data for the structure solution and refinement was collected on a STOE-Stadi-P diffractometer ($\text{Cu K}\alpha_1$ -radiation) equipped with a PSD-detector. The synchrotron-XRPD data for the refinement of CAU-10-H was measured at the beamline P8 of the PETRA-accelerator ring at the DESY in Hamburg. The wavelength was set to 0.495 Å and the pattern was recorded on a 2D-CCD-detector. The raw data was converted with the fit2D-program.^[23] The suitability of this setup was confirmed by the successful refinement of the NIST-standard CeO_2 and the Al-based MOF CAU-1-NH₂.²⁴ Temperature dependent XRPD-data was measured in capillaries on a STOE-Stadi-P diffractometer equipped with an image plate detector using $\text{Cu K}\alpha_1$ -radiation. The software used for the structure determination was Expo2009,^[25] the refinements were performed with TOPAS.^[26] The software used for force-field-calculations, to complete structural fragments and to optimize some of the structures by forcefield-calculations was Materials Studio 5.0.^[27] IR-spectra measured ambient conditions were measured with a Bruker ALPHA-FT-IR A220/D-01 spectrometer

equipped with an ATR-unit. The Raman-spectra were measured with a Bruker IFS 66 FRA 106 spectrometer in the range of 0-3300 cm^{-1} using a Nd/YAG-Laser (1064 nm). NMR-spectra in solution were measured on a Bruker DRX 500 spectrometer. Solid-state CP-MAS-NMR spectra were recorded on a Bruker DSX Avance 400 FT NMR spectrometer in a 7 mm ZrO_2 -rotor at a rotation frequency of 5 kHz. Thermogravimetric measurements were performed on a NETZSCH STA 409 CD analyzer under a flow of air with a heating rate of 4 K/min in Al_2O_3 -crucibles. The data was corrected for buoyancy and current effects. EDX-measurements were performed with a Phillips ESEM XL-30. SEM-micrographs were recorded with a Zeiss Gemini Ultra Plus. Sorption experiments were carried out with a BEL JAPAN INC. Belsorp_{max}. Temperature dependent IR-spectra were recorded with a Bruker Tensor 27 spectrometer equipped with an MCT detector and working with the spectral resolution of 2 cm^{-1} . All presented spectra, except the ones at RT, were measured at 50 °C. For the IR experiment a silicon wafer was covered by a thin layer of the material by evaporating on its surface a few drops of the corresponding dispersion in methanol.

In the SHG microscope the sample is illuminated wide-field under normal incidence with femtosecond pulsed infrared (IR) laser light at 800 nm (Spectra Physics, Tsunami ®). The polarization of the incident IR light is varied by a zero-order half-wave plate for 800 nm. The sample is irradiated by a long focal length lens ($f=7.5$ cm), so that the incident fundamental light can be considered in good approximation as a collimated beam, and electric field components along the propagation direction (Z) can be neglected. Behind the sample, a high-power objective (Thorlabs, LMU-15X-NUV) collimates the transmitted light. An interference filter (Melles-Griot, FWHM) centered at 400 nm selectively transmits the second-harmonic light. A Glan-Taylor polarizer can be inserted as analyzer. Finally, an EM-CCD camera (C9100, Hamamatsu) collects the transmitted light.

Synthesis. CAU-10-H (**1**) was synthesized from a mixture of 200 mg 1,3-H₂BDC (1.20 mmol), 800 mg of $\text{Al}_2(\text{SO}_4)_3 \cdot 18\text{H}_2\text{O}$ (1.20 mmol), 1 mL N,N-dimethylformamid (DMF) and 4 mL H_2O . The reactants were dosed into a teflon-lined steel-autoclave with a volume of 37 mL and placed in an oven for 12 h at 135 °C. After cooling to room temperature, the product was filtered off and the obtained solid was redispersed in water by sonication and stirring, until a homogenous mixture was obtained. The dispersion was filtered again and the white microcrystalline solid was dried in air. Elemental analysis: C 40.2 %, H 4.6 %. Calculated values based on the deduced sum formula $[\text{Al}(\text{OH})(\text{O}_2\text{C-C}_6\text{H}_4\text{-CO}_2)] \cdot 1.7 \text{ H}_2\text{O}$: C 40.2 %, H 3.1 %. This synthesis procedure is also applicable in larger teflon reactors with a comparably low filling degree (15 to 20 %), while in glass reactors the formation of an unknown crystalline byproduct was observed.

The methylated MOF CAU-10-CH₃ (**2**) was synthesized in a 100 mL glass reactor with screw cap. Therefore 0.80 g (4.44 mmol) 5-methylisophthalic acid, 2.96 g $\text{Al}_2(\text{SO}_4)_3 \cdot 18\text{H}_2\text{O}$ (4.44 mmol), 4 mL DMF and 16 mL H_2O were mixed thoroughly and

heated for 12 h to 130 °C. After cooling to room temperature, the filtered product was redispersed in ~ 200 mL water by sonication and stirring. Afterwards, the mixture was filtered again and the pale yellow solid was dried under ambient conditions. Elemental analysis: C 46.1%, H 4.1 %, N 1.4 %. Calculated values based on the deduced sum formula $[\text{Al}(\text{OH})(\text{O}_2\text{C}-\text{C}_6\text{H}_4\text{OCH}_3-\text{CO}_2)] \cdot 0.73 \text{ H}_2\text{O} \cdot 0.25 \text{ DMF}$: C 46.1 %, H 4.1, N 1.4 %. The synthesis in teflon-lined autoclaves results in the formation of the same reaction product, but DMF-molecules are occluded inside the pores of this product, which could not be removed by heating or evacuation.

The OCH₃-functionalized MOF CAU-10-OCH₃ (**3**) was also synthesized in a 100 mL glass reactor with screw cap. 1.20 g (6.12 mmol) 5-methoxyisophthalic acid, 2.04 g Al₂(SO₄)₃·18H₂O (4.44 mmol), 3 mL DMF and 12 mL H₂O were mixed thoroughly and heated for 12 h at 130 °C. After cooling to room temperature, the white microcrystalline product was processed in the same way as CAU-10-CH₃. Elemental analysis: C 44.9 %, H 3.6 %, N 1.2 %. Calculated values based on the deduced sum formula $[\text{Al}(\text{OH})(\text{O}_2\text{C}-\text{C}_6\text{H}_4\text{OCH}_3-\text{CO}_2)] \cdot 1.3 \text{ H}_2\text{O} \cdot 0.24 \text{ DMF}$: C 42.9 %, H 4.1, N 1.2 %.

For the other three compounds, we had to develop a different synthesis route, since the stronger polarity of the NO₂-, the NH₂- and the OH-group led to the occlusion of sulfate ions inside the channels of the MOF, as measured by EDX-analysis.

The NO₂-functionalized CAU-10-NO₂ (**4**) was synthesized using a 2 M solution of AlCl₃·6H₂O in water as the Al³⁺-source. Thus, 1440 mg (6.82 mmol) 5-nitroisophthalic acid, 3.4 mL Al³⁺-solution (6.80 mmol), 4 mL DMF and 12.6 mL H₂O were filled into a 100 mL glass reactor with screw cap. The mixture was heated at 120 °C for 12 h, and the product was worked up in the same way as the other compounds. Elemental analysis: C 38.1 %, H 2.5 %, N 6.8 %. Calculated values based on the deduced sum formula $[\text{Al}(\text{OH})(\text{O}_2\text{C}-\text{C}_6\text{H}_4\text{NO}_2-\text{CO}_2)] \cdot 0.41 \text{ DMF}$: C 39.1 %, H 2.4, N 7.0 %.

The NH₂-functionalized CAU-10-NH₂ (**5**) was synthesized by dosing 1200 mg (6.63 mmol) 5-aminoisophthalic acid, 3.3 mL Al³⁺-solution (6.6 mmol), 4 mL DMF and 12.7 mL H₂O into a 100 mL glass reactor with screw cap. The mixture was heated at 120 °C for 12 h, and the resulting pale pink solid was filtered off. The reaction product was redispersed in water by sonication for 30 minutes, filtered off again and dried for one hour at 200 °C in air. Elemental analysis: C 42.8 %, H 2.9 %, N 6.4 %. Calculated values based on the deduced sum formula $[\text{Al}(\text{OH})(\text{O}_2\text{C}-\text{C}_6\text{H}_4\text{NH}_2-\text{CO}_2)]$: C 42.8 %, H 2.9, N 6.4 %. Although the analysis matches the chemical formula, NMR-experiments indicate that the NH₂-group is partially formylated during the synthesis (see SI, paragraph XI).

The OH-functionalized CAU-10-OH (**6**) was synthesized by dosing 1000 mg (5.49 mmol) 5-hydroxyisophthalic acid, 2.8 mL Al³⁺-solution (5.6 mmol), 4 mL DMF and 13.2 mL H₂O into a 100 mL glass reactor with screw cap. The mixture was heated at 120 °C for 12 h, and the resulting white solid was filtered off. The reaction product was redispersed in water by sonication for 30 minutes, filtered off again and dried for one hour at 200 °C in

air. Elemental analysis: C 41.3 %, H 4.5 %. Calculated values based on the deduced sum formula $[\text{Al}(\text{OH})(\text{O}_2\text{C}-\text{C}_6\text{H}_4\text{OH}-\text{CO}_2)] \cdot 0.5 \text{ H}_2\text{O}$: C 41.2 %, H 2.6.

The compounds contain no residual chloride or sulfate ions, according to the EDX analysis. The yield is in all cases between 60 % and 70 % based on the amount of linker. Temperature-dependent IR-spectra and Raman-spectra measured under ambient conditions of all compounds can be found in the supporting information (Fig S23-S34).

Structure determination and refinement of 1, 2 and 3. All compounds were obtained as microcrystalline powders, therefore the structures had to be determined from powder diffraction data.

Indexing of the powder pattern of CAU-10-H (**1**) suggested a tetragonal cell with the space group *I*4₁. Based on this cell, the structure was solved from in-house XRPD-data by direct methods using the program Expo2009 [25]. The inorganic building units were unambiguously located while the organic parts of the framework were inserted as recently described.[28] Utilizing the program Materials Studio[27] the aromatic moieties were introduced at the appropriate positions and the structure was optimized by force-field calculations keeping the positions of the inorganic units fixed. Employing this model as a starting structure, the crystal structure was successfully confirmed by Rietveld-methods using synchrotron XRPD data (Fig. 1). For the measurement at the synchrotron, the sample was heated to 180 °C to remove adsorbed solvent molecules and filled into a 0.7 mm capillary which was immediately sealed. This procedure was necessary since the occluded solvent molecules had a strong influence on the observed intensities. Some parameters of this refinement are summarized in Tab.1. Further details are summarized in the supporting information.

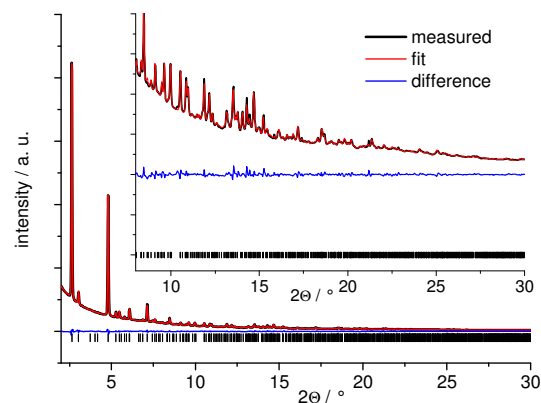


Figure 1: Rietveld plot for the refinement of activated CAU-10-H ($\lambda = 0.495 \text{ \AA}$). The observed intensities are shown in black, the calculated intensities in red. The blue line is the difference plot, vertical bars mark the Bragg reflection positions.

For CAU-10-CH₃ (**2**), a symmetry transition was observed upon removal of the occluded solvent molecules. The compound crystallizes in a tetragonal cell with extinction conditions matching the chiral space group *P*4₁ in its *as(as synthesized)*-form (Fig. S4). The chirality was confirmed by second-harmonic generation measurements (*vide infra*). Heating of **2-as** at 200 °C for one hour in air re-

sulted in small changes in the unit cell parameters. However, indexing of the XRPD pattern led to the space group $I4_1/amd$. We did not observe any reversibility of this transition under ambient conditions even after several months. The structure of this activated compound **2** was solved from in-house XRPD-data using Expo2009. All non-hydrogen atoms of the framework were directly obtained from the structure solution. The structural model was refined by Rietveld-methods (Fig. 2, Tab. 1).

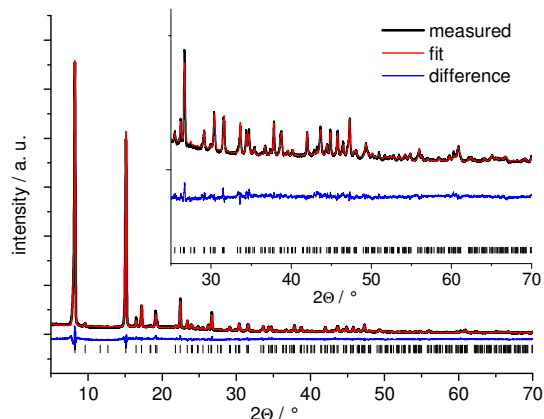


Figure 2: Rietveld plot for the refinement of activated CAU-10-CH₃ (Cu-K α_1 radiation). The observed intensities are shown in black, the calculated intensities in red. The blue line is the difference plot, vertical bars mark the Bragg reflection positions.

The structure of the CAU-10-OCH₃ (**3**) was also solved from XRPD-data. The pattern measured for the as synthesized compound could be indexed in the space group $I4_1/a$. Using direct methods, all framework atoms except the methyl group could be located, and therefore the linker molecule was completed using Materials Studio. This model was successfully refined by Rietveld-methods using TOPAS (Fig. 3).

Table 1: Results of the Rietveld refinements.

CAU-10-X	-H (1)	-CH ₃ (2)	-OCH ₃ (3)
space group	$I4_1$	$I4_1/amd$	$I4_1/a$
$a = b$ [Å]	21.55(7)	21.4917(6)	21.3609(3)
c [Å]	10.38(3)	10.1810(5)	10.5699(2)
R _{wp}	0.019	0.071	0.076
R _{Bragg}	0.004	0.021	0.043
GoF	2.208	2.474	2.817
wavelength	0.495 Å	Cu K α_1	Cu K α_1
atoms	28	10	17
restraints	45	7	22

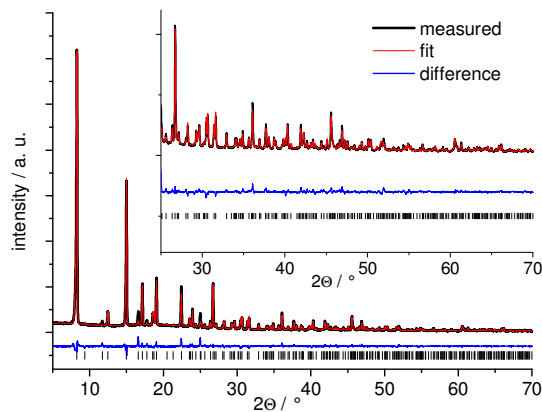


Figure 3: Rietveld plot for the refinement of as synthesized CAU-10-OCH₃ (Cu-K α_1 radiation). The observed intensities are shown in black, the calculated intensities in red. The blue line is the difference plot, vertical bars mark the Bragg reflection positions.

Second-harmonic generation (SHG) or frequency doubling is a second order nonlinear optical process in which photons of frequency ω are converted in photons with the doubled frequency 2ω . Within the electric dipole approximation, SHG is described by the second-order nonlinear polarization $\mathbf{P}^{(2)}(2\omega)$ as in following equation:

$$\mathbf{P}^{(2)}(2\omega) = \chi^{(2)} : \mathbf{E}(\omega)\mathbf{E}(\omega) \quad \text{Eq. 1}$$

with $\chi^{(2)}$ the second-order susceptibility and $\mathbf{E}(\omega)$ the electric field of the incoming light at frequency ω . For a centrosymmetric medium the electric field and polarization transform under the action of a centre of inversion as $\mathbf{P} \rightarrow -\mathbf{P}$ and $\mathbf{E} \rightarrow -\mathbf{E}$. This means that equation 1 transforms to

$$-\mathbf{P}^{(2)} = \chi^{(2)} : (-\mathbf{E})(-\mathbf{E}) = \chi^{(2)} : \mathbf{E}\mathbf{E} = \mathbf{P}^{(2)} \quad \text{Eq. 2}$$

which implies that $\chi^{(2)}$ must be zero. Thus centrosymmetric media cannot generate SHG. In fact SHG is especially sensitive to the symmetry relations and organization of a system. As a consequence SHG-microscopy is increasingly used to deduce structural information from materials. Examples include determination of domain structures,^{29,30} host/guest systems^{31,32} and structural transitions.³³

Recently, a methodology based on polarization dependent SHG-microscopy to determine the point group symmetry of non-centrosymmetric structures has been developed by some of us.³⁴ The methodology has been verified experimentally on systems of known symmetry³⁵ and employed to determine the symmetry of molecular crystals of unknown structure successfully.³⁶

Here we used a derivative methodology, only including the tetragonal non-centrosymmetric point group symmetries. Two polarization dependent tests were used for the determination: in test 1 the plane of polarization of the linearly polarized light incident on the sample is rotated over 360° while all second-harmonic light is detected, test 2 is identical except that an analyzer is placed in front of the detector, meaning that only the second-harmonic light of one linear polarization is detected. These tests lead to polarization plots in which the number of null points – called zeroes ‘z’ – and the number of times the plot

behaves as an even function around a maximum or minimum intensity can be counted – called symmetry axes ‘sa’. For monocrystalline, tetragonal structures the expected observables are listed for each point group symmetry. Depending on whether the crystals are aligned with their crystallographic c-axis with the sample plane of the microscope, or have a different (called arbitrary) orientation, these differ, as can be seen in table 2. As can be seen from this table, the results of test 1 and 2 can be used to distinguish between the different non-centrosymmetric point group symmetries.

If the material is not SHG-active, it means it belongs to a centrosymmetric point group, more specifically C_{4h} or D_{4h} . Indeed, for activated CAU-10- CH_3 (**2**) and CAU-10- OCH_3 (**3**), we could detect no SHG-activity, which confirms the space groups assigned via Rietveld refinement of the XRPD-data.

In contrast, for the non-activated compound CAU-10- CH_3 (**2**) we could detect SHG-activity. An SHG-image is shown in figure 5a. To assign a point group symmetry via polarized SHG-microscopy, we need to ensure that the analyzed particles are indeed monocrystalline products. Via scanning electron microscopy we confirmed that structures with a size of several μm with a distinct crystal habit are present (Fig. S38). For the analysis particles in the range of 2-3 μm were selected. In a first step the polarization dependency of the SHG intensity in test 1 and 2 was compared between different parts of the same particle. Only those particles that showed the same (albeit differently scaled) polarization dependence for all parts were chosen. Of these the majority showed the following observables in both test 1 and 2: 0 z and 0 sa. A minority of the particles showed the following observables: 0 z and 4 sa for test 1, and 0 z and 0 sa for test 2 (see figure 5b-e). This corresponds to the point group C_4 . The possible space groups derived from the le Bail fit are $P4_1$, and $P4_122$ but only the first belongs to the point group symmetry C_4 . Thus, the SHG-results allow to assign the correct space group and confirm the symmetry transition of CAU-10- CH_3 (**2**) upon activation from a non-centrosymmetric to a centrosymmetric structure. Recently, for amino-functionalized MIL-53(Al) also a symmetry transition that greatly diminished the SHG-activity was observed, not upon activation, but upon adsorption of guest molecules.^{37c}

The same analysis was performed for CAU-10-H (**1**) with qualitatively the same results (Fig. S43), meaning that also this structure belongs to the point group C_4 , which is also in accordance with the determined space group $I4_1$.

The compounds **4**, **5** and **6** crystallize in primitive tetragonal space groups, as determined by indexing of their powder patterns and the observed extinction conditions. The cell parameters were confirmed by Le Bail-methods for these compounds (Tab. S2, Fig. S5-S7), but due to the crystallographic complexity of these structures it was not possible up to now to refine the structural models. In fact it's also difficult to unambiguously assign a space group by the observed extinction conditions. One reason is the fact, that several space groups show identical extinction conditions in the XRPD-pattern. Moreover, in the case of the CAU-10-series, the differences between the extinction conditions are marginal. Therefore the results of the SHG-measurements greatly en-

hance the information about the non-refined members of the CAU-10-series.

For compound **5** CAU-10- NH_2 no SHG can be detected. This is in accordance with the assignment of a centrosymmetric space group by the Le Bail method. Compound **4** and **6** also showed SHG-activity, proving their non-centrosymmetric nature. However, SEM images (Fig. S40 and 42) show that only polycrystalline particles are present, meaning that a point group symmetry assignment based on SHG-microscopy cannot be performed. By XRPD we cannot distinguish the space groups $P4_1$ and $P4_122$ for CAU-10- NO_2 (**4**). However, performing SHG measurements using parallel polarizers a distinction can be made, since only the space group $P4_122$ belongs to D_4 -symmetry. A structure with point group D_4 regardless of its orientation cannot generate SHG when placed between parallel polarizers (SI paragraph VIII). An agglomeration of such structures or polycrystalline sample will neither generate SHG under these conditions, if the plane of polarization of the incident and second-harmonic generated light is not significantly rotated while passing through the polycrystalline particle. The latter condition was experimentally verified. When measuring compound **4** between parallel polarizers, a distinct SHG-signal was observed (Fig. 4). Thus the space group $P4_1$ is the correct one for this compound.

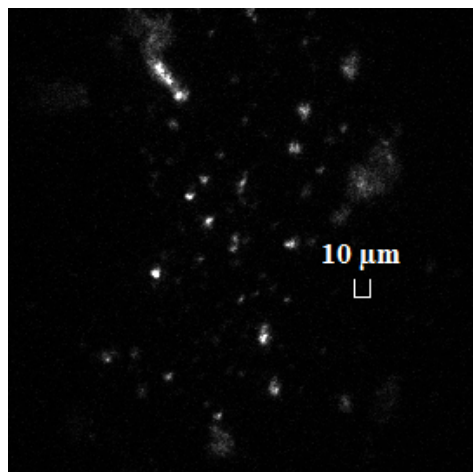


Figure 4: An SHG-image of CAU-10-NO₂ (**4**) in which the plane of linear polarization of the incident light is parallel with the polarization state that the analyzer at the detection site transmits.

Table 2: Observables in polarization dependent SHG-microscopy tests for all non-centrosymmetric tetragonal point group symmetries.

Point group [‡]	orientation*	Test 1 [†]	Test2 [†]
C _{4v}	all	0z, 4sa	0z, 0sa
C ₄	arbitrary	0z, 0sa	0z, 0sa
	c-axis in sample plane	0z, 4sa	0z, 0sa
S ₄	arbitrary	0z, 0sa	0z, 0sa
	c-axis in sample plane	2z, 4sa	2z, 0sa
D ₄	all	2z, 4sa	4z, 4sa
D _{2d}	arbitrary	0z, 0sa	0z, 0sa
	c-axis in sample plane	2z, 4sa	2z, 0sa

[‡] Schoenflies notation * the orientations in which no SHG can be generated were not taken into account. [†] z = number of zeros; sa = number of symmetry axis or minima and maxima around which the graphs behaves as an even function; Kleinmann symmetry was not assumed.

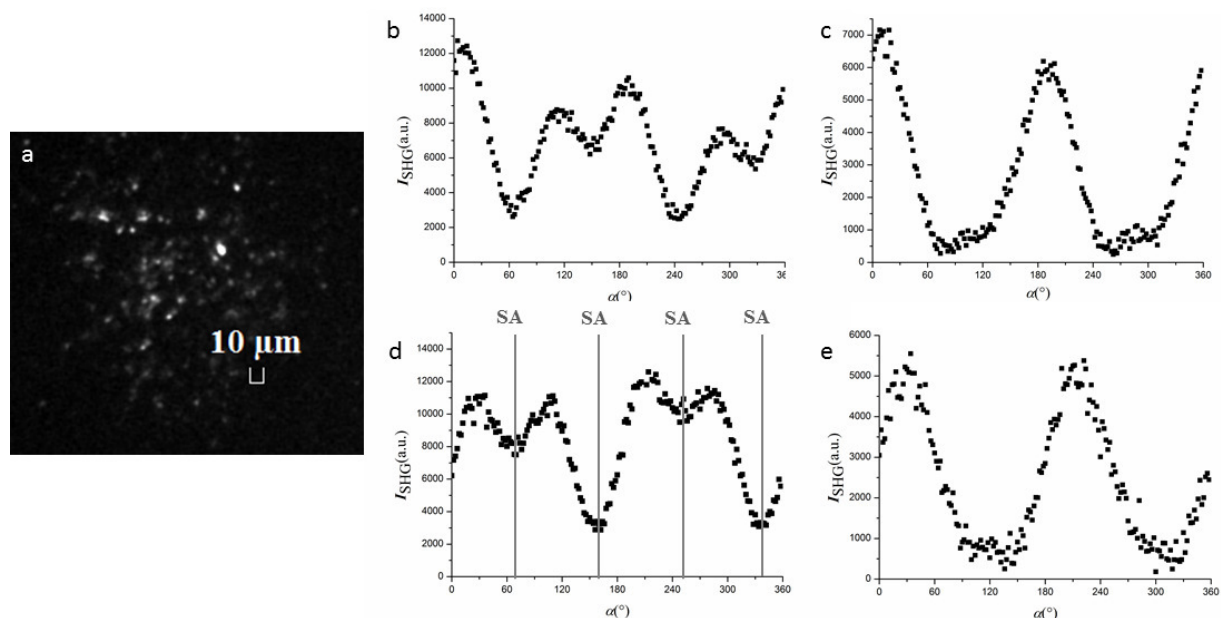


Figure 5: a) SHG-image of as synthesized CAU-10-CH₃ (**2**). SHG intensity of this structure for tests 1 and 2 resp. corresponding to an arbitrarily oriented crystallite (b and c resp.) and a crystallite oriented with its c-axis aligned with the sample plane (d and e resp.) while varying the plane of polarization of the incident light (α). The incident light is linearly polarized and rotated along the direction of light propagation. Note that when the plane of polarization is 180° different, the plane of polarization of the incident light is identical.

Structural description. The inorganic building unit of the CAU-10-framework is a chain of *cis*-connected, corner sharing AlO₆-polyhedra. Four of the oxygen atoms are part of four different carboxylate groups, while two bridging OH⁻ ions in *cis*-position to each other complete the octahedral coordination of the Al-center. By this connectivity mode, helices are formed (Fig. 6). This helical inorganic building unit is remarkable since most often linear chains of *trans*-connected M(III)O₆-polyhedra are observed in MOFs with one-dimensional inorganic units. Examples are the framework compounds with MIL-53 topology. Chains of edge-sharing AlO₆-polyhedra are also known^[38] but to the best of our knowledge there are only two Sc-based MOFs which contain such fourfold helical *cis*-connected chains of M(III)O₆-polyhedra.^[39]

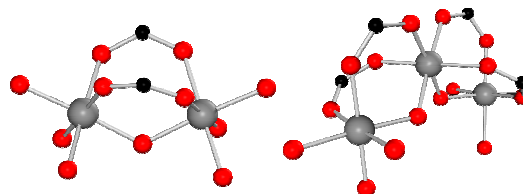


Figure 6: A dimeric unit of corner-sharing AlO₆-octahedra on the left. A trimeric subunit is shown on the right, which hints at the formation of a helical arrangement. Aluminium atoms are shown in grey, oxygen in red and carbon in black.

The framework of CAU-10 is formed by the connection of each helix to four adjacent inorganic building

units of alternating rotational orientation via the organic linker molecules (Fig.7). Thus, square-shaped, sinusoidal channels are formed, which exhibit a maximum diameter of $\sim 7 \text{ \AA}$.

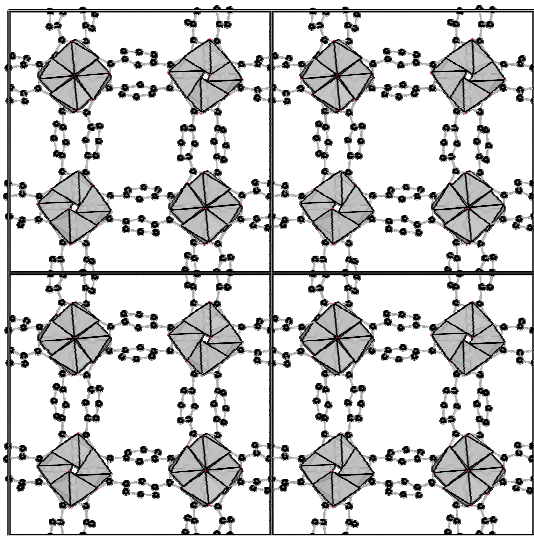


Figure 7: A 2×2 supercell of the framework of CAU-10-H (**1**) as seen along the c -axis, showing the fourfold connectivity of the helices and the square-shaped channels that are formed.

Depending on the functional groups, the framework structures are only slightly changed while the topology itself is retained. Due to the size of the channels in the sub-nanometer range, these small changes have a massive impact on the accessibility of the pores for guest molecules. Therefore the structures of **2** and **3** are described herein in detail. While two symmetry independent helices are observed in **1**, the change of the linker molecules to methylisophthalic acid in **2** leads to a more symmetric structure ($I4_1$ vs. $I4_1/amd$). The adjacent AlO_6 -helices are related by a mirror plane which is parallel to the b - c -plane (Fig. 8) and passes through the carbon atoms in 2- and 5-position and the methyl-group of the organic moieties.

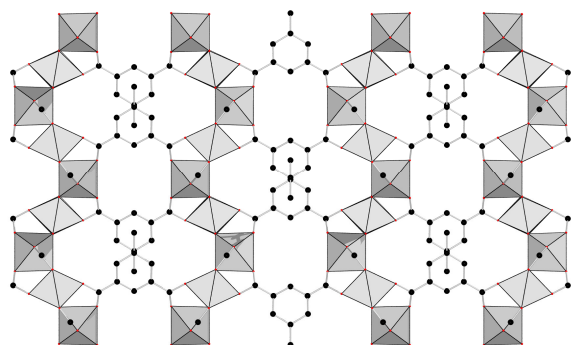


Figure 8: The arrangement of the helices in the framework of CAU-10-CH₃ (**2**) as seen along the b -axis. AlO_6 -polyhedra are shown in grey, oxygen atoms in red and carbon atoms in black.

In the structure of CAU-10-OCH₃ (**3**) which crystallises in the space group $I4_1/a$, only one crystallographically independent helix is observed. The helices are related by an inversion axis, which is

running parallel to the c -axis between four helices (Fig.9).

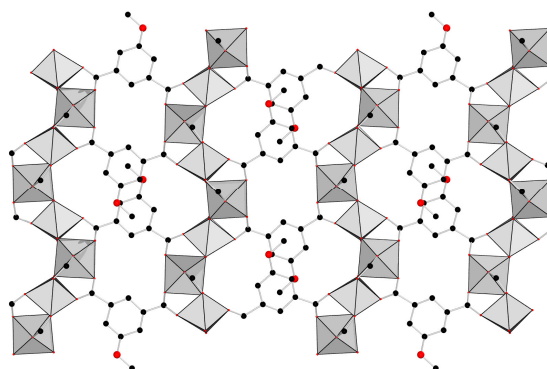


Figure 9: The arrangement of the helices in the framework of CAU-10-OCH₃ (**3**) as seen along the b -axis. AlO_6 -octahedra are shown in grey, oxygen atoms in red and carbon atoms in black.

The different arrangements of the helices result as well in different alignments of the organic building units. The framework of CAU-10-CH₃ (**2**) has the structure of highest symmetry. This results in functional groups which are protruding directly into the channels (Fig. 10, right). The shortest distance between two methyl-carbon atoms is 5.8 \AA (center to center). The lower symmetry in CAU-10-OCH₃ (**3**) results in a distortion of the framework, which gives rise to a slightly larger distance between the oxygen-atoms of the functional groups of 6.4 \AA (center to center) (Fig. 10, left). In CAU-10-H (**1**), the distance of the aromatic carbon atoms in 5-position is 6.8 \AA .

The exact structures of the NO₂⁻, NH₂⁻ and OH-functionalized MOFs remain yet unknown due to their crystallographic complexity and/or the rather insufficient crystallinity. However, the sorption behavior points at structural similarities between CAU-10-NO₂ (**4**) and CAU-10-H (**1**) as well as CAU-10-NH₂ (**5**) / CAU-10-OH (**6**) and CAU-10-CH₃ (**2**) / CAU-10-OCH₃ (**3**).

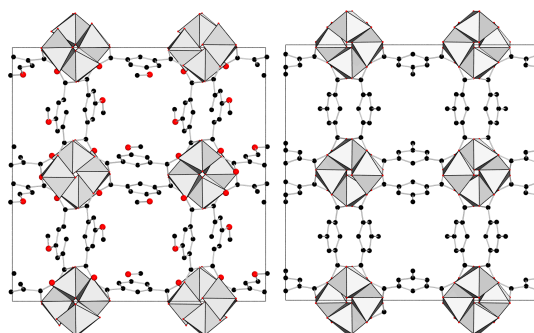


Figure 10: Direct comparison of the framework structures of CAU-10-OCH₃ on the left and CAU-10-CH₃ on the right, as seen along the c -axis. AlO_6 -octahedra are shown in grey, oxygen atoms in red and carbon atoms in black.

The differences in the CAU-10-X structures are due to a combination of the differences in the steric requirements of the functional groups and the interactions (inter ring distances $< 3.4 \text{ \AA}$) of the aromatic moieties.

We object to the framework topology of CAU-10 as an archetype, which should be likely to form with

several other trivalent cations as well as further V-shaped linker molecules, in analogy to the diversity observed for MIL-53-topology. This is supported by the recent discovery of a very similar MOF based on Sc^{3+} and the V-shaped 2,5-thiophenedicarboxylic acid.^[39]

Sorption behaviour. The subtle structural differences of these microporous compounds, i.e. the diameter of the pore aperture and the flexibility of the organic building units should result in drastically altered sorption properties. Therefore, the sorption behavior of all six members of the CAU-10-series in the low pressure regime (up to 1 bar) was measured using nitrogen and hydrogen at 77 K and carbon dioxide and water vapor at 298 K. Prior to every measurement, the samples were activated in vacuum (0.1 mbar) at 200 °C. The sorption isotherms for N_2 at 77 K are shown in Figure 11. For CAU-10-H (**1**) and CAU-10- NO_2 (**4**), a type I isotherms was observed, indicating microporosity.

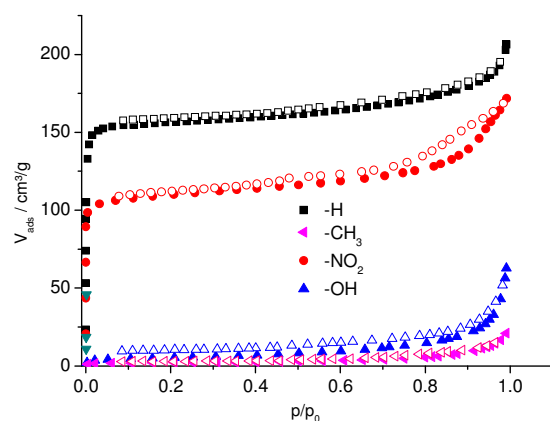


Figure 11: Sorption isotherms of CAU-10-X compounds for nitrogen at 77 K. Filled symbols represent the adsorption, empty symbols the desorption branches.

While we observed isotherms typical for non porous compounds for **2** and **6** ($-\text{CH}_3$ and $-\text{OH}$), for CAU-10- OCH_3 (**3**) and $-\text{NH}_2$ (**5**) (not shown) only an initial uptake of gas was measured. Due to the very slow equilibration, it was not possible to measure full curves for **3** and **5** with appropriate precision. However, higher tolerance values for the pressure fluctuation during the measurements hint at the existence of accessible micropores. We attribute this behavior to the narrow channels, which slow down the free diffusion of gas molecules in case of N_2 -adsorption, and thus extend the equilibration times. Thus, the functional groups have a massive impact on the accessibility of the channels in the case of N_2 -sorption. The specific surface areas S_{BET} are $635 \text{ m}^2/\text{g}$ and $440 \text{ m}^2/\text{g}$ for CAU-10-H (**1**) and CAU-10- NO_2 (**4**), respectively. Their micropore volumes, determined by single point calculation at $p/p_0=0.5$, are $0.25 \text{ cm}^3/\text{g}$ (for **1**) and $0.18 \text{ cm}^3/\text{g}$ (for **4**). The experimental value for the CAU-10-H (**1**) is in very good agreement with the theoretical pore volume of $0.23 \text{ cm}^3/\text{g}$ as obtained from a single point adsorption simulation by force-field methods.^[40]

The curves for the hydrogen adsorption show an uptake of this gas for all members of the series except CAU-10- CH_3 (**2**) (Fig. 12).

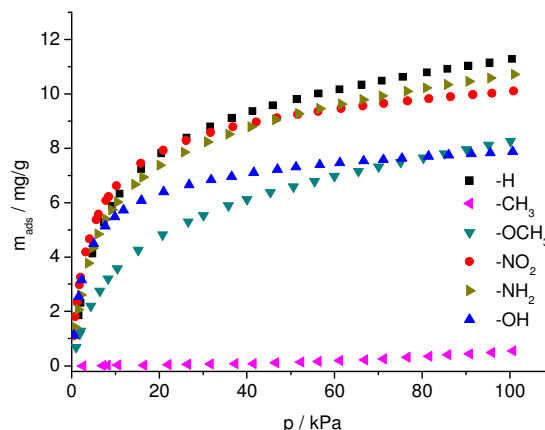


Figure 12: Adsorption isotherms of **1** - **6** for hydrogen at 77 K.

The influence of the functional groups on the adsorption is clearly demonstrated. Their impact on the capacity is not only due to their size but also to the subtle structural differences caused by these groups. Moreover the affinity towards H_2 is varied. Although the micropore volumes of CAU-10-H (**1**) and CAU-10- NO_2 (**4**) differ substantially, similar H_2 uptakes at pressures below 40 kPa are observed. The reason for this result is probably the polar nature of the functional group, which induces a stronger affinity towards H_2 in **4**. The accessibility of the channels for H_2 molecules is hardly influenced due to its smaller kinetic diameter (N_2 : 3.6 \AA , H_2 : 2.6 \AA), except for CAU-10- CH_3 (**2**).

The adsorption isotherms for CO_2 were measured at 298 K and clearly prove the porosity of all members of the CAU-10-series (Fig. 13).

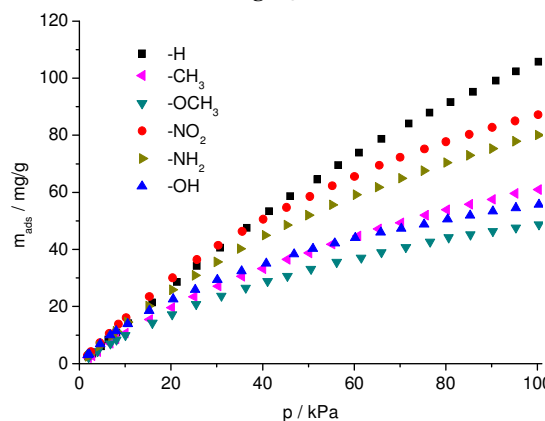


Figure 13: Adsorption isotherms for CO_2 at 298 K.

Even the pores of CAU-10- CH_3 (**2**) are accessible towards CO_2 molecules which can be attributed to the higher experimental temperature of 298 K and stronger host-guest interactions. Although the kinetic diameter of CO_2 molecules (3.3 \AA) is larger than the one of H_2 molecules (2.6 \AA), the increased flexibility of the framework at 298 K makes the pores of **2** accessible for CO_2 , while H_2 is not adsorbed at 77 K. Similar trends for capacities are found, as observed for the H_2 adsorption. In comparison with the unfunctionalized compound **1**, sub-

stantially lower uptakes of gas are observed for **2**, **3** and **6**. The NO_2 -group in **4** and the NH_2 -group in **5** lead to intermediate capacities for these two MOFs.

A pronounced influence of the functional groups was observed for the adsorption of water vapor, measured at 298 K (Fig. 14).

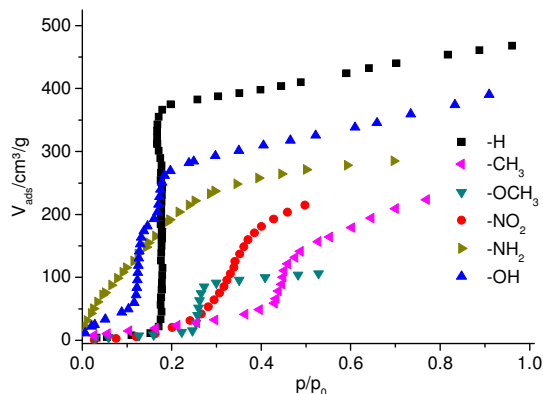


Figure 14: Adsorption isotherms of **1** - **6** for H_2O at 298 K.

All MOFs show an uptake of water vapor and the amount is mainly determined by the size of the functional group. CAU-10- NH_2 (**5**) and CAU-10- OH (**6**) show pronounced uptakes of H_2O molecules at low relative pressure which can be explained by the existence of strong hydrogen-bonds between the functional groups in the MOF and the adsorbate (the broad band of the hydrogen-bonded water molecules are visible for non-dehydrated sample in the IR-spectra – Fig. S31, S33). Besides this, the point of condensation, at which the pores are filled with liquid adsorbate, is altered by the functionalization. The highest affinity towards H_2O is observed for the highly polar groups in CAU-10- NH_2 (**5**) and CAU-10- OH (**6**). The exact amounts of H_2 and CO_2 adsorbed at 100 kPa and the amount of H_2O that was adsorbed after condensation are summarized in Table 3.

Table 3: Total amounts of adsorbed gas or vapour.

R	H_2 [mg/g] (at 100 kPa)	CO_2 [mg/g] (at 100 kPa)	H_2O [cm^3/g] (at $p/p_0 =$)
-H	11.2	105.7	382 (0.26)
- CH_3	0.5	60.9	140 (0.48)
- OCH_3	8.2	48.7	92 (0.30)
- NO_2	10.1	87.1	181 (0.40)
- NH_2	10.7	80.0	271 (0.50)
- OH	7.9	55.7	284 (0.25)

Interestingly, the high affinity observed during water adsorption is not reflected during the activation of the series of CAU-10-X samples as observed in the IR-spectra. For all the samples, molecular water is removed already during evacuation at RT. The fingerprint region of the CAU-10-X are not changed after water desorption (Fig. S23-S34). This suggests that dehydration leads at most to minor changes in the structure.

Correlation of Sorption Properties and Structure. In the framework of CAU-10- H (**1**), the

channels are open and easily accessible for all measured gas molecules. The framework of CAU-10- CH_3 (**2**) is only able to adsorb CO_2 at 298 K, but at 77 K, no adsorption could be observed. In CAU-10- OCH_3 (**3**), the size of the adsorbate seems to be the crucial parameter which determines the accessibility of the pores. To understand this sorption behavior, the H-atoms must be added to the framework structure. This was accomplished by an automatic algorithm implemented in the Materials Studio software.^[27]

The van-der-Waals-model of CAU-10- CH_3 (**2**) shows, that only a very small aperture with a diameter of 1.4 Å allows the diffusion into the channels (Fig. 15).

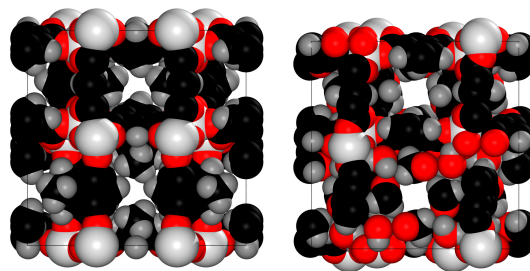


Figure 15: Unit cell of CAU-10- CH_3 (**2**) on the left and CAU-10- OCH_3 (**3**) on the right, shown as van-der-Waals models. Aluminium atoms are light grey, oxygen atoms are red, carbon atoms are black and hydrogen atoms are dark grey.

In the framework of CAU-10- OCH_3 (**3**), this smallest diameter is 2.5 Å. This increase of the diameter by ~ 1 Å is mainly due to the functional group. In **2**, the protons of the methyl-group limit the accessibility. In **3**, the hydrogen atoms can be almost neglected, since the unprotonated oxygen-atoms of the methoxy-groups are limiting the diameter of the aperture (Fig.12). In the unfunctionalized CAU-10- H (**1**), the accessible diameter according to the crystal structure is 4 Å, which allows the adsorption of all measured gases (Fig. 16).

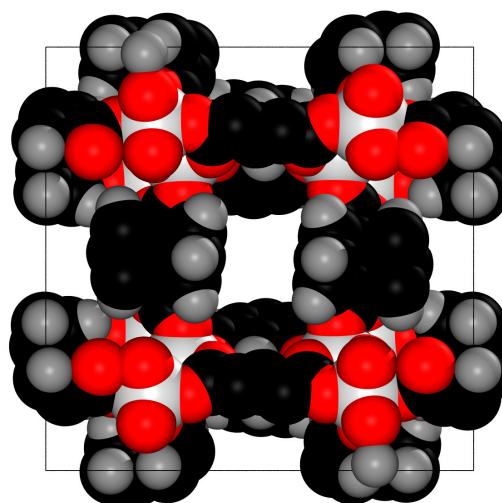


Figure 16: Van-der-Waals model of CAU-10- H (**1**). Aluminium atoms are light grey, oxygen atoms are red, carbon atoms are black and hydrogen atoms are dark grey.

Therefore, the accessibility of **1** for all gases is in agreement with its crystal structure. For CAU-10-

OCH₃ (**3**), we must assume that the framework possesses a certain degree of flexibility, since the kinetic diameters of the gas molecules are larger than the channel openings. In the framework of CAU-10-CH₃ (**2**), the flexibility of the MOF must be even higher than in **3**, since the pore opening is smaller. Therefore, only at an elevated temperature of 298 K, gas molecules can be adsorbed in **2**. At 77 K, its flexibility is too low to permit the adsorption of gases.

Stability measurements. The stabilities in aqueous solutions depending on the pH-value as well as under solvothermal conditions in water were investigated by XRPD- and IR-measurements (Fig. S11-S16). For these tests, 50 mg of each MOF were stirred for 18 hours at room temperature in 4 mL of 0.01 M hydrochloric acid or 0.01 M sodium hydroxide solution. According to these results, the MOFs are stable in a pH-range from 2 to 8. Stirring under more basic conditions does not lead to a complete decomposition, but the pH-value is lowered to 8, indicating that the compounds are dissolved until a final pH-value of 8 is reached. The treatment in acidic solution (pH of 2), does not lead to additional bands in the IR-spectra, indicating that no isophthalic acid derivatives are formed by solvolysis of the MOFs, confirming their stability. Upon treatment with water at 130 °C under stirring for 3 hours, no decomposition is observed as well. This stability is lower compared to the series of zirconium based MOFs^[7] but it is nevertheless very remarkable, especially in comparison with several MOFs based on divalent metal ions.^[18]

According to the thermogravimetric experiments, all of the MOFs decompose at temperatures around 400 °C (Fig. S17-S22). The temperature dependent XRPD-measurements for CAU-10-H (**1**) show a decomposition at ~ 430 °C (Fig. 17 and Fig. S8). While the removal of the adsorbed solvent molecules leads to changes in the relative intensities, the broadening of the reflections at 430 °C marks the beginning of the decomposition of the framework. These observations were also supported by temperature-dependent FTIR spectroscopy (see SI).

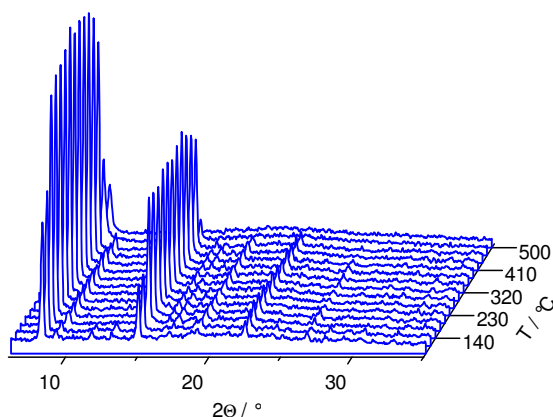


Figure 17: Temperature dependent XRPD-data of CAU-10-H measured in a capillary.

For CAU-10-NO₂ (**4**) and CAU-10-OH (**6**) we observed similarly high thermal stabilities in the temperature dependent XRPD-measurements (Fig. S9-S10). The decomposition starts at temperatures above 410 °C. During the heating, we observed al-

most no shift of the reflections for **1**. For **4**, a shift towards lower angles is observed. Thus, the unit cell of CAU-10-NO₂ (**4**) is slightly expanding upon heating while it remains rather rigid in case of CAU-10-H (**1**).

A slightly lower stability is observed in the temperature dependent IR-spectra (Fig. S23-S33), mainly attributed to the different measurement conditions in vacuum. Thus CAU-10-H (**1**) and CAU-10-CH₃ (**2**) decompose at 350 °C, while the decomposition of CAU-10-NO₂ (**4**) starts already at 300 °C in vacuum. From the CAU-10-series, CAU-10-NH₂ (**5**) and CAU-10-OCH₃ (**3**) revealed the highest thermal stability under vacuum, decomposing only at 450 °C. The lowest stability was observed for CAU-10-OH (**6**), for which sample damage appeared already at 250 °C. The lower stability compared to XRPD experiments can be attributed to the different measurement conditions. Temperature dependent IR spectra allowed also to follow the removal of traces of DMF and water molecules occluded inside the pores, which are removed up to 150 °C. In neither sample free isophthalic acid was observed in the IR-spectra.

Nonlinear optical properties. While inorganic materials are still nearly exclusively used in practical applications of nonlinear optical (NLO) materials, it is widely recognized that molecular-based materials can surpass these materials in their nonlinear optical characteristics: ultrafast response times, higher NLO-responses and a better processibility into devices.^{41,42} Metal-organic frameworks have been investigated as a route to obtain nonlinear optical molecular-based materials.^{43,44k}

We quantified the SHG-response for the structure that has the highest SHG activity, namely CAU-10-NO₂ (**4**). Assuming monocrystalline particles, the effective second order nonlinear optical coefficient averaged over all orientations $\langle d_{\text{eff}} \rangle$ was found to be 0.0002 pm/V (SI paragraph X). However, the generated SHG intensity scales quadratically with the thickness of a single crystal, but only linearly with the number of crystallites. As the CAU-10-NO₂ (**4**) sample consists in fact of a polycrystalline powder, this determined value is an underestimation of the effective nonlinear optical coefficient with at least several orders of magnitude. Typical commercial NLO materials (such as KDP, BBO, KTP and LiIO₃) show d_{eff} values between 0.4 and 15 pm/V. The true value of d_{eff} CAU-10-NO₂ (**4**) will likely be in this range.

Conclusions

Summarizing the results, a series of six MOFs was synthesized exhibiting the same framework topology, but different functional groups. The detailed characterisation clearly shows that subtle structural differences have a massive impact on the sorption capacity and affinity, as well as on the second-order nonlinear optical activity. The combination of XRPD and SHG measurements allows following structural changes upon activation and the determination of the correct space group. The straightforward synthesis of the compounds under very similar reaction conditions could be helpful in tuning the sorption

properties by using mixed linker systems. Moreover the topology of the CAU-10-series could be starting point for the synthesis of isoreticular compounds based on V-shaped ligands and trivalent cations. This would expand the range of opportunities for the modulation of the sorption behavior.

Supporting Information available. Crystallographic data and details about the refinements, Le Bail-fits, results of the thermogravimetric measurements, XRPD-data for the stability tests, temperature dependent IR-spectra and Raman-spectra under ambient conditions, NMR-spectra, the description of the HT-experiments, SEM-images, additional SHG-data and the theoretical treatment of the SHG results. This material is available free of charge via the Internet at <http://pubs.acs.org>.

AUTHOR INFORMATION

Corresponding Author

* Norbert Stock, Institut für Anorganische Chemie, Christian-Albrechts-Universität zu Kiel, Max-Eyth-Straße 2, D-24118 Kiel, Germany; stock@ac.uni-kiel.de

Funding Sources

This work has been supported by the DFG (SPP 1362). The research leading to these results has received funding from the European Community's Seventh Framework Programme (FP7/2007-2013) under grant agreement no 228862. The IR studies (BG and BM) were carried out with the equipment purchased thanks to the financial support of the European Regional Development Fund in the framework of the Polish Innovation Economy Operational Program (contract no. POIG.02.01.00-12-023/08). MAVdV thanks the FWO Vlaanderen for a postdoctoral fellowship. TV and MAVdV acknowledge financial support from the KU Leuven (GOA).

ACKNOWLEDGMENT

The help of Christin Szillus and Lorenz Kienle (CAU Kiel) recording the SEM-micrographs is gratefully acknowledged. We thank master student Ward Ceunen for performing part of the SHG-measurements under the guidance of MAVdV.

REFERENCES

- Morris, R. E.; Wheatley, P. E., *Angew. Chem. Int. Ed.* **2008**, *47*, 4966-4981.
- Li, J. R.; Kuppler, R. J.; Zhou, H. C.; *Chem. Soc. Rev.* **2009**, *38*, 1477-1504.
- Kreno, L. E.; Leong, K.; Farha, O. K.; Allendorf, M.; Van Duyne, R. P.; Hupp, J. T.; *Chem. Rev.* **2012**, *112*, 1105-1125.
- Horcajada, P.; Gref, R.; Baati, T.; Allan, P. K.; Maurin, G.; Couvreur, P.; Férey, G.; Morris, R. E.; Serre, C.; *Chem. Rev.* **2012**, *112*, 1232-1268.
- O'Keeffe, M.; *Chem. Soc. Rev.* **2009**, *38*, 1215-1217.
- Cavka, J. H.; Jakobsen, S.; Olsbye, U.; Guillou, N.; Lamberti, C.; Bordiga, S.; Lillerud, K. P.; *J. Am. Chem. Soc.* **2008**, *130*, 13850-13851.
- Schaate, A.; Roy, P.; Godt, A.; Lippke, J.; Waltz, F.; Wiebcke, M.; Behrens, P.; *Chem. Eur. J.* **2011**, *17*, 6643-6651.
- Loiseau, T.; Serre, C.; Huguenard, C.; Fink, G.; Taulelle, F.; Henry, M.; Bataille, T.; Férey, G.; *Chem. Eur. J.* **2004**, *10*, 1373-1382.
- Gaab, M.; Trukhan, N.; Maurer, S.; Gummaraju, R.; Müller, U.; *Micropor. Mesopor. Mater.* **2012**, *157*, 131-136.
- Senkovska, I.; Hoffmann, F.; Fröba, M.; Getzschmann, J.; Böhlmann, W.; Kaskel, S.; *Micropor. Mesopor. Mater.*, **2009** *122*, 93-98.
- Devic, T.; Horcajada, P.; Serre, C.; Salles, F.; Maurin, G.; Moulin, B.; Heurtaux, D.; Clet, G.; Vimont, A.; Greneche, J.-M.; Le Ouay, B.; Moreau, F.; Magnier, E.; Filinchuk, Y.; Marrot, J.; Lavalley, J.-C.; Daturi, M.; Férey, G.; *J. Am. Chem. Soc.*, **2010**, *132*, 1127-1136.
- Biswas, S.; Ahnfeldt, T.; Stock, N.; *Inorg. Chem.* **2011**, *50*, 9518-9526.
- Mowat, J. P. S.; Miller, S. R.; Slawin, A. M. Z.; Seymour, V. R.; Ashbrook, S. E.; Wright, P. A.; *Micropor. Mesopor. Mater.* **2011**, *142*, 322-333.
- Whitfield, T. R.; Wang, X.; Liu, L.; Jacobson, A. J.; *Solid State Sci.* **2005**, *7*, 1096-1103.
- Serre, C.; Millange, F.; Thouvenot, C.; Noguès, M.; Marsolier, G.; Louër, D.; Férey, G.; *J. Am. Chem. Soc.* **2002**, *124*, 13519-13526.
- Anokhina, E. V.; Vougo-Zanda, M.; Wang, X.; Jacobson, A. J.; *J. Am. Chem. Soc.* **2005**, *127*, 15000-15001.
- Volklinger, C.; Loiseau, T.; Guillou, N.; Férey, G.; Elkaïm, E.; Vimont, A.; *Dalton Trans.* **2009**, *12*, 2241-2249.
- Cychosz, K. A.; Matzger, A. J.; *Langmuir* **2010**, *26*, 17198-17202.
- Bernt, S.; Guillermin, V.; Serre, C.; Stock, N.; *Chem. Commun.* **2011**, *47*, 2838-2840.
- Stock, N.; *Micropor. Mesopor. Mater.* **2010**, *129*, 287-295.
- Stock, N.; Biswas, S.; *Chem. Rev.* **2012**, *112*, 933-969.
- Biemmi, E.; Christian, S.; Stock, N.; Bein, T.; *Micropor. Mesopor. Mater.* **2009**, *117*, 111-117.
- Hammersley, A. P.; Svensson, S. O.; Hanfland, M.; Fitch, A. N.; Häusermann, D.; *High Pressure Research* **1996**, *14*, 235-248.
- Ahnfeldt, T.; Guillou, N.; Gunzelmann, D.; Margiolaki, I.; Loiseau, T.; Férey, G.; Senker, J.; Stock, N.; *Angew. Chem. Int. Ed.* **2009**, *28*, 5163-5166.
- Altomare, A.; Camalli, M.; Cuocci, C.; Giacobozzo, C.; Moliterni, A.; Rizzi, R.; *J. Appl. Cryst.* **2009**, *42*, 1197-1202.
- Topas Academics 4.2, Coelho Software, **2007**.
- Materials Studio Version 5.0, Accelrys Inc., San Diego, CA, **2009**.
- Reinsch, H.; Feyand, M.; Ahnfeldt, T.; Stock, N.; *Dalton Trans.* **2012**, *41*, 4164-4171.
- Kim, H.; Lim, T.K.; Shin, S.T.; Lee, C.K.; Araoka, F.; Ofuji, M.; Takanishi, Y.; Takezoe, H., *Phys. Rev. E* **2004**, *69*, 061701.
- Kaneshiro, J.; Kawado, S.; Yokota, H.; Uesu, Y.; Fukui, T., *J. Appl. Phys.* **2008**, *104*, 054112.
- van der Veen, M.A.; Sels, B.F.; De Vos, D.E.; Verbiest, T., *J. Am. Chem. Soc.* **2010**, *132*, 6630-6631.
- van der Veen, M.A.; Van Noyen, J.; Sels, B.F.; Jacobs, P.A.; Verbiest, T.; De Vos, D.E., *Phys. Chem. Chem. Phys.* **2010**, *12*, 10688-10692.

- ³³ De Sa Peixoto, P.; Deniset-Besseau, A.; Schanne-Kleinb, M.C.; Mosser G., *Soft Matter* **2011**, *7*, 11203-11210.
- ³⁴ van der Veen, M.A. Vermoortele, F., De Vos, D.E., Verbiest, T., *Anal. Chem.*, 2012, DOI: 10.1021/ac300936q
- ³⁵ van der Veen, M.A. Vermoortele, F., De Vos, D.E., Verbiest, T., *Anal. Chem.*, 2012, DOI: 10.1021/ac3011318
- ³⁶ Vancleuvenbergen, S.; Hennrich, G.; Willot, P.; Koeckelberghs, G.; Clays, K.; Verbiest, T., van der Veen, M.A., *J. Phys. Chem. C* **2012**, *116*, 12219-12225.
- ³⁷ Serra-Crespo, P.; van der Veen, M.A.; Gobechiya, E.; Houthoofd, K.; Filinchuk, Y.; Kirschhock, C.E.A.; Martens, J.A.; Sels, B.F.; De Vos, D.E.; Kapteijn, F.; Gascon, J., *J. Am. Chem. Soc.* **2012**, *134*, 8314-8317.
- ³⁸ Volkringer, C.; Loiseau, T.; Haouas, M.; Taulelle, F.; Popov, D.; Burghammer, M.; Riekel, C.; Zlotea, C.; Cuevas, F.; Latroche, M.; Phanon, D.; Knöfelv, C.; Llewellyn, P. L.; Férey, G.; *Chem. Mater.* **2009**, *21*, 5783-5791.
- ³⁹ Ibarra, I. A.; Yang, S.; Lin, X.; Blake, A. J.; Rizkallah, P. J.; Nowell, H.; Allan, D. R.; Champness, N. R.; Hubberstey, P.; Schröder, M.; *Chem. Commun.* **2011**, *47*, 8304-8306.
- ⁴⁰ Reinsch, H.; Krüger, M.; Wack, J.; Senker, J.; Salles, F.; Maurin, G.; Stock, N.; *Micropor. Mesopor. Mater.* **2012**, *157*, 50-55.
- ⁴¹ Lacroix, P.G.; *Eur. J. Inorg. Chem.* **2001**, 339-348.
- ⁴² Verbiest, T., Houbrechts, S., Kauranen, M., Clays, K., Persoons, A.; *J. Mater. Chem.* **1997**, *7*, 2175.
- ⁴³ van der Veen, M.A.; Verbiest, T.; De Vos D.E., *Micropor. Mesopor. Mater.* **2012**, DOI: 10.1016/j.micromeso.2012.04.051.
- ⁴⁴ Evans, O.R., Lin, W.; *Chem. Rev.* **2012**, *112*, 1084-1104.
-

4.5.2 Mixed-linker MOFs with CAU-10-structure: synthesis and gas sorption characteristics

Das vorliegende Manuskript wurde im Oktober 2012 im Journal "Dalton Transactions" eingereicht.

Ausgehend von der Struktur der Serie von CAU-10-MOFs wurde die Möglichkeit untersucht, die Eigenschaften der Verbindungen durch die Verwendung von Mischungen verschiedener Isophthalsäurederivate zu modulieren. Dazu wurden die auf 5-Bromisophthalsäure basierende Verbindung CAU-10-Br sowie die auf Isophthalsäure und 5-Bromisophthalsäure basierende Verbindung CAU-10-H/Br synthetisiert. Außerdem wurden eine Mischung von 5-Nitroisophthalsäure und 5-Aminoisophthalsäure zur Synthese von CAU-10-NO₂/NH₂ und eine Mischung von Isophthalsäure und 5-Methylisophthalsäure zur Synthese von CAU-10-H/CH₃ eingesetzt. Die Charakterisierungsmethoden umfassten die Röntgenpulverbeugung, Elementaranalyse, IR-Spektroskopie, NMR-Spektroskopie, Vis-Spektroskopie, Rasterelektronenmikroskopie, Thermogravimetrie und Gassorption. Auch die Reproduzierbarkeit der Synthesen bezüglich der eingebauten Linkerverhältnisse und der daraus resultierenden Sorptionseigenschaften wurde untersucht.

Die Struktur von CAU-10-Br konnte mittels Rietveldverfeinerung bestätigt werden. CAU-10-H/Br zeigte im Vergleich zu CAU-10-H eine verminderte Kapazität für die Adsorption von N₂, H₂ und CO₂. Alle analytischen Ergebnisse weisen darauf hin, dass Bromisophthalsäure homogen im Netzwerk verteilt vorliegt. Die Reproduzierbarkeit der Synthese konnte ebenfalls nachgewiesen werden. Für CAU-10-H/CH₃ konnte zwar ein erfolgreicher Einbau von Methylisophthalsäure in das Netzwerk nachgewiesen werden, ebenso wurde eine Abnahme der Sorptionskapazität beobachtet. Allerdings variierten die Eigenschaften sowie die Zusammensetzung teilweise drastisch. Für CAU-10-NO₂/NH₂ konnte ebenfalls bewiesen werden, dass beide Linkermoleküle in das Produkt eingebaut werden und die Sorptionseigenschaften weisen einen hohen Grad an Reproduzierbarkeit auf. Zusätzlich konnte über die optischen Eigenschaften der Verbindung gezeigt werden, dass sich die Linkermoleküle bevorzugt komplementär paarweise anordnen. Die Verbindung zeigte außerdem erhöhte Kapazitäten für H₂ und CO₂ im Vergleich zu CAU-10-NO₂ und CAU-10-NH₂, was auf eine zusätzliche Polarisation der

Porenoberfläche durch den komplementären Einbau der Linkermoleküle hindeuten könnte.

Cite this: DOI: 10.1039/c0xx00000x

www.rsc.org/xxxxxx

ARTICLE TYPE

Mixed-linker MOFs with CAU-10 structure: synthesis and gas sorption characteristics

Helge Reinsch,^a Steve Waitschat^a and Norbert Stock^a

Received (in XXX, XXX) Xth XXXXXXXXX 20XX, Accepted Xth XXXXXXXXX 20XX

DOI: 10.1039/b000000x

The metal-organic framework compound [Al(OH)(BDC-Br)] (**1**) (BDC-Br²⁻ = 5-bromo-1,3-benzenedicarboxylate) denoted CAU-10-Br was synthesised under solvothermal reaction conditions. Its structure was successfully refined by Rietveld methods. The framework is based on the connection of infinite helical chains of *cis*-connected AlO₆-polyhedra via BDC-Br²⁻ ions. Thus non-intersecting parallel channels are formed each periodically varying in diameter between 1.1 and 6.6 Å. Nevertheless **1** adsorbs CO₂ at 298 K, while it's non-porous towards H₂ and N₂ at 77 K. Employing high-throughput (HT) methods we identified synthesis conditions that lead to the formation of mixed-linker MOFs with CAU-10 topology. Starting with a molar ratio H₂BDC : H₂BDC-Br = 3 : 1 we established a synthesis procedure for the partially bromo-functionalised mixed-linker-MOF [Al(OH)(BDC)_{0.8}(BDC-Br)_{0.2}] (**2**) denoted as CAU-10-H/Br. Starting with a molar ratio H₂BDC-NH₂ : H₂BDC-NO₂ = 1 : 1 the partially NO₂- and NH₂-functionalised mixed-linker MOF [Al(OH)(BDC-NO₂)_{0.55}(BDC-NH₂)_{0.23}(BDC-NHCHO)_{0.22}] (**3**) denoted as CAU-10-NO₂/NH₂ was synthesised, in which the NH₂-groups were found to be partially formylated. In **2**, the BDC-Br²⁻ ions are statistically incorporated in the framework while in **3** the different linker molecules are arranged preferentially pair-wise. The partial bromo-functionalisation in CAU-10-H/Br (**2**) leads to a lower sorption capacity in comparison with the parent structure CAU-10-H, while the pore accessibility is comparable. The incorporation of NO₂-, NH₂- and NHCHO-groups in CAU-10-NO₂/NH₂ (**3**) does not only affect the accessibility of the pores for N₂, but results also in an increased capacity for H₂ and CO₂ in comparison with the parent structure CAU-10-NO₂. The reproducibility of the synthesis procedures was tested regarding the composition of the MOFs and the resulting gas sorption properties. In **2** a molar fraction of (BDC)²⁻ = 80±2% is found, while in **3** a molar fraction of (BDC-NO₂)²⁻ = 55±2% is observed. Starting from the molar ratio H₂BDC : H₂BDC-CH₃ = 1 : 1 mixed linker MOFs denoted as CAU-10-H/CH₃ (**4**) were also obtained. In contrast to **2** and **3** the molar ratios of BDC²⁻ / BDC-CH₃²⁻ as well as the sorption properties differ substantially for every batch. The compounds were further characterised by X-ray powder diffraction, thermogravimetric / elemental analysis, NMR / Vis / IR-spectroscopy, and gas sorption measurements.

Introduction

Metal-organic frameworks (MOFs) are porous materials which have been intensively studied¹ due to their potential for several applications like gas storage,² separation of gases³ or liquids,⁴ catalytic processes⁵ or in sensor devices.⁶ The main advantage of these compounds is their modular construction principle. MOFs are built up by the connection of defined inorganic units - mostly metal ions or metal-oxo clusters - and organic building units, most often polytopic carboxylate ions. Replacement of the building units by geometrically similar ones, e. g. replacement of 1,4-benzenedicarboxylate in the framework of Cr-MIL-101⁷ (MIL stands for Matériaux de l'Institut Lavoisier) by 2,6-naphthalenedicarboxylate⁸ or 2-nitro-1,4-

benzenedicarboxylate⁹ allows the synthesis of an extended or the respective nitro-functionalised framework structure. This approach is called isorecticular synthesis and has attracted considerable interest, but only few framework structures are known, in which this principle was successfully applied.^{10,11,12,13} Recently it was demonstrated that the use of mixtures of differently functionalised linker molecules with identical denticity can enhance the sorption properties.¹⁴ This approach is known as Mix-MOF concept or solid solution approach.¹⁵ It was also shown that the stability of the resulting compounds,^{16,17} the affinity towards gases¹⁸ or the selectivity towards mixtures of gases can be altered.¹⁹ Often the improved performance is attributed to a specific arrangement of the linker molecules, but experimental evidence for such ordering is not always

given.

Aluminium-based MOFs have shown to be of interest for industrial applications since they are non-toxic, chemically and thermally stable and inexpensive.²⁰ Moreover, the isoreticular synthesis approach was successfully applied for at least two series of Al-based MOFs (Al-MIL-53²¹ and CAU-3²²). In the case of the flexible framework of Al-MIL-53 it was further shown that the use of mixtures of linker molecules leads to modulated “breathing” properties, i. e. the flexibility of the framework is tuned, depending on the molar ratio of different linker molecules.²³

We have recently reported a series of functionalised aluminium MOFs denoted as CAU-10 (CAU stands for Christian-Albrechts-Universität).²⁴ All members of this series are based on isophthalate ions (BDCX²⁻) that bear functional groups in 5-position (X = -H, -CH₃, -OCH₃, -NO₂, -NH₂ or -OH). Depending on the functional group, the crystal structures are slightly altered and the capacities, affinities and accessibilities of the pores for various gases are changed.

In this study we used the framework structure of CAU-10 as a platform for the synthesis of MOFs based on mixtures of linker molecules. As a reference, the bromo-functionalised member of the CAU-10-series was first synthesised and characterised in detail. Subsequently a mixed linker MOF was synthesised starting from H₂BDC and H₂BDC-Br. Moreover, a mixture of H₂BDC and H₂BDC-CH₃ as well as H₂BDC-NO₂ and H₂BDC-NH₂ was employed to synthesise MOFs with CAU-10-topology. These MOFs were thoroughly characterised by X-ray powder diffraction (XRPD), IR- / NMR- / Vis-spectroscopy, CHNS-analysis, sorption measurements and scanning electron microscopy.

Experimental

Materials. All used chemicals are commercially available and were used without further purification.

Methods. The synthesis was carried out in 100 mL Duran glass reactors with screw cap. X-ray powder diffraction (XRPD) data for the refinement of CAU-10-Br (1) and for CAU-10-H/Br (2) was measured on a Bruker PANalytical Empyrean diffractometer (CuK_α-radiation) in transmission geometry. Therefore the samples were loaded into capillaries (Ø = 0.5 mm). The data for CAU-10-NO₂/NH₂ (3), CAU-10-H (5), CAU-10-NO₂ (6) and CAU-10-NH₂ (7) was measured on a STOE Stadi-P powder diffractometer equipped with a linear position sensitive detector system (Cu-K_{α1} radiation) in transmission geometry. The data for CAU-10-H/CH₃ (4) and CAU-10-CH₃ (8) was recorded on a Stadi P Combi diffractometer with CuK_{α1}-radiation equipped with an image-plate detector system and a xy-stage. Crystallographic analysis was carried out with TOPAS.²⁵ Elemental analyses were obtained using an Eurovektor EuroEA Elemental Analyzer. EDX-spectra were measured with a Philips ESEM XL 30. SEM-micrographs were recorded with a Zeiss Gemini Ultra Plus microscope. IR-spectra were measured on a Bruker ALPHA-FT-IR A220/D-01 spectrometer equipped with an ATR-unit. UV/Vis-spectra were recorded on a Varian Cary 5000. The thermogravimetric analyses were recorded using an NETSCH STA 409 CD analyzer. The samples were

heated in Al₂O₃ crucibles at a rate of 4 K min⁻¹ under a flow of air (25 ml min⁻¹). The TG data were corrected for buoyancy and current effects. Solid-state CP-MAS-NMR spectra were measured on a Bruker DSX Avance 400 FT NMR spectrometer in 7 mm ZrO₂-rotors at a rotation frequency of 5 kHz with glycine as the reference. NMR spectra in solution were measured on a Bruker DRX 500 after dissolution of the compounds in 5% NaOD/D₂O. Sorption experiments were performed using a BEL JAPAN INC. Belsorp_{max}.

Synthesis. CAU-10-Br (1) was synthesised by heating a mixture of 1680 mg 5-bromoisophthalic acid (H₂BDC-Br, 6.85 mmol), 6.88 mL of a 0.5 M solution of Al₂(SO₄)₃·18H₂O (6.88 mmol Al³⁺), 9.12 mL H₂O and 4 mL N,N-dimethylformamide (DMF) to 120 °C for 12 h. The product was recovered by filtration and redispersed in water by sonication for 30 minutes. The product was filtered off and the obtained white powder was dried at 200 °C for 1 h. CHNS-analysis: C 35.1 %, H 2.1 %, N 1.6 %. Calculated values based on the formula: [Al(OH)(BDC-Br)]·0.5DMF: C 35.3 %, H 2.2 %, N 2.2 %. To establish the synthesis procedures of the mixed-linker MOFs, high-throughout (HT) -methods were employed.²⁶ Reactant compositions were identified which were suitable for a high degree of mixing (i. e. a molar ratio of linker molecules as close as possible to 1 : 1) while preserving a high degree of crystallinity. A set up of such a HT-experiment is described in the supplementary material (Tab. S3). The optimised reaction conditions were successfully scaled up to the g-scale as described below.

CAU-10-H/Br (2) was synthesised by heating a mixture of 600 mg isophthalic acid (H₂BDC, 3.6 mmol), 292 mg H₂BDC-Br (1.2 mmol), 2.4 mL of a 2 M solution of AlCl₃·6H₂O (4.8 mmol Al³⁺), 13.6 mL H₂O and 4 mL DMF to 120 °C for 12 h. The product was recovered by filtration and redispersed in water by sonication for 30 minutes. The mixture was filtered off and the obtained white powder was dried at 200 °C for 1 h. CHNS-analysis: C 40.0 %, H 2.4 %, N 0.2 %. Calculated values based on the formula [Al(OH)(BDC)_{0.8}(BDC-Br)_{0.2}]·0.92H₂O·0.035DMF: C 40.0 %, H 2.8 %, N 0.2 %. The molar ratio BDC²⁻ : BDC-Br²⁻ of 4:1 in the product was further confirmed by NMR-experiments (Fig. S1). It is noteworthy that the reaction mixture contains 25 % H₂BDC-Br, while the final product contains only 20 % BDC-Br²⁻.

CAU-10-NO₂/NH₂ (3) was synthesised by heating a mixture of 720 mg 5-nitroisophthalic acid (H₂BDC-NO₂, 3.4 mmol), 618 mg 5-aminoisophthalic acid (H₂BDC-NH₂, 3.4 mmol), 3.4 mL of a 2 M solution of AlCl₃·6H₂O (6.8 mmol Al³⁺), 12.6 mL H₂O and 4 mL DMF to 120 °C for 12 h. The product was recovered by filtration and redispersed in water by sonication for 30 minutes. The mixture was filtered off and the obtained yellow powder was dried at 200 °C for 1 h. CHNS-analysis: C 39.2 %, H 2.8 %, N 6.2 %. Calculated values based on the formula: [Al(OH)(BDC-NO₂)_{0.55}(BDC-NH₂)_{0.23}(BDCNHCHO)_{0.22}]: C 40.0 %, H 2.0 %, N 5.7 %. The molar ratio of linker molecules and the degree of formylation of the NH₂-group were confirmed by NMR-spectroscopy (Fig. S2, S8). It is noteworthy that the reaction mixture contains both linker molecules in equal molar amounts, while the product contains an excess of BDC-NO₂²⁻ (55 %).

CAU-10-H/CH₃ (**4**) was synthesised by heating a mixture of 400 mg H₂BDC (2.4 mmol), 436 mg 5-methylisophthalic acid (H₂BDC-CH₃, 2.4 mmol), 2.4 mL of a 2 M solution of AlCl₃·6H₂O (4.8 mmol Al³⁺), 13.6 mL H₂O and 4 mL DMF to 125 °C for 12 h. The product was recovered by filtration and redispersed in water by sonication for 30 minutes. The mixture was filtered off and the obtained pale yellow powder was dried at 200 °C for 1 h. According to the characterisation, the fraction of BDC-CH₃²⁻ varies from ~ 21-25%. Typical values for the CHNS-analysis: C 44.6-46.7 %, H 2.6-3.2 %, N 0.2-0.5 %. For the common formula [Al(OH)(BDC)_{1-n}(BDC-CH₃)_n·solvent this corresponds to a maximum molar fraction of BDC-CH₃²⁻ of 25 %.

The other CAU-10 compounds that were employed for comparison with the mixed-linker MOFs (CAU-10-H (**5**), -NO₂ (**6**), -NH₂ (**7**) and -CH₃ (**8**)) were synthesised according to the recently reported procedures.²⁴ SEM-micrographs of **1**, **2** and **3** are shown in the supporting information (Fig. S11-S13). The absence of chloride or sulphate ions in the products after extensive washing was proven by CHNS-analysis and EDX-measurements.

Results and Discussion

XRPD and Crystal Structure

The XRPD pattern of CAU-10-Br (**1**) (Fig. 1) was successfully indexed in a tetragonal unit cell with extinction conditions that correspond to the space group *I4₁/amd*. Therefore, the crystal structure of the isotypic compound CAU-10-CH₃²⁴ was used as a starting model for the Rietveld refinement. The methyl-carbon atoms were replaced by bromine atoms and the structural model could be subsequently refined to satisfying figures of merit restraining five C-C-, two C-O- and one Al-O-distance. The final Rietveld plot is shown in Figure 1.

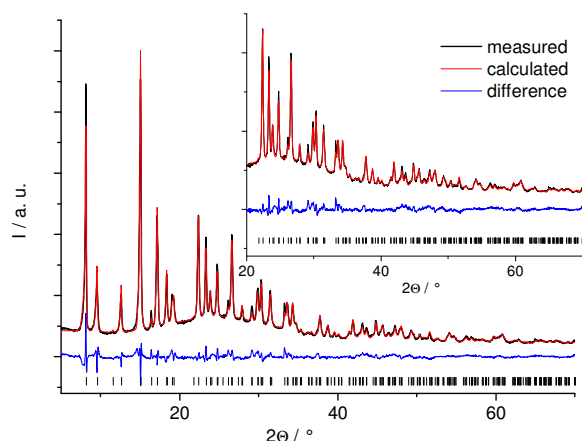


Fig. 1 The Rietveld plot of the structure refinement of CAU-10-Br (**1**). The black line is the experimental data, the red line represents the fit and the blue line the difference curve. Vertical bars mark the Bragg reflection positions.

The final parameters of this refinement are summarised in Tab. 1. Characteristic bond lengths and the asymmetric unit can be found in the supporting information (Fig. S4, Tab. S1).

Table 1 Final parameters for the Rietveld refinement of CAU-10-Br (**1**).

formula	AlO ₃ C ₈ H ₃ Br
M / g/mol	283
crystal system	tetragonal
space group	<i>I4₁/amd</i>
<i>a</i> / Å	21.5064(14)
<i>c</i> / Å	10.1648(12)
V/10 ⁶ Å ³	4701.5(8)
R _{wp} / %	5.74
R _{Exp} / %	1.97
R _{Bragg} / %	2.03
GoF	2.92
independent atoms	10
restraints	9

The structure is based on the interconnection of helical chains of *cis*-connected AlO₆-polyhedra by BDC-Br²⁻ ions (Fig. 2). This interconnection leads to pairs of BDC-Br²⁻ ions with a distance of 3.2 Å between the linker molecules (Fig. 3, top). Thus a framework with square-shaped channels is obtained.²⁴

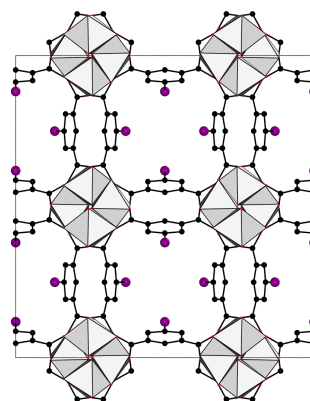


Fig. 2 Structure of CAU-10-Br (**1**) as seen along the *c*-axis.

The minimum diameter of these channels is only 1.1 Å, based on the van-der-Waals radii of the atoms, while the maximum diameter is 6.6 Å (Fig. 3, bottom).

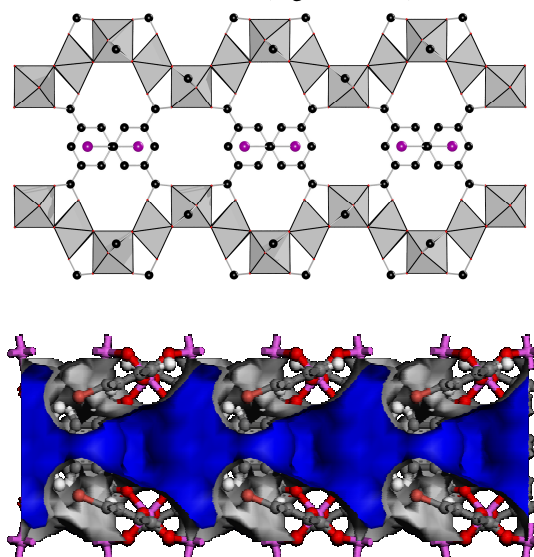


Fig. 3 Top: The connection of two helices by BDC-Br²⁻ ions as seen along [010] showing the pairs of linker molecules. Bottom: Representation of a channel in CAU-10-Br (**1**), as seen along [010]. Aluminium in pink, carbon in grey, oxygen in red and hydrogen in white. The accessible solvent surface is shown in blue.

According to the XRPD-pattern of CAU-10-H/Br (**2**) (Fig. 4), the product is not a mixture of CAU-10-H (**5**) and CAU-10-Br (**1**). The relative intensities of the Bragg reflections and fractions of linker molecules incorporated in the product (80 % BDC²⁻), indicate that **2** is a BDC-Br²⁻ doped derivative of CAU-10-H (**5**) (Fig. 4). The rather broad peaks observed in **2** could be due to the disorder of Br-groups in the framework.

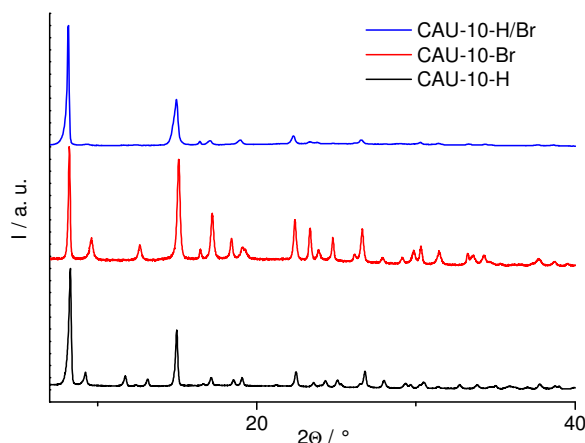


Fig. 4 The XRPD-patterns for CAU-10-Br (**1**) in red, CAU-10-H/Br (**2**) in blue and CAU-10-H (**5**) in black.

The Le Bail fit for CAU-10-H/Br (**2**) (Fig. S5) in the space group $I4_1$ confirms its phase purity. The refined cell parameters ($a = b = 21.485(5)$ Å, $c = 10.407(3)$ Å) are closer to the ones reported for CAU-10-H (**5**) ($a = b = 21.55(7)$ Å, $c = 10.38(3)$ Å) than to the cell parameters of **1** (Table 1). Although the differences between the different MOFs seem to be small, they can have a strong influence on the properties, as reported for the CAU-10-series.²⁴ The structural relationship of **2** and **5** indicates that the pore openings and therefore also the accessibility for guest molecules should be similar.

The major amount of incorporated linker molecules in CAU-10-NO₂/NH₂ (**3**) consists of BDC-NO₂²⁻ ions. Thus it is reasonable to assume that the structure is a derivative of CAU-10-NO₂ (**6**) doped with BDC-NH₂²⁻ ions. CAU-10-NO₂ (**6**) crystallises in the space group $P4_1$. The Le Bail fit of **3** in this space group (Fig. 5, $R_{WP} = 4.1$ %) confirms its phase purity and resulted in the cell parameters $a = b = 21.4924(6)$ and $c = 10.5260(6)$ Å.

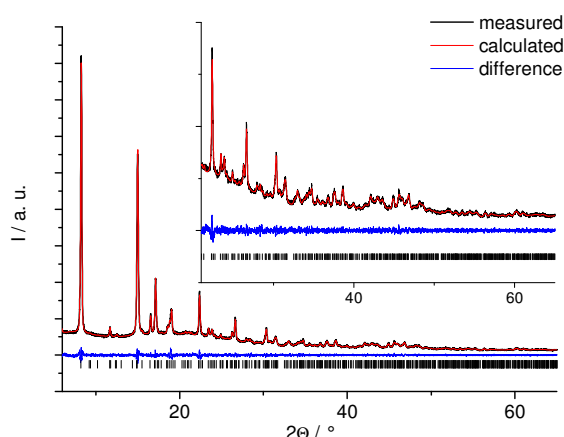


Fig.5 Le Bail fit for the lattice parameter determination of CAU-10-NO₂/NH₂ (**3**). The black line represents the experimental data, the red line is the calculated fit and the blue line the difference curve. Vertical bars mark the Bragg reflection positions.

The observed unit cell dimensions for **3** are closer to the parameters reported for CAU-10-NO₂ (**6**) ($a = b = 21.4707(3)$ Å, $c = 10.3777(2)$ Å, space group $P4_1$) than to the cell parameters of CAU-10-NH₂ (**7**) ($a = b = 21.4567(4)$ Å, $c = 10.8452(3)$ Å, space group $P\bar{4}n2$). The quality of the Le Bail fit and the shifted cell parameters demonstrate, that **3** is a mixed-linker MOF and not a mixture between the CAU-10-NO₂ (**6**) and CAU-10-NH₂ (**7**).

For CAU-10-H/CH₃ (**4**) large differences in the composition of the products - obtained under identical reaction conditions - were observed. The XRPD-pattern shows that **4** exhibit unambiguously the CAU-10 framework structure (Fig. S6).

Spectroscopic Characterisation

The pair-wise arrangement of BDC-NO₂²⁻ and BDC-NH₂²⁻ / BDC-NHCHO²⁻ in **3** can be evidenced by Vis-spectroscopy and the yellow colour of the compound. In CAU-10-NO₂ (**6**), every aromatic ring is neighboured to a chemically identical nitroisophthalate moiety. In CAU-10-NH₂ (**7**) every aromatic ring is neighboured to an NH₂- or NHCHO-functionalised aromatic moiety. This results in a white colour for **6** and a pale pink colour for **7**. The mixing of linker molecules in **3** results in the formation of a yellow solid. Thus, the different environments of the linker molecules induce an absorption behaviour that is substantially changed in comparison with the parent compounds (Fig. 6).

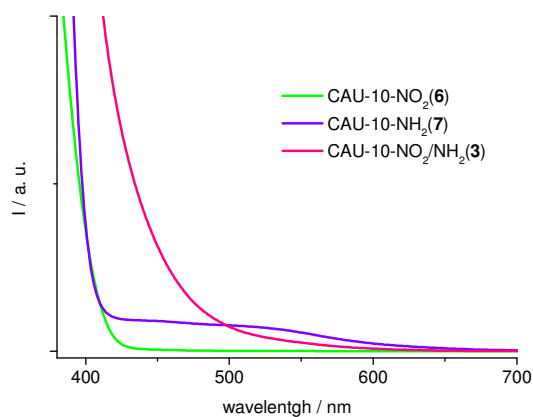


Fig. 6 Vis-spectra of CAU-10-NO₂/NH₂ (**3**) in pink, CAU-10-NO₂ (**6**) in green and CAU-10-NH₂ (**7**) in purple.

This can be explained by interactions between the aromatic moieties or between the aromatic moieties and the respective functional groups,²⁷ which can affect the electronic transitions in aromatic systems.²⁸ The distances between the aromatic rings in the frameworks in the CAU-10-series are ≤ 3.4 Å (Fig. 7).²⁴ Thus in **3**, the interaction between BDC-NO₂²⁻ ions and BDC-NH₂²⁻ / BDC-NHCHO²⁻ ions apparently induces energetic changes in the π -electron systems, which results in the yellow colour. However, since the majority of linker molecules in **3** are BDC-NO₂²⁻ ions, this pairing is not possible throughout the whole framework. Thus the structure must be still considered as a massively BDC-NH₂²⁻-doped derivative of CAU-10-NO₂ (**6**).

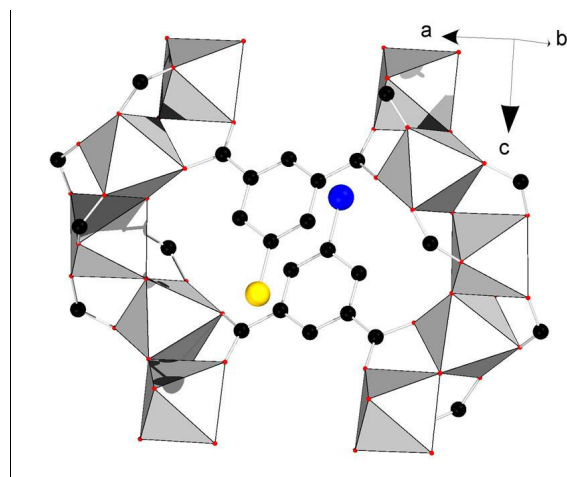


Fig. 7 A part of the structure of CAU-10-X, showing the proximity of the aromatic moieties. AlO₆-polyhedra are represented in grey, oxygen atoms in red, carbon atoms in black and the functional groups are displayed in blue and yellow, respectively.

The solid-state ¹³C-CP-MAS-NMR spectra (Fig. S7, Tab. S2) clearly prove that the respective linker molecules are incorporated into the frameworks of **2** and **3**. Moreover, the partial formylation of NH₂-groups that was observed for CAU-10-NH₂ (**7**)²⁴ is found as well in CAU-10-NO₂/NH₂ (**3**). The statistical incorporation of linker molecules in **2** and the pair-wise arrangement in **3** do not have a strong influence on the chemical shifts of the ¹³C signals.

The IR-spectra further confirm the incorporation of both kinds of linker molecules into the frameworks of the mixed-

linker MOFs **2**, **3** and **4**. As an example the spectra of CAU-10-Br (**1**), CAU-10-H/Br (**2**) and CAU-10-H (**5**), are shown in Fig. 8. It can be clearly observed, that the spectrum of the mixed-linker MOF **2** can be obtained by a summation of the spectra of **1** and **5** (Fig. 8).

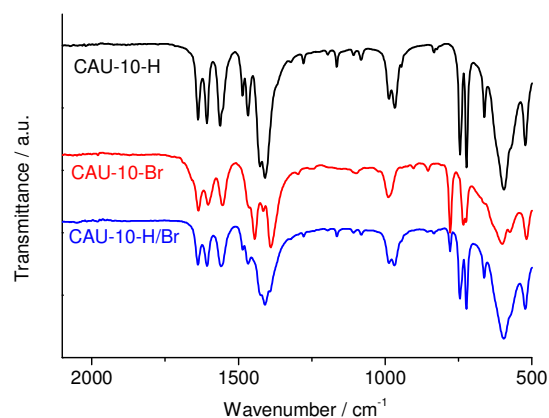


Fig. 8 IR-spectra of **1**, **2** and **5** in the region between 2100 and 500 cm⁻¹.

Especially the bands of the C-H-out-of-plane vibrations of the aromatic ring confirm the existence of both molecules in the framework. For the 1,3-substituted linker molecule in **5**, these bands are observed at 722 and 744 cm⁻¹, while the 1,3,5-substitution in **1** leads to the bands at 779 and 736 cm⁻¹.²⁹ In the spectrum of **2**, a combination of these absorption bands is observed. The full spectra for **1**, **2** and **5** as well as the IR-spectra for the other described MOFs can be found in the supporting information (Fig. S8-S10) and confirm this observation for the other MOFs based on mixtures of linker molecules.

Thermal Stability

According to the thermogravimetric experiment, CAU-10-Br (**1**) decomposes above 400 °C in air (Fig. 9).

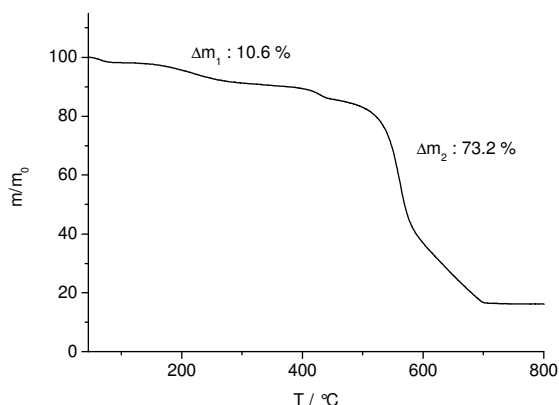


Fig. 9 TG-curve for CAU-10-Br (**1**). The measurement was carried out with a heating rate of 4 K/min under air.

The first small two steps up to 350 °C (mass loss of 10.6 %) correspond to the removal of occluded guest molecules (H₂O, DMF) from the pores. The small third and the large fourth step (mass loss of 73.2 %) above 400 °C correspond to the decomposition of the framework and are in good agreement with the expected value (75 %). This shows that the stability of **1** is comparable to the other members of the CAU-10-series.²⁴

Sorption Behavior

Prior to the sorption measurements, all samples were activated at 200 °C under vacuum (0.1 mbar) for 15-20 h. The shapes of the N₂ sorption isotherms measured at 77 K (Fig. 10) demonstrate, that CAU-10-H/Br (2) is microporous, since a type I isotherm is observed.

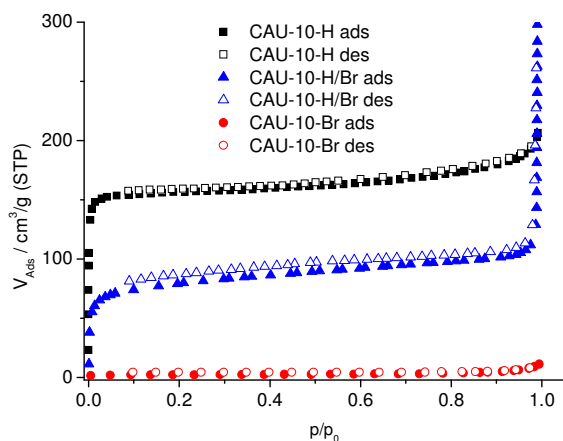


Fig.10 Nitrogen isotherms for CAU-10-Br (1), CAU-10-H/Br (2) and CAU-10-H (5), measured at 77 K.

CAU-10-Br (1) shows no uptake of nitrogen, which is in good agreement with the expected accessibility based on the crystal structure (the minimum diameter of the pores is only 1.1 Å). The observed surface areas and micropore volumes (calculated from the amount adsorbed at $p/p_0 = 0.5$) are $S_{\text{BET}} = 640 \text{ m}^2/\text{g}$ and $V_{\text{Mic}} = 0.25 \text{ cm}^3/\text{g}$ for CAU-10-H (5) and $S_{\text{BET}} = 305 \text{ m}^2/\text{g}$ and $0.14 \text{ cm}^3/\text{g}$ for CAU-10-H/Br (2). Thus the structural similarity of 2 and 5 does indeed result in a similar sorption behaviour towards nitrogen. This further confirms that the partially bromo-functionalised title compound 2 can be considered as a BDC-Br²⁻-doped version of CAU-10-H (5) with a similar accessibility for guest molecules but a lowered capacity.

This is further confirmed by the CO₂-adsorption isotherms measured at 298 K (Fig. 11). While CAU-10-Br (1) is non-porous towards nitrogen at 77 K, we observe an uptake of CO₂ at 298 K which is due to the higher intrinsic dynamics of the framework at elevated temperatures. For the unfunctionalised CAU-10-H (5) and the doped CAU-10-H/Br (2), the same tendencies as for the nitrogen sorption are observed regarding the capacities. The maximum uptakes of CO₂ at 298 K and 1 bar are 10.6 %, 3.6 % and 8.1 % for 5, 1 and 2, respectively.

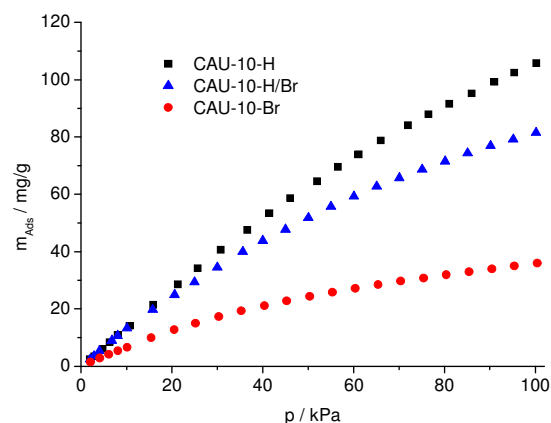


Fig.11 Adsorption isotherms of CO₂ for CAU-10-Br (1), CAU-10-H/Br (2) and CAU-10-H (5), measured at 298 K.

For CAU-10-NO₂/NH₂ (3), we observed a completely different trend, since the mixing of the linker molecules leads to an increase of adsorbed CO₂ in comparison with CAU-10-NO₂ (6) and CAU-10-NH₂ (7) (Fig. 12). The maximum amounts adsorbed at 298 K and 1 bar are 8.7, 8.0 and 9.8 % for 6, 7 and 3, respectively.

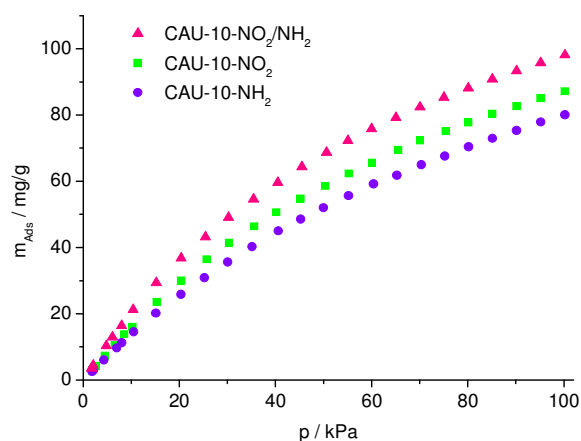


Fig.12 Adsorption isotherms of CO₂ for CAU-10-NO₂/NH₂ (3), CAU-10-NO₂ (6) and CAU-10-NH₂ (7), measured at 298 K.

The increase of capacity for CO₂ can be explained by the incorporation of the smaller NH₂-groups ($\varnothing \sim 4.5 \text{ Å}$) into the framework of 3, compared to the larger NO₂-groups ($\varnothing \sim 5.5 \text{ Å}$) in CAU-10-NO₂ (6), while the NHCHO-groups ($\varnothing \sim 5.5 \text{ Å}$) are comparable in size to the NO₂-groups. The diameter of the functional groups was calculated based on the van-der-Waals radii of the atoms, assuming a spherical shape for the functional group, thus representing a maximum size. Moreover the interactions between the linker molecules due to the pair-wise arrangement may have a polarizing effect on the pore surface,²⁸ which could increase the affinity towards CO₂.³⁰

In the N₂ sorption experiments (Fig. S14) we observed that the pores of 3 are accessible for nitrogen molecules, but the equilibration times are very long (a typical measurement for 3 takes ca. 10 times longer compared to an identical measurement of 5 or 6). Long measurement times are also necessary for the N₂ sorption of CAU-10-NH₂ (7) and we have observed that very often measurements are automatically aborted due to the exceeding of the maximum

measurement time (ca. 62 h). Moreover the ad- and desorption curves do not coincide, which would be expected for a microporous compound. This is most probably due to a hindered diffusion of gas molecules into and out of the pores. A similar sorption behaviour was already observed for CAU-10-OCH₃.²⁴

The hydrogen adsorption isotherms of the CAU-10 compounds **1-3** and **5-7** are shown in Figure 13.

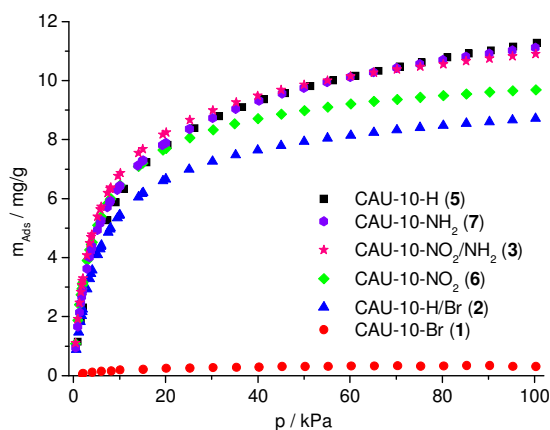


Fig.13 Hydrogen adsorption isotherms for **1** (red circles), **2** (blue triangles), **3** (pink stars), **5** (black squares), **6** (green diamonds) and **7** (purple hexagons) measured at 77 K

The influence of the bromo-group on the sorption properties of CAU-10-Br (**1**) and CAU-10-H/Br (**2**) as observed in the N₂ sorption measurements is confirmed. At 77 K, the pores in CAU-10-Br (**1**) are not accessible for hydrogen molecules, although the kinetic diameter of H₂ (2.6 Å) is much lower than the diameter of N₂ (3.6 Å) and CO₂ (3.3 Å). Thus at this low temperature, the intrinsic rigidity of the framework inhibits adsorption, while CO₂ molecules can enter the pores at 298 K. For the partially bromo-functionalised **2**, the statistical distribution of the Br-groups leads to a decrease in sorption capacity compared to CAU-10-H (**5**) (maximum amounts adsorbed at 1 bar: 1.13 % for **5** and 0.87 % for **2**).

The mixed linker compound CAU-10-NO₂/NH₂ (**3**) exhibits an interesting adsorption behaviour towards H₂. The sorption capacity is higher compared to CAU-10-NO₂ (**6**) but similar to CAU-10-NH₂ (**7**) with maximum amounts adsorbed of 1.09, 1.01 and 1.11 % for **3**, **6** and **7**, respectively, at 1 bar. The increase in capacity for **3** compared to **6** is in agreement with the observations in the CO₂ adsorption measurements and can be explained by the differences in the steric demand of NH₂- and NO₂-groups. At pressures below 40 kPa, the uptake of H₂ for CAU-10-NO₂/NH₂ (**3**) even exceeds the values measured for all other members of the CAU-10-series. This could be due to additional polarisation of the pore surface, resulting from the pair-wise arrangement of the linker molecules. However, this behaviour is not yet fully understood and subject of further investigations.

To evaluate the reproducibility of the synthesis procedures, we measured isotherms on products of different batch reactions. For different batches of CAU-10-H/Br (**2**) and CAU-10-NO₂/NH₂ (**3**) the respective isotherms are almost identical (Fig. S15 and S16). In contrast to these results, the CO₂ isotherms of different CAU-10-H/CH₃ (**4**) samples

vary from batch to batch (Fig. 14), although the synthesis conditions in each batch were identical. These differences could be explained by the variation of the composition, which is in agreement with the results of NMR-spectroscopy (Fig. S3).

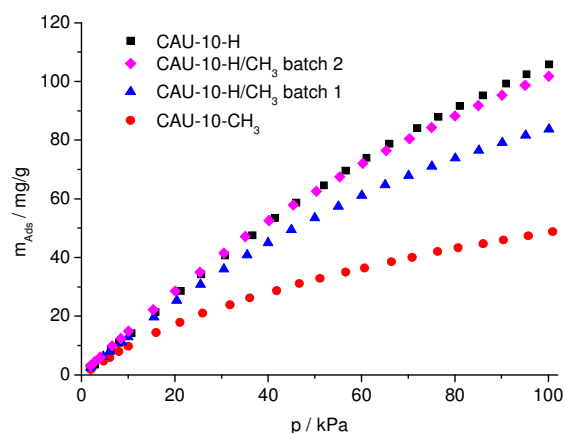


Fig.14 Adsorption isotherms of CO₂ for CAU-10-H (**5**), CAU-10-CH₃ (**8**) and two different samples of CAU-10-H/CH₃ (**4**) measured at 298 K.

Conclusions

The availability of mixed-linker CAU-10 compounds and their detailed characterization demonstrates that the capacity and the accessibility of the micropores for different gas molecules can be changed by this approach. Moreover, the detailed characterisation indicates that the synthesis procedures must be carefully evaluated regarding their reproducibility. To the best of our knowledge, the preferential pair-wise arrangement of the linker molecules as observed in CAU-10-NO₂/NH₂ has not yet been reported. This opens up the opportunity not only to modulate the sorption behaviour but also other properties, such as the optical properties as reported in this study.

Acknowledgement

The help of Dr. Alexandra Lieb (OvGU Magdeburg) for recording the XRPD data and Dr. Jan Krahmer (CAU Kiel) for recording the NMR-spectra is gratefully acknowledged. This work has been financially supported by the DFG (SPP 1362). The research leading to these results has received funding from the European Community's Seventh Framework Programme (FP7/2007-2013) under grant agreement n° 228862".

Notes and references

- ¹ N. Stock, S. Biswas, *Chem. Rev.*, 2012, **112**, 933.
 - ² M. P. Suh, H. J. Park, T. K. Prasad, D. Lim, *Chem. Rev.*, 2012, **112**, 782.
 - ³ J. Liu, P. K. Thallapally, B. P. McGrail, D. R. Brown, J. Liu, *Chem. Soc. Rev.*, 2012, **41**, 2308.
- ⁴ Institut für Anorganische Chemie, Christian-Albrechts-Universität Kiel, Max-Eyth-Straße 2, 24118 Kiel, Germany; stock@ac.uni-kiel.de
[†] Electronic Supplementary Information (ESI) available: NMR-spectra after dissolution, results of the Rietveld refinement, additional XRPD-data, solid-state-NMR-spectra, IR-spectra, SEM-micrographs, additional sorption isotherms. See DOI: 10.1039/b000000x/

- ⁴ F. Vermoortele, M. Maes, P. Modhadam, M. Lennox, F. Ragon, M. Boulhout, S. Biswas, K. Laurier, I. Beurroies, R. Denoyel, M. Roeffaers, N. Stock, T. Düren, C. Serre, D. De Vos, *J. Am. Chem. Soc.*, 2011, **133**, 18529.
- ⁵ A. Corma, H. García, F. X. Llabrés i Xamena, *Chem. Rev.*, 2010, **110**, 4606.
- ⁶ O. Shekhah, J. Liu, R. A. Fischer, C. Wöll, *Chem. Soc. Rev.*, 2011, **40**, 1081.
- ⁷ G. Férey, C. Mellot-Draznieks, C. Serre, F. Millange, J. Dutour, S. Surblé, I. Margiolaki, *Science*, 2005, **23**, 2040.
- ⁸ A. Sonnauer, F. Hoffmann, M. Fröba, L. Kienle, V. Duppel, M. Thommes, C. Serre, G. Férey, N. Stock, *Angew. Chem. Int. Edt.*, 2009, **48**, 3791.
- ⁹ S. Bernt, V. Guillermin, C. Serre, N. Stock, *Chem. Commun.* 2011, **47**, 2838.
- ¹⁰ J. H. Cavka, S. Jakobsen, U. Olsbye, N. Guillou, C. Lamberti, S. Bordiga, K. P. Lillerud, *J. Am. Chem. Soc.*, 2008, **130**, 13850; A. Schaate, P. Roy, A. Godt, J. Lippke, F. Waltz, M. Wiebcke, P. Behrens, *Chem. Eur. J.*, 2011, **17**, 6643; M. Kandiah, M. H. Nilsen, S. Usseglio, S. Jakobsen, U. Olsbye, M. Tilset, C. Larabi, E. A. Quadrelli, F. Bonino, K. P. Lillerud, *Chem. Mater.* 2010, **22**, 6632; G. Wißmann, A. Schaate, S. Lillenthal, I. Bremer, A. M. Schneider, P. Behrens, *Micropor. Mesopor. Mater.*, 2012, **152**, 64.
- ¹¹ C. Serre, F. Millange, S. Surblé, G. Férey, *Angew. Chem. Int. Edt.* 2004, **43**, 6285; P. Horcajada, F. Salles, S. Wuttke, T. Devic, D. Heurtaux, G. Maurin, A. Vimont, M. Daturi, O. David, E. Magnier, N. Stock, Y. Filinchuk, D. Popov, C. Riekel, G. Férey, C. Serre, *J. Am. Chem. Soc.* 2011, **133**, 17839.
- ¹² M. Eddaoudi, J. Kim, N. L. Rosi, D. T. Vodak, J. Wachter, M. O'Keeffe, O. M. Yaghi, *Science*, 2002, **295**, 469.
- ¹³ K. Barthelet, J. Marrot, D. Riou, G. Férey, *Angew. Chem. Int. Edt.* 2004, **41**, 281; Y. Liu, K. Leus, M. Grzywa, D. Weinberger, K. Strubbe, H. Vrielinck, R. Van Deun, D. Volkmer, V. Van Speybroeck, P. Van Der Voort, *Eur. J. Inorg. Chem.*, 2012, **16**, 2819; A. Centrone, T. Harada, S. Speakman, T. A. Hatton, *Small*, 2010, **15**, 1598.
- ¹⁴ H. Deng, C. J. Doonan, H. Furukawa, R. B. Ferreira, J. Towne, C. B. Knobler, B. Wang, O. M. Yaghi, *Science*, 2010, **327**, 846.
- ¹⁵ A. D. Burrows, *CrystEngComm.*, 2011, **13**, 3623.
- ¹⁶ S. Marx, W. Kleist, J. Huang, M. Maciejewski, A. Baiker, *Dalton Trans.*, 2010, **39**, 3795.
- ¹⁷ M. L. Foo, S. Horike, T. Fukushima, Y. Hijikata, Y. Kubota, M. Takata, S. Kitagawa, *Dalton Trans.*, 2012, DOI: 10.1039/c2dt31195j.
- ¹⁸ H. Chun, D. N. Dybtsev, H. Kim, K. Kim, *Chem.- Eur. J.*, 2005, **11**, 3521.
- ¹⁹ S. Horike, Y. Inubushi, T. Hori, T. Fukushima, S. Kitagawa, *Chem. Sci.*, 2012, **3**, 116.
- ²⁰ M. Gaab, N. Trukhan, S. Maurer, R. Gummaraju, U. Müller, *Micropor. Mesopor. Mater.*, 2012, **157**, 131.
- ²¹ T. Loiseau, C. Serre, C. Huguenard, G. Fink, F. Taulelle, M. Henry, T. Bataille, G. Férey, *Chem. Eur. J.*, 2004, **10**, 1373; I. Senkowska, F. Hoffmann, M. Fröba, J. Getzschmann, W. Böhlmann, S. Kaskel, *Micropor. Mesopor. Mater.*, 2009, **122**, 93; S. Biswas, T. Ahnfeldt, N. Stock, *Inorg. Chem.*, 2011, **50**, 9518.
- ²² H. Reinsch, M. Feyand, T. Ahnfeldt, N. Stock, *Dalton Trans.*, 2012, **41**, 4164.
- ²³ T. Lescouet, E. Kockrick, G. Bergeret, M. Pera-Titus, D. Farrusseng, *Dalton Trans.*, 2011, **40**, 11359.
- ²⁴ H. Reinsch, M. A. Van der Veen, B. Gil, B. Marszalek, T. Verbiest, D. De Vos, N. Stock, 2012, x, xyz.
- ²⁵ Topas Academics 4.2, Coelho Software, **2007**.
- ²⁶ N. Stock, *Micropor. Mesopor. Mater.*, 2010, **129**, 287.
- ²⁷ C. Janiak, *J. Chem. Soc., Dalton Trans.*, 2000, 3885.
- ²⁸ C. A. Hunter, K. R. Lawson, J. Perkins, C. J. Urch, *J. Chem. Soc., Perkin Trans. 2*, 2001, 651.
- ²⁹ G. Socrates, *Infrared and Raman Characteristic Group Frequencies: Tables and Charts*, 3rd ed.; Wiley & Sons: West Sussex, U.K., 2004.
- ³⁰ S. Barman, H. Furukawa, O. Blacque, K. Venkatesan, O. M. Yaghi, H. Berke, *Chem. Commun.*, 2010, **46**, 7981.

4.5.3 The first keto-functionalized microporous Al-based metal-organic framework: [Al(OH)(O₂C-C₆H₄-CO-C₆H₄-CO₂)]

Dieses Manuskript wurde im September 2012 im Journal „Inorganic Chemistry“ eingereicht.

Das solvothermale System Al³⁺ / 4,4'-Benzophenondicarbonsäure (H₂BPDC) / H₂O / DMF wurde mittels Hochdurchsatzmethoden untersucht. Dabei konnten Synthesebedingungen identifiziert werden, unter denen die Verbindung [Al(OH)(BPDC)] oder CAU-8 als phasereines Pulver entsteht. Des Weiteren konnten Bedingungen gefunden werden, unter denen sich makroskopische Einkristalle von CAU-8 bildeten. Die Struktur von CAU-8 wurde mittels Einkristalldiffraktometrie bestimmt. Das phasenreine mikrokristalline Produkt CAU-8 wurde mittels Röntgenpulverbeugung, Elementaranalyse, IR-Spektroskopie, Thermogravimetrie und Gassorption charakterisiert. Das Netzwerk von CAU-8 basiert auf Ketten *trans*-verknüpfter AlO₆-Polyeder, die über die Linkermoleküle so verknüpft werden, dass voneinander isolierte Kanäle mit einem Durchmesser von 8 Å entstehen. Die Oberfläche dieser Kanäle ist mit den Ketogruppen der Linkermoleküle ausgekleidet. Eine topologische Analyse der Gerüststruktur zeigte, dass dieses Netzwerk mit der Struktur einer tetragonalen Kugelpackung korreliert. Dabei wurde eine Herangehensweise für die Handhabung eindimensionaler periodischer Baueinheiten für die topologische Klassifizierung erarbeitet und verwendet, die ebenso für andere Verbindungen mit eindimensionalen Baueinheiten genutzt wurde. Es zeigte sich, dass die Topologien in hervorragender Weise die Netzwerkstrukturen beschreiben.

The first keto-functionalized microporous Al-based metal-organic framework: [Al(OH)(O₂C-C₆H₄-CO-C₆H₄-CO₂)]

Helge Reinsch,^a Martin Krüger,^b Jerome Marrot,^b Norbert Stock^{a}*

^a Institut für Anorganische Chemie, Christian-Albrechts-Universität zu Kiel, Max-Eyth-Straße 2, D-24118 Kiel (Germany), E.mail: stock@ac.uni-kiel.de; ^b Institute Lavoisier (UMR CNRS 8180), Porous Solids Group, Université de Versailles Saint Quentin en Yvelines, 45, Avenue des Etats-Unis, 78035 Versailles, France.

KEYWORDS metal-organic frameworks; aluminium carboxylates; porous materials; solvothermal synthesis; high-throughput methods

ABSTRACT Based on the V-shaped linker molecule 4,4'-benzophenonedicarboxylic acid, the new carbonyl-functionalized metal-organic framework (MOF) [Al(OH)(O₂C-C₆H₄-CO-C₆H₄-CO₂)], denoted as CAU-8, was discovered employing high-throughput methods. The compound is obtained from 4,4'-benzophenonedicarboxylic acid, Al₂(SO₄)₃·18 H₂O in a mixture of, N,N-dimethylformamide (DMF) and water under solvothermal conditions. The structure was determined from single-crystal X-ray diffraction data (*I*₄/a, *a* = *b* = 13.0625(5), *c* = 52.565(2) Å). The framework is based on infinite inorganic building units of *trans*-connected, corner-

sharing AlO_6 -polyhedra. Parallel Al-O-chains are arranged in layers perpendicular to [001]. Within a layer an inter-chain distance of ~ 1.1 nm is observed. The orientation of the Al-O-chains within neighboring layers is perpendicular to each other - along [100] and [010], respectively - and an ABCDA stacking of these layers is observed. The interconnection of these orthogonally oriented chains by the V-shaped dicarboxylate ions results in the formation a three-dimensional framework structure containing one-dimensional channels with a diameter of ca. 8 Å. The pore walls are lined by the keto-groups. CAU-8 was thoroughly characterized by X-ray powder diffraction (XRPD), thermogravimetric measurements, IR- and Raman-spectroscopy, elemental analysis and gas sorption experiments using N_2 and H_2 as adsorptives. CAU-8 is stable up to 350 °C in air and exhibits a moderate porosity with a specific surface area of $S_{\text{BET}} = 600$ m^2/g and a micropore volume of 0.23 cm^3/g . Moreover a detailed topological analysis of the framework was carried out and an approach for the topological analysis of MOFs based on infinite 1-periodic building units is proposed.

Introduction

Porous metal-organic frameworks (MOFs) are attracting considerable interest in academic as well as industrial research.^{1,2,3} The main reason for this is probably the opportunity to modulate their properties by crystal engineering. Once the synthesis of a new framework compound is established, the replacement of the building units by topologically identical ones during the synthesis allows in principle the tuning of the compound's properties.⁴ This was demonstrated for example for Al^{3+} -MOFs based on linear dicarboxylate ions.^{5,6,7,8,9} The framework-topology of Al-MIL-53 (MIL stands for Matériaux de l'Institut Lavoisier) is based on the connection of linear chains of *trans*-connected corner-sharing AlO_6 -polyhedra by dicarboxylate ions.⁵ Employing larger or smaller dicarboxylate ions, isorecticular compounds with altered pore size^{3,6,7}

as well as chemically functionalized framework structures can be obtained.^{8,9} By alteration of the synthesis conditions, the formation of different inorganic nodes such as cyclic cationic clusters can be preferred, which lead to the formation of uninodal frameworks with cubic topology, denoted CAU-3 (CAU stands for Christian-Albrechts Universität).¹⁰ For this framework structure, the extension and the functionalization of the framework were only possible employing high-throughput (HT) methods.¹¹ The change of the linker molecules can strongly affect the synthesis conditions that allow the crystallisation of the targeted compound and HT-methods speed up the screening of large parameter spaces and thus ease the optimization of synthesis conditions.¹² We have focused our investigations on the synthesis of new aluminium-based MOFs, since these compounds have shown to be thermally and chemically very stable.¹³ Furthermore, Al³⁺ is non-toxic and the inorganic reactants are inexpensive, which makes these MOFs interesting materials for industrial applications.³ Their stability allows the facile post-synthetic modification (PSM) of these compounds,^{14,15,16} which is a versatile method to generate functional groups in a MOF which are not accessible via conventional synthesis methods. Moreover a large variety of different functional groups can be readily introduced into Al-MOFs in order to “tune” their sorption properties.¹⁷

In this contribution, we report the solvothermal synthesis at the gram-scale of the new metal-organic framework [Al(OH)(O₂C-C₆H₄-CO-C₆H₄-CO₂)] denoted as CAU-8, based on 4,4'-benzphenonedicarboxylate. This compound was thoroughly characterized by single-crystal X-ray diffraction as well as X-ray powder diffraction (XRPD), thermogravimetric analysis, IR- and Raman-spectroscopy, elemental analysis and gas sorption measurements. Moreover its topology is described in detail.

Experimental Section

Chemicals. All chemicals are commercially available and were used as purchased, except for 4,4'-benzophenonedicarboxylic acid (H₂BPDC), which was ground prior to the synthesis.

Methods. HT-experiments were carried out in custom made steel-multiclaves in Teflon-lined reaction vessels with a maximum volume of 2 mL.¹¹ The large-scale synthesis was carried out in a glass-reactor with screw-cap and a volume of 100 mL (DURAN® GL 45). Single-crystal X-ray diffraction data was collected on a Bruker X8-APEX2 CCD area-detector diffractometer using Mo-K_{α1} radiation. X-ray powder diffraction data was collected on a STOE Stadi-P powder diffractometer in transmission geometry (Cu-K_{α1} radiation) using a linear position sensitive detector (PSD) system. SEM-micrographs were recorded on a Philips ESEM-XL 30 microscope. IR spectra were recorded on a Bruker ALPHA-FT-IR A220/D-01 spectrometer equipped with an ATR-unit. FT-Raman spectra were recorded on a Bruker IFS 66 FRA 106 spectrometer in the range of 0-3300 cm⁻¹ using a Nd/YAG-Laser (1064 nm). The thermogravimetric (TG) analyses were carried out using a NETSCH STA 409 CD analyzer. The samples were heated in Al₂O₃ crucibles at a rate of 4 K min⁻¹ under a flow of air (25 ml min⁻¹). The TG data were corrected for buoyancy and current effects. Gas sorption experiments were performed using a BEL JAPAN INC. Belsorp_{max} instrument. The programs used for the topological analysis were Systre¹⁸ and TOPOS.¹⁹

HT-Investigation. The solvothermal system Al³⁺ / H₂BPDC / DMF / H₂O was investigated using different Al³⁺-sources. After discovery of CAU-8 (Fig. 2), the synthesis parameters were systematically varied in order to optimize the purity and the crystallinity of the product. Different Al³⁺-sources were employed (Al(NO₃)₃·9H₂O, AlCl₃·6H₂O and Al₂(SO₄)₃·18H₂O) and the absolute concentrations as well as the molar ratios of Al³⁺ and H₂BPDC were varied (30-200 g/L H₂BPDC; molar ratio Al³⁺:H₂BPDC between 2:1 and 1:1). The composition of the solvent

mixture was altered as well (0-80 vol.% DMF). Moreover the influence of the pH was investigated using hydrochloric acid and sodium hydroxide as additives. The reaction time was varied between 12 and 36 h and the temperature was varied between 120 °C and 145 °C. All samples were characterized by XRPD measurements.

Synthesis of Single Crystals of CAU-8

Single-crystals of CAU-8 suitable in size for the structure determination (Fig. 1) were isolated during the HT optimisation experiments from a 2 mL-reactor. These were accompanied by the microcrystalline, unporous byproduct. In this experiment, 60 mg H₂BPDC (0.22 mmol), 148 mg Al₂(SO₄)₃·18H₂O (0.22 mmol), 250 μL DMF and 250 μL H₂O were heated for 12 hours at 140 °C.

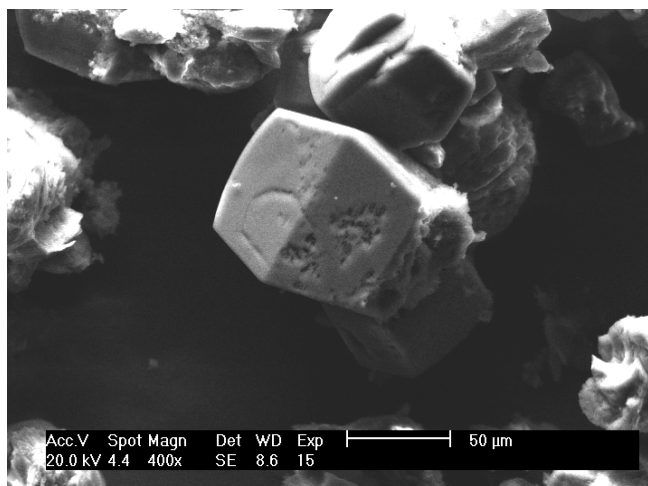


Figure 1. SEM-micrograph of a single crystal of CAU-8.

Scale-up Syntheses

Larger amounts phase-pure CAU-8 can be only obtained as microcrystalline powder after an additional activation step. For this synthesis, 2000 mg H₂BPDC (7.4 mmol), 7.4 mL of a 0.5 M solution of Al₂(SO₄)₃·18H₂O (7.4 mmol Al³⁺), 0.6 mL H₂O and 12 mL DMF are heated at 140 °C for 12 hours. After filtration, a buff colored powder is obtained. This raw product contains

recrystallized linker molecules, and therefore is treated with DMF (20 mL) at 85 °C over night. After filtration, the now white solid is thoroughly washed with water and dried under ambient conditions. The yield is ~ 1.2 g (~ 40 %). CHNS-analysis: N 1.6 %, C 47.6 %, H 3.4 %. Calculated from the chemical formula $[\text{Al}(\text{OH})(\text{O}_2\text{C}-\text{C}_6\text{H}_4-\text{CO}-\text{C}_6\text{H}_4-\text{CO}_2)] \cdot 0.5\text{DMF} \cdot 3.7 \text{H}_2\text{O}$: N 1.7 %, C 47.7 %, H 4.8 %.

Structure determination

A suitable single crystal was carefully selected and glued onto a glass fibre. The structure was solved using direct methods, developed by successive difference Fourier syntheses and refined by full-matrix least-squares on all F^2 data using SHELXTL. Diffuse electron density inside the framework due to occluded solvent molecules was corrected with the program SQUEEZE,²⁰ a part of the PLATON package of crystallographic software used to calculate the solvent or counterions disorder area and to remove its contribution to the overall intensity data. Results of the crystallographic work are summarized in Table 1. Crystallographic data for CAU-8 has been deposited with the Cambridge Crystallographic Data Centre as supplementary publication no. CCDC 899228. A copy of the data can be obtained, free of charge, on application to CCDC, 12 Union Road, Cambridge CB2 1EZ, U.K. (fax +44 1223 336033 or email deposit@ccdc.cam.ac.uk).

Table 1: Crystal data for CAU-8.

empirical formula	C ₁₅ H ₉ AlO ₆
formula weight	312.20 g/mol
crystal system	tetragonal
space group	<i>I</i> 4 ₁ / <i>a</i> (No. 88)
<i>a</i> = <i>b</i> , <i>c</i> [Å]	13.0625(5), 52.565(2)
<i>V</i> [Å ³]	8969.1(6)
<i>Z</i>	16
ρ (calc) [g/cm ³]	0.925
F (000)	2560
crystal size [mm]	0.02 x 0.06 x 0.08
temperature (K)	296
radiation [Å]	0.71073
theta min-max [°]	1.5, 5.0
limiting indices	-15 > <i>h</i> > 15 -15 > <i>k</i> > 15 -62 > <i>l</i> > 62
reflections collected/unique	44877 / 3950
R(int)	0.112
observed data [<i>I</i> > 2 σ (<i>I</i>)]	1901
number of reflections, parameters	3950, 205
R1	0.0791
wR2	0.2299
S	1.02
residual electron density [e/Å ³]	min. -0.20, max. 0.24

Results and Discussion

HT Investigation

CAU-8 was discovered during the investigation of the system Al^{3+} / H_2BPDC / DMF / H_2O under solvothermal reaction conditions employing $\text{Al}(\text{NO}_3)_3 \cdot 9\text{H}_2\text{O}$ and $\text{Al}_2(\text{SO}_4)_3 \cdot 18\text{H}_2\text{O}$ as Al^{3+} -sources. In the first experiment that led to the discovery of CAU-8, the molar ratio Al^{3+} : H_2BPDC was kept constant at 1 : 1 and the absolute concentration of the reactants as well as the ratio H_2O : DMF was varied at a filling degree of 500 mL. The exact composition of the reaction mixtures can be found in the supporting information (Tab. S1). The experiment and the results which are based on XRPD measurements are visualized in Fig. 2. Employing both Al^{3+} -sources the formation of CAU-8 is observed. For $\text{Al}_2(\text{SO}_4)_3 \cdot 18\text{H}_2\text{O}$, the minimum amount of DMF necessary for the synthesis of CAU-8 is 200 μL while lower fractions of DMF result only in the recrystallization of H_2BPDC . Higher concentrations of the reactants induce the formation of a non-porous byproduct but lead also to better crystalline CAU-8 products. Using $\text{Al}(\text{NO}_3)_3 \cdot 9\text{H}_2\text{O}$ as Al^{3+} -source necessitates higher fractions of DMF (at least 300 μL) to induce the formation of CAU-8 and in all cases the formation of the byproduct is observed. At higher absolute concentrations the non-porous compound becomes the main product and CAU-8 is observed only in minor amounts. In general, less crystalline products are obtained when $\text{Al}(\text{NO}_3)_3 \cdot 9\text{H}_2\text{O}$ is employed as the Al^{3+} -source. Further detailed HT-investigations (~150 reactions) optimising the reactant concentrations, the temperature-time program, and the solvent ratio led to the optimized synthesis procedure, which could also be successfully up-scaled to larger reactors.

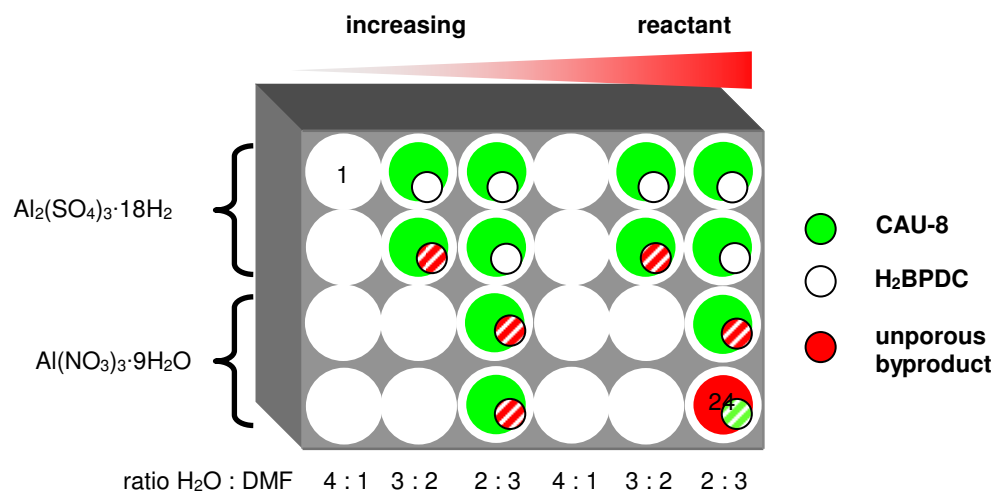


Figure 2. Schematic representation of the obtained products and the observed tendencies in the HT-experiment that led to the discovery of CAU-8. The results are based on the XRPD measurements.

Crystal Structure of CAU-8. The crystal structure of CAU-8 was determined from single crystal X-ray diffraction data. The formation of single crystals of Al-based MOFs suitable for in-house acquisition of diffraction data is remarkable and to the best of our knowledge it has only been reported once up to now.²¹ Most often Al-based MOFs are only obtained as microcrystalline products.^{22,23}

The asymmetric unit of CAU-8 contains two independent Al^{3+} -ions bridged by one μ_2 -OH-group and one complete linker molecule (Fig. S1). Some characteristic bond lengths are summarised in Tab. S2. The inorganic building unit of CAU-8 is an infinite linear chain of *trans*-connected, corner-sharing AlO_6 -polyhedra, and it is therefore identical to the building unit in the MIL-53 framework,⁵ but the arrangement of these units as well as the framework structure are substantially different. In MIL-53 all Al-O chains are parallel to each other and each chain is connected to four neighbouring chain. Thus one-dimensional lozenge-shaped channels are formed. In contrast, in CAU-8 parallel chains of *trans*-connected, corner-sharing AlO_6 -polyhedra

are arranged in layers of parallel chains with a distance of ~ 1.1 nm between each other. An ABCDA stacking of these layers is observed in which the chains in the layers A+C and B+D exhibit the same orientation (Fig. 3, top). The orientation of the chains within neighboring layers is perpendicular to each other. The interconnection of two chains from adjacent layer is accomplished via four benzophenonedicarboxylate molecules as shown in Figure 3 (bottom) and thus a three-dimensional framework with one-dimensional channels is formed. The concave sides of the linker molecules surround small cavities ($\varnothing = 6.5$ Å), which possess very small windows with a diameter below 2 Å based on van-der-Waals radii. These windows are blocked by linker molecules of neighboring cages.

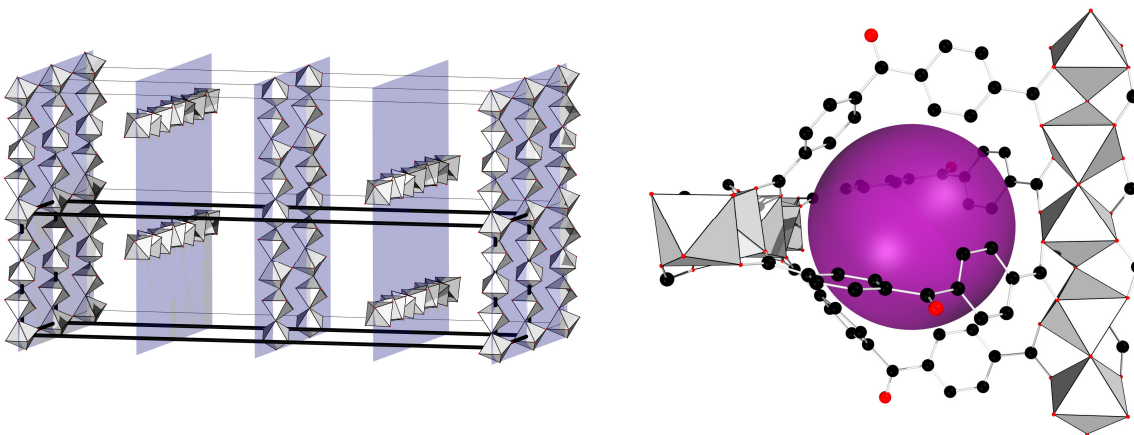


Figure 3. Left: ABCDA-stacking of the layers of AlO_6 -chains in a $2 \times 2 \times 1$ supercell as observed in the framework of CAU-8. The corresponding lattice planes are emphasized in blue. Right: Connection of two adjacent Al-O-chains via four benzophenonedicarboxylate molecules (both viewed along $[100]$). The cavity between the linker molecules is displayed as a purple sphere. The unit cell is shown in black, bold lines.

The convex sides of the linker molecules build up uniform, non-intersecting channels along $[100]$ and $[010]$ with a diameter of ~ 8 Å. The inner walls of the channels are lined with keto-groups (Fig. 4).

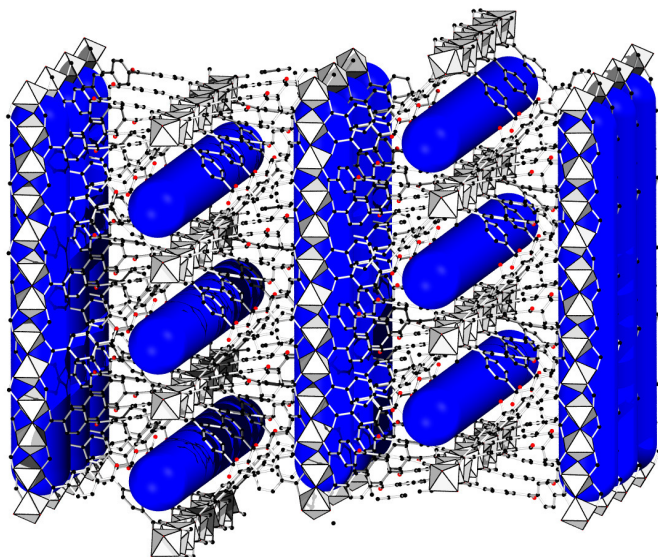


Figure 4. Representation of the framework structure of CAU-8. The keto-lined channels are represented as blue tubes. AlO_6 -polyhedra in grey, carbon atoms in black, oxygen atoms in red, hydrogen atoms were omitted for clarity.

The building units as well as the arrangement of the channels observed in CAU-8 are very similar to the ones recently reported for $[\text{In}(\text{OH})(\text{O}_2\text{C}-\text{C}_6\text{H}_4\text{OC}_6\text{H}_4-\text{CO}_2)]$.^{24,25} The structure of this compound is based on linear chains of *trans*-connected InO_6 -polyhedra which are interconnected by 4,4'-oxybisbenzoate ions. Thus the building units are very similar to the ones in CAU-8, but the connectivity is substantially different. While two chains are connected via four linker molecules at each crossing point in CAU-8, they are only connected by two linker molecules in the In-based MOF. Thus, $[\text{In}(\text{OH})(\text{O}_2\text{C}-\text{C}_6\text{H}_4\text{OC}_6\text{H}_4-\text{CO}_2)]$ exhibits a remarkable breathing effect, while CAU-8 possesses a rigid framework structure (Fig. 6).

Thermal Stability and XRPD

According to the results of the thermogravimetric measurement, the framework of CAU-8 decomposes at a temperature of 350 °C in air (Fig. 5).

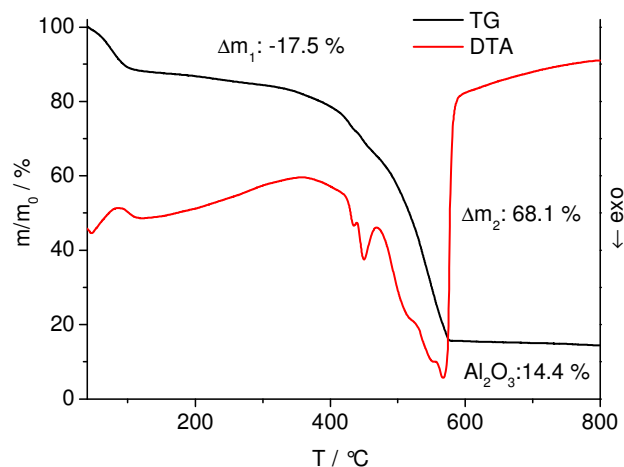


Figure 5. TG- and DTA-curves of CAU-8, measured with a heating rate of 4 K/min under air.

Up to a temperature of ~ 200 °C, occluded solvent molecules (H₂O, DMF) are removed (mass loss: 17.5 %), which is an endothermic reaction according to the DTA-curve. Between 200 and 350 °C a continuous mass loss is observed which can be attributed to the removal of small amounts of residual linker molecules from the pores. Above 350 °C, the framework is decomposed in a strongly exothermic reaction. The mass loss above 350 °C (68.1 %) is in very good agreement with the expected value (67.6 %) based on the chemical formula [Al(OH)(O₂C-C₆H₄-CO-C₆H₄CO₂)]. The XRPD-measurements further prove the thermal stability of CAU-8 framework structure upon moderate thermal treatment. After activation under vacuum at 200 °C, no loss of crystallinity is observed and the structure is fully retained (Fig. 6).

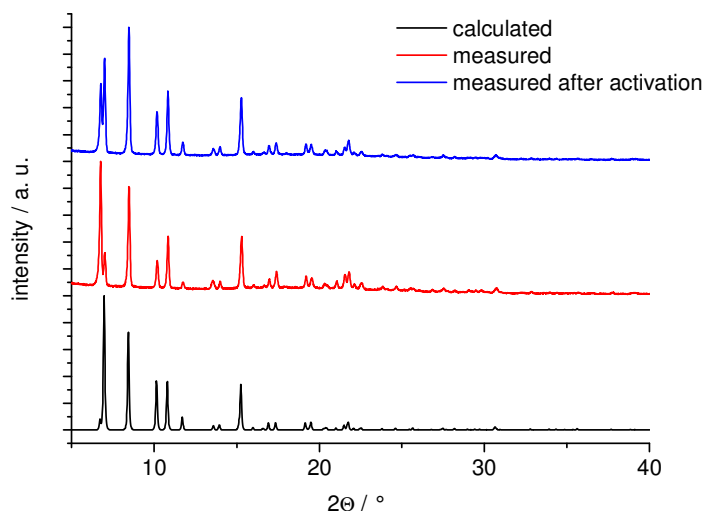


Figure 6. XRPD-data for CAU-8. Pattern calculated from single crystal data in black, experimental pattern of the MOF before activation in red and after activation at 200 °C in vacuum in blue.

The rigidity of the framework is demonstrated since no shift the Bragg peaks upon thermal treatment is observed. However, the relative intensities strongly vary. While the first peak at 6.7° has hardly any intensity according to single crystal data, it is the peak of highest intensity for the as synthesized CAU-8 and still shows high intensity in the activated product. We attribute this to the different amounts of guest molecules occluded inside the pores. These species have not taken into account in the single crystal structure, since the diffuse electron density of the disordered solvent molecules was treated with the SQUEEZE routine during the structure determination.

Vibrational Spectroscopy

The IR- and the Raman-spectra of CAU-8 are displayed in Figure 7. The most prominent band in both spectra is the asymmetric ν_{CO} -band of the carboxylate-groups at 1603 cm^{-1} . The absorption of the corresponding symmetric vibration can be observed at 1433 cm^{-1} . The ν_{CO} -band of the

keto-group in the linker molecule is observed at 1667 cm^{-1} . Some residual linker molecules could not be removed by solvent treatment. The band at 1714 cm^{-1} can be attributed to the ν_{CO} -band of free carboxylic acid groups and is due to the inclusion of small amounts of linker molecules inside the channels. This result is consistent with the continuous mass loss between 200 and $350\text{ }^{\circ}\text{C}$ observed in the TG-experiment (Fig. 5).

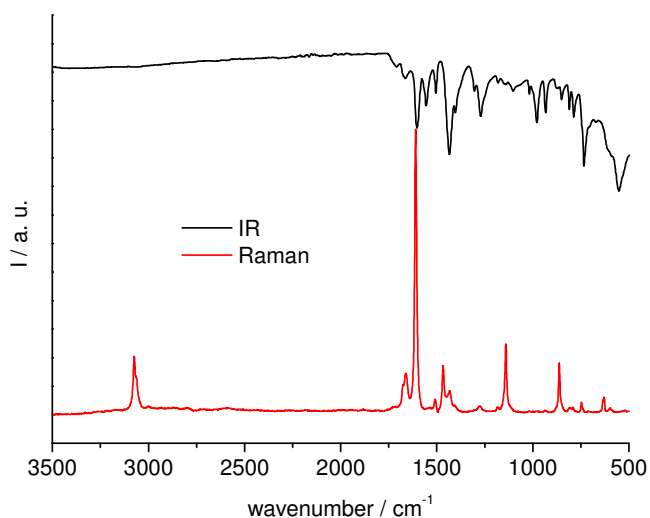


Figure 7. IR-spectrum (black line) and Raman-spectrum (red line) of CAU-8.

The ν_{CH} -band of the aromatic ring is clearly observed in the Raman-spectrum at 3074 cm^{-1} . The δ_{CH} -band for 1,4-substituted benzene rings is found at 864 cm^{-1} . The ν_{CC} -band of the bond between the benzene core and the CO-group is observed at 1140 cm^{-1} .

Sorption Properties

Prior to the sorption measurement, the MOF was activated for 18 h at $200\text{ }^{\circ}\text{C}$ under vacuum (0.1 mbar). The nitrogen sorption experiment clearly yields a type-I-isotherm, proving the microporosity of CAU-8 (Fig. 8).

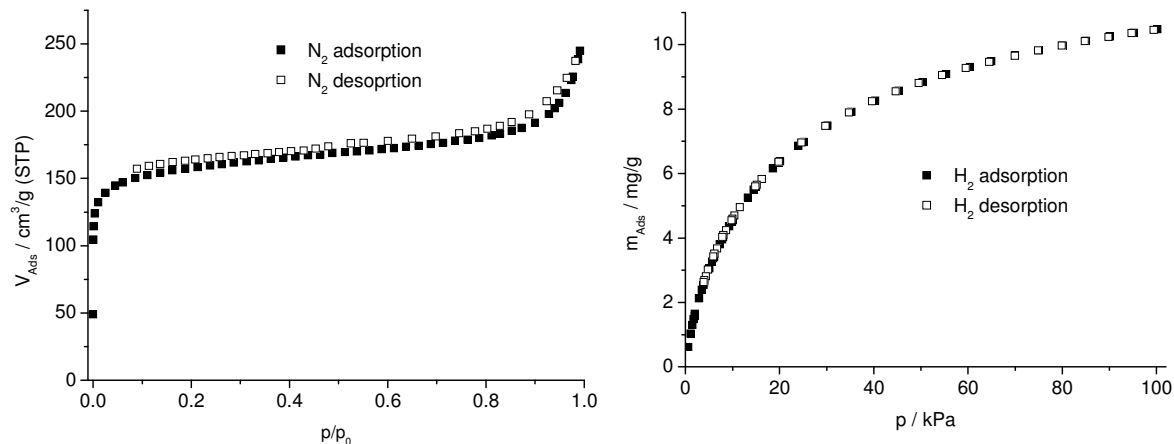


Figure 8. N₂- and H₂-sorption isotherms for CAU-8 measured at 77 K. Filled symbols represent the adsorption, empty symbols represent the desorption branch.

The specific surface area according to the BET-method is $S_{\text{BET}} = 600 \text{ m}^2/\text{g}$ and the observed micropore volume is $V_{\text{MIC}} = 0.23 \text{ cm}^3/\text{g}$, calculated from the amount adsorbed at $p/p_0 = 0.5$. The maximum uptake of hydrogen at 77 K and 1 bar is 1.04 wt. %.

Topological Analysis

The infinite aluminium-oxo-chain can be considered in different ways for the topological analysis. It was recently proposed,²⁶ to view such an infinite building unit as a ladder-like fragment of the network. This expands the one-periodic building unit into a two-dimensional fragment. However, in nearly all cases for MOFs based on finite inorganic building units, the zero-periodic character of the building blocks is retained by merging the points of extension into a “zero-dimensional” point for the topological classification. Therefore, we consider a different approach for the handling of the one-periodic building unit in CAU-8, which does not convert the infinite chain into a 2-dimensional, ladder-like fragment, but into a zig-zag-line for the topological analysis (Fig. 9). In this approach two points of extension are merged into one.

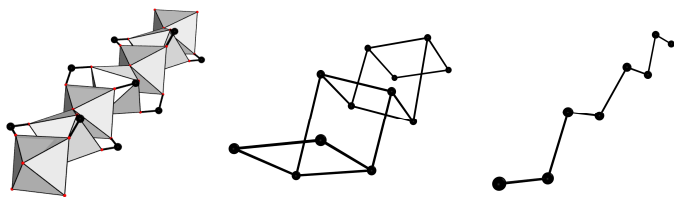


Figure 9. A part of the infinite chain as observed in CAU-8 (left), the ladder like model (middle) and the zig-zag-line (right) used for the topological analysis in this contribution.

For the topological analysis the embedding of highest symmetry was calculated using the program Systre.¹⁸ Subsequently this embedding was further analyzed with TOPOS.¹⁹ According to this procedure, the underlying net of CAU-8 has been reported, but no three-letter code has been assigned up to now. The net is a uninodal, four-connected $4/5/t1$ net with the point symbol $5^4.8^2$ (Fig. 10). The vertex symbol of this net is $5.5_2.5.8.5.8$. The notation $4/5/t1$ was introduced by Fischer, who reported on tetragonal homogenous sphere packings.²⁷ This representation in the form $k/l/m$ describes that every vertex has k nearest neighbors and that the shortest circuit is an l -ring. The t represents the crystal system, in this case tetragonal, while m is a number.

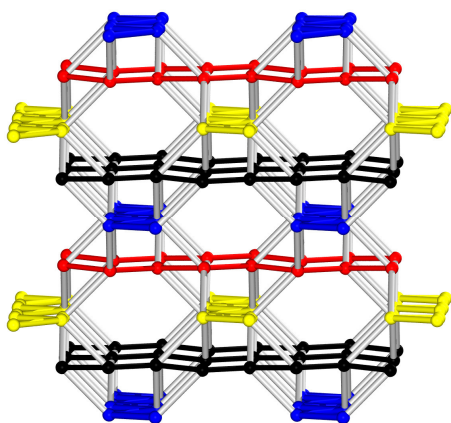


Figure 10. Representation of the underlying net of CAU-8 as seen along the b -axis. The fragments which represent the Al-oxo-chains are emphasized in blue, black, yellow and red,

corresponding to the respective layer. The bonds between the colored chains (grey) represent the V-shaped organic moieties.

This net is a very accurate representation of the CAU-8-framework. The character of the Al-O chains can be clearly identified in the topology (emphasized in blue, black, yellow and red in Fig. 10) as well as the arrangement in an ABCD-fashion. Thus, the one-periodic character of the inorganic units as well as the structural features of the MOF is retained. To set this result in a broader context, we have applied this procedure to various other MOFs, which are based on infinite, one-periodic building units. Thus this analysis was carried out for the frameworks of MIL-53,⁵ MIL-68,²⁸ CAU-4,²⁹ CAU-6³⁰ and CAU-10.¹⁷ In all cases we observed a very accurate representation of the underlying net for the selected frameworks by merging adjacent points of extension whenever appropriate (Fig. S2-S11, Tab. S3).

Conclusions

CAU-8 is a rare example of a keto-functionalized MOF and was readily synthesized from commercially available chemicals. It extends the number of framework structures of MOFs based on linear chains of *trans*-connected M(III)O₆-polyhedra of which the most important members are the ones of the MIL-53-family. The keto-group should be chemically accessible and thus post-synthetic modification reactions should be feasible. First studies have been carried out by us, but the reactivity seems to be inferior compared to MOFs containing aldehyde groups. The proposed topological approach towards the handling of infinite one-periodic building units shows promising results and could turn out as a versatile method for the classification of such materials.

Supporting Information. Exact composition of the reaction mixtures in the high-throughput experiment; the asymmetric unit and selected bond lengths; topological analysis of MOFs based

on infinite one-periodic building units. This material is available free of charge via the Internet at <http://pubs.acs.org>.

Corresponding Author

*Norbert Stock, Institut für Anorganische Chemie, Christian-Albrechts-Universität, Max-Eyth-Straße 2, 24118 Kiel, Germany; email: stock@ac.uni-kiel.de

Funding Sources

This work has been supported by the DFG (SPP 1362). The research leading to these results has received funding from the European Community's Seventh Framework Programme (FP7/2007-2013) under grant agreement no 228862.

References

-
- 1 Stock, N.; Biswas, S.; *Chem. Rev.* **2012**, *112*, 933–969.
 - 2 Janiak, C.; Vieth, J. K.; *New J. Chem.* **2010**, *34*, 2366-2388.
 - 3 Gaab, M.; Trukhan, N.; Maurer, S.; Gummaraju, R.; Müller, U.; *Micropor. Mesopor. Mater.* **2012**, *157*, 131-136.
 - 4 O’Keeffe, M.; *Chem. Soc. Rev.* **2009**, *38*, 1215-1217.
 - 5 Loiseau, T. ; Serre, C. ; Huguenard, C. ; Fink, G. ; Taulelle, F.; Henry, M. ; Bataille, T. ; Ferey, G. ; *Chem. Eur. J.* **2004**, *10*, 1373-1382.
 - 6 Senkovska, I.; Hoffmann, F.; Fröba, M.; Getzschmann, J.; Böhlmann, W.; Kaskel, S.; *Micropor. Mesopor. Mater.* **2009**, *122*, 93-98.
 - 7 Biswas, S.; Ahnfeldt, T.; Stock, N.; *Inorg. Chem.* **2011**, *50*, 9518-9526.
-

- 8 Comotti, A.; Bracco, S.; Sozzani, P.; Horike, S.; Matsuda, R.; Chen, J.; Takata, M.; Kubota, Y.; Kitagawa, S.; *J. Am. Chem. Soc.* **2008**, *130*, 13664-13672.
 - 9 Reimer, N., Gil, B., Marszalek, B., Stock, N., *CrystEngComm* **2012**, *14*, 4119-4125.
 - 10 Reinsch, H.; Feyand, M.; Ahnfeldt, T.; Stock, N.; *Dalton Trans.* **2012**, *41*, 4164-4171.
 - 11 Stock, N.; *Micropor. Mesopor. Mater.* **2010**, *129*, 287-295.
 - 12 Sonnauer, A.; Hoffmann, F.; Fröba, M.; Kienle, L.; Duppel, V.; Thommes, M.; Serre, C.; Ferey, G.; Stock, N.; *Angew. Chem. Int. Edt.* **2009**, *48*, 3791-3794.
 - 13 Cychosz, K. A.; Matzger, A. J.; *Langmuir* **2010**, *26*, 17198-17202.
 - 14 Ahnfeldt, T.; Gunzelmann, D.; Loiseau, T.; Hirsemann, D.; Senker, J.; Ferey, G.; Stock, N.; *Inorg. Chem.* **2009**, *48*, 3057-3064.
 - 15 Goesten, M. G.; Stavitski, E.; Juan-Alcaniz, J.; Ramos-Fernandez, E. V.; Sai Sankar Gupta, K. B.; van Bekkum, H.; Gascon, J.; Kapteijn, F., *J. Catalysis* **2011**, *281*, 177-187.
 - 16 Ahnfeldt, T.; Gunzelmann, D.; Wack, J.; Senker, J.; Stock, N.; *CrystEngComm* **2012**, *14*, 4126-4136.
 - 17 Reinsch, H.; Van der Veen, M. A.; Gil, B.; Marszalek, B.; Verbiest, T.; De Vos, D.; Stock, N.; *submitted*.
 - 18 Delgado-Friedrichs, O.; O’Keeffe, M.; *Acta Crystallogr. A* **2003**, *59*, 351–360.
 - 19 Blatov, V. A.; *Cryst. Rev.* **2004**, *10*, 249–318.
 - 20 van der Sluis, P.; Spek, A. L. *Acta Crystallogr., Sect. A* **1990**, *46*, 194.
 - 21 Loiseau, T.; Lecroq, L. ; Volkringer, C. ; Marrot, J. ; Férey, G. ; Haouas, M. ; Taulelle, F. ; Burrelly, S. ; Llewellyn, P. L. ; Latroche, M. ; *J. Am. Chem. Soc.* **2006**, *128*, 10223-10230.
-

- 22 Ahnfeldt, T.; Guillou, N.; Gunzelmann, D.; Margiolaki, I.; Loiseau, T.; Férey, G.; Senker, J.; Stock, N.; *Angew. Chem. Int. Ed.* **2009**, *28*, 5163-5166.
- 23 Fateeva, A.; Chater, P. A.; Ireland, C. P.; Tahir, A. A.; Khimyak, Y. Z.; Wiper, P. V.; Darwent, J. R.; Rosseinsky, M. J.; *Angew. Chem. Int. Ed.* **2012**, *51*, 7440-7444.
- 24 Jin, Z.; Zhao, H.-Y.; Zhao, X.-J.; Fang, Q.-R.; Long, J. R.; Zhu, G.-S.; *Chem. Commun.* **2010**, *46*, 8612-8614.
- 25 Tan, Y.-X.; Wang, F.; Kang, Y.; Zhang, J.; *Chem. Commun.* **2011**, *47*, 770-772.
- 26 O’Keeffe, M.; Yaghi, O. M.; *Chem. Rev.* **2012**, *112*, 675-702.
- 27 Fischer, W.; *Z. Kristallographie* **1993**, *205*, 9-26.
- 28 Volkringer, C.; Meddouri, M.; Loiseau, T.; Guillou, N.; Marrot, J.; Férey, G.; Haouas, M.; Taulelle, F.; Audebrand, N.; Latroche, M.; *Inorg. Chem.* **2008** *47*, 11892-11901.
- 29 Reinsch, H.; Krüger, M.; Wack, J.; Senker, J.; Salles, F.; Maurin, G.; Stock, N.; *Micropor. Mesopor. Mater.* **2012**, *157*, 50–55.
- 30 Reinsch, H.; Marszalek, B.; Wack, J.; Senker, J.; Gil, B.; Stock, N.; *Chem. Commun.* **2012**, DOI:10.1039/c2cc34909d.
-

5. Zusammenfassung

Im Rahmen dieser Arbeit wurde eine Vielzahl von solvothermalen Reaktionssystemen untersucht, wobei in fast allen Fällen Hochdurchsatzmethoden angewendet wurden. Dies führte zur Entdeckung von 18 neuen Verbindungen (Tabelle 5.1). Die Syntheseparameter konnten meist soweit optimiert werden, dass hochkristalline Verbindungen isoliert werden konnten, deren Strukturbestimmung meistens aus Röntgenpulverbeugungsdaten erfolgte. Soweit möglich wurden die optimierten Synthesebedingungen von der Hochdurchsatzreaktorgröße auf größere Reaktoren übertragen und die Verbindungen ausführlich charakterisiert. Dabei standen insbesondere die Sorptionseigenschaften im Vordergrund.

Basierend auf linearen aromatischen Dicarbonsäuren konnte eine Serie von drei zueinander isoretikulären Verbindungen im System Al^{3+} / Linkermolekül / Methanol / NaOH erhalten werden (CAU-3-X). Durch die Wahl von 2-Propanol als Lösungsmittel entstand unter ähnlichen Bedingungen die Verbindung CAU-6. Beide Gerüsttypen weisen sehr ungewöhnliche und bisher unbekannte anorganische Baueinheiten auf, deren Bildung entscheidend durch das Lösungsmittel bestimmt wird. Ausgehend von dreifach funktionalisierten aromatischen Carbonsäuren konnte ein neuer Al^{3+} -basierter MOF im System Al^{3+} / 1,3,5-Benzotrisbenzoesäure / DMF erhalten werden (CAU-4). Des Weiteren wurde die Bildung von Mn^{3+} - aus Mn^{2+} -Ionen unter solvothermalen Bedingungen in Methanol beobachtet, was die Synthese von Mn-MIL-100 ermöglichte. Zusätzlich konnten zwei neue Netzwerkstrukturen basierend auf gewinkelten aromatischen Dicarbonsäuren hergestellt werden. Die Verbindung CAU-8 basiert auf Benzophenondicarbonsäure (H_2BPDC) und wird im System Al^{3+} / H_2BPDC / DMF / H_2O hergestellt. Die Serie von Verbindungen mit CAU-10-Netzwerkstruktur hingegen enthält Isophthalsäure oder ein funktionalisiertes Derivat dieses Linkermoleküls. Die CAU-10-Gerüststruktur erwies sich als wertvoller Archetyp für die Synthese neuer Aluminium-MOFs. Im System Al^{3+} / Linkermolekül / DMF / H_2O konnten insgesamt 10 verschiedene Verbindungen basierend auf dieser Topologie hergestellt werden, wodurch massiv Einfluss auf die Materialeigenschaften genommen werden konnte.

Tabelle 5.1: Die in dieser Arbeit hergestellten und charakterisierten Verbindungen.

Trivialname	Summenformel	Strukturbestimmung
CAU-3-BDC	[Al ₂ (OCH ₃) ₄ (1,4-BDC)]	mittels XRPD + Rietveld
CAU-3-BDC-NH₂	[Al ₂ (OCH ₃) ₄ (1,4-BDC-NH ₂)]	mittels XRPD + Rietveld
CAU-3-NDC	[Al ₂ (OCH ₃) ₄ (2,6-NDC)]	mittels XRPD + Rietveld
CAU-4	[Al(BTB)]	mittels XRPD + Kraftfeldrechnungen
CAU-6	[Al ₁₃ Cl ₆ (H ₂ O) ₆ (OH) ₂₇ (1,4-BDC-NH ₂) ₃ (C ₃ H ₇ OH) ₆]	mittels XRPD + Kraftfeldrechnungen
CAU-8	[Al(OH)(BPDC)]	Einkristalldaten
CAU-10-H	[Al(OH)(1,3-BDC)]	mittels XRPD + Rietveld
CAU-10-CH₃	[Al(OH)(1,3-BDC-CH ₃)]	mittels XRPD + Rietveld
CAU-10-CH₃(as)	[Al(OH)(1,3-BDC-CH ₃)]	Indizierung + SHG
CAU-10-OCH₃	[Al(OH)(1,3-BDC-OCH ₃)]	mittels XRPD + Rietveld
CAU-10-NO₂	[Al(OH)(1,3-BDC-NO ₂)]	Indizierung + SHG
CAU-10-NH₂	[Al(OH)(1,3-BDC-NH ₂)]	Indizierung + SHG
CAU-10-OH	[Al(OH)(1,3-BDC-OH)]	Indizierung + SHG
CAU-10-Br	[Al(OH)(1,3-BDC-Br)]	mittels XRPD + Rietveld
CAU-10-H/Br	[Al(OH)(1,3-BDC) _{0,8} (1,3-BDC-Br) _{0,2}]	Indizierung
CAU-10-H/CH₃	[Al(OH)(1,3-BDC) _{1-x} (1,3-BDC-CH ₃) _x]	XRPD-Vergleich
CAU-10-NO₂/NH₂	[Al(OH)(1,3-BDC-NO ₂) _{0,55} (1,3-BDC-NH ₂) _{0,45}]	Indizierung
Mn-MIL-100	[Mn ₃ (O)(H ₂ O) ₃ (BTC) ₂]	XRPD-Vergleich

mittels XRPD: Strukturlösung aus Pulverbeugungsdaten; Rietveld: Struktur mittels Rietveldmethoden verfeinert; Indizierung: Diffraktogramm indiziert und Zellparameter verfeinert; SHG: Raum- oder Auslöschungsgruppe mittels SHG-Messungen bestätigt

5.1 Aluminium-MOFs basierend auf linearen Dicarbonsäuren

Bei der explorativen Untersuchung des solvothermalen System Al^{3+} / Terephthalsäure (H_2BDC) / Methanol / NaOH konnten vier verschiedene Verbindungen identifiziert werden. Es wurde die Bildung von Al-MIL-53 beobachtet, ebenso wie das unfunctionalisierte Analogon von CAU-1 und eine unbekannte, nur schwach kristalline Verbindung. Daneben konnte CAU-3-BDC erhalten werden. Die Syntheseparameter wurden in etwa 200 Hochdurchsatzreaktionen optimiert. Durch Kombination von Thermogravimetrie, Elementaranalyse und IR-Spektroskopie konnte die Summenformel zu $[\text{Al}_2(\text{OCH}_3)_4(\text{BDC})]$ bestimmt werden. Die Struktur konnte aus Pulverbeugungsdaten bestimmt und verfeinert werden. In weiteren Hochdurchsatzuntersuchungen konnten ausgehend von 2-Aminoterephthalsäure ($\text{H}_2\text{BDC-NH}_2$) und 2,6-Naphthalendicarbonsäure (H_2NDC) CAU-3-BDC- NH_2 und CAU-3-NDC erhalten werden (Abb. 5.1), deren Strukturen ebenfalls mit Rietveldmethoden verfeinert werden konnten.

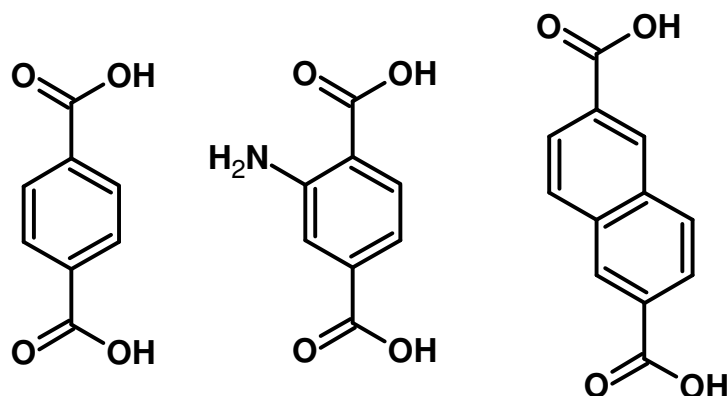


Abbildung 5.1: Linkermoleküle, die erfolgreich in die Struktur des CAU-3-Gerüst eingebaut werden konnten. Von links nach rechts: Terephthalsäure, 2-Aminoterephthalsäure und 2,6-Naphthalendicarbonsäure.

Während für CAU-3-BDC- NH_2 die Kristallstruktur von CAU-3-BDC mittels Fouriersynthese ergänzt wurde, wurde das Startmodell für die Verfeinerung von CAU-3-NDC mittels Kraftfeldrechnungen erstellt. CAU-3-BDC- NH_2 enthält geringe Mengen eines röntgenamorphen Nebenprodukts und die Aminogruppen werden während der Synthese teilweise methyliert. Die relativ basischen Synthesebedingungen führen außerdem zu einer partiellen Deaminierung der Linkermoleküle. Im Fall von CAU-3-NDC wurden Verunreinigungen durch Chloridionen sowie Naphthalendicarbonsäure beobachtet. Alle drei Verbindungen

wurden ausführlich mittels Elementaranalyse, Thermogravimetrie, IR- und Raman-Spektroskopie sowie Gassorptionsmessungen charakterisiert. Dabei zeigte sich, dass CAU-3-NDC eine der höchsten bisher beobachteten spezifischen Oberflächen aufwies ($\sim 2300 \text{ m}^2/\text{g}$, CAU-3-BDC: $\sim 1500 \text{ m}^2/\text{g}$; CAU-3-BDC-NH₂: $\sim 1250 \text{ m}^2/\text{g}$). Durch die Verwendung der verschiedenen Linkermoleküle konnten die Sorptionseigenschaften gegenüber Stickstoff und Wasserdampf moduliert werden. Die drei Verbindungen sind zueinander isoretikulär und basieren auf dem gleichen [Al₁₂(OCH₃)₂₄]¹²⁺-cluster, der durch Carboxylatgruppen abgesättigt wird (Abb. 5.2, rechts). Zusammen mit der anorganischen Baueinheit die in CAU-1 beobachtet wird (Abb. 5.2 links) stellen diese beiden Netzwerkstrukturen die einzigen Beispiele für zyklische Aluminium-Cluster dar.

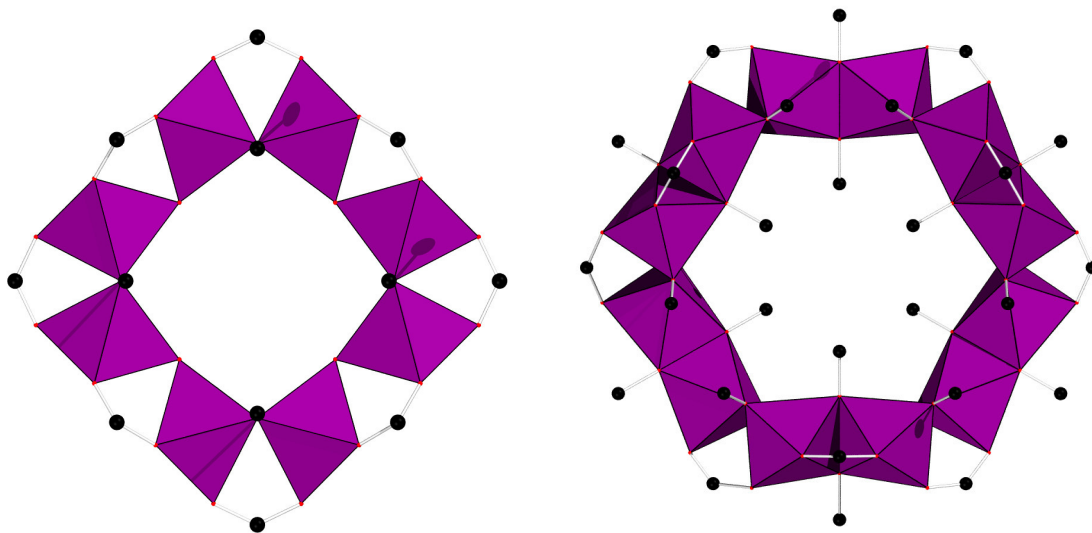


Abbildung 5.2: Strukturen der anorganischen Baueinheiten in CAU-1 (links) und CAU-3 (rechts). AlO₆-Polyeder in violett, Kohlenstoffatome in schwarz.

In beiden Fällen ist deren Vorkommen auf MOFs beschränkt. Die anorganischen Baueinheiten von CAU-3 sind im Gerüst zwölfmal zu benachbarten Baueinheiten verknüpft, so dass das Netzwerk analog zur kubisch flächenzentrierten Kugelpackung aufgebaut ist (**fcc**-Topologie). Durch die anisotrope Ringform kristallisieren die Strukturen allerdings nicht kubisch sondern in rhomboedrisch zentrierten Zellen. Dadurch entstehen tetraedrische und oktaedrische Poren, deren Durchmesser zwischen 1 und 3.8 nm variiert und die über trigonale Fenster mit einem Durchmesser von ca. 8 Å verbunden werden. Die Synthese der CAU-3-Familie gab den Anlass zur Untersuchung weiterer solvothermaler Systeme mit Alkoholen als Lösungsmittel.

Während in Ethanol ausschließlich literaturbekannte Verbindungen beobachtet wurden, konnte im System $\text{AlCl}_3 \cdot 6\text{H}_2\text{O}$ / Aminoterephthalsäure ($\text{H}_2\text{BDC-NH}_2$) / 2-Propanol die neue Verbindung CAU-6 synthetisiert werden. Durch eine Kombination von Elementaranalyse, IR-Spektroskopie, Festkörper-NMR-Spektroskopie, Thermogravimetrie und EDX-Spektroskopie konnte für CAU-6 die Summenformel $[\text{Al}_{13}\text{Cl}_6(\text{H}_2\text{O})_6(\text{OH})_{27}(\text{BDC-NH}_2)_3(\text{C}_3\text{H}_7\text{OH})_6]$ bestimmt werden. Ausgehend von dieser Summenformel konnte ein Modell der Struktur von CAU-6 aus Synchrotronpulverbeugungsdaten erstellt werden. Dieses Modell wurde mit Kraftfeldrechnungen optimiert. Da die Position der Chloridionen und der Solvensmoleküle im Gerüst nicht bestimmt werden konnte, war eine Verfeinerung mittels Rietveldmethoden allerdings nicht möglich. Alle experimentellen Messwerte sind aber in sehr guter Übereinstimmung mit dem erhaltenen Modell. Die Struktur von CAU-6 basiert auf säulenförmigen anorganischen Ketten. Diese lassen sich theoretisch ableiten, wenn dreizehnkernige $[\text{Al}_{13}(\text{OH})_{24}(\text{H}_2\text{O})_{24}]\text{Cl}_{15} \cdot 13\text{H}_2\text{O}$ -Cluster unter Wasserabspaltung kondensiert würden. Diese säulenförmigen Baueinheiten enthalten Hohlräume und sind über die Linkermoleküle miteinander verknüpft (Abb. 5.3).

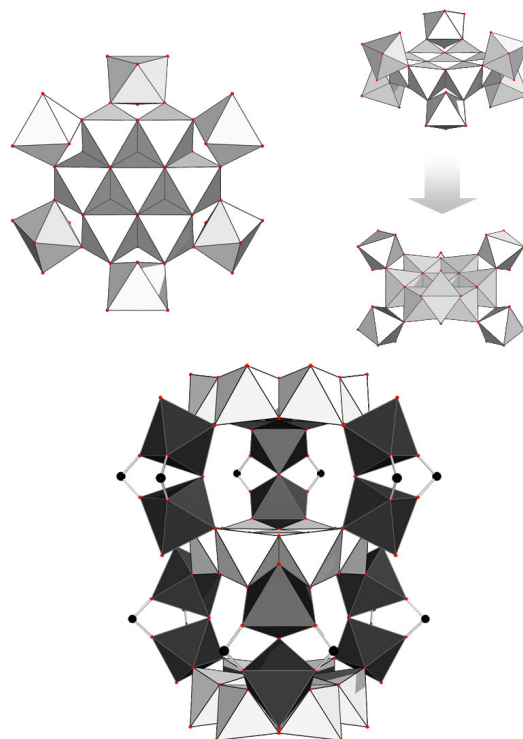


Abbildung 5.3: Darstellung der hypothetischen Kondensation von $[\text{Al}_{13}(\text{OH})_{24}(\text{H}_2\text{O})_{24}]\text{Cl}_{15} \cdot 13\text{H}_2\text{O}$ -Clustern zu Säulen. AlO_6 -Polyeder in hell- bzw. dunkelgrau, Kohlenstoffatome in schwarz.

So entstehen trigonale Kanäle, die Chloridionen und Solvensmoleküle enthalten. Diese Spezies lassen sich nur teilweise entfernen ohne das Gerüst zu zersetzen. Die Kombination aus eingelagerten Anionen und protischen OH- und NH₂-Gruppen führt allerdings dazu, dass für die Wasserdampfsorption eine Typ-I-Isotherme gemessen wird, was für MOFs sehr ungewöhnlich ist, da diese sonst eher hydrophobe Eigenschaften zeigen.

5.2 MOFs basierend auf dreifach funktionalisierten Linkermolekülen

Im solvothermalen System Al³⁺ / 1,3,5-Bezentrisbenzoesäure (H₃BTB) / DMF konnte mit Hilfe von Hochdurchsatzmethoden eine hochporöse aber nur gering kristalline neue Verbindung hergestellt werden (CAU-4). Mittels Thermogravimetrie, Elementaranalyse und IR-Spektroskopie konnte die Summenformel [Al(BTB)] bestimmt werden. Für eine reproduzierbare Synthese wurde Benzoesäure als Additiv benötigt. Ein Strukturmodell konnte mittels Kraftfeldrechnungen aus der Kristallstruktur des Lanthanoid-basierten Tb-MIL-103 entwickelt werden. Die Struktur basiert auf der Verbrückung von Al³⁺-Ionen über Carboxylatgruppen, wodurch eine unendlich lange Reihe voneinander isolierter AlO₆-Polyeder entsteht. Diese sind über die Linkermoleküle so verknüpft, dass hexagonale Kanäle mit einem Durchmesser von ~ 1 nm entstehen. Dieses Modell wurde an das gemessene Diffraktogramm angepasst und ist in guter Übereinstimmung mit den weiteren Eigenschaften der Verbindung. Die Güte des Modells wurde außerdem durch Festkörper-NMR-Spektroskopie überprüft, die die Existenz von zwei kristallographisch unabhängigen Aluminiumatomen bestätigte. Die scheinbare spezifische Oberfläche von CAU-4 beträgt ~1500 m²/g und die Verbindung ist bis ca. 400 °C in Luft stabil.

In dem solvothermalen System Mn²⁺ / Trimesinsäure (H₃BTC) / Methanol konnte beobachtet werden, dass bei Verwendung von Mn(NO₃)₂·4H₂O unter solvothermalen Bedingungen eine Oxidation von Mn²⁺-Ionen stattfindet. Nach relativ kurzen Reaktionszeiten bildete sich die auf Mn³⁺-basierte Verbindung Mn-MIL-100, deren Struktur analoge basierend auf Fe³⁺, Cr³⁺ oder Al³⁺ bereits bekannt waren. Als entscheidend für die Oxidation von Mn²⁺ stellte sich das Gegenion heraus. Die anorganischen Baueinheiten für diese MOFs sind trimere Cluster aus μ₃-O verknüpften Kationen. Im Falle von Mangan bestehen diese aus zwei Mn³⁺-Ionen und einem Mn²⁺-Ion. Diese Cluster bilden die Ecken eines Supertetraeders, dessen

Flächen durch die Trimesationen gebildet werden. Die Supertetraeder sind dann analog zu den tetraedrischen Knotenpunkten im zeotypen MTN-Netzwerk angeordnet. Dadurch entsteht eine mesoporöse Verbindung, die zwei Arten von Kavitäten enthält. Die in Mn-MIL-100 eingelagerten Lösungsmittelmoleküle können unter Vakuum oder durch thermische Aktivierung entfernt werden. Die thermische Aktivierung führt allerdings zu einer irreversiblen Amorphisierung des MOFs. Dies weist darauf hin, dass durch die thermische Aktivierung koordinativ ungesättigte Mn-Zentren entstehen, was zur Zersetzung des Gerüsts führt. Beide Aktivierungsmethoden führen allerdings zu einer vergleichbaren Porosität. Die Kristallisation von Mn-MIL-100 wurde mittels energiedispersiver Röntgenbeugung unter solvothermalen Bedingungen untersucht. Diese Experimente wurden nach zwei verschiedenen Modellen (nach Avrami bzw. nach Gualtieri) ausgewertet. Trotz der in-situ Oxidation von Mn^{2+} -Ionen konnten allerdings keine ungewöhnlichen kinetischen Phänomene beobachtet werden, unabhängig von dem Modell das zur kinetischen Auswertung herangezogen wurde.

5.3 Aluminium-MOFs basierend auf gewinkelten Dicarbonsäuren

Ausgehend von Benzophenondicarbonsäure (H_2BPDC) konnte im System $Al^{3+} / H_2BPDC / DMF / H_2O$ unter solvothermalen Bedingungen die Bildung von zwei neuen kristallinen Verbindungen beobachtet werden, von denen sich eine als porös erwies und deshalb näher untersucht wurde. Mittels Hochdurchsatzmethoden wurden Synthesebedingungen gefunden, die zur Bildung von makroskopischen Einkristallen von $[Al(OH)BPDC]$ (CAU-8) führten. Außerdem wurde ein Syntheseweg für phasereines, mikrokristallines CAU-8 entwickelt. Die Strukturlösung erfolgte aus Einkristallbeugungsdaten. Das Netzwerk von CAU-8 basiert auf unendlich langen Ketten von *trans*-eckenverknüpften AlO_6 -Polyedern. Diese Ketten wiederum sind parallel in Schichten angeordnet. Dabei unterscheidet sich die Orientierung der Ketten in benachbarten Schichten jeweils um 90° . Die Verknüpfung über die Linkermoleküle resultiert in Kanälen mit einem Durchmesser von ca. 8 \AA , deren Wände mit Keto-Gruppen ausgekleidet sind. Die Kanäle sind voneinander isoliert und verlaufen analog zur Orientierung der Ketten schichtweise parallel mit einer Verdrehung von 90° relativ zu den benachbarten Kanälen. Das mikrokristalline Produkt wurde mittels IR-Spektroskopie, Elementaranalyse, Thermogravimetrie,

Röntgenpulverbeugung und Gassorption charakterisiert. Dabei zeigte sich, dass Linkermoleküle in geringen Mengen in die Kanäle eingelagert sind. Dennoch besitzt CAU-8 eine scheinbare spezifische Oberfläche von $\sim 600 \text{ m}^2/\text{g}$. CAU-8 ist ein weiteres Beispiel für Aluminium-MOFs, die auf Ketten von AlO_6 -Polyedern basieren. Allerdings entsteht durch die Verwendung von Benzophenondicarbonsäure eine neue, bisher unbekannte Netzwerkstruktur. Die Topologien von CAU-8 und weiteren Verbindungen mit eindimensionalen anorganischen Baueinheiten wurden eingehend analysiert. Dafür wurde eine Herangehensweise für die Handhabung solcher eindimensionaler Baueinheiten für die topologische Klassifizierung genutzt, die akkurate Darstellungen der Kristallstrukturen lieferte. Die für CAU-8 beobachtete Topologie entspricht dabei der Struktur eines hypothetischen Zeoliths, die aus einer tetragonalen Kugelpackung abgeleitet werden kann.

Des Weiteren wurde basierend auf Isophthalsäure (H_2BDC) die neue Verbindung $[\text{Al}(\text{OH})\text{BDC}]$ (CAU-10-H) hergestellt. Die Struktur konnte aus Pulverbeugungsdaten bestimmt und mittels Rietveldmethoden verfeinert werden. Die chirale Raumgruppe $I4_1$ konnte mit Hilfe von SHG-Mikroskopie bestätigt werden. Die anorganische Baueinheit in CAU-10-H ist eine helicale Kette von *cis*-eckenverknüpften AlO_6 -Polyedern (Abb. 5.4 links). Dabei sind Helices verschiedener Orientierung abwechselnd im Netzwerk angeordnet und über die Isophthalationen verknüpft, so dass viereckige Kanäle entstehen (Abb. 5.4 rechts).

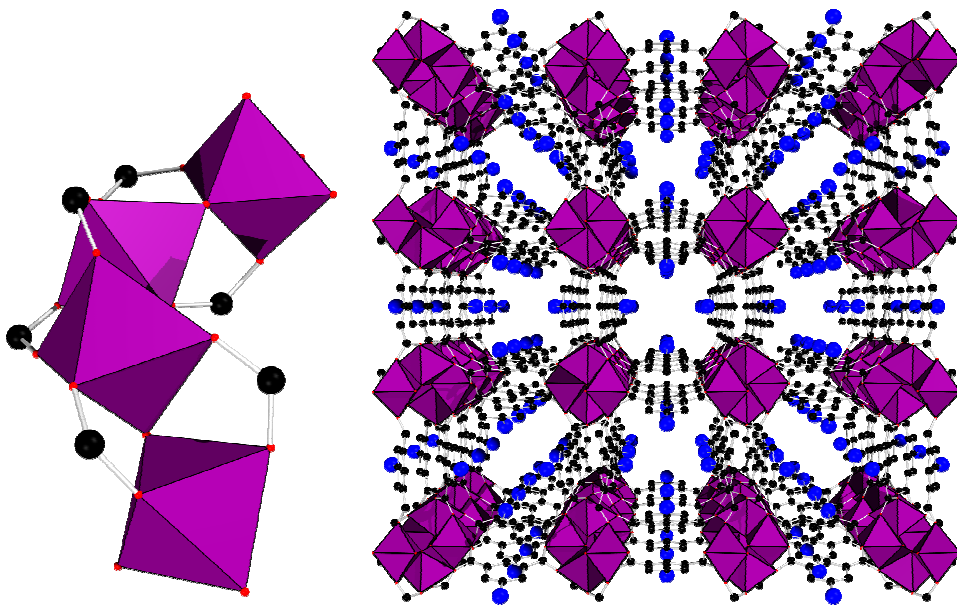


Abbildung 5.4: Links die *cis*-Verknüpfung der AlO_6 -Polyeder, rechts die Anordnung der Helices im Kristall. AlO_6 -Polyeder in violett, Kohlenstoffatome in schwarz, potentielle funktionelle Gruppen in blau.

Neben dem unfunktionalisierten CAU-10-H konnten weitere Verbindungen ausgehend von in 5-Position funktionalisierten Isophthalsäuren hergestellt werden (CAU-10-X). Die Strukturen von CAU-10-Br, CAU-10-OCH₃ und CAU-10-CH₃ konnten ebenfalls aus Pulverbeugungsdaten gelöst und mittels Rietveldmethoden verfeinert werden. Für CAU-10-CH₃ wurde ein Phaseübergang bei der thermischen Aktivierung beobachtet. Die Verbindung kristallisiert in der Raumgruppe *P4*₁, die mittels SHG-Mikroskopie bestätigt werden konnte. Allerdings konnte nur die Struktur der bei 200 °C kalzinierten Verbindung auch verfeinert werden (Raumgruppe *I4*₁/*amd*). Außerdem konnten CAU-10-NO₂, CAU-10-NH₂ und CAU-10-OH hergestellt werden. Die Kristallinität dieser Verbindungen reichte allerdings nicht aus, um deren Strukturen zu verfeinern. Allerdings konnten durch Kombination von Röntgenpulverbeugung und SHG-Mikroskopie Raum- und Auslöschungsgruppen ermittelt werden. Im Fall von CAU-10-NH₂ wurde eine partielle Formylierung der Aminogruppen während der Synthese mittels NMR-Spektroskopie bestätigt. Alle Mitglieder der CAU-10-Serie wurden detailliert charakterisiert und zeigten eine sehr hohe thermische und chemische Stabilität. Außerdem konnten die Sorptionseigenschaften gegenüber Stickstoff, Wasserstoff, Kohlendioxid und Wasserdampf durch den Einbau verschiedener Linkermoleküle massiv moduliert werden. Neben der Kapazität konnten auch die Affinität und die Zugänglichkeit der Poren verändert werden.

Eine weitere Möglichkeit zur Einflussnahme auf die Sorptionseigenschaften wurde durch die Verwendung von Mischungen von Linkermolekülen demonstriert. Dabei konnte durch die Verwendung von Mischungen von Isophthalsäure und Methyl-, bzw. Bromisophthalsäure die Sorptionskapazität moduliert werden. Im Falle von CAU-10-H/Br konnte ein hoher Dotierungsgrad bei gleichzeitiger sehr hoher Reproduzierbarkeit der Synthese erreicht werden. Die Synthese von CAU-10-NO₂/NH₂ zeigte, dass sich die Sorptionskapazität gegenüber Wasserstoff und Kohlendioxid durch den Einsatz von Mischungen von Linkermolekülen auch erhöhen lässt. In diesem speziellen Fall wurde beobachtet, dass sich die Linkermoleküle komplementär paarweise im Gerüst anordnen, was zu veränderten optischen Eigenschaften führte. Zusätzlich kann dies auch zu einer Polarisierung der Porenoberfläche führen, die einen Faktor für die erhöhte Kapazität darstellen könnte.

Einige Eigenschaften und Syntheseparameter sind zum Vergleich mit den im Abschnitt 4.1 beschriebenen literaturbekannten Verbindungen (Tab. 4.1) in Tabelle 5.2 zusammengefasst.

Tabelle 5.2: Eigenschaften und Syntheseparameter der in dieser Arbeit hergestellten Verbindungen.

Trivialname	Lösungsmittel	thermische Stabilität	S_{BET} bzw. Porosität gegenüber
CAU-3-BDC	Methanol	200 °C	~ 1500 m ² /g
CAU-3-BDC-NH₂	Methanol	200 °C	~ 1250 m ² /g
CAU-3-NDC	Methanol	200 °C	~ 2300 m ² /g
CAU-4	DMF	400 °C	~ 1500 m ² /g
CAU-6	Isopropanol	150 °C	~ 620 m ² /g
CAU-8	DMF + H ₂ O	350 °C	~ 600 m ² /g
CAU-10-H	H ₂ O + DMF	430 °C	~ 630 m ² /g
CAU-10-CH₃	H ₂ O + DMF	~ 380 °C	CO ₂ , H ₂ O
CAU-10-OCH₃	H ₂ O + DMF	~ 400 °C	H ₂ , CO ₂ , H ₂ O
CAU-10-NO₂	H ₂ O + DMF	410 °C	~ 440 m ² /g
CAU-10-NH₂	H ₂ O + DMF	~ 350 °C	H ₂ , CO ₂ , H ₂ O
CAU-10-OH	H ₂ O + DMF	~ 250 °C	H ₂ , CO ₂ , H ₂ O
CAU-10-Br	H ₂ O + DMF	400 °C	CO ₂
CAU-10-H/Br	H ₂ O + DMF	-	~ 300 m ² /g
CAU-10-H/CH₃	H ₂ O + DMF	-	variierend
CAU-10-NO₂/NH₂	H ₂ O + DMF	-	H ₂ , CO ₂
Mn-MIL-100	Methanol	120 °C	~ 1600 m ²

6. Ausblick

Strukturelle Analoga der neuen beobachteten Aluminium-Oxo-Cluster lassen sich häufig ausgehend von Übergangsmetallionen als molekulare Verbindungen herstellen. Dies eröffnet zum einen die Möglichkeit die auf Übergangsmetallen basierenden MOFs als lohnendes Synthesziel zu definieren. Diese könnten komplett veränderte magnetische und unter Umständen auch katalytische Eigenschaften zeigen, wie im Fall des Ti^{4+} -basierten Analogon von CAU-1 bereits beobachtet wurde. Somit könnten auch Ti^{4+} - oder Cr^{3+} -basierte Analoga der CAU-3-Familie präparativ zugänglich sein. Im Hinblick auf CAU-6 böte sich die Substitution von Al^{3+} durch Ga^{3+} an, da der dreizehnkernige molekulare Cluster für dieses Kation ebenfalls bekannt ist. Zum anderen ist es durchaus möglich, dass verschiedene andere molekulare Architekturen basierend auf Al^{3+} zugänglich sind und potentiell ein MOF-Netzwerk ausbilden könnten. Die Strukturvielfalt der (zyklischen) molekularen Magneten lässt hier viele neue Strukturen zu (Abb. 6.1).

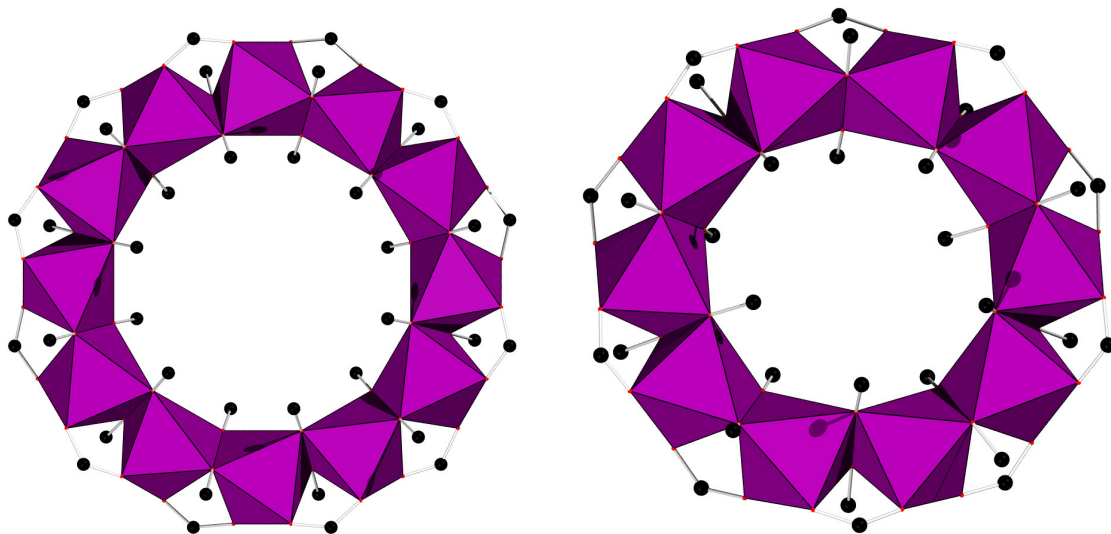


Abbildung 6.1: Links: Struktur eines zwölkernigen Eisen-Oxo-Clusters¹²⁷; Rechts: Struktur eines zehnkernigen Eisen-Oxo-Clusters.¹²⁸

Da Mn-MIL-100 als erster MOF die Mn-basierte trimere Baueinheit enthält, wäre die Synthese weiterer Mn-MOFs basierend auf diesem Cluster erstrebenswert. Hier bieten sich die Strukturen von MIL-101¹²⁹, MIL-88¹³⁰ oder MIL-59¹³¹ als Synthesziel an. Die weitere explorative Untersuchung der Bildung von Mn^{3+} -basierten Verbindungen könnte allerdings auch zu völlig anderen Strukturen führen und bietet ein weites Feld für die Forschung. Mechanistisch wäre insbesondere von Interesse,

warum sich unter solvothermalen Bedingungen Mn^{3+} bildet und wie diese Spezies stabilisiert wird. Des Weiteren lassen sich möglicherweise auch weitere „ungewöhnliche“ Oxidationsstufen von Übergangsmetallionen in-situ generieren und durch den Einbau in einen MOF stabilisieren, wie beispielsweise V^{2+} , Mn^{4+} , Co^{3+} oder Ni^{3+} .

Basierend auf der Struktur von CAU-8 beschäftigt sich die aktuelle Forschung im Arbeitskreis mit der Synthese von isoretikulären Verbindungen basierend auf ähnlichen Linkermolekülen (abb. 6.2).

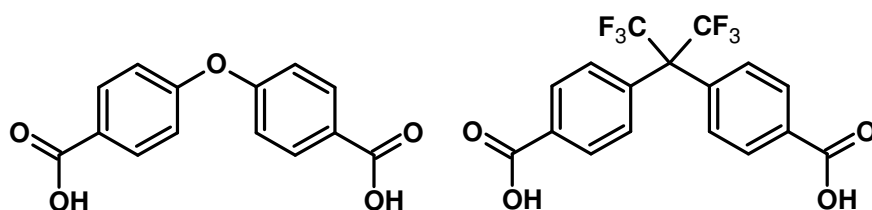


Abbildung 6.2: Mögliche Linkermoleküle für die Synthese von Verbindungen mit CAU-8-Struktur.

Außerdem bieten die funktionellen Keto-Gruppen eine Möglichkeit zur post-synthetischen Modifizierung. So wird im Moment eine Syntheseprozedur zur Iminbildung sowie zur Reduktion zum Alkohol untersucht. Aktuelle Arbeiten haben allerdings gezeigt, dass die Reaktivität der Keto-Gruppe geringer ist als die Reaktivität von Aldehydgruppen in MOFs.

Basierend auf weiteren gewinkelten Dicarbonsäuren sollte es ebenso möglich sein eine Verbindung mit CAU-10-Struktur mit größerem Porendurchmesser zu synthetisieren. Hier bieten sich Linkermoleküle an, bei denen die Säuregruppen in einer Ebenen mit den aromatischen Ringen stehen, wie 2,7-Naphthalendicarbonsäure oder 2,8-Anthracendicarbonsäure. Auch die Verwendung weiterer funktionalisierter Isophthalsäuren wie 5-Cyanoisophthalsäure könnte zu neuen Verbindungen mit CAU-10-Struktur führen. Für CAU-10-NO₂ wurde zudem beobachtet, dass sich bei der photochemischen Umsetzung mit Alkoholen Radikale auf den Linkermolekülen bilden. Der Mechanismus dieser Reaktion und die Modulation der Reaktivität durch den Einsatz von Mischungen von Linkermolekülen zur Synthese von CAU-10-MOFs sind Gegenstand aktueller Forschung. Die beobachtete Formylierung der Aminogruppen während der Synthese von CAU-10-NH₂ könnte ebenfalls eine vielversprechende Methode zur gezielten Modifizierung sein. Möglicherweise lässt sich Dimethylformamid in der Synthese durch

Dimethylacetamid ersetzen, wodurch eine in-situ Acetylierung möglich scheint. Aktuelle Arbeiten haben gezeigt, dass auch die Synthese von CAU-10-NH₂ ohne den Zusatz von DMF möglich scheint. So sollte auch der nicht modifizierte MOF präparativ zugänglich sein. Die für CAU-10-NO₂/NH₂ beobachtete erhöhte Kapazität und Affinität gegenüber Wasserstoff und CO₂ wird weiter untersucht. Dazu sind kalorimetrische Messungen geplant, ebenso wie die Charakterisierung mit photochemischen Methoden. Diese Experimente sollen weitere Beweise für die paarweise Anordnung von NO₂- und NH₂-funktionalisierten Linkermolekülen erbringen.

Nicht zuletzt zeigt die Vielzahl an neuen Verbindungen, die in dieser Arbeit synthetisiert werden konnten, dass die explorative Untersuchung von solvothermalen Systemen mittels Hochdurchsatzmethoden eine ideale Möglichkeit bietet neue Verbindungen mit hochinteressanten Eigenschaften herzustellen. Die Vielfalt an kommerziell erhältlichen und präparativ zugänglichen Carbonsäuren bietet ein praktisch unbegrenztes Forschungsgebiet für die Synthese neuer Aluminium-MOFs.

7. Anhänge

High-Throughput Studies of Highly Porous Al-based MOFs Supporting Information

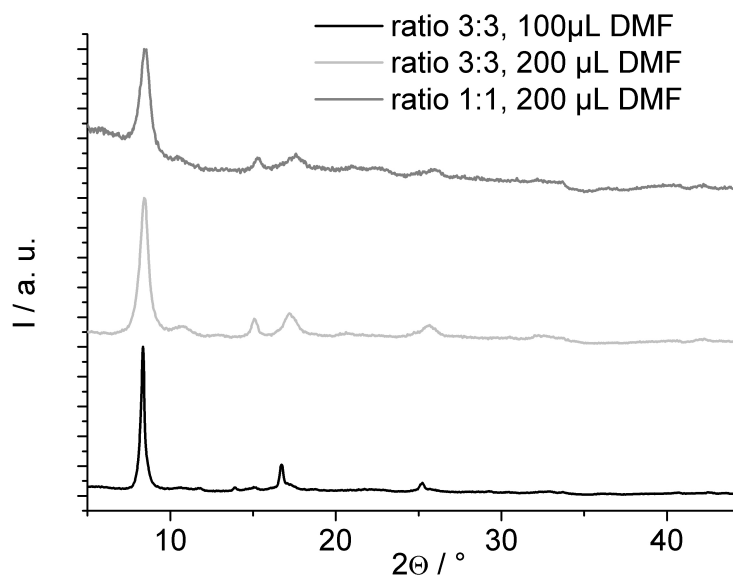


Figure S1: The powder patterns of three products obtained with trimellitic acid and the corresponding composition of the reactant mixture ($\text{Al}_2(\text{SO}_4)_3 \cdot 18\text{H}_2\text{O}$: linker).

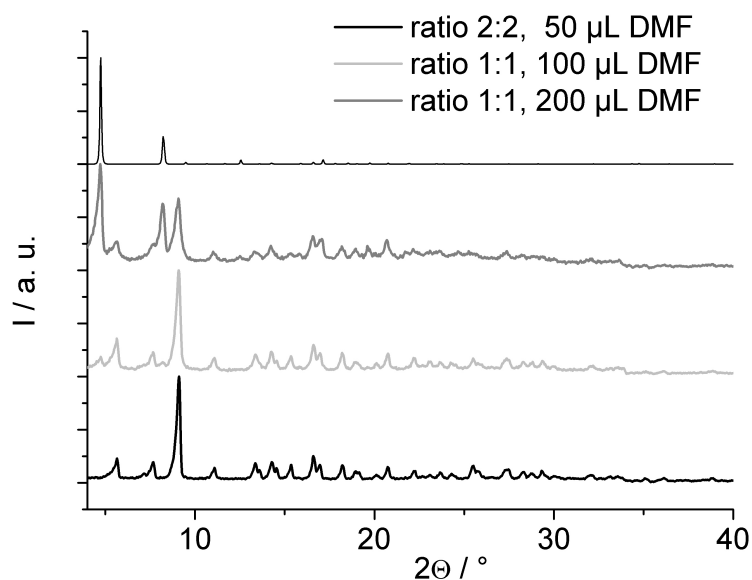


Figure S2: The powder patterns of three products obtained with trimesic acid and the corresponding composition of the reactant mixture ($\text{Al}_2(\text{SO}_4)_3 \cdot 18\text{H}_2\text{O}$: linker). On top, a calculated pattern for MIL-110.

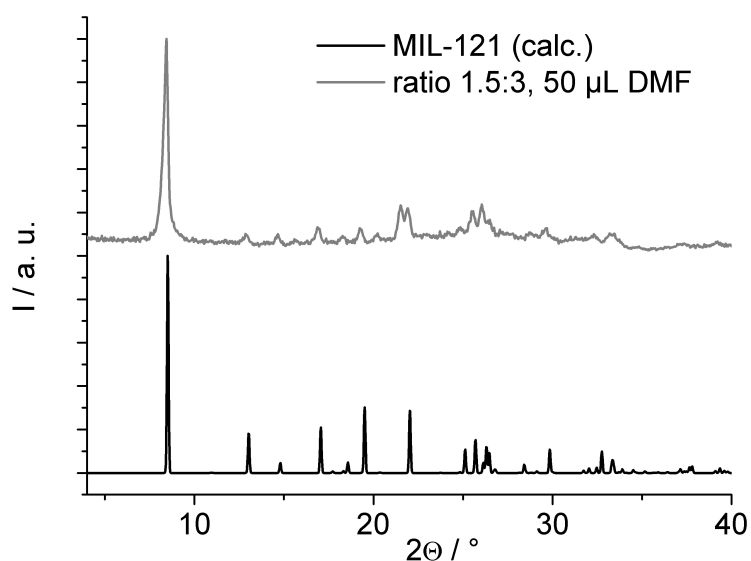


Figure S3: The powder pattern of a product obtained with pyromellitic acid with the corresponding composition $\text{Al}_2(\text{SO}_4)_3 \cdot 18\text{H}_2\text{O}$: linker in grey and a calculated pattern for MIL-121 in black.

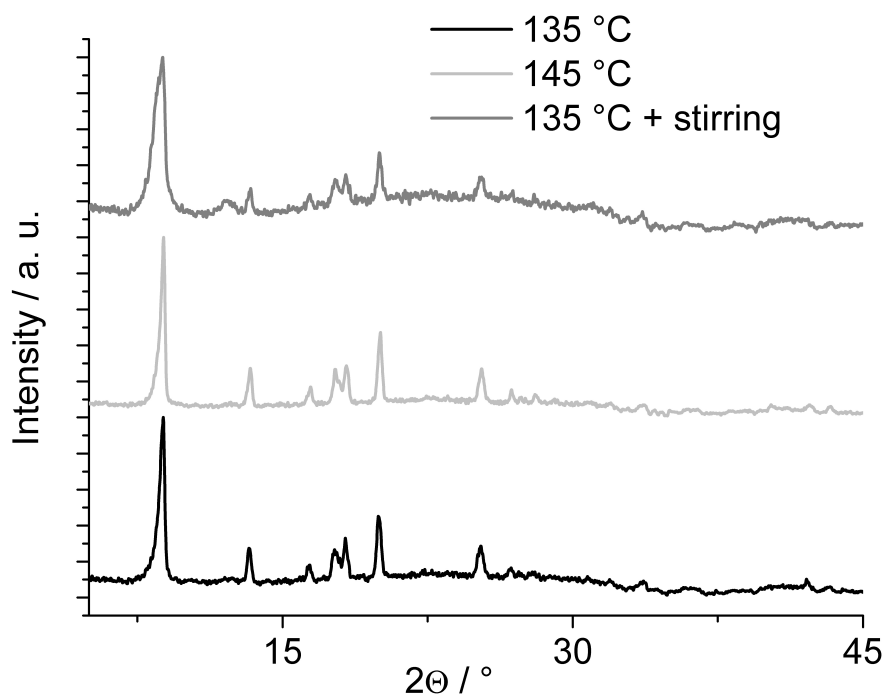


Figure S4: The powder patterns of three products obtained with pyromellitic acid in the microwave oven under different synthesis conditions, and the corresponding composition of the reactant mixture ($\text{Al}_2(\text{SO}_4)_3 \cdot 18\text{H}_2\text{O}$: linker).

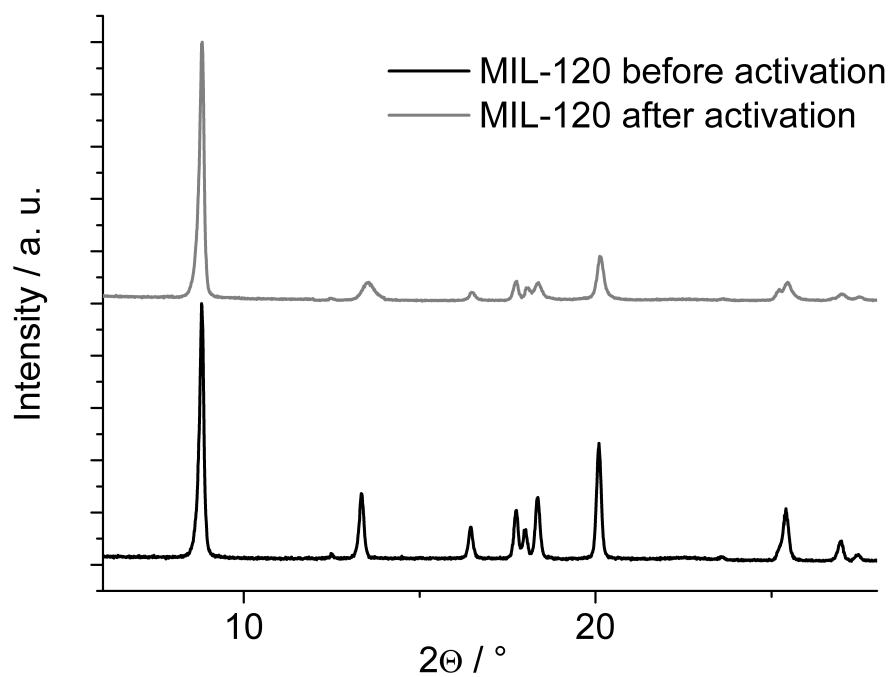


Figure S5: Powder pattern of the as synthesized MIL-120 and of the same compound after thermal activation showing the peak broadening due to the thermal treatment.

Supporting Information

CAU-3: A new family of porous MOFs with a novel Al-based brick: $[\text{Al}_2(\text{OCH}_3)_4(\text{O}_2\text{C-X-CO}_2)]$ (X=aryl)

Helge Reinsch, Mark Feyand, Tim Ahnfeldt and Norbert Stock

Institute of Inorganic Chemistry, Christian-Albrechts-Universität, Max-Eyth-Straße 2, 24118
Kiel, Germany

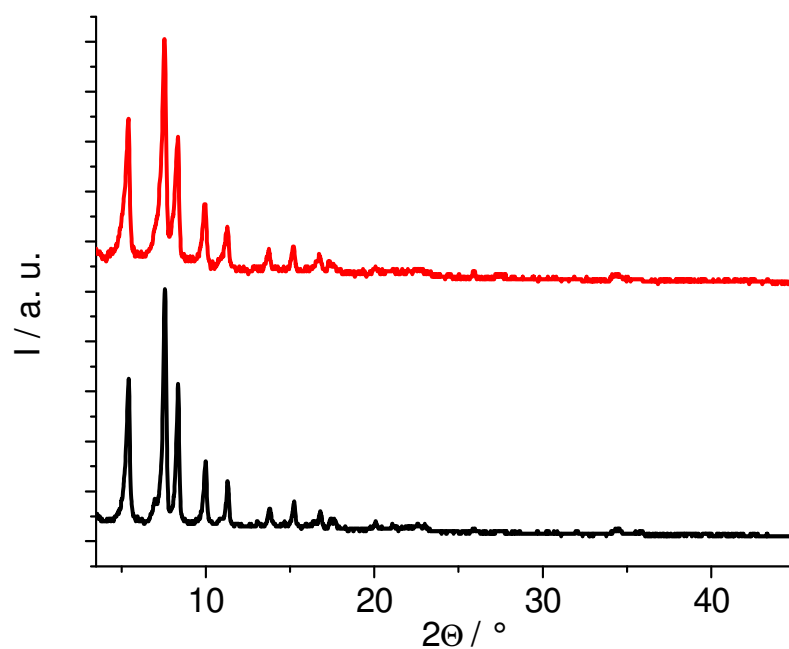


Figure S1: Powder pattern of an “as”-sample of CAU-3-BDC (black), and a sample after activation procedure and sorption measurement (red).

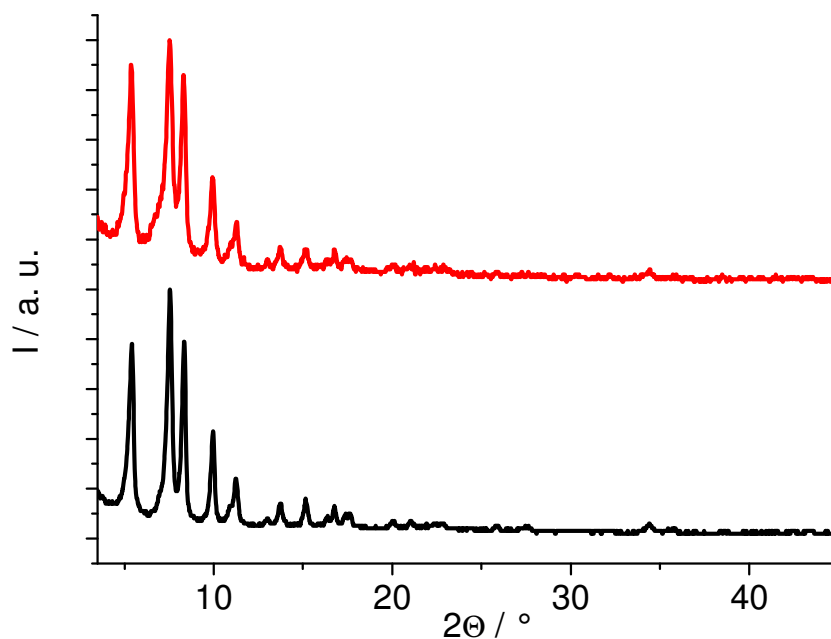


Figure S2: Powder pattern of an “as”-sample of CAU-3-BDC-NH₂ (black), and a sample after activation procedure and sorption measurement (red).

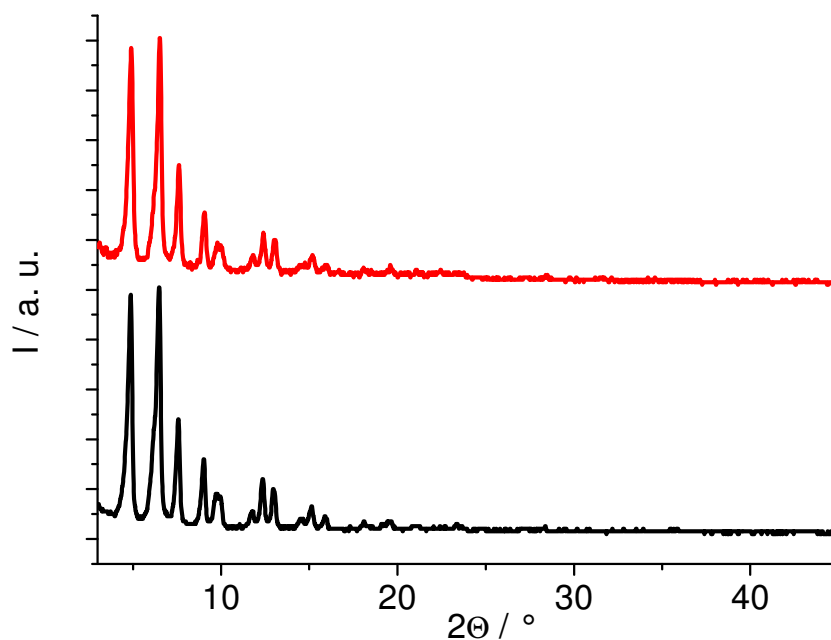


Figure S3: Powder pattern of an “as”-sample of CAU-3-NDC (black), and a sample after activation procedure and sorption measurement (red).

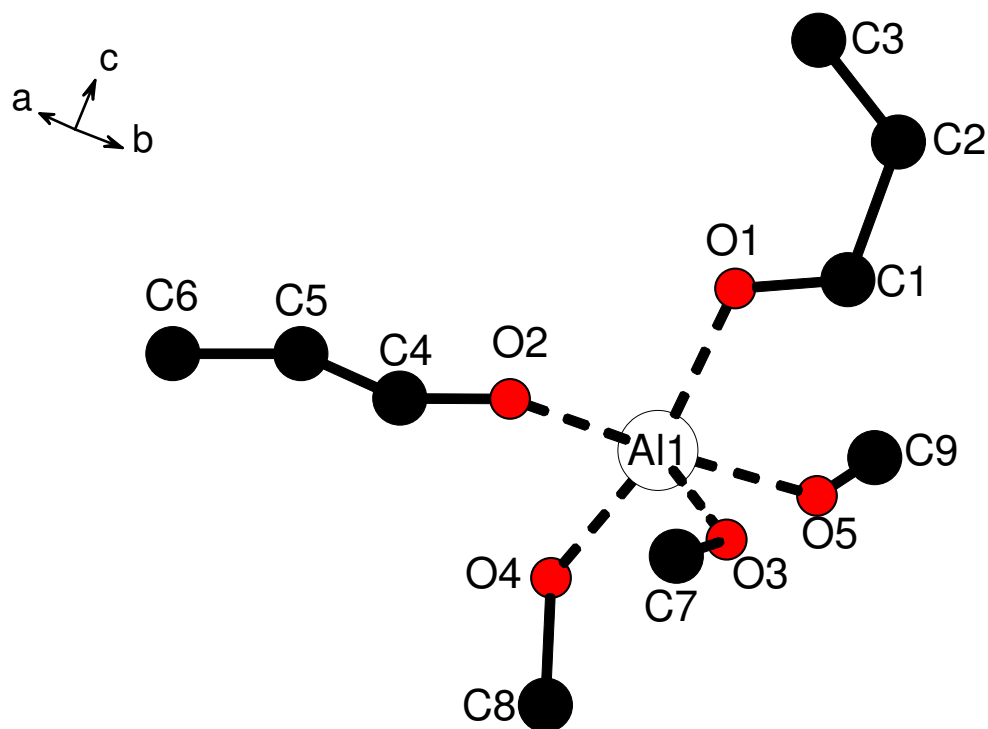


Figure S4: Asymmetric unit of CAU-3-BDC with numbering scheme.

Table S1: Selected bond lengths in CAU-3-BDC [Å].

<i>Atom 1</i>	<i>Atom 2</i>	<i>d / Å</i>			
Al1	O1	1.96(1)	C2	C3	1.39(1)
	O2	1.98(2)	O2	C4	1.23(1)
	O3	1.92(1)	C5	C6	1.37(1)
	O4	1.83(1)	O3	C7	1.47(3)
	O5	1.89(2)	O4	C8	1.46(2)
O1	C1	1.22(2)	O5	C9	1.51(3)
C1	C2	1.54(1)	C9	O5	1.51(3)

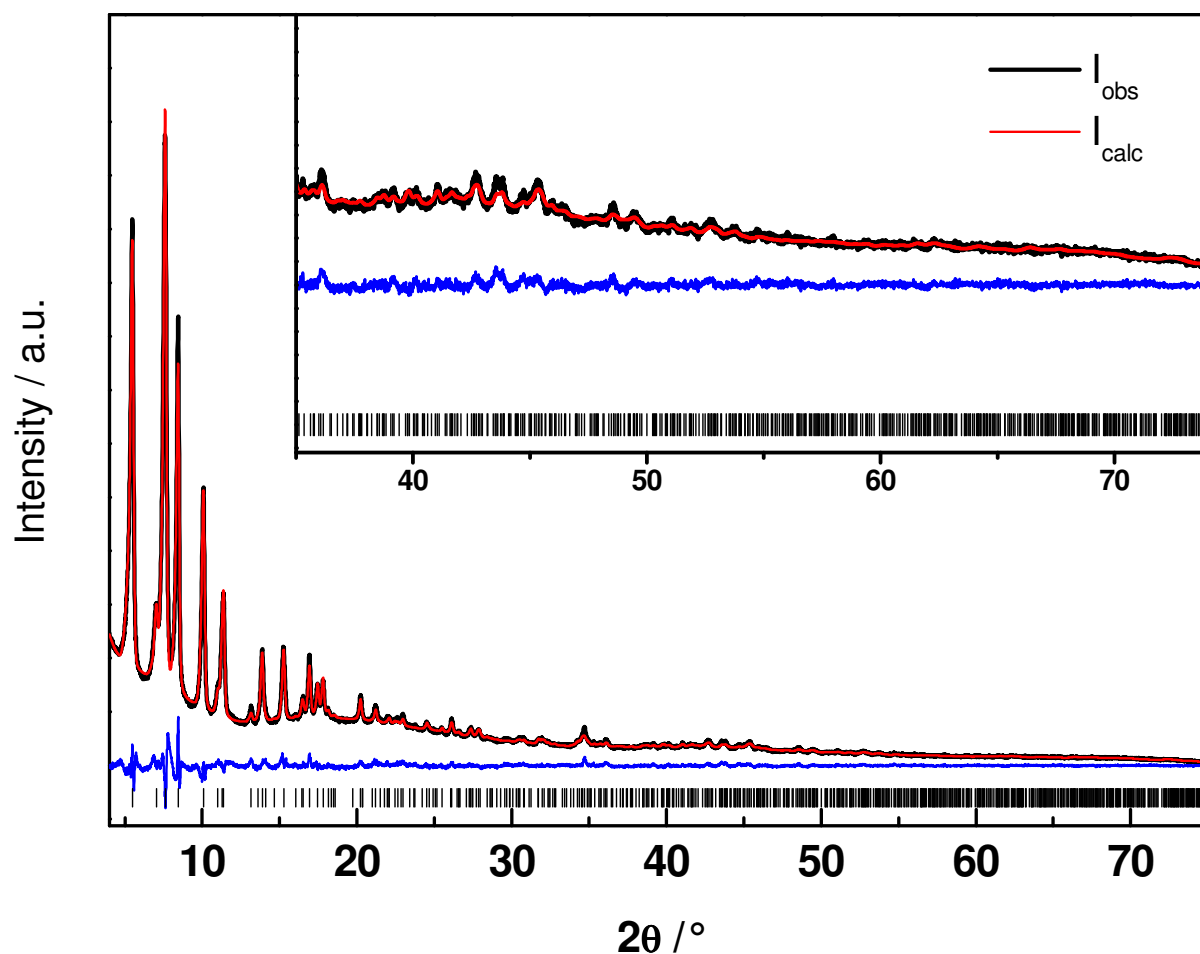


Figure S5: Final Rietveld plot of the refinement of CAU-3-BDC-NH₂. The observed intensities are shown in black, the calculated intensities are shown in red. The difference curve is shown below in blue, vertical bars mark the Bragg positions. The insert shows a plot enlargement from 35 -75 °2θ.

Table S2: Selected bond lengths in CAU-3-BDC-NH₂ [Å].

<i>Atom 1</i>	<i>Atom 2</i>	<i>d / Å</i>			
Al1	O1	1.99(2)	C3	C3	1.39(3)
	O2	1.80(2)	O2	C4	1.39(5)
	O3	1.74(2)	C4	O2	1.39(3)
	O4	1.87(3)		C5	1.53(9)
	O5	1.99(4)	C5	C6	1.33(5)
O1	C1	1.23(5)	N1	C3	1.5 (1)
C1	C2	1.60 (2)	N2	C6	1.5(1)
C2	C3	1.38 (6)			

Table S3: Atomic coordinates of CAU-3-NDC obtained from the force field calculations using Materials Studio 5.0.

<i>Symbol</i>	<i>x/a</i>	<i>y/b</i>	<i>z/c</i>
Fe1	0.25217	0.05104	0.51501
O2	0.27995	0.07593	0.55811
O3	0.32005	0.02894	0.51211
O4	0.21924	0.01434	0.47145
C5	0.26741	0.0306	0.44692
C6	0.24497	0.90175	0.2889
C7	0.24115	0.91213	0.32179
C8	0.19049	0.86321	0.34061
C9	0.14677	0.7935	0.29296
C10	0.19805	0.84234	0.27414
Fe11	0.0794	0.26015	0.48371
O12	0.11136	0.28559	0.44055
O13	0.06741	0.33477	0.4861
O14	0.04232	0.23563	0.52706
C15	0.05494	0.18882	0.54084
C16	0.5384	0.61932	0.48658
C17	0.47766	0.56072	0.48441
C18	0.47197	0.50052	0.49396
C19	0.58885	0.55858	0.50829
C20	0.59464	0.61894	0.49844
C21	0.29241	0.12878	0.57297
O22	0.31378	0.14379	0.50389
C23	0.34838	0.16804	0.47475
O24	0.18921	0.08691	0.51862
C25	0.15431	0.07905	0.54788
C26	0.31919	0.97871	0.49943
H27	0.31796	0.05445	0.456
H28	0.26201	0.06152	0.42827
H29	0.26215	0.9876	0.43382
H30	0.28504	0.94023	0.27504
H31	0.27804	0.9583	0.33253
H32	0.11043	0.7473	0.28205
H33	0.10738	0.20825	0.54132
H34	0.03412	0.14329	0.52646
H35	0.04152	0.18272	0.56665
H36	0.54135	0.665	0.47882
H37	0.43518	0.56247	0.47513
H38	0.63177	0.55735	0.51734
H39	0.31608	0.15723	0.45372
H40	0.3848	0.15121	0.47182
H41	0.3791	0.22248	0.47602
H42	0.1003	0.04938	0.54346
H43	0.16228	0.12602	0.55768
H44	0.16881	0.05767	0.56752

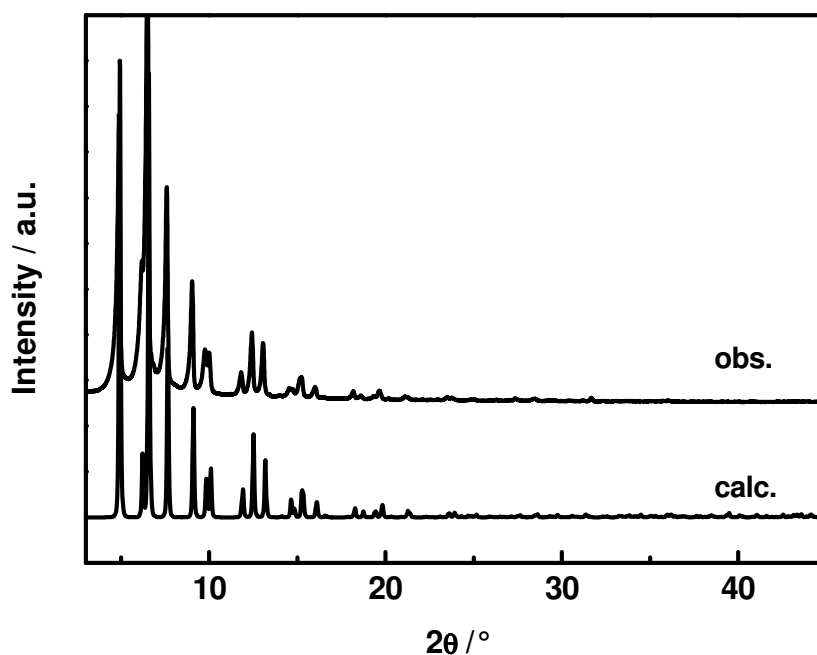


Figure S6: Calculated and observed powder pattern obtained from force field calculation.

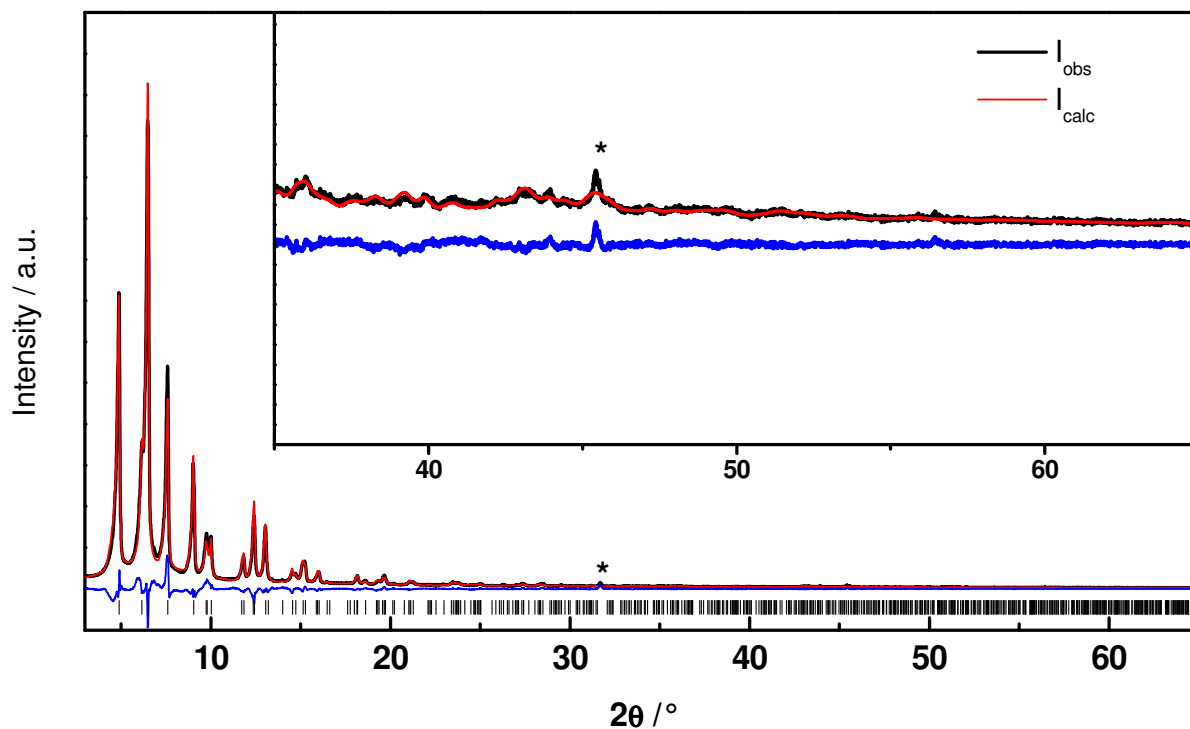


Figure S7: Final Rietveld plot of CAU-3-NDC. The asterisks correspond to NaCl as a by-product. The observed intensities are shown in black, the calculated intensities are shown in red. The difference curve is shown below in blue, vertical bars mark the Bragg positions. The insert shows a plot enlargement from 35 -65 °2θ.

Table S4: Selected bond lengths of CAU-3-NDC [Å]

Atom 1	Atom 2	d /				
			C3	C4	1.4(3)	
Al1	O1	1.8(2)	C4	C5	1.3(3)	
	O4	1.8(2)	C5	C5	1.3(4)	
	O5	1.9(2)		C6	1.5(6)	
	O6	1.9(2)	O3	C7	1.2(3)	
	O7	1.8(1)	O4	C7	1.2(2)	
	O8	2.0(3)	C7	C8	1.5(2)	
	Al2	O2	1.8(2)	C8	C9	1.3(6)
		O3	1.8(1)		C12	1.4(6)
O5		2.0(3)		C7	1.5(2)	
O6		1.9(3)	C9	C10	1.3(4)	
O7		1.9(2)	C10	C11	1.3(7)	
O8		2.0(2)	C11	C12	1.3(4)	
O1		C1	1.2(4)	O5	C13	1.4(2)
O2		C1	1.2(4)	O6	C16	1.3(4)
C1	C2	1.4(3)	O7	C14	1.3(2)	
C2	C3	1.4(1)	O8	C15	1.4(2)	
	C6	1.4(4)				

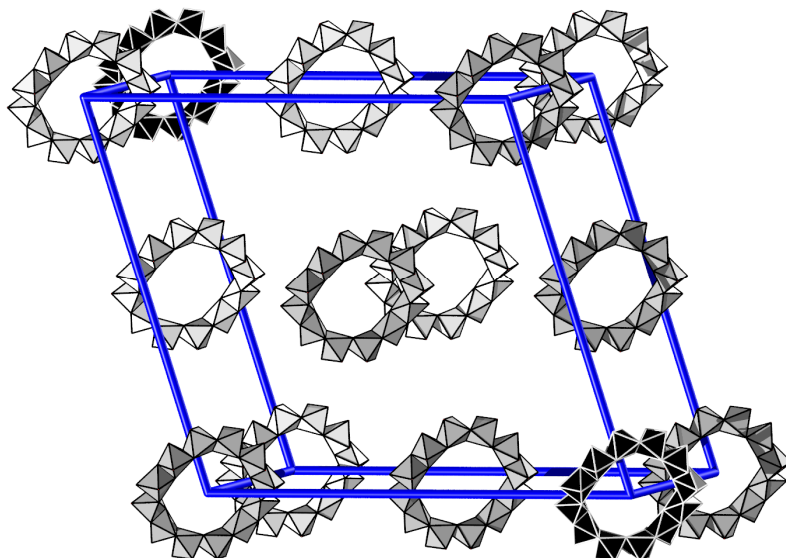


Figure S8: Pseudo-fcc-arrangement of the inorganic units. The colours emphasize the ABC-stacking.

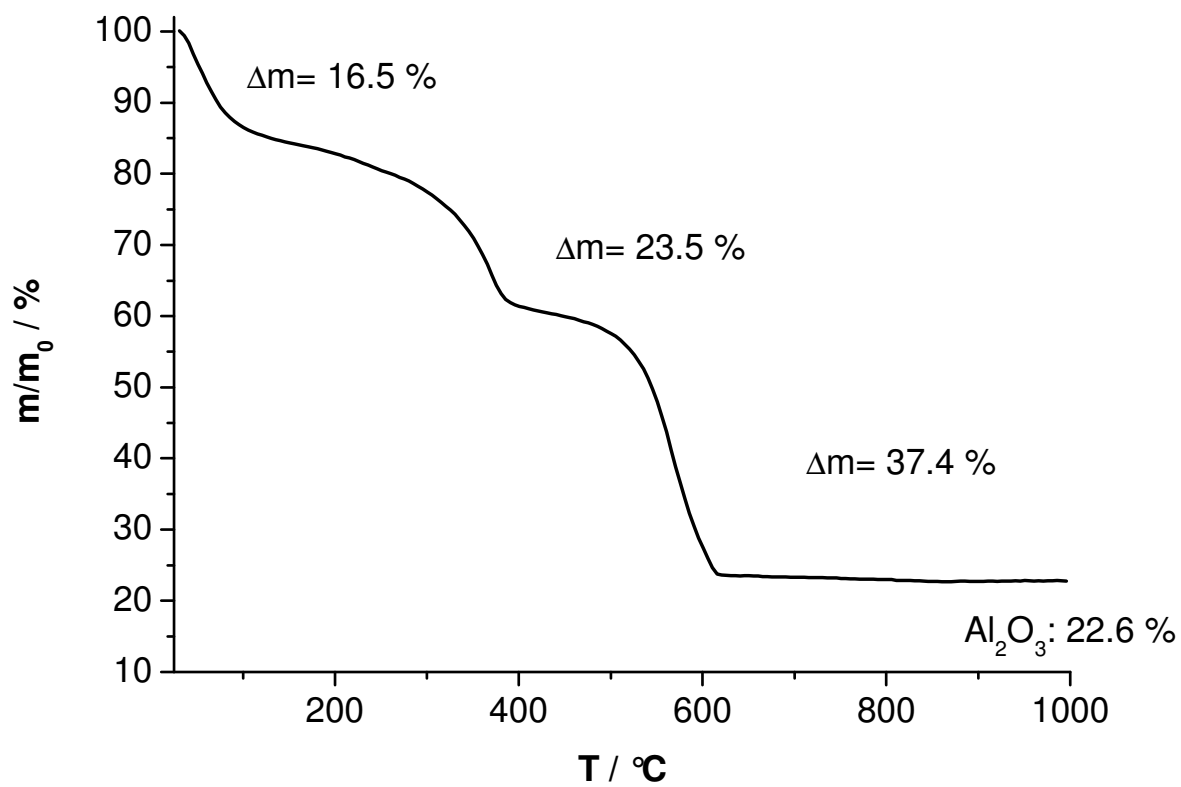


Fig. S9: TG-curve for CAU-3-BDC (1).

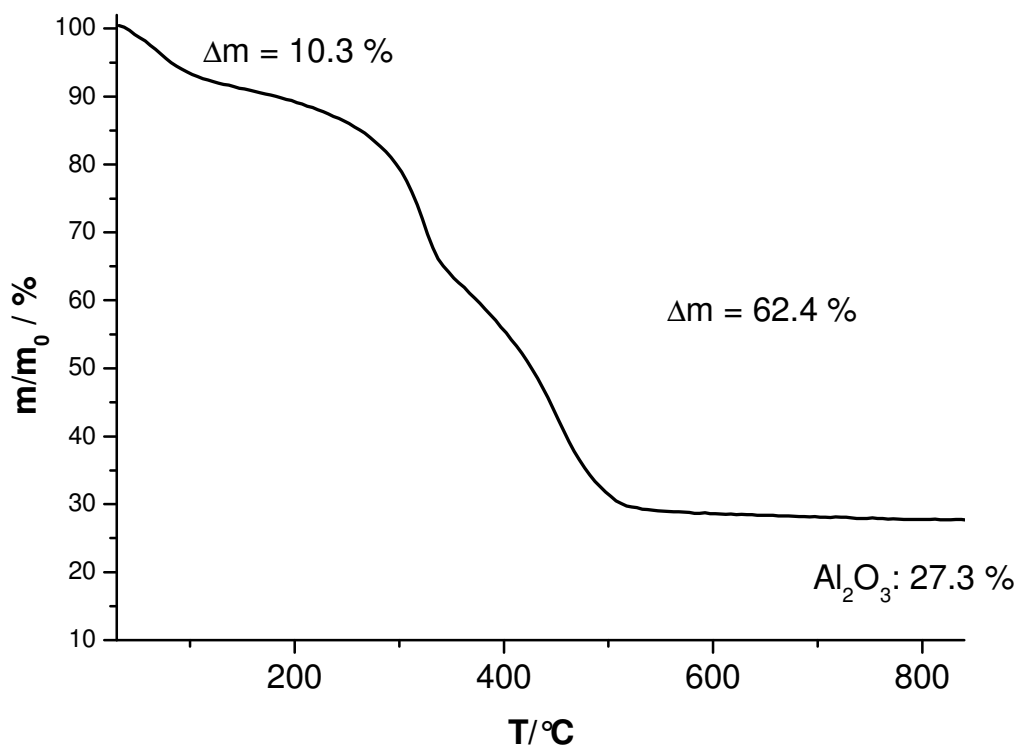


Figure S10. TG-diagram of the decomposition of CAU-3-BDC-NH₂ (**2**).

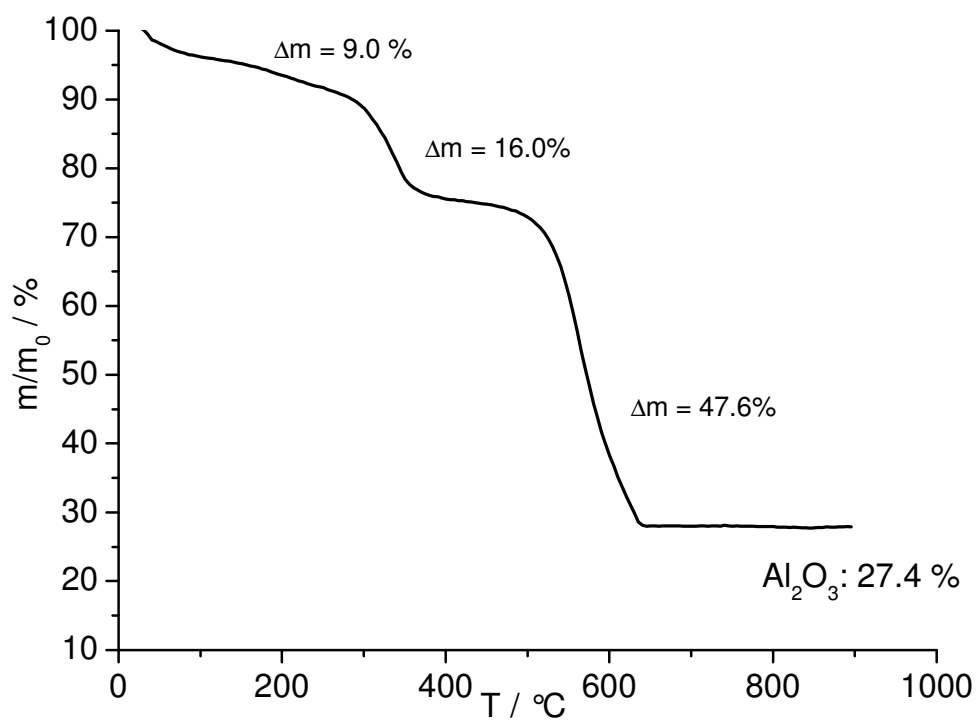


Figure S11. TG-diagram of the decomposition of CAU-3-NDC (**3**).

Table S5: Exact amounts of starting materials used in the discovery of CAU-3-BDC.

Reaktor No.	molar ratio H ₂ BDC	molar ratio AlCl ₃ *6H ₂ O	molar ratio NaOH	amount H ₂ BDC [μmol]	amount AlCl ₃ *6H ₂ O [μmol]	amount NaOH [μmol]	mass H ₂ BDC [mg]	mass AlCl ₃ *6H ₂ O [mg]	volume NaOH [μL]	volume MeOH [μL]
1	0,25	1	0,5	32	128	64	5	31	32	1368
2	0,25	1	0,75	32	128	96	5	31	48	1352
3	0,25	1	1,25	32	128	160	5	31	80	1320
4	0,25	1	1,5	32	128	192	5	31	96	1304
5	0,25	1	1,75	32	128	224	5	31	112	1288
6	0,25	1	2	32	128	256	5	31	128	1272
7	0,25	1	1	32	128	130	5	31	65	935
8	0,25	1	1	32	128	130	5	31	65	1185
9	0,25	1	1	32	128	130	5	31	65	1435
10	0,50	2	2	64	256	260	11	62	130	870
11	0,50	2	2	64	256	260	11	62	130	1120
12	0,50	2	2	64	256	260	11	62	130	1370
13	0,50	2	1	64	256	128	11	62	64	1336
14	0,50	2	1,25	64	256	160	11	62	80	1320
15	0,50	2	1,50	64	256	192	11	62	96	1304
16	0,50	2	1,75	64	256	224	11	62	112	1288
17	0,50	2	2	64	256	256	11	62	128	1272
18	0,50	2	2,5	64	256	320	11	62	160	1240
19	1	4	1,55	128	512	198	21	124	99	1301
20	1	4	2,18	128	512	279	21	124	140	1260
21	1	4	2,81	128	512	360	21	124	180	1220
22	1	4	3,43	128	512	439	21	124	220	1180
23	1	4	4,06	128	512	520	21	124	260	1140
24	1	4	4,68	128	512	599	21	124	300	1100

A new Al-MOF based on an unique column-shaped inorganic building unit exhibiting strongly hydrophilic sorption behaviour

Helge Reinsch^a, Bartosz Marszałek^b, Julia Wack^c, Jürgen Senker^c, Barbara Gil^b, Norbert Stock^a

^a *Institute of Inorganic Chemistry, Christian-Albrechts-Universität Kiel, Max-Eyth-Straße 2, 24118 Kiel, Germany; E-mail: stock@ac.uni-kiel.de*

^b *Faculty of Chemistry, Jagiellonian University, ul. Ingardena 3, 30-060 Kraków, Poland*

^c *Inorganic Chemistry I, Universität Bayreuth, Universitätsstraße. 30, 95447 Bayreuth, Germany*

Supplementary Information

S1: Materials and Methods

S2: High-Throughput Investigations

S3: Data for Al-MIL-68

S4: Details about Synthesis and Characterisation of CAU-6

S5: XRPD-data and structure determination of CAU-6

S6: Solid-State NMR-spectra of CAU-6

S7: Temperature-dependent IR-spectra

S8: Crystallographic Information

S1: Materials and Methods

Chemicals. $\text{AlCl}_3 \cdot 6\text{H}_2\text{O}$ (Riedel-de Haen, $\geq 99\%$), terephthalic acid (H_2BDC) ABCR, 98 %), 2-aminoterephthalic acid ($\text{H}_2\text{BDC-NH}_2$, Fluka, $\geq 98\%$), 2-propanol (BASF, purum) were used as purchased. The synthesis was performed in custom made Teflon inserts in steel autoclaves with a volume of 30 mL. X-ray powder diffraction data for the cell refinement was collected on a Panalytical Xpert Highscore diffractometer in reflection geometry. Temperature dependent X-ray powder diffraction data was measured on a STOE Stadi-P diffractometer in transmission geometry equipped with an image plate detector (IPDS) using $\text{Cu-K}\alpha_1$ radiation. The XRPD-synchrotron data was collected at beamline G3 at the DORIS-accelerator ring at DESY, Hamburg with a wavelength of 1.54295 Å in transmission geometry. Therefore, the sample was transferred into a 0.5 mm capillary. One dimensional solid state Magic-Angle-Spinning Nuclear Magnetic Resonance spectra were acquired on the APOLLO console (Tecmag) at the magnetic field of 7.05 T (Magnex). The one dimensional ^{27}Al MAS NMR spectra was recorded using the 2 μs rf pulse ($\pi/6$ flipping angle), 8 kHz spinning speed, and 1000 scans with acquisition delay 1 s. The ^{27}Al MQMAS spectrum was measured with a Bruker Avance II 300 spectrometer operating at 7.05 T with a resonance frequency for ^{27}Al of 78.2045 MHz. The sample was packed in a ZrO_2 rotor with an outer diameter of 2.5 mm and mounted in a standard triple resonance MAS probe. The experiment was carried out at a rotation frequency of 25 kHz, using a three-pulse sequence² with nutation frequencies of 110 kHz for the excitation (2.2 μs) and conversion (1.2 μs) and 16 kHz for the selective 90° pulse. The coherence pathway ($0 \rightarrow \pm 3 \rightarrow -1$) was selected via a cog-wheel phase cycle $\text{COG60}\{11,1,0;30\}$.³ During t_1 and t_2 a cw(continuous wave)-decoupling with a nutation frequency of 45 kHz was applied, while the recycle delay was set to 1s. Two dimensional FTIR spectra were recorded with a Bruker Tensor 27 spectrometer equipped with an MCT detector and working with the spectral resolution of 2 cm^{-1} . For the IR experiment a silicon wafer was covered by a thin layer of the material by evaporating on its surface a few drops of the CAU-6 dispersion in methanol. The thermogravimetric analysis was carried out using a NETSCH STA 409 CD analyzer. The samples were heated in Al_2O_3 crucibles at a rate of 4 K min^{-1} under a flow of air (75 ml/min). The TG data were corrected for buoyancy and current effects. Sorption experiments were performed using a Belsorp-max instrument (BEL JAPAN INC.). The molecular modelling software used was Materials Studio 5.0.

² J.P. Amoureux, C. Fernandes, S. Steuernagel, *J. Magn. Reson. A*, 1996, **123**, 116.

³ A. Jerschow, R.J. Kumar, *J. Magn. Reson.*, 2003, **160**, 59.

S2: High-Throughput Investigations

CAU-6 and Al-MIL-68 were initially obtained from one single HT-experiment. The synthesis was carried out in a Teflon-lined HT-reactor using microwave-assisted heating (Anton Paar Synthos 3000 multimode microwave unit employing a 4x24MG5 rotor). The reaction temperature was set to 120 °C and the reaction time was 4 h. The composition of the reaction mixtures is given in Tab. S1. The observed tendencies and products are represented in Fig. S1.

Tab. S1: Composition of the reaction mixtures in the initial HT-experiment.

Reactor No	linker	n (linker) [mmol]	n (AlCl ₃ ·6H ₂ O) [mmol]	m (linker) [mg]	m (AlCl ₃ ·6H ₂ O) [mg]	V 2-propanol [μL]
1	H ₂ BDC-NH ₂	0.066	0.033	12	8	1000
2	H ₂ BDC-NH ₂	0.066	0.066	12	16	1000
3	H ₂ BDC-NH ₂	0.066	0.099	12	24	1000
4	H ₂ BDC-NH ₂	0.066	0.132	12	32	1000
5	H ₂ BDC-NH ₂	0.066	0.199	12	48	1000
6	H ₂ BDC-NH ₂	0.066	0.265	12	64	1000
7	H ₂ BDC-NH ₂	0.132	0.066	24	16	1000
8	H ₂ BDC-NH ₂	0.132	0.132	24	32	1000
9	H ₂ BDC-NH ₂	0.132	0.199	24	48	1000
10	H ₂ BDC-NH ₂	0.132	0.265	24	64	1000
11	H ₂ BDC-NH ₂	0.132	0.397	24	96	1000
12	H ₂ BDC-NH ₂	0.132	0.530	24	128	1000
13	H ₂ BDC	0.055	0.055	9	13	1000
14	H ₂ BDC	0.055	0.110	9	27	1000
15	H ₂ BDC	0.055	0.221	9	53	1000
16	H ₂ BDC	0.055	0.442	9	107	1000
17	H ₂ BDC	0.110	0.110	18	27	1000
18	H ₂ BDC	0.110	0.221	18	53	1000
19	H ₂ BDC	0.110	0.442	18	107	1000
20	H ₂ BDC	0.110	0.662	18	160	1000
21	H ₂ BDC	0.221	0.221	37	53	1000
22	H ₂ BDC	0.221	0.442	37	107	1000
23	H ₂ BDC	0.221	0.883	37	213	1000
24	H ₂ BDC	0.221	1.104	37	266	1000

Thus $\text{H}_2\text{BDC-NH}_2$ was employed in two different absolute concentrations in six different molar ratios $\text{H}_2\text{BDC-NH}_2 : \text{AlCl}_3 \cdot 6\text{H}_2\text{O}$. H_2BDC was employed in three different absolute concentrations in four different molar ratios $\text{H}_2\text{BDC} : \text{AlCl}_3 \cdot 6\text{H}_2\text{O}$.

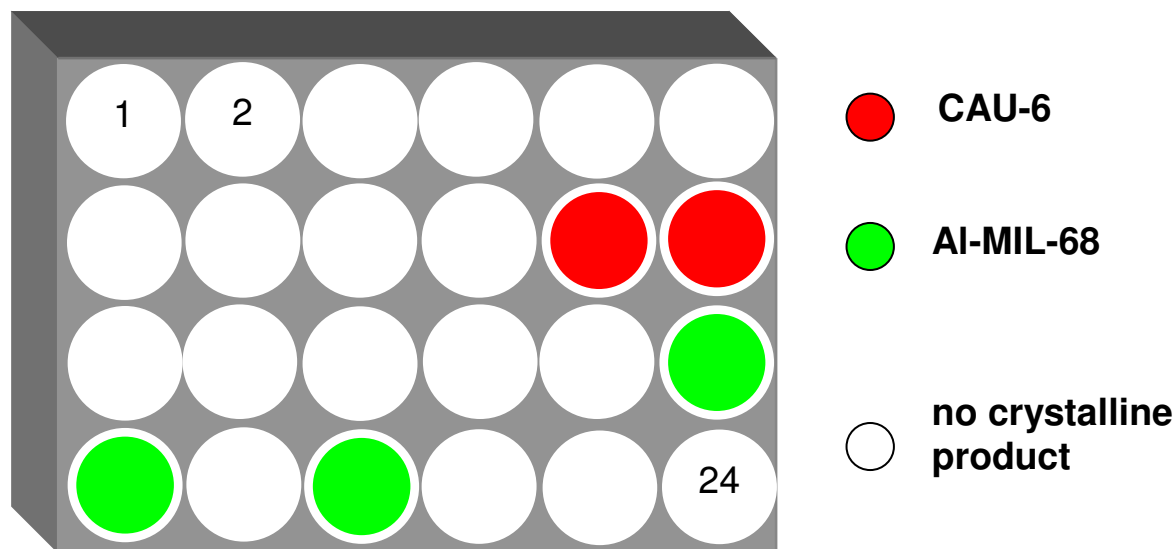


Fig. S1: Products that were obtained from the initial HT-experiment.

Only in few vessels, the formation of a crystalline product was observed. CAU-6 is only formed at high concentrations of $\text{H}_2\text{-BDC-NH}_2$ and if $\text{AlCl}_3 \cdot 6\text{H}_2\text{O}$ is used in large excess (molar ratio $\text{H}_2\text{BDC-NH}_2 : \text{AlCl}_3 \cdot 6\text{H}_2\text{O} < 1 : 3$). AI-MIL-68 is obtained from reaction mixtures with medium and high concentrations of H_2BDC and if at least equal amounts of $\text{AlCl}_3 \cdot 6\text{H}_2\text{O}$ are used (molar ratio $\text{H}_2\text{BDC} : \text{AlCl}_3 \cdot 6\text{H}_2\text{O} < 1 : 1$). Subsequent optimization and upscaling of the reaction conditions led to the synthesis procedures given in S3 and S4.

S3: Data for Al-MIL-68

For the up-scaled synthesis 300 mg (1.8 mmol) terephthalic acid, 2.2 g $\text{AlCl}_3 \cdot 6\text{H}_2\text{O}$ (9.1 mmol) and 10 mL 2-propanol were heated in a Teflon-lined autoclave in 4 h to 130°C , held at this temperature for 12 h and cooled down to room temperature during 4 h. The product exhibits the MIL-68-topology, as shown by XRPD-measurements (Fig. S2).

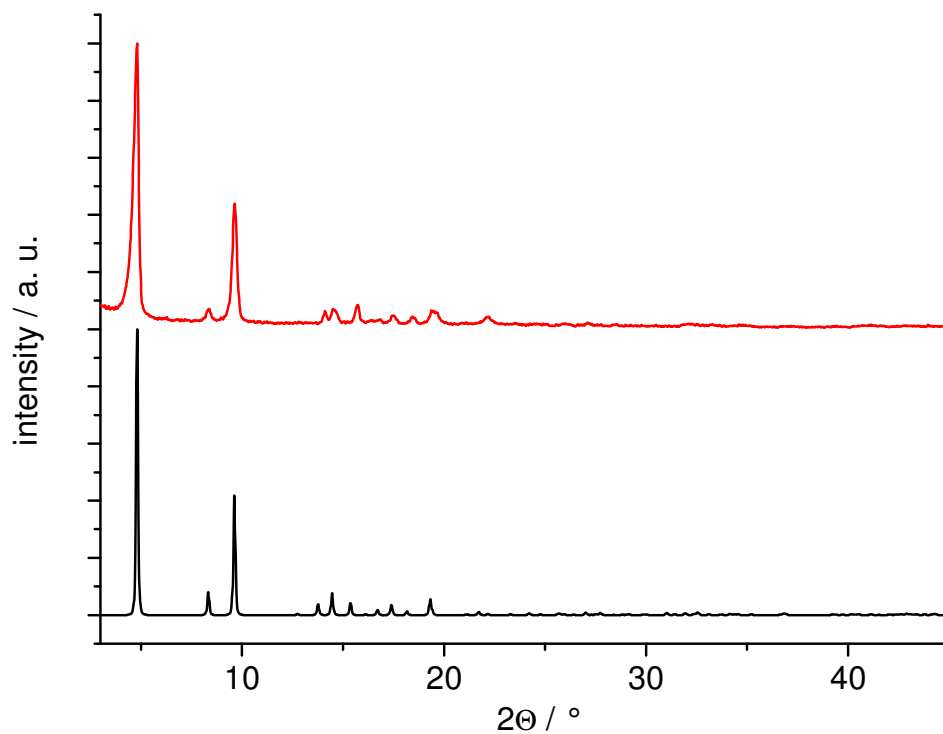


Fig. S2: Powder pattern of the obtained Al-MIL-68 (red line), in comparison with simulated data (black line).⁴

⁴ K. Barthelet, J. Marrot, G. Férey, D. Riou, *Chem. Commun.* 2004, 520.

S4: Details of Synthesis and Characterisation of CAU-6

Optimized synthesis. 150 mg (0.83 mmol) H₂BDC-NH₂, 800 mg (3.32 mmol) AlCl₃·6H₂O and 5 mL 2-propanol were transferred into a Teflon-lined autoclave and mixed thoroughly. It should be mentioned that the synthesis yields the title compound only if Teflon-lined reactors are used, while the reaction in glass vessels result in X-ray amorphous products. The mixture was heated slowly during twelve hours to 120 °C, held at this temperature for twelve hours and cooled to room temperature over twelve hours. The filtered product was treated in 300 mL water by stirring for twelve hours, filtered again and dried under ambient conditions. This washing procedure was repeated four more times, and the final product was obtained as yellow, microcrystalline powder (Fig. S5). During the washing process, the molar ratio of Al:Cl was decreased from 1:1 to 13:6, as measured by EDX-analysis. Furthermore, the cell parameters are slightly shifted (Fig S3, S4). Elemental analysis of the final product: C 25.2 %, H 4.9 %, N 3.2 %. Theoretical values based on the sum formula [Al₁₃(OH)₂₇(H₂O)₆(BDC-NH₂)₃Cl₆(C₃H₇OH)₆]: 24.9 %, H 5.0 %, N 2.1 %.

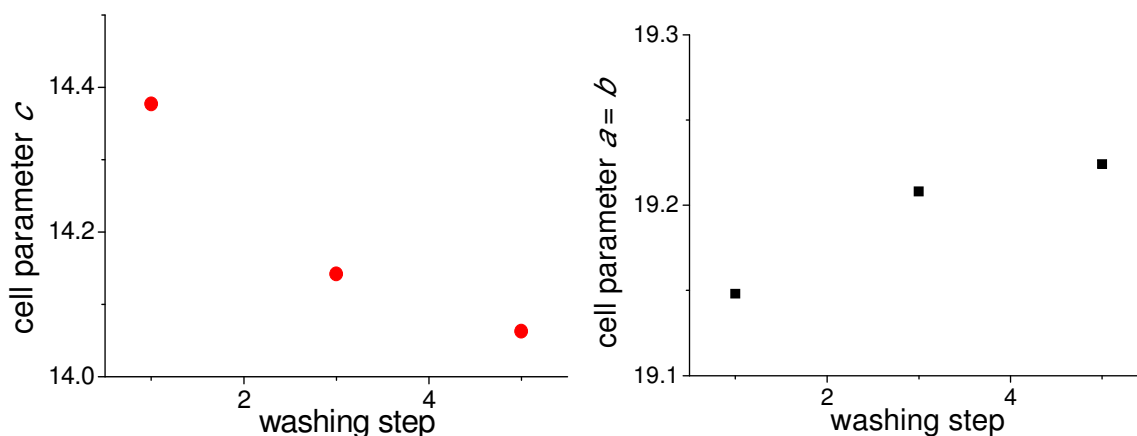


Fig. S3: Cell parameters for *c* (left) and *a = b* (right), as obtained by the le Bail-Fit method. Error bars lie within the symbols.

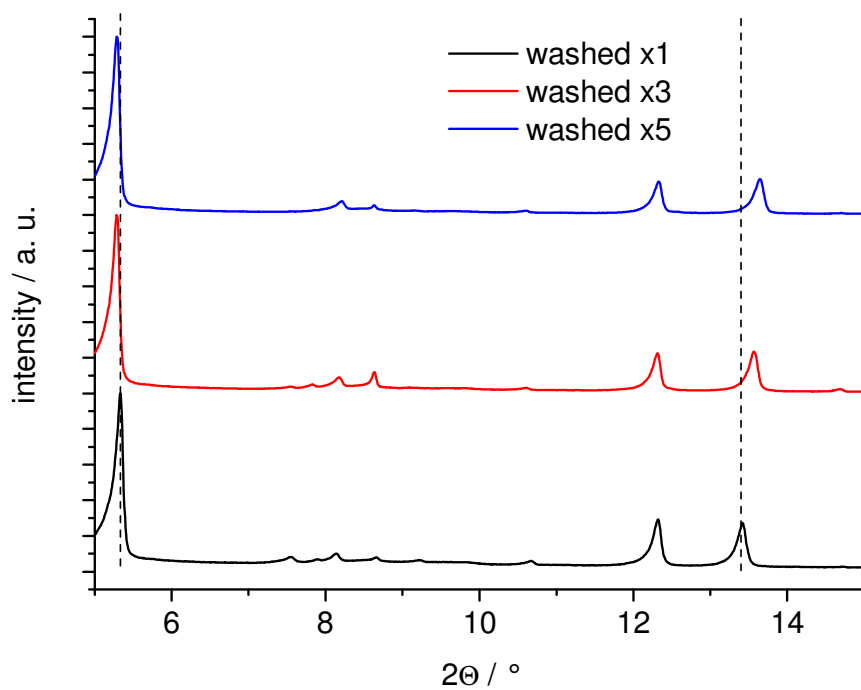


Fig. S4: Low-angle region of the powder patterns measured after washing 1, 3 and 5 times. The dashed lines were inserted to guide the eye.

SEM micrographs

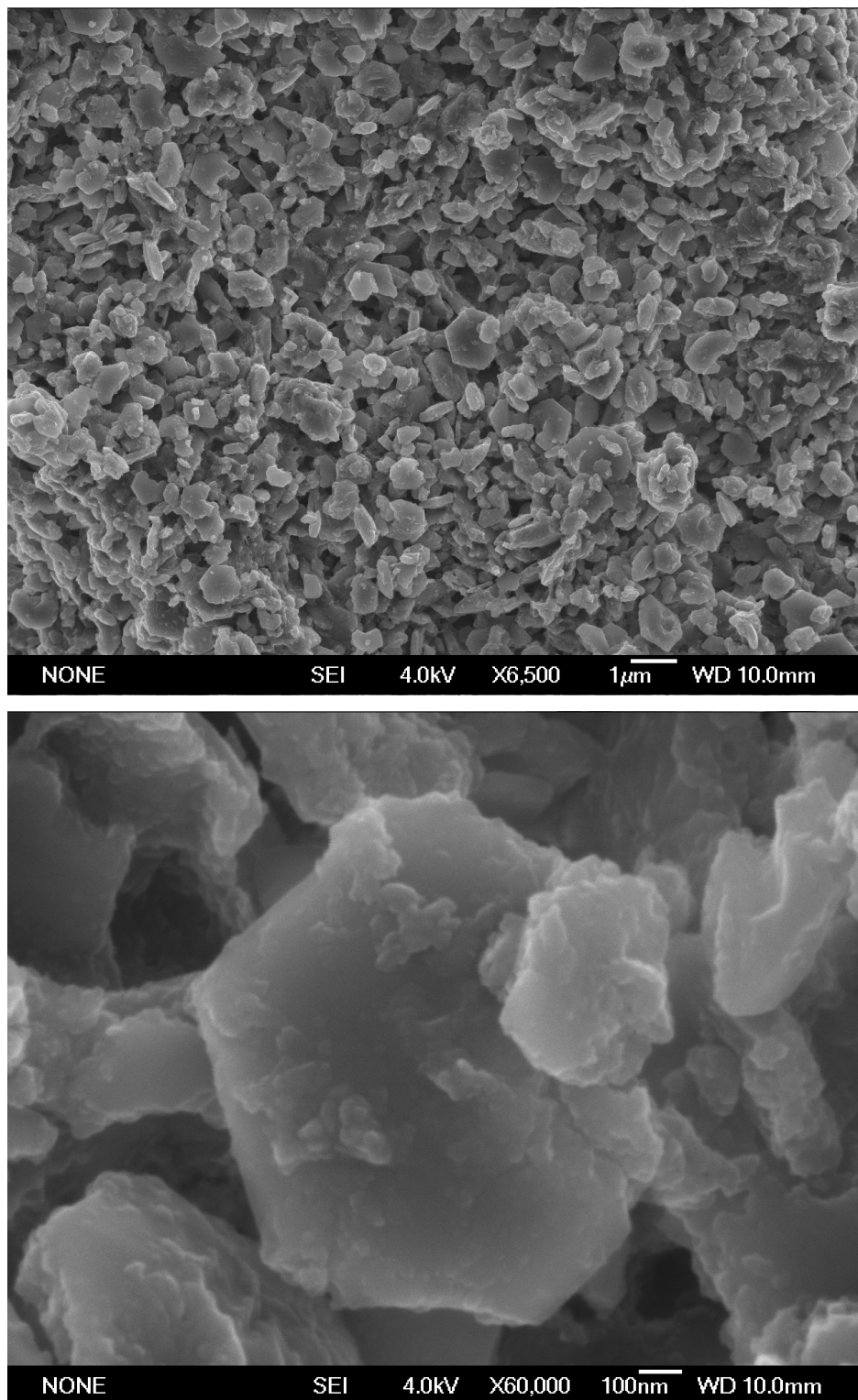


Fig. S5: SEM-micrographs of CAU-6, showing the microcrystalline habitus and the preferentially hexagonal crystal shape.

Thermal Stability. The TG-curve in Fig. S6 shows three steps. During the first weight loss up to ~ 180 °C, adsorbed solvent is removed from the channels of the MOF, which gives rise to the measured porosity. Two additional steps lead to the decomposition of the framework by further removal of solvent molecules and decomposition of the linker molecules. The measured weight losses (first step: 8 %; second and third step: 58 %, residual mass: 34 %) are in good agreement with the expected value based on the sum formula (expected residual mass: 32.7 %).

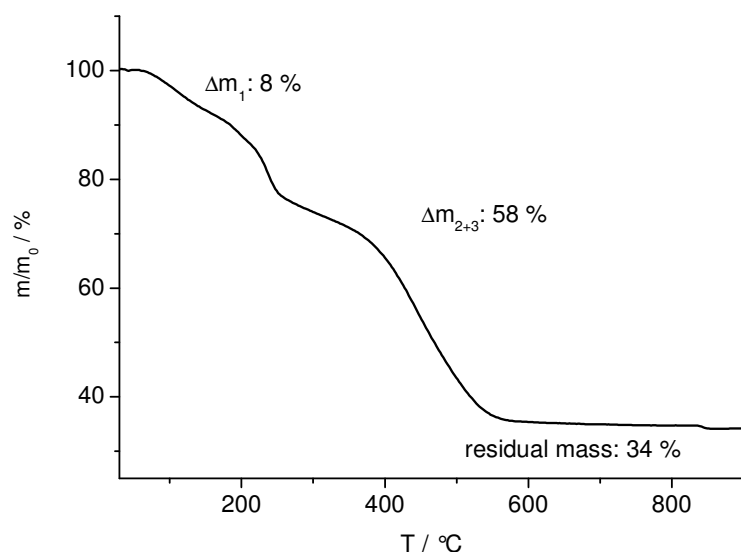


Fig. S6: TG-curve for CAU-6 measured in air with a heating rate of 4 K/min.

The temperature-dependent XRPD-data (Fig. S7) shows an increasing intensity of the peaks up to ~ 240 °C, due to the partial removal of occluded solvent. It further confirms the decomposition above 240 °C. The higher stability compared to TG-data is due to the measurement in a capillary.

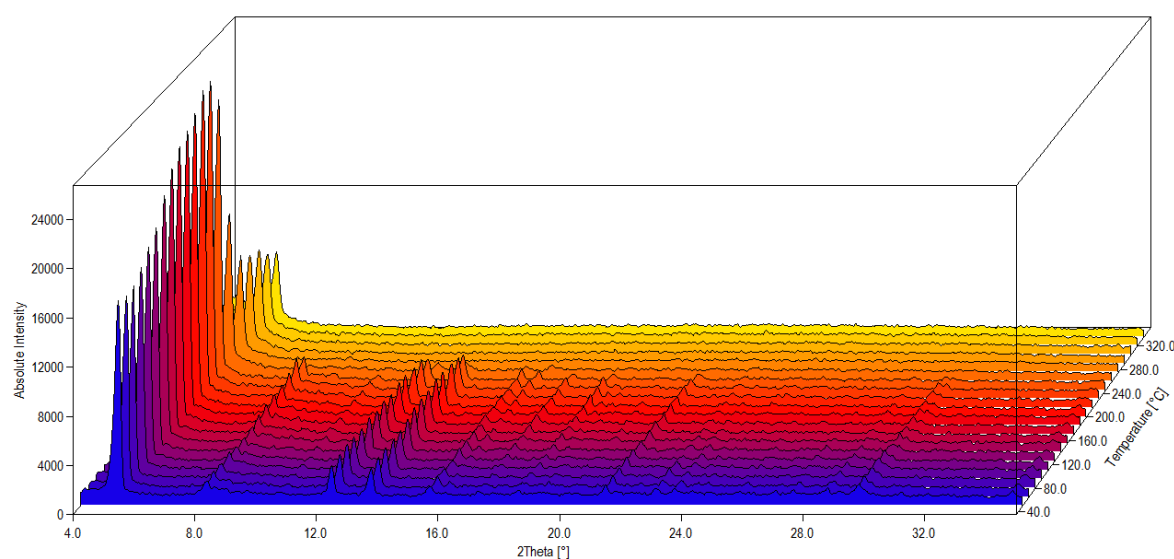


Fig. S7: TDXRD-data for CAU-6 measured in a capillary under air.

Sorption Properties

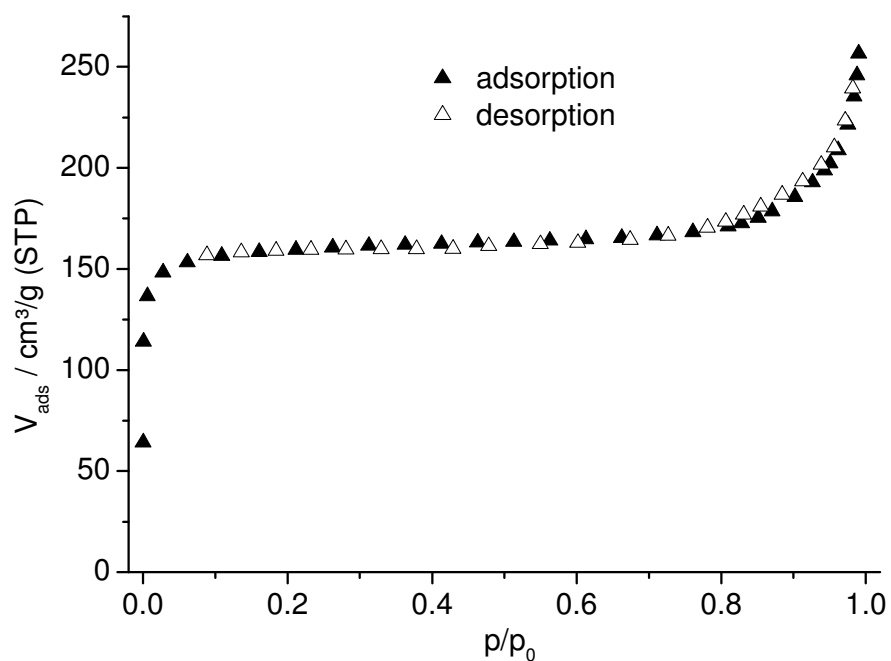


Fig. S8: Nitrogen sorption isotherm measured at 77 K after activation of the MOF at 130 °C in vacuum (0.1 mbar).

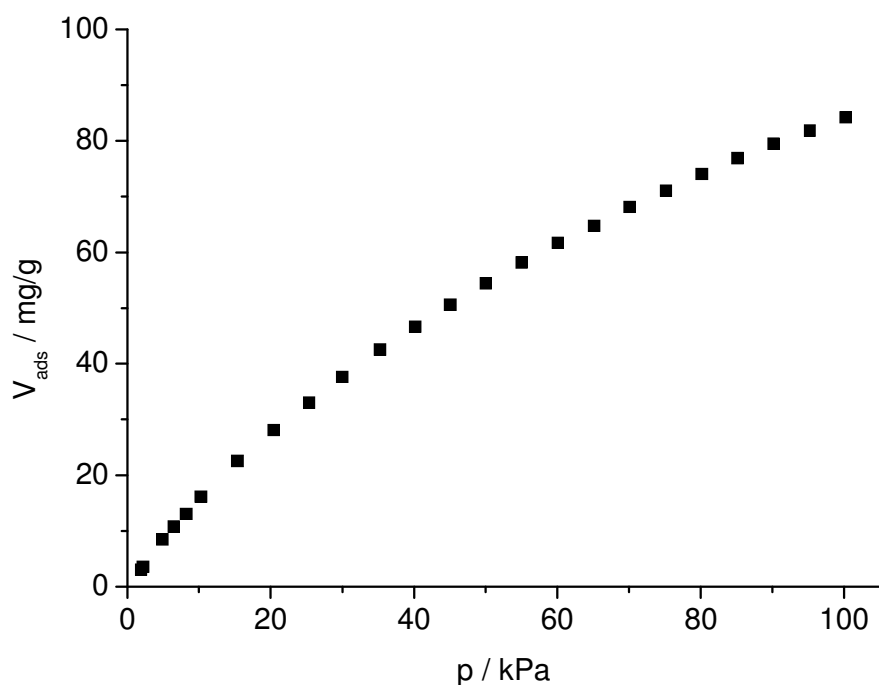


Fig. S9: CO₂ adsorption isotherm measured at 298 K after activation of the MOF at 130 °C in vacuum (0.1 mbar).

S5: XRPD-data and structure determination of CAU-6

Structure Determination. The XRPD-data for structure determination was recorded at the beamline G3 at the DORIS accelerator Ring at the DESY, Hamburg. The MOF was filled into a 0.5 mm capillary and measured with a wavelength of 1.54295 Å. Indexing of the powder pattern resulted in a hexagonal/trigonal cell with the refined cell parameters $a = b = 19.2275(3)$ Å and $c = 14.0741(3)$ Å (Fig. S10). The extinction conditions were suitable for the space groups $P31c$, $P-31c$, $P-62c$, $P6_3mc$ and $P6_3/mmc$.

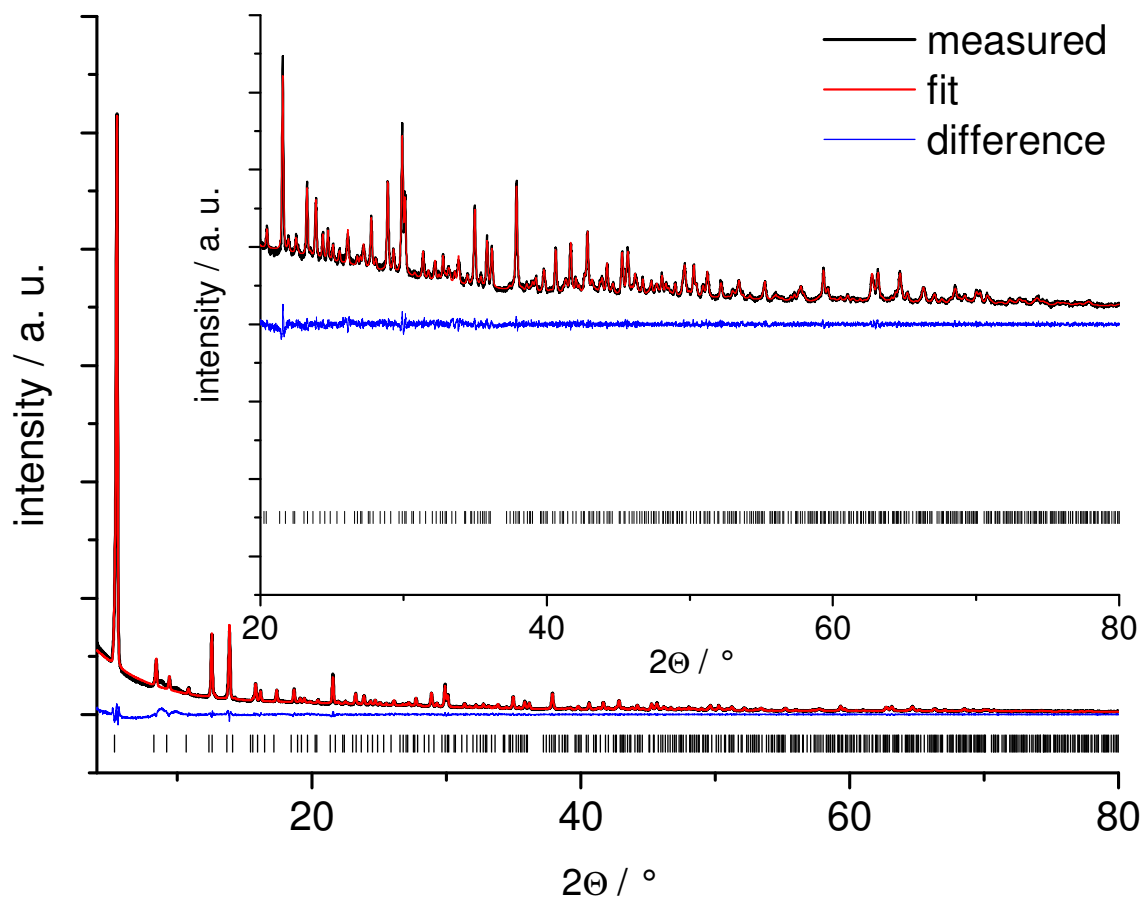


Fig. S10: Le-Bail-fit of CAU-6 in the space group $P6_3/mmc$. The obtained figures of merit are $R_{WP} = 5.2 \%$ and $R_{exp} = 2.5 \%$.

The structure solution by direct methods⁵ resulted in plausible structural fragments in the space groups $P-31c$ and $P-62c$. The inorganic building units could be unambiguously identified. The structures obtained in $P-31c$ and $P-62c$ were found to exhibit the higher

⁵ A. Altomare, M. Cavalli, R. Calandro, C. Cuocci, C. Giacovazzo, A. Gagliardi, A. G. G. Moliterni, R. Rizzi, EXPO2004. Program for Solving Crystal Structures from Powder Data by direct Methods, 2004.

symmetry of the space group $P6_3/mmc$, as tested with Material Studio⁶ and Platon.⁷ Residual electron density indicated, that the carboxylate groups were coordinated to the bridging AlO_6 -dimers between the heptanuclear cores. Therefore, the linker molecules were inserted at the corresponding positions and were structurally optimized using force-field methods, employing Material Studio. We tried to complete this crystallographic model by Fourier-synthesis using TOPAS⁸, but none of the remaining fragments (chloride ions, solvent molecules) could be located, even if structural models of lower symmetry were employed. We interpret this as a sign of disorder of the remaining structural fragments. Therefore, the attempted Rietveld refinement did not result in satisfying figures of merit. The measured pattern and a simulated one of the framework model are compared in Fig. S11.

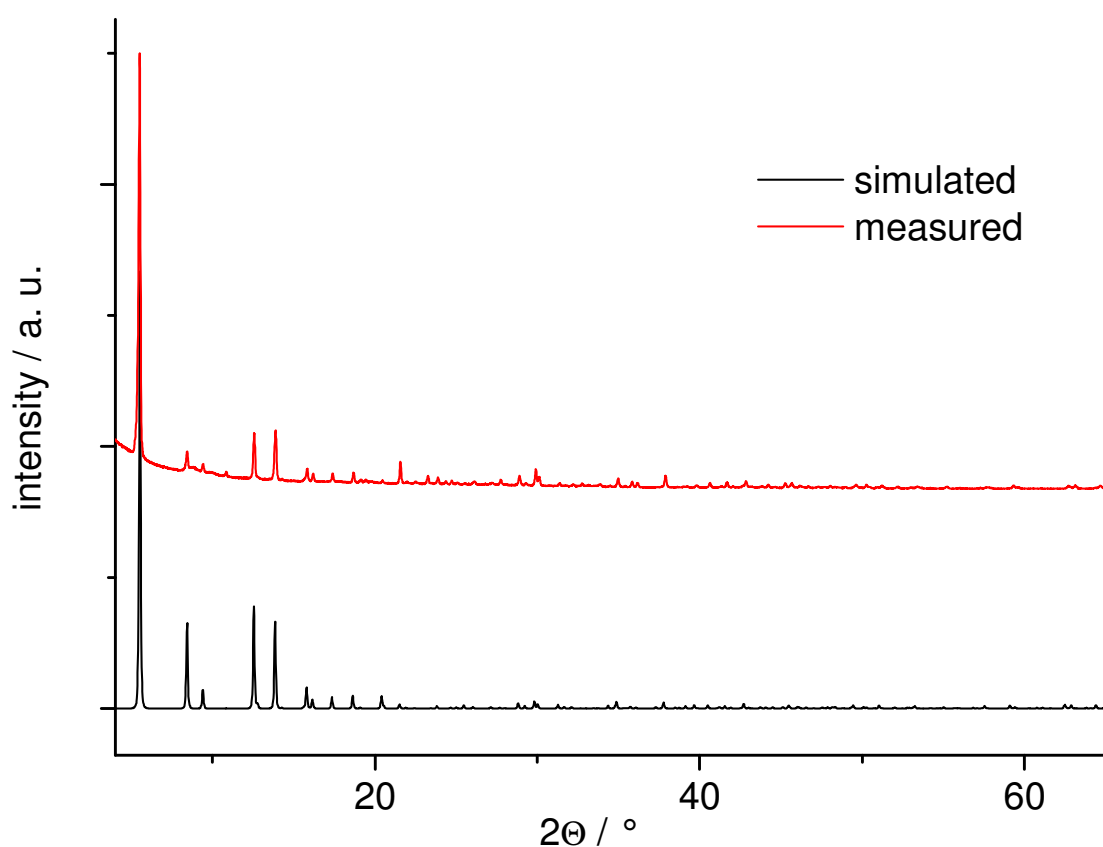


Fig. S11: Comparison of the simulated and the measured XRPD-pattern ($\lambda = 1.54295 \text{ \AA}$).

The structural model is given in .cif-format at the end of this document. The asymmetric unit is shown in Fig. S12 and the relevant bond distances are summarized in Tab. S1.

⁶ Materials Studio Version 5.0, Accelrys Inc., San Diego, CA, 2009.

⁷ A.L. Spek, PLATON, A Multipurpose Crystallographic Tool, Utrecht University, Utrecht, The Netherlands, 2010.

⁸ Topas Academics 4.2, Coelho Software, 2007.

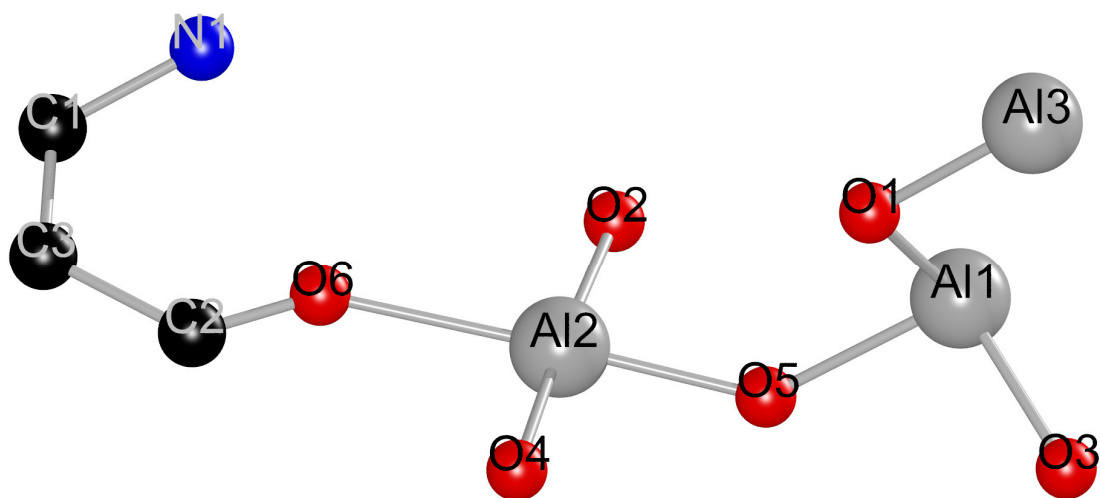


Fig. S12: Asymmetric unit of CAU-6 with numbering scheme as in Tab. S2.

Tab. S2: Bond distances in CAU-6.

Al1	O3	1.8691
	O5	1.8909
	O1	2.0229
Al2	O5	1.7646
	O2	1.9336
	O4	1.9985
	O6	2.0397
Al3	O1	1.7750
O6	C2	1.1544
C1	C1	1.3971
	C3	1.4114
	N1	1.4281
C2	C3	1.4803
N1	C1	1.428

Construction principle of the structure of CAU-6 starting from Al₁₃-clusters

The Al₁₃ cluster as observed in [Al₁₃(OH)₂₄(H₂O)₂₄]Cl₁₅·13H₂O⁹ can be used to construct the framework of CAU-6. Taking into account that bridging between the Al³⁺ ions is exclusively accomplished by OH⁻ ions (presented as red spheres), condensation of the [Al₁₃(OH)₂₄(H₂O)₂₄]¹⁵⁺ ions lead to columns of the composition [Al₁₃(OH)₂₇(H₂O)₁₈]¹²⁺ (Fig. S13). Water molecules are presented as blue spheres. Twelve water molecules per formula unit are formally replaced by bridging dicarboxylate ions which leads to the final composition [Al₁₃(OH)₂₇(H₂O)₆(O₂CR)₆]⁶⁺. Since the dicarboxylate ions BDC-NH₂²⁻ are interconnecting the inorganic columns the final framework composition [Al₁₃(OH)₂₇(H₂O)₆(BDC-NH₂)₃]⁶⁺ is expected (Fig. S14). This is in agreement with the observed formula.

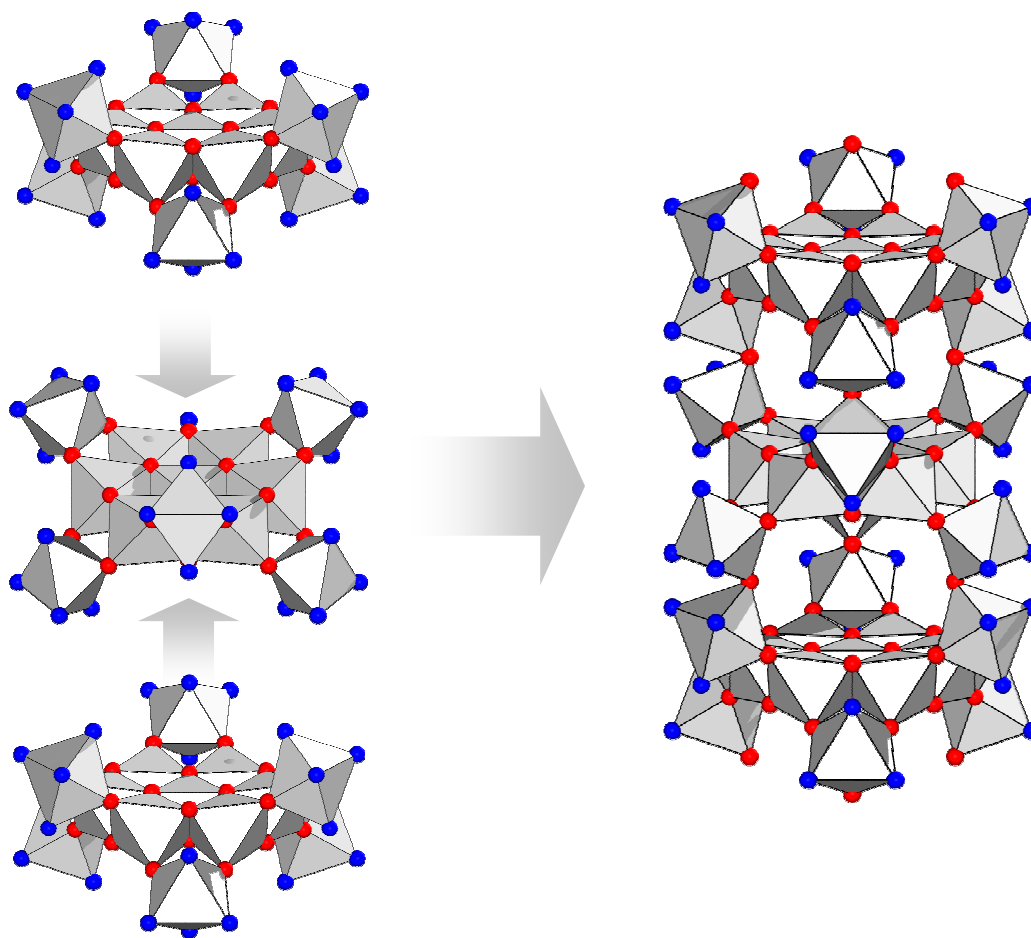


Fig. S13: Schematic representation of the formal condensation of Al₁₃-cluster into the column observed in CAU-6.

⁹ W. Seichter, H. Mögel, P. Brand, D. Salah, *Eur. J. Inorg. Chem.* 1998, **6**, 795.

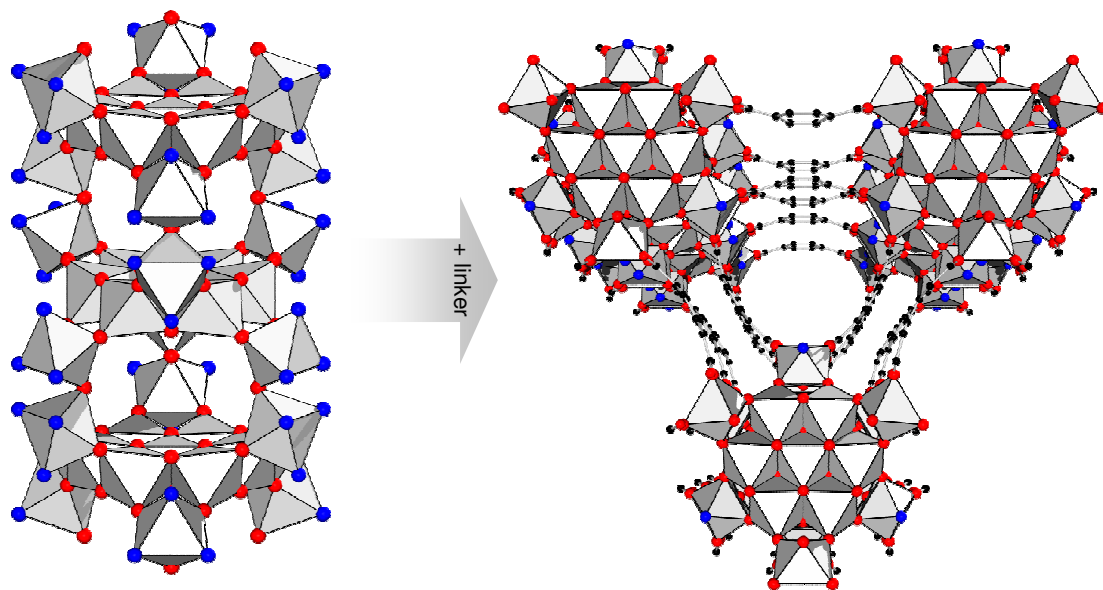


Fig. S14: Schematic representation of the interconnection of columns by linker molecules.

S6: Solid-State NMR-spectra of CAU-6

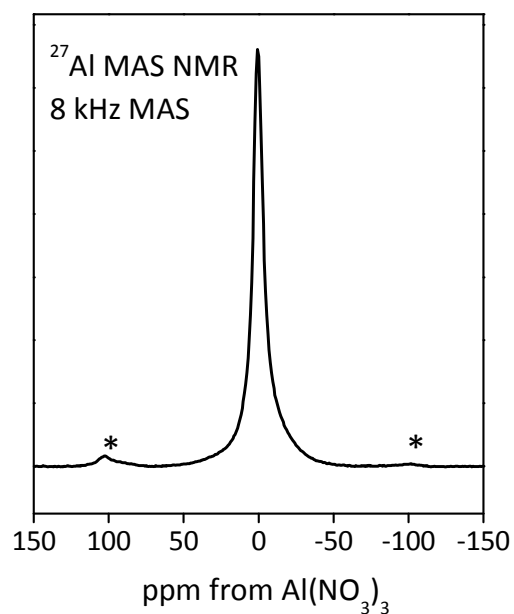


Fig. S15: Solid-state ^{27}Al -MAS-NMR spectrum of CAU-6. The spinning side-bands are marked with asterisks.

The one dimensional ^{27}Al -MAS-NMR spectrum shows that all Al atoms are located in octahedral environment of oxygen atoms in the first coordination sphere. The symmetry of the second coordination sphere is not influencing the symmetry of the AlO_6 units.

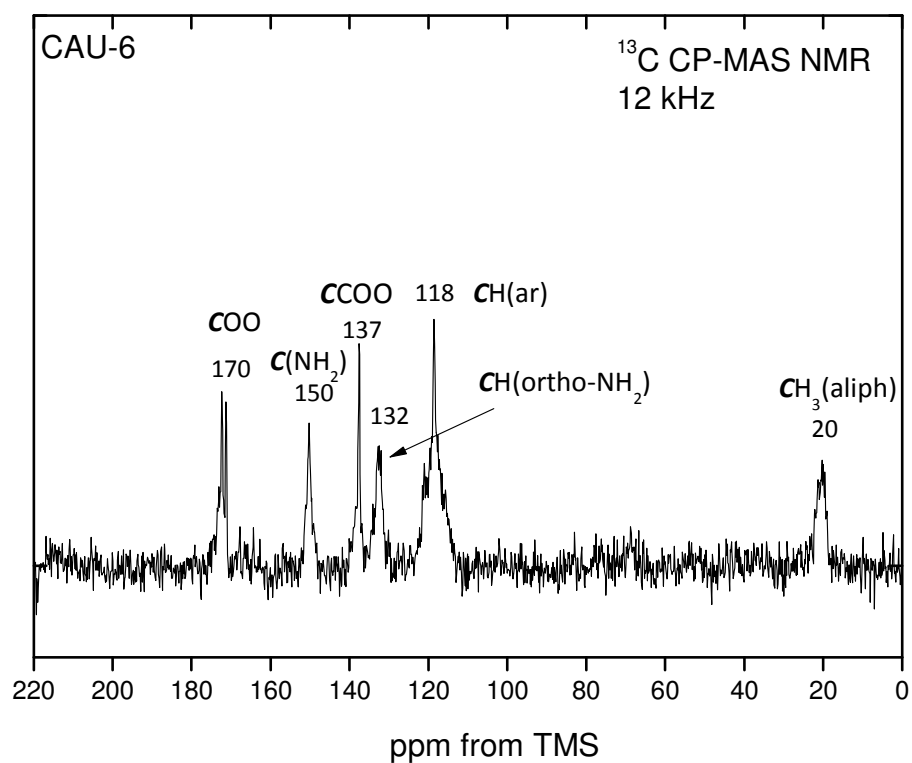
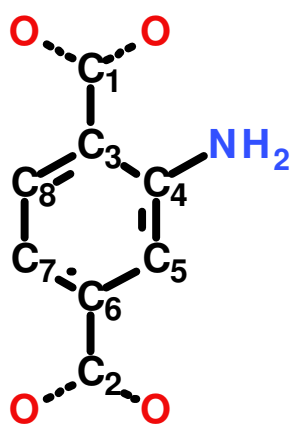


Fig. S16: Solid-state ^{13}C - ^1H -CP-MAS-NMR spectrum of CAU-6.

The ^{13}C - ^1H -CP-MAS-NMR spectrum was recorded to characterise the aminoterephthalate ions incorporated in CAU-6. The signals can be assigned in table S3.



C-atom	Chemical shift (ppm)
C1, C2	170
C4	150
C3, C6	137
C5	132
C7, C8	118

The signal at 20 ppm can be assigned to a CH₃ group from aliphatic species and is due to isopropanol molecules that were not removed by extensive washing.

1D ²⁷Al spectra are broadened due to the strong quadrupolar coupling, hence it is not possible to distinguish between different signals with similar chemical shift. 2D ²⁷Al MQMAS spectrum helps to overcome this problem because it provides the opportunity to separate the CSA interaction from the quadrupolar interaction. The spectrum reveals two different signals caused by different surroundings of aluminium atoms in the structure.

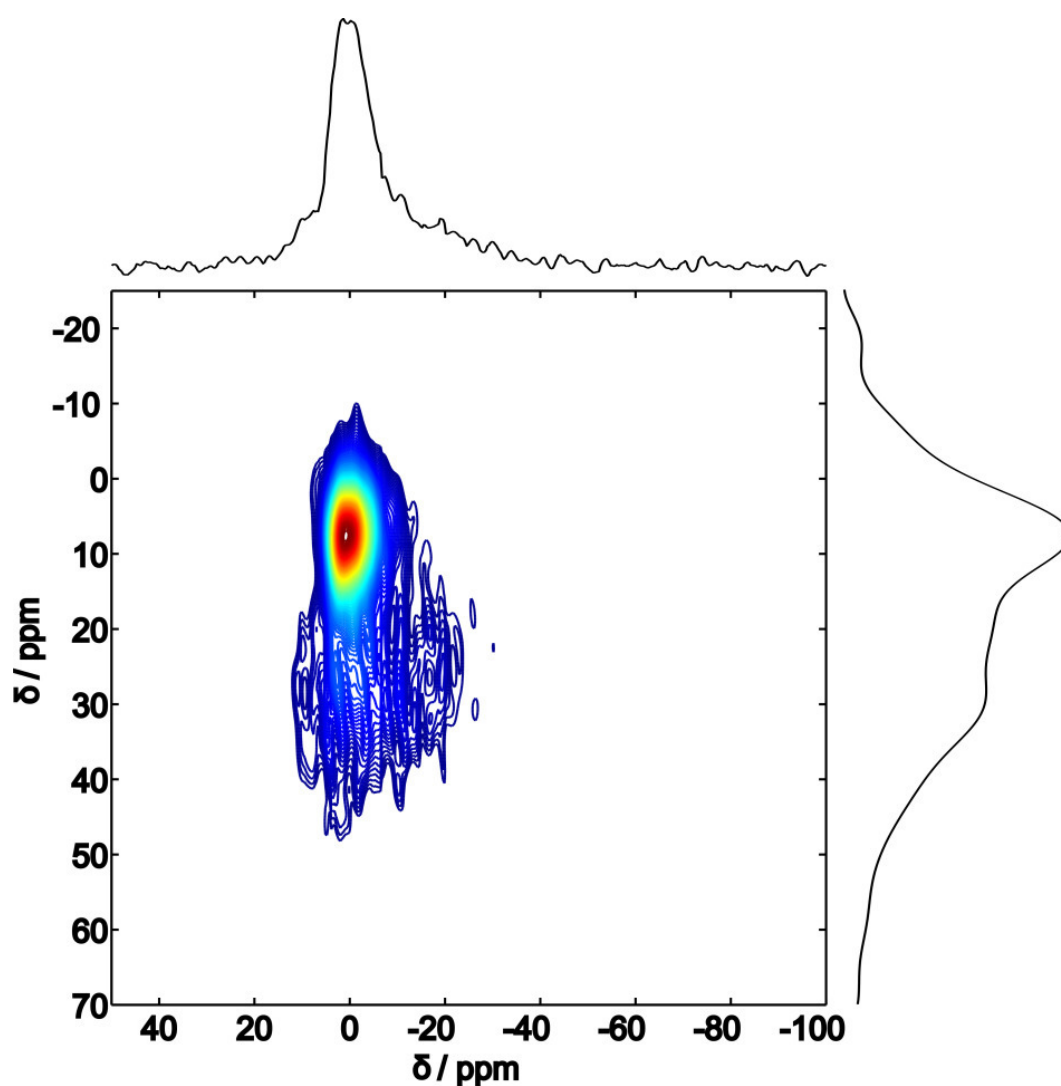


Fig. S17: Two dimensional ²⁷Al MQMAS spectrum of CAU-6.

S7: Temperature-dependent IR-spectra

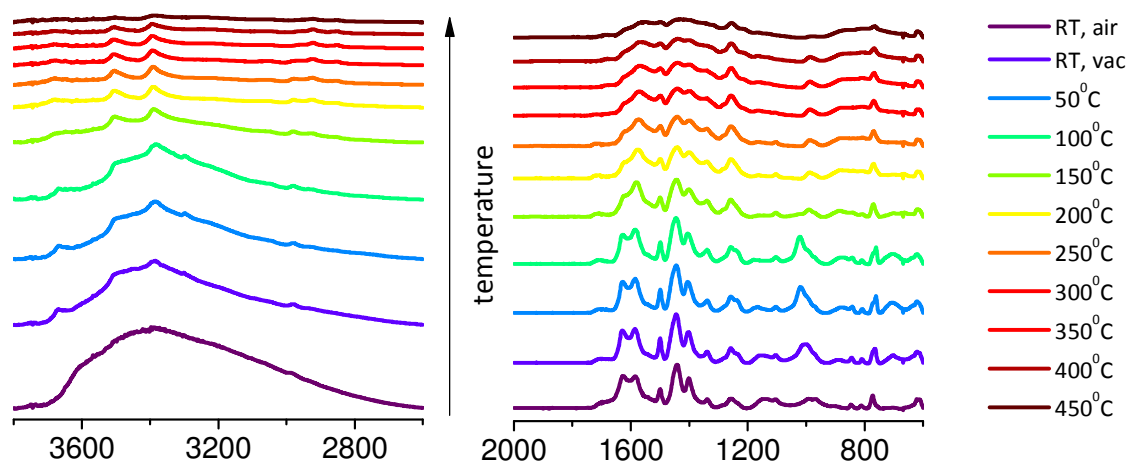


Fig. S18: Temperature-dependent IR spectra of CAU-6. All spectra (except for marked as RT) at 50°C.

The IR spectra show that it is not possible to remove all solvent and/or water molecules from the pores without damaging the framework by thermal activation. The intensity of the broad absorption around 3400 cm^{-1} , characteristic of hydrogen-bonded OH groups, is substantially decreased by applying vacuum and further lowered by heating of the sample (in vacuum). This band can be assigned both to hydrogen-bonded water and propanol. During heating, the OH-band of hydroxyl-groups at 3670 cm^{-1} and the NH_2 -bands at 3500 cm^{-1} and 3380 cm^{-1} gain intensity, but already at 150 °C, the peaks in the spectrum are flattened. Decrease of the intensities occurs especially in the region 1800 – 1300 cm^{-1} where C-C- and C=O vibrations are observed and marks the beginning decomposition of the framework. The complete removal of the solvent and water molecules, which is achieved at ~250 °C based on the IR-spectra, the TG-experiments and the TDXRPD-data, thus substantially damages the framework structure. It can be observed that water molecules are removed at lower temperature region: decrease of the intensity of the band at 3400 cm^{-1} is accompanied by the increase of the C-O band at 1025 cm^{-1} .¹⁰ This means that water-propanol interactions are replaced by propanol-propanol interactions and finally, with further temperature increase, by propanol desorption (disappearance of the 1025 cm^{-1} band).

¹⁰ J.J. Max, C. Chapados, *J. Chem. Phys.*, 2009, **130**, 124513.

S8: Crystallographic Information File

```
data_CAU-6
_symmetry_space_group_name_H-M 'P63/MMC'
_symmetry_Int_Tables_number 194
_symmetry_cell_setting hexagonal
loop_
_symmetry_equiv_pos_as_xyz
  x,y,z
  -y,x-y,z
  -x+y,-x,z
  -x,-y,z+1/2
  y,-x+y,z+1/2
  x-y,x,z+1/2
  y,x,-z
  x-y,-y,-z
  -x,-x+y,-z
  -y,-x,-z+1/2
  -x+y,y,-z+1/2
  x,x-y,-z+1/2
  -x,-y,-z
  y,-x+y,-z
  x-y,x,-z
  x,y,-z+1/2
  -y,x-y,-z+1/2
  -x+y,-x,-z+1/2
  -y,-x,z
  -x+y,y,z
  x,x-y,z
  y,x,z+1/2
  x-y,-y,z+1/2
  -x,-x+y,z+1/2
_cell_length_a 19.2275
_cell_length_b 19.2275
_cell_length_c 14.0741
_cell_angle_alpha 90.0000
_cell_angle_beta 90.0000
_cell_angle_gamma 120.0000
loop_
_atom_site_label
_atom_site_type_symbol
_atom_site_fract_x
_atom_site_fract_y
_atom_site_fract_z
_atom_site_U_iso_or_equiv
_atom_site_adp_type
_atom_site_occupancy
Al1 Al 0.15864 0.15864 0.00000 0.02533 Uiso 1.00
Al2 Al 0.30662 0.15331 0.12799 0.02533 Uiso 1.00
Al3 Al 0.00000 0.00000 0.00000 0.02533 Uiso 1.00
O1 O 0.09506 0.04753 0.05707 0.02533 Uiso 1.00
O2 O 0.35854 0.17927 0.00510 0.02533 Uiso 1.00
```

O3	O	0.09789	0.19578	0.06295	0.02533	Uiso	1.00
O4	O	0.24522	0.12261	0.25000	0.02533	Uiso	1.00
O5	O	0.24672	0.19169	0.08346	0.02533	Uiso	1.00
O6	O	0.37641	0.11062	0.18232	0.02533	Uiso	1.00
C1	C	0.49691	0.06648	0.16360	0.02533	Uiso	1.00
C2	C	0.40052	0.09594	0.25000	0.02533	Uiso	1.00
C3	C	0.46280	0.07214	0.25000	0.02533	Uiso	1.00
N1	N	0.46119	0.06657	0.07467	0.02533	Uiso	0.25

Supporting Information

A new aluminum-based microporous metal-organic framework: Al(BTB) (BTB = 1,3,5-benzenetrisbenzoate)*

Helge Reinsch, Martin Krüger, Norbert Stock*

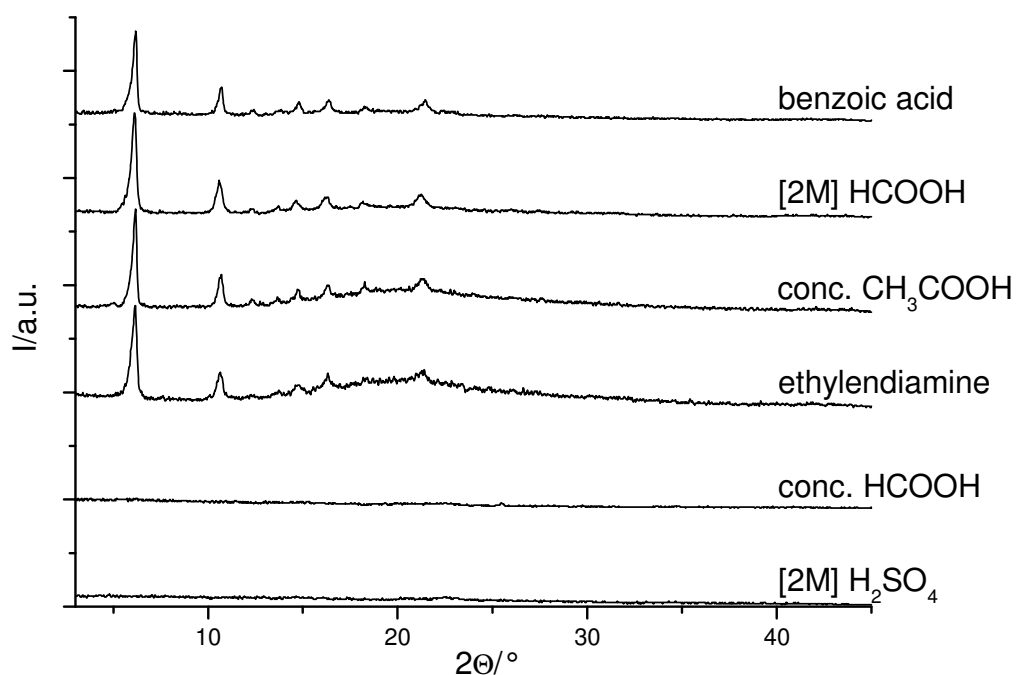


Figure S1: Comparison of the influence of additives on the formation of CAU-4.

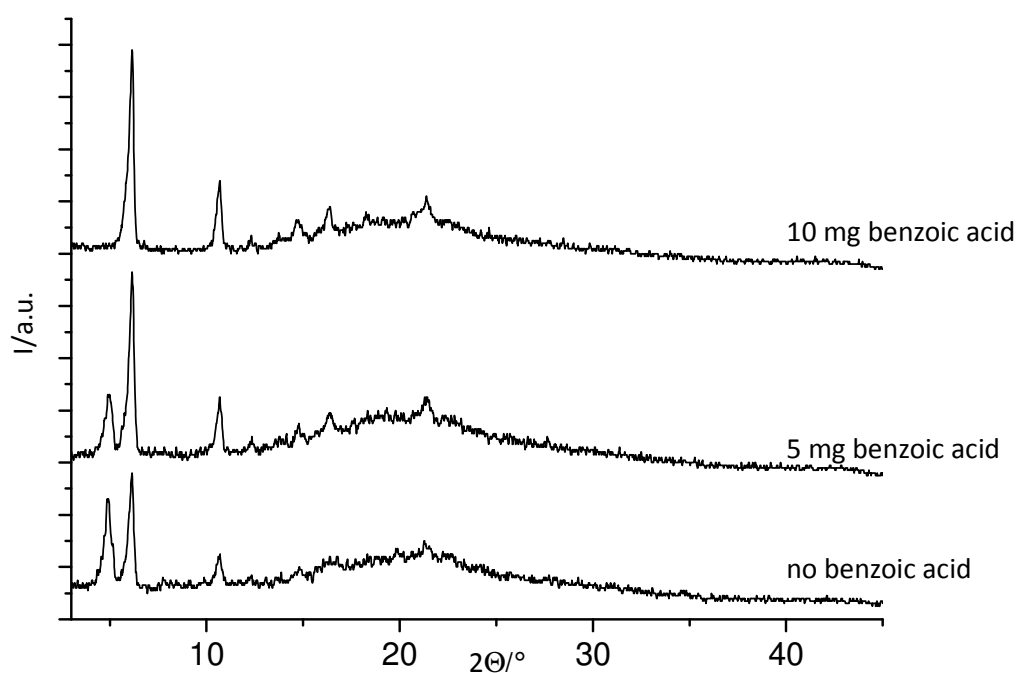


Figure S2: Influence of the addition of benzoic acid on the formation of the byproduct using technical DMF as the solvent.

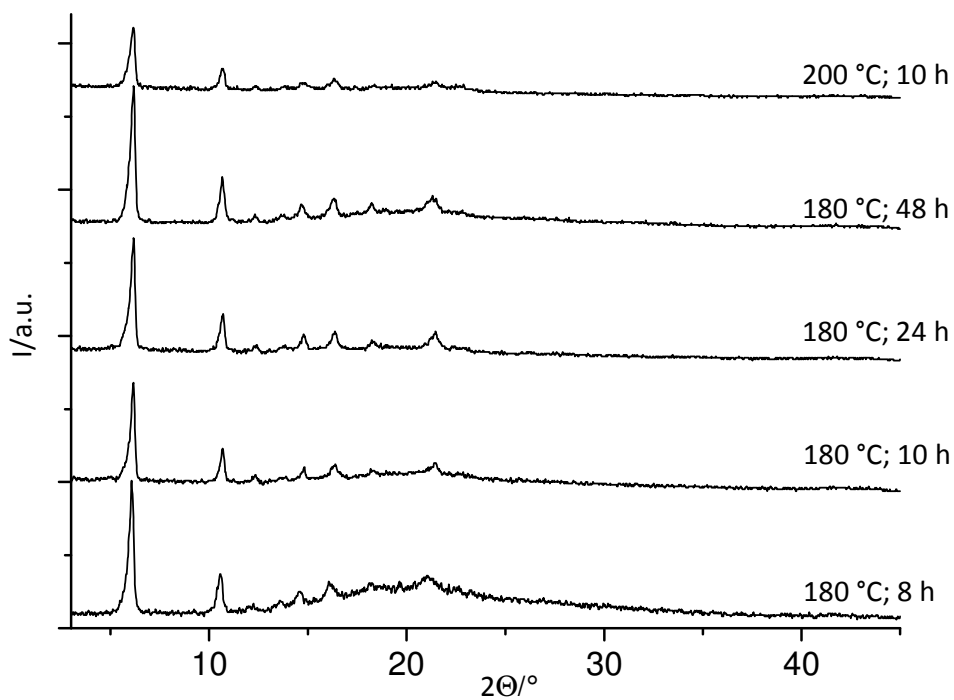


Figure S3: Time and temperature dependence of the crystallinity of CAU-4. The molar ratio $\text{Al}^{3+} : \text{H}_3\text{BTB} : \text{benzoic acid} : \text{DMF} = 7 : 14 : 10 : 142$ was used.

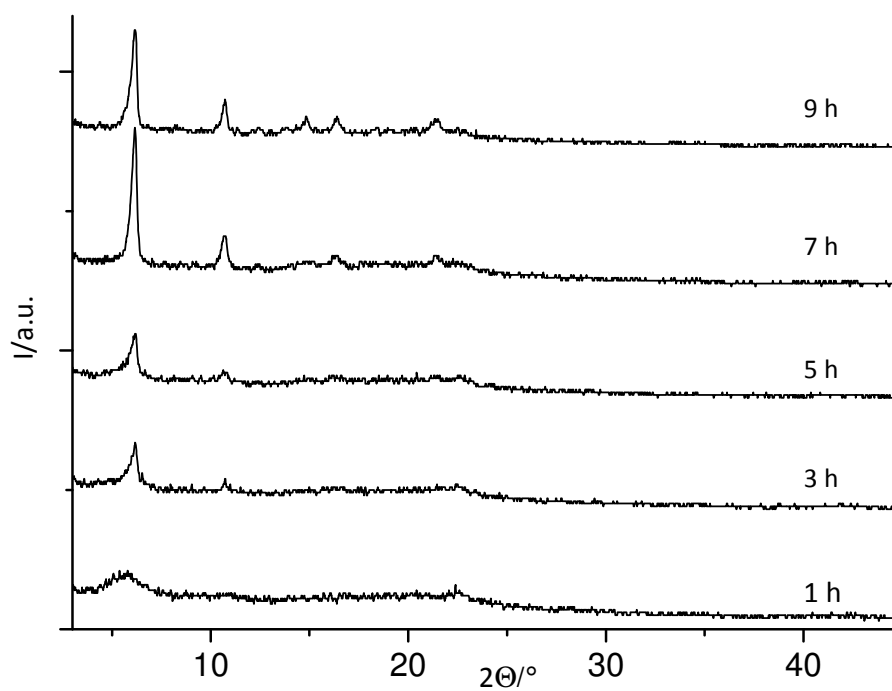


Figure S4: Ex-situ investigation of the formation of CAU-4 under stirring in pyrex glass tubes. The molar ratio $\text{Al}^{3+} : \text{H}_3\text{BTB} : \text{benzoic acid} : \text{DMF} = 7 : 14 : 10 : 142$ was used

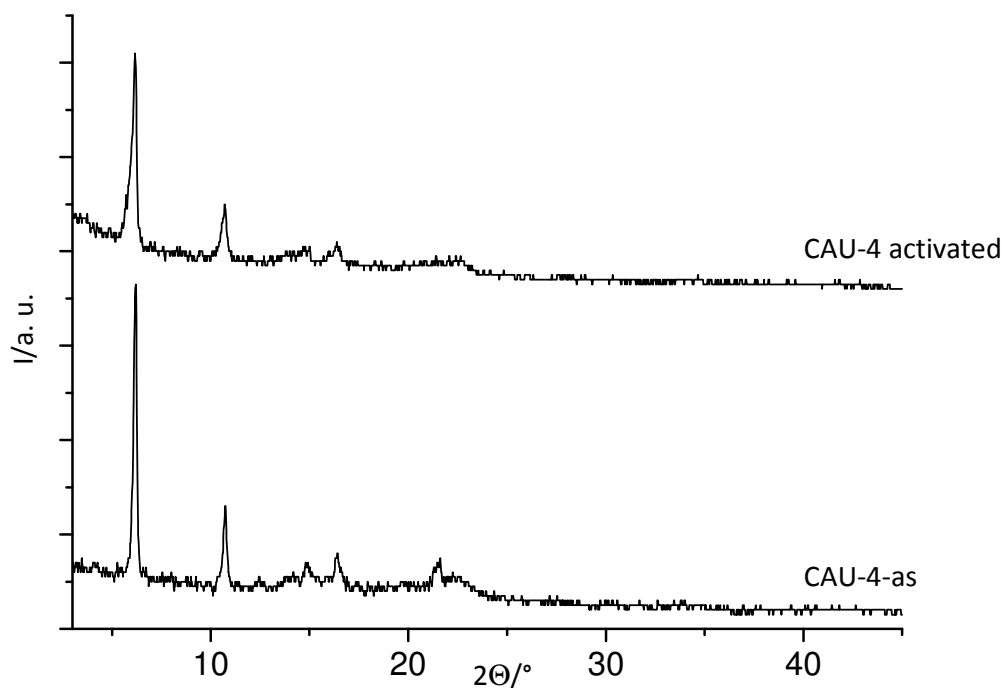


Figure S5: XRPD patterns of CAU-4-as and activated CAU-4.

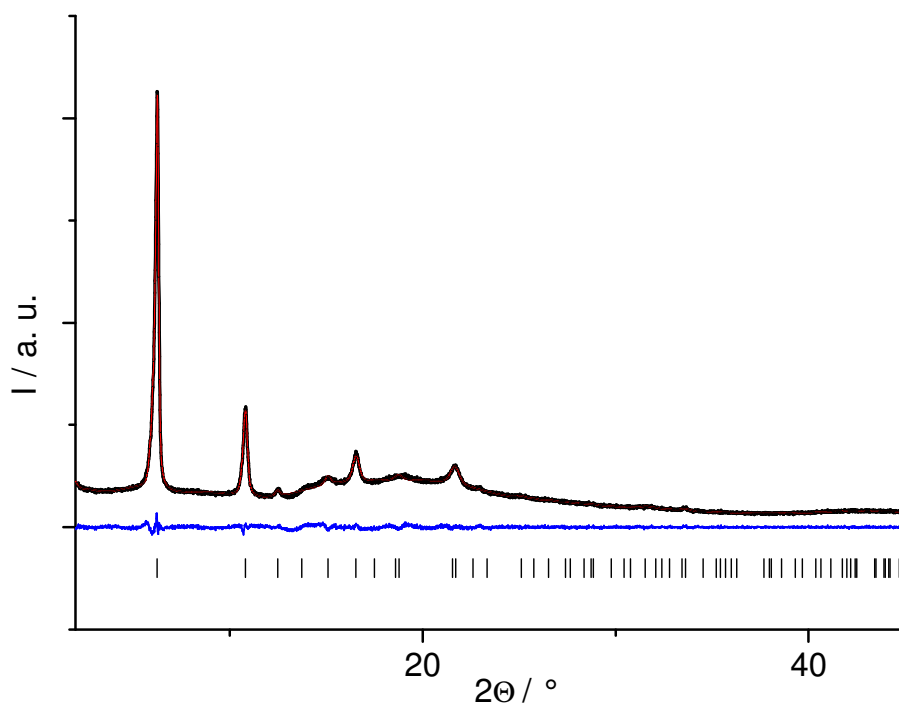


Figure S6: Pawley fit for CAU-4. The observed intensities are shown in black, the calculated intensities are shown in red. The difference curve is shown below in blue, vertical bars mark the Bragg positions.

Tab S7: Atomic parameters of the structural model of CAU-4 obtained using Materials Studio software.

Atom	x/a	y/b	z/c	occupancy
Al1	0.33333	0.66667	0.00000	1.00
Al2	0.33333	0.66667	0.50000	1.00
O1	0.33840	0.56557	0.13781	1.00
O2	0.33840	0.56557	0.63781	1.00
C3	0.41632	0.44222	0.19376	1.00
C4	0.41632	0.44222	0.69376	1.00
C5	0.46595	0.39283	0.19131	1.00
C6	0.46595	0.39283	0.69131	1.00
C7	0.56783	0.28392	0.25000	1.00
C8	0.61620	0.23240	0.25000	1.00
C9	0.56266	0.12533	0.25000	1.00
C10	0.46197	0.92394	0.25000	1.00
C11	0.40983	0.81965	0.25000	1.00
H12	0.34230	0.40570	0.14848	1.00
H13	0.34230	0.40570	0.64848	1.00
H14	0.42767	0.32070	0.13592	1.00
H15	0.42767	0.32070	0.63592	1.00
H16	0.49193	0.24596	0.25000	1.00

Supporting Information

Formation and Characterisation of Mn-MIL-100

Helge Reinsch and Norbert Stock

Activation under vacuum at room temperature

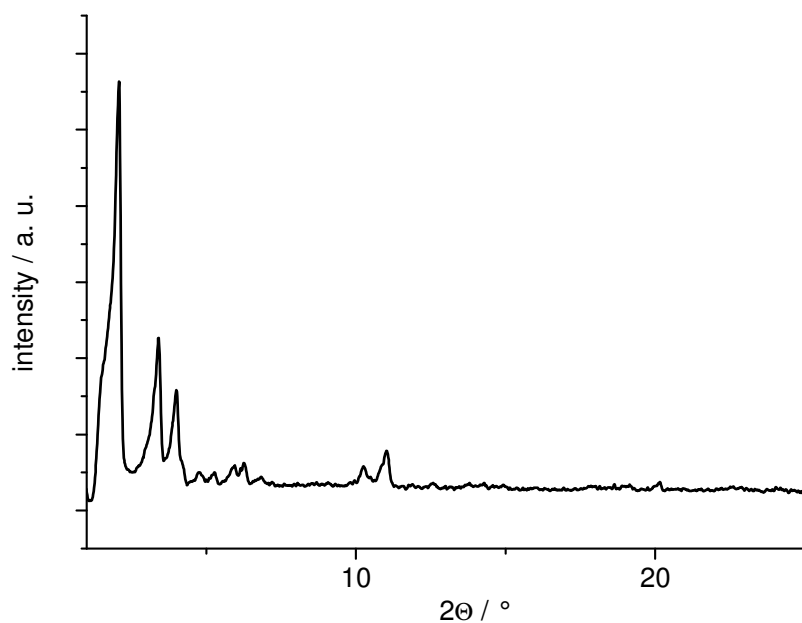


Fig. S1: XRPD pattern of Mn-MIL-100 washed in ethanol and activated at 0.1 mbar at room temperature after the sorption experiment. The XRPD pattern was recorded using the STADI P Combi diffractometer equipped with an image plate detector (measurement time 3 min).

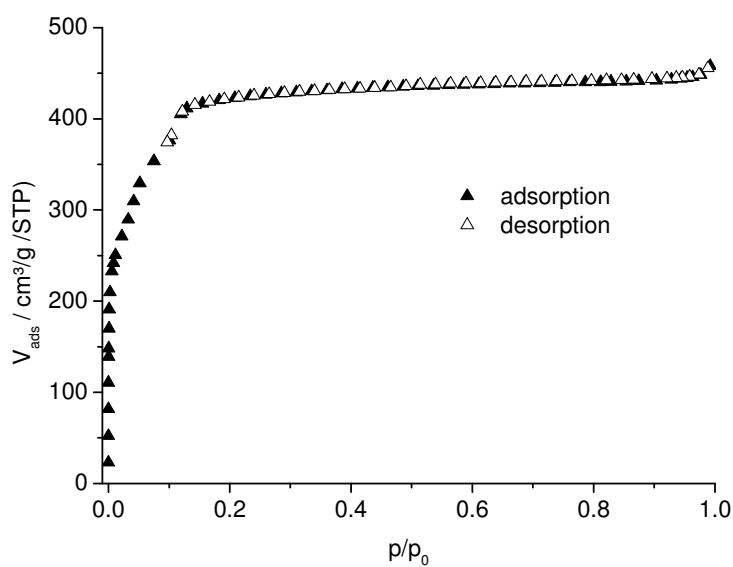


Fig. S2: Nitrogen sorption isotherm (measured at 77 K) of Mn-MIL-100 washed in ethanol and activated at 0.1 mbar at room temperature.

IR-spectroscopy

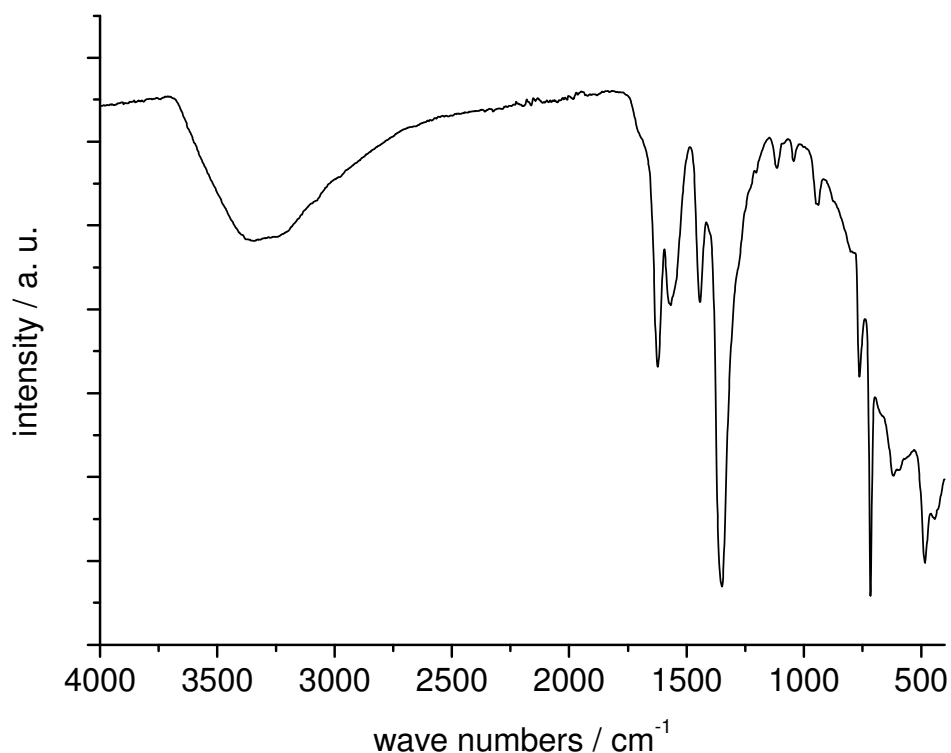


Fig. S3: IR-spectrum of as-synthesized Mn-MIL-100.

The IR-spectrum of Mn-MIL-100 exhibits a strong band around 3300 cm⁻¹, which is due to the hydrogen bonds of the occluded solvent molecules. Furthermore, the asymmetric CO₂-stretching band at 1620 cm⁻¹ belongs to the trimesate anions, while the shoulder at 1700 cm⁻¹ can be attributed to residual acid, which can be washed out by treatment with ethanol. Strong absorptions are also observed at 1350 cm⁻¹ and 713 cm⁻¹. The first is due to the symmetric CO₂-stretching of the carboxylate and the latter is the ring-out-of-plane vibration of the 1,3,5-substituted benzene core of the linker molecules.

Sharp-Hancock-Plots and Fits

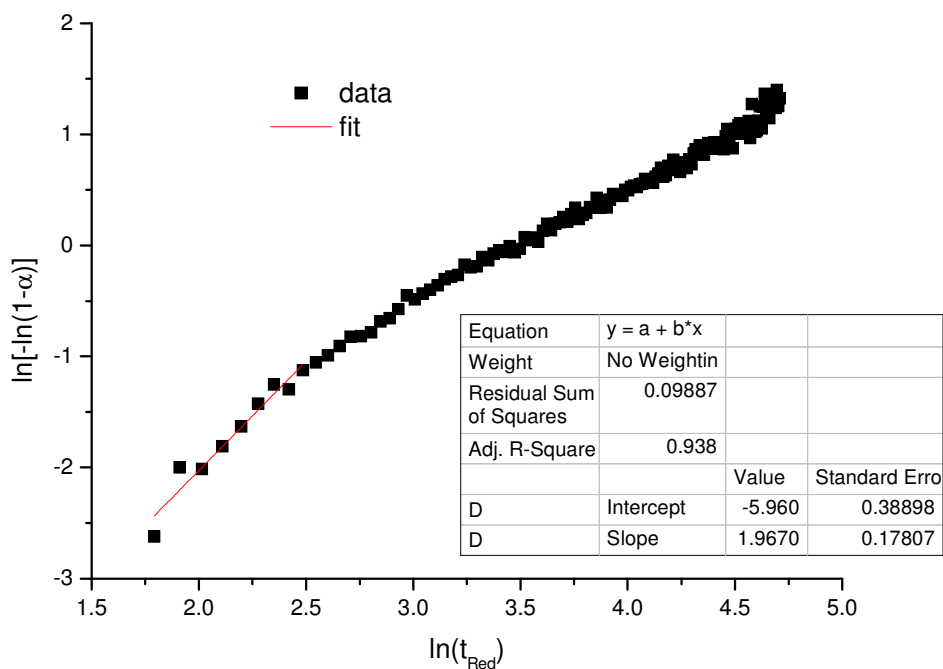


Fig. S4: SH-Plot for the initial reaction stage at 125 °C.

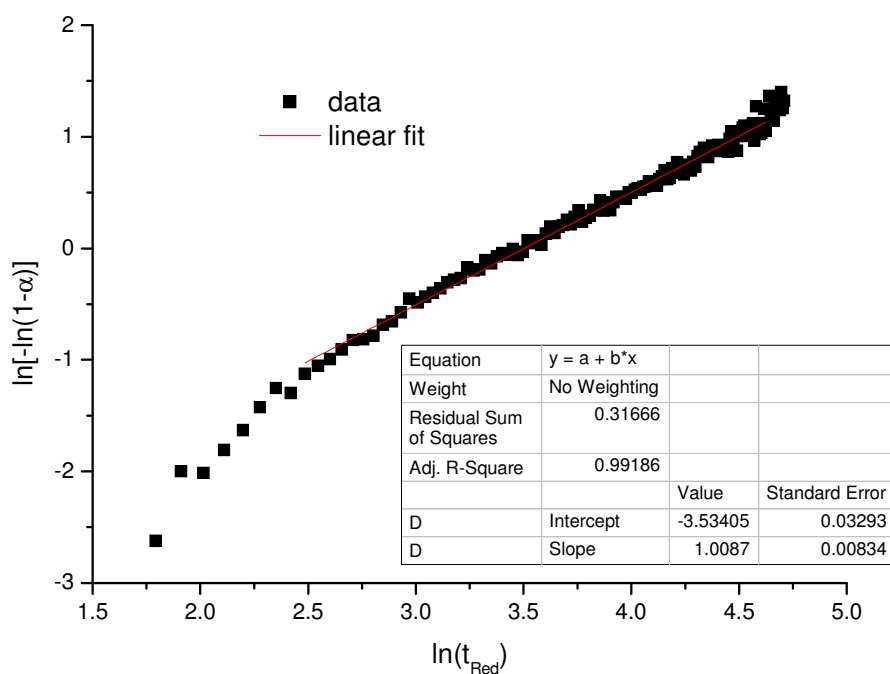


Fig. S5: SH-Plot for the second reaction stage at 125 °C.

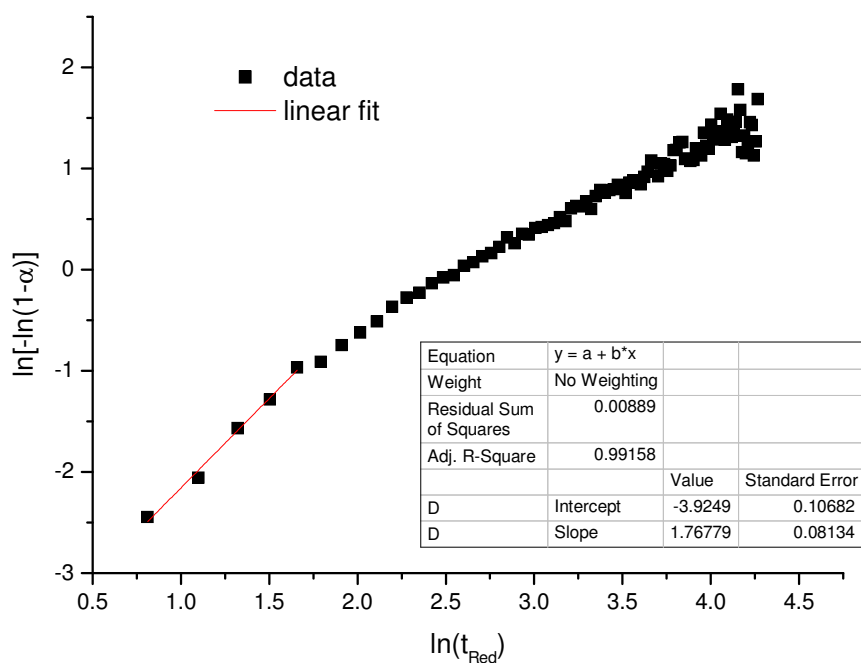


Fig. S6: SH-Plot for the initial reaction stage at 135 °C.

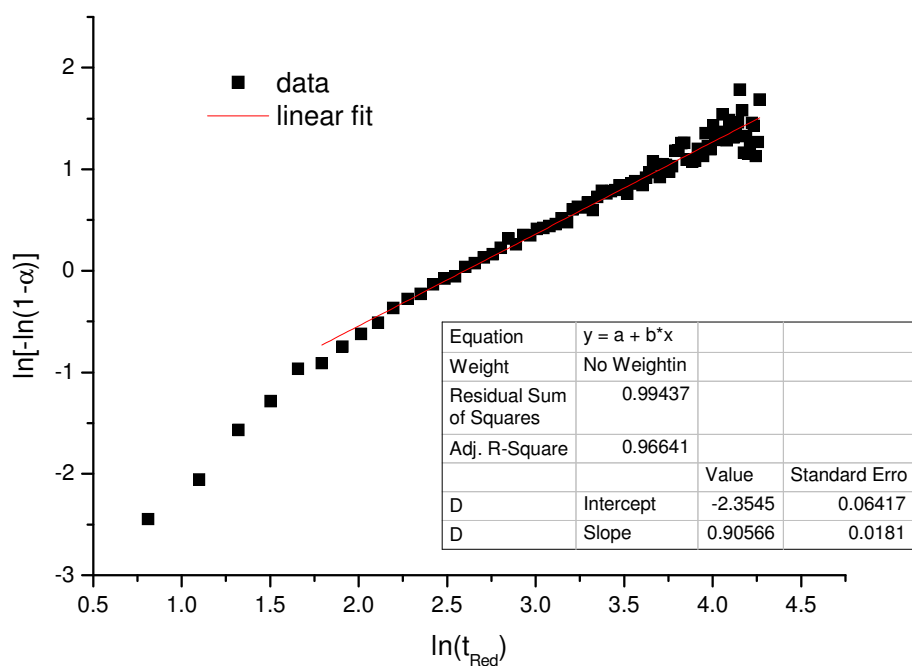


Fig. S7: SH-Plot for the second reaction stage at 135 °C.

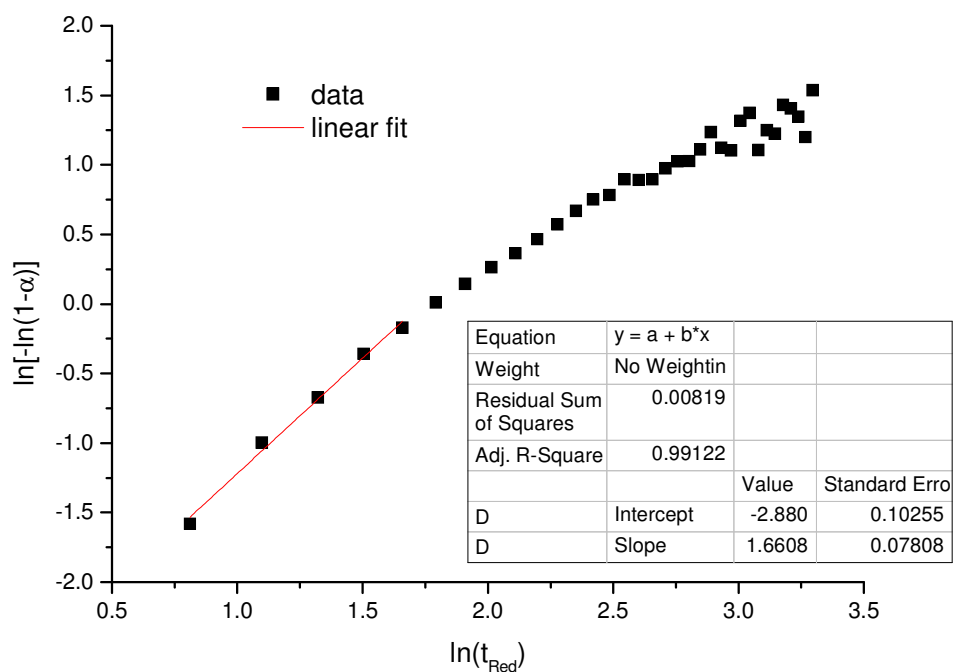


Fig. S8: SH-Plot for the initial reaction stage at 145 °C.

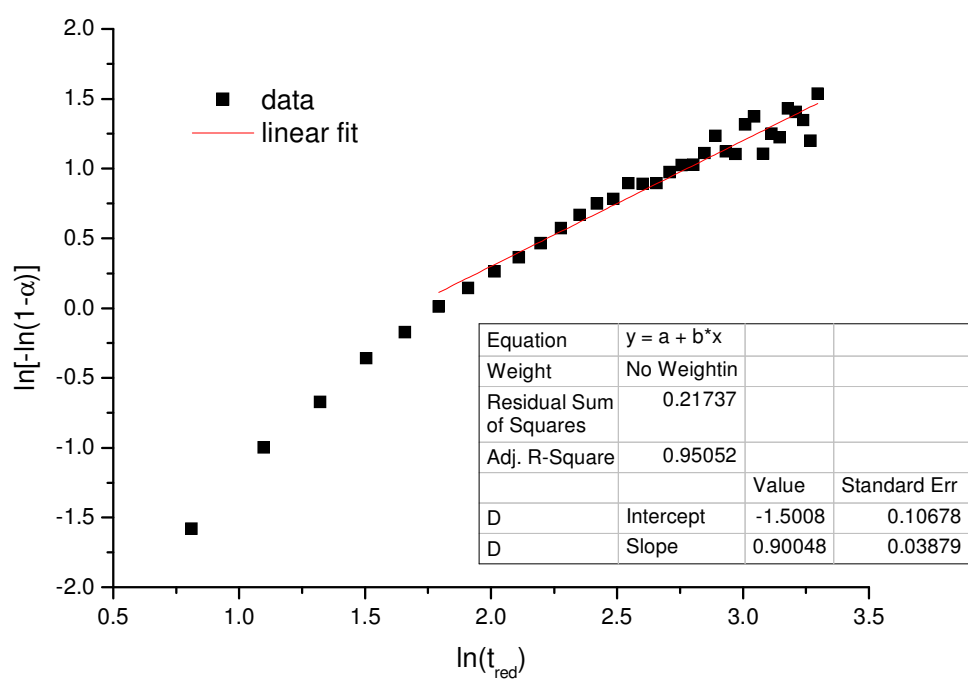


Fig. S9: SH-Plot for the second reaction stage at 145 °C.

Gualtieri-Fits

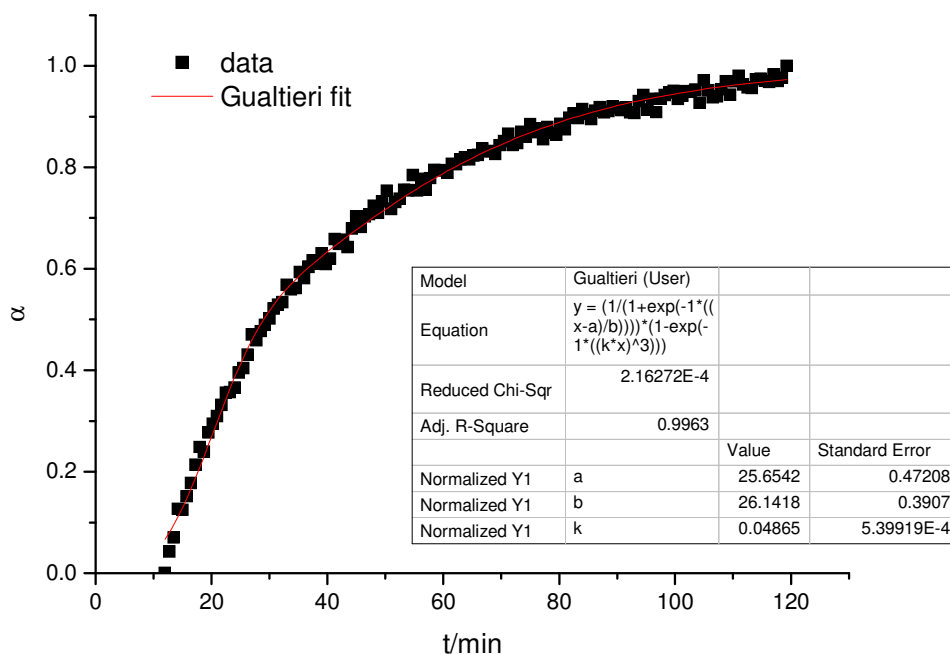


Fig. S10: Gualtieri-Fit for the reaction at 125 °C.

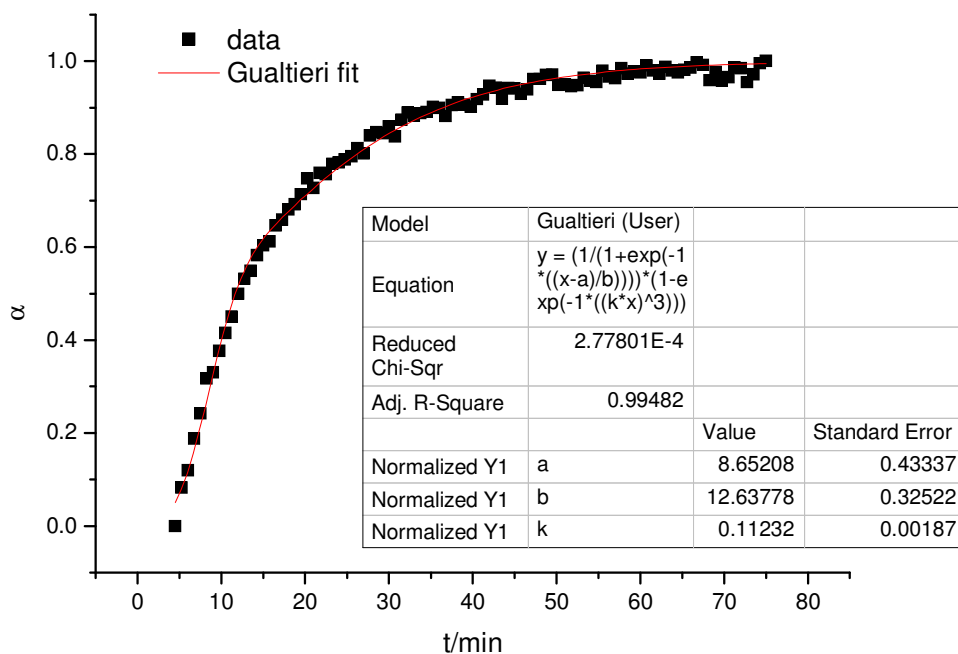


Fig. S11: Gualtieri-Fit for the reaction at 135 °C.

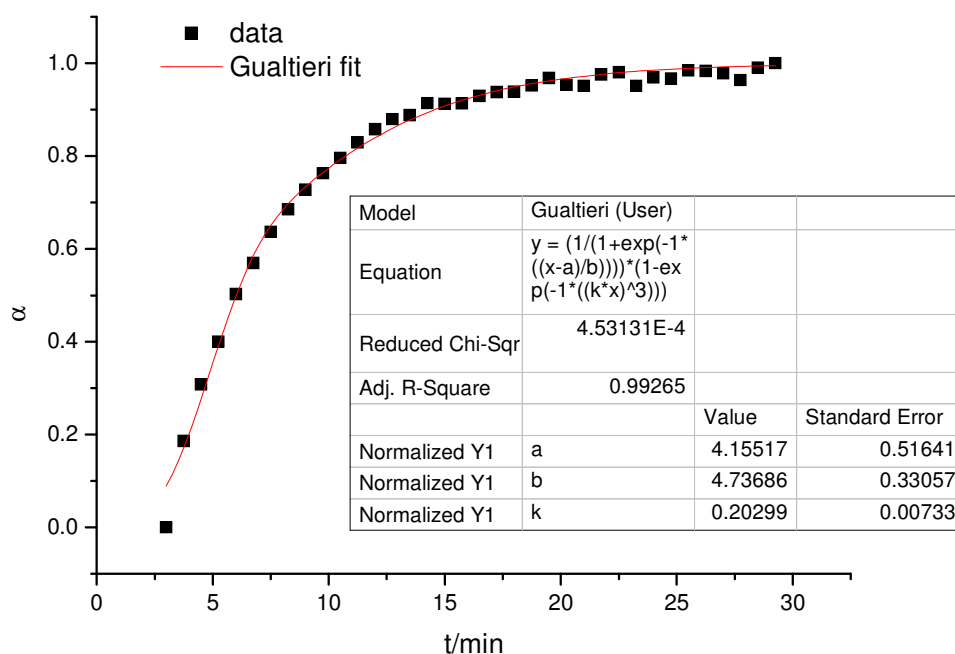


Fig. S12: Gualtieri-Fit for the reaction at 145 °C.

Arrhenius Plots

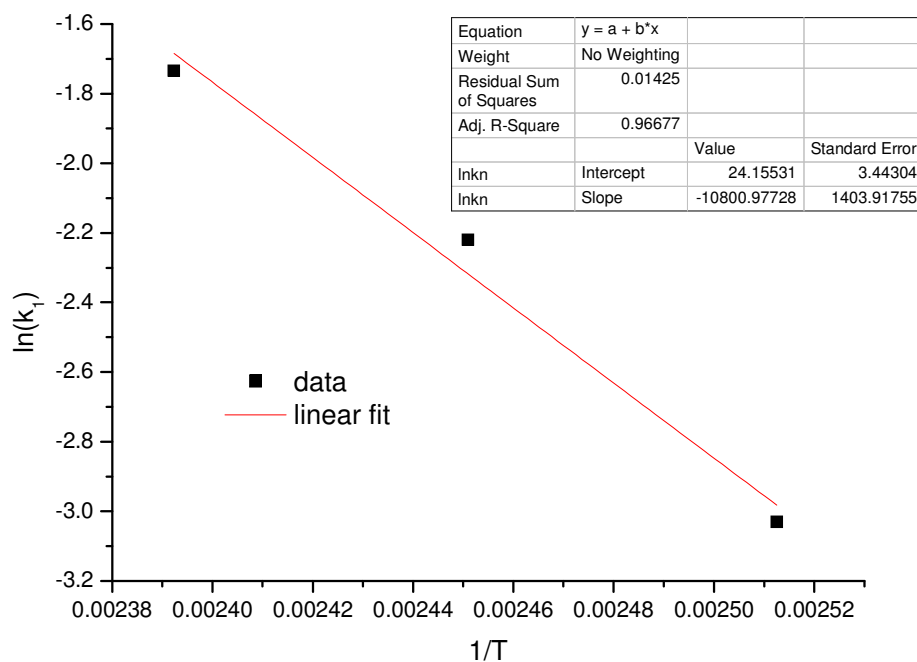


Fig. S13: Arrhenius-Plot for the initial reaction rate constant obtained from SH-Plot.

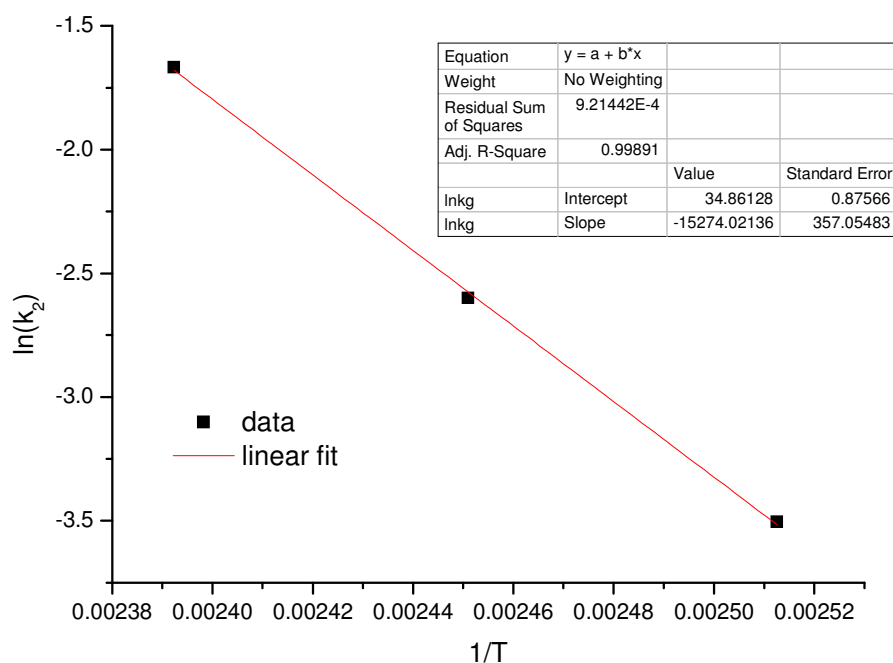


Fig. S14: Arrhenius-Plot for the second reaction rate constant obtained from SH-Plot.

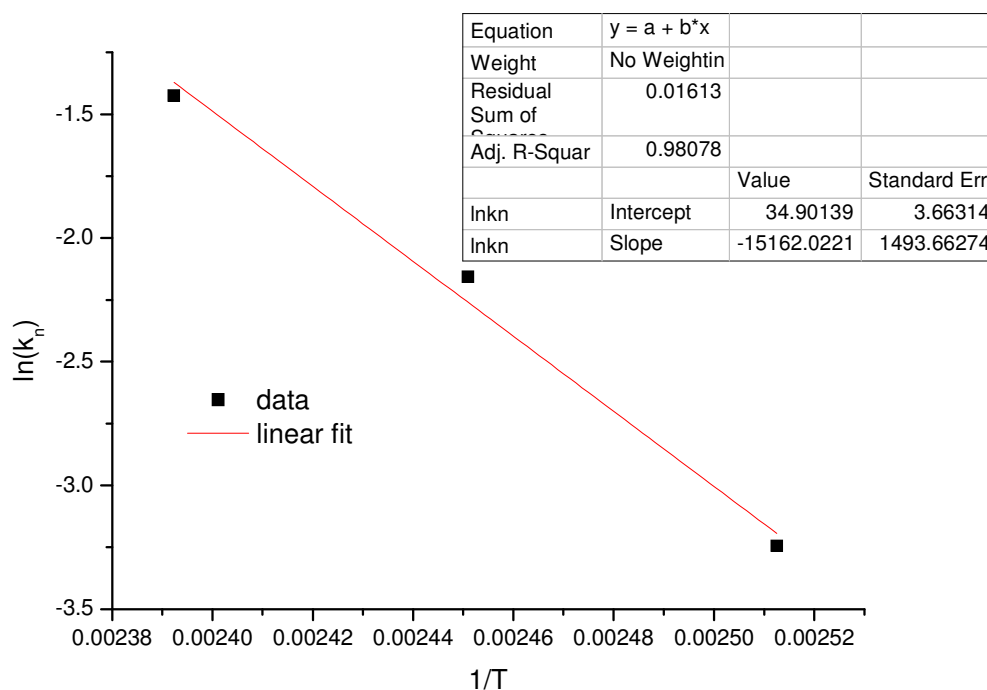


Fig. S15: Arrhenius-Plot for the nucleation rate constant obtained from Gualtieri-Plot.

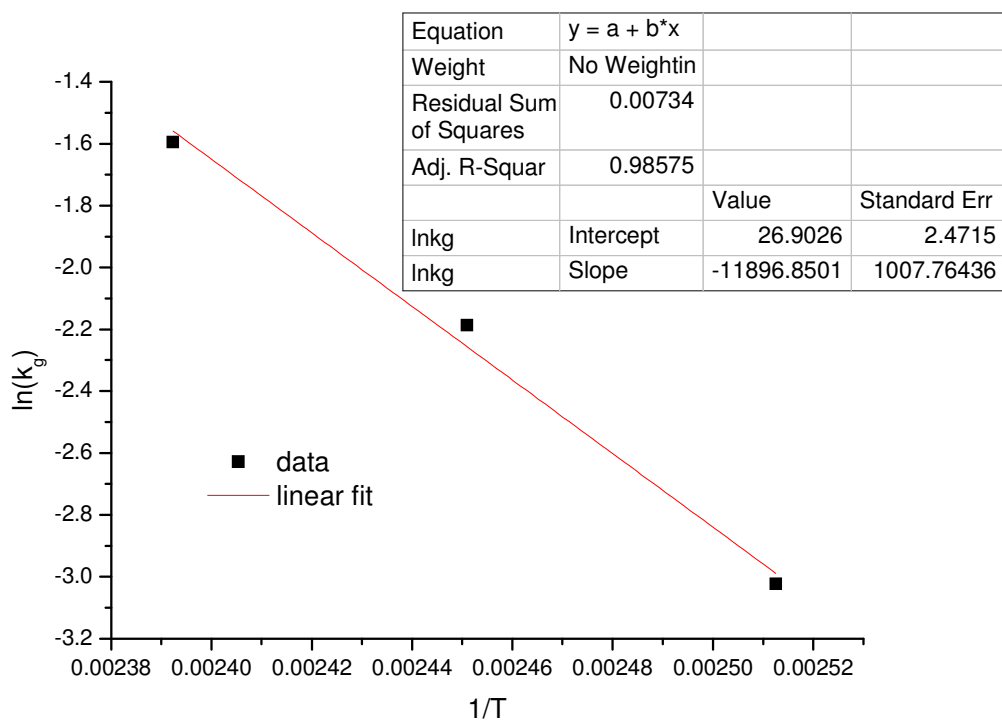


Fig. S16: Arrhenius-Plot for the growth rate constant obtained from Gualtieri-Plot.

Supporting Information

Structures, sorption characteristics and nonlinear optical properties of a new series of highly stable aluminium MOFs

Helge Reinsch, Monique Van der Veen, Barbara Gil, Bartosz Marszalek, Thierry Verbiest,

Dirk de Vos, Norbert Stock

- I. Details of the refinements**
 - II. Temperature dependent XRPD-data**
 - III. Stability tests of CAU-10-X dispersions under aqueous conditions**
 - IV. Results of the thermogravimetric measurements**
 - V. Vibrational spectra**
 - VI. Description of the High-throughput experiments**
 - VII. Scanning electron microscopy images**
 - VIII. SHG polarization dependency of compound 1**
 - IX. Theoretical treatment of SHG for D4 symmetry**
 - X. Determination of the effective second-order nonlinear coefficient**
 - XI. In-situ-formylation of CAU-10-NH₂ (5)**
-

I. Details of the refinements

Tab. S1: Results of the Rietveld refinements.

compound	CAU-10-H (1)	CAU-10-CH ₃ (2)	CAU-10-OCH ₃ (3)
space group	<i>I</i> 4 ₁	<i>I</i> 4 ₁ /amd	<i>I</i> 4 ₁ /a
<i>a</i> = <i>b</i> [Å]	21.55(7)	21.4917(6)	21.3609(3)
<i>c</i> [Å]	10.38(3)	10.1810(5)	10.5699(2)
formula	Al ₂ O ₁₀ C ₁₆ H ₁₀	Al _{0.5} O _{2.5} C _{4.5} H _{3.5}	AlO ₇ C ₉ H ₇
<i>Z</i>	8	32	16
thermal factors	28	3	17
cell parameters	2	2	2
restraints	45	7	22
R _{WP} [%]	1.9	7.1	7.6
R _{Exp} [%]	0.9	2.9	2.7
R _{Bragg} [%]	0.4	2.1	4.3

Tab. S2: Results of the Le Bail fits.

compound	CAU-10-NO ₂ (4)	CAU-10-NH ₂ (5)	CAU-10-OH (6)
space group	<i>P</i> 4 ₁	<i>P</i> $\bar{4}$ n2	<i>P</i> 4
<i>a</i> = <i>b</i> [Å]	21.4707(3)	21.4567(4)	21.3072(5)
<i>c</i> [Å]	10.3777(2)	10.8452(3)	38.6974(9)
R _{WP} [%]	3.2	4.9	4.8

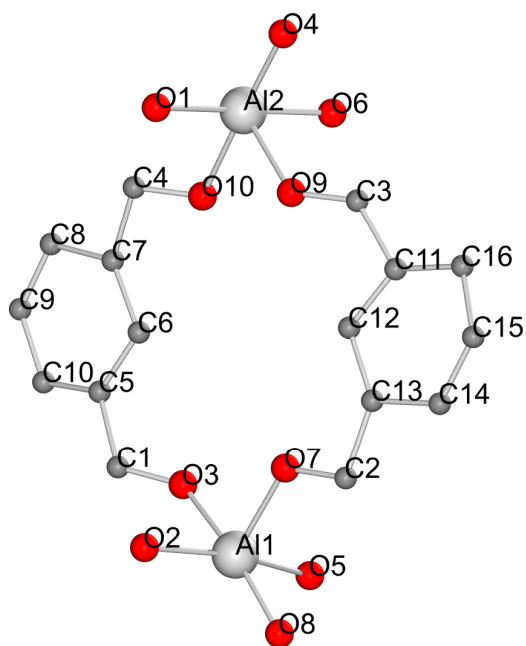


Fig.S1: Asymmetric unit of CAU-10-H with numbering scheme used in Tab. S1.

Tab.S1: Bond lengths (Å) in the structure of CAU-10-H.

Al1	O8	1.803(46)	O9	1.281(48)	
	O2	1.952(33)	C11	1.511(36)	
	O3	1.971(38)	C4	O6	1.271(58)
	O7	1.996(43)	O10	1.297(46)	
	O5	1.999(38)	C7	1.496(49)	
Al2	O6	1.809(37)	C5	C6	1.353(50)
	O4	1.821(62)	C10	1.381(47)	
	O1	1.955(41)	C6	C7	1.453(52)
	O10	1.973(50)	C7	C8	1.427(52)
	O9	1.993(47)	C8	C9	1.359(43)
C1	O5	1.234(53)	C9	C10	1.421(46)
	O3	1.288(47)	C11	C12	1.374(44)
	C5	1.519(31)	C16	1.415(41)	
C2	O2	1.241(62)	C12	C13	1.428(45)
	O7	1.296(46)	C13	C14	1.449(47)
	C13	1.491(38)	C14	C15	1.411(57)
C3	O1	1.221(59)	C15	C16	1.409(57)

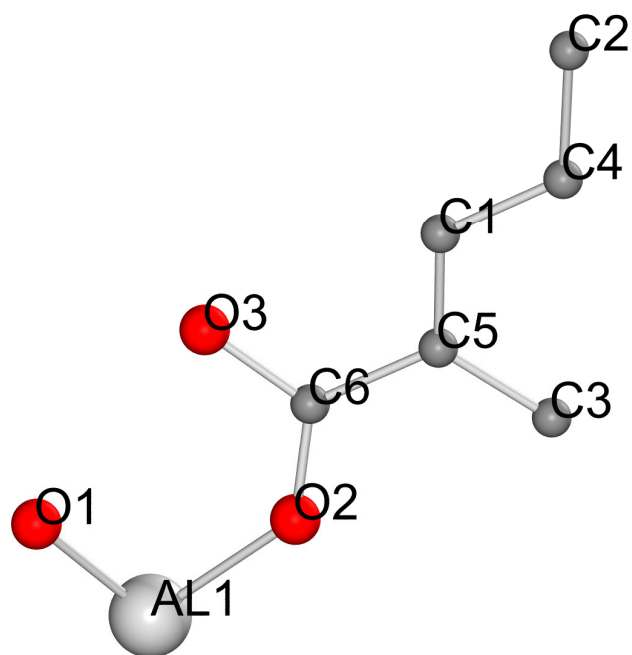


Fig.S2: Asymmetric unit of CAU-10-CH₃ with numbering scheme used in Tab S2.

Tab.S2: Bond lengths (Å) in the structure of CAU-10-CH₃.

Al1	O1	1.773(6)	C2	C4	1.527(12)
	O3	1.895(7)	C3	C5	1.393(10)
	O2	1.951(8)	C5	C6	1.464(10)
C1	C5	1.361(13)	C6	O2	1.229(15)
	C4	1.418(8)		O3	1.323(11)

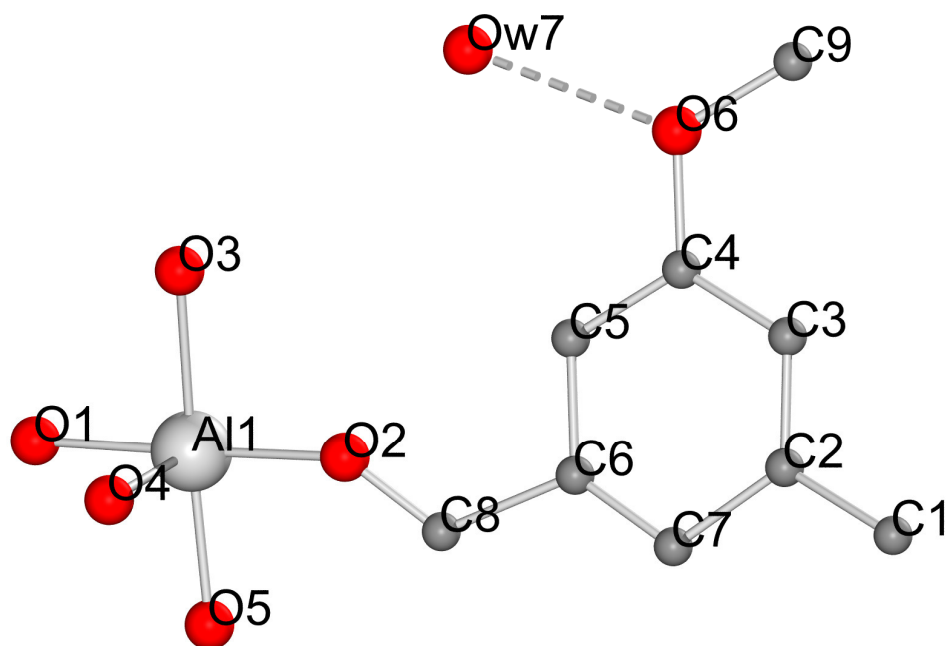


Fig.S3: Asymmetric unit of CAU-10-OCH₃ with numbering scheme used in Tab S3.

Tab.S3: Bond lengths (Å) in the structure of CAU-10-OCH₃.

Al1	O2	1.812(7)	C4	C5	1.383(11)
	O5	1.832(11)	C5	C6	1.425(12)
	O1	1.847(7)	C6	C7	1.348(11)
	O5	1.883(10)		C8	1.574(9)
	O4	1.926(8)			
	O3	1.984(8)			
O1	C1	1.254(10)			
O2	C8	1.267(9)			
O3	C8	1.269(9)			
O4	C1	1.257(10)			
O5	Ow7	2.855(12)			
O6	C9	1.416(20)			
	C4	1.430(12)			
	Ow7	2.934(12)			
C1	C2	1.510(9)			
C2	C3	1.360(13)			
	C7	1.453(12)			
C3	C4	1.429(10)			

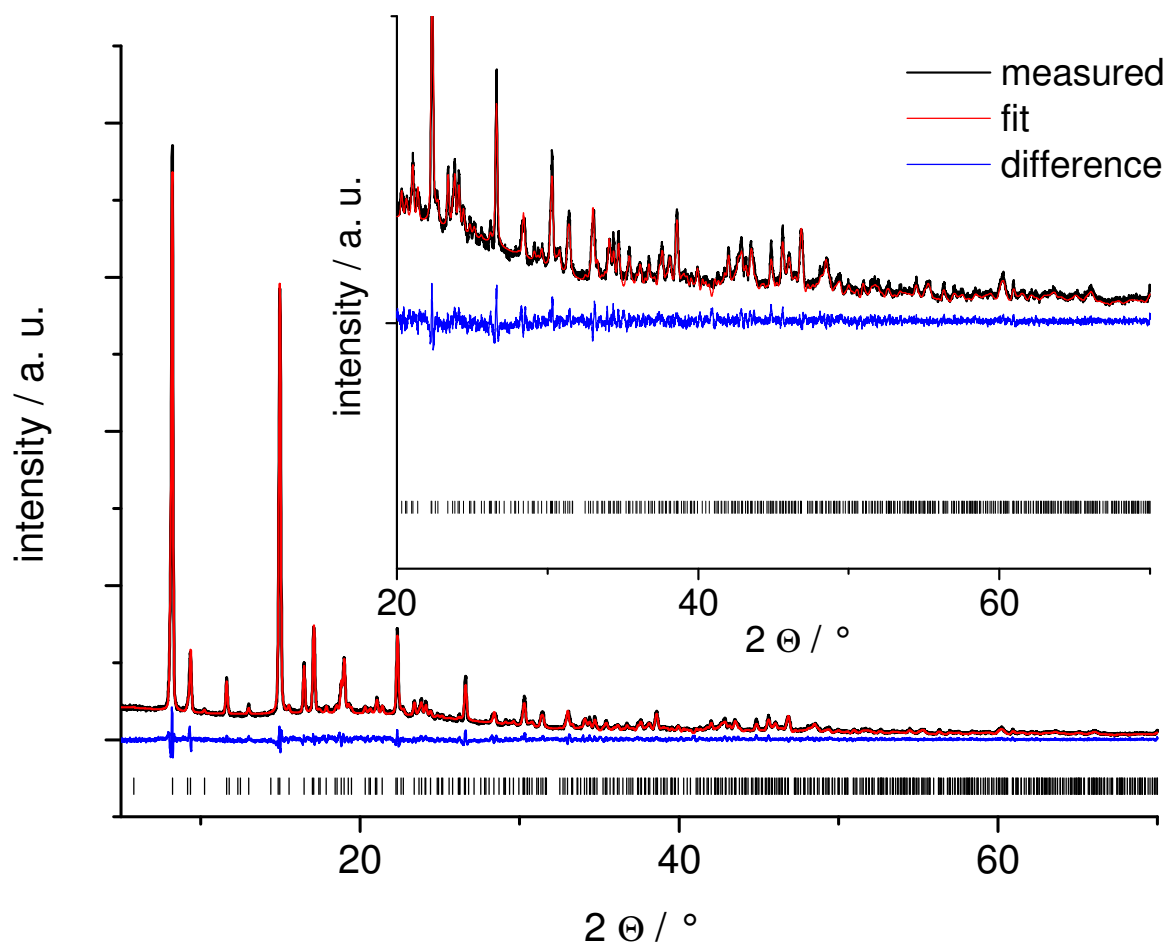


Fig.S4: Le Bail fit for as synthesized CAU-10-CH₃ (**2**) in the space group $P4_1$. The peak shape was modelled by a Thompson-Cox-Hastings function; the number of background parameters was 10. The obtained cell parameters are $a = 21.4900(6)$ Å and $c = 10.4828(4)$ Å. The R_{WP} value is 6.8 %.

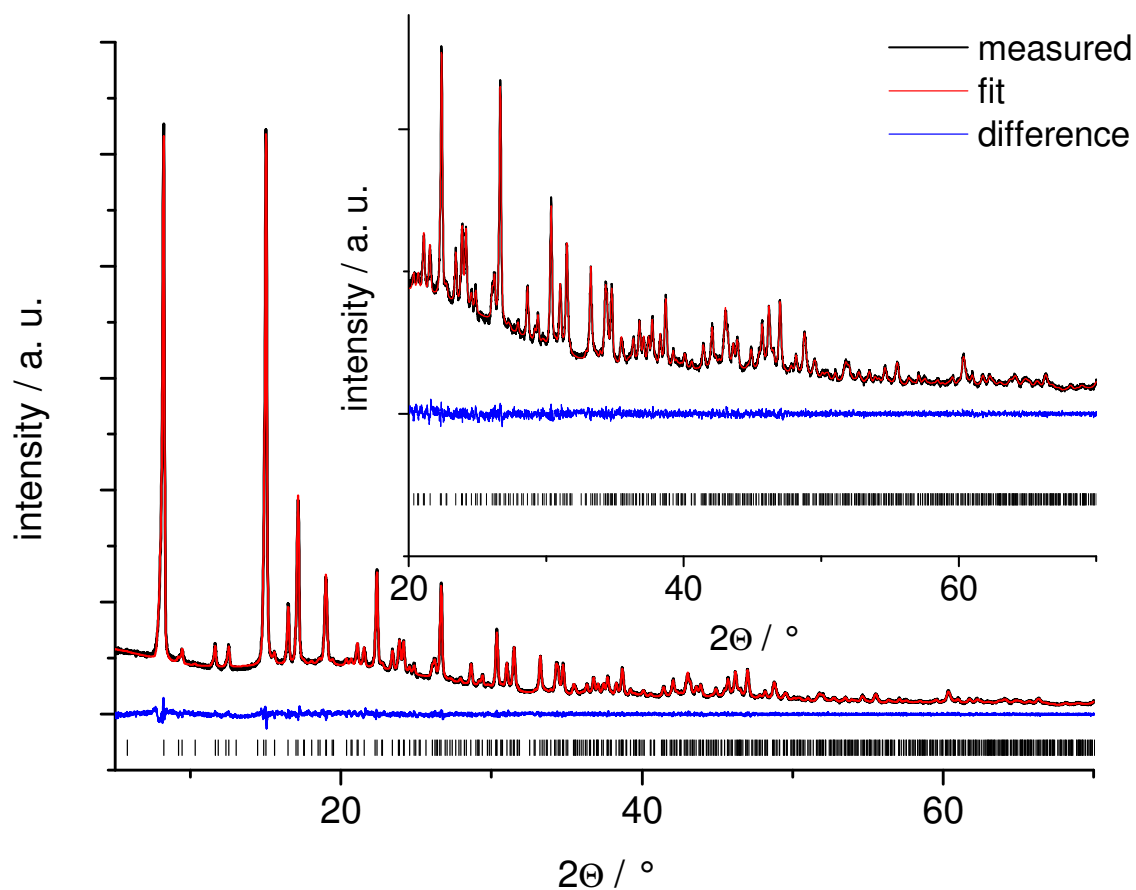


Fig.S5: Le Bail fit for the activated CAU-10-NO₂ (**4**) in the space group $P4_1$. The peak shape was modelled by a Thompson-Cox-Hastings function; the number of background parameters was 10. The obtained cell parameters are $a = 21.4707(3)$ Å and $c = 10.3777(2)$ Å. The R_{WP} value is 3.2 %.

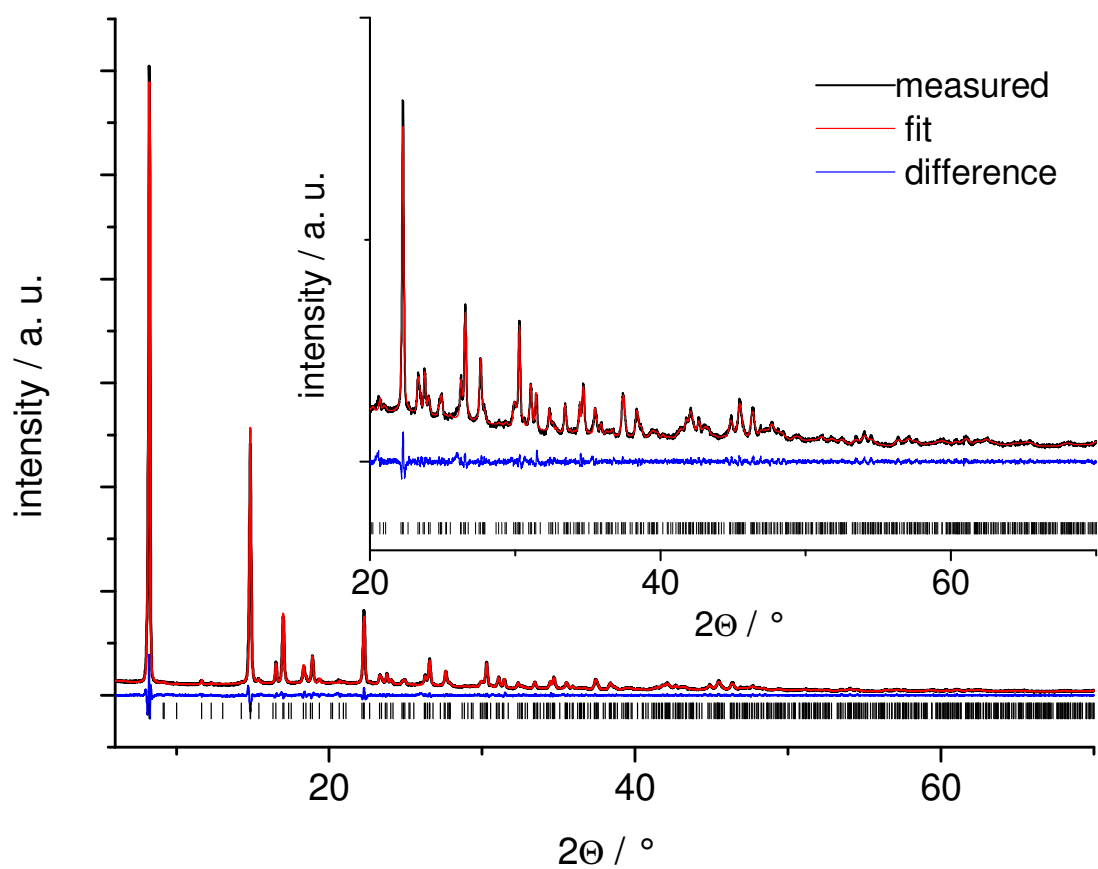


Fig.S6: Le Bail fit for the activated CAU-10-NH₂ (**5**) in the space group $P\bar{4}n2$. The peak shape was modelled by a Thompson-Cox-Hastings function; the number of background parameters was 12. The obtained cell parameters are $a = 21.4567(4)$ Å and $c = 10.8452(3)$ Å. The R_{WP} value is 4.9 %.

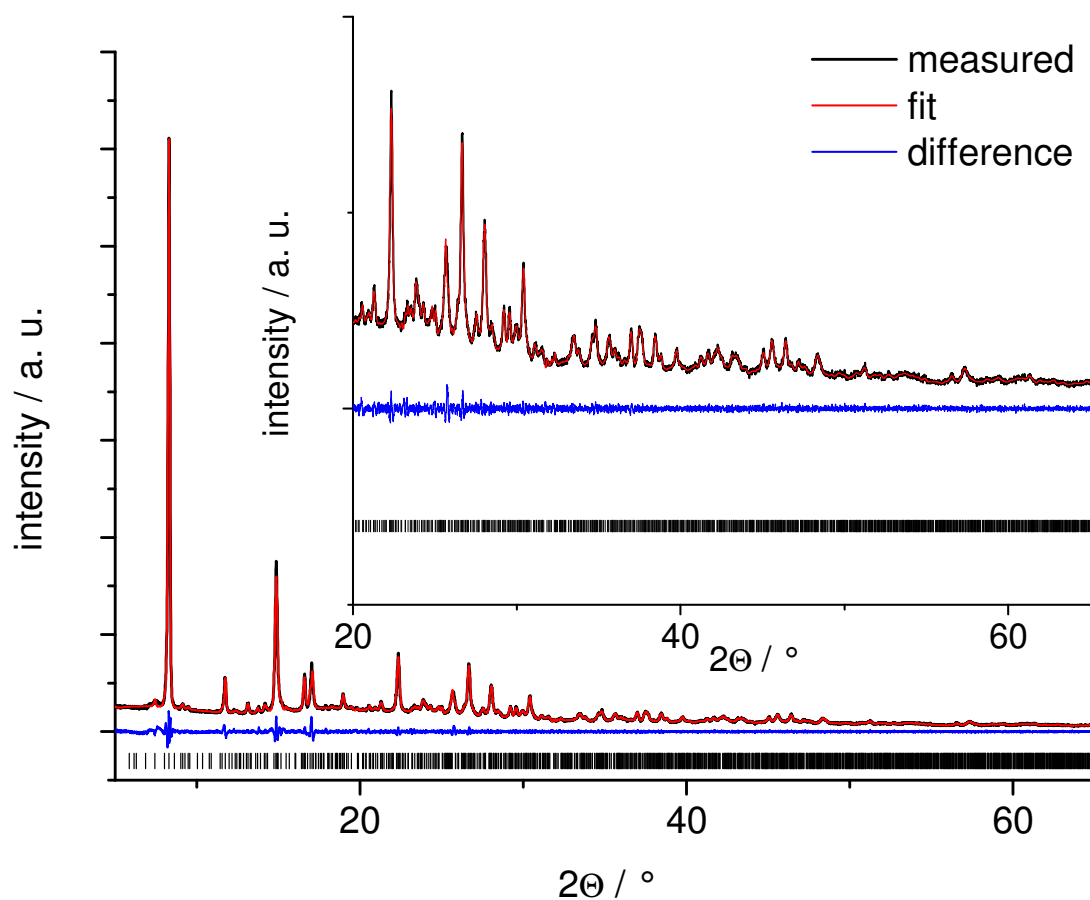


Fig.S7: Le Bail fit for the activated CAU-10-OH (**6**) in the space group $P4$. The peak shape was modelled by a PearsonVII function, the number of background parameters was 14. The obtained cell parameters are $a = 21.3072(5) \text{ \AA}$ and $c = 38.6974(9) \text{ \AA}$. The R_{WP} value is 4.8 %. Thus the compound crystallizes in a unit cell four times as large as the other members of the CAU-10-series.

II. Temperature-dependent XRPD-data

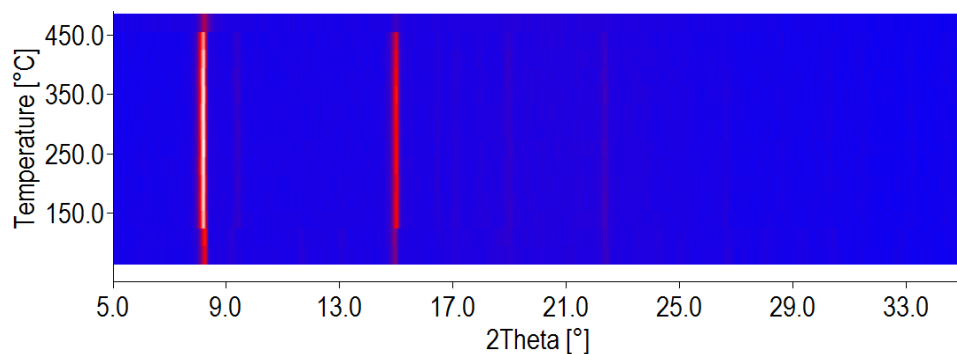


Fig. S8: The contour plot for the TDXPDP-measurements of as synthesized CAU-10-H (**1**). The intensities of the first two reflections increase upon heating, but hardly any shift of the reflection positions is observed.

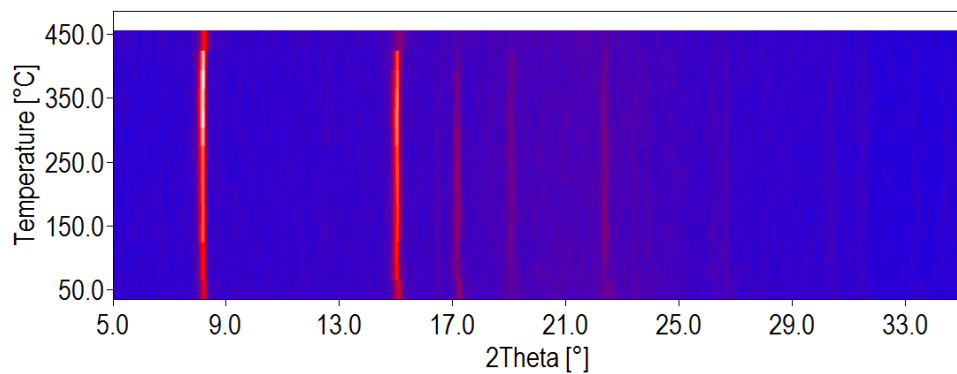
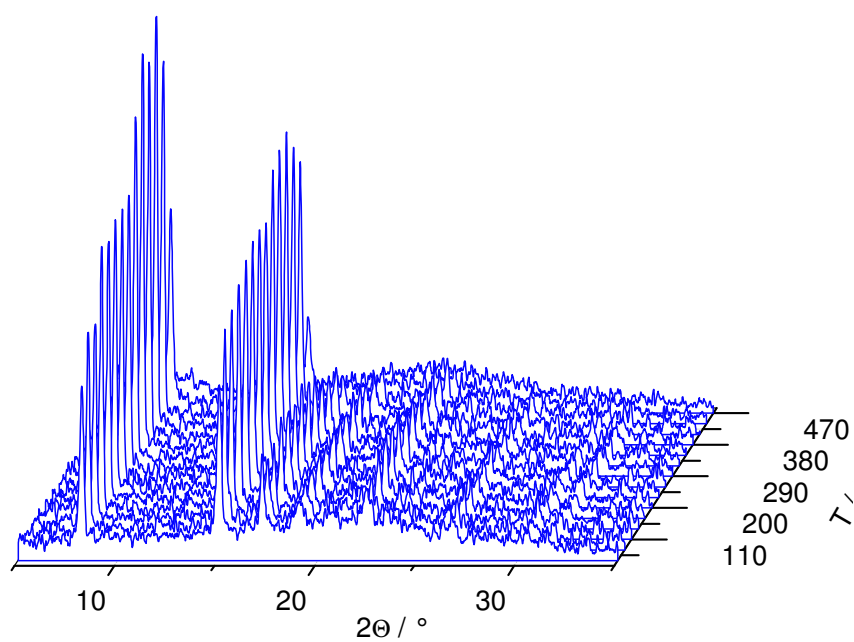


Fig. S9: TDXPDP-data for as synthesized CAU-10-NO₂ (**4**). The contour plot shows higher intensities of the first two reflections at elevated temperatures. At low temperatures a small shift of reflection positions is observed.

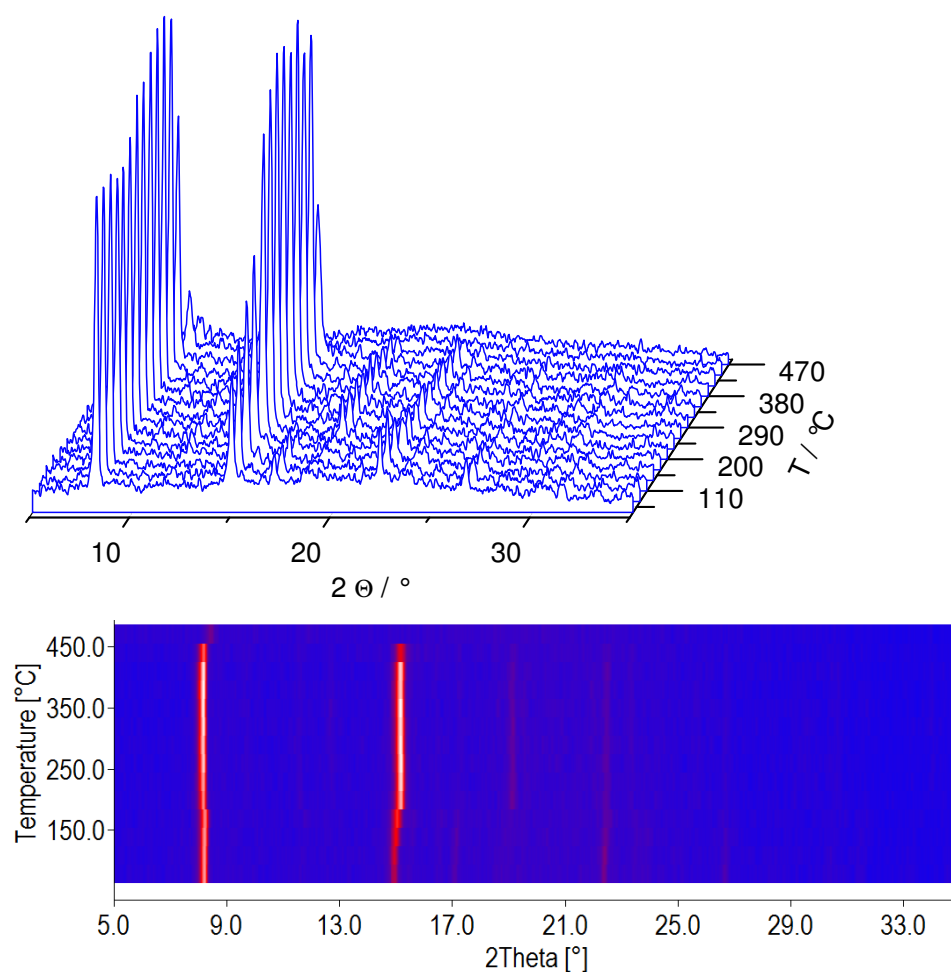


Fig. S10: TDXRPD-data for as synthesized CAU-10-OH (**6**). The contour plot shows the change of intensities of the first two reflections as well as the appearance and disappearance of reflections upon increase of temperature. Up to ca. 175 °C a shift of reflection positions is observed.

III. Stability tests of CAU-10-X dispersions under aqueous conditions

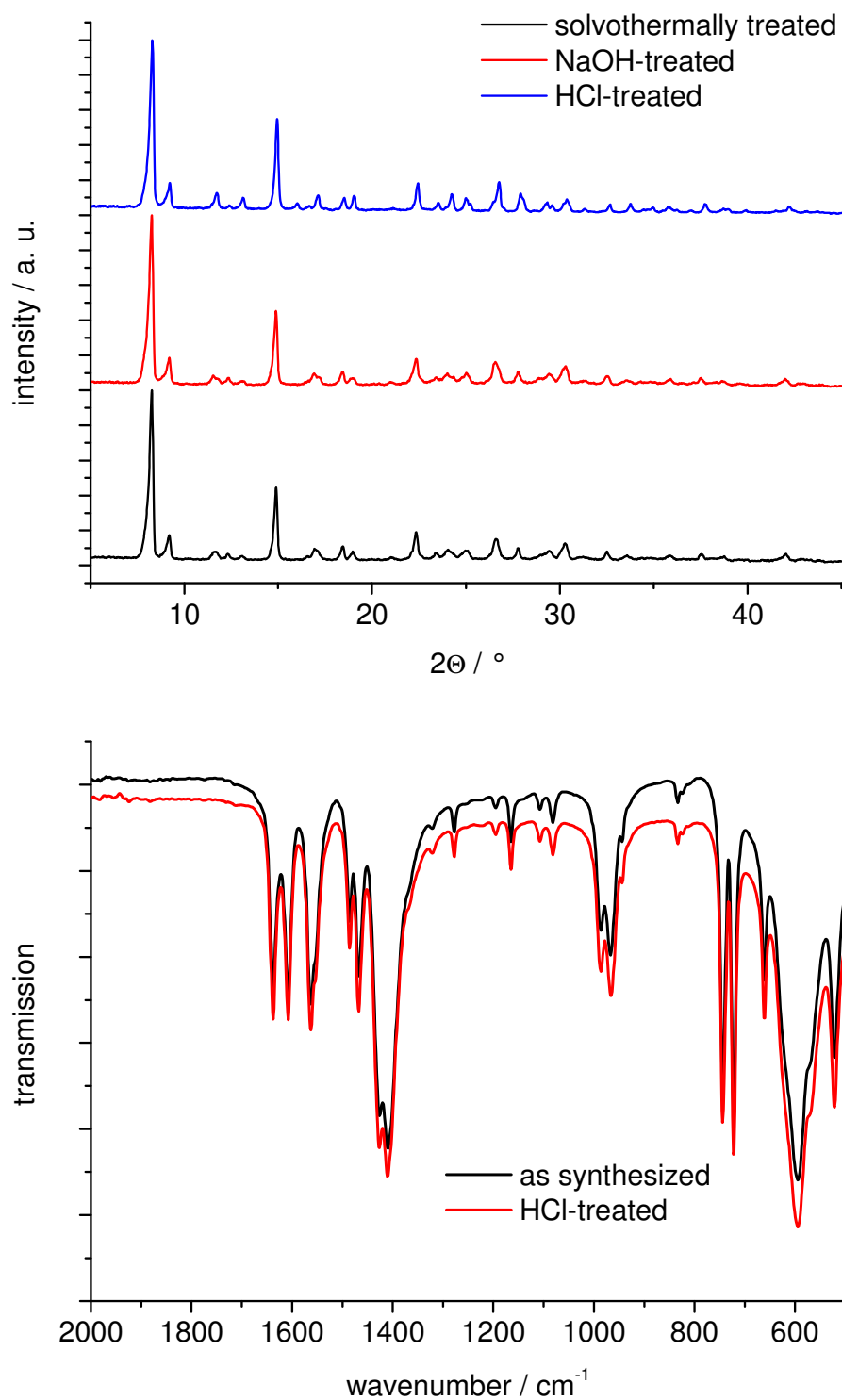


Fig. S11: XRPD-data and IR-spectra of as synthesized CAU-10-H (**1**). Intensities and peak shapes vary slightly. No additional peaks appear in the IR-spectrum due to hydrolysis.

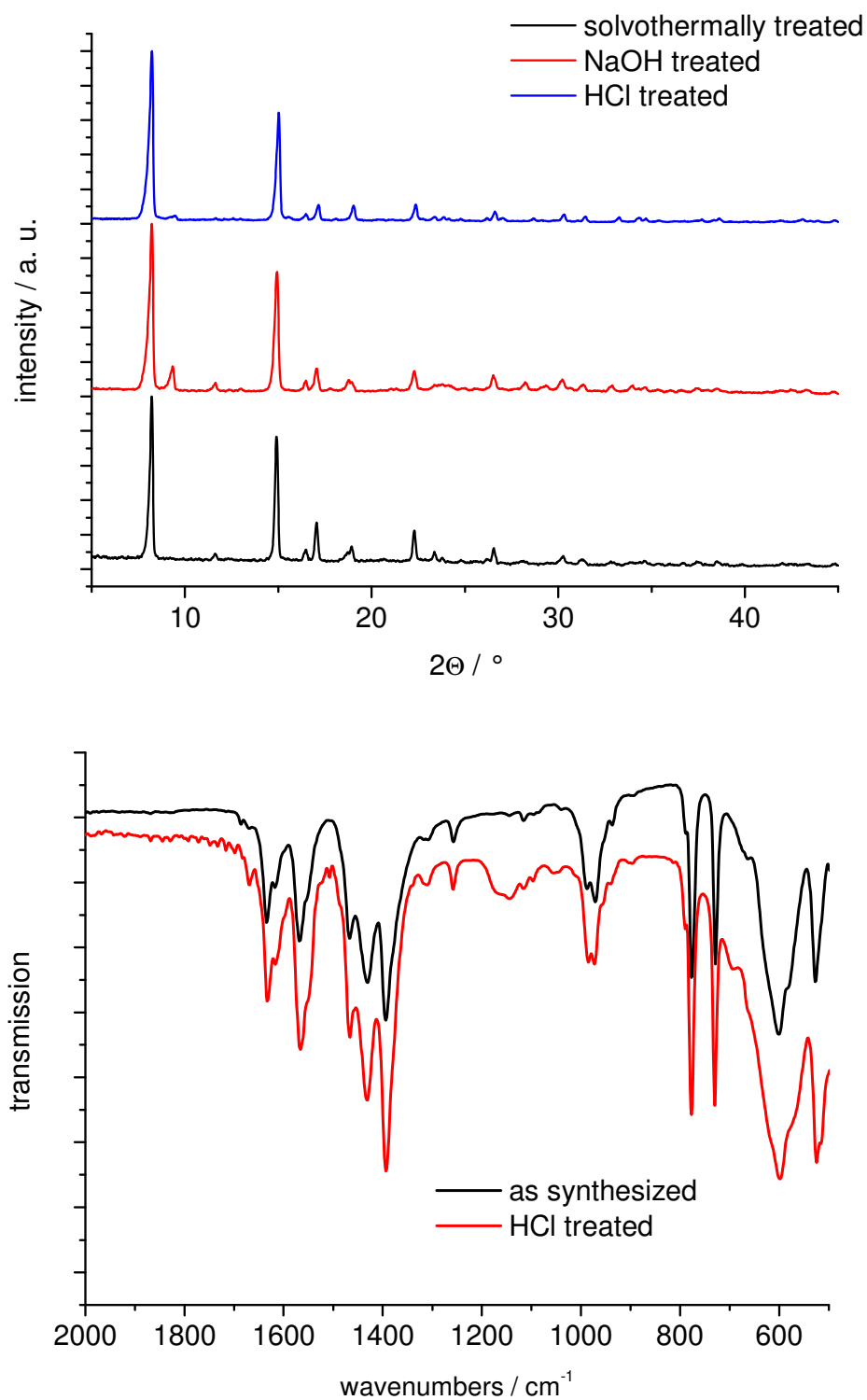


Fig. S12: XRPD-data and IR-sepectra of as synthesized CAU-10-CH₃ (**2**). Intensities and peak shapes vary slightly. No additional peaks appear in the IR-spectrum due to hydrolysis.

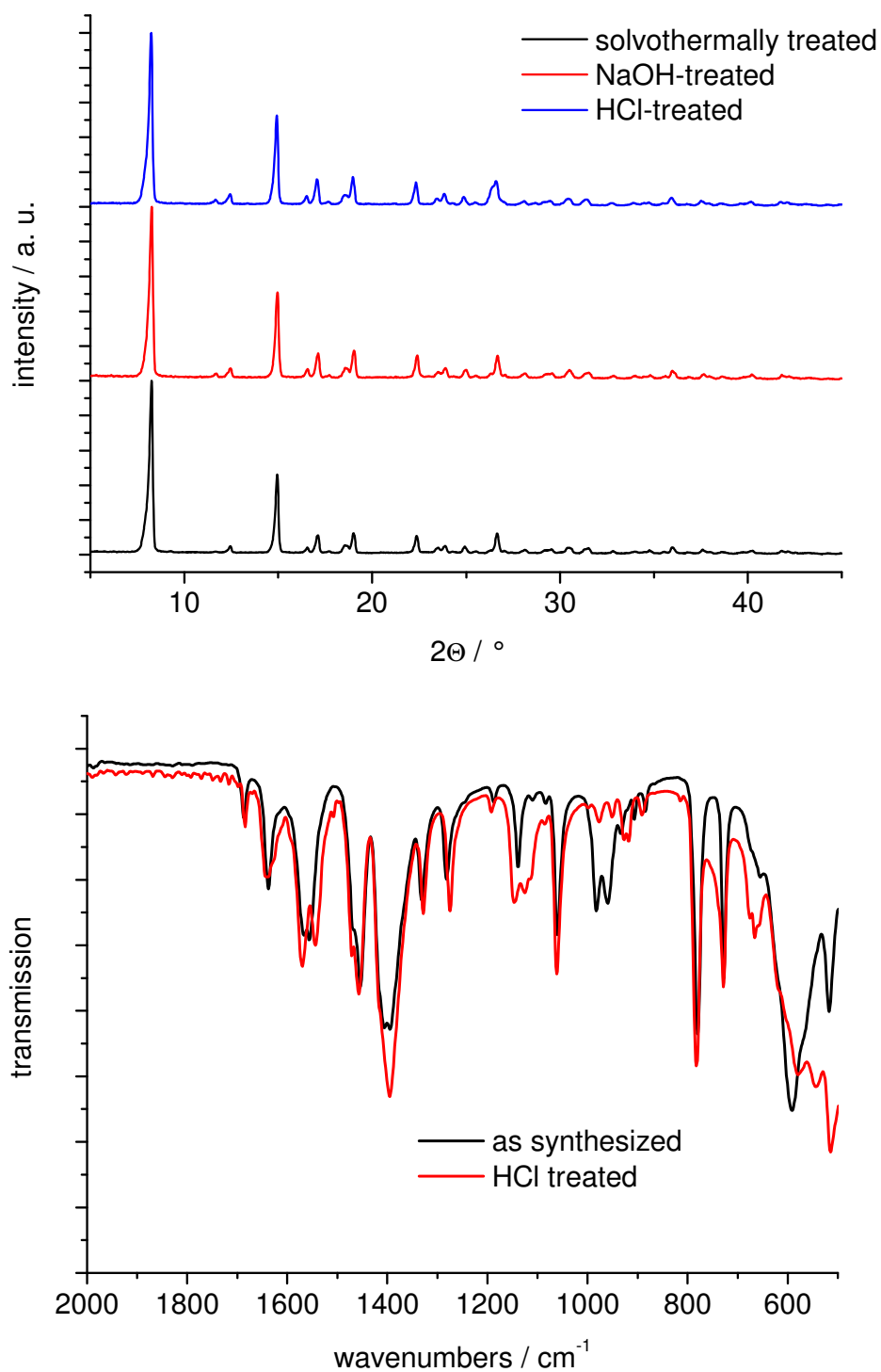


Fig. S13: XRPD-data and IR-sepectra of as synthesized CAU-10-OCH₃ (**3**). Intensities and peak shapes vary slightly. No additional peaks appear in the IR-spectrum due to hydrolysis.

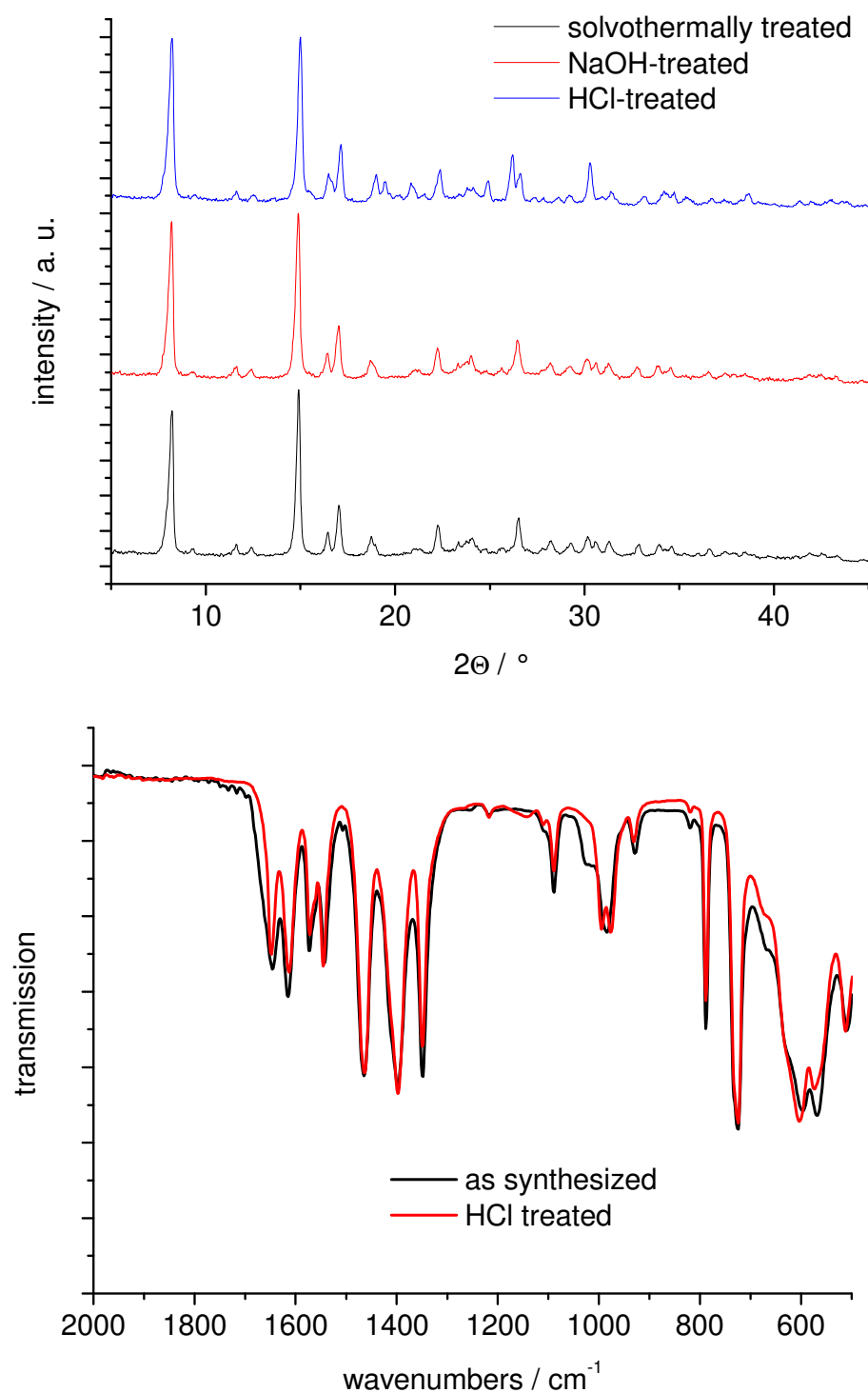


Fig. S14: XRPD-data and IR-spectra of as synthesized CAU-10-NO₂ (**4**). Intensities and peak shapes vary slightly. No additional peaks appear in the IR-spectrum due to hydrolysis.

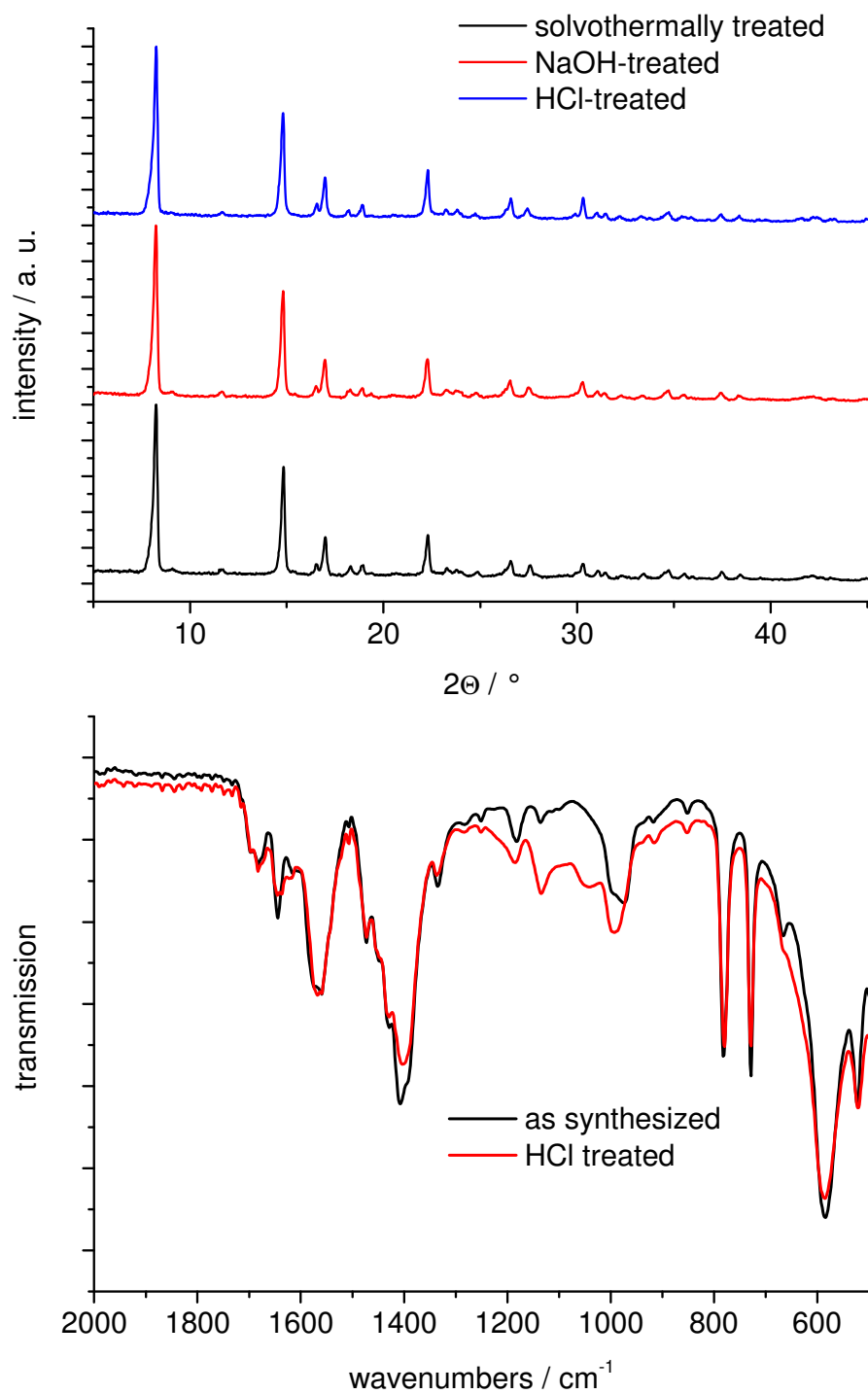


Fig. S15: XRPD-data and IR-spectra of as synthesized CAU-10-NH₂ (**5**). Intensities and peak shapes vary slightly. No additional peaks appear in the IR-spectrum due to hydrolysis.

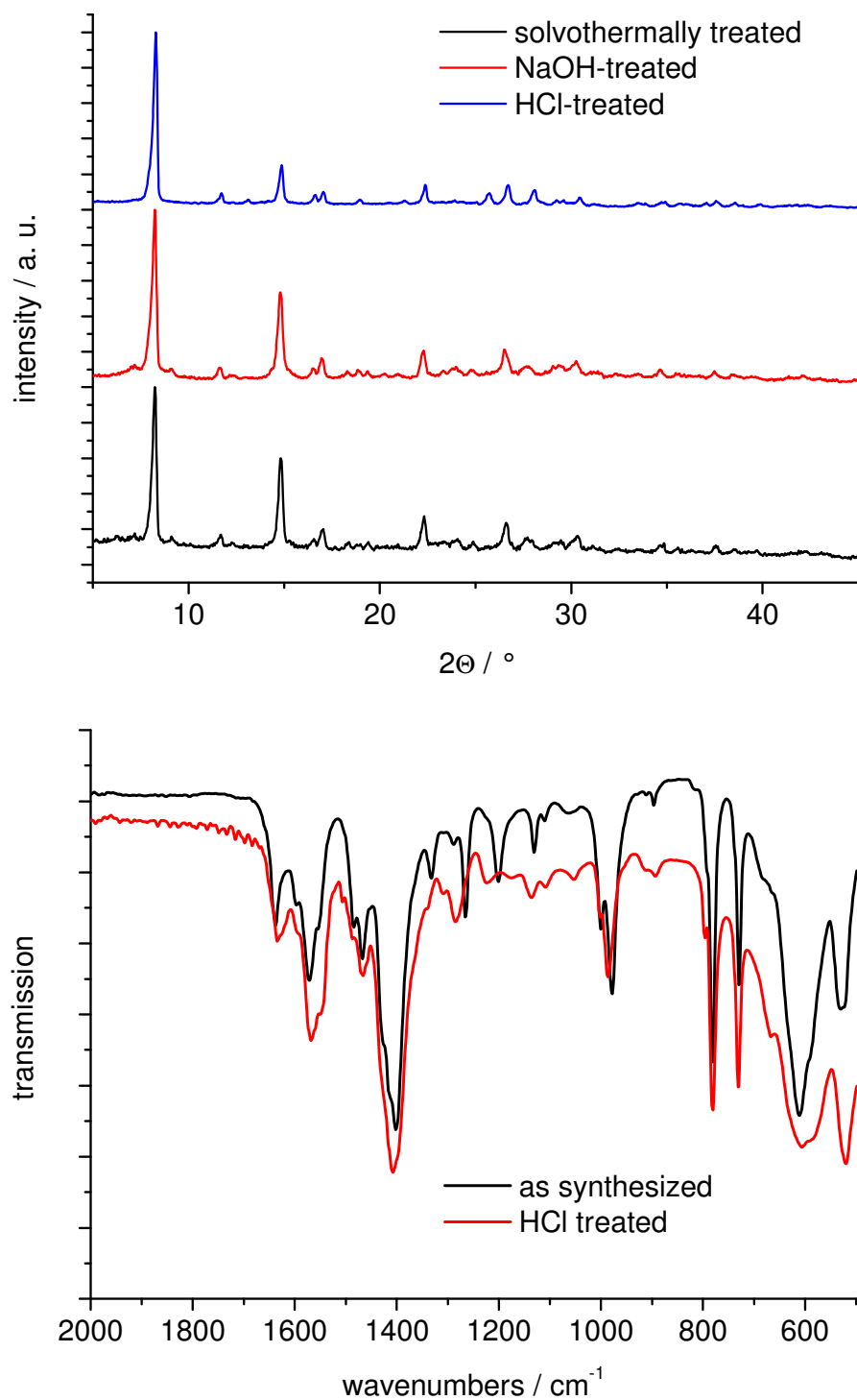


Fig. S16: XRPD-data and IR-sepectra of as synthesized CAU-10-OH (**6**). Intensities and peak shapes vary slightly. No additional peaks appear in the IR-spectrum due to hydrolysis.

IV. Results of the thermogravimetric measurements

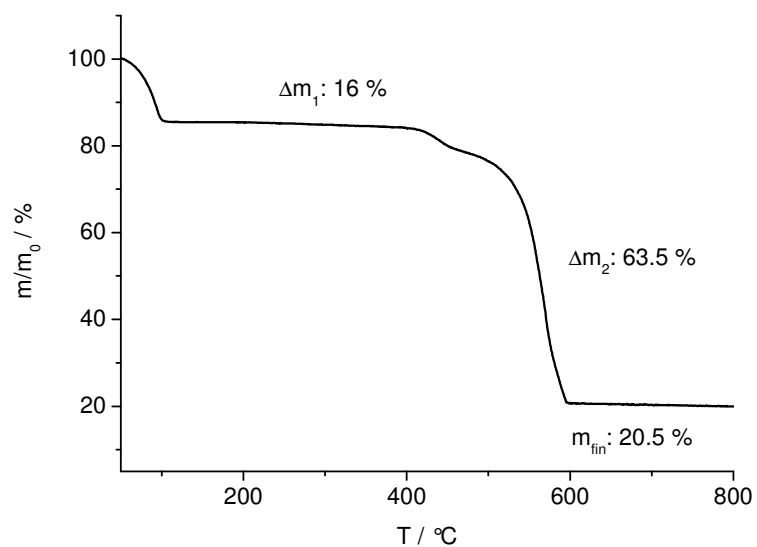


Fig. S 17: TG-curve for as synthesized CAU-10-H (1). The calculated value for the decomposition above 400 °C (63.1 %) is in good agreement with the experimental value.

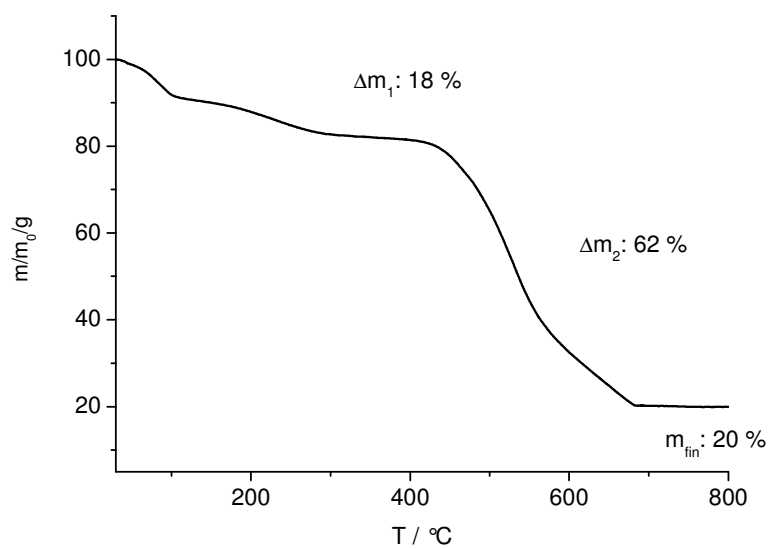


Fig. S 18: TG-curve for as synthesized CAU-10-CH₃ (2). The calculated value for the decomposition above 400 °C (67 %) is in reasonable agreement with the experimental value.

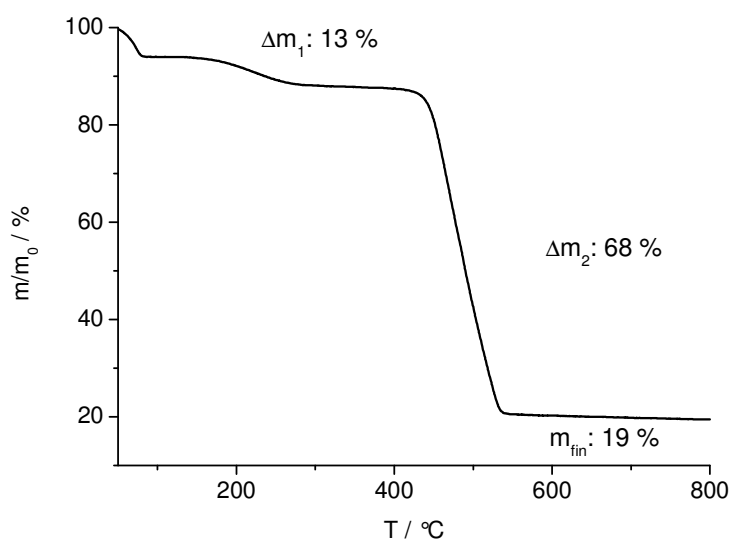


Fig. S 19: TG-curve for as synthesized CAU-10-OCH₃ (**3**). The calculated value for the decomposition above 400 °C (69.7 %) is in good agreement with the experimental value.

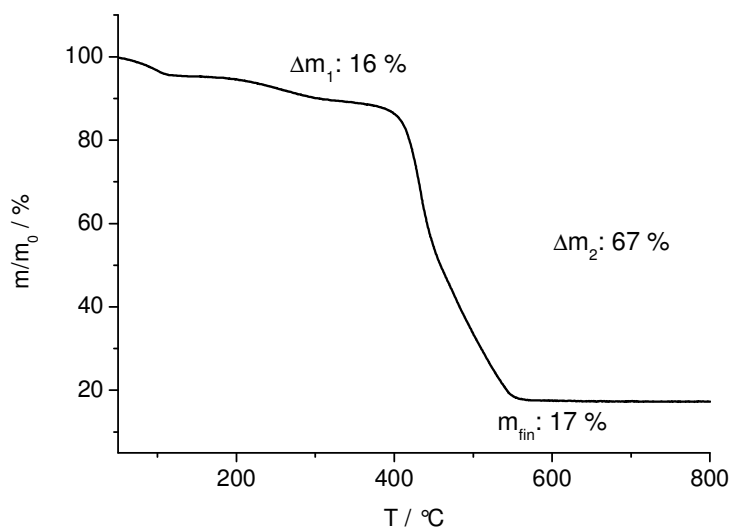


Fig. S 20: TG-curve for as synthesized CAU-10-NO₂ (**4**). The calculated value for the decomposition above 400 °C (67.3 %) is in good agreement with the experimental value.

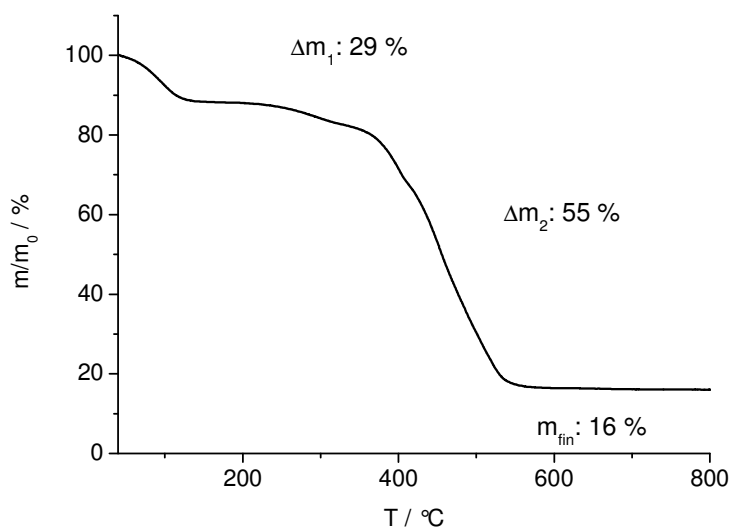


Fig. S 21: TG-curve for as synthesized CAU-10-NH₂ (5). The calculated value for the decomposition above 400 °C (54.0 %) is in good agreement with the experimental value.

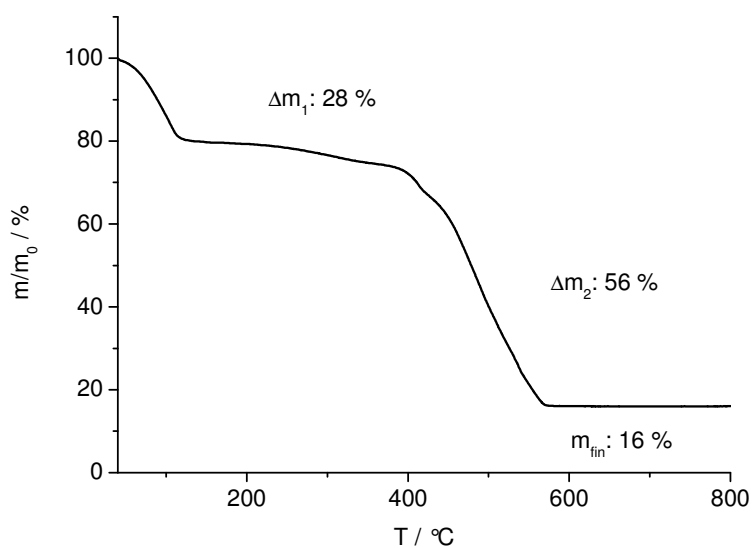


Fig. S 22: TG-curve for as-synthesized CAU-10-OH (6). The calculated value for the decomposition above 400 °C (54.3 %) is in good agreement with the experimental value.

V. Vibrational spectra

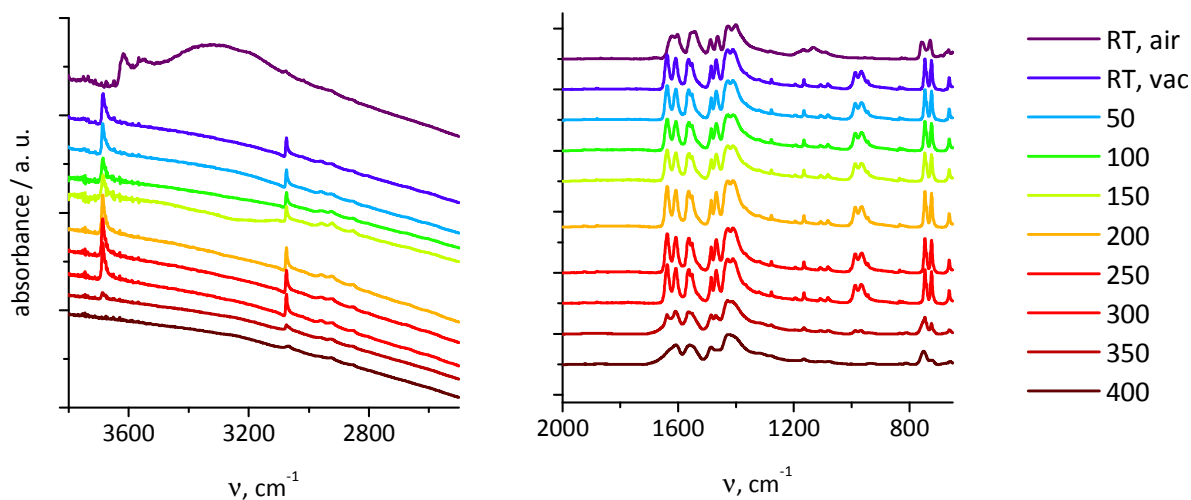


Fig. S 23: Temperature dependent IR-spectra of CAU-10-H (1).

By application of vacuum, the broad band of the hydrogen-bonds of adsorbed water molecules around 3300 cm^{-1} disappears. The peak of the ν_{OH} -vibration at 3615 cm^{-1} is therefore shifted to 3685 cm^{-1} after solvent removal. Furthermore, the ν_{CH} -vibration of the aromatic ring at 3075 cm^{-1} is clearly observed. The bands at 755 cm^{-1} and 724 cm^{-1} are characteristic for 1,3-substituted benzene-rings (out-of-plane-deformation of C-H bonds). The absence of a band at $\sim 1685\text{ cm}^{-1}$ proves that no DMF is occluded inside the pores. The broadening of the peaks at $350\text{ }^{\circ}\text{C}$ marks the beginning decomposition of the MOF.

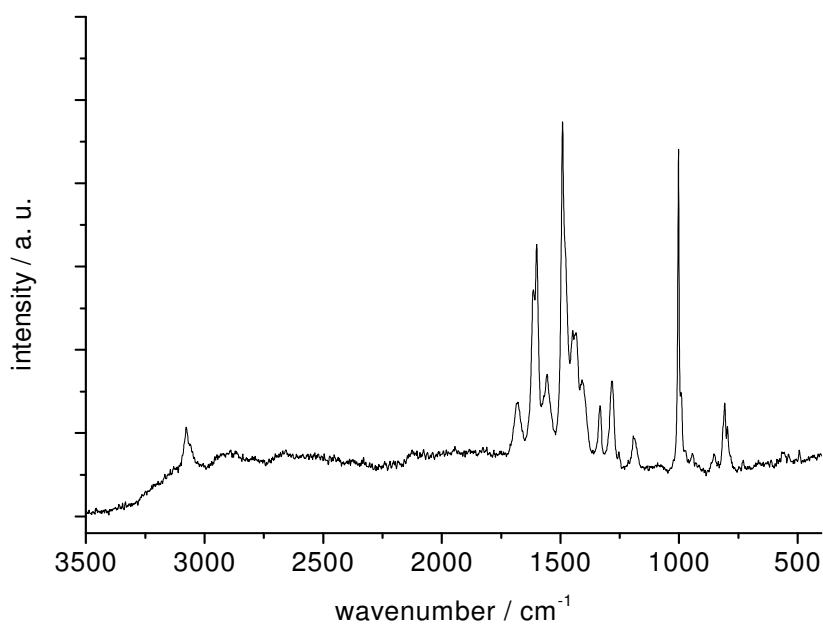


Fig. S 24: Raman-spectrum of CAU-10-H (1).

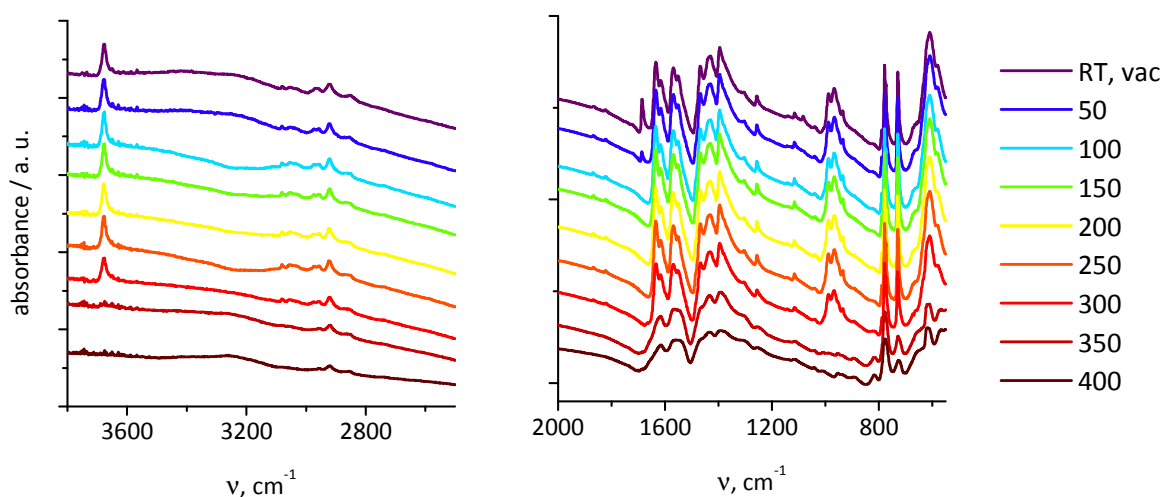


Fig. S 25: Temperature dependent IR-spectra of CAU-10-CH₃ (**2**).

The peak of the ν_{OH} -vibration at 3676 cm^{-1} is prominent in the spectrum. Beside the ν_{CH} -vibration of the aromatic ring at 3075 cm^{-1} , the ν_{CH} -vibrations of the CH₃-group 2916 cm^{-1} (asymmetric) and 2845 cm^{-1} (symmetric) are clearly observed. The bands at 777 cm^{-1} and 730 cm^{-1} are characteristic for 1,3,5-substituted benzene-rings (out-of-plane-deformation of C-H bonds). The band at $\sim 1685\text{ cm}^{-1}$ which belongs to the ν_{CO} -vibration of DMF disappears already at $100\text{ }^{\circ}\text{C}$. The broadening of the peaks at $350\text{ }^{\circ}\text{C}$ marks the beginning of the decomposition of the MOF.

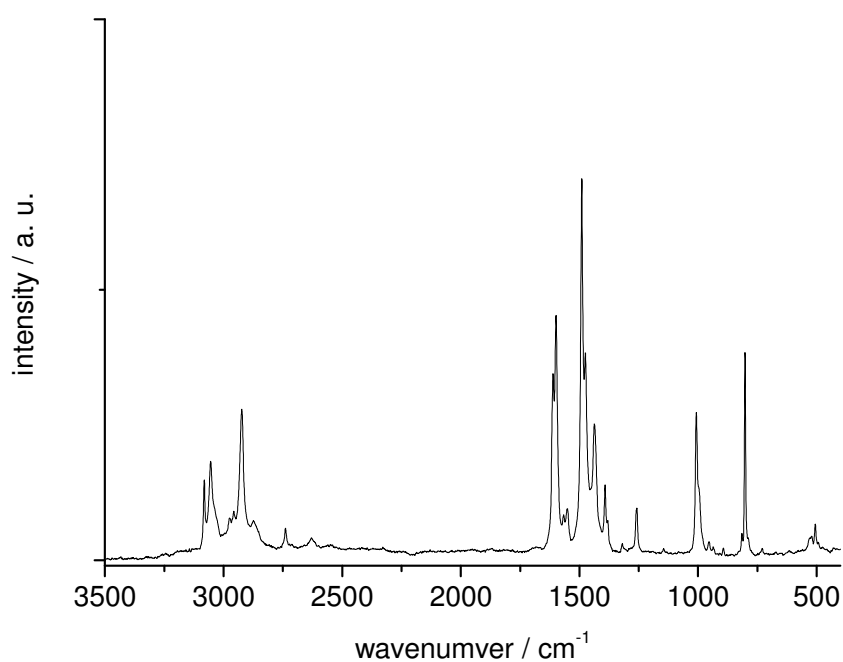


Fig. S 26: Raman-spectrum of CAU-10-CH₃ (**2**).

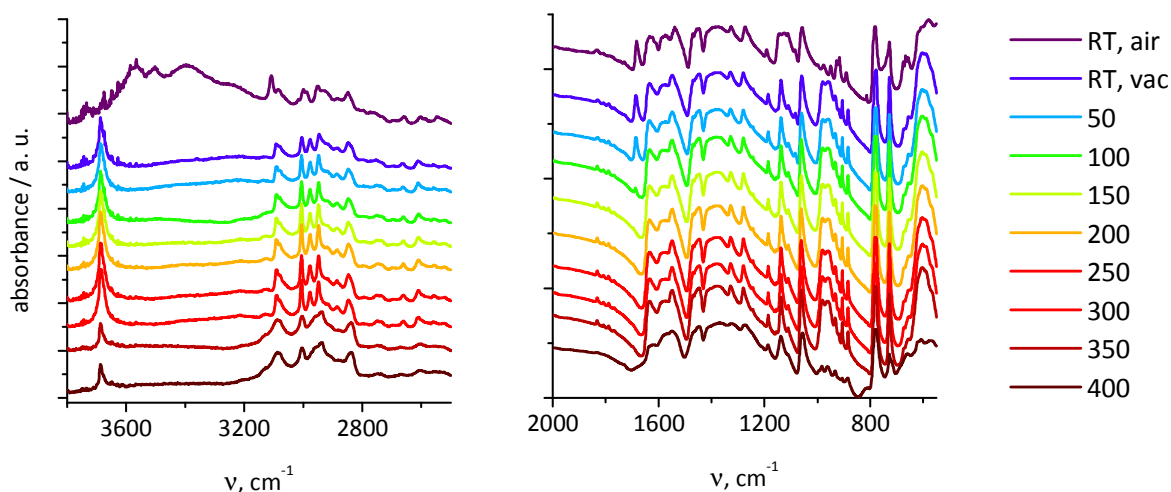


Fig. S 27: Temperature dependent IR-spectra of CAU-10-OCH₃ (**3**).

By application of vacuum, the broad band of the hydrogen-bonds of adsorbed water molecules around 3300 cm⁻¹ disappears. The peak of the ν_{OH} -vibration at 3686 cm⁻¹ is prominent in the spectrum. Besides the ν_{CH} -vibrations of the aromatic ring at 3092 and 3006 cm⁻¹, three bands of the ν_{CH} -vibrations of the OCH₃-group at 2975 and 2945 cm⁻¹ (asymmetric) and 2845 cm⁻¹ (symmetric) are clearly observed. The bands at 784 and 728 cm⁻¹ are characteristic for 1,3,5-substituted benzene-rings (out-of-plane-deformation of C-H bonds). The band at ~1685 cm⁻¹ which belongs to the ν_{CO} -vibration of DMF disappears already at 100 °C. The broadening of the peaks at 400 °C marks the beginning of the decomposition of the MOF.

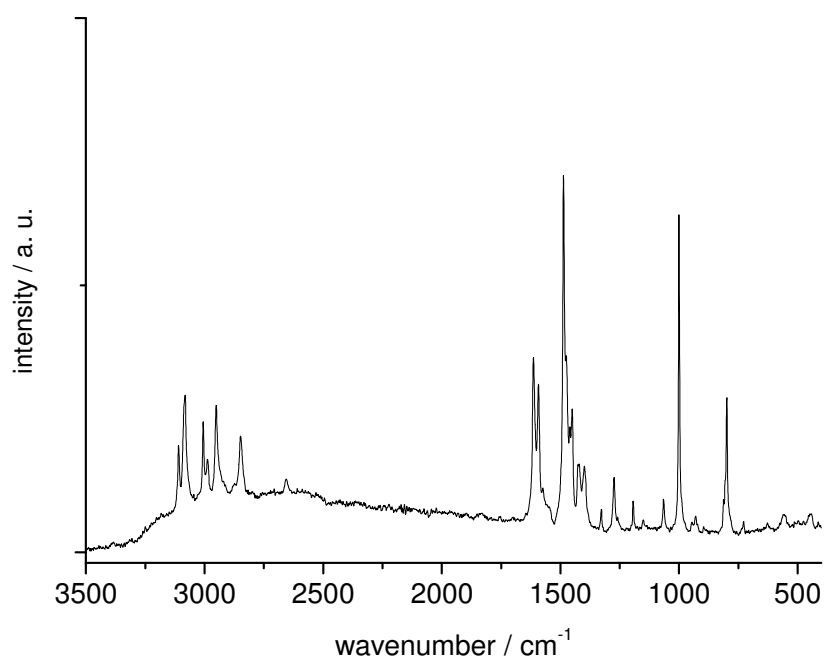


Fig. S 28: Raman-spectrum of CAU-10-OCH₃ (**3**).

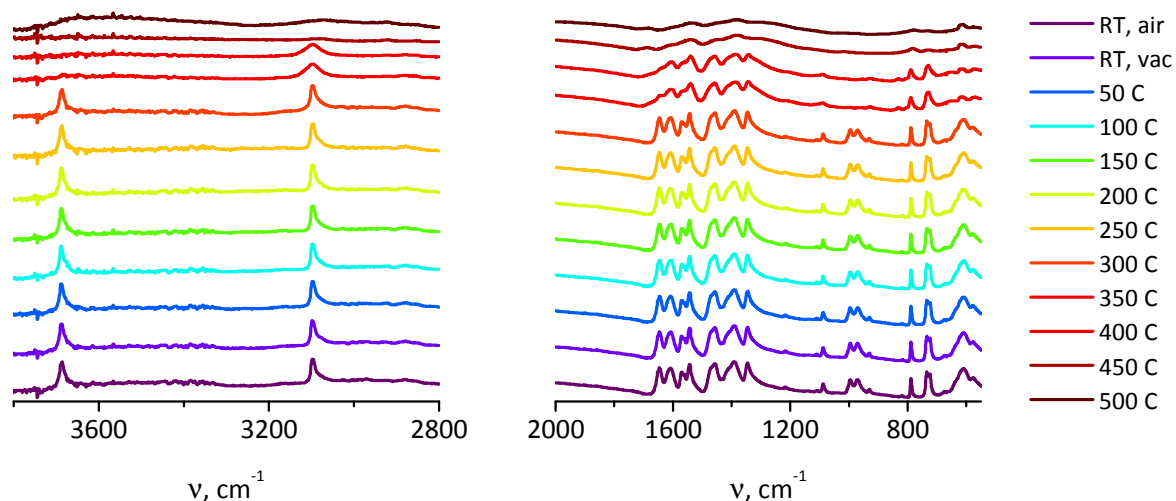


Fig. S 29: Temperature dependent IR-spectra of CAU-10-NO₂ (4).

The peak of the ν_{OH} -vibration at 3693 cm^{-1} is prominent in the spectrum. The ν_{CH} -vibrations of the aromatic ring at 3096 cm^{-1} is clearly observed. The bands at 787 cm^{-1} and 724 cm^{-1} are characteristic for 1,3,5-substituted benzene-rings (out-of-plane-deformation of C-H bonds). The broadening of the peaks at $350 \text{ }^\circ\text{C}$ marks the beginning of the decomposition of the MOF.

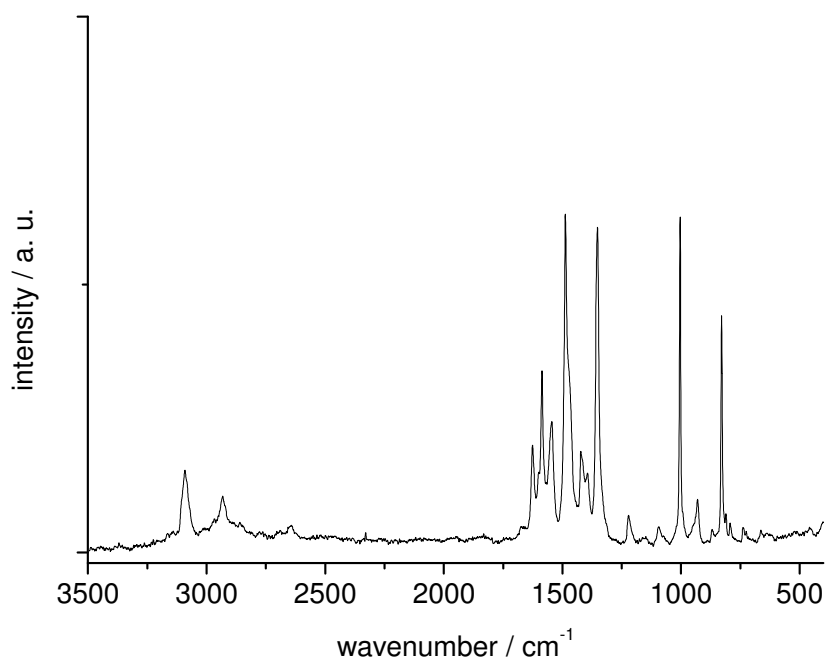


Fig. S 30: Raman-spectrum of CAU-10-NO₂ (4).

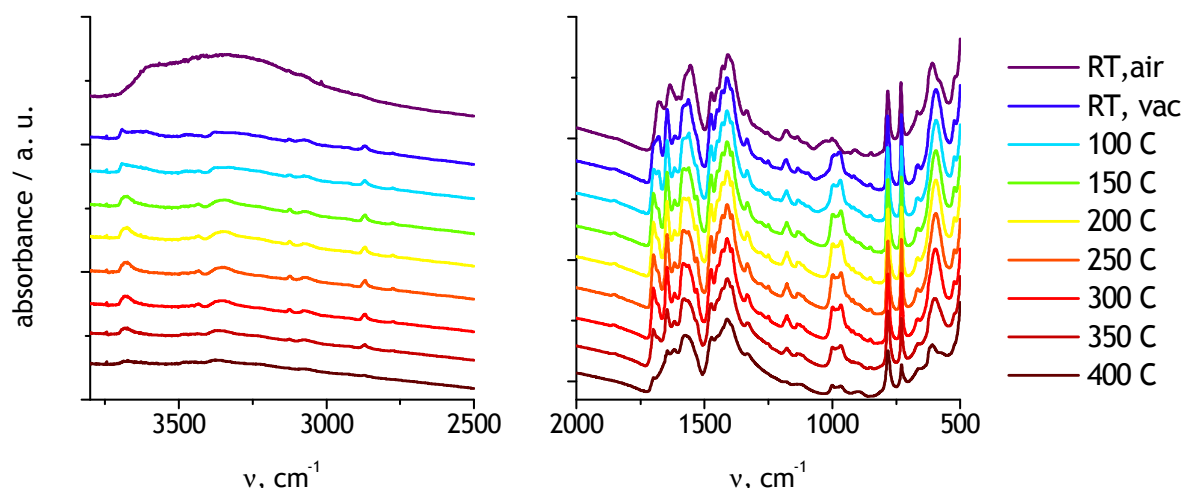


Fig. S 31: Temperature dependent IR-spectra of CAU-10-NH₂ (**5**).

The peak of the ν_{OH} -vibration at 3693 cm^{-1} is very weak in the spectrum as well as the ν_{CH} -vibrations of the aromatic ring at 3068 cm^{-1} . The broad band at 3330 cm^{-1} (ν_{NH} -vibration) and the band at 2845 cm^{-1} (ν_{CH} -vibration) can be explained by the partial formylation of the NH_2 -group during the synthesis (see paragraph XI). This is further confirmed by the ν_{CO} -band for amides at 1682 cm^{-1} . The bands at 786 and 727 cm^{-1} are characteristic for 1,3,5-substituted benzene-rings (out-of-plane-deformation of C-H bonds). The broadening of the peaks at $400\text{ }^\circ\text{C}$ marks the beginning of the decomposition of the MOF.

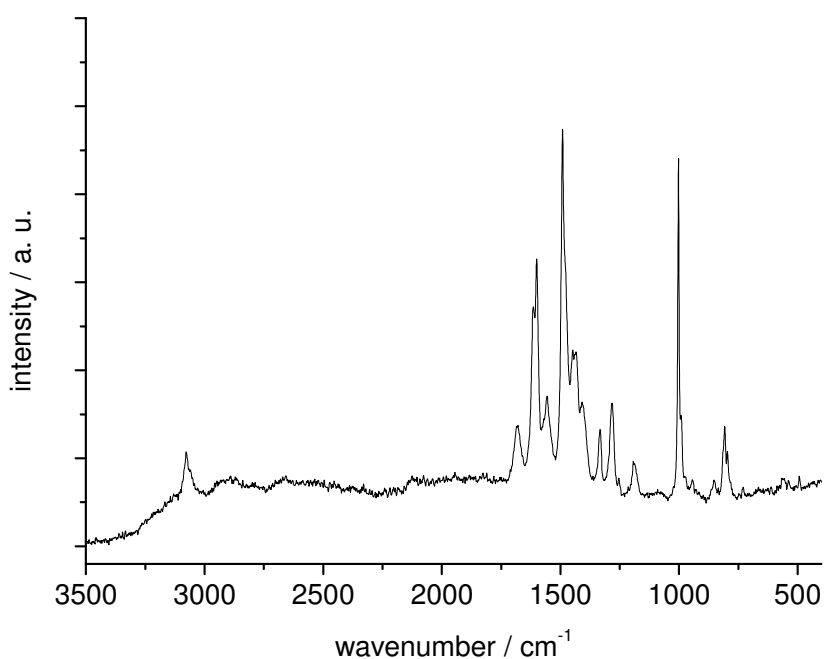


Fig. S 32: Raman-spectrum of CAU-10-NH₂ (**5**).

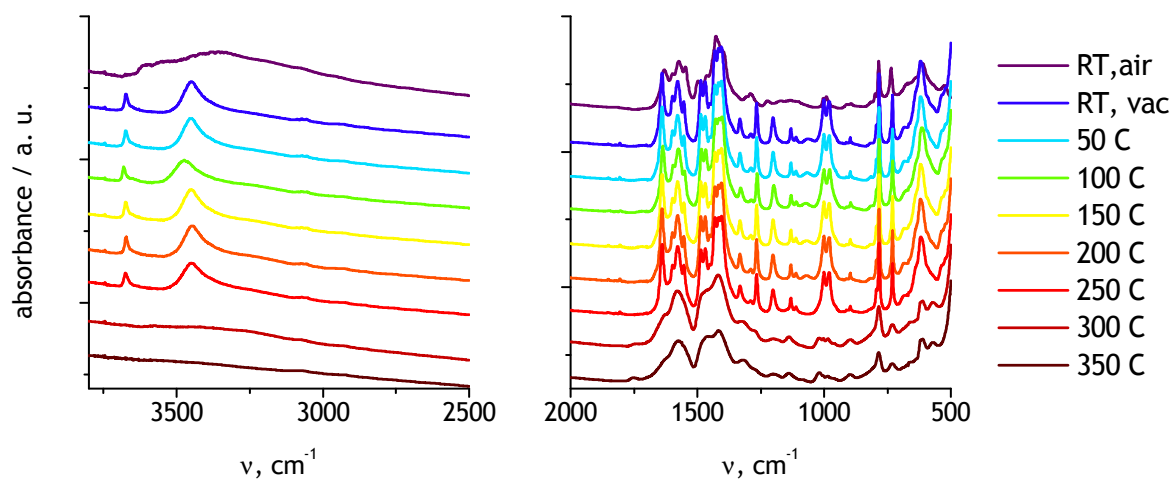


Fig. S 33: Temperature dependent IR-spectra of CAU-10-OH (**6**).

By application of vacuum, the broad band of the hydrogen-bonds of adsorbed water molecules around 3300 cm^{-1} disappears. The peak of the ν_{OH} -vibration at 3615 cm^{-1} is thus only visible upon activation, as well as the peak at 3450 cm^{-1} which belongs to the ν_{OH} -group at the aromatic ring. The bands at 786 cm^{-1} and 727 cm^{-1} are characteristic for 1,3,5-substituted benzene-rings (out-of-plane-deformation of C-H bonds). The broadening of the peaks at $300\text{ }^{\circ}\text{C}$ marks the beginning of the decomposition of the MOF.

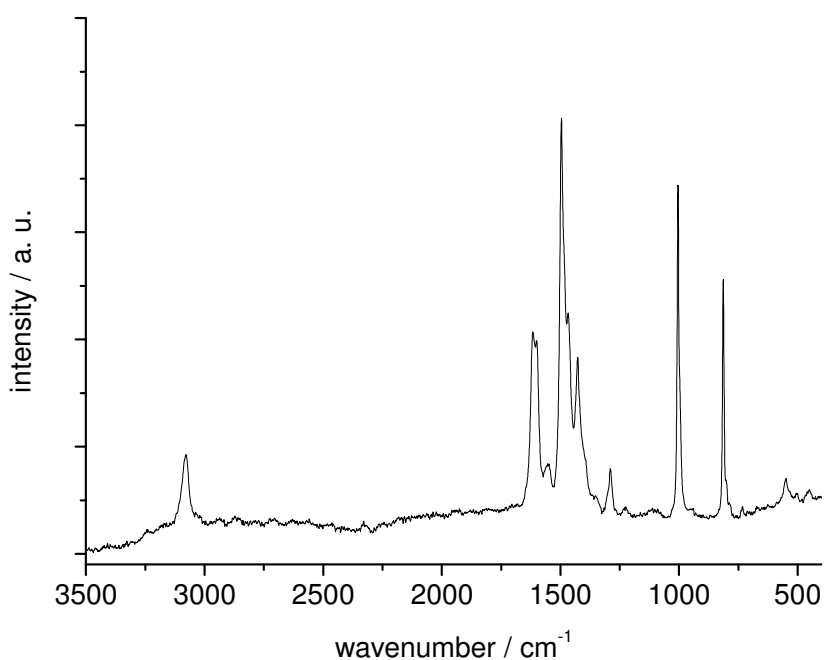


Fig. S 34: Raman-spectrum of CAU-10-OH (**6**).

VI. Description of the HT-experiments

CAU-10-H (**1**) was discovered as the first MOF of the CAU-10-series. The investigated system was Al^{3+} / isophthalic acid / DMF-water mixture and the 24-reactor HT-setup was used. Two different aluminium salts were employed as Al^{3+} -source in different molar ratios Al^{3+} : linker. A 4:1 mixture of water and DMF (500 μL) was used as solvent (Tab. S4). The reactions were carried out at 145 °C for 12 h.

Tab. S4: Exact amounts of starting materials during the HT-experiment that led to the discovery of CAU-10-H (**1**).

number	n (Al^{3+}) [mmol]	n (linker) [mmol]	m (AIX) [mg]	m (linker) [mg]	Al-source
1	0.030	0.060	7.3	10.0	$\text{AlCl}_3 \cdot 6\text{H}_2\text{O}$
2	0.060	0.060	14.5	10.0	$\text{AlCl}_3 \cdot 6\text{H}_2\text{O}$
3	0.120	0.060	29.0	10.0	$\text{AlCl}_3 \cdot 6\text{H}_2\text{O}$
4	0.045	0.090	10.9	15.0	$\text{AlCl}_3 \cdot 6\text{H}_2\text{O}$
5	0.090	0.090	21.8	15.0	$\text{AlCl}_3 \cdot 6\text{H}_2\text{O}$
6	0.181	0.090	43.6	15.0	$\text{AlCl}_3 \cdot 6\text{H}_2\text{O}$
7	0.602	0.120	145.2	20.0	$\text{AlCl}_3 \cdot 6\text{H}_2\text{O}$
8	0.723	0.120	174.2	20.0	$\text{AlCl}_3 \cdot 6\text{H}_2\text{O}$
9	0.843	0.120	203.3	20.0	$\text{AlCl}_3 \cdot 6\text{H}_2\text{O}$
10	0.753	0.151	181.5	25.0	$\text{AlCl}_3 \cdot 6\text{H}_2\text{O}$
11	0.904	0.151	217.8	25.0	$\text{AlCl}_3 \cdot 6\text{H}_2\text{O}$
12	1.054	0.151	254.1	25.0	$\text{AlCl}_3 \cdot 6\text{H}_2\text{O}$
13	0.904	0.181	217.8	30.0	$\text{AlCl}_3 \cdot 6\text{H}_2\text{O}$
14	1.084	0.181	261.3	30.0	$\text{AlCl}_3 \cdot 6\text{H}_2\text{O}$
15	1.265	0.181	304.9	30.0	$\text{AlCl}_3 \cdot 6\text{H}_2\text{O}$
16	1.054	0.211	254.1	35.0	$\text{AlCl}_3 \cdot 6\text{H}_2\text{O}$
17	1.265	0.211	304.9	35.0	$\text{AlCl}_3 \cdot 6\text{H}_2\text{O}$
18	1.476	0.211	355.7	35.0	$\text{AlCl}_3 \cdot 6\text{H}_2\text{O}$
19	0.361	0.120	120.4	20.0	$\text{Al}_2(\text{SO}_4)_3 \cdot 18\text{H}_2\text{O}$
20	0.482	0.120	160.5	20.0	$\text{Al}_2(\text{SO}_4)_3 \cdot 18\text{H}_2\text{O}$
21	0.602	0.120	200.6	20.0	$\text{Al}_2(\text{SO}_4)_3 \cdot 18\text{H}_2\text{O}$
22	0.723	0.151	240.7	25.0	$\text{Al}_2(\text{SO}_4)_3 \cdot 18\text{H}_2\text{O}$
23	0.964	0.151	321.0	25.0	$\text{Al}_2(\text{SO}_4)_3 \cdot 18\text{H}_2\text{O}$
24	1.205	0.151	401.2	25.0	$\text{Al}_2(\text{SO}_4)_3 \cdot 18\text{H}_2\text{O}$

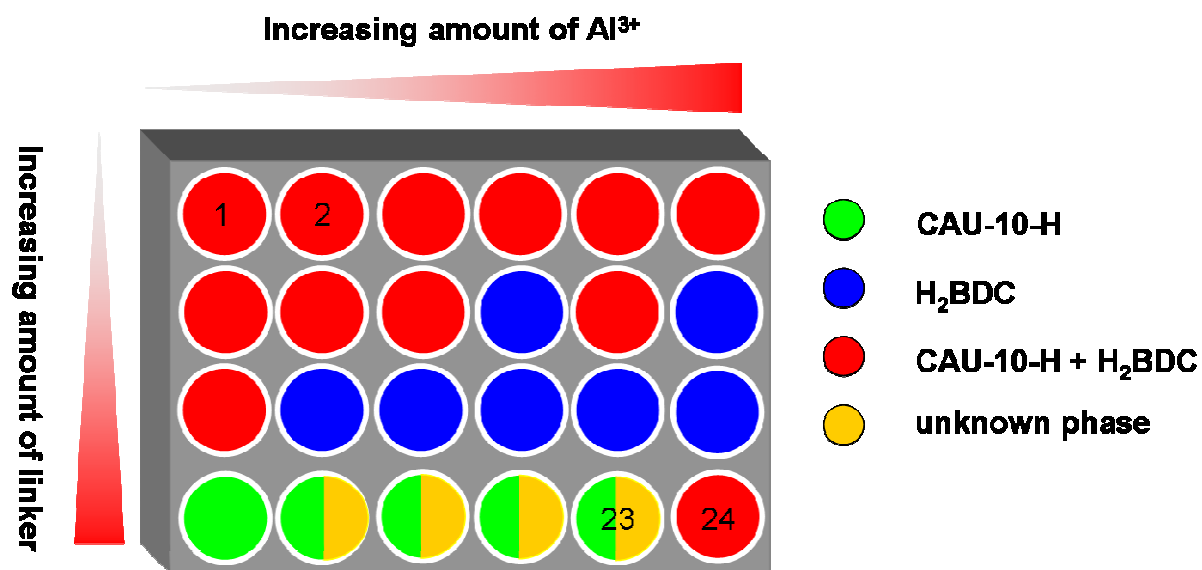


Fig. S35: Products and tendencies that were observed during the discovery of CAU-10-H (**1**).

Employing $\text{AlCl}_3 \cdot 6\text{H}_2\text{O}$ as the Al^{3+} -source, **1** could be synthesized but not as pure compound. In most cases, recrystallised isophthalic acid was observed as byproduct or in its pure form, no matter which molar ratio Al^{3+} :linker was employed. In the last row, the Al^{3+} -source was changed to the sulfate. In most reactions, the formation of **1** was observed accompanied by an unknown byproduct. Only for the molar ratio Al^{3+} :linker 3:1, CAU-10-H was obtained as a single phase product. Further optimization of the reaction conditions and composition led to the optimized synthesis conditions described in the article.

For the synthesis of the functionalized analogues of **1**, an archetypical HT-experiment is described in Tab. S5 and Fig S36. Two different aluminium sources were employed. Different concentrations of reactants were employed at a constant ratio Al^{3+} :linker in mixtures of water and DMF in varying ratios. The synthesis was carried out at 135 °C for 12 h.

Tab. S5: Exact amounts of starting materials during the HT-experiment that led to the discovery of CAU-10-NO₂ (**4**).

number	n (Al ³⁺) [mmol]	n (linker) [mmol]	m (AlX) [mg]	m (linker) [mg]	Al-source	V H ₂ O [μL]	V DMF [μL]
1	0.076	0.076	28.4	16.0	Al(NO ₃) ₃ ·9H ₂ O	500.0	0.0
2	0.076	0.076	28.4	16.0	Al(NO ₃) ₃ ·9H ₂ O	400.0	100.0
3	0.076	0.076	28.4	16.0	Al(NO ₃) ₃ ·9H ₂ O	300.0	200.0
4	0.076	0.076	28.4	16.0	Al(NO ₃) ₃ ·9H ₂ O	200.0	300.0
5	0.114	0.114	42.7	24.0	Al(NO ₃) ₃ ·9H ₂ O	500.0	0.0
6	0.114	0.114	42.7	24.0	Al(NO ₃) ₃ ·9H ₂ O	400.0	100.0
7	0.114	0.114	42.7	24.0	Al(NO ₃) ₃ ·9H ₂ O	300.0	200.0
8	0.114	0.114	42.7	24.0	Al(NO ₃) ₃ ·9H ₂ O	200.0	300.0
9	0.152	0.152	56.9	32.0	Al(NO ₃) ₃ ·9H ₂ O	500.0	0.0
10	0.152	0.152	56.9	32.0	Al(NO ₃) ₃ ·9H ₂ O	400.0	100.0
11	0.152	0.152	56.9	32.0	Al(NO ₃) ₃ ·9H ₂ O	300.0	200.0
12	0.152	0.152	56.9	32.0	Al(NO ₃) ₃ ·9H ₂ O	200.0	300.0
13	0.076	0.076	50.5	16.0	Al ₂ (SO ₄) ₃ ·18H ₂ O	500.0	0.0
14	0.076	0.076	50.5	16.0	Al ₂ (SO ₄) ₃ ·18H ₂ O	400.0	100.0
15	0.076	0.076	50.5	16.0	Al ₂ (SO ₄) ₃ ·18H ₂ O	300.0	200.0
16	0.076	0.076	50.5	16.0	Al ₂ (SO ₄) ₃ ·18H ₂ O	200.0	300.0
17	0.114	0.114	75.8	24.0	Al ₂ (SO ₄) ₃ ·18H ₂ O	500.0	0.0
18	0.114	0.114	75.8	24.0	Al ₂ (SO ₄) ₃ ·18H ₂ O	400.0	100.0
19	0.114	0.114	75.8	24.0	Al ₂ (SO ₄) ₃ ·18H ₂ O	300.0	200.0
20	0.114	0.114	75.8	24.0	Al ₂ (SO ₄) ₃ ·18H ₂ O	200.0	300.0
21	0.152	0.152	101.0	32.0	Al ₂ (SO ₄) ₃ ·18H ₂ O	500.0	0.0
22	0.152	0.152	101.0	32.0	Al ₂ (SO ₄) ₃ ·18H ₂ O	400.0	100.0
23	0.152	0.152	101.0	32.0	Al ₂ (SO ₄) ₃ ·18H ₂ O	300.0	200.0
24	0.152	0.152	101.0	32.0	Al ₂ (SO ₄) ₃ ·18H ₂ O	200.0	300.0

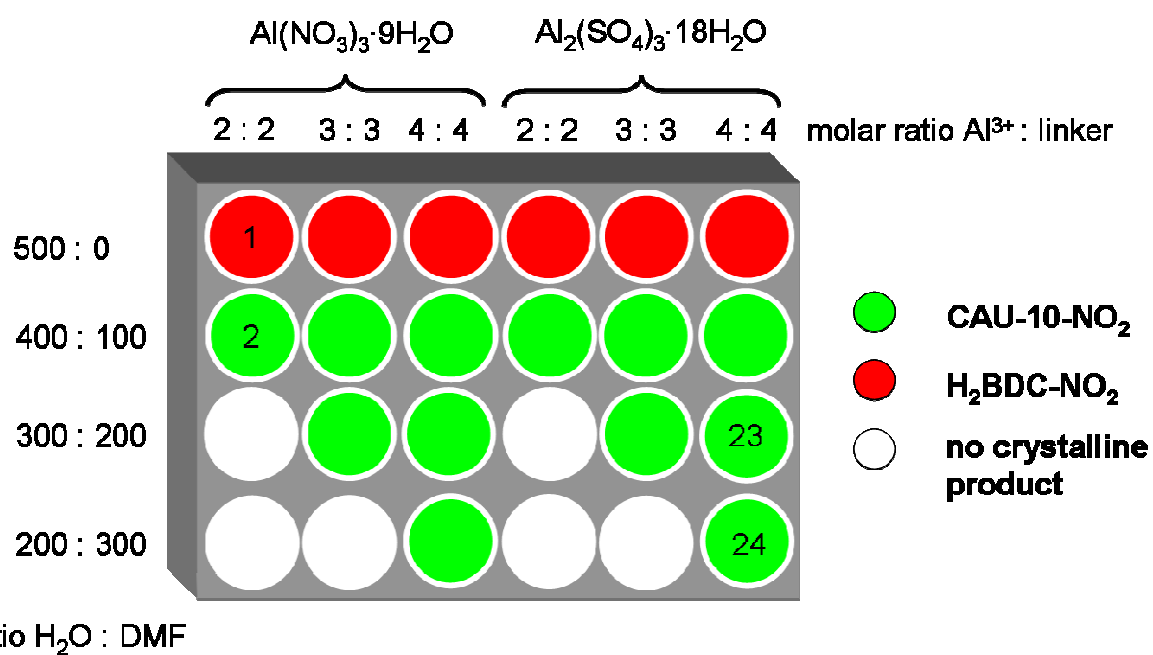


Fig. S36: Products and tendencies that were observed during the discovery of CAU-10-NO₂ (4).

In this experiment the role of DMF for the synthesis becomes clearer. The use of pure water as solvent (reactions 1, 5, 9, 13, 17, 21) results not in the formation of a MOF, but in the recrystallization of the linker molecule. CAU-10-NO₂ (4) is only obtained, if mixtures of water and DMF are employed. The formation of the MOF is apparently almost independent of the Al³⁺-source but strongly depends on the amount of Al³⁺ salt and DMF employed. Further optimization of the synthesis conditions led to the procedure described in the paper.

VII. Scanning electron microscopy images

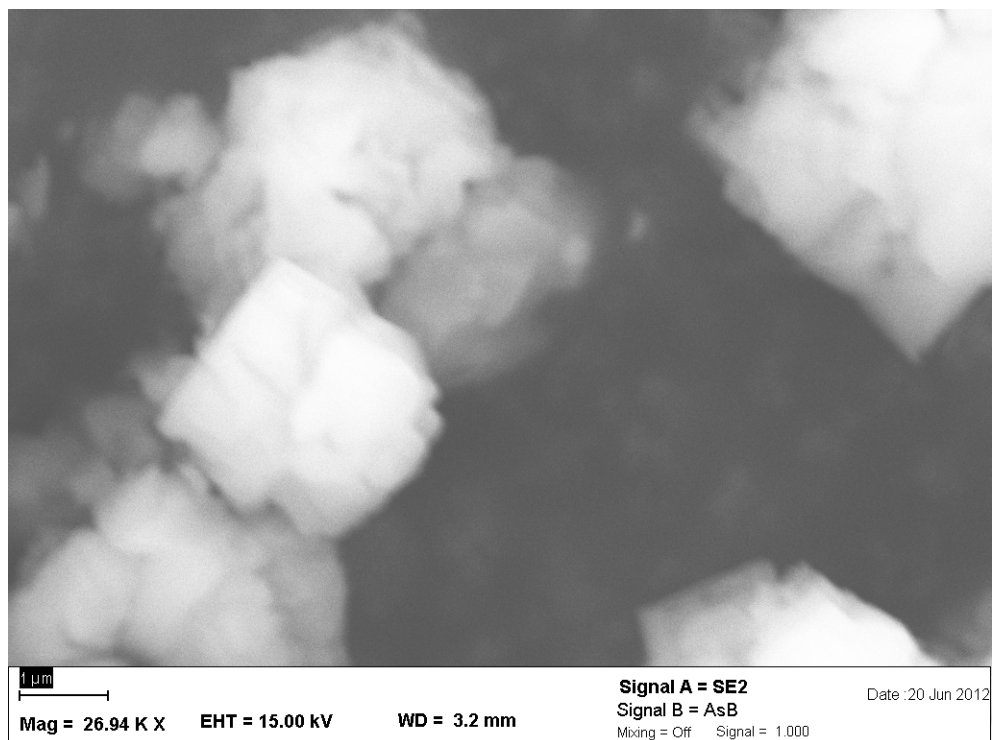


Fig. S37: SEM-Micrograph of CAU-10-H (1).

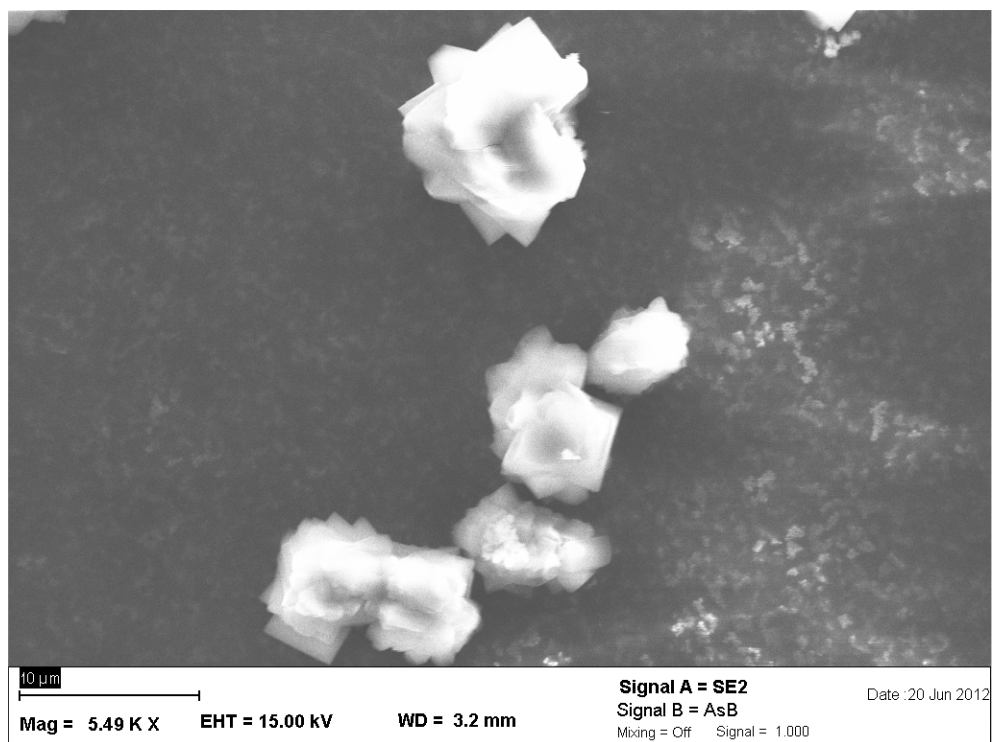


Fig. S38: SEM-Micrograph of CAU-10-CH₃ (2).

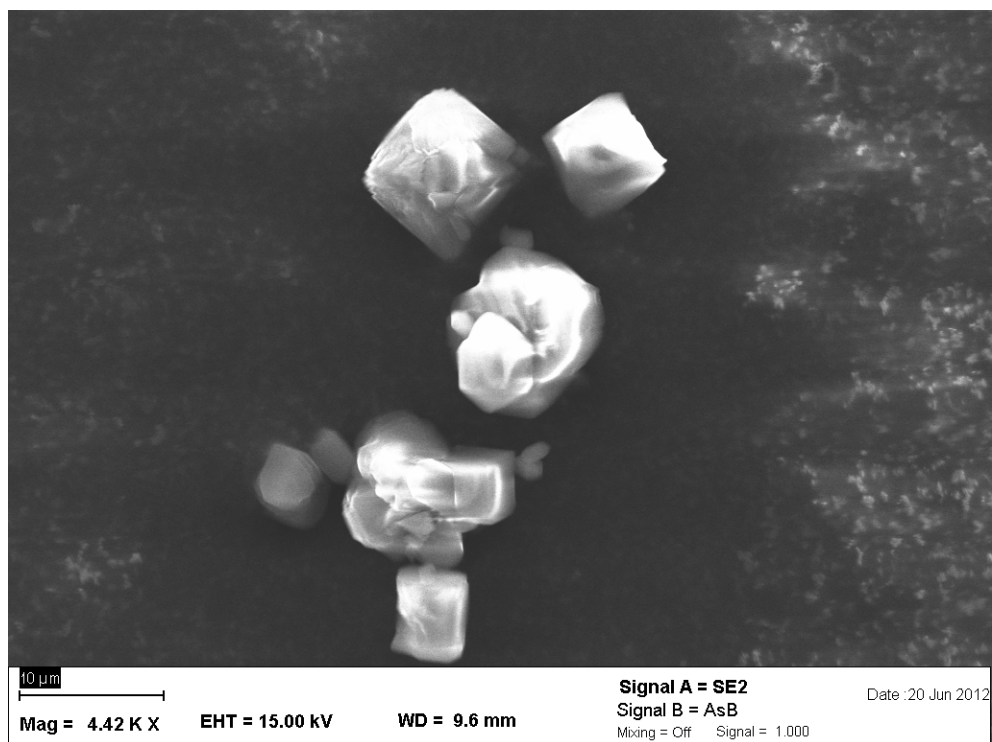


Fig. S39: SEM-Micrograph of CAU-10-OCH₃ (3).

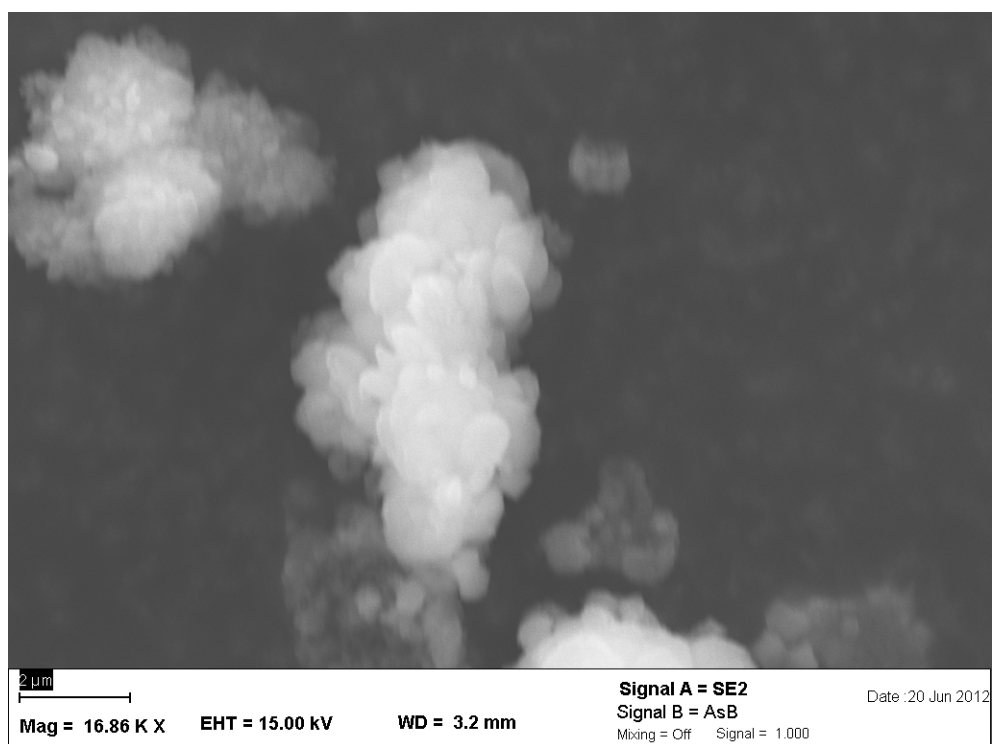


Fig. S40: SEM-Micrograph of CAU-10-NO₂ (4).

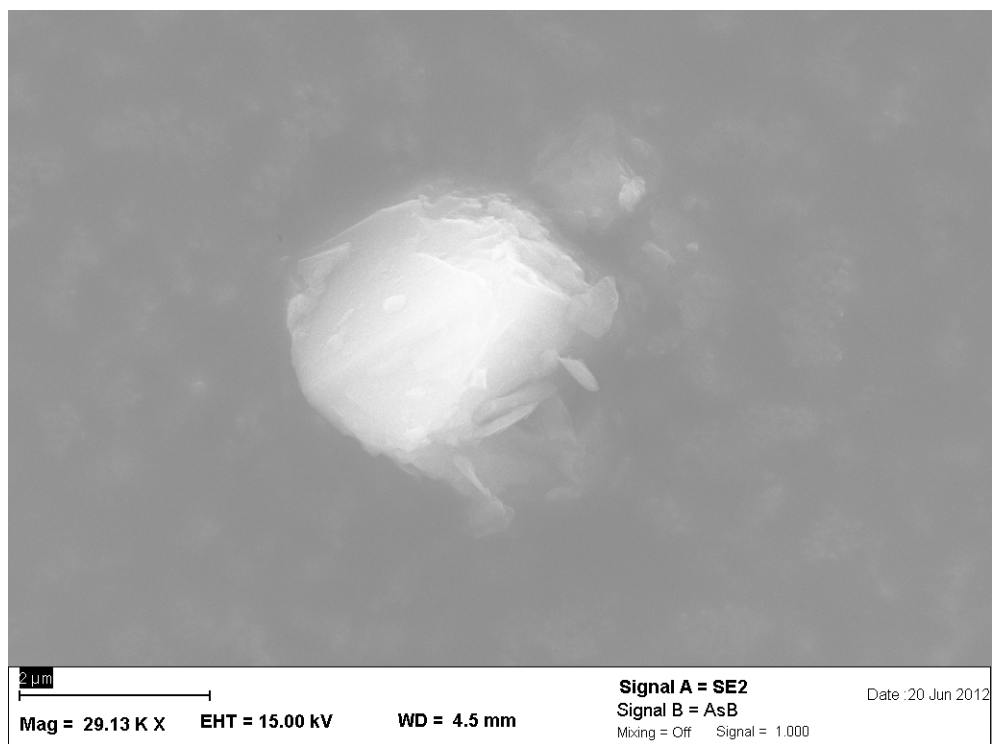


Fig. S41: SEM-Micrograph of CAU-10-NH₂ (5).

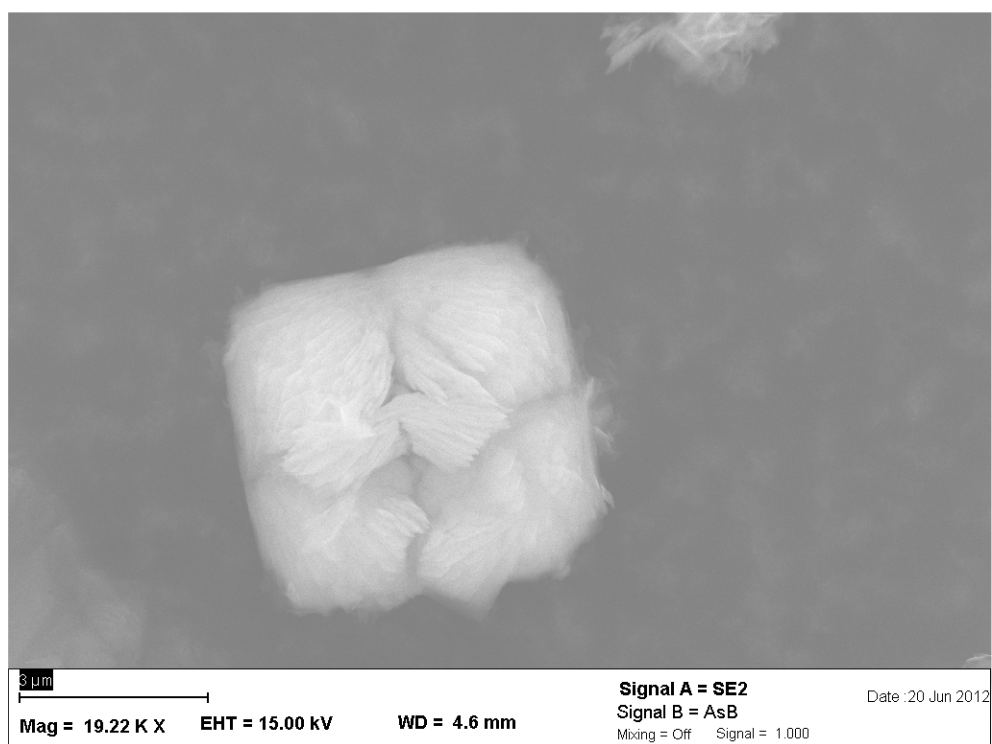


Fig. S42: SEM-Micrograph of CAU-10-OH (6).

VIII. SHG polarization dependency of compound 1

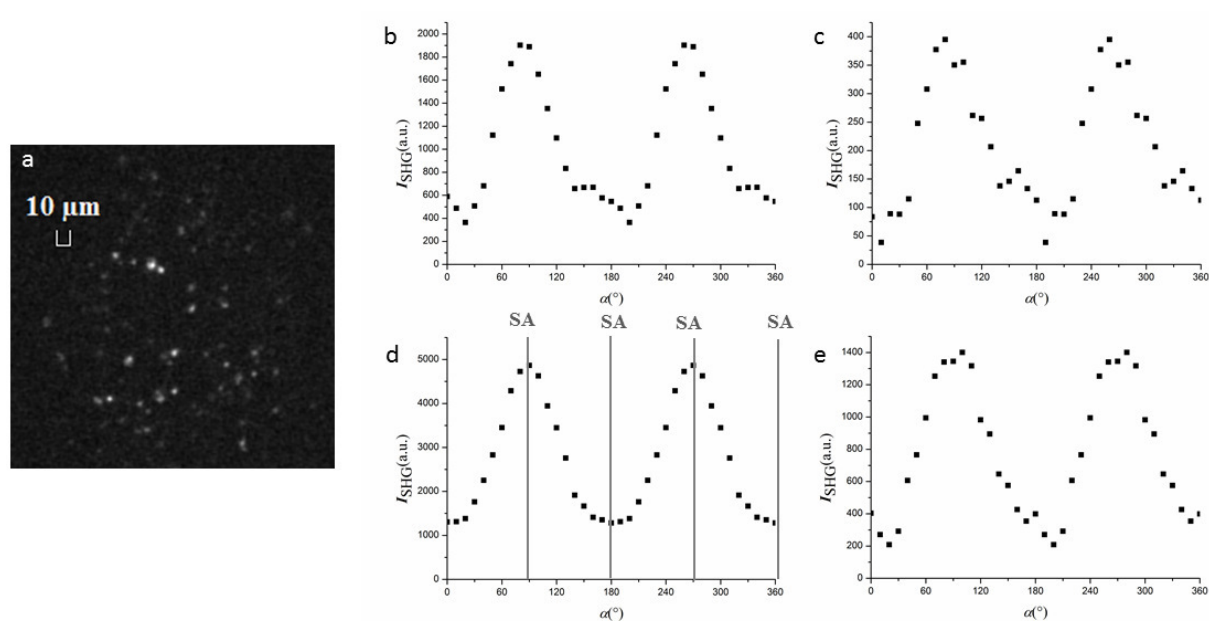


Figure S43: a) SHG-image of activated CAU-10-H (1). SHG intensity of this structure for tests 1 and 2 resp. corresponding to an arbitrarily oriented crystallite (b and c resp.) and a crystallite oriented with its c-axis aligned with the sample plane (d and e resp.) while varying the plane of polarization of the incident light (α). The incident light is linearly polarized and rotated along the direction of light propagation. Note that when the plane of polarization is 180° different, the plane of polarization of the incident light is identical.

IX. Theoretical treatment of SHG for D4 symmetry

Equation 1 of the main text of the article can be rewritten as

$$P_i^{(2)} = \sum_{j,k} \chi_{ijk}^{(2)} E_j E_k \quad \text{Eq. S 1}$$

in which the indices ijk refer to the Cartesian coordinates. Equation S 1 connects the components $P_i^{(2)}$ of the polarization vector with the components E_i of the electric field vector via the susceptibility tensor components $\chi_{ijk}^{(2)}$. For a structure with D_4 only following susceptibility tensor components are non-zero: $\chi_{xyz} = \chi_{xzy} = -\chi_{yzx} = -\chi_{yxz}$ and $\chi_{zxy} = -\chi_{zyx}$. In the latter tensor components the indices refer directly to the natural coordinate system of the structure with D_4 symmetry.

The measured SHG intensity $I_L^{2\omega}$ polarized along the L direction is directly related to the polarization $P_L^{(2)}$:

$$I_L^{2\omega} \sim |P_L^{(2)}|^2 \quad \text{Eq. S 2}$$

Employing equation S 1 and S 2 for a structure of D_4 symmetry of any orientation yield following equation

$$I_X^{2\omega} \sim \chi_{xyz}^{(2)} E_Y^2 (E_X \cos(\varphi) - E_Y \sin(\varphi))^2 \sin^2(2\theta) \quad \text{Eq. S 3}$$

in which θ and φ described the orientation of the crystal with respect to the Cartesian laboratory XYZ frame. θ is the angle between the z and the Z axis, φ is the angle between the projection of the z axis in the XY plane with the X axis. For light polarized parallel with the polarization direction of the detected second-harmonic intensity X , the component of the electric field of the incident light E_Y is zero. As can be seen from Eq. S 3 this means that the detected second harmonic intensity $I_X^{2\omega}$ is zero. Thus a structure of D_4 symmetry, regardless of its orientation, cannot generate SHG when placed between parallel polarizers.

X. Determination of the effective second-order nonlinear coefficient

As a reference material a thin (100 μm thick) beta barium borate (BBO) crystal of which the second-order nonlinear properties are very well characterized was used. The crystal was cut to achieve type I phase-matching and optimize the quadratic nonlinear response ($\theta = 29.2^\circ$, $\varphi = 90^\circ$; Eksma optics, BBO-601H). We compared the intensity of the second-harmonic light of activated CAU-10-NO₂ (5) with that of the reference crystal by placing them consecutively in the SHG-microscope.

Following equations describes the intensity of the SHG-light $I^{2\omega}$ of the CAU-10-NO₂ (5) crystallites (Eq.1) and the reference crystal (Eq. 2):

$$I^{2\omega} = A \frac{\langle d_{\text{eff}} \rangle^2}{n_{2\omega} n_{\omega}^2} r^2 (I^{\omega})^2 \quad \text{Eq. S 4}$$

$$I^{2\omega} = A \frac{d_{\text{ooe}}^2}{n_{\theta,2\omega} n_{\omega,\omega}^2} L^2 (I^{\omega})^2 \quad \text{Eq. S 5}$$

In which A contains all variables that are identical in both equations, and I^{ω} is the intensity of the incident laser light. In equation S 4, n_{ω} and $n_{2\omega}$ are the refractive index of CAU-10-NO₂ at the frequency of the incident light and second-harmonic light respectively, r is the size of the crystallites and $\langle d_{\text{eff}} \rangle$ is the effective nonlinearity coefficient averaged over all orientations of the particles. In equation S 5 $n_{\omega,\omega}$ is the ordinary refractive index of BBO at the frequency of the incident light and $n_{\theta,2\omega}$ the extraordinary refractive index at the frequency of the second-harmonic light propagating at an angle θ with the optical axis of the crystal, L is the thickness of the crystal and d_{ooe} is the effective nonlinearity coefficient for the Type I phase-matched interaction.

Reported values for the refractive index of metal-organic frameworks vary between 1.2 and 1.65 in the VIS to NIR spectral region (Adv. Mater. 2008, 21, 1931–1935; Inorg. Chem. 2010, 49, 10283–10290; Phys. Chem. Chem. Phys., 2012, 14, 4713–4723). We used here the intermediate value of 1.4 for both n_{ω} and $n_{2\omega}$ of CAU-10-NO₂. For determination of the intensity of the second-harmonic light linearly polarized incident light was used, while all generated second-harmonic light was collected. The intensity per particle was averaged for four different orientations of the plane of polarization of the incident light (all 45° apart) and corrected with the size of the particle estimated from the microscopic image was used for r

(typically 3-4 μm). The average SHG intensity of 15 particles corrected for their size was used to compare with the SHG intensity of the reference.

Eq. S 4 is deduced for monocrystalline particles. However, as can be seen from the SEM-image (see figure S 40) these are not present. However as the SHG intensity $I^{2\omega}$ scales quadratically with the crystallite size but only linearly with amount of crystallites, deducing $\langle d_{\text{eff}} \rangle$ via eq. S 4 leads to a coefficient that is a gross underestimation for polycrystalline particles.

XI. In-situ-formylation of CAU-10-NH₂ (5)

To prove the partial formylation of the amino-group, a ¹H-NMR-spectrum of CAU-10-NH₂ (5) dissolved in 5% NaOD in D₂O was measured (Fig. S 44).

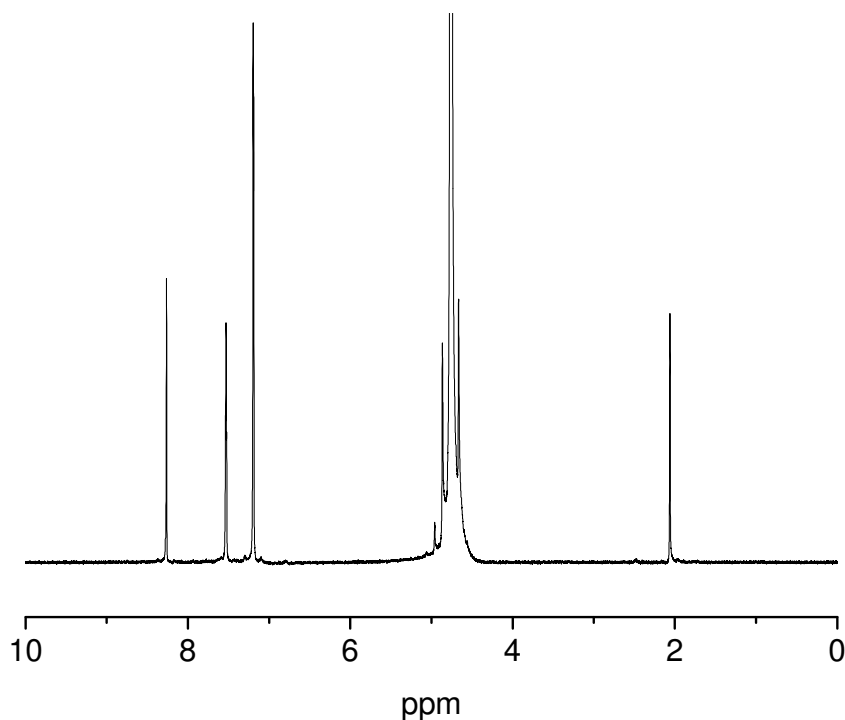


Figure S44: ¹H-NMR-spectrum of CAU-10-NH₂ (5) dissolved in 5% NaOD in D₂O (reference: TMS).

The signals at 7.53 ppm (triplet) and 7.18 ppm (duplet) are the signals of the H-atom in 2-position and the H-atoms in 4- and 6-position of the benzene ring, respectively. The signal at 2.06 ppm (singlet) corresponds to dimethylamine and the signal at 8.26 ppm (singlet) to formic acid. Both species are observed due to the solvolysis of DMF in basic solution, but the ratio of integrals of 1:1 does not match the expected value of 6:1 for HN(CH₃)₂ : HCOOH. Thus only a minor amount of formic acid is observed due to traces of DMF in the MOF, but the main amount is obtained by solvolysis of the formylated aminoisophthalate. The degree of formylation based on integrals is ~ 50%.

This was further confirmed by solid-state NMR-spectra. The signals of the CP-MAS-¹³C-spectrum (Fig. S45) are attributed to the respective atoms in Tab. S6.

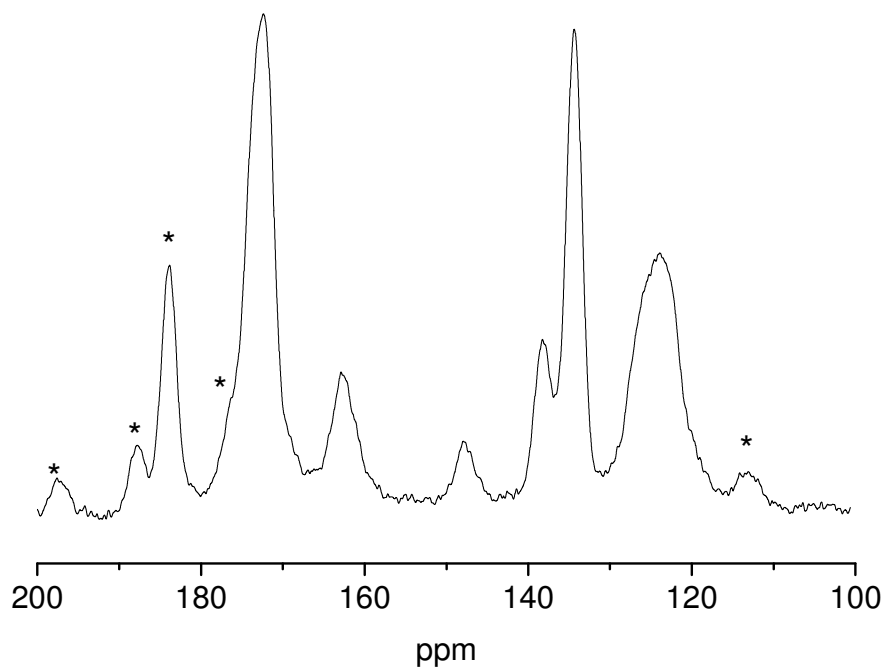
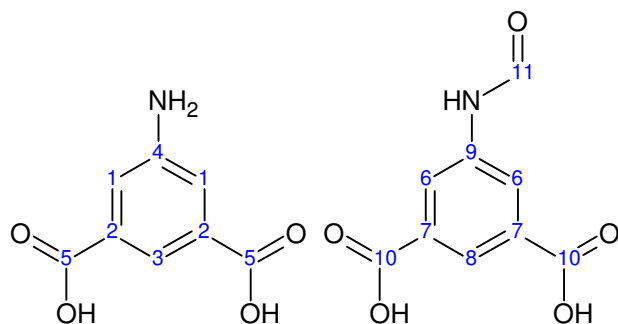


Figure S45: CP-MAS-¹³C-NMR-spectrum of CAU-10-NH₂ (**5**) at a rotation frequency of 5 kHz. Asterisks mark spinning side bands.



C-atom	ppm
5, 10	172
11	163
4	148
9	138
2, 7	134
1, 3, 6, 8	124

The CP-MAS-¹⁵N-NMR-spectrum clearly shows a signal at -264 ppm, which is characteristic for amide-nitrogen atoms. A very weak signal for the NH₂-group can be observed at 350 ppm.

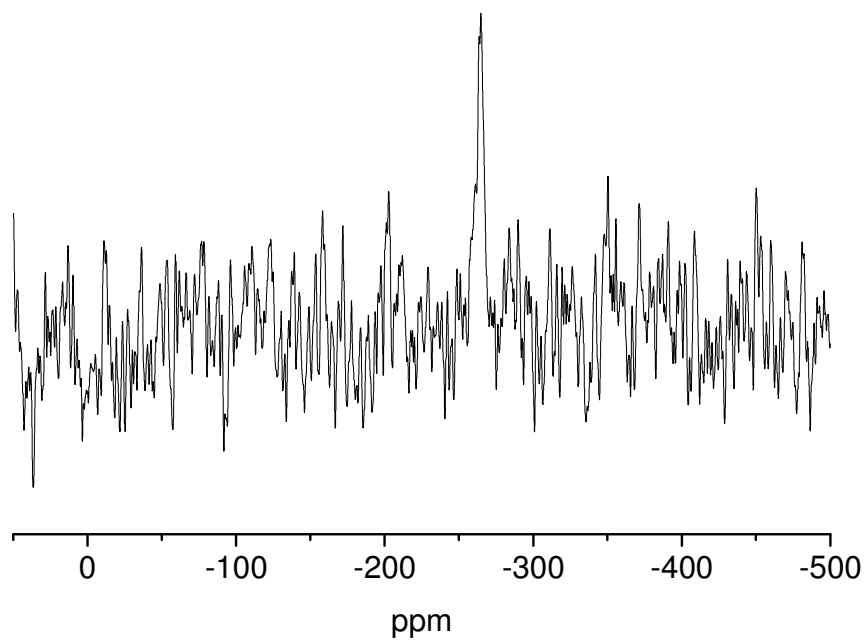


Figure S46: CP-MAS-¹⁵N-NMR-spectrum of CAU-10-NH₂ (**5**) at a rotation frequency of 5 kHz.

Supporting Information

Mixed-linker MOFs with CAU-10-structure: synthesis and gas sorption characteristics

Helge Reinsch, Steve Waitschat and Norbert Stock

- S1: ¹H-NMR-spectra of dissolved CAU-10-X samples in solution**
 - S2: Results of the Rietveld refinement**
 - S3: Additional XRPD-data for CAU-10-H/Br (2) and for CAU-10-H/CH₃ (4)**
 - S4: Solid-state NMR-spectroscopy**
 - S5: IR-spectroscopy**
 - S6: Scanning electron microscopy**
 - S7: Additional Sorption Isotherms**
 - S8: Crystallographic information file for CAU-10-Br**
 - S9: HT-experiment for mixed-linker MOFs**
-

S1: ^1H -NMR-spectra of dissolved CAU-10-X samples in solution

CAU-10-H/Br (2)

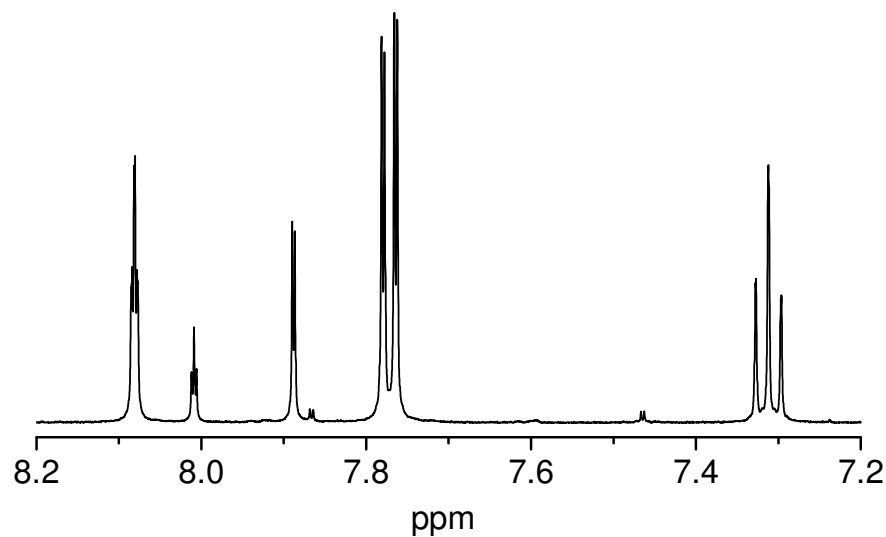


Figure S1: ^1H -NMR-spectrum of CAU-10-H/Br (2) after dissolution of the MOF in 5% NaOD in D_2O .

^1H -NMR spectrum of dissolved **2** (200 MHz, 5% NaOD in D_2O , 300 K, TMS): $\delta = 8.08$ (m, BDC, 2-position), 8.01 (t, BDC-Br, 2-position), 7.89 (d, BDC-Br, 4,6-position), 7.77 (m, BDC, 4,6-position), 7.31 (t, BDC, 5-position) ppm.

CAU-10-NO₂/NH₂ (5)

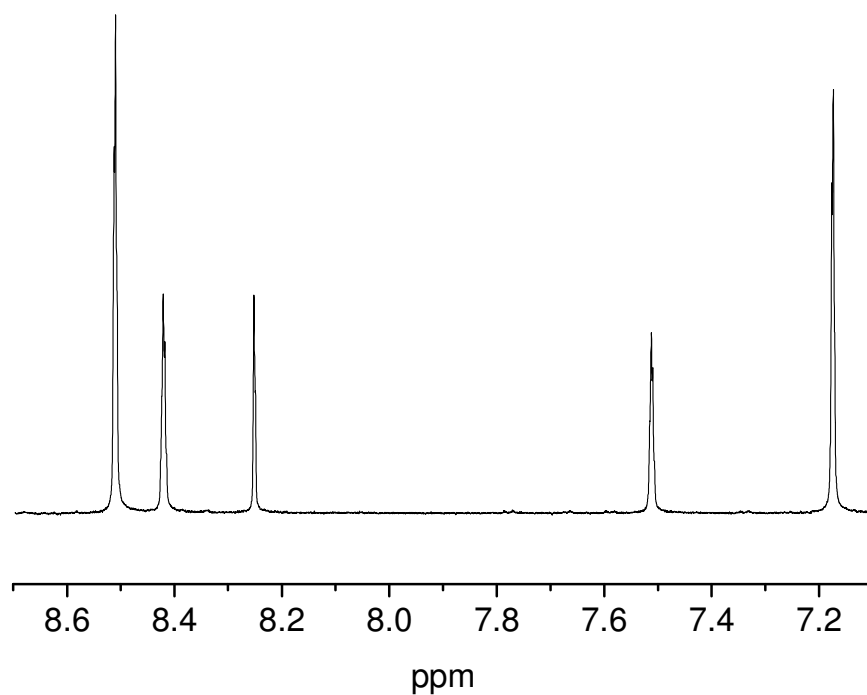


Figure S2: ¹H-NMR-spectrum of CAU-10-NO₂/NH₂ (**5**) after dissolution of the MOF in 5% NaOD in D₂O.

¹**H-NMR** spectrum of dissolved **5** (200 MHz, 5% NaOD in D₂O, 300 K, TMS): δ = 8.51 (d, BDC-NO₂, 4,6-position), 8.42 (t, BDC-NO₂, 2-position), 8.25 (s, formic acid), 7.51 (t, BDC-NH₂, 2-position), 7.17 (d, BDC-NH₂, 4,6-position) ppm. According to the integrals, the ratio BDC-NO₂ : BDC-NH₂ varies slightly between 5 : 4 and 4.7 : 4, thus the fraction of BDC-NH₂ is 44% to 46 %.

CAU-10-H/CH₃ (4)

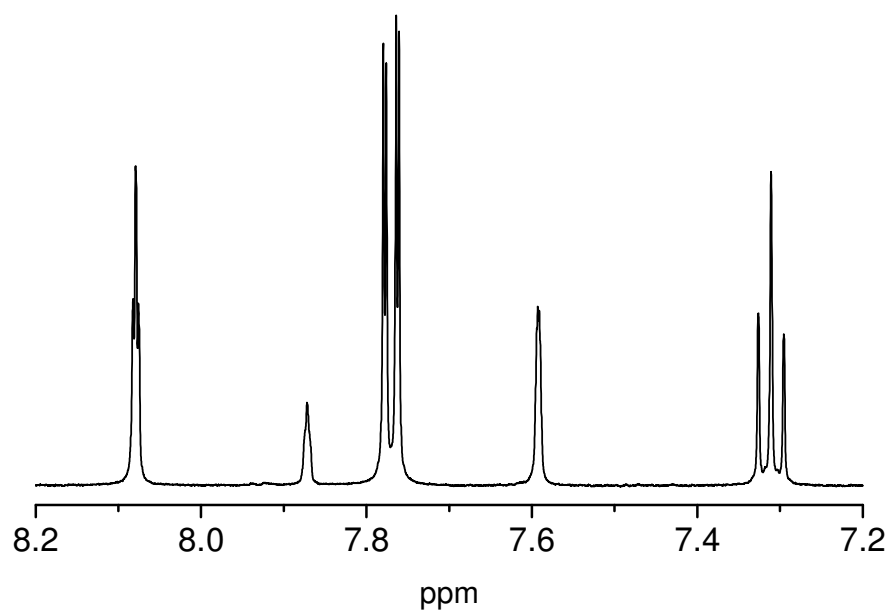


Figure S3: ¹H-NMR-spectrum of CAU-10-H/CH₃ (**4**) after dissolution of the MOF in 5% NaOD in D₂O.

¹**H-NMR** spectrum of dissolved **4** (200 MHz, 5% NaOD in D₂O, 300 K, TMS): δ = 8.08 (m, BDC, 2-position), 7.87 (s, BDC-CH₃, 2-position), 7.77 (m, BDC, 4,6-position), 7.59 (s, BDC-CH₃, 4,6-position), 7.31 (t, BDC, 5-position) ppm. According to the integrals, the ratio BDC : BDC-CH₃ varies between 3.6 : 1 and 3 : 1, thus the fraction of BDC-CH₃ is 21% to 25 %.

S2: Results of the Rietveld refinement of CAU-10-Br (1)

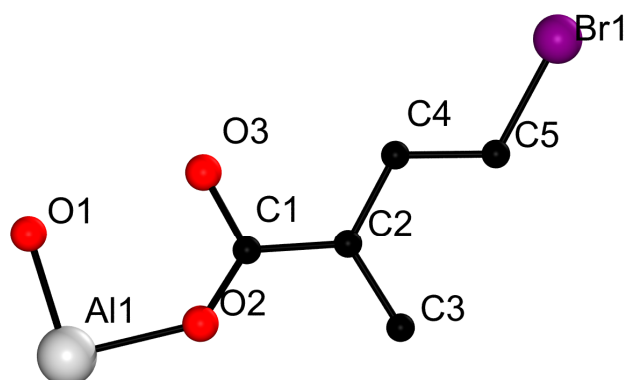


Figure S4: Assymmetric unit of CAU-10-Br (1) with numbering scheme used in Tab. S1.

Table S1: Bond lengths in CAU-10-Br (1) in Å.

Al1	O1	1.83(2)
	O2	1.92(2)
	O3	1.95(2)
O2	C1	1.29(2)
O3	C1	1.29(2)
C1	C2	1.42(2)
C2	C3	1.39(1)
	C4	1.42(2)
C4	C5	1.41(1)
	C2	1.42(2)
C5	Br1	1.82(2)

S3: Additional XRPD-data for CAU-10-H/Br (2) and for CAU-10-H/CH₃ (4)

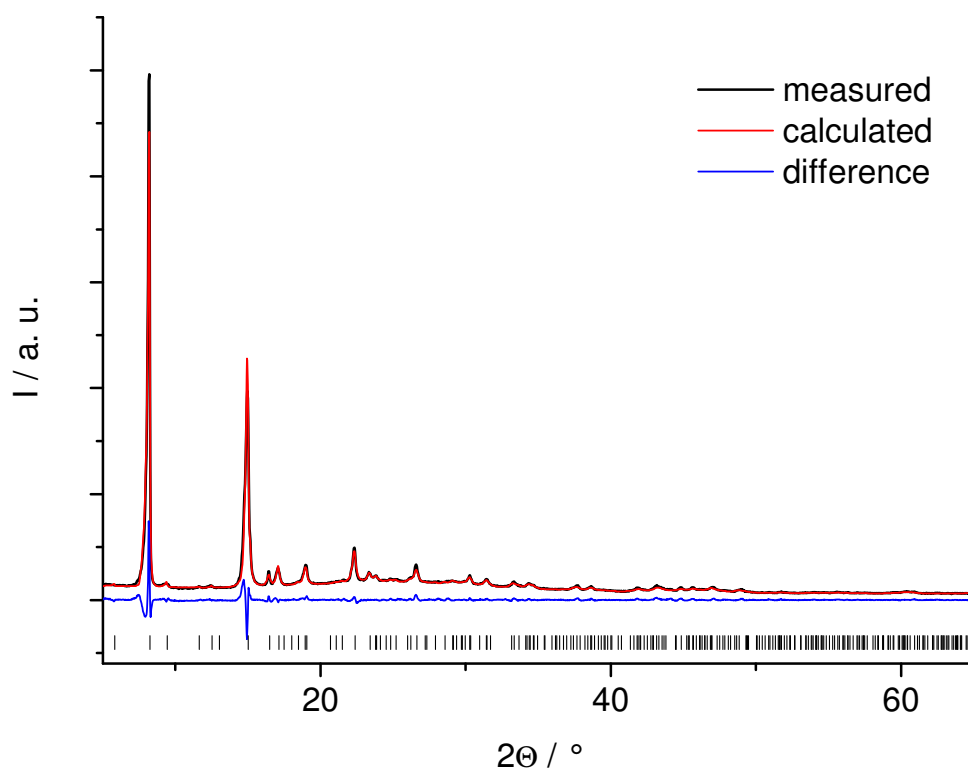


Figure S5: LeBail fit for CAU-10-H/Br (2) in the space group $I4_1$. The final R_{WP} is 7.5 %, the refined cell parameters are $a = b = 21.485(5)$ and $c = 10.407(3)$ Å.

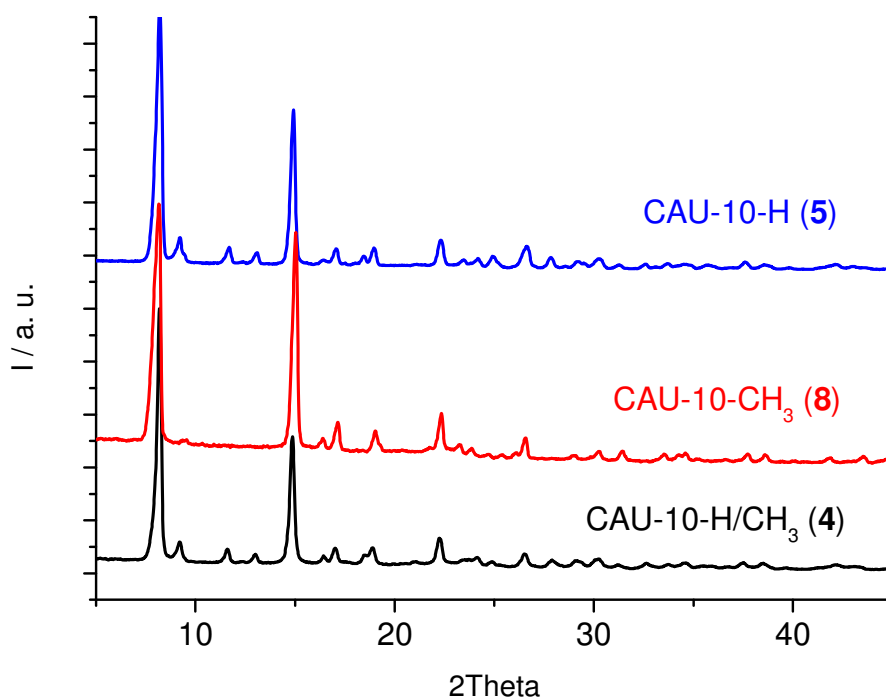


Figure S6: Comparison of the XRPD-patterns of CAU-10-H (5), CAU-10-CH₃ (8) and CAU-10-H/CH₃ (4), measured on a Stadi P Combi diffractometer equipped with an xy-stage with CuK_{α1}-radiation.

S4: Solid-state NMR spectroscopy

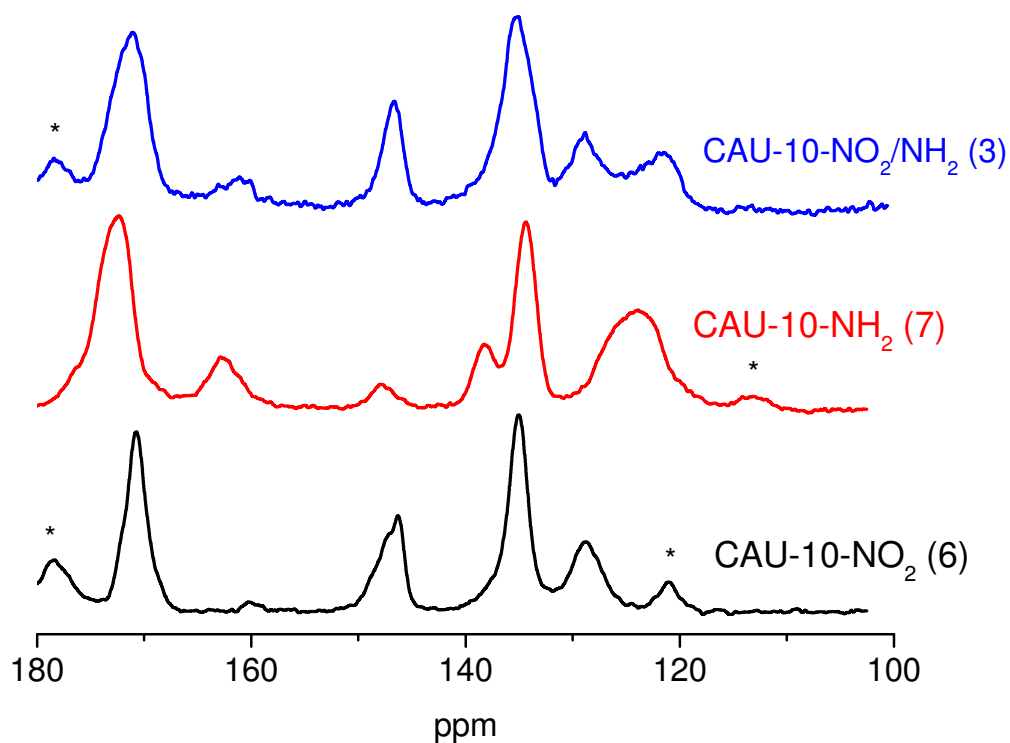
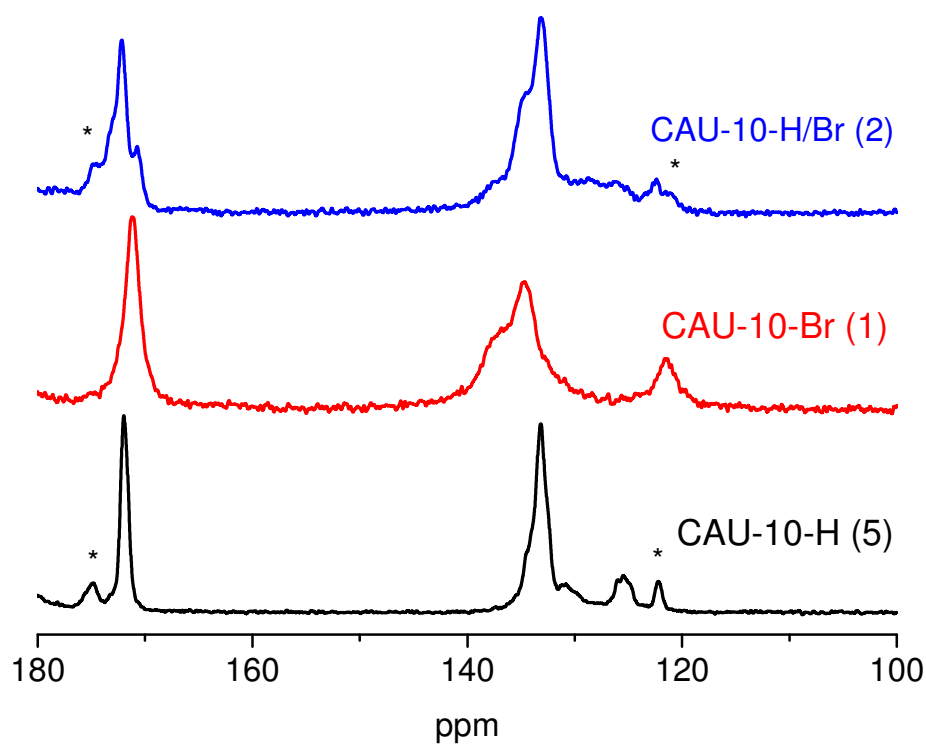
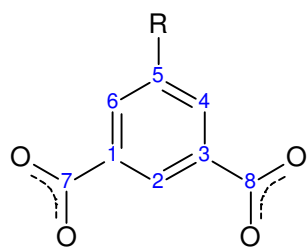


Figure S7: ^{13}C -CP-MAS-NMR spectra of **1**, **2**, **3**, **5**, **6**, and **7**. The MOFs based on mixtures of linker molecules clearly show a spectrum that results from the combination of the pure-linker MOFs. Asterisks mark spinning side bands.

Table S2: Assignment of ^{13}C -NMR-signals (ppm).

C-atom	CAU-10-H	CAU-10-Br	CAU-10-NO ₂	CAU-10-NH ₂
7,8	172	171	171	172
1,3	133	134	135	134
2	131	134	135	124
4,6	135	138	129	124
5	125	121	146	148, 138
9				163



The ^{13}C -signals were assigned using data measured in solution.¹¹ Due to the limited resolution of the spectra, the signals for the mixed-linker MOFs are not assigned in detail. The signal for atom 9 is caused by the partial formylation of the NH₂-group in **3** and **7** during the synthesis and thus belongs to the CHO-NH-aryl-group. This modification causes also two signals for the atom in 5-position of aminoisophthalate in these compounds. The signal at 148 ppm belongs to the formylated molecule, while the signal at 138 ppm is characteristic for the non-modified aminoisophthalate.

¹¹ SDBSWeb : <http://riodb01.ibase.aist.go.jp/sdbs/> (National Institute of Advanced Industrial Science and Technology, 20.8.2012)

S5: IR-spectroscopy

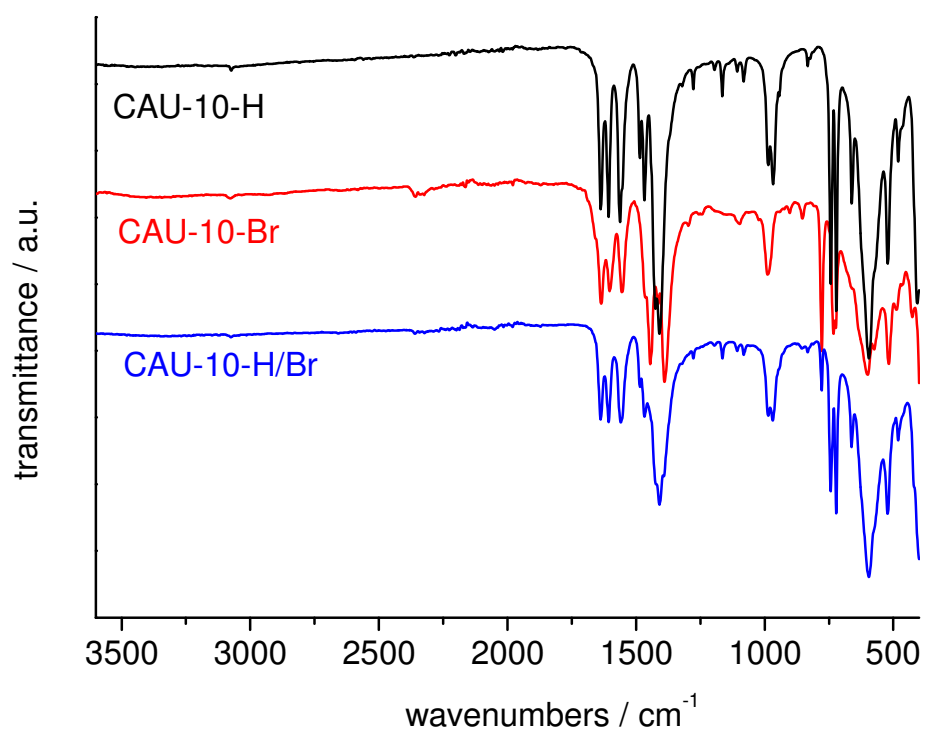


Figure S8: IR-spectra of CAU-10-H (5), CAU-10-Br (1) and CAU-10-H/Br (2).

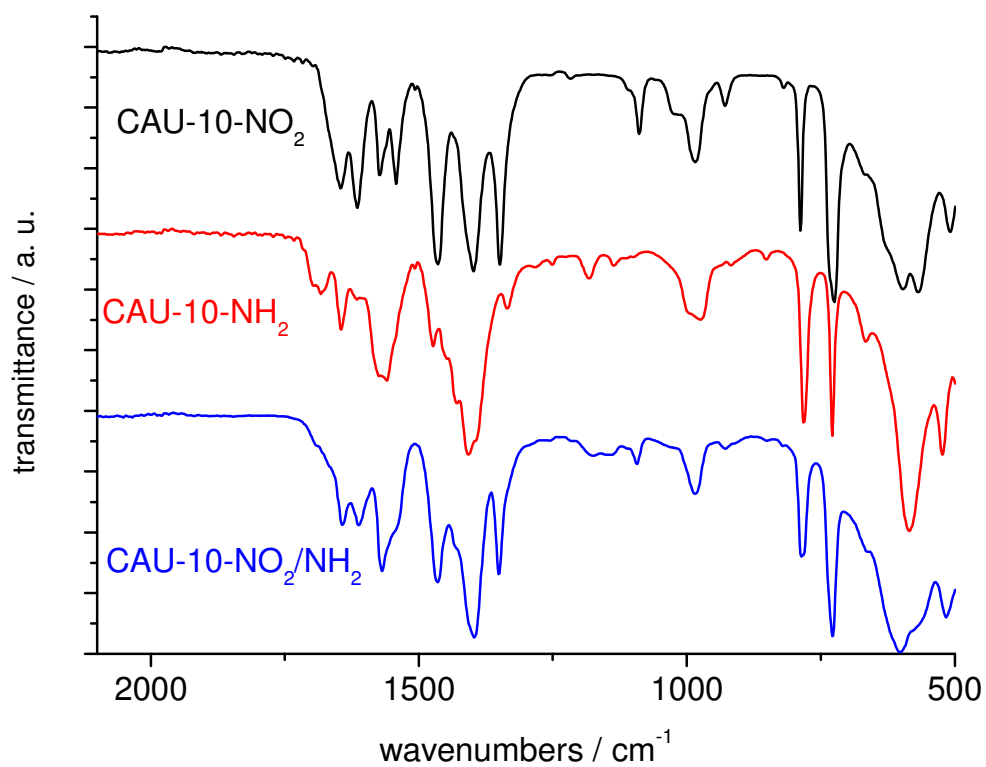
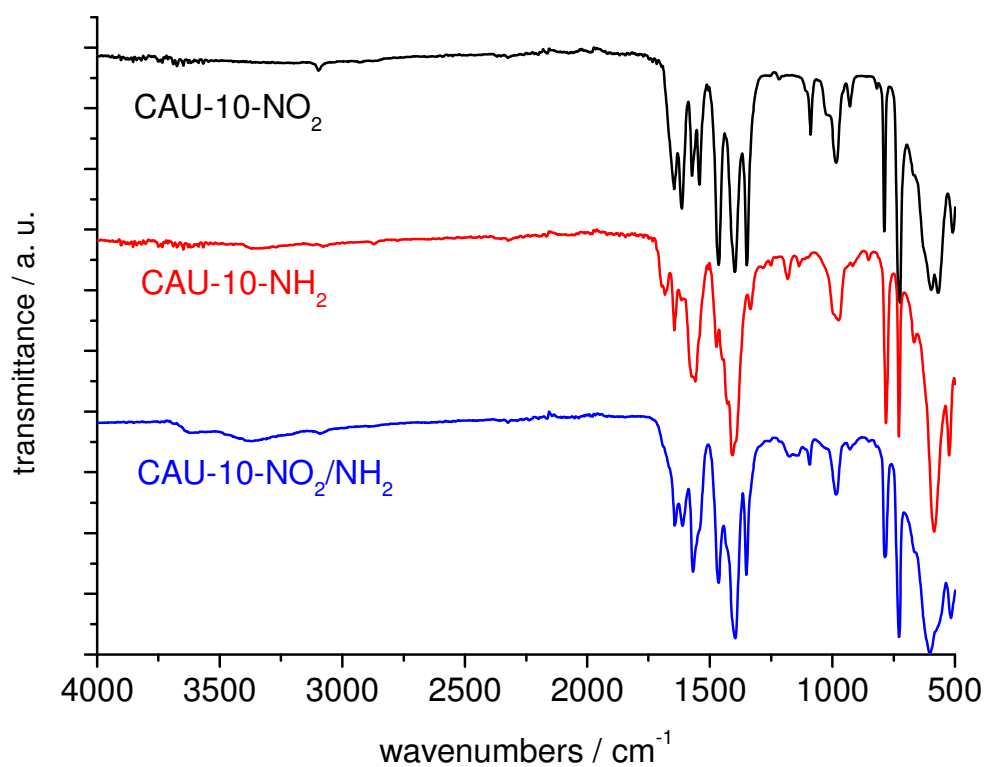


Figure S9: IR-spectra of CAU-10-NO₂ (6), CAU-10-NH₂ (7) and CAU-10-NO₂/NH₂ (3). Top: full spectra; bottom: region between 2100 and 500 cm^{-1} .

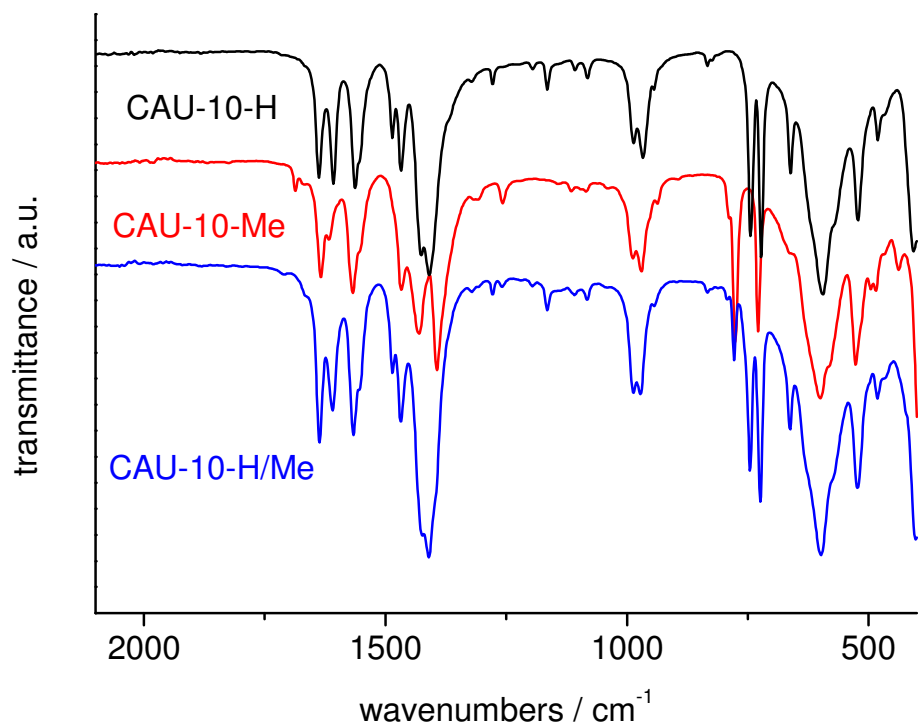
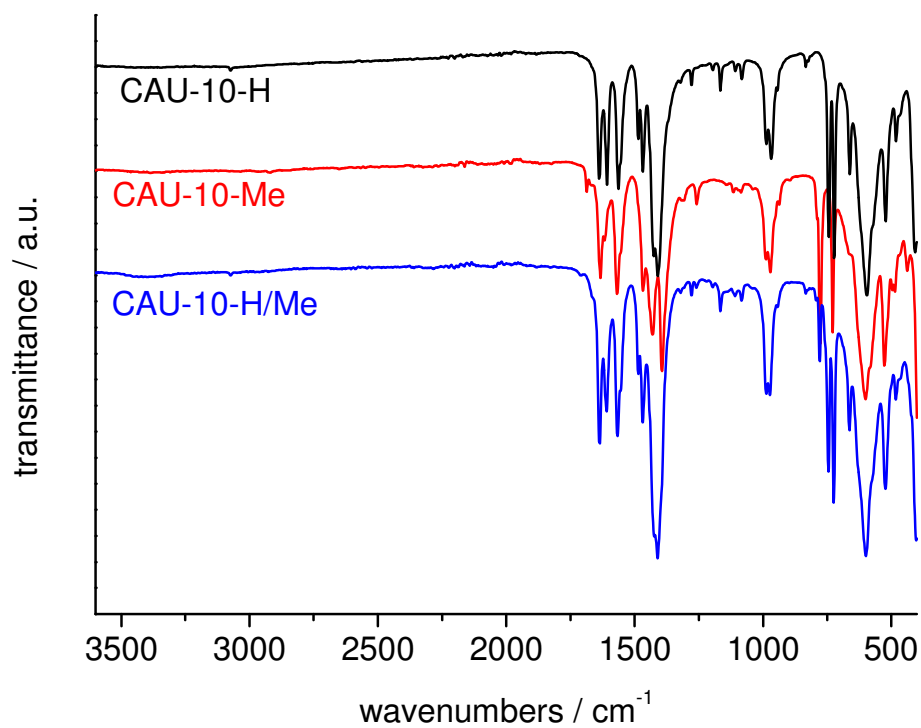


Figure S10: IR-spectra of CAU-10-H (**5**), CAU-10-CH₃ (**8**) and CAU-10-H/CH₃ (**4**). Top: full spectra; bottom: region between 2100 and 500 cm⁻¹.

S6: Scanning electron microscopy

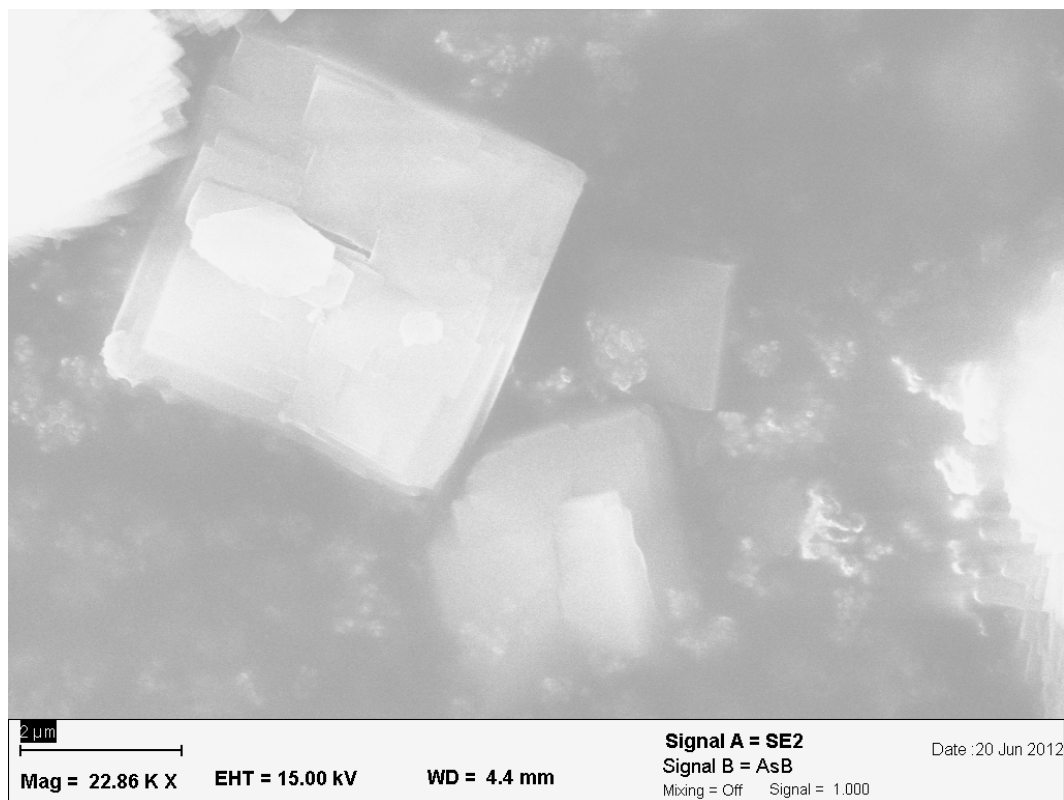


Figure S11: SEM-micrograph of crystals of CAU-10-Br (1).

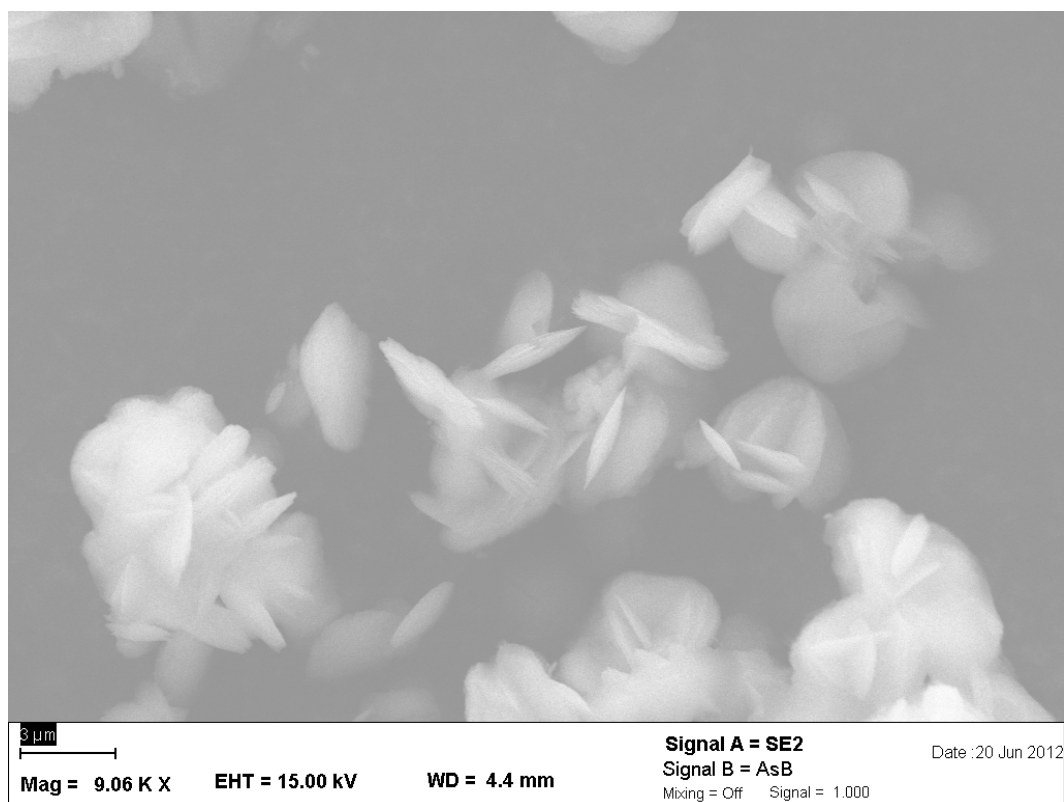


Figure S12: SEM-micrograph of crystals of CAU-10-H/Br (2)

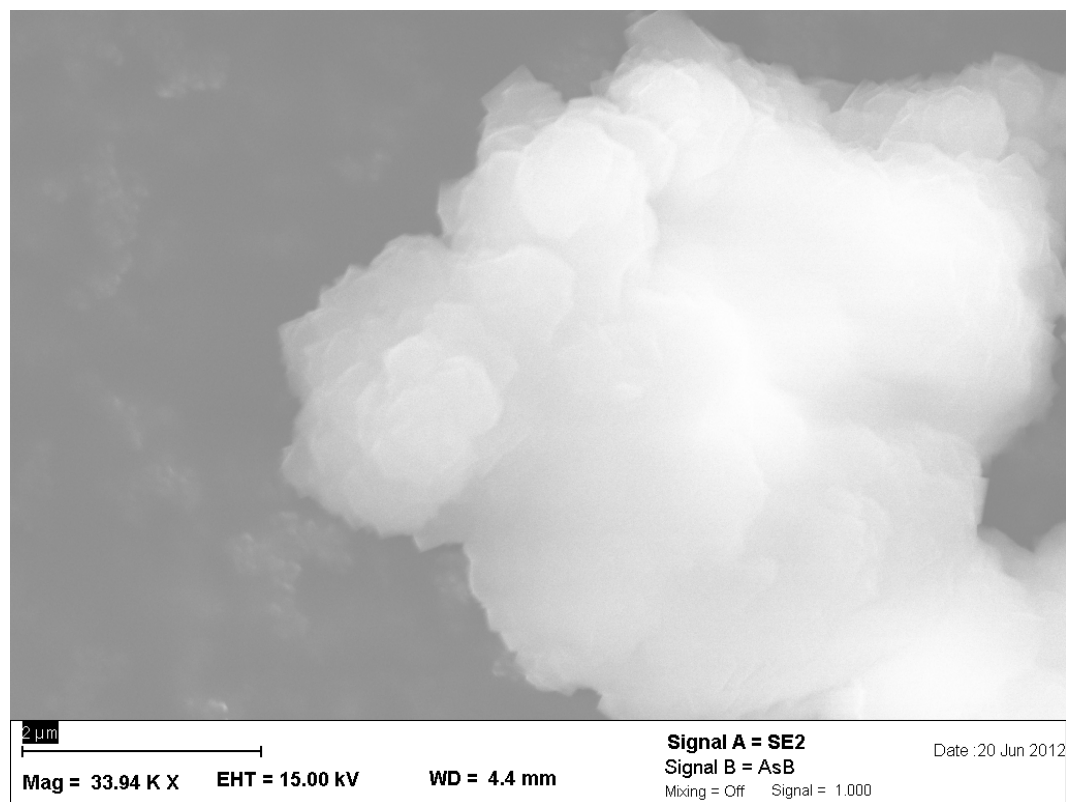


Figure S13: SEM-micrograph of crystals of CAU-10-NO₂/NH₂ (3).

S7: Additional Sorption Isotherms

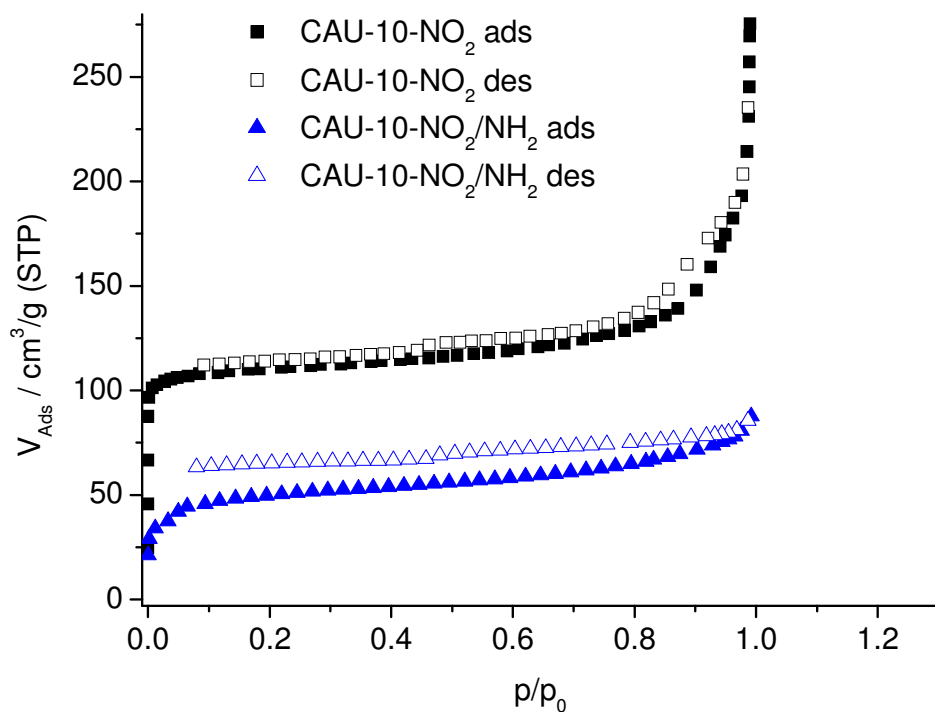


Figure S14: Nitrogen sorption isotherms for **6** and **3** measured at 77 K.

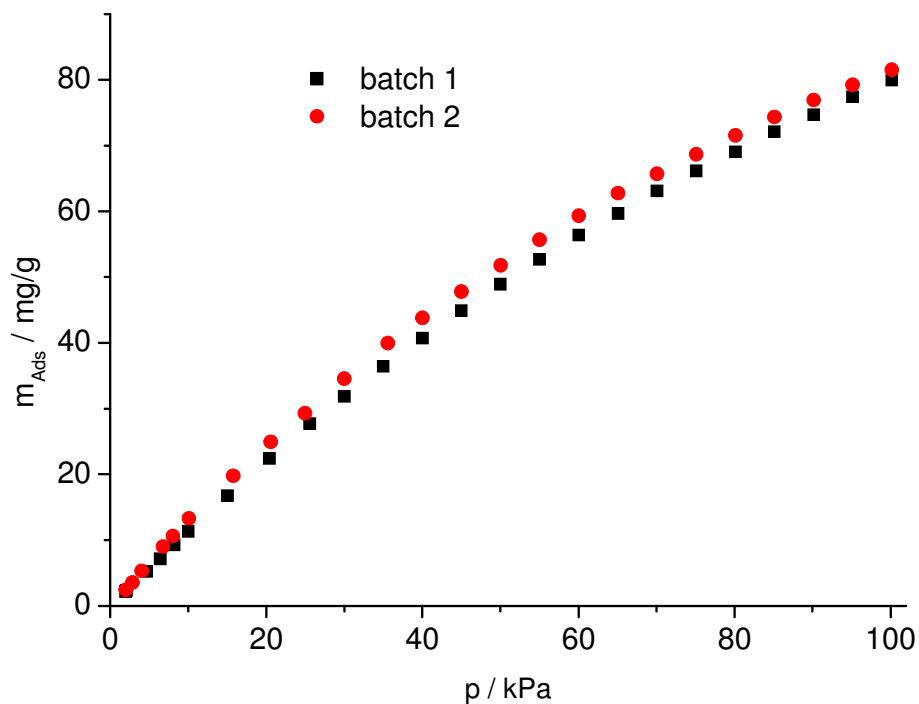


Figure S15: CO₂ adsorption isotherms for different batches of **2** measured at 298 K.

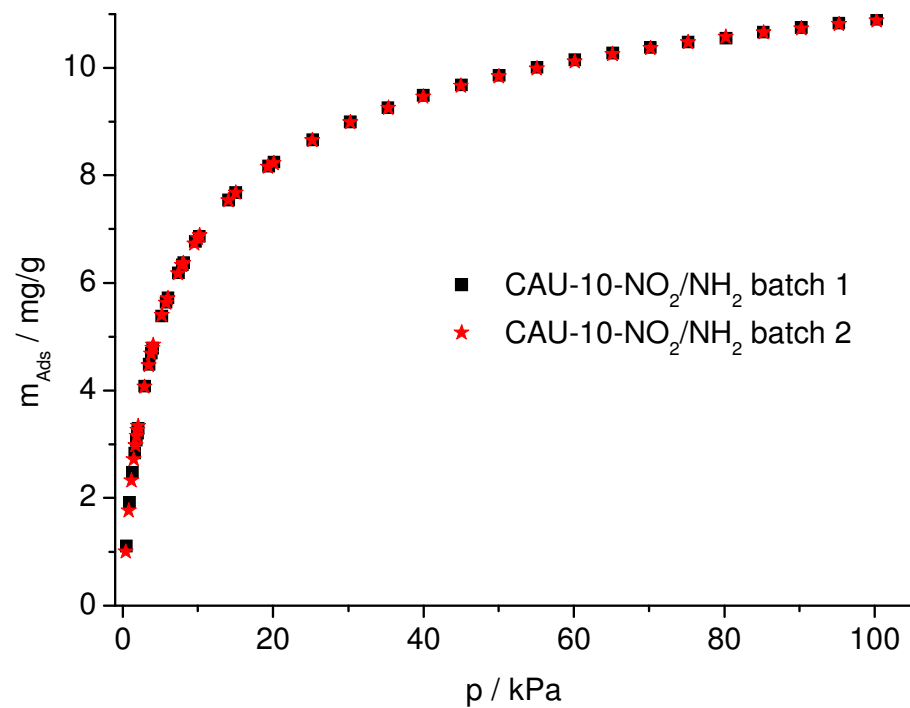


Figure S16: Hydrogen adsorption isotherms for different batches of **3** measured at 77 K.

S8: Crystallographic information file for CAU-10-Br

```
data_
_chemical_name_mineral CAU-10-Br
_cell_length_a 21.5064(14)
_cell_length_b 21.5064(14)
_cell_length_c 10.1648(12)
_cell_angle_alpha 90
_cell_angle_beta 90
_cell_angle_gamma 90
_cell_volume 4701.48(80)
_symmetry_space_group_name_H-M I41/amdz
loop_
_symmetry_equiv_pos_as_xyz
'-x, -y, -z'
'-x, -y+1/2, z'
'-x, y, z'
'-x, y+1/2, -z'
'-x+1/2, -y, z+1/2'
'-x+1/2, -y+1/2, -z+1/2'
'-x+1/2, y, -z+1/2'
'-x+1/2, y+1/2, z+1/2'
'-y+1/4, -x+1/4, -z-1/4'
'-y+1/4, -x-1/4, z+1/4'
'-y+1/4, x+1/4, -z-1/4'
'-y+1/4, x-1/4, z+1/4'
'-y-1/4, -x+1/4, z-1/4'
'-y-1/4, -x-1/4, -z+1/4'
'-y-1/4, x+1/4, z-1/4'
'-y-1/4, x-1/4, -z+1/4'
'y+1/4, -x+1/4, z-1/4'
'y+1/4, -x-1/4, -z+1/4'
'y+1/4, x+1/4, z-1/4'
'y+1/4, x-1/4, -z+1/4'
'y-1/4, -x+1/4, -z-1/4'
'y-1/4, -x-1/4, z+1/4'
'y-1/4, x+1/4, -z-1/4'
'y-1/4, x-1/4, z+1/4'
'x, -y, -z'
'x, -y+1/2, z'
'x, y, z'
'x, y+1/2, -z'
'x+1/2, -y, z+1/2'
'x+1/2, -y+1/2, -z+1/2'
'x+1/2, y, -z+1/2'
'x+1/2, y+1/2, z+1/2'
loop_
_atom_site_label
_atom_site_type_symbol
_atom_site_symmetry_multiplicity
_atom_site_fract_x
_atom_site_fract_y
_atom_site_fract_z
_atom_site_occupancy
_atom_site_B_iso_or_equiv
Al1 Al 0 0.31709(73) 0 0 1 0.20(65)
O1 O 0 0.25586(90) 0.00586(90) 0.125 1 0.6(13)
O2 O 0 0.38258(88) 0.00832(71) 0.1278(13) 1 0.20(61)
O3 O 0 0.33965(39) 0.07041(79) 0.2802(19) 1 0.20(77)
C1 C 0 0.38756(74) 0.04378(63) 0.2293(13) 1 1.2(14)
C2 C 0 0.44351(46) 0.0570(11) 0.2986(16) 1 0.2(13)
C3 C 0 0.5 0.0476(13) 0.2345(16) 1 0.2(16)
C4 C 0 0.44325(43) 0.0828(11) 0.4267(16) 1 0.2(14)
C5 C 0 0.5 0.0876(14) 0.4945(18) 1 0.2(18)
Br1 Br 0 0.5 0.11892(28) 0.66128(65) 1 3.11(39)
```

S9: HT-experiment for mixed-linker MOFs

For the first synthesis of a mixed-linker-MOF we usually choose the same Al^{3+} -source as well as the same temperature program as for the synthesis of the parent-MOF. The molar ratios of Al^{3+} : linker molecules were varied slightly as well as the fraction of DMF and the absolute concentrations of the reactants (Tab. S2). Based on XRPD-measurements, we thus identified reaction conditions that lead to products with a high degree of mixing and sufficiently good crystallinity.

Table S3: Composition of the reaction mixtures in an archetypical HT-experiment.

linker 1 [%]	linker 2 [%]	linker 1 [mmol]	linker 2 [mmol]	Al^{3+} [mmol]	V H_2O [μL]	V DMF [μL]
87.5	12.5	0.11	0.02	0.12	400	100
75	25	0.09	0.03	0.12	400	100
50	50	0.06	0.06	0.12	400	100
87.5	12.5	0.11	0.02	0.12	350	150
75	25	0.09	0.03	0.12	350	150
50	50	0.06	0.06	0.12	350	150
87.5	12.5	0.21	0.03	0.24	400	100
75	25	0.18	0.06	0.24	400	100
50	50	0.12	0.12	0.24	400	100
87.5	12.5	0.21	0.03	0.24	350	150
75	25	0.18	0.06	0.24	350	150
50	50	0.12	0.12	0.24	350	150
87.5	12.5	0.11	0.02	0.24	400	100
75	25	0.09	0.03	0.24	400	100
50	50	0.06	0.06	0.24	400	100
87.5	12.5	0.11	0.02	0.24	350	150
75	25	0.09	0.03	0.24	350	150
50	50	0.06	0.06	0.24	350	150
87.5	12.5	0.21	0.03	0.48	400	100
75	25	0.18	0.06	0.48	400	100
50	50	0.12	0.12	0.48	400	100
87.5	12.5	0.21	0.03	0.48	350	150
75	25	0.18	0.06	0.48	350	150
50	50	0.12	0.12	0.48	350	150

A new keto-functionalized microporous Al-based
metal-organic framework: [Al(OH)(O₂C-C₆H₄-
CO-C₆H₄-CO₂)]

Helge Reinsch^a, Martin Krüger^a, Jerome Marrot^b, Norbert Stock^{a}*

I: List of HT-reactions

II: Asymmetric unit of CAU-8

**II: Topological analysis of MOFs based on infinite one-periodic building
units**

I: List of HT-reactions

Table S1: Exact compositions of the reaction mixtures in the HT-experiment.

number	n (Al ³⁺) [mmol]	n (linker) [mmol]	m (AlX) [mg]	m (linker) [mg]	Al-source	V H ₂ O [μL]	V DMF [μL]
1	0.11	0.11	111.1	30.0	Al ₂ (SO ₄) ₃ ·18H ₂ O	400.0	100.0
2	0.11	0.11	111.1	30.0	Al ₂ (SO ₄) ₃ ·18H ₂ O	300.0	200.0
3	0.11	0.11	111.1	30.0	Al ₂ (SO ₄) ₃ ·18H ₂ O	200.0	300.0
4	0.15	0.15	148.1	40.0	Al ₂ (SO ₄) ₃ ·18H ₂ O	400.0	100.0
5	0.15	0.15	148.1	40.0	Al ₂ (SO ₄) ₃ ·18H ₂ O	300.0	200.0
6	0.15	0.15	148.1	40.0	Al ₂ (SO ₄) ₃ ·18H ₂ O	200.0	300.0
7	0.19	0.19	185.2	50.0	Al ₂ (SO ₄) ₃ ·18H ₂ O	400.0	100.0
8	0.19	0.19	185.2	50.0	Al ₂ (SO ₄) ₃ ·18H ₂ O	300.0	200.0
9	0.19	0.19	185.2	50.0	Al ₂ (SO ₄) ₃ ·18H ₂ O	200.0	300.0
10	0.22	0.22	222.2	60.0	Al ₂ (SO ₄) ₃ ·18H ₂ O	400.0	100.0
11	0.22	0.22	222.2	60.0	Al ₂ (SO ₄) ₃ ·18H ₂ O	300.0	200.0
12	0.22	0.22	222.2	60.0	Al ₂ (SO ₄) ₃ ·18H ₂ O	200.0	300.0
13	0.11	0.11	55.6	30.0	Al(NO ₃) ₃ ·9H ₂ O	400.0	100.0
14	0.11	0.11	55.6	30.0	Al(NO ₃) ₃ ·9H ₂ O	300.0	200.0
15	0.11	0.11	55.6	30.0	Al(NO ₃) ₃ ·9H ₂ O	200.0	300.0
16	0.15	0.15	74.1	40.0	Al(NO ₃) ₃ ·9H ₂ O	400.0	100.0
17	0.15	0.15	74.1	40.0	Al(NO ₃) ₃ ·9H ₂ O	300.0	200.0
18	0.15	0.15	74.1	40.0	Al(NO ₃) ₃ ·9H ₂ O	200.0	300.0
19	0.19	0.19	92.6	50.0	Al(NO ₃) ₃ ·9H ₂ O	400.0	100.0
20	0.19	0.19	92.6	50.0	Al(NO ₃) ₃ ·9H ₂ O	300.0	200.0
21	0.19	0.19	92.6	50.0	Al(NO ₃) ₃ ·9H ₂ O	200.0	300.0
22	0.22	0.22	111.1	60.0	Al(NO ₃) ₃ ·9H ₂ O	400.0	100.0
23	0.22	0.22	111.1	60.0	Al(NO ₃) ₃ ·9H ₂ O	300.0	200.0
24	0.22	0.22	111.1	60.0	Al(NO ₃) ₃ ·9H ₂ O	200.0	300.0

II: Asymmetric unit of CAU-8

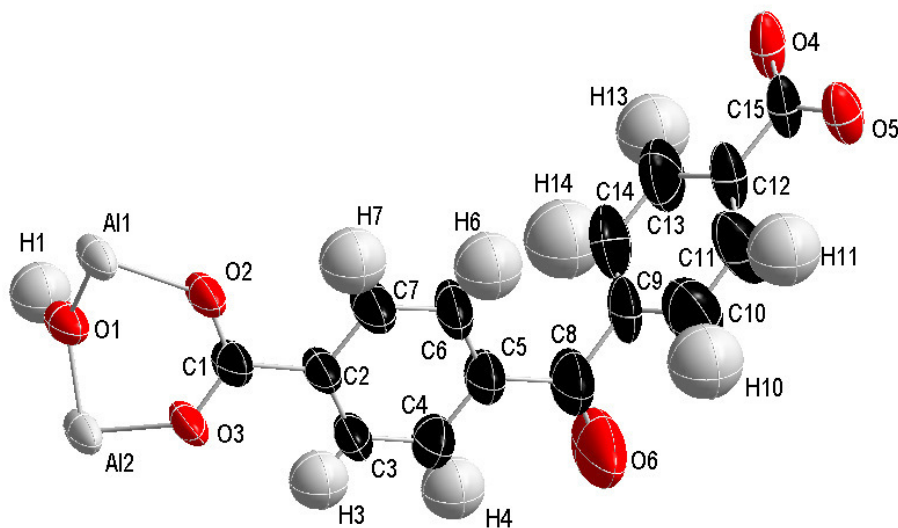


Fig. S1: Assymmetric unit of CAU-8 with numbering scheme as use in Tab. S2.

Tab. S2: Bond lengths in CAU-8 in Angstrom.

Al1	O1	1.8431(11)
	O2	1.9029(11)
	O5	1.9034(11)
Al2	O1	1.8216(11)
	O4	1.9079(12)
	O3	1.9217(13)
O1	H1	0.9526(83)
O2	C1	1.2713(20)
O3	C1	1.2480(19)
O4	C15	1.2458(20)
O5	C15	1.2508(19)
O6	C8	1.2378(35)
C1	C2	1.4960(23)
	C3	1.3564(24)
	C7	1.3758(26)
C3	H3	0.9305(17)
	C4	1.3620(23)
C4	H4	0.9292(20)
	C5	1.3892(27)
C5	C6	1.3712(29)
	C8	1.4924(27)
C6	H6	0.9319(19)
	C5	1.3712(29)
C7	C7	1.3719(27)
	H7	0.9308(20)
C8	C9	1.4809(32)
C9	C14	1.3338(37)
	C10	1.3739(35)

C10	H10	0.9304(26)
	C11	1.3575(36)
C11	H11	0.9314(23)
	C12	1.3931(31)
C12	C13	1.4069(31)
	C15	1.4780(27)
C13	H13	0.9297(26)
	C14	1.3872(34)
C14	H14	0.9292(24)

III: Topological analysis of MOFs based on infinite one-periodic building units

Tab. S3. MOFs based on infinite inorganic building units and their topologies as observed in this study.

compound	MIL-53	MIL-68	MIL-120	CAU-4	CAU-6	CAU-10
building unit	chain	chain	helices	bridged ions	columns	helices
connectivity	uninodal 4	binodal 4,4	bimodal 3,4	bimodal 3,5	uninodal 8	uninodal 4
name	dia	bik	nor-3,4-C2/m	hms	ecf	gis
SG (MOF)	Pnma	Cmcm	C2/m	P312	P6 ₃ /mmc	I41/amd
SG (net)	Fd-3m	Cmcm	C2/m	P-6m2	P6 ₃ /mmc	I41/amd
point symbol	(6 ⁶)	(5.6 ⁵)(5 ⁴ .6 ⁸) ₂	(6.8 ²) ₄ (6 ² .8 ² .10 ²)	(6 ³)(6.9 ⁸)	(3 ⁸ .4 ¹⁰ .5 ⁸ .6 ²)	4 ³ .6 ² .8

In MIL-53 (Fig. S2) and MIL-68 (Fig. S3), the inorganic units are identical to the ones observed in CAU-8. Thus the infinite chains were considered in the same way as for CAU-8.

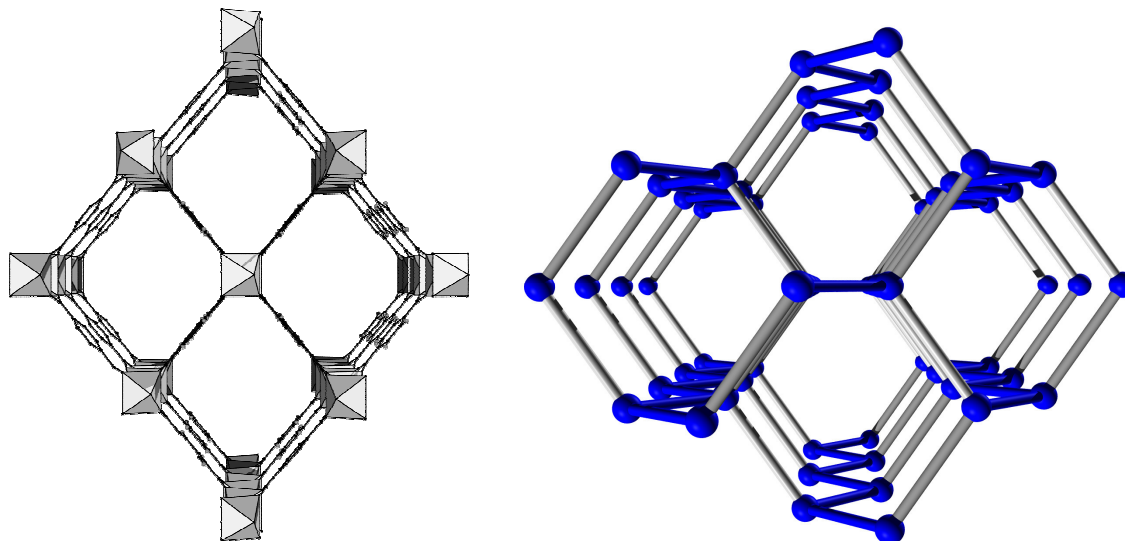


Fig. S2: Left: Framework structure of MIL-53. Right: Representation of the underlying **dia**-net with the fragments corresponding to the Al-oxo-chains emphasized in blue. Intra-chain bonds are colored in blue, bonds representing the organic linker molecules are colored in grey.

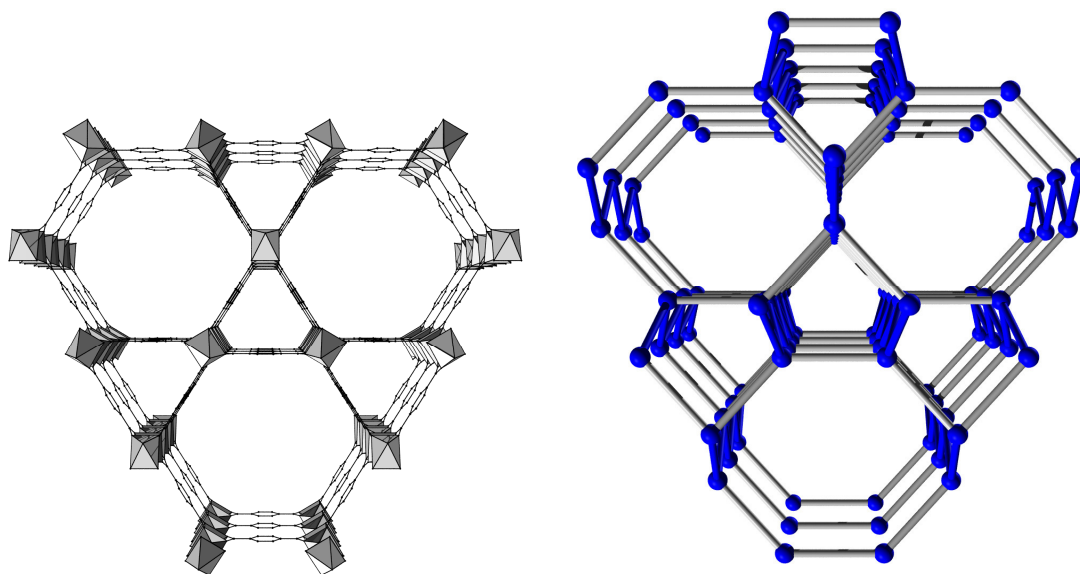


Fig. S3: Left: Framework structure of MIL-68. Right: Representation of the underlying **bkn**-net with the fragments corresponding to the Al-oxo-chains emphasized in blue. Intra-chain bonds are colored in blue, bonds representing the organic linker molecules are colored in grey.

In both cases, the chain-like character is retained in a similar way as observed for CAU-8 and the pore system is accurately represented by the respective topology.

In the framework of MIL-120 which is based on chains of edge-sharing AlO_6 -polyhedra 1,2,4,5-benzenetetracarboxylate, the infinite inorganic building unit exhibits a helical shape and the linker molecule is represented by a 4-connected node (Fig. S4). No merging of the points of extension seems possible.

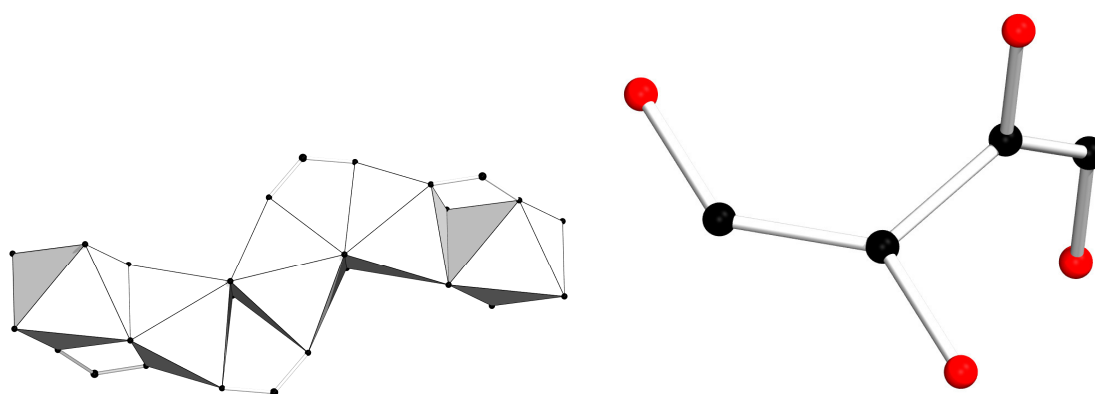


Fig. S4: Left: A fragment of the inorganic unit in MIL-120. Right: Corresponding helical representation of this infinite building unit. The red spheres represent the four-connected organic linker molecules.

Although the infinite unit has a different shape, our analysis resulted in a suitable, accurate topology (Fig. S5).

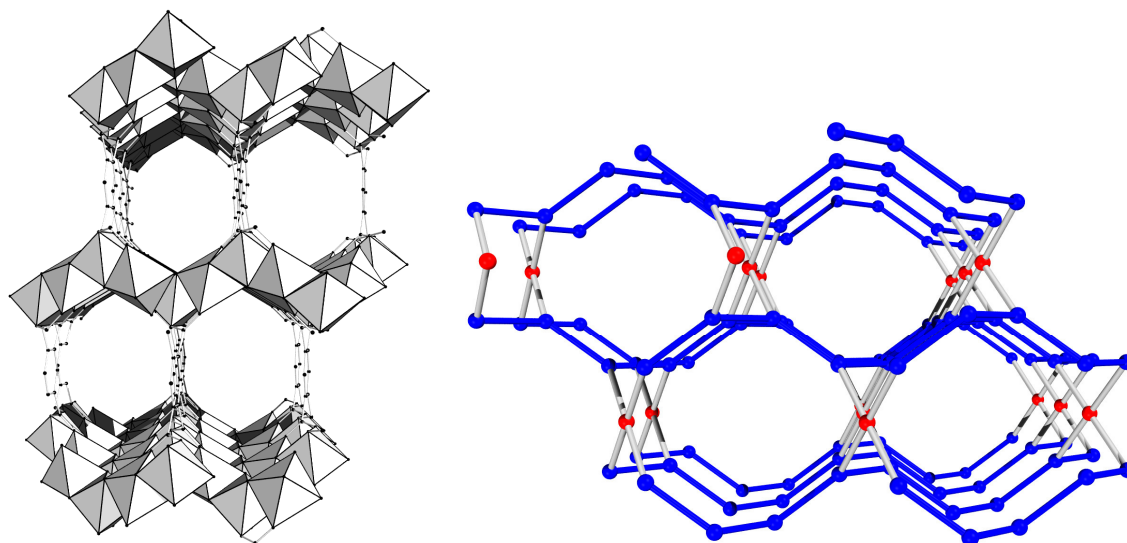


Fig. S5: Left: Framework structure of MIL-120. Right: Representation of the underlying **nor**-net with the fragments corresponding to the Al-oxo-chains emphasized in blue and the nodes corresponding to the linker molecules represented in red. Intra-chain bonds are colored in blue, bonds representing the organic linker molecules are colored in grey.

Another MOF based on infinite helical building units is CAU-10. This compound is based on chains of *cis*-connected corner-sharing AlO_6 -polyhedra bridged by 1,3-benzenedicarboxylate. Two polyhedra are bridged by two carboxylate groups and thus these points of extension were merged into one point (Fig. S6).

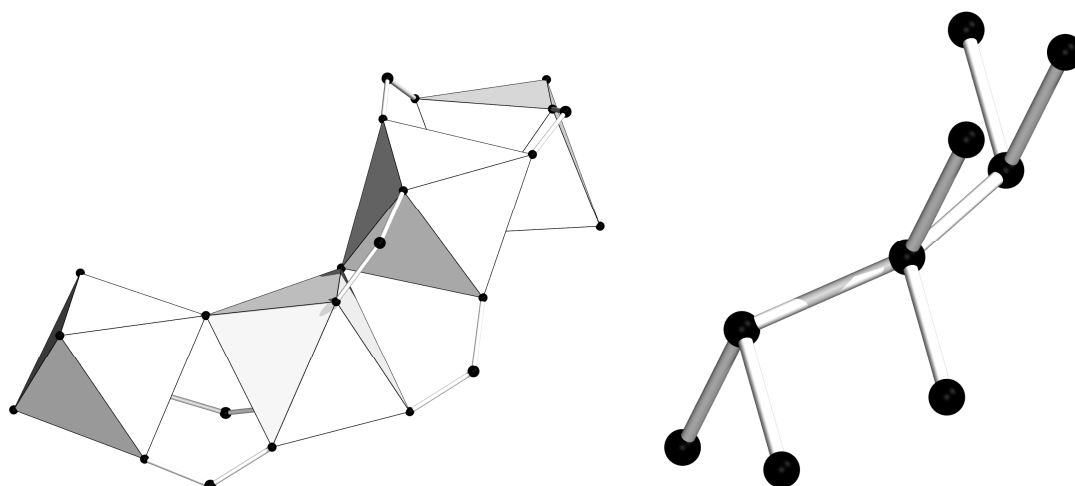


Fig. S6: Left: A fragment of the inorganic unit in CAU-10. Right: Corresponding helical representation of this infinite building unit.

The underlying topology of CAU-10 is the **gis**-network (Fig. S7).

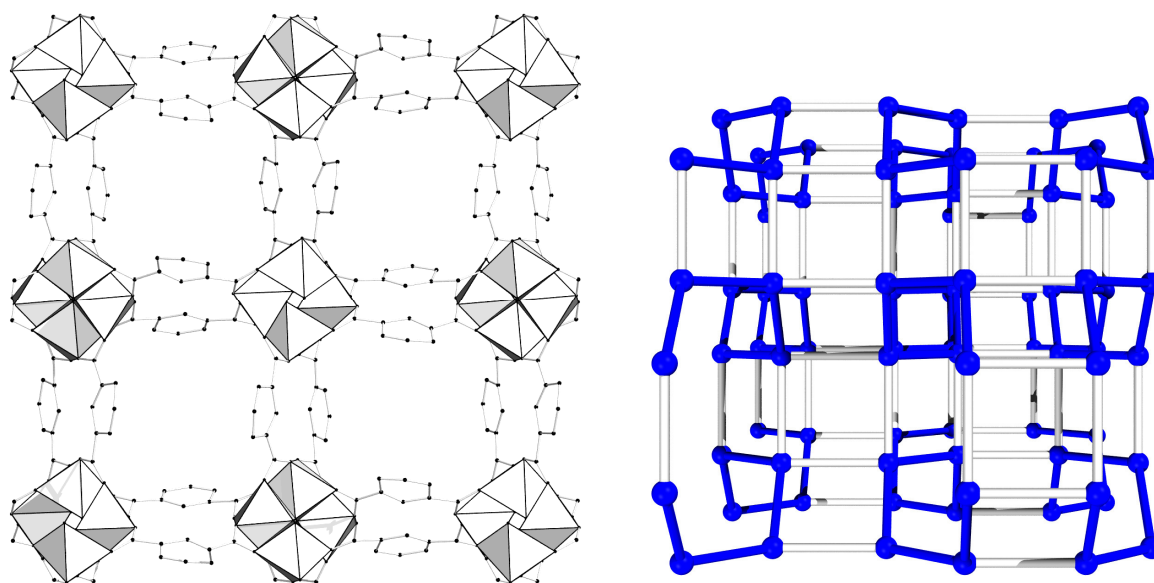


Fig. S7: Left: Framework structure of CAU-10. Right: Representation of the underlying **gis**-net with the helical fragments corresponding to the Al-oxo-chains emphasized in blue. Intra-chain bonds are colored in blue, bonds representing the organic linker molecules are colored in grey.

Another MOF which is based on infinite building units is CAU-4, in which the inorganic unit consists of carboxylate-bridged Al^{3+} -ions (Fig. S8) which are connected via tritopic 1,3,5-

benzenetrisbenzoate linker molecules. Thus three points of extension are merged into one point.

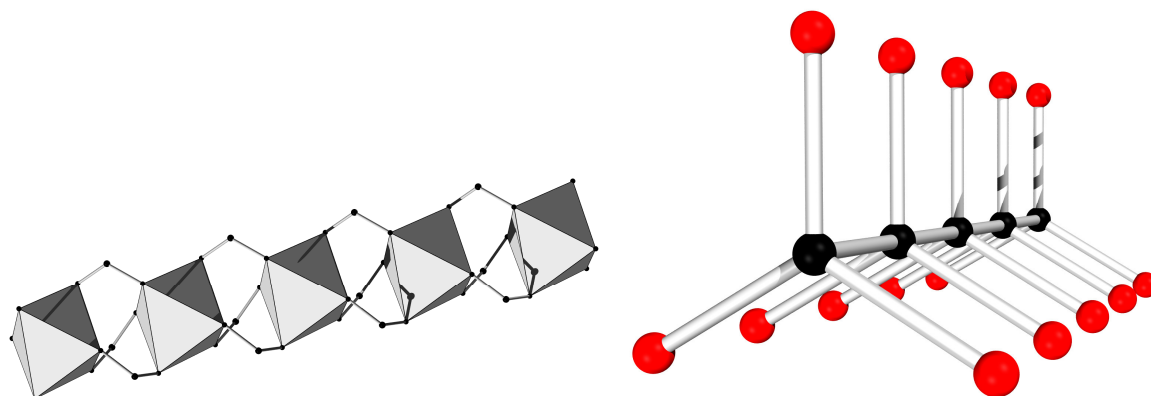


Fig. S8: Left: A fragment of the inorganic unit in CAU-4. Right: Corresponding representation of this infinite building unit. The red spheres represent the three-connected organic linker molecules.

This framework exhibits the binodal **hms**-topology (Fig. S9).

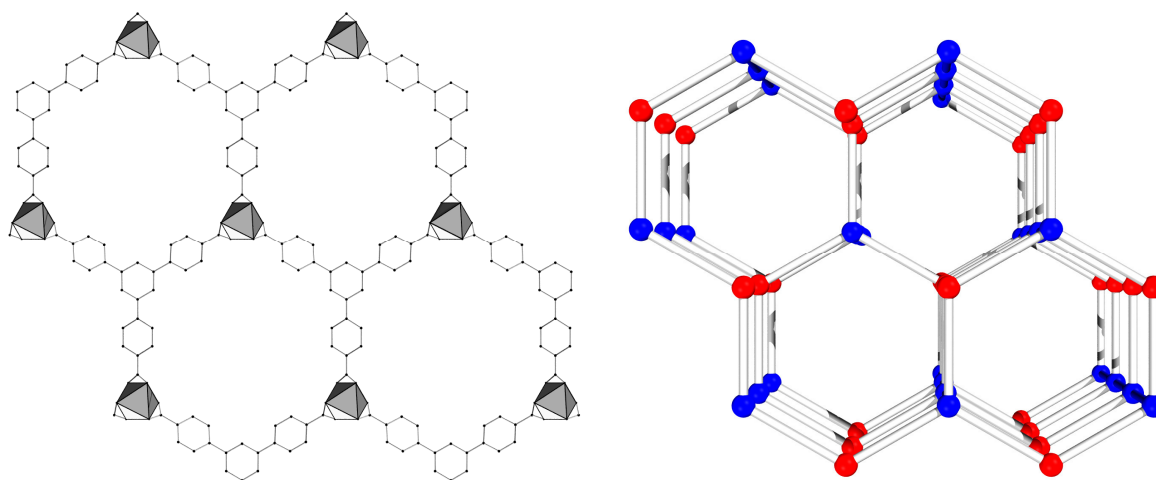


Fig. S9: Left: Framework structure of CAU-4. Right: Representation of the underlying **hms**-net with the linear fragments corresponding to the Al-oxo-chains emphasized in blue and the three-connected organic nodes emphasized in red. Intra-chain bonds are colored in blue, bonds representing the organic linker molecules are colored in grey.

A very special framework is observed in the MOF CAU-6, which is based on column-like infinite inorganic units which are connected via 2-amino-1,4-benzenedicarboxylate molecules. The points of extension for this column-like unit were generated as shown in Fig. S10. Thus two carboxylate groups were merged into one point of extension.

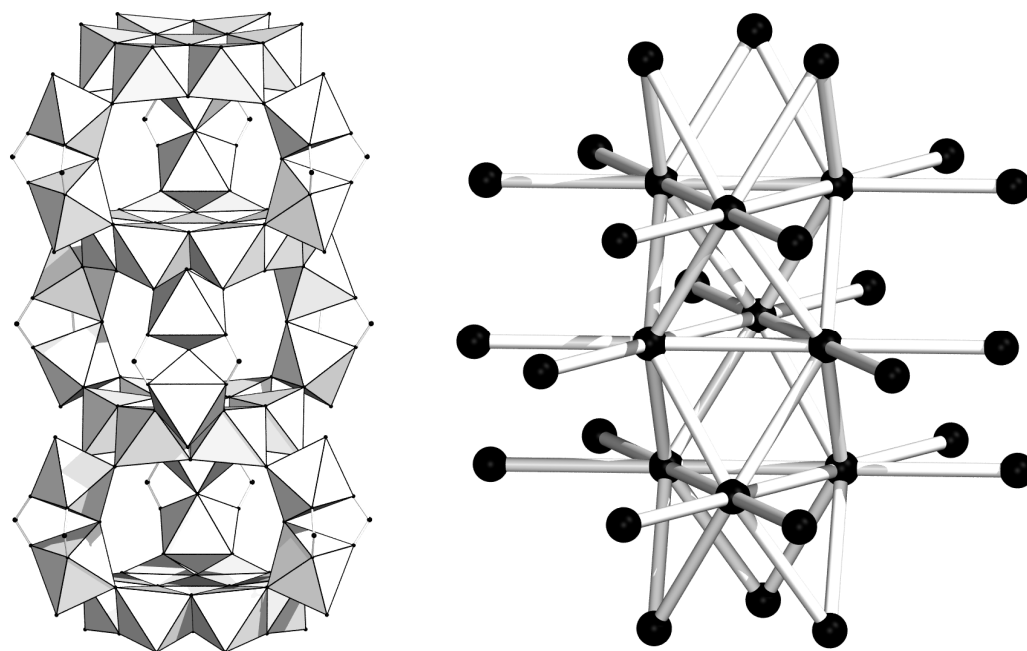


Fig. S10: Left: A fragment of the inorganic unit in CAU-6. Right: Corresponding representation of this infinite building unit.

On every “level”, six linker molecules are coordinating pair wise and thus after merging these pairs into three distinct points, triangles are obtained which are alternating oriented at each level. The observed topology is the *ecf*-net (Fig. S11).

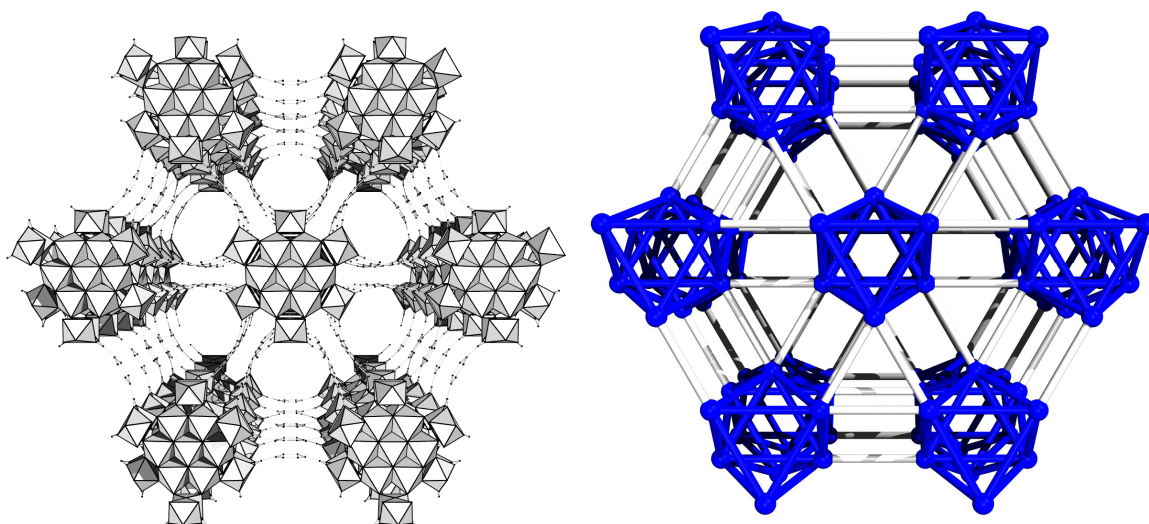


Fig. S11: Left: Framework structure of CAU-6. Right: Representation of the underlying *ecf*-net with the “linear” fragments corresponding to the Al-oxo-columns emphasized in blue. Intra-chain bonds are colored in blue, bonds representing the organic linker molecules are colored in grey.

Thus in all structures discussed herein, the approach presented in the paper resulted in accurate topological representations of the corresponding frameworks.

8. Literatur

- ¹ A. U. Czaja, N. Trukhan, U. Müller, *Chem. Soc. Rev.*, **2009**, *38*, 1284.
- ² M. Gaab, N. Trukhan, S. Maurer, R. Gummaraju, U. Müller, *Microporous Mesoporous Mater.*, **2012**, *157*, 131.
- ³ J. L. C. Rowsell, O. M. Yaghi, *Microporous Mesoporous Mater.*, **2004**, *73*, 3.
- ⁴ G. Férey, *Chem. Soc. Rev.*, **2008**, *37*, 191.
- ⁵ N. Stock, S. Biswas, *Chem. Rev.*, **2012**, *112*, 933.
- ⁶ S. R. Batten, N. R. Champness, X.-M. Chen, J. Garcia-Martinez, S. Kitagawa, L. Öhrström, M. O'Keeffe, M. P. Suh, J. Reedijk, *CrystEngComm*, **2012**, *14*, 3001.
- ⁷ D. J. Tranchemontagne, J. L. Mendoza-Cortés, M. O'Keeffe, O. M. Yaghi, *Chem. Soc. Rev.*, **2009**, *38*, 1257.
- ⁸ S. Hausdorf, F. Baitalow, T. Böhle, D. Rafaja, F. O. R. L. Mertens, *J. Am. Chem. Soc.*, **2010**, *132*, 10978.
- ⁹ S. Surble, F. Millange, C. Serre, G. Férey, R. I. Walton, *Chem. Commun.*, **2006**, 1518.
- ¹⁰ V. Guillermin, S. Gross, C. Serre, T. Devic, M. Bauer, G. Férey, *Chem. Commun.*, **2010**, *46*, 767.
- ¹¹ D. J. Tranchemontagne, J. L. Mendoza-Cortés, M. O'Keeffe, O. M. Yaghi, *Chem. Soc. Rev.*, **2009**, *38*, 1257.
- ¹² N. L. Rosi, J. Kim, M. Eddaoudi, B. Chem, M. O'Keeffe, O. M. Yaghi, *J. Am. Chem. Soc.*, **2005**, *127*, 1504.
- ¹³ T. Devic, P. Horcajada, C. Serre, F. Salles, G. Maurin, B. Moulin, D. Heurtaux, G. Clet, A. Vimont, J. Grenèche, B. Le Ouay, F. Moreau, E. Magnier, Y. Filinchuk, J. Marrot, J. Lavalley, M. Daturi, G. Férey, *J. Am. Chem. Soc.*, **2010**, *132*, 1127.
- ¹⁴ C. Volkringer, T. Loiseau, *Mater. Res. Bull.*, **2006**, *41*, 948.
- ¹⁵ M. L. Foo, S. Horike, Y. Inubushi, S. Kitagawa, *Angew. Chem., Int. Edt.*, **2012**, *51*, 6107.
- ¹⁶ K. J. Gagnon, H. P. Perray, A. Clearfield, *Chem. Rev.*, **2012**, *112*, 1034.
- ¹⁷ J. Perles, N. Snejkó, M. Iglesias, M. Á. Monge, *J. Mater. Chem.*, **2009**, *19*, 6504.
- ¹⁸ R. Banerjee, A. Phan, B. Wang, C. Knobler, H. Furukawa, M. O'Keeffe, O. M. Yaghi, *Science*, **2008**, *319*, 939.
- ¹⁹ J. P. Zhang, X. M. Chen, *Chem. Commun.*, **2006**, 1689.
- ²⁰ P. Pachfule, R. Banerjee, *Cryst. Growth Des.*, **2011**, *11*, 5176.
- ²¹ J. H. Cavka, S. Jakobsen, U. Olsbye, N. Guillou, C. Lamberti, S. Bordiga, K. P. Lillerud, *J. Am. Chem. Soc.*, **2008**, *130*, 13850.
- ²² V. Guillermin, F. Ragon, M. Dan-Hardi, T. Devic, M. Vishnuvarthan, B. Campo, A. Vimont, G. Clet, Q. Yang, G. Maurin, G. Férey, A. Vittadini, S. Gross, C. Serre, *Angew. Chem., Int. Edt.*, **2012**, DOI: 10.1002/anie.201204806
- ²³ M. Eddaoudi, J. Kim, N. L. Rosi, D. T. Vodak, J. Wachter, M. O'Keeffe, O. M. Yaghi, *Science*, **2002**, *295*, 469.
- ²⁴ S. R. Miller, G. M. Pearce, P. A. Wright, F. Bonino, S. Chavan, S. Bordiga, I. Margiolaki, N. Guillou, G. Férey, S. Bourrelly, P. L. Llewellyn, *J. Am. Chem. Soc.*, **2008**, *130*, 15967.
- ²⁵ M. T. Wharmby, G. M. Pearce, J. P. S. Mowat, J. M. Griffin, S. E. Ashbrook, P. A. Wright, L.-H. Schilling, A. Lieb, N. Stock, S. Chavan, S. Bordiga, E. Garcia, G. D. Pirngruber, M. Vreeke, L. Gora, *Micropor. Mesopor. Mater.*, **2012**, *157*, 3.
- ²⁶ F. Jeremias, A. Khutia, S. K. Henninger, C. Janiak, *J. Mater. Chem.*, **2012**, *22*, 10148.
- ²⁷ A. Schaate, S. Dühnen, G. Platz, S. Lilienthal, A. M. Schneider, P. Behrens, *Eur. J. Inorg. Chem.*, **2012**, *5*, 790.
- ²⁸ G. Wißmann, A. Schaate, S. Lilienthal, I. Bremer, A. M. Schneider, P. Behrens, *Microporous Mesoporous Mater.*, **2012**, *152*, 64.
- ²⁹ M. Kandiah, M. H. Nilsen, S. Usseglio, S. Jakobsen, U. Olsbye, M. Tilset, C. Larabi, E. A. Quadrelli, F. Bonino, K. P. Lillerud, *Chem. Mater.*, **2010**, *22*, 6632.
- ³⁰ M. Mendt, B. Jee, N. Stock, T. Ahnfeldt, M. Hartmann, D. Himsl, A. Pöpl, *J. Phys. Chem. C*, **2010**, *114*, 19443.
- ³¹ T. Lescouet, E. Kockrick, G. Bergeret, M. Pera-Titus, D. Farrusseng, *Dalton Trans.*, **2011**, *40*, 11359.
- ³² H. Furukawa, N. Ko, Y. B. Go, N. Aratani, S. B. Choi, E. Choi, A. O. Yazaydin, R. Q. Snurr, M. O'Keeffe, J. Kim, O. M. Yaghi, *Science*, **2010**, *239*, 424.
- ³³ M. P. Suh, H. J. Park, T. K. Prasad, D.-W. Lim, *Chem. Rev.*, **2012**, *112*, 782.

- 34 J. R. Li, J. Sculley, H.-C. Zhouk *Chem. Rev.*, **2012**, *112*, 869.
- 35 A. Corma, H. García, F. X. Llabrés i Xamena, *Chem. Rev.*, **2010**, *110*, 4606.
- 36 L. E. Kreno, K. Leong, O. K. Farha, M. Allendorf, R. P. Van Duyne, J. T. Hupp, *Chem. Rev.*,
2012, *112*, 1105
- 37 P. Horcajada, R. Gref, T. Baati, P. K. Allan, G. Maurin, P. Couvreur, G. Férey, R. E. Morris, C.
Serre, *Chem. Rev.*, **2012**, *112*, 1232.
- 38 K. A. Cychosz, A. J. Matzger, *Langmuir*, **2010**, *26*, 17198.
- 39 C. Volkringer, D. Popov, T. Loiseau, G. Férey, M. Burghammer, C. Riekel, M. Haouas, F.
Taulelle, *Chem. Mater.*, **2009**, *21*, 5695.
- 40 C. Volkringer, D. Popov, T. Loiseau, N. Guillou, G. Férey, M. Haouas, F. Taulelle, C. Mellot-
Draznieks, M. Burghammer, C. Riekel, *Nature Materials*, **2007**, *6*, 760.
- 41 T. Loiseau, C. Serre, C. Huguenard, G. Fink, F. Taulelle, M. Henry, T. Bataille, G. Férey,
Chem.-Eur. J., **2004**, *10*, 1373.
- 42 I. Senkowska, F. Hoffmann, M. Fröba, J. Getzschmann, W. Böhlmann, S. Kaskel, *Microporous*
Mesoporous Mater., **2009**, *122*, 93.
- 43 S. Biswas, T. Ahnfeldt, N. Stock, *Inorg. Chem.*, **2011**, *50*, 9518.
- 44 N. Reimer, B. Gil, B. Marszalek, N. Stock, *CrystEngComm*, **2012**, *14*, 4119.
- 45 C. Volkringer, T. Loiseau, T. Devic, G. Férey, D. Popov, M. Burghammer, C. Riekel,
CrystEngComm, **2010**, *12*, 3225
- 46 A. Comotti, S. Bracco, P. Sozzani, S. Horike, R. Matsuda, J. Chen, M. Takata, Y. Kubota, S.
Kitagawa, *J. Am. Chem. Soc.*, **2008**, *130*, 13664.
- 47 T. Ahnfeldt, N. Guillou, D. Gunzelmann, I. Margiolaki, T. Loiseau, G. Férey, J. Senker, N.
Stock, *Angew. Chem.*, **2009**, *121*, 5265.
- 48 C. Volkringer, T. Loiseau, N. Guillou, G. Férey, M. Haouas, F. Taulelle, N. Audebrand, I.
Margiolaki, D. Popov, M. Burghammer, C. Riekel, *Cryst. Growth Des.*, **2009**, *9*, 2927.
- 49 C. Volkringer, T. Loiseau, N. Guillou, G. Férey, M. Haouas, F. Taulelle, E. Elkaim, N. Stock,
Inorg. Chem., **2010**, *49*, 9852.
- 50 W. L. Bragg, *Nature*, **1912**, 410.
- 51 W. Massa, *Kristallstrukturbestimmung*, Vol. 5, Teubner-Verlag, Stuttgart, Leipzig,
Wiesbaden, **2005**.
- 52 R. Allmann, *Röntgenpulverdiffraktometrie*, Vol. 2, Springer-Verlag, Berlin Heidelberg
New York, **2003**.
- 53 P.-E. Werner, L. Eriksson; M. Westdahl, *J. Appl. Crystallogr.*, **1985**, *18*, 367.
- 54 A. Boultif, D. Louër, *J. Appl. Crystallogr.*, **1991**, *24*, 987.
- 55 J. W. Visser, *J. Appl. Crystallogr.*, **1969**, *2*, 89.
- 56 G. S. Pawley, *J. Appl. Cryst.*, **1981**, *14*, 357.
- 57 A. Le Bail, H. Duroy, J. L. Fourquet, *Mater. Res. Bull.*, **1988**, *23*, 447
- 58 J. Karle, H. Hauptman, *Acta Cryst.*, **1956**, *9*, 635.
- 59 K. D. M. Harris, M. Tremayne, B. M. Kariuki, *Angew. Chem., Int. Edt.*, **2001**, *40*, 1626.
- 60 H. M. Rietveld, *Acta Cryst.*, **1967**, *22*, 151.
- 61 T. Hahn, *International Tables for Crystallography Vol. A*, fifth Edt., Springer, **2005**.
- 62 C. Serre, F. Millange, C. Thouvenot, M. Nogues, G. Marsolier, D. Louer, G. Férey, *J. Am.*
Chem. Soc., **2002**, *124*, 13519.
- 63 A. Altomare, M. Camalli, C. Cuocci, C. Giacovazzo, A. Moliterni, R. Rizzi, *J. Appl. Cryst.*,
2009, *42*, 1197.
- 64 Topas Academics 4.2, Coelho Software, **2007**.
- 65 WINXPOW Version 2.11, Stoe & Cie GmbH: Darmstadt, Germany, **1999**.
- 66 W. Kraus, G. Nolze, PowderCell 2.4, **2000**.
- 67 Materials Studio version 5.0, Accelrys Inc. San Diego, CA, USA, **2009**.
- 68 A. Pichon, A. Lazuen-Garay, S. L. James, *CrystEngComm* **2006**, *8*, 211.
- 69 P. J. Beldon, L. Fabian, R. S. Stein, A. Thirumurugan, A. K. Cheetham, T. Friscic, *Angew.*
Chem. Int Ed. **2010**, *49*, 9640.
- 70 N. Stock, S. Biswas, *Chem. Rev.*, **2012**, *112*, 933.
- 71 P. Maniam, N. Stock, *Inorg. Chem.*, **2011**, *50*, 5085.
- 72 M. Li, M. Dincă, *J. Am. Chem. Soc.*, **2011**, *133*, 12926.
- 73 T. Chalati, P. Horcajada, R. Gref, P. Couvreur, C. Serre, *J. Mater. Chem.*, **2011**, *21*, 2220.
- 74 A. Rabenau, *Angew. Chem.*, **1985**, *97*, 1017.
- 75 D. R. Modeshia, R. I. Walton, *Chem. Soc. Rev.*, **2010**, *39*, 4303.
- 76 R. I. Walton, *Chem. Soc. Rev.*, **2002**, *31*, 230.
- 77 C. S. Cundy, *Chem. Rev.*, **2003**, *103*, 663.

- 78 G. Férey, C. Mellot-Draznieks, C. Serre, F. Millange, J. Dutour, S. Surble, I. Margiolaki, *Science*, **2005**, *309*, 2040.
- 79 C. Serre, F. Millange, C. Thouvenot, M. Nogues, G. Marsolier, D. Louer, G. Férey, *J. Am. Chem. Soc.*, **2002**, *124*, 13519.
- 80 T. Ahnfeldt, N. Guillou, D. Gunzelmann, I. Margiolaki, T. Loiseau, G. Férey, J. Senker, N. Stock, *Angew. Chem.*, **2009**, *121*, 5265.
- 81 S. Biswas, T. Ahnfeldt, N. Stock, *Inorg. Chem.*, **2011**, *50*, 9518.
- 82 T. Ahnfeldt, D. Gunzelmann, J. Wack, J. Senker, N. Stock, *CrystEngComm*, **2012**, *14*, 4126.
- 83 E. Biemmi, S. Christian, N. Stock, T. Bein, *Micropor. Mesopor. Mater.*, **2009**, *117*, 111.
- 84 I. Tickle, A. Sharff, M. Vinkovic, J. Yon, H. Jhoti, *Chem. Soc. Rev.*, **2004**, *33*, 558.
- 85 C. Jäkel, R. Paciello, *Chem. Rev.*, **2006**, *106*, 2912.
- 86 R. A. Potyrailo, V. M. Mirsky, *Chem. Rev.*, **2008**, *108*, 770.
- 87 S. Bauer, N. Stock, *Angew. Chem. Int. Ed.*, **2007**, *46*, 6857.
- 88 T. Loiseau, C. Serre, C. Huguenard, G. Fink, F. Taulelle, M. Henry, T. Bataille, G. Férey, *Chem. Eur. J.*, **2004**, *10*, 1373.
- 89 V. Finsy, C. Kirschhock, G. Vedts, M. Maes, L. Alaerts, D. De Vos, G. Baron, J. Denayer, *Chem.-Eur. J.*, **2009**, *15*, 7724.
- 90 S. Biswas, T. Ahnfeldt, N. Stock, *Inorg. Chem.*, **2011**, *50*, 9518.
- 91 N. Reimer, B. Gil, B. Marszalek, N. Stock, N., *CrystEngComm*, **2012**, *14*, 4119.
- 92 T. Loiseau, C. Mellot-Draznieks, H. Muguerra, G. Férey, M. Haouas, F. Taulelle, *C. R. Chimie*, **2005**, *8*, 765.
- 93 I. Senkovska, F. Hoffmann, M. Fröba, J. Getzschmann, W. Böhlmann, S. Kaskel, *Micropor. Mesopor. Mater.*, **2009**, *122*, 93.
- 94 T. Ahnfeldt, D. Gunzelmann, T. Loiseau, D. Hirsemann, G. Férey, J. Senker, N. Stock, *Inorg. Chem.*, **2009**, *48*, 3057.
- 95 S. Couck, J. F. M. Denayer, G. V. Baron, T. Rémy, J. Gascon, F. Kapteijn, *J. Am. Chem. Soc.*, **2009**, *131*, 6326.
- 96 P. Serra-Crespo, M. A. van der Veen, E. Gobechiya, K. Houthoofd, Y. Filinchuk, C. E. A. Kirschhock, J. A. Martens, B. F. Sels, D. E. De Vos, F. Kapteijn, J. Gascon, *J. Am. Chem. Soc.*, **2012**, *134*, 8314.
- 97 E. Stavitski, M. Goesten, J. Juan-Alcañiz, A. Martinez-Joaristi, P. Serra-Crespo, A.V. Petukhov, J. Gascon, F. Kapteijn, *Angewandte Chemie Int. Ed.*, **2011**, *50*, 9624.
- 98 P. Serra-Crespo, E. V. Ramos-Fernandez, J. Gascon, F. Kapteijn, *Chem. Mater.*, **2011**, *23*, 2565.
- 99 J. Juan-Alcañiz, Maarten Goesten, A. Martinez-Joaristi, E. Stavitski, A. V. Petukhov, J. Gascon, F. Kapteijn, *Chem. Commun.*, **2011**, *47*, 8578.
- 100 C. Volkringer, T. Loiseau, M. Haouas, F. Taulelle, D. Popov, M. Burghammer, C. Riekel, C. Zlotea, F. Cuevas, M. Latroche, D. Phanon, C. Knöfelv, P. L Llewellyn, G. Férey, *Chem. Mater.*, **2009**, *21*, 5783.
- 101 M. Haouas, C. Volkringer, T. Loiseau, G. Férey, F. Taulelle, *J. Phys. Chem. C*, **2011**, *115*, 17934.
- 102 C. Volkringer, H. Leclerc, J. Lavalley, T. Loiseau, G. Férey, M. Daturi, A. Vimont, *J. Phys. Chem. C*, **2012**, *116*, 5710.
- 103 C. Volkringer, D. Popov, T. Loiseau, N. Guillou, G. Férey, M. Haouas, F. Taulelle, C. Mellot-Draznieks, M. Burghammer, C. Riekel, *Nature Materials*, **2007**, *6*, 760.
- 104 T. Loiseau, L. Lecroq, C. Volkringer, J. Marrot, G. Férey, M. Haouas, F. Taulelle, S. Bourrelly, P. L. Llewellyn, M. Latroche, *J. Am. Chem. Soc.*, **2006**, *128*, 10223.
- 105 E. A. Mainicheva, O. A. Gerasko, L. A. Sheludyakova, D. Y. Naumov, M. I. Naumova, V. P. Fedin, *Russian Chemical Bulletin, Int. Ed.*, **2006**, *55*, 267.
- 106 M. Maes, L. Alaerts, F. Vermoortele, R. Ameloot, S. Couck, V. Finsy, J. Denayer, D. De Vos, *J. Am. Chem. Soc.*, **2010**, *132*, 2284.
- 107 C. Volkringer, T. Loiseau, N. Guillou, G. Férey, M. Haouas, F. Taulelle, E. Elkaim, N. Stock, *Inorg. Chem.*, **2010**, *49*, 9852.
- 108 C. Volkringer, T. Loiseau, M. Haouas, F. Taulelle, D. Popov, M. Burghammer, C. Riekel, C. Zlotea, F. Cuevas, M. Latroche, D. Phanon, C. Knöfelv, P. L Llewellyn, G. Férey, *Chem. Mater.*, **2009**, *21*, 5783.
- 109 C. Volkringer, T. Loiseau, N. Guillou, G. Férey, M. Haouas, F. Taulelle, N. Audebrand, I. Margiolaki, D. Popov, M. Burghammer, C. Riekel, *Cryst. Growth Des.*, **2009**, *9*, 2927.
- 110 A. Fateeva, P. A. Chater, C. P. Ireland, A. A. Tahir, Y. Z. Khimiyak, P. V. Wiper, J. R. Darwent, M. J. Rosseinsky, *Angew. Chem.*, **2012**, *124*, 7558.

- 111 T. Ahnfeldt, N. Guillou, D. Gunzelmann, I. Margiolaki, T. Loiseau, G. Férey, J. Senker, N. Stock, *Angew. Chem.*, **2009**, *121*, 5265.
- 112 T. Ahnfeldt, J. Moellmer, V. Guillerm, R. Staudt, C. Serre, N. Stock, *Chem.-Eur. J.*, **2011**, *17*, 6462.
- 113 T. Ahnfeldt, D. Gunzelmann, J. Wack, J. Senker, N. Stock, *CrystEngComm*, **2012**, *14*, 4126.
- 114 C. Volkringer, T. Loiseau, N. Guillou, G. Férey, E. Elkaim, *Solid Stat. Sci.*, **2009**, *11*, 1507.
- 115 C. Volkringer, T. Loiseau, T. Devic, G. Férey, D. Popov, M. Burghammer, C. Riekel, *CrystEngComm*, **2010**, *12*, 3225.
- 116 M. Vougo-Zanda, J. Huang, E. Anokhina, W. Wang, A. J. Jacobson, *Inorg. Chem.*, **2008**, *47*, 11535.
- 117 C. Volkringer, M. Meddouri, T. Loiseau, N. Guillou, J. Marrot, G. Férey, M. Haouas, F. Taulelle, N. Audebrand, M. Latroche, *Inorg. Chem.*, **2008**, *47*, 11892.
- 118 T. R. Whitfield, X. Wang, L. Liu, A. J. Jacobson, *Solid State Sci.*, **2005**, *7*, 1096.
- 119 C. Volkringer, T. Loiseau, G. Férey, *Solid Stat. Sci.*, **2009**, *11*, 29.
- 120 S. Bauer, C. Serre, T. Devis, P. Horcajada, J. Marrot, G. Férey, N. Stock, *Inorg. Chem.*, **2008**, *47*, 7568.
- 121 C. Serre, F. Millange, C. Thouvenot, M. Nogues, G. Marsolier, D. Louer, G. Férey, *J. Am. Chem. Soc.*, **2002**, *124*, 13519.
- 122 K. Barthelet, J. Marrot, G. Férey, D. Riou, *Chem. Commun.*, **2004**, 520.
- 123 J. P.S. Mowat, S. R. Miller, A. M.Z. Slawin, V. R. Seymour, S. E. Ashbrook, P. A. Wright, *Micropor. Mesopor. Mater.*, **2011**, *142*, 322.
- 124 K. Barthelet, D. Riou, G. Férey, *Chem. Commun.*, **2002**, 1492.
- 125 S. Surble, C. Serre, C. Mellot-Draznieks, F. Millange, G. Férey, *Chem. Commun.*, **2006**, 284.
- 126 M. Dan-Hardi, C. Serre, T. Frot, L. Rozes, G. Maurin, C. Sanchez, G. Férey, *J. Am. Chem. Soc.*, **2009**, *131*, 10857.
- 127 A.-A. H. Abu-Nawwas, J. Cano, P. Christian, T. Mallah, G. Rajaraman, S. J. Teat, R. E. P. Winpenny, Y. Yukawa, *Chem. Commun.* **2004**, 314.
- 128 G. Jiang, Y. Li, W. Hua, Y. Song, J. Bai, S. Li, M. Scheer, X. You, *CrystEngComm* **2006**, *8*, 314.
- 129 G. Férey, C. Mellot-Draznieks, C. Serre, F. Millange, J. Dutour, S. Surble, I. Margiolaki, *Science*, **2005**, *309*, 2040.
- 130 S. Surble, C. Serre, C. Mellot-Draznieks, F. Millange, G. Férey, *Chem. Commun.*, **2006**, 284.
- 131 K. Barthelet, D. Riou, G. Férey, *Chem. Commun.*, **2002**, 1492.
-

9. Liste der Publikationen und Beiträge

Vorträge

[Al₂(OCH₃)₄(O₂C-X-CO₂)] or CAU-3: Isorecticular porous MOFs with a novel inorganic brick

Helge Reinsch, Mark Feyand, Tim Ahnfeldt, Norbert Stock,
12. Norddeutsches Doktorandenkolloquium 2009, Oldenburg.

CAU-3: A new family of porous MOFs with a novel inorganic brick: [Al₂(OCH₃)₄(O₂C-X-CO₂)] (X=aryl)

Helge Reinsch, Mark Feyand, Tim Ahnfeldt, Norbert Stock,
22. Deutsche Zeolith-Tagung 2010, München.

CAU-10: A new series of porous metal-organic frameworks

Helge Reinsch
AC-Kolloquium Februar 2011, Kiel.

Poster

CAU-3: A new family of porous MOFs with a novel inorganic brick: [Al₂(OCH₃)₄(O₂C-X-CO₂)] (X=aryl)

Helge Reinsch, Mark Feyand, Tim Ahnfeldt, Norbert Stock,
MOF 2010, Marseille, Frankreich.

Formation and Characterization of Mn-MIL-100

Helge Reinsch, Norbert Stock,
23. Deutsche Zeolith-Tagung 2011, Erlangen.

Formation and Characterization of Mn-MIL-100

Helge Reinsch, Norbert Stock,
British Zeolite Conference 2011, Edinburgh.

A new series of Al-based MOFs

Helge Reinsch, Norbert Stock

24. Deutsche Zeolith-Tagung 2012, Magdeburg.

Ligand “doping” in the Al-based MOF [Al(OH)(1,3-BDC)]

Steve Waitschat, Helge Reinsch, Norbert Stock

24. Deutsche Zeolith-Tagung 2012, Magdeburg.

Sorption characteristics and photochemistry of a new series of Al-based MOFs

Helge Reinsch, Norbert Stock, Arne Klinkebiel

MOF 2012, Edinburgh, Schottland.

Publikationen

A new aluminium-based microporous metal–organic framework: Al(BTB) (BTB = 1,3,5-benzenetrisbenzoate), H. Reinsch, M. Krüger, J. Wack, J. Senker, F. Salles, G. Maurin and N. Stock, *Micropor. Mesopor. Mater.*, **2012**, *157*, 50-55.

CAU-3: A new family of porous MOFs with a novel Al-based brick: [Al₂(OCH₃)₄(O₂C-X-CO₂)] (X = aryl), Helge Reinsch, Mark Feyand, Tim Ahnfeldt, Norbert Stock, *Dalton Trans.*, **2012**, *41*, 4164-4171.

A new Al-MOF based on a unique column-shaped inorganic building unit exhibiting strongly hydrophilic sorption behaviour, Helge Reinsch, Bartosz Marszałek, Julia Wack, Jürgen Senker, Barbara Gil and Norbert Stock, *Chem. Commun.*, **2012**, *48*, 9486-9488.

Structures, sorption characteristics and nonlinear optical properties of a new series of highly stable aluminium MOFs, Helge Reinsch, Monique Van der Veen, Barbara Gil, Bartosz Marszalek, Thierry Verbiest, Dirk de Vos, Norbert Stock, *Chem. Mater.*, submitted.

Formation and Characterisation of Mn-MIL-100, Helge Reinsch, Norbert Stock, *CrystEngComm*, submitted.

The first keto-functionalized microporous Al-based metal-organic framework: [Al(OH)(O₂C-C₆H₄-CO-C₆H₄-CO₂)], Helge Reinsch, Martin Krüger, Jerome Marrot, Norbert Stock, *Inorg. Chem.*, submitted.

High-Throughput Studies of Highly Porous Al-based MOFs, Helge Reinsch, Norbert Stock, *Micropor. Mesopor. Mater.*, submitted.

Mixed-linker MOFs with CAU-10-structure: synthesis and gas sorption characteristics, Helge Reinsch, Steve Waitschat, Norbert Stock, *Dalton Trans.*, submitted.

Curriculum Vitae

Helge Reinsch

Persönliche Daten

Geburtsdatum: 26. Oktober 1984

Geburtsort: Preetz

Familienstand: ledig

Staatangehörigkeit: deutsch

Ausbildung

seit 06/2009 Promotion im Institut für Anorganische Chemie

bei Prof. Dr. Norbert Stock an der Christian-Albrechts-Universität zu Kiel.

Thema: *Synthese und Eigenschaften poröser metall-organischer Gerüstverbindungen basierend auf dreiwertigen Kationen*

10/2004 - 05/2009 Diplomstudiengang Chemie

an der Christian-Albrechts-Universität zu Kiel mit Abschluss als Diplom-Chemiker, Diplomarbeit bei Prof. Dr. Norbert Stock

Thema: *Synthese und Charakterisierung aluminiumhaltiger poröser Gerüstverbindungen*

08/2003 - 05/2004 Zivildienst

08/1994 - 06/2003 Gymnasium Wellingdorf, Kiel

08/1991 - 07/1994 Adolf-Reichwein-Grundschule, Kiel

Eidesstattliche Erklärung

Hiermit versichere ich an Eides statt, dass ich die vorliegende Arbeit selbständig – abgesehen von der wissenschaftlichen Betreuung durch meinen Lehrer – und nur unter Verwendung der angegebenen Hilfsmittel angefertigt habe. Die Dissertation wird ausschließlich an dieser Stelle zur Promotion vorgelegt. Teile der Arbeit wurden in den genannten Journalen als wissenschaftliche Beiträge bereits veröffentlicht oder wurden zur Veröffentlichung eingereicht. Ich erkläre hiermit, dass ich noch keinen Promotionsversuch unternommen habe und dass die Arbeit unter Einhaltung der Regeln guter wissenschaftlicher Praxis der Deutschen Forschungsgesellschaft entstanden ist.

Kiel, Oktober 2012
